

Geotechnical, Geological and Earthquake Engineering

Jian Chu

Sri P.R. Wardani

Atsushi Iizuka *Editors*

Geotechnical Predictions and Practice in Dealing with Geohazards



Springer

Geotechnical Predictions and Practice in Dealing with Geohazards

GEOTECHNICAL, GEOLOGICAL AND EARTHQUAKE ENGINEERING

Volume 25

Series Editor

Atilla Ansal, *School of Engineering, Özyeğin University, Istanbul, Turkey*

Editorial Advisory Board

Julian Bommer, *Imperial College London, U.K.*

Jonathan D. Bray, *University of California, Berkeley, U.S.A.*

Kyriazis Pitilakis, *Aristotle University of Thessaloniki, Greece*

Susumu Yasuda, *Tokyo Denki University, Japan*

For further volumes:

<http://www.springer.com/series/6011>

Jian Chu • Sri P.R. Wardani • Atsushi Iizuka
Editors

Geotechnical Predictions and Practice in Dealing with Geohazards

 Springer

Editors

Jian Chu
Department of Civil, Construction
& Environmental Engineering
Iowa State University
Ames, IA
USA

Sri P.R. Wardani
Department of Civil Engineering
Diponegoro University
Semarang, Indonesia

Atsushi Iizuka
Research Center for Urban Safety
and Security
Kobe University
Kobe, Hyogo
Japan

ISSN 1573-6059

ISBN 978-94-007-5674-8

ISBN 978-94-007-5675-5 (eBook)

DOI 10.1007/978-94-007-5675-5

Springer Dordrecht Heidelberg New York London

Library of Congress Control Number: 2013940209

Chapter 23: © Springer (outside the USA) 2013

© Springer Science+Business Media Dordrecht 2013

This work is subject to copyright. All rights are reserved by the Publisher, whether the whole or part of the material is concerned, specifically the rights of translation, reprinting, reuse of illustrations, recitation, broadcasting, reproduction on microfilms or in any other physical way, and transmission or information storage and retrieval, electronic adaptation, computer software, or by similar or dissimilar methodology now known or hereafter developed. Exempted from this legal reservation are brief excerpts in connection with reviews or scholarly analysis or material supplied specifically for the purpose of being entered and executed on a computer system, for exclusive use by the purchaser of the work. Duplication of this publication or parts thereof is permitted only under the provisions of the Copyright Law of the Publisher's location, in its current version, and permission for use must always be obtained from Springer. Permissions for use may be obtained through RightsLink at the Copyright Clearance Center. Violations are liable to prosecution under the respective Copyright Law.

The use of general descriptive names, registered names, trademarks, service marks, etc. in this publication does not imply, even in the absence of a specific statement, that such names are exempt from the relevant protective laws and regulations and therefore free for general use.

While the advice and information in this book are believed to be true and accurate at the date of publication, neither the authors nor the editors nor the publisher can accept any legal responsibility for any errors or omissions that may be made. The publisher makes no warranty, express or implied, with respect to the material contained herein.

Printed on acid-free paper

Springer is part of Springer Science+Business Media (www.springer.com)

Preface

The 3rd International Conference on Geotechnical Engineering for Disaster Mitigation and Rehabilitation was held in Semarang, Indonesia, May 18–20, 2001. A One-Day International Symposium on Recent Advances in Geotechnical Engineering was also organized by the Conference Organizing Committee led by Prof. S.P.R. Wardani and the Technical Committee TC303 under the International Society for Soil Mechanics and Geotechnical Engineering (ISSMGE). This Symposium also marked the 40-year contributions of Professor Hideki Ohta in research and development in the area of soil mechanics and geotechnical engineering. Professor Ohta is a Professor of Research and Development Initiative at Chuo University, Japan. Before his retirement in 2009, he was a Professor at the Tokyo Institute of Technology (TIT). Prof. Ohta started his professional career in geotechnical engineering in 1971 at Kyoto University. He also worked at the University of Cambridge, Asian Institute of Technology, and Kanazawa University. He was the vice president (1999–2001) and later the president (2004–2006) of the Japanese Geotechnical Society. He has received many awards, including awards from the Japan Society of Civil Engineers (1971, 2002, and 2004), and awards from the Japanese Geotechnical Society (1986, 1991, 1999, and 2008). His major research interests include constitutive model of soils, deformation of soft clays, dam engineering, and rock slope stability. Professor Ohta is one of the key founders of TC303 (the TC39 then) and has been a sought-after keynote and invited speaker at international conferences.

The theme of the symposium was the recent advances in geotechnical predictions and practices dealing with geohazards. Fourteen invited speakers, including Prof. Ohta and a number of other leading world researchers, presented their latest research works at the symposium. This volume comprises the written version of the lectures presented at the symposium and several other invited contributions. The book contains 23 chapters and is divided into three sections: Geotechnical Aspects of Some Recent Disasters; Geotechnical Predictions; and Geotechnical Practices in Dealing with Geohazards. A prologue is also provided to share a glimpse of Prof. Hideki Ohta's life and achievements in the past 40 years. The recent earthquake disasters in Japan and a series of other disasters in the world

have again highlighted the need for more reliable geotechnical prediction, better methods for geotechnical design, particularly dealing with geohazards. It is hoped that this book will provide a timely review and summary of the recent advances in theories, analyses, and methods for geotechnical predictions and the most up-to-date practices in geotechnical engineering and particularly in dealing with geohazards.

We would like to take this opportunity to thank all the contributors for their valuable contributions as well as their time and patience. We want to thank Professor Ohta in particular for his considerable effort in reading through many of the chapters in this book. We also thank Hermine Vloemans of Springer for her professional handling of the publication process and her patience in waiting for the manuscripts to be fully completed.

Ames
Semarang
Kobe, Hyogo

Jian Chu
Sri P.R. Wardani
Atsushi Iizuka



A group photo of Prof. Hideki Ohta (in traditional Kazakhstani costume) with invited speakers and participants to the One-Day International Symposium

Contents

Part I Geotechnical Aspects of Some Recent Disasters

1	Tsunami Induced by 2011 Tohoku-Pacific Ocean Earthquake and a Possible Renewal Plan	3
	Hideki Ohta, Susumu Iai, Yukihiko Nishida, Shu Morioka, and Atsushi Iizuka	
2	Tsunami Damage: What Is Unexpected?	19
	Koji Ichii	
3	Past Earthquakes in Indonesia and New Seismic Hazard Maps for Earthquake Design of Buildings and Infrastructures	33
	Masyhur Irsyam, Hendriyawan, M. Asrurifak, M. Ridwan, Fahmi Aldiamar, I. Wayan Sengara, Sri Widiyantoro, Wahyu Triyoso, Danny Hilman, Engkon Kertapati, Irwan Meilano, Suhardjono, and Anita Firmanti	
4	Lessons Learned from the Recent Natural Disasters in Indonesia	47
	Sri Prabandiyani Retno Wardani and Agus Setyo Muntohar	
5	Behavior of Slope Protection and Retaining Structures During the Wenchuan Earthquake on May 12, 2008	61
	Jianhui H. Deng, Fei Chen, Jinbing B. Wei, and Jiajia J. Tai	

Part II Geotechnical Predictions

6	Consolidation and Creep Settlement of Embankment on Soft Clay: Prediction Versus Observation	77
	S. Robert Lo, M.R. Karim, and C.T. Gnanendran	

7 Numerical Simulation of Soil Structures Reinforced by Geosynthetics	95
Masafumi Hirata, Atsushi Iizuka, Hideki Ohta, Takayuki Yamakami, Yoshihiro Yokota, and Koji Ohmori	
8 Deformation Prediction of a Structure Placed on Soft Clay in Tokyo Bay Affected by Heavy Deep Well Pumping	115
Koki Matsumoto, Akira Kobayashi, and Hideki Ohta	
9 Elasto-Plastic FEM Analysis and Safety Evaluation of Large Rockfill Dams During Reservoir Filling	131
Tetsuo Fujiyama, Takeshi Ishiguro, Yoshihisa Uchita, and Hideki Ohta	
10 Three Dimensional Soil/Water Coupled Analysis of Reverse Concreting Excavation Work	149
Shigehiko Sugie, Hideki Ohta, and Atsushi Iizuka	
11 Spatial Discretization of a Water Head in Soil–Water Coupled Finite Element Method Analysis Using the Hybrid-Type Penalty Method	163
Masafumi Hirata, Atsushi Iizuka, Hideki Ohta, Tetsuo Fujiyama, and Tomohide Takeyama	
12 Theoretical Analysis for Noncoaxiality of Toyoura Sand	181
Shinya Tachibana and Jiro Kuwano	
13 Threshold of Friction Stabilizes Self-Weight Transmission in Gravitating Loose Sand Heaps	199
Thirapong Pipatpongsa and Hideki Ohta	
14 Elasto-Plastic Constitutive Model for Unsaturated Soils with Subloading Surface Concept	215
Shintaro Ohno, Katsuyuki Kawai, Atsushi Iizuka, Shinya Tachibana, Shin-ichi Kanazawa, and Hideki Ohta	
15 Stress–Strain Relationship for the Singular Point on the Yield Surface of the Elasto-Plastic Constitutive Model and Quantification of Metastability	229
Tomohide Takeyama, Thirapong Pipatpongsa, Atsushi Iizuka, and Hideki Ohta	
16 Analysis of Earth Pressure Problems by Upper and Lower Equilibrium Methods	241
Akira Nishihara, Shinji Shimamoto, and Hideki Ohta	

Part III Geotechnical Practices in Dealing with Geo-hazards

17 Rehabilitation of the Old Rossio Railway Station Building: Enlargement and Underpinning 253
 Pedro Simão Sêco e Pinto, João Barradas, and Arlindo Sousa

18 Analysis of Slope Stability and Landslide in Seismic Active Regions 281
 Askar Zhussupbekov, Rauan Ermagambetovich Lukpanov, Serik Beisengalievich Yenkebayev, and Vitaliy Analolievich Khomyakov

19 Recent Developments of PVD Soft Ground Improvement: Laboratory Test Results and Simulations 297
 Dennes T. Bergado, Suthasinee Artidteang, Jaturonk Saowapakpiboon, and Yip Poon Lai

20 Study on Regional Ground Upheaval Phenomenon Caused by the Rising of Groundwater Level and Its Effect on Underground Infrastructure 321
 Sokkheang Sreng, Hiroshi Tanaka, Tejiro Saito, Takuya Kusaka, Tamio Ito, and Atsushi Koizumi

21 A Robust Control Approach for Decision Making and Reliability Design of Soil Structures 337
 Takeshi Sato, Takeshi Nagae, and Hirofumi Nishida

22 Development of a Portable Triaxial Testing Apparatus—*Smart Triaxial* 353
 Eiki Nakayama, Ichizo Kobayashi, Atsushi Iizuka, Moriyuki Taya, and Hideki Ohta

23 Innovation in Disaster Mitigation Technologies 375
 Jian Chu

Index 385



Professor Hideki Ohta (Born in Tokyo on 31st January, 1944): lifetime contributor to solving challenges in Geotechnical engineering

Prologue: 40 Years Contributions to Geotechnical Engineering of Prof. Hideki Ohta

Atsushi Iizuka

Hideki Ohta was born in Tokyo, Japan on January 31, 1944. He grew up in Kyoto and received his Bachelor's degree from Kyoto University in 1966. He went on to earn his Master's degree in 1968 and his Doctorate in 1972 at the Graduate School of Kyoto University. His doctoral thesis, entitled "Analysis of Deformation of Soils Based on the Theory of Plasticity and Application to Settlement of Embankments," and his early achievements were pioneer works in the field of theoretical soil mechanics. They stimulated the research on elasto-plastic/elasto-viscoplastic constitutive modeling of soils and theoretical/analytical interpretation of soil behavior, particularly in his own country of Japan.

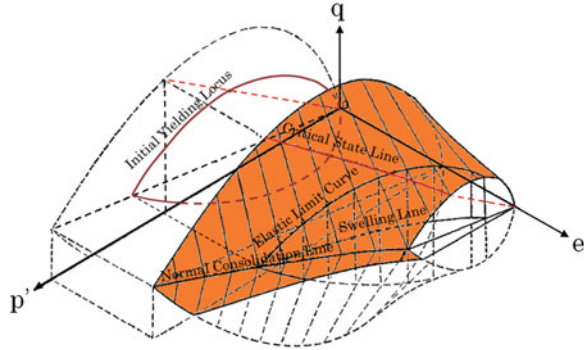
In 1971, he began his career as Assistant Professor in the Department of Civil Engineering at Kyoto University and was promoted to Associate Professor in 1972. He married his wife, Saeko, in 1972 and they have two sons, Taisuke and Kosuke. From August 1973 to October 1974, Professor Ohta visited Cambridge University in the United Kingdom, as an Overseas Fellow-Commoner. His stay in Cambridge was fruitful and he developed lifelong friendships with colleagues there. These include Prof. Peter Wroth, Prof. Andrew Schofield, Prof. David Muir Wood, Prof. Mark Randolph, and many others. In the preface of a book by Prof. David Muir Wood, the author mentions Professor Ohta, saying, "This book took shape in the course of discussions with Hideki Ohta in our smoke-filled room at Kanpur." In Cambridge, he polished his work on constitutive modeling, sometimes called the Kamo Clay model (Kamo is the name of the river that flows through the center of Kyoto), and discovered that the Kamo Clay model could be regarded as a rational extension of the original Cam-clay model to initially anisotropic stress state.

He also presented a clearly physical interpretation showing that the plastic shear dissipation energy assumed in the derivation of Cam-clay models is nothing more than a description for dilatancy behavior of soil materials.

A. Iizuka (✉)

Research Center for Urban Safety and Security, Kobe University, Japan.

Fig. 1 State boundary surface of Kamo Clay model (Ohta and Hata, Proc. JSCE, No.196, 1971)



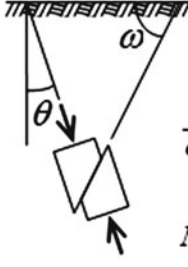



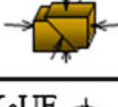


Professor Hideki Ohta has a broad range of research interests, from theoretical/fundamental soil mechanics to geotechnical engineering practice, from laboratory and in situ testing to full-scale model tests. He developed a new triaxial test apparatus named COWK that is capable of measuring K_0 value and then shearing the undisturbed soil specimen where in situ anisotropic stress state was initially preserved.

During the period from September 1980 to September 1982, he was transferred to the Asian Institute of Technology as Associate Professor in the Geotechnical and Transportation Engineering Department. In 1984, he moved to Kanazawa to be Associate Professor in the Civil Engineering Department at Kanazawa University. He was then promoted to professor there in 1985. This period, his so-called Kanazawa period, was challenging for him as he tackled geotechnical disaster problems such as landslides, ground subsidence, and so forth. A topic certainly worth mentioning here is that Professor Ohta supervised elementary schoolchildren in extracurricular scientific activities in which they observed movement of the ground where they lived and measured the amount of movement by means of fixed mirrors and targets that were installed in the ground.

In 1998, Professor Ohta moved to Tokyo to become a professor in the International Development Engineering Department at Tokyo Institute of Technology. He is a firm believer in the value of continuing education. His private seminar, called Terakoya, is a typical example of this attitude. It has continued to be held almost once a month since his Kanazawa period.

Terakoya is open to anyone who wants to join. Here, not only theoretical issues in soil mechanics are discussed, but also various problems related to the practice of geotechnical engineering are explored, with sessions going past midnight (and sometimes including alcohol). Not a few engineers who attended these sessions earned their Doctorate degrees for academic achievements that were made right at Terakoya. During Professor Ohta's Tokyo period, he served on our societies as chairman of many of the technical committees, and was a councilor to academic societies, an adviser to consulting firms and worked on various other projects. In 2004, Professor Ohta became President of the Japanese Geotechnical Society.

Table 1 Undrained strength derived from Sekiguchi and Ohta's model (Ohta, Nishihara and Morita, Proc. 11th ICSMFE, 1985)

type of test	reduced equation for specified test on normally consolidated clay	Blue marine clay ($I_p = 20-21$, $\phi' = 33^\circ$, $K_0 = 0.5$)	
		measured	calculated
 $\frac{s_u}{\sigma'_{v0}} = \frac{OCR^{-\Lambda}(1+2K_0)M \exp(-\Lambda)}{3\sqrt{3}(\cosh\beta - \sinh\beta \cos 2\theta)}$ $\frac{\tau}{\sigma'_{v0}} = \frac{OCR^{-\Lambda}(1+2K_0)M \exp(-\Lambda)}{3\sqrt{3}\left(\sqrt{\cosh^2\beta - \sinh^2\beta \cos^2 2\omega} - \sinh\beta \sin 2\omega\right)}$ $M = \frac{6 \sin\phi'}{3 - \sin\phi'}, \Lambda = 1 - \frac{C_s}{C_c}, \eta_0 = \frac{3(1-K_0)}{1+2K_0}, \beta = \frac{\sqrt{3}\eta_0\Lambda}{2M}$			
 K ₀ PUC	K ₀ -consolidated Plane strain Comp. $\frac{s_u}{\sigma'_{v0}} = \frac{(1+2K_0)M \exp(-\Lambda)}{3\sqrt{3}(\cosh\beta - \sinh\beta)}$	0.34	0.347
 K ₀ UC	K ₀ -consolidated triaxial Comp. $\frac{s_u}{\sigma'_{v0}} = \frac{(1+2K_0)}{6} M \exp\left(\frac{\Lambda\eta_0}{M} - \Lambda\right)$	0.33	0.318
 DSS	Direct Simple Shear $\frac{\tau_{max}}{\sigma'_{v0}} = \frac{(1+2K_0)}{3\sqrt{3}} M \exp(-\Lambda)$	0.20	0.239
 K ₀ PUE	K ₀ -consolidated Plane strain Ext. $\frac{s_u}{\sigma'_{v0}} = \frac{(1+2K_0)M \exp(-\Lambda)}{3\sqrt{3}(\cosh\beta + \sinh\beta)}$	0.19	0.165
 K ₀ UE	K ₀ -consolidated triaxial Ext. $\frac{s_u}{\sigma'_{v0}} = \frac{(1+2K_0)}{6} M \exp\left(-\frac{\Lambda\eta_0}{M} - \Lambda\right)$	0.155	0.135
 FV	Field Vane $\frac{\tau_h}{\sigma'_{v0}} = \frac{(1+2K_0)}{3\sqrt{3}} M \exp(-\Lambda)$ $\frac{\tau_v}{\sigma'_{v0}} = \frac{(1+2K_0)}{3\sqrt{3}} \sqrt{\left(\frac{Mp'}{\Lambda p'_0} \ln \frac{p'}{p'_0}\right)^2 - \left(1 - \frac{p'}{p'_0}\right)^2 \eta_0^2}$	0.19	0.182

(data by Ladd, 1973)



Fig. 2 A photo of Terakoya with Professor Ohta's students



Fig. 3 A snap of Professor Ohta enjoying skiing

Professor Ohta is a keen observer of all phenomena and has a knack for providing logical interpretations for what he sees. Sometimes, it seems as if he is actually drawing theoretically initial/boundary value problems in his brain to create his explanations. Although he is famous as a theoretical researcher and it is widely recognized that his work has made great contributions to the development of



Fig. 4 Professor Hideki Ohta and his wife, Ms. Saeko

theoretical soil mechanics, in fact he is a civil engineer who is rich in ideas. He, himself, wishes to be recognized for this too. The motivation for his research has always been firm and consistent since the beginning of his career as a researcher, and he had hoped to establish an academic field highlighting construction works for soil structures. He therefore needed constitutive modeling and soil–water coupled initial/boundary value formulation consisting of simultaneous partial differential equations. At present, his ambitious spirit in this field is definitely carried on by his many disciples.

Professor Ohta has published close to 400 journal articles, conference papers, and research reports. Also, he has authored 12 technical books. For his contributions in the field of geotechnical engineering, Professor Ohta has received a number of awards, including The Outstanding Paper Award for a Young Researcher from the Japan Society of Civil Engineers (1971) for “On the State Surface of Anisotropically Consolidated Clays”; The Outstanding Paper Award from the Japanese Geotechnical Society (1986) for “Undrained Stability of Ko-Consolidated Clays”; The Reader’s Award from the Japanese Geotechnical Society (2001) for “Development of Constitutive Equations for Soils”; The Outstanding Paper Award from Japan Society of Civil Engineers (2004) for “Compressibility and Material Constants of In-situ Compacted Rock Material under high Overburden Pressure”; the Annual Outstanding Article Award from the Japanese Geotechnical Society (2005) for “New Technology for Maintenance/Retrofit and Renewal Works in Geotechnical Engineering”; and The Innovative Technical Development Award from the Japanese Geotechnical Society (2008) for “Development and Application of DACSAR: Soil-water Coupled Elasto-viscoplastic Finite Element Code.”

In 2009, Professor Ohta retired from Tokyo Institute of Technology at the age of 65, and is currently Professor of Research & Development Initiatives at Chuo University. He is still very energetically involved in various research activities.

Professor Ohta was a field hockey player. He loves playing golf by swinging his club in the hockey style, and is good at skiing.

Contributors

Fahmi Aldiamar Team for Revision of Seismic Hazard Maps of Indonesia, Jakarta, Indonesia

Suthasinee Artidteang School of Engineering and Technology, Asian Institute of Technology, Klong Luang, Pathumthani, Bangkok, Thailand

M. Asrurifak Team for Revision of Seismic Hazard Maps of Indonesia, Jakarta, Indonesia

João Barradas Geotechnical Department, National Laboratory of Civil Engineering (LNEC), Lisbon, Portugal

Dennes T. Bergado School of Engineering and Technology, Asian Institute of Technology, Klong Luang, Pathumthani, Bangkok, Thailand

Fei Chen Water Resources and Hydropower Engineering, Sichuan University, Chengdu, China

Jian Chu Department of Civil, Construction and Environmental Engineering, Iowa State University, Ames, IA, USA

Jianhui H. Deng Water Resources and Hydropower Engineering, Sichuan University, Chengdu, China

Anita Firmanti Research Institute for Human Settlements, Indonesia Ministry of Public Works, Jakarta, Indonesia

Tetsuo Fujiyama Science and Technology Department, Engineering Division, Nuclear Waste Management Organization of Japan (NUMO), Minato-ku, Tokyo, Japan

Technical Research Institute, Maeda Corporation, Nerima-ku, Tokyo, Japan

C.T. Gnanendran University of New South Wales, Canberra, ACT, Australia

Hendriyawan Team for Revision of Seismic Hazard Maps of Indonesia, Jakarta, Indonesia

Faculty of Civil and Environmental Engineering, Institute of Technology Bandung, Bandung, Indonesia

Danny Hilman Team for Revision of Seismic Hazard Maps of Indonesia, Jakarta, Indonesia

Masafumi Hirata Technical Research Institute, Maeda Corporation, Nerima-ku, Tokyo, Japan

Susumu Iai Disaster Prevention Research Institute, Kyoto University, Uji, Kyoto, Japan

Koji Ichii Graduate School of Engineering, Hiroshima University, Higashi-Hiroshima, Hiroshima, Japan

Atsushi Iizuka Research Center for Urban Safety and Security, Kobe University, Nada-ku, Kobe, Hyog, Japan

Masyhur Irsyam Faculty of Civil and Environmental Engineering, Institute of Technology Bandung, China, Indonesia

Team for Revision of Seismic Hazard Maps of Indonesia, Jakarta, Indonesia

Takeshi Ishiguro CDS Project Section, Maeda Corporation, Chiyoda-ku, Tokyo, Japan

Tamio Ito Watershed Management Division, Geology and Geotechnology Department, Nippon Koei Co., Ltd., Tokyo, Japan

Shin-ichi Kanazawa Department of Civil and Environmental Engineering, Faculty of Science and Engineering, Chuo University, Bunkyo-ku, Tokyo, Japan

M.R. Karim University of New South Wales, Canberra, ACT, Australia

Katsuyuki Kawai Research Center for Urban Safety and Security, Kobe University, Kobe, Hyogo, Japan

Engkon Kertapati Team for Revision of Seismic Hazard Maps of Indonesia, Jakarta, Indonesia

Vitaliy Analolievich Khomyakov Department Civil Engineering, The Kazakh Leading Academy of Architecture and Civil Engineering (KazGASA), Kazakhstan

Akira Kobayashi Faculty of Environmental and Urban Engineering, Kansai University, Suita City, Osaka, Japan

Ichizo Kobayashi Technical Research Institute, Kajima Corporation, Chofu, Tokyo, Japan

Atsushi Koizumi Faculty of Creative Science and Engineering, Waseda University, Tokyo, Japan

Takuya Kusaka Research and Development Center, Nippon Koei Co., Ltd., Tsukubashi, Ibaraki, Japan

The University of Tokushima, Tokushima, Japan

Jiro Kuwano Geosphere Research Institute, Saitama University, Sakura-ku, Saitama, Japan

Yip Poon Lai AnchorSol Co Ltd., Kuala Lumpur, Malaysia

S. Robert Lo University of New South Wales, Canberra, ACT, Australia

Rauan Ermagambetovich Lukpanov Department Civil Engineering, Eurasian National University of L.N. Gumilyov, Astana, Kazakhstan

Koki Matsumoto Civil Engineering Division, Hazama Ando Corporation, Tokyo, Japan

Irwan Meilano Team for Revision of Seismic Hazard Maps of Indonesia, Jakarta, Indonesia

Shu Morioka West Japan Highway Maintenance Corporation, Ibaraki, Osaka, Japan

Agus Setyo Muntohar Department of Civil Engineering, Universitas Muhammadiyah, Yogyakarta, Indonesia

Takeshi Nagae Department of Management Science and Technology, Tohoku University, Aoba-ku, Sendai, Miyagi, Japan

Graduate School of Engineering, Tohoku University, Aoba, Miyagi, Sendai

Eiki Nakayama Core Laboratory, OYO Corporation, Kita-ku, Saitama, Japan

Hirofumi Nishida Kanagawa Water Supply Authority, Asahi-ku, Yokohama, Kanagawa, Japan

Yukihiro Nishida West Japan Highway Maintenance Corporation, Ibaraki, Osaka, Japan

Akira Nishihara Department of Architecture and Civil Engineering, Faculty of Engineering, Fukuyama University, Fukuyama, Hiroshima, Japan

Koji Ohmori Research Institute of Digital Geo-Environment, Kanazawa, Ishikawa, Japan

Shintaro Ohno Civil Engineering Design Division, Kajima Corporation, Minato-ku, Tokyo, Japan

Hideki Ohta Research and Development Initiative, Chuo University, Bunkyo-ku, Tokyo, Japan

Pedro Simão Sêco e Pinto Geotechnical Department, University of Coimbra, Coimbra, Portugal

Geotechnical Department, National Laboratory of Civil Engineering (LNEC), Lisbon, Portugal

Thirapong Pipatpongsa Global Scientific Information and Computing Center, Tokyo Institute of Technology, Meguro-ku, Tokyo, Japan

M. Ridwan Team for Revision of Seismic Hazard Maps of Indonesia, Jakarta, Indonesia

Teijiro Saito Civil Engineering Division, Nishimatsu Construction Co., Ltd., Tokyo, Japan

Jaturonk Saowapakpiboon Department of Highways, Bangkok, Thailand

Takeshi Sato Civil Design and Service Department of Osaka Head Office, Toyo Construction Co., Ltd., Chuo-ku, Osaka, Japan

I. Wayan Sengara Faculty of Civil and Environmental Engineering, Institute of Technology Bandung, Bandung, Indonesia

Team for Revision of Seismic Hazard Maps of Indonesia, Jakarta, Indonesia

Shinji Shimamoto Load and Traffic Design Division, CTI Engineering Co., Ltd., Osaka-shi, Osaka, Japan

Arlindo Sousa Geotechnical Department, National Laboratory of Civil Engineering (LNEC), Lisbon, Portugal

Sokkheang Sreng Research and Development Center, Nippon Koei Co., Ltd., Tsukuba-shi, Ibaraki, Japan

Shigehiko Sugie Technical Research Institute, Obayashi Corporation, Kiyose, Tokyo, Japan

Suhardjono Team for Revision of Seismic Hazard Maps of Indonesia, Jakarta, Indonesia

Shinya Tachibana Geosphere Research Institute, Saitama University, Sakura-ku, Saitama, Japan

Jiajia J. Tai Water Resources and Hydropower Engineering, Sichuan University, Chengdu, China

Tomohide Takeyama Department of Civil Engineering, Tokyo Institute of Technology, Meguro-ku, Tokyo, Japan

Hiroshi Tanaka Research and Development Center, Nippon Koei Co., Ltd., Tsukuba-shi, Ibaraki, Japan

Moriyuki Taya Head Office, OYO Corporation, Chiyoda-ku, Tokyo, Japan

Wahyu Triyoso Team for Revision of Seismic Hazard Maps of Indonesia, Jakarta, Indonesia

Yoshihisa Uchita Construction Department, Tokyo Electric Power Company, Chiyoda-ku, Tokyo, Japan

Sri Prabandiyani Retno Wardani Department of Civil Engineering, Diponegoro University, Semarang, Indonesia

Jinbing B. Wei Water Resources and Hydropower Engineering, Sichuan University, Chengdu, China

Sri Widiyantoro Team for Revision of Seismic Hazard Maps of Indonesia, Jakarta, Indonesia

Takayuki Yamakami Information Media Center, Kanazawa University, Kanazawa, Ishikawa, Japan

Serik Beisengalieвич Yenkebayev Department Civil Engineering, Eurasian National University of L.N. Gumilyov, Astana, Kazakhstan

Yoshihiro Yokota Maeda Kohsen Corporation, Nihonbashi, Chuo-ku, Tokyo, Japan

Askar Zhussupbekov Department Civil Engineering, Eurasian National University of L.N. Gumilyov, Astana, Kazakhstan

Part I
Geotechnical Aspects of Some
Recent Disasters

Chapter 1

Tsunami Induced by 2011 Tohoku-Pacific Ocean Earthquake and a Possible Renewal Plan

Hideki Ohta, Susumu Iai, Yukihiko Nishida, Shu Morioka,
and Atsushi Iizuka

1.1 Introduction

Several sequential waves of tsunami induced by the 2011 Tohoku-Pacific Ocean Earthquake on March 11, 2011, struck a huge area of near-shore zones in the Sanriku area, where human activities virtually disappeared in cities, towns, and villages. The land near the seashore settled 0.5–1.5 m during the earthquake and rendered the area more dangerous to live in than it used to be. People there have been advised to shift their homes and workplaces farther from the seashore to inland areas that are higher and therefore safer than the coastal area. However, people have their own reasons for not moving their daily activities. Their economic activities require them to live very close to the sea, even after experiencing the disaster, which has happened many times in the history of the region and will most likely happen again. How reasonably safe residential areas near the shore be provided for the people in the region?

H. Ohta (✉)
Research and Development Initiatives, Chuo University,
1-13-27, Kasuga, 112-8551 Bunkyo-ku, Tokyo, Japan
e-mail: ohtaoffice@kib.biglobe.ne.jp

S. Iai, D.Eng.
Disaster Prevention Research Institute, Kyoto University, Uji, Kyoto 611-0011, Japan
e-mail: iai@geotech.dpri.kyoto-u.ac.jp

Y. Nishida, D.Eng. • S. Morioka
West Japan Highway Maintenance Corporation, 5-1 Nishi-ekimae cho,
567-0032 Ibaraki, Osaka, Japan
e-mail: y.nishida@w-m-kansai.co.jp; s.morioka@w-m-kansai.co.jp

A. Iizuka, D.Eng.
Research Center for Urban Safety and Security, Kobe University,
1-1 Rokkodai, Nada-ku, 657-8501 Kobe, Hyogo, Japan
e-mail: iizuka@kobe-u.ac.jp

The worldwide standard size of containers currently widely used in international trading is 45 ft. However, 45-ft containers are not yet in domestic use throughout Japan because railways, trailers, and road facilities are designed for smaller size containers. Bigger trailers and road facilities are needed. It is obvious that the future development of the Japanese economy requires new transportation systems and infrastructures that accept the use of 45-ft containers. It is also obvious that current Japanese transportation systems and facilities cannot be replaced by new ones because the cost of replacement is prohibitive. Therefore, how can the Japanese system change into one that is suitable for 45-ft containers?

Young people in Japan want to work after school but have serious difficulty obtaining jobs in their home towns. Many retired people in Japan want to contribute to society by offering what they can, but cannot find opportunities to do so. The near-shore areas struck by the 2011 tsunami no longer have economic activities; at the moment, there are practically no jobs and no chance to contribute to local communities. People are moving away from the region that suffered from the tsunami. How can we induce people to move back to their home towns?

This chapter proposes a combined renewal plan of breakwaters, cities, and villages in the Sanriku area that hopes to answer these questions.

1.2 Tsunami Disaster Induced by 2011 Tohoku-Pacific Ocean Earthquake

An earthquake with a Japan Meteorological Agency (JMA) magnitude 9.0 hit north east Japan at 14:46, March 11, 2011. The Japan Meteorological Agency named this earthquake the 2011 Tohoku-Pacific Ocean earthquake. This earthquake registered the greatest magnitude since the modern earthquake monitoring system was established in Japan.

The recorded heights of the tsunamis were higher than 7.3 m at Soma, 4.2 m at Oarai, and 4.1 m at Kamaishi.

The impact of the tsunamis was also the greatest since modern design methodology was adopted for designing breakwaters. A typical example of the damage was the Kamaishi Harbor breakwater. In this example, the breakwater was specifically designed for protection against the impact of a tsunami and was constructed at the mouth of the Kamaishi harbor at a depth of 63 m or less over a length of 990 m in the northern part and 670 m in the southern part, with an opening of 300 m in between. However, the breakwater was devastated by the tsunami. This may be partly owing to the failure of the adopted design as well as being a symbolic event that indicates the magnitude of a tsunami.

Figure 1.1 shows a cross-section of the breakwater. The breakwater is a composite caisson and rubble mound. Based on the visual data (video) monitored from the coastline, the tsunami first arrived at about 15:24 (about 40 min after the earthquake). The breakwater was not damaged by this first arrival. However, there was a continual overtopping of water at the top of the breakwater. At about 15:32, when the height of

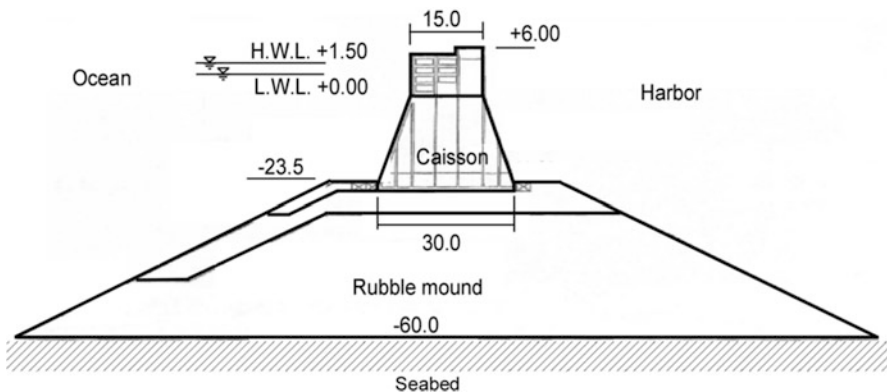


Fig. 1.1 Cross-section of a breakwater at Kamaishi Port (north breakwater, third section)

the tsunami was reduced, serious devastation of the breakwater was visually confirmed by the monitored visual data. At 15:59, the devastation had progressed further and many of the caissons fell into the harbor from the rubble mound. The rubble mound was also seriously devastated as about half of it was lost.

Experts in hydrodynamics claimed that erosion was the primary cause of the damage to the breakwater. Some geotechnical engineering experts, including the authors, pointed out that loss in the bearing capacity of the rubble mound because of seepage of sea water from the ocean side to the harbor side could be significant. The study is underway.

Figure 1.2 shows the loss of the breakwaters that existed at the mouth of Onagawa Bay before the disaster on March 11, 2011. Figure 1.2, which was taken after the disaster, shows no structure on the surface of the sea. However, on an information board at the left lower corner of the photograph, a pair of breakwaters is clearly shown on this and the other side of the bay, with an opening between them. This indicates that the breakwaters were sitting in the sea at a depth of about 20 m and then disappeared at the time of the tsunami. The huge breakwater structure, wider than 50 m at the bottom, has completely disappeared, as seen in Fig. 1.2. It has been reported that many of the concrete caisson blocks were found on the ocean side of the original location after the tsunami. This indicates that the breakwaters were devastated when the tsunami wave receded from the bay after striking the harbor and the town.

The harbor and the town of Onagawa were completely swept away by the tsunami, as seen in Fig. 1.3a and b. Two cars on top of two three-story concrete buildings were evidence the height of tsunami waves, which traveled from the seashore. A concrete building knocked down by the tsunami was found to be accompanied by concrete piles hanging from the building base slab which stands vertically after the disaster rather than sitting horizontally on the ground as before. This implies either that the knock down force of the tsunami wave was hard enough to pull the piles out or that the foundation of the building was liquified when the tsunami wave reached the building.



Fig. 1.2 Breakwaters at the mouth of Onagawa Bay disappeared at the time of the tsunami disaster (Professor Jiro Kuwano is standing by the information board)

There were practically no buildings remaining along the streets after the tsunami disaster in flat areas directly facing the sea that did not have protective seawalls, as seen in Fig. 1.4a, which was taken from the top of a 6-m hill in the town of Yuriage. Almost an entire town adjacent to a fishery harbor at the seaside disappeared. The sea side of the Sendai-Tobu highway, running north to south along the seashore south of Sendai, Miyagi, suffered from the tsunami (as seen in Fig. 1.4b), whereas the inland side remained relatively unaffected because the highway embankment unexpectedly worked as a long seawall preventing the tsunami waves to come further into the inland areas.

Even the areas heavily protected by seawalls suffered from the tsunami in 2011, as seen in Fig. 1.5a and b. The seawalls in the town of Taro in the Sanriku area (shown in Fig. 1.5) were constructed after experiencing tsunami disasters in 1896 and 1933. They worked satisfactorily to protect Taro when it was struck by a tsunami that arose from the earthquake that occurred in Chile at 4:10 am (Japanese local time) on May 23, 1960, which traveled 17,000 km across the Pacific Ocean, reached the Sanriku area 22.5 h after the earthquake, and killed 142 Japanese people. It should be noted that the Sanriku area previously suffered from tsunamis in 1611, 1677, 1896, 1933, 1960, 1978, and in 2011.

Many other areas along the Japanese coastline suffered from tsunami disasters. One of those areas, Hiro in Wakayama, is famous among the Japanese people for its public education about tsunami disaster mitigation and rehabilitation, which was performed in Japanese primary schools from 1937 to 1947. A short story written by

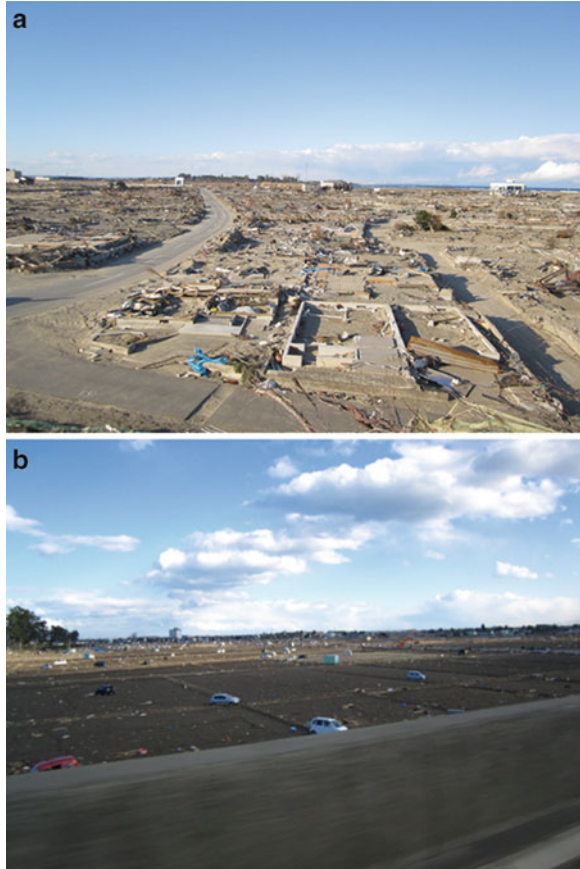
Fig. 1.3 Onagawa immediately after suffering from the tsunami disaster. **(a)** Onagawa harbor completely washed out. **(b)** Cars on top of two buildings



Nakai (1937) in a schoolbook compiled by the state for fifth grade primary school children told what a man did during a tsunami in 1854 to give a clear warning to the village by setting fire to a number of rice stacks, which the farmers had worked all year to produce. Because of the fire, the village people hurried to the plateau and were saved from the violence of oncoming tsunami. After the disaster, Gihei Hamaguchi sponsored construction of a protective seawall embankment (Fig. 1.6) 5 m high and 20 m wide at the base to create continuous part-time jobs (Ohta et al. 2005).

In front of the embankment, black pine trees were planted that could withstand the sea breeze. Spindle trees were planted on the seaside slope of the embankment and wax trees for sumac wax on the other slope. The village people were wise enough to plant trees that would yield cash afterward. The embankment placed along the coastline for a length of 600 m was completed in 1858 and eventually protected the village when another tsunami struck in 1946. This sort of success

Fig. 1.4 Areas with no protective seawall. (a) Yuriage with no houses left along the streets. (b) The sea side of Sendai-Tobu highway running north to south along the seashore south of Sendai, Miyagi



story is still influential among Japanese people even today. The authors believe that forthcoming measures chosen by people living on the coastline of Japan to protect themselves from possibly extraordinary tsunami waves in the future will most likely consist of protective seawalls, even after experiencing tsunami waves higher than those in the town of Taro.

1.3 Seawall Highway with Residential Functions

Aiming at overcoming the difficulties introduced in Chap. 1 (Introduction), the authors propose an idea for renewal of the region. Let us construct two parallel highways running from south to north along the shoreline, as shown in Fig. 1.7. One highway runs through inland area and is already partly in service. The blue line in

Fig. 1.5 Areas heavily protected by seawalls. (a) Huge seawall at Taro, Miyako. (b) Inland area behind the seawall at Taro



Fig. 1.6 Protective seawall embankment at Hiro

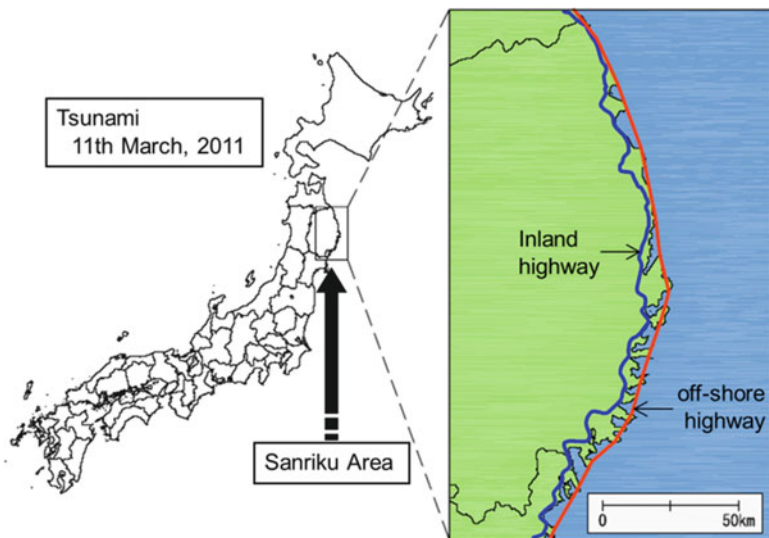


Fig. 1.7 Two parallel highways running along the coastline

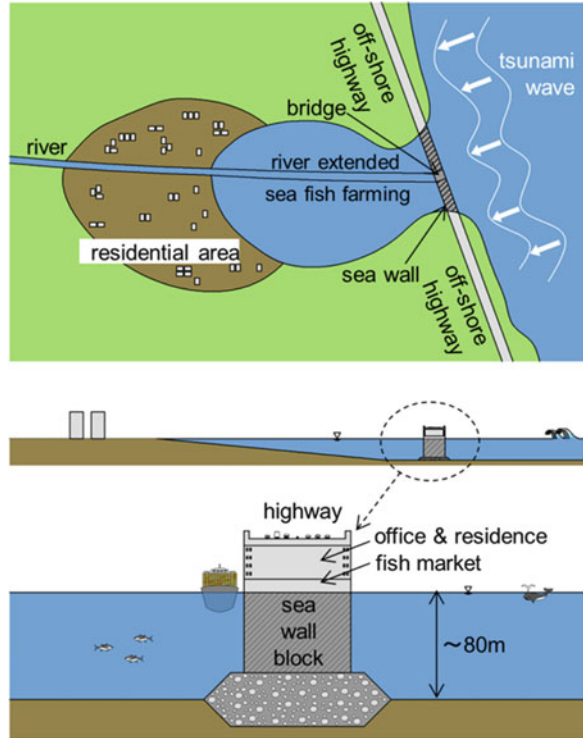
Fig. 1.7 shows the approximate location of the whole route of the inland highway, which was planned before the 2011 earthquake. An additional highway is needed that will run through the offshore area and sit on top of the huge seawall, which is mainly located in the sea about 80 m deep. This offshore highway will run across the bays and connect the tips of the small peninsulas. These two highways will have an area about 10–20 km wide between them.

As shown in Fig. 1.8, the authors propose to have four- or five-story residential building to be used for apartments and offices underneath the offshore highway. The lowest part of the building above sea level may be used for fish markets and fishery-related industries. The whole structure is supposed to work as a huge seawall and an emergency exit in the event of a tsunami after a huge earthquake.

Because the offshore highway will inevitably enclose the bays, special considerations are needed to keep the natural environment of the water so it can be used for fish farming, which will become the major fishery industry in the future when fish hunting becomes unacceptable for ecological reasons. The control of water flow coming into and going out from the enclosed bay area will be a challenging engineering problem to be solved by carefully selected specialists in a wide variety of academic and practical fields. The source of energy needed to control the environment in the enclosed bay area is another problem to be solved.

As drawn in Fig. 1.8, harbor facilities can be constructed inside the offshore highway for small fishery boats because they can go through the river-outlet gate, which is kept open except during a tsunami. Large-scale harbor facilities for tall container carriers should be constructed by placing pier-type structures along the highway on the side facing the ocean. The length of the offshore highway running across the mouth of the bay is more than enough to provide the space to construct jetties for huge vessels loading 45-ft containers.

Fig. 1.8 The off-shore highway concept



Obviously many other important factors must be carefully considered when planning the construction of a huge seawall, which will function not only as a breakwater to block tsunami waves, but also as a residential, industrial, fishery, and commercial space accompanied by harbor facilities. Particularly the stability of the rubble mound supporting the concrete structure must be guaranteed by some new technology, such as the one proposed by Kikuchi (2011). A totally new concept for the structure's foundation, similar to a piled raft foundation, may be needed.

It is also important for the local people to discuss whether they are willing to accept a huge structure that will completely change the landscape they have enjoyed throughout their long history in the region. The financial feasibility of the project is another important subject to discuss. The authors think the project should be treated as a private finance initiative combined with input from the national budget.

The road network covering the area between the inland and offshore highways should be reconstructed over the land that was almost completely swept away by the 2011 earthquake-induced tsunami. This new road system should be designed in such a way that the whole area covered by the network can accept 45-ft container carriage. Thus, the area that suffered from the 2011 tsunami will become the only one in Japan in which 45-ft containers are acceptable and hence the only Japanese area competitive in the world industry.

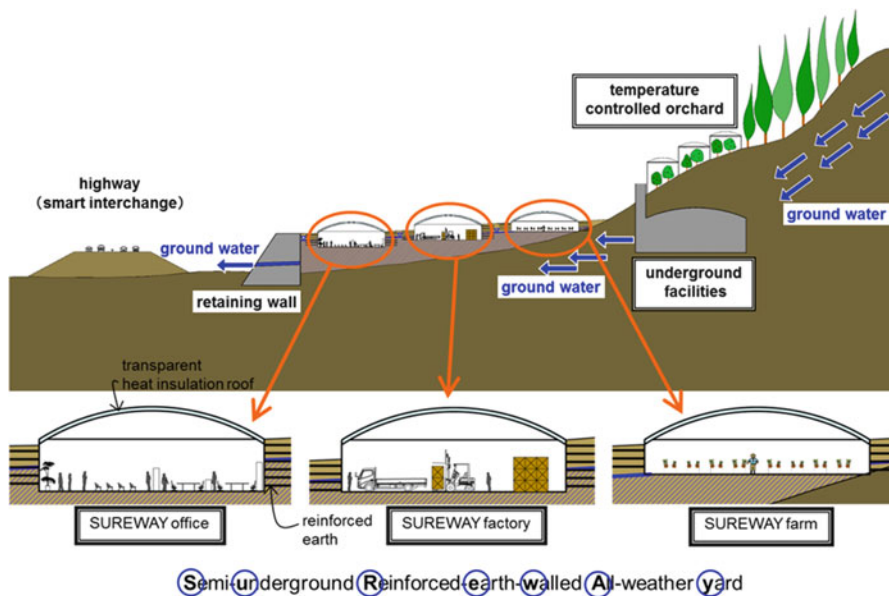


Fig. 1.9 The inland highway with semi-underground facilities (SUREWAY)

1.4 Inland Highway with Semi-underground Facilities

Construction of the planned inland highway, as shown in Fig. 1.7, will inevitably result in an excessive volume of excavated soil and rock because it runs through a relatively hilly area. As seen in Fig. 1.7, the inland highway runs from south to north crossing a number of small rivers flowing down from west to east along small valleys; that is, the inland highway embankment blocks the small rivers as if the highway is a fill-dam. The river water goes to downstream through box culverts underneath the highway embankment in the usual way; therefore, there are no reservoirs on the upstream side of the highway. Instead of having reservoirs, the authors propose to construct embankments using the excavated soil and rock to fill the small valleys, making it possible to construct semi-underground facilities such as shown in Fig. 1.9.

Figure 1.9 shows projected area of semi-underground offices, factories, and vegetable plants along the inland highway route shown in Fig. 1.7. In our concept, offices, factories, and vegetable plants are contained in buildings. However, the authors propose all-weather outdoor facilities that are basically outdoor and yet perfectly protected from the rain and wind and are even air conditioned. The use of ground water in the facilities' temperature control is advantageous because the ground water is available inexpensively in many parts of Japan. It is the key point that the facilities are primarily outdoors and are not contained in any kind of structures defined as buildings. If the facilities are contained in buildings, construction costs

cannot be drastically reduced because buildings have to conform to traditional building codes. The idea of having primarily outdoor-type facilities is vitally needed to drastically reduce the cost of construction by applying new technology. It is essential that the timing of construction of the inland highway should be identical with that of the embankment containing the semi-underground facilities. Parallel advancement of these two construction works can drastically reduce the cost both of the highway and semi-underground facilities.

The semi-underground facilities schematically shown in Fig. 1.9 sit directly on the ground and their roofs are supported by reinforced earth walls rather than the columns used in ordinary buildings. The reinforced earth walls are strong enough to support the roofs and floor slabs (if the facilities are multistory) compared with columns and stable enough even during severe earthquakes, as introduced by Tatsuoka (2011). The roof and floor slabs of semi-underground facilities shown in Fig. 1.9 are structurally independent from the inside facilities. It should be emphasized that the roofs can be transparent and heat insulated so the facilities can be used as temperature-controlled vegetable factories.

Many of the small valleys crossed by the planned inland highway were finely divided paddy fields cultivated in earlier days. The water coming out of the ground at the highest upstream of the valley becomes a small stream that people used to supply water to their paddy fields. The temperature of the water is almost constant (about 14–16 °C) throughout the year. The constant temperature of the water was believed to be essential in growing rice plants of high quality. This was the reason why people spent time and paid effort to take care of their finely divided and therefore labor-consuming paddy fields.

Now the people who used to look after paddy fields in these small valleys are getting older and becoming unable to continue their rice production activities. Consequently, many of the paddy fields are left uncultivated and are covered by weeds. The water goes downstream without giving moisture to rice plants anymore.

The authors propose to (1) place an earth dam or a retaining wall, (2) fill the upstream side of the valley with the soil and rock excavated during constructing the inland highway, and (3) make the land flat where semi-underground facilities protected by reinforced earth walls are placed, as shown in Fig. 1.9. A small stream will be dammed up in the reclaimed land and form a sort of underground reservoir, making it easy to use the ground water in the deeper part of the filled land. The room temperature in the semi-underground facilities is expected to be inexpensively controlled by effective circulation both of the ground water and the air whose temperature is controlled to be cooler than outside air in the summer and warmer in the winter by experiencing a travel through a pipe placed in the ground water.

A group of facilities such as those shown in Fig. 1.9 can provide extremely inexpensive places for economic activities in the field of industrial production, commercial business, and vegetable farming. If the road network covering the region between two trunk highways, one off-shore highway and the other the inland highway, is renewed in such a way that 45-ft container carriage is acceptable, then the region can become a new industrial center of Japan, with a number of harbor facilities along the offshore highway combined semi-underground production facilities along the inland highway.

Hopefully, this area will induce many companies to shift production facilities to the region from their present places of business, which can be sold for relatively good prices. A number of these new villages along the inland highway can provide equitable jobs not only to the native people who want to work near their homes, but also to those who want to move from remote mega-cities in urban areas after selling their houses for good prices.

The lifestyle of the people who become to be involved in the economic activities in the newly developed villages along the inland highway would be somewhat different from what they had before joining the new villages. Many of them are supposed to work in one of the semi-underground factories and semi-underground offices for a certain period of time, most likely shorter than before. After or before work, they are supposed to look after the vegetable factories as well as their neighbors' families in addition to their own families.

Members of the newly born villages have to help each other because almost all of them are newcomers. Children and elderly people have to do their part to support village life as well, such as picking and delivering the vegetables, looking after young children, and so on. In this way, everybody works as much as possible and gets paid for it. By doing so, a kind of new lifestyle can be created. This is what the authors are dreaming and expecting. We need a new lifestyle that looks like the one we used to have earlier when people's daily life was limited to their village because there were no cars.

The whole project proposed by the authors requires nationwide agreement before it is seriously considered as a possible renewal plan for the region that seriously suffered from the 2011 tsunami, which swept away practically all human activities in the region. The financial aspects should be considered carefully by the nation because the national budget is forbiddingly tight. Construction of the inland highway and some part of the offshore highway may be supported by the national budget, but the majority of the project should be supported by a private finance initiative, which needs the agreement of a wide variety of people who wish to invest in this business enterprise from Japan as well as from abroad.

1.5 Use of the Ground Water in Temperature Control of Facilities

One of the essential points in materializing the semi-underground factories, offices, and vegetable factories is that these are basically outdoor facilities. By this, the cost of construction could be drastically reduced compared with those contained in structures defined as buildings, because we do not necessarily need structural members such as columns and beams to support the load. Columns in ordinary buildings are replaced by reinforced earth walls. Beams to support the roof and floor slabs (in case the room is multistory) are fixed into the reinforced earth, not to the columns.

Second key point is the use of ground water in controlling the temperature inside semi-underground rooms. To demonstrate the possibility, the authors constructed

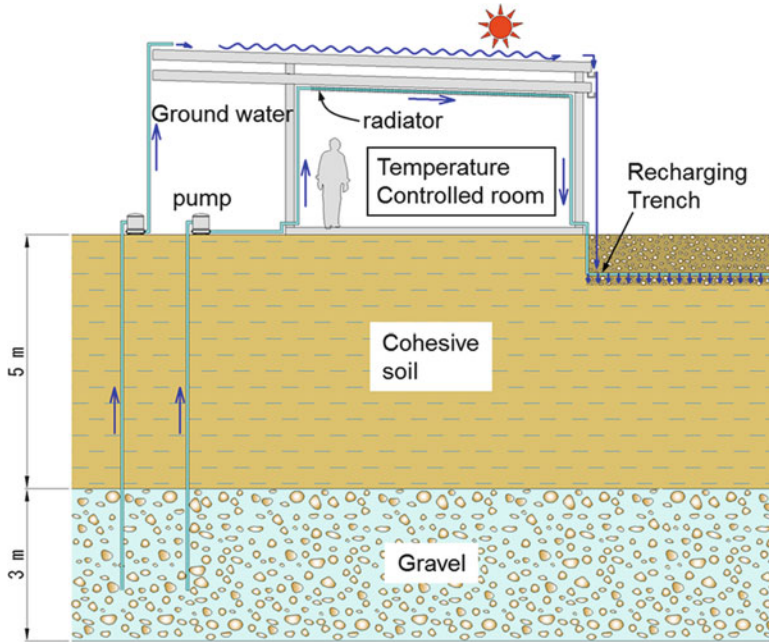


Fig. 1.10 The room temperature control using ground water

the room shown in Fig. 1.10. The ground water circulates in the room through radiator placed under a fan fixed on the ceiling. During the summer of 2011, the temperature inside the room was 28°C at the highest, whereas the outside temperature was around $33\text{--}35^{\circ}$. The temperature of the ground water available at the site of this experiment is 19° , which is a little warmer than the authors expected. This is not advantageous to keep the room temperature cooler than outside in the summer but it is convenient to use the ground water in warming the room in the winter when the outside temperature becomes lower than the freezing point. In addition to the use of the ground water being circulated through a pipe in the room, air temperature is controlled to be nearly equal to the that of ground water by circulating it in the ground water through a thin pipe. This is less expensive compared with circulation of ground water itself because air weighs much less than water.

Figure 1.11 shows a mini-greenhouse, the wall of which is made of soil reinforced by nonwoven geosynthetics. The ground water is circulated in the planting bed to keep the temperature of the planter cooler than outside air temperature in the summer and warmer in the winter to realize the relatively mild variation in temperature throughout the year, and making it possible to have four-season vegetable production. The use of air temperature controlled by circulating it in a pipe buried in the ground is also applicable in addition to the use of the ground water itself. The progress of these trials is reported by Ohta et al. (2011a, b, c).

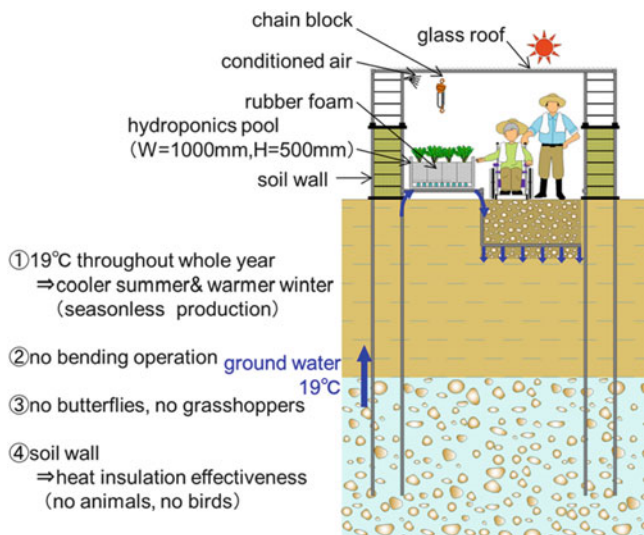


Fig. 1.11 Mini-greenhouse using ground water for temperature control

The authors expect that this type of soil-walled greenhouse will make vegetable production possible throughout the year without sharp peak of labor demand. Hopefully, this will give elderly people an easier opportunity to be involved in agricultural activities because it will not require peak labor concentration. It will also be advantageous that soil-walled greenhouses will prevent butterflies and grasshoppers from laying eggs on the vegetables and therefore practically no insecticide will be needed. Soil-walled greenhouses will also prevent animals from invading vegetable plantation yards; therefore, there will be no need to kill animals such as rabbits, wild boars, deer, bears, and monkeys.

It should be mentioned that the authors feel it is necessary to demonstrate the performance of the trials shown in Figs. 1.10 and 1.11, which are not identical with semi-underground outdoor facilities. The inland highway with semi-underground facilities as shown in Fig. 1.9 is definitely a new concept with practically no existing successful examples. This means there is a very high risk for possible investment in the projects. However, trials such as those shown in Figs. 1.10 and 1.11 require much smaller investment accompanied by lower risk and therefore are easier to be tried by those particularly living in the region north of the big market of Tokyo and south of the nuclear power plant that failed due to the tsunami waves induced by the 2011 earthquake.

In the past few decades, people who used to be involved in agricultural production in Japan were unable to sustain this endeavor, which is not as highly mechanized as rice production and hence is extremely labor intensive. This continued with the rise of the farmers' average age. In Japan at this moment, there is a huge area of land for agricultural use being left idle simply because elderly farmers cannot supply the power needed to take care of their lands. The main difficulty is the need for a very short period of peak labor concentration in

vegetable plantation. For this reason, only a small area of their land is cultivated to plant vegetables, just enough for the family use.

However, after the failure of the nuclear power plant caused by the huge tsunami, people in the region who are producing vegetables mainly for their families are not fully confident that vegetables produced by them in their farm lands will be safe for their grandchildren. The authors expect that a greenhouse such as that shown in Fig. 1.11 may attract attention because it requires a continuous supply of labor throughout the year rather than seasonal concentration periods. In addition, basically it does not need insecticide and is much safer from radiation, mainly accompanied by occasional wind and rain.

If the greenhouse model with temperature controlled by ground water as shown in Fig. 1.11 becomes widely accepted, the concept of semi-underground outdoor facilities hopefully will become very familiar to the people and therefore more acceptable not only psychologically, but also economically.

1.6 Concluding Remarks

The proposed renewal plan of the area that suffered from a tsunami disaster on March 11, 2011 is currently a sort of dream and is not realistic from any point of view. However, the authors believe that their dream can eventually become reality if the idea is carefully studied by the nation. The authors believe that the famous words of wisdom “Let it be” should not be applied to the renewal of the region that suffered from the 2011 earthquake-induced tsunami. A big challenge is needed. Any constructive suggestions for this renewal plan are most welcome and actively needed.

Acknowledgments This work was supported by JSPS Grant-in-Aid for Scientific Research (No. 23310119, 23560594).

References

- Kikuchi Y (2011) Lessons from damage of port and airport facilities during the 2011 off the Pacific coast of Tohoku earthquake. *Geosyn Tech Inf (Japan Chapter of the International Geosynthetic Society)* 27(3):16–25
- Nakai TM (1937) Fire set to rice-stacks. In Japanese school book for 5th grade children compiled by the state, 1937–1947
- Ohta H, Thirapong P, Ohmori T (2005) Public education of tsunami disaster mitigation and rehabilitation performed in Japanese primary schools. In: Chu, Poon, Yong (eds) *Proceedings of international conference on geotechnical engineering for disaster mitigation and rehabilitation*. World Scientific Publishing Company, Hong Kong, pp 141–150. ISBN 981-256-469-1
- Ohta H, Nishida Y, Morioka S, Iizuka A (2011a) Possibility of temperature control of semi-underground all-weather yard by using the ground water. In: 38th annual meeting of Kanto Branch, Japan Society of Civil Engineers, III-40, Tokyo

- Ohta H, Nishida Y, Morioka S, Iizuka A (2011b) Concept of SUREWAY (Semi-underground reinforced-earth-walled all-weather yard). In: 46th annual meeting of Japanese Geotechnical Society, no. 767, Kobe
- Ohta H, Nishida Y, Morioka S, Iizuka A (2011c) Possibility of semi-underground all-weather outdoor yard by using the ground water. In: 66th annual meeting of Japan Society of Civil Engineers, III-126, Matsuyama
- Tatsuoka F (2011) The 2011 Great East Japan earthquake and geosynthetic engineering. *Geosyn Tech Inf (Japan Chapter of the International Geosynthetic Society)* 27(3):1–10

Chapter 2

Tsunami Damage: What Is Unexpected?

Koji Ichii

2.1 Introduction

The 2011 Great East Japan Earthquake was a nightmare. The trust that society had for engineers turned into disappointment. More than 15,000 people died in the earthquake and the failure of the nuclear power plant forced society to face the invisible hazard of radiation.

The main reason for the disaster was the large scale of the earthquake and tsunami. A 9.0-magnitude (M_w) earthquake was unexpected. However, the presidents of the Japanese Society of Civil Engineers (JSCE) and other societies jointly appeal that engineers should not use the word “unexpected” as an excuse. This appeal might be correct. The author believes the event was really unexpected, and our unawareness of the event made the scale of the disaster larger. In addition, engineers should carefully check what was unexpected and discuss why this was so.

This chapter is written to start the discussion. It focuses on the unexpected issues related to tsunamis and geotechnical structures. First, brief outlines of our conventional effort for tsunami hazard mitigation and real phenomena in the 2011 Great East Japan Earthquake are introduced. Then, unexpected issues are discussed. Finally, a proposal for the safety and relief of society is presented.

This chapter was written in September 2011. The detail of the damage caused by the 2011 Great East Japan Earthquake is still under investigation by numerous researchers and engineers. In this sense, the report of the earthquake is not fixed. It will take years to establish and share common understandings of what happened in the earthquake. However, the discussion needs to start immediately, even if there is only limited information.

K. Ichii, D.Eng. (✉)
Graduate School of Engineering, Hiroshima University, 1-4 Kagamiyama,
739-8527 Higashi-Hiroshima, Hiroshima, Japan
e-mail: ichiikoji@hiroshima-u.ac.jp

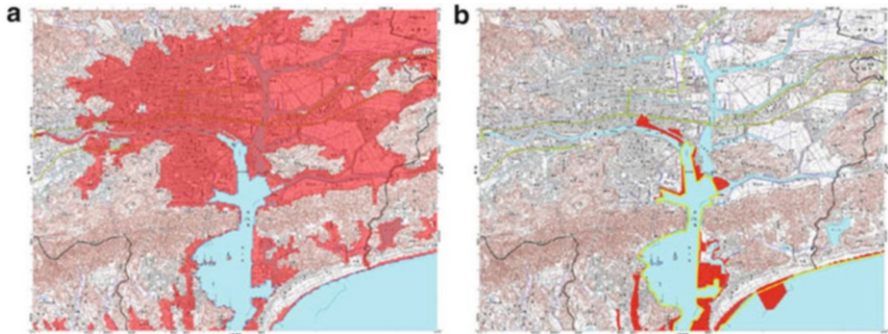


Fig. 2.1 An example of published tsunami hazard maps (Kochi Prefecture). (Note that this map is not the latest version). (a) The case when embankments and floodgates work well. (b) The case when embankments and floodgates do not work

2.2 Efforts for Tsunami Hazard Mitigation

It is true that scientists have been working hard to prepare for future earthquakes and tsunamis. First it is necessary to summarize the conventional efforts to mitigate tsunami disaster.

One of the problems in the tsunami hazard evaluation was that the seismic resistance of coastal protection structures was not appropriately evaluated. This is mainly because of a budget shortage. It was reported that seismic performance evaluations were not conducted for almost 60 % of Japanese coastal structures in 2006. Apparently, in most cases unless an earthquake occurs far away, strong ground motion attacks structures before tsunamis. These strong ground motions sometimes trigger liquefaction in structural foundations, and coastal structures such as embankments and floodgates are damaged. The damage to these structures magnifies the tsunami disaster.

Figure 2.1 shows an example of tsunami hazard maps. This is not the latest version of the maps, but was made public by the Kochi Prefecture several years ago. The maps were prepared for two circumstances: one in which embankments, floodgates, or other coastal protection structures do not work, and the other in which these structures work well. These were the best- and worst-case scenarios. They prepared these two types of hazard maps because they did not know the seismic performance of coastal structures. Another reason was that the real situation was close to the worst case (shown on the left-hand side of Fig. 2.1). If more attention is paid to seismic performance evaluation and improvement, the situation could improve (closer to the best case shown in the right-hand side). In other words, the left side of the figure was the anticipated situation to realize the necessity of the countermeasures, and the right side was the target to be accomplished by engineers.

Based on this idea, seismic performance evaluation was performed with enthusiasm. Figure 2.2 shows an example of seismic performance evaluation of seaside

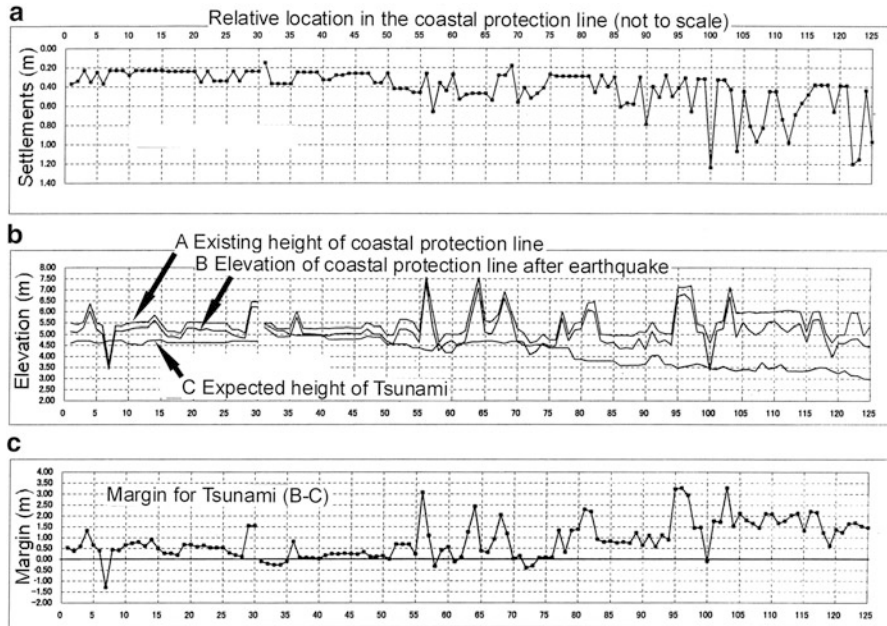


Fig. 2.2 An example of seismic performance evaluation along a coastline (Osaka Prefecture). (a) Settlements of coastal structures. (b) Elevations of coastal protection lines before and after earthquakes and the expected height of a tsunami. (c) Margin of a tsunami

structures along a coastline of the Osaka Prefecture. In this area, 125 total types of structures are located on the 70-km coastline. For each structure, settlement induced by the anticipated ground motion was evaluated (Fig. 2.2a). Then subtracting the evaluated settlement from the height of the structure (A in Fig. 2.2b), the residual height of the coastal structure could be evaluated (B in Fig. 2.2b). The margin for tsunamis (Fig. 2.2c) could be evaluated by comparing the residual height (B in Fig. 2.2b) and the anticipated tsunami height announced by the Japanese government (C in Fig. 2.2b). In the case shown in Fig. 2.2, there was no margin at approximately seven parts, and further detailed investigations or countermeasures were necessary.

The evaluation of the settlement shown in Fig. 2.2 was performed by referring the summary of finite element method (FEM) parametric studies. An example of FEM analysis is shown in Fig. 2.3. Not only the deformation pattern, but also the settlement at the crest can be evaluated. The applicability of FEM analysis for coastal structures has been widely published (i.e., Iai et al. 1998). However, it was not cost effective to build a FEM model for each site. Therefore, a simple but cost-effective system to evaluate the settlement of coastal structures by referring the summary of FEM parametric studies was proposed, and it was applied to obtain the result shown in Fig. 2.2. The author was a member of the project that proposed the system.

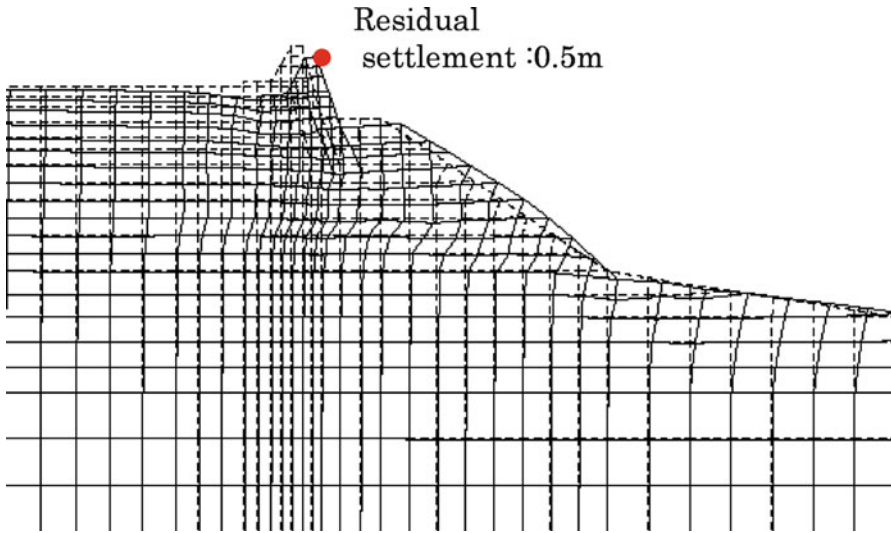


Fig. 2.3 An example of finite element method analysis of a seawall

Although the details of the system were not published in English, the essential concept (without the data used in the final system) can be found in a paper by Ichii and Donahue (2005).

Numerous parametric studies were performed to establish the system; then the effects of the differences in the conditions (e.g., thickness of rubble slope, slope inclination) were summarized. In the application of the system to a target site, the case most similar to the target site is picked up. Based on the differences between the pick-up case and the target site, the calculated settlement of the case is corrected for the site. The summary of the parametric study is used to evaluate the amount of correction in this procedure.

Appropriate evaluation of the possible settlement is usually difficult. However, the proposed system is dedicated to be used only for the purpose of screening (i.e., selection of relatively weak sites). This clear definition of the purpose made it easy to establish the system. In other words, the system was designed to answer the safer side estimation. Figure 2.4 shows a comparison between the estimation by the proposed system and the FEM results. For half of the cases, the estimations agree well; but for the other half, the simple proposed system gives safer side values.

It should be emphasized that engineers pursue the safer side if there are unclear elements. Figure 2.1a is a worst-case scenario in which no embankment or flood-gate works. In other words, because usually not all embankments or floodgates are broken, one can expect the real situation to be better than that represented in Fig. 2.1a. Figure 2.2 shows a discussion of the tsunami hazard based on the anticipated tsunami height. This anticipated height is usually calculated from the worst-case scenario. Figure 2.4 shows the accuracy of the seismic performance evaluation. This result also indicates the existence of a safety margin related to the

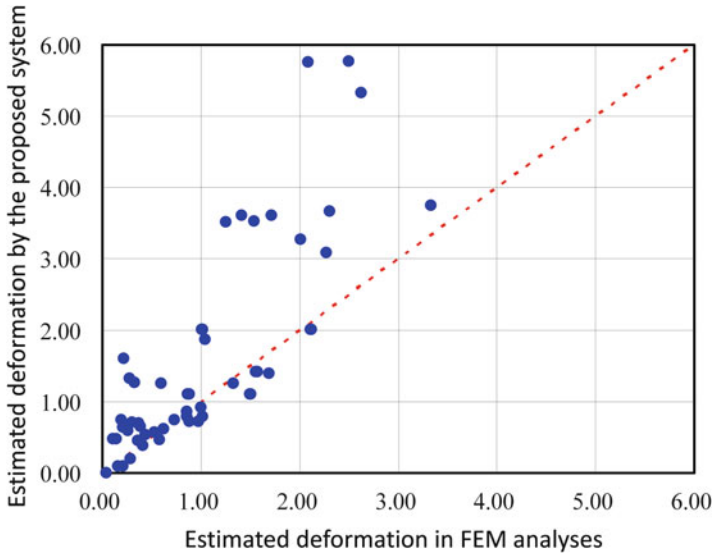


Fig. 2.4 Comparison of the results of detailed analyses (FEM) and of a simple (but safer side) system

method used in practice. Thus, we believe that there are usually many safety margins in the practice to consider uncertainties.

An example of countermeasures should be noted here. For the Kuji, Kamaishi, and Ofunato ports, breakwaters were constructed both at the gate of the port and the harbors. Figure 2.5 shows the Kamaishi Port Gate Breakwaters, which were constructed to mitigate the impact of tsunamis.

The construction of structures as a countermeasure is usually a large project that benefits the civil engineering industry. Appropriate (or exaggerated?) estimation of future disasters is necessary to realize the project. In this sense, not only the engineers but also almost all the people related to the civil engineering industry are familiar with the concept of safety margin.

In a sense, almost no one tends to cut the safety margin. Engineers have believed that they should point out the risks and hazards of earthquakes and tsunamis, and should make progress in seismic assessments and countermeasures. These efforts create a safer society, and the knowledge of these efforts gratifies engineers.

2.3 What Happened in the 2011 Great East Japan Earthquake

The 2011 Great East Japan Earthquake ($M_w = 9.0$) was a huge-scale event. Figure 2.6 shows the estimated slippage at the fault. Both the area of moved fault and amount of slippage were quite large. This large movement under the sea bottom induced an extensive tsunami. The detailed mechanism of the tsunami is still under

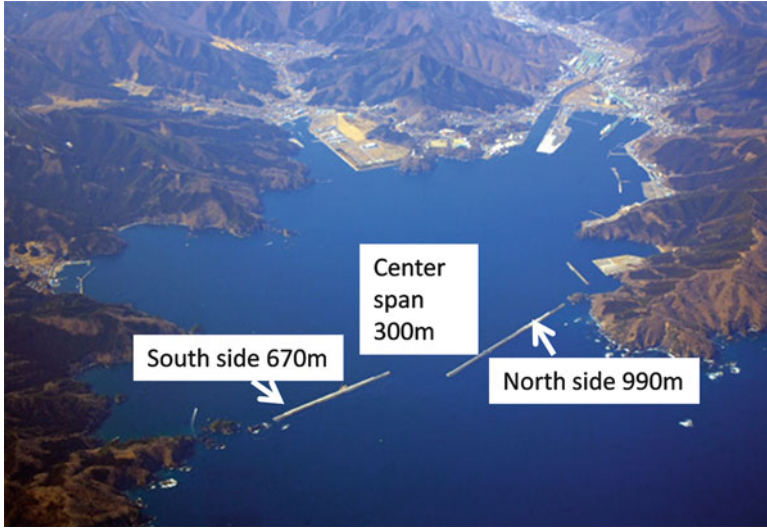


Fig. 2.5 Kamaishi Port Gate breakwaters (Kamaishi Port Office)

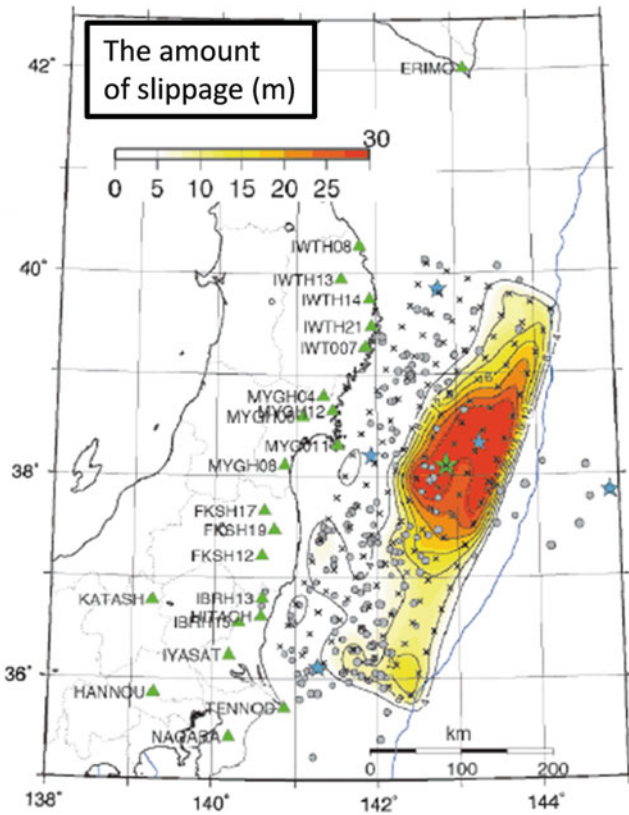


Fig. 2.6 Contours of the estimated slippage (Cabinet Office, Government of Japan)



Fig. 2.7 Snapshots of the moment of tsunami (anonymous official). (a) The moment of tsunami. (b) Tsunami covered everything

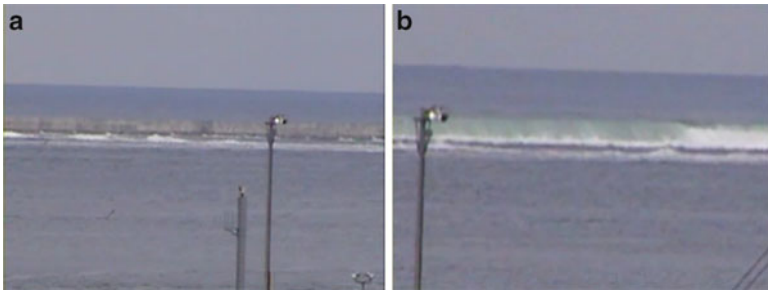


Fig. 2.8 Snapshots of the Kamaishi Port Gate Breakwater (anonymous official). (a) Bubbles behind the caisson walls. (b) Overflowed tsunami

investigation, but the fact is that the significant height of the tsunami was observed on the eastern coast of Japan.

Figure 2.7 shows snapshots from the video recorded by a government official. He evacuated to the roof terrace of a building and recorded the entire event from the terrace. The tsunami height shown on the left side of Fig. 2.7a was almost as high as a two-story house, and the houses shown in the figure were swept away. The entire city was covered by the tsunami, as shown in the right side of Fig. 2.7b. These scenes were recorded at the Kamaishi Port, where breakwaters were installed as shown in Fig. 2.5.

The observed tsunami height was larger than expected in the design of breakwaters. The real performance and effect of breakwaters for the mitigation of tsunami impact were still under investigation and discussion. The situation at the first tsunami wave at the breakwater site was recorded by the official mentioned in the preceding. Figure 2.8 shows the tsunami at the breakwaters. In the beginning, white bubbles were observed behind the caissons of breakwaters (Fig. 2.8a). The reason of this phenomenon might be the difference of the water level between the front (tsunami) and back (port) sides. But there is a discussion that this was caused by the water flow between caissons or upward flow from rubble foundations owing to the high permeability in the foundations. Nevertheless, a few moments later, the tsunami overflowed as shown in the right side of Fig. 2.8b.

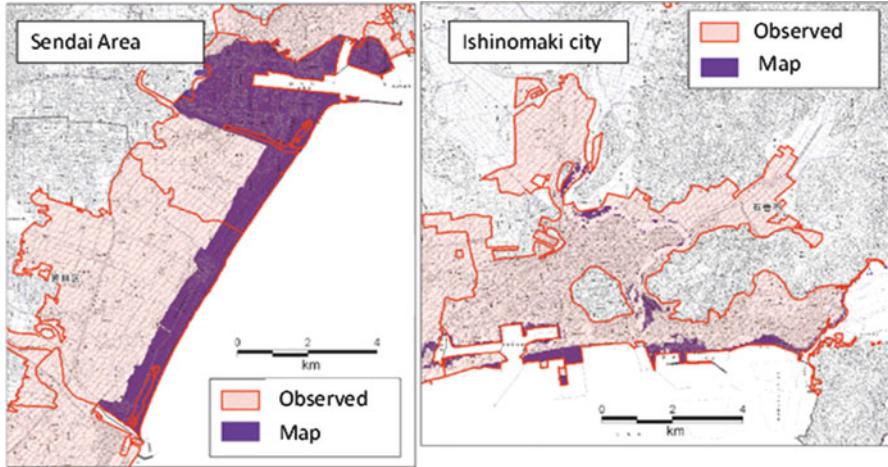


Fig. 2.9 Tsunami inundation areas observed in reality and shown in the hazard maps (Cabinet Office, Government of Japan)

As a result of the unexpected height of the tsunami, the observed inundation was far beyond the area earlier imagined. Figure 2.9 shows the comparison between the tsunami inundation areas shown in the hazard maps and those observed in reality. The reality was much more severe than imagined.

Many people died as a result of the discrepancy between projected inundation and the reality. In addition to the people who *could not* evacuate, some people *did not* evacuate. The reason why they did not evacuate might be as follows.

“I did not imagine the tsunami would come to my place, which is far from the coast.”

“I believed the breakwaters and seawalls made us safe.”

These comments are fictitious as the author did not actually conduct interviews. But similar comments were heard several times from interviews on broadcast television with people who were actually in danger. Similar comments also can be found in discussions related to the failure of the Fukushima nuclear power plant. Note that because of the limited information opened for public discussion, the debate related to the nuclear power plant failure is skipped in this chapter. However, as a philosophical issue, it might suggest similar problems.

2.4 From a Field Survey

The author joined the field survey team of the JSCE and visited the damaged area in July 2011. The following are more realistic reports.

Figure 2.10 shows the damage to the Rikuzentakata City Office. About one third of city officers died in the earthquake (more than 80 people out of approximately

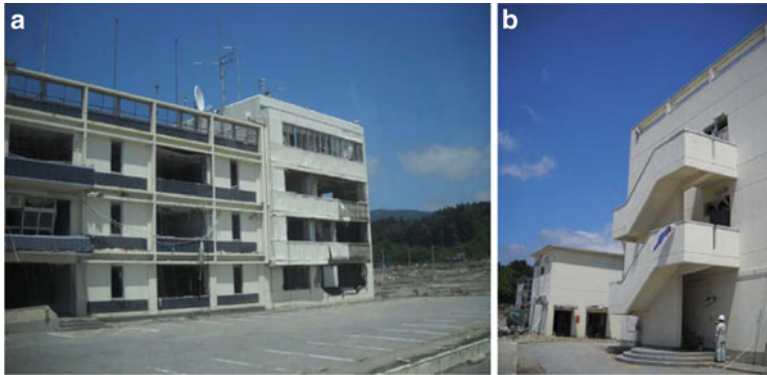


Fig. 2.10 Photos of Rikuzentakata City Office. (a) The damaged Rikuzentakata city office. (b) Emergency stairs of the office

300 people). The height of the tsunami was unbelievable, reaching the third floor, as shown in Fig. 2.10a. A tsunami of such a height was a completely unexpected event.

What was disappointing was the fact that the emergency stairs did not reach to the roof terrace, as shown in Fig. 2.10b. Actually, some people on the roof terrace survived. (The video of evacuated people on the terrace was recorded and broadcast throughout the Internet.) Therefore, there may have been another way to evacuate to the roof terrace, which was effective. But if the emergency stairs had reached the roof, more people could have been evacuated.

It might be impossible for us to imagine that such a high tsunami would attack the office. Otherwise, more efforts would have been made. Obviously, even for such a high tsunami, more effort could have been expended to mitigate the disaster, such as extension of the stairs to the roof, preparation of a rubber boat on the roof, and so on. The point is that it is unlikely to imagine such an unbelievably high tsunami in advance, and accept the budget required for evacuation efforts that would usually be needless.

Figure 2.11 shows damaged sea walls at Ofunato city. Emergency repairs were ongoing at the time of the survey, as shown in Fig. 2.11a. The side part of the seawall survived, and the cross-section of the wall can be observed as shown in Fig. 2.11b. An old small sea wall was recognized at the cross-section, and it was obvious that the seawalls were improved before the tsunami.

Here, the improvement of sea walls means the increase of the wall height and width. Although the details (e.g., the time of improvement) are unknown, efforts were made to ensure stronger coastal protection. Unfortunately, the tsunami height was greater than expected, and the disaster could not be prevented. The problem is that how high seawalls need to be is not known.

If there were a physical limitation to the possible height of tsunamis, the problem would be easy. For example, there might be a physical upper limit in the level of the possible strong motion because the strong motions propagate through the ground, and strong shear forces caused by strong ground motions require large shear strain in the ground. Usually, the ground has strong nonlinear characteristics, and large shear strain



Fig. 2.11 Photos of seawalls with improvements prior to the tsunami. (a) Damaged sea walls in Ofunato City. (b) Evidence of improvements

decreases the shear stiffness. Thus, strong motions cannot be transmitted without losing the features of motions. However, a tsunami is the movement of a water mass. It looks like the larger movement of sea bottom ground could induce larger water mass movement. Furthermore, not only earthquakes, but also any types of sea bottom movement, such as landslides, can create tsunami. Therefore, it appears that there is no upper limit to tsunami height. This implies that completely sufficient countermeasures are impossible. The level of safety or relief can be increased; however, the possibility of an unexpected event and disaster always remains.

2.5 Safety and Relief

The expectation for civil engineers is to build a safe society and offer reassurance to the people. However, the facts observed in the 2011 Great East Japan Earthquake disaster remind us that it is almost impossible to build a safe and reassured society. From the previous discussion, the following has been learned.

- (a) Although engineers tend to choose safer options, in reality the hazard can be far beyond the expectation.
- (b) Publication of hazard maps or construction of breakwaters as countermeasures was believed to be effective to mitigate tsunami disaster. However, these efforts not only give the society a false feeling of relief, but also restrain people from evacuating. Therefore, once the real hazard becomes more severe than the expectation, the damage could be magnified.
- (c) Even for the magnificently high tsunami observed after the earthquake, something could have been done to mitigate the disaster; for example, the extension of emergency stairs and preparation of rubber boats.
- (d) Efforts to improve coastal structures have been carried out and may contribute to more safety. However, the tsunami height was greater than expected. This fact confirms the fact that nobody can identify enough improvements to ensure complete safety.

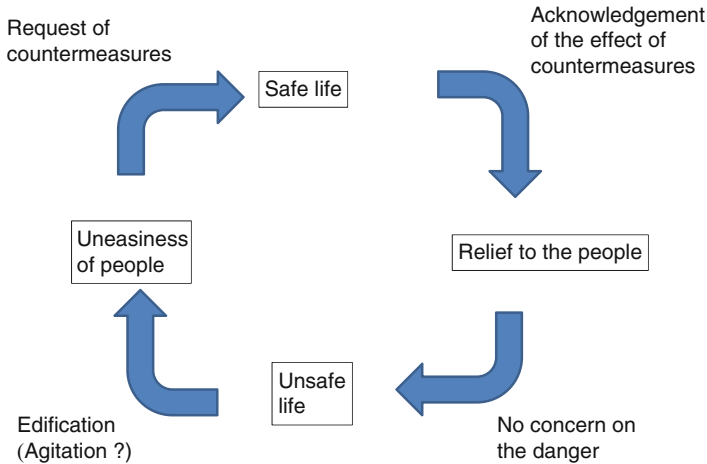


Fig. 2.12 The relationship between “safety” and “relief”

The author thinks that these lessons are related to the relationship between safety and relief. Lately, safety and relief have been buzz words in Japanese public administration and civil engineering. Many politicians try to guarantee the safety and relief of society. Many projects have been put into practice to build a safe society and give relief to the people.

The relationship between safety and relief can be schematically illustrated as shown in Fig. 2.12. Safety can be established by the preparation of countermeasures, and relief can be realized by the acknowledgment of the effect of countermeasures. However, once the people obtain relief, they lose the concern about the danger. A situation that does not have a consciousness of danger is a truly unsafe condition. Therefore, engineers should work hard to educate the people. In a sense, this edification is a kind of agitation to make the people request countermeasures. As a result of education, they may feel unease and request countermeasures. Thus, civil engineering projects to provide a safe society can be conducted at the request of the people. This is an endless cycle, and will not ensure safety for all.

Considering the cycle shown in Fig. 2.12, what we should learn from the experience to stop the cycle is summarized in Fig. 2.13. There are three main lessons.

(a) *Develop imagination skills*

The development of more imagination is needed. In a sense, it was not recognized before the earthquake that the people were too reassured and were therefore unsafe. Engineers were also too reassured considering that they tend to choose safe practices. This was actually because of the shortage of imagination. Not only the tsunami phenomenon itself, but also the limited collective imagination was unexpected in this disaster.

(b) *Be a friend of Kassavndra*

Kassavndra was a female prophet in Troy. Her prediction was right, but nobody believed her. It is not clear whether there was a person who pointed out the possibility of such a great disaster in advance. However, people would not

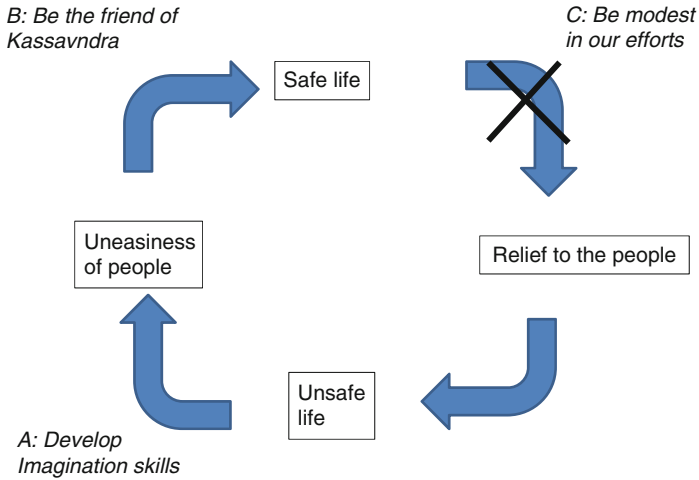


Fig. 2.13 What should be done to stop the endless cycle

believe it until it really happened. Therefore, even if somebody foretold the event, the extension of the emergency stairs at the city office would not have been done. The calamitous story is often ignored, and the person who tells it is regarded as a kind of Kassavndra because it is not expected. We must become a friend of Kassavndra and learn how to adapt to the story.

(c) *Be modest in our efforts*

Engineers often pride themselves on their efforts for society, especially those efforts to build a safe society, which contribute to the relief of people. However, in a sense, these efforts were overrated by the people, and their relief made the disaster worse. This was truly an unexpected situation. Engineers should be more modest. This is an especially severe issue in the discussion related to the failure of the nuclear power plant.

2.6 Conclusions

As mentioned earlier, it will need years to establish and share common understandings of what really happened in the earthquake. This chapter is written to start the discussion of the unexpected issues related to tsunamis and geotechnical structures. The event was truly unexpected, and this ignorance of the possibility of such an event enlarged the disaster. What and why was unexpected must be carefully reviewed and discussed.

As a result, some unexpected factors in the relationship between safety and relief have been pointed out. Shortage of imagination, avoiding unhappy stories, and overestimation of the effort for countermeasures could have been improved. These kinds of unexpected matters should be carefully checked to avoid future failures.



Fig. 2.14 Decoration for a festival at the temporary office

In addition to these unexpected matters that amplified the disaster, some unexpected benefits were also observed. For example, Fig. 2.14 shows a decoration at the temporary office of Rikuzentakata City. This decoration encouraged the people, especially the children of the city. The mutual cooperation and undefeated attitude of the people in the damaged area were also admirable. Human virtues beyond expectation were demonstrated.

References

- Anonymous Official (2011) The video tape recorded on the roof terrace of Kamaishi port Office, Anonymous government official in Kamaishi Port who recoded the video
- Cabinet Office (2011) White paper on disaster management 2011, Government of Japan (In Japanese with English executive summary on the website, <http://www.bousai.go.jp/hakusho/h23/index.htm>, downloaded on September, 2011)
- Iai S, Ichii K, Liu H, Morita T (1998) 'Effective stress analyses of port structures', Special issue of soils and foundations. *Jpn Geotech Soc* 29:97–114
- Ichii K, Donahue MJ (2005) Evaluation of sea dike settlement due to seismic shaking prior to tsunami attack. In: *Solutions to coastal disasters 2005*, ASCE, Charleston, pp 616–629
- Kamaishi Port Office. The outline of Kamaishi Port Gate breakwaters, http://www.pa.thr.mlit.go.jp/kamaishi/bousai/b01_03.html in Japanese, downloaded on September, 2011
- Kochi Prefecture: Website of Kochi prefecture in a past time (downloaded on September 1, 2007) (The latest version can be found at: <http://www.pref.kochi.lg.jp/soshiki/010201/tunamisin-suiyosoku.html>) (in Japanese)
- Osaka Prefecture: Non-published information related to the committee of disaster prevention along the coastal line, the committee was organized from 2005 to 2006

Chapter 3

Past Earthquakes in Indonesia and New Seismic Hazard Maps for Earthquake Design of Buildings and Infrastructures

Masyhur Irsyam, Hendriyawan, M. Asrurifak, M. Ridwan, Fahmi Aldiamar, I. Wayan Sengara, Sri Widiyantoro, Wahyu Triyoso, Danny Hilman, Engkon Kertapati, Irwan Meilano, Suhardjono, and Anita Firmanti

3.1 Introduction

The Indonesian region is located in the Circum-Pacific belt, also known as the Ring of Fire, which is the most active belt in the world (Fig. 3.1). This region experiences about 90 % of the world's earthquakes, nearly half of which are great earthquakes (Kramer 1996). Because of its location, the seismic activities in Indonesia are affected by three major active tectonic plates of the earth, the Eurasian, Indo-Australian, and Pacific Philippine plates. Moreover, some active faults exist and are identified offshore and onshore of Indonesia such as the Great Sumateran fault, the Palu-Koro fault, the Molucca fault, the Sorong fault, and many others. The tectonic setting around Indonesia can be seen in Fig. 3.2.

A massive earthquake occurred within 150 km of Aceh Province in 2004 and followed by a massive tsunami increased public and government awareness regarding seismic activities in Indonesia. The earthquake devastated the human population living on the coastline of Aceh Province and parts of North Sumatra Province. According to Bappenas' report (2005), because of the earthquake 165,708 were classified as dead, 12,132 as missing, and 703,518 as displaced. The huge natural

M. Irsyam, Ph.D. • Hendriyawan (✉) • I.W. Sengara, Ph.D.
Team for Revision of Seismic Hazard Maps of Indonesia, Jakarta, Indonesia

Faculty of Civil and Environmental Engineering, Institute of Technology Bandung,
Bandung 40132, Indonesia
e-mail: masyhur.irsyam@yahoo.co.id

M. Asrurifak • M. Ridwan • F. Aldiamar • S. Widiyantoro • W. Triyoso • D. Hilman
• E. Kertapati • I. Meilano • Suhardjono
Team for Revision of Seismic Hazard Maps of Indonesia, Jakarta, Indonesia

A. Firmanti
Research Institute for Human Settlements, Indonesia Ministry of Public Works, Jakarta, Indonesia



Fig. 3.1 Pacific Ring of Fire (Source: http://en.wikipedia.org/wiki/File:Pacific_Ring_of_Fire.svg)

disaster, one of the largest ever on a global scale, triggered several researchers in earthquake engineering to consider the new conceptual approach and technological shift shown in the transition of UBC 1997 to ASCE 2010.

3.2 Lesson Learned from Great Earthquakes in Indonesia

Some great earthquakes that repeatedly occurred in Indonesia over the last few years have caused catastrophic damage to structures and devastated the human population. Some of the great earthquakes can be seen in Table 3.1. Based on several sources, the estimated total losses owing to the earthquake can be seen in Fig. 3.3.

Table 3.1 shows that since 2004 almost every year great earthquakes with a magnitude greater than 6.5 occur in Indonesia. According to Fig. 3.3, the total losses from 2004 to 2010 vary from US\$39 million to US\$4,745 million and almost 200,000 were killed because of the earthquake's activities. Examples of the earthquake's effects are illustrated in Figs. 3.4, 3.5, and 3.6.

The total losses caused by previous earthquakes have increased the awareness to the Indonesian people regarding the seismic effects on structures such as buildings, bridges, dams, and other critical facilities. Therefore, to mitigate the effects of earthquakes more comprehensive studies in earthquake engineering have been performed to revise the previous Indonesia seismic hazard map and update the Indonesian seismic code. The results of the study are used to improve the policy or guidelines in Indonesian seismic codes.

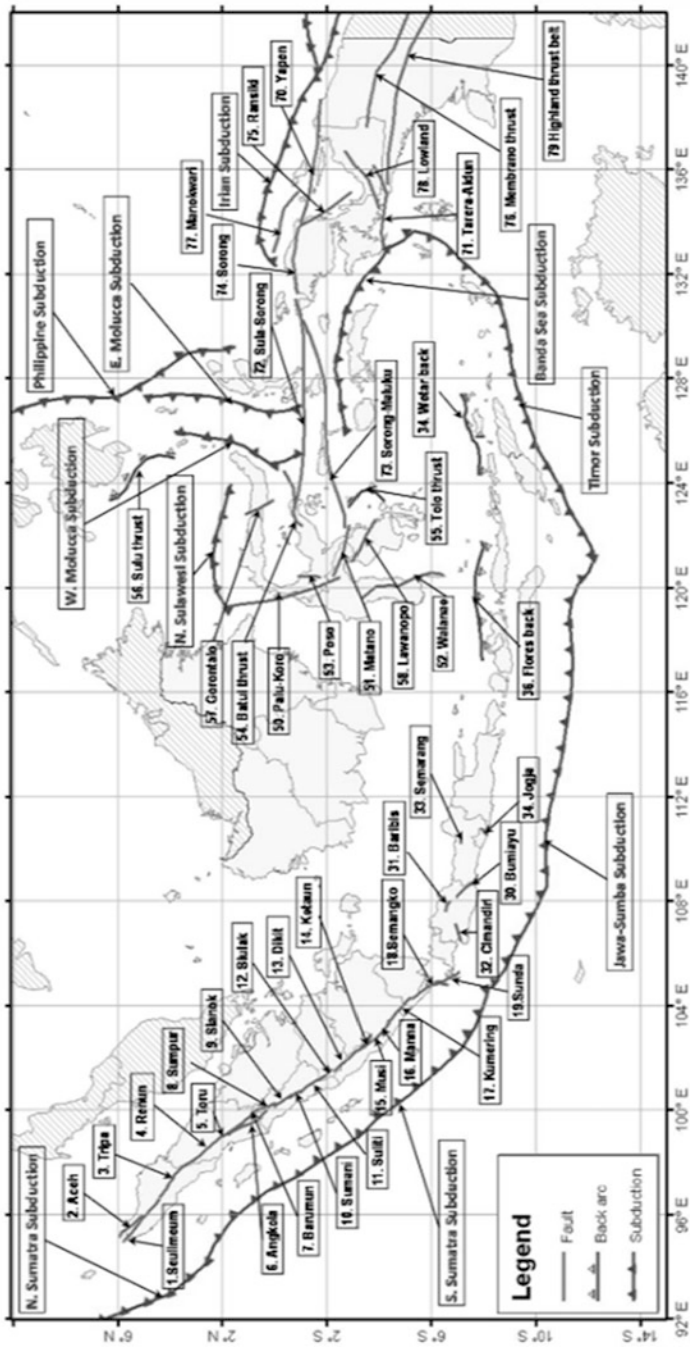


Fig. 3.2 Tectonic setting of Indonesia (Irsyam et al. 2010)

Table 3.1 Significant earthquakes in Indonesia from 2004 to 2011

Year	Location	<i>M</i>	Effect	Source
2004	Aceh	9.0–9.3	Earthquake was followed by tsunami. 165,708 were accounted for as dead, 12,132 as missing, and 703,518 as displaced. More than 1,600 villages and hundreds of public facilities were damaged.	Bappenas (2005)
2005	Nias	8.7	The total number of dead varied from 150 to 870. The earthquake also affected Simeulue in Aceh. In Simuelue, 10–15 % of buildings were visibly damaged. According to local people, dozens were killed, whereas 80 were injured.	IFRC (2005)
2006	Jogya	6.3	The earthquake killed more than 5,700 people, injured between 40,000 and 60,000 more, and damaged or destroyed hundreds of thousands of villages.	Bappenas (2006)
2007	West Sumatera	8.4	The most severely affected areas were the provinces of West Sumatera and Bengkulu. About 25 people were killed and 160 injured. More than 48,000 houses were damaged or destroyed.	Bappenas (2007)
2009	Padang	7.6	More than 1,000 people were killed and 1,200 injured. Around 135,000 houses were severely damaged and an estimated 1,250,000 were made homeless or otherwise severely affected.	Grundy (2010)
	West Java	7.4	More than 81 people were killed, 1,917 injured, and 100 villages wrecked or damaged. Some public facilities were damaged.	Bappenas (2009)
2010	Mentawai	7.5	The earthquake was followed by a tsunami. It is estimated that 509 people were killed and 110,000 were displaced. More than 1,200 villages and some public facilities were damaged.	Bappenas (2010)

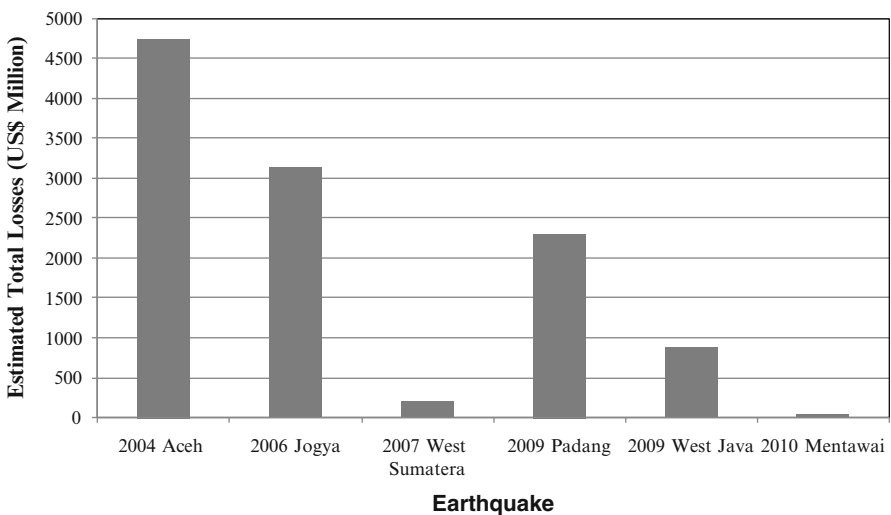


Fig. 3.3 Estimated total losses in US\$ Million



Fig. 3.4 The damages of buildings and facilities due to the 2004 Aceh Earthquake



Fig. 3.5 Buildings failures and ground cracking due to the 2007 West Sumatera Earthquake (Source: Bappenas 2007)

3.3 Development of a New Seismic Hazard Map of Indonesia

The comprehensive study in earthquake engineering was started in 2005 after the 2004 Aceh earthquake. Studies were performed by individuals from several institutions. In 2009, The Public Works of Indonesia assigned 11 researchers as a Team for Revision of Seismic Hazard Maps of Indonesia. The team was assigned to develop new Indonesian seismic hazard maps. The team also collaborated with the United States Geological Survey. The procedure and methodology used in the



Fig. 3.6 Ground cracking and landslide due to the 2009 Padang Earthquake

seismic hazard assessment considered the new conceptual approach and technological shift shown in the transition of UBC 1997 to ASCE 2010.

Several issues were considered in developing new seismic hazard maps. The issues, such as recent seismic activities, the latest research works regarding fault characteristics around Indonesia, improvements of the method in seismic hazard analysis, and the latest provisions in the International Building Code (ASCE 2010) were considered in developing the maps.

Several great earthquake occurrences in Indonesia in the last few years inquire revision of seismic hazard parameters. The earthquake events were considered in determining seismic hazard parameters, especially maximum credible earthquake magnitude (MCE). For instance, the previous seismic hazard maps use MCE for Sumatera smaller than the 2004 Aceh earthquake and the 2005 Nias earthquake. The seismic hazard parameters used in developing new seismic hazard maps can be seen in Fig. 3.7.

The previous Indonesian seismic hazard map was developed using area sources model. This two-dimensional (2-D) model has some limitations in modeling fault source geometries. The fault source model or three-dimensional (3-D) model could improve the modeling of seismic sources significantly. This model can represent the geometry of fault source more reliably than the 2-D model. Therefore, this model was used in developing the new Indonesian seismic hazard maps.

The recent studies regarding paleoseismology of the Sumatran Subduction Zone (SSZ) and neotectonics of the Sumatran Fault Zone (SFZ) conducted by Sieh and Natawidjaja (2000) and Natawijaya (2002) show the unique characteristics of SSZ and the fault segmentation of SFZ. The research also shows that the Sumatran fault is highly segmented. These results could affect the seismic hazard assessment, especially in modeling the seismic sources for Sumatra. Therefore, the results of these seismotectonic conditions were taken into account in developing the new seismic hazard maps for the Sumatra region. The latest researches regarding seismotectonic conditions for Eastern Indonesia were also considered in the study.

The characteristics of the major tectonic feature used in this study are developed by combining historical earthquakes data in the catalog and the seismotectonic

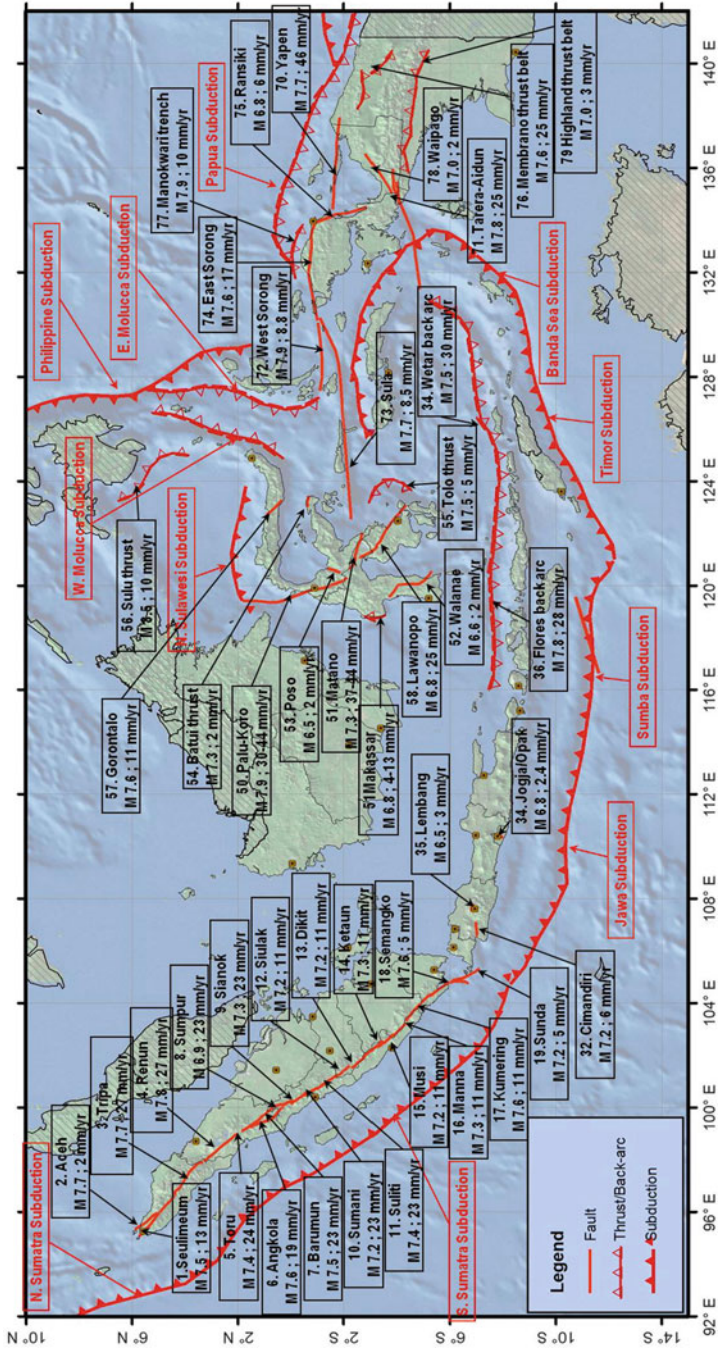


Fig. 3.7 Seismic hazard parameters used in revising Indonesia seismic hazard map

Table 3.2 Sources model with attenuation relationships

Sources model	Attenuation
Shallow background	<ol style="list-style-type: none"> 1. Boore-Atkinson NGA (Boore and Atkinson 2008) 2. Campbell-Bozorgnia NGA (Campbell and Bozorgnia 2008) 3. Chiou-Youngs NGA (Chiou and Youngs 2008)
Deep background	<ol style="list-style-type: none"> 1. Atkinson-Boore intraslab (Atkinson and Boore 2003) 2. Geomatrix slab seismicity rock (Youngs et al. 1997) 3. Atkinson-Boore intraslab seismicity world data BC-rock condition (Atkinson and Boore 1995)
Fault	<ol style="list-style-type: none"> 1. Boore-Atkinson NGA (Boore and Atkinson 2008) 2. Campbell-Bozorgnia NGA (Campbell and Bozorgnia 2008) 3. Chiou-Youngs NGA (Chiou and Youngs 2008)
Subduction	<ol style="list-style-type: none"> 1. Geomatrix subduction (Youngs et al. 1997) 2. Atkinson-Boore BC rock and global source (Atkinson and Boore 1995) 3. Zhao et al., with variable V_{s-30} (Zhao John et al. 2006)

setting of Indonesia. The seismic source model used in this study is composed of background seismicity, fault sources, and subduction sources.

Background seismicity is used to account for random earthquakes on unmapped faults and smaller earthquakes on mapped faults. Background sources are defined based on a declustered earthquake catalog that begins in 1963. A gridded model based on spatially smoothed earthquake rates as proposed by Frankel (1995) was used for modeling background seismicity. This model accounts for the observation that big earthquakes ($M \geq 5$) occur near small earthquakes ($M \geq 4$ or 5).

Fault or line sources represent individual faults for which data are sufficient to determine maximum earthquake magnitudes distributions and slip rate estimates. The area versus magnitude and subsurface rupture length versus magnitude relations (all earthquake types) developed by Wells and Coppersmith (1994) were used in estimating the maximum earthquake magnitude distributions for the fault sources.

Subduction mechanism occurred when an oceanic plate is being subducted under an island arc or continent. Thrust fault mechanism may occur along the interface, whereas normal faulting may occur toward and along outer arc high and in the trench. Here reverse and strike-slip faulting events that occurred in the upper plate are considered to fall within this classification as long as they are near a convergent boundary of the subduction zone.

A relatively simple mechanism of subduction occurs where oceanic crust is subducted beneath the continental platform, such as in Sumatera, Java, and Nusa Tenggara. A double arc collision in northern Molucca Sea seems to be originated as a typical arc collision complex in the form of inverted U-shaped oceanic slabs to the eastward-dipping Benioff Zone beneath the Halmahera Island in the east and the westward dipping Benioff Zone beneath the Sangihe Island in the west (Silver 1978). Active and/or inactive subduction zone, volcanic belt, fault and thrust/shallow crustal faults are common features of the Indonesian archipelago.

The activities of background source zone were modeled by fitting a Gutenberg-Richter (GR) truncated exponential curve to the historical seismicity data. For big earthquakes, the planar fault source and interplate/megathrust subduction source were modeled by means of the fault slip-rate in conjunction with the pure characteristic magnitude model. For moderate earthquakes, magnitude distributions were modeled by fitting GR truncated exponential curves to the historical seismicity data.

Several new attenuation functions were also used in the study. In addition, three next generation attenuations (NGA) were used in the study. The list of attenuation functions used in the study can be seen in Table 3.2.

The existing Indonesian seismic hazard map is based on PGA at bedrock for 10 % probability of exceedance (PE) in 50 years (475 years return period of earthquakes). The existing seismic hazard map can be seen in Fig. 3.8. This is because the existing code (SNI-1726 2002) partially adopts the concept of UBC 1997. The new Indonesia Seismic Code will adopt the International Building Code (ASCE 2010). This code implements spectral hazard maps for 2 % PE in the design time period of 50 years (2,500 years return period of earthquakes). The maps are based on spectral acceleration rather than peak ground acceleration (PGA), peak ground velocity (PGV), or zone factors. Two spectral hazard maps are used in this provision: short period (0.2 s) and long period (1.0 s).

The Indonesia Seismic Hazard Map Revision Team produced spectral hazard maps for several return periods of earthquake, such as 475 and 2,475 years. For each return period, three spectral hazard maps were developed, i.e., PGA, short period (0.2 s) and long period (1.0 s). The PGA maps for 475 and 2,475 years return periods of earthquakes can be seen in Figs. 3.9 and 3.10, respectively. In 2010, the seismic hazard maps were officially approved and signed by the Ministry of Public Work of Indonesia.

The result for the 475-year return period is relatively higher than the PGA from the existing Indonesian Seismic Code (SNI 03-1726-2002) especially at near fault locations. This is because the maximum magnitudes used in that study are larger than the previous study. For instance, the value of maximum magnitude of the Sumatra Subduction Fault near Aceh has been increased from 8.5 to 9.2. The increase of the maximum magnitudes are affected by great earthquakes that have occurred since 2004.

3.4 Future Research in Seismic Hazard

At the moment, research on seismic maps is continuously performed by enhancing risk maps and microzonation maps for several cities in Indonesia. In 2011, the Ministry Coordinator for People's Welfare of Indonesia started coordinating several institutions in Indonesia such as BMKG (Meteorological, Climatological and Geophysical Agency), Ministry of Research and Technology, Universities (ITB, UI), BPPT (The Agency for the Assessment and Application of Technology), Public

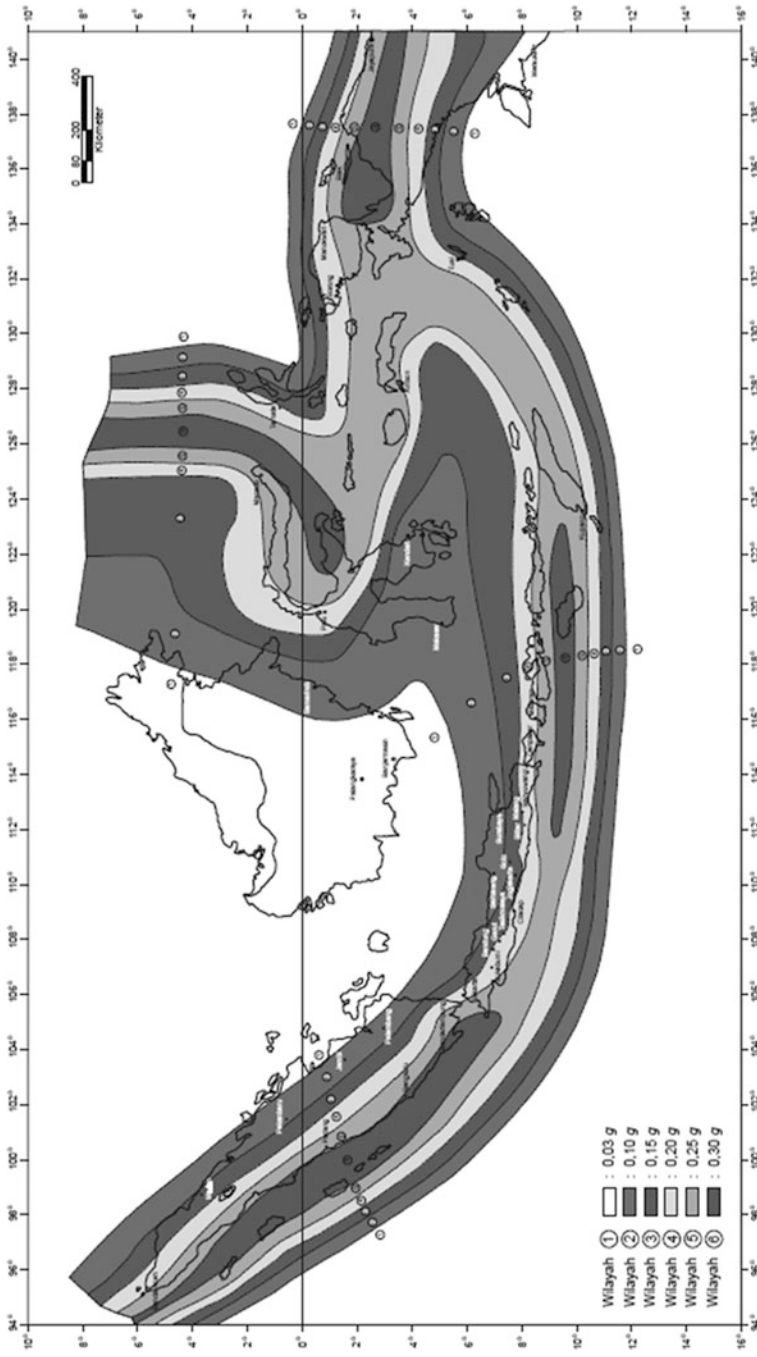


Fig. 3.8 Maximum peak ground acceleration at bedrock of Indonesia for 500 year return period (SNI-1726 2002)

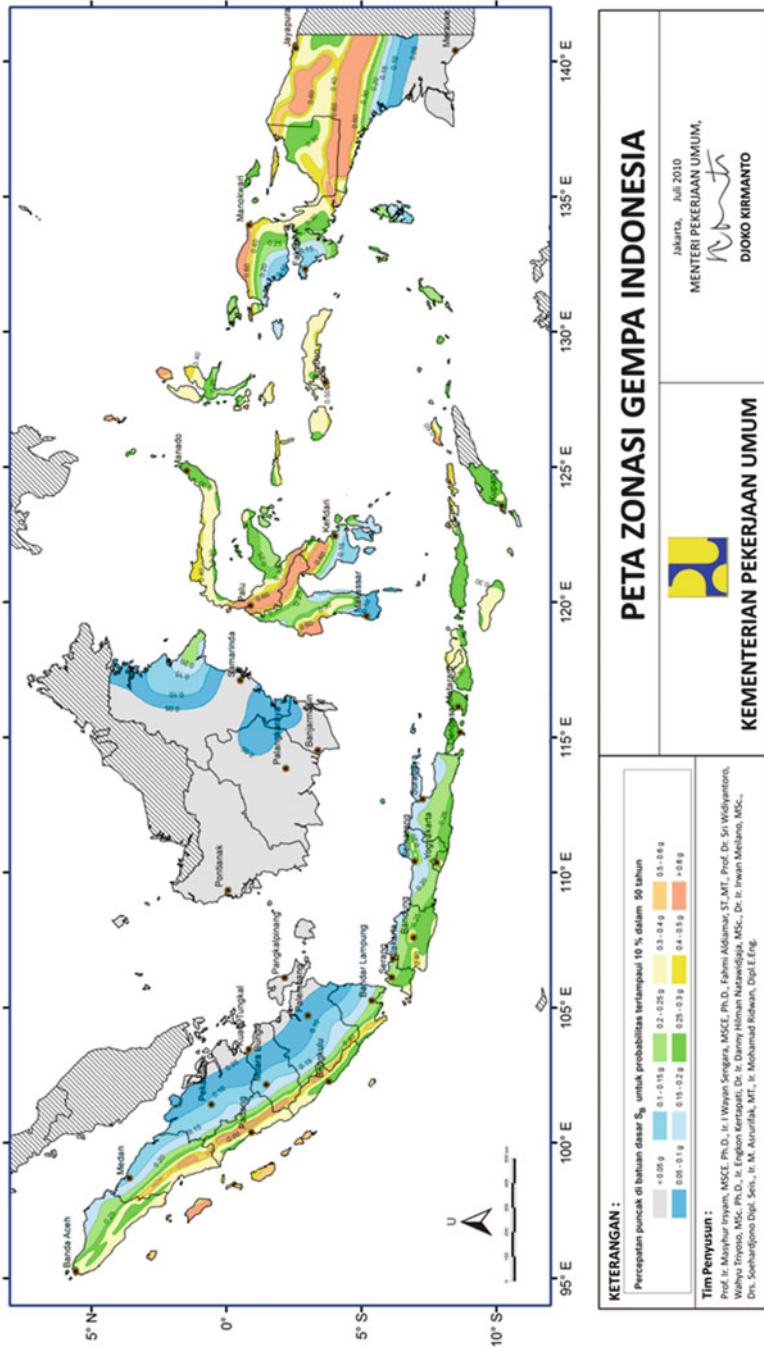


Fig. 3.9 PGA contour maps for 10 % PE in 50 years (475 years)

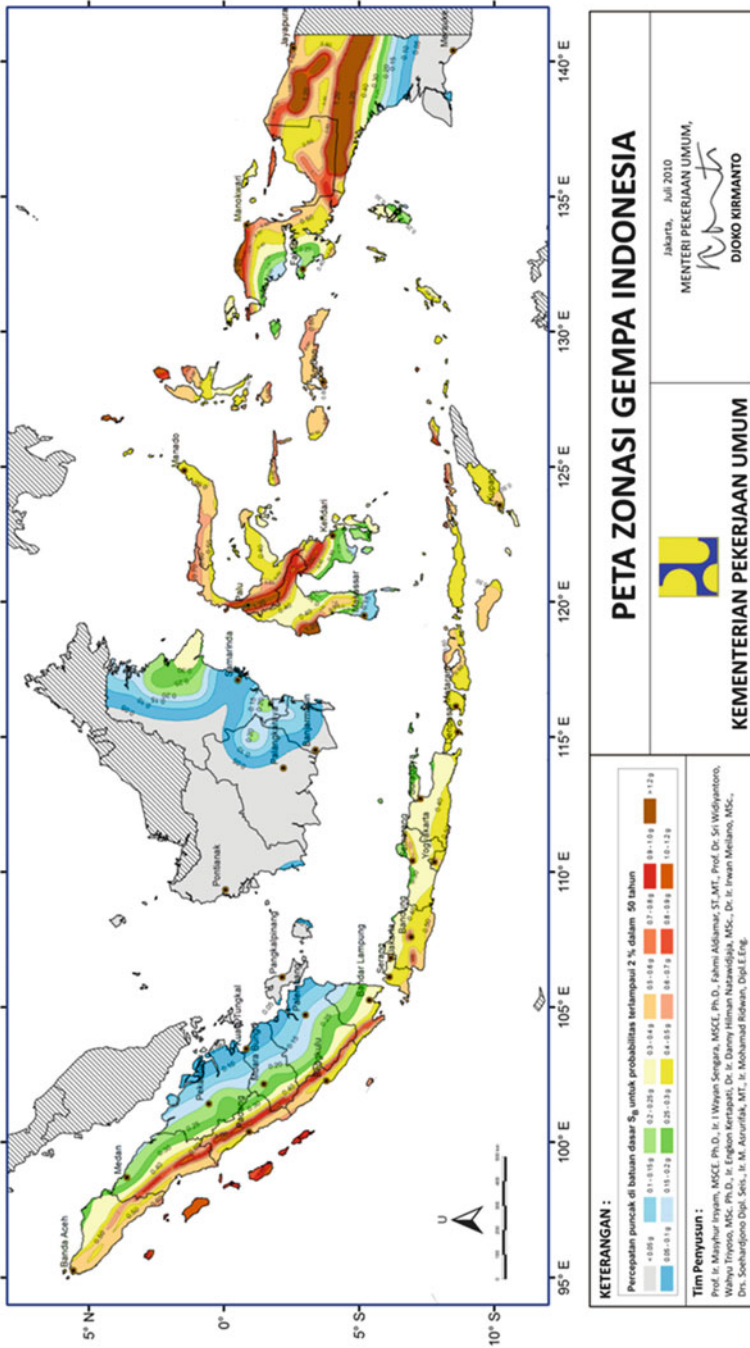


Fig. 3.10 PGA contour maps for 2 % PE in 50 years (2.475 years)

Works, Bappenas (The Agency for National Planning Development), BNPB (The Agency for National Disaster Management), and professional associations.

The focus of the teams is on developing microzonation maps for several cities in Indonesia. Several field investigations, including deep boring (down to 350 m) and geophysical surveys such as seismic downhole and microtremor array are performed for gathering primary data. The research also covers the development of synthetic time histories as input in local site effects analysis.

3.5 Conclusion

Several great earthquakes repeatedly occurred in Indonesia over the last few years. This has triggered several Indonesian researchers to conduct comprehensive studies of earthquake engineering to improve and revise the previous Indonesian seismic hazard map and Indonesian seismic code. The new spectral hazard maps of Indonesia have been developed by the Indonesia Seismic Hazard Map Revision Team. The maps have been officially signed by the Ministry of Public Work Indonesia. The maps were developed based on the latest data and methodology. The team has developed several return periods of earthquake, such as 475 and 2,475 years. For each return period, three spectral hazard maps are developed, such as PGA, short period (0.2 s) and long period (1.0 s).

At the moment, research in seismic hazard mitigation is continuing by developing risk maps and microzonation maps for several cities in Indonesia. The research is performed with the collaboration of several institutions such as universities, and government and professional associations under the coordination of the Ministry Coordinator for People's Welfare of Indonesia.

Acknowledgments The team would like to thank the Department of Public Works, Science and Technology Empowerment and Socialization—Ministry of Research and Technology, National Disaster Management Agency (BNPB), Geology Research and Development Centre Indonesia (ESDM), Indonesian Institute of Sciences (LIPI), AIFDR (Australia-Indonesia Facility for Disaster Reduction), and the United States Geological Survey for their support and assistance for this study. Last but not least, the authors want to express grateful thanks to Endra Susila, PhD, for his helpful discussion.

References

- ASCE (2010) Minimum design loads for buildings and other structures, ASCE/SEI 7-10. Standard published American Society of Civil Engineers, Reston
- Atkinson G, Boore D (1995) New ground motion relations for Eastern North America. *Bull Seismol Soc Am* 85:17–30
- Atkinson GM, Boore DM (2003) Empirical ground-motion relations for subduction zone earthquakes and their application to Cascadia and other regions. *Bull Seismol Soc Am* 93 (4):1703–1729

- Bappenas (2005) Indonesia: the preliminary damage and loss assessment the 26 December 2004 natural disaster, a technical report
- Bappenas (2006) The preliminary damage and loss assessment Yogyakarta and Central Java Natural Disaster, a technical report, Jakarta
- Bappenas (2007) Report of damage and loss assessment post earthquake disaster in Bengkulu and West Sumatra provinces, a technical report.
- Bappenas (2009) Action plan for the rehabilitation and reconstruction post-earthquake disaster areas in the province of West Java and district Cilacap, Central Java Province, 2 September 2009, a technical report
- Bappenas (2010) Action plan for the rehabilitation and reconstruction accelerated development post earthquake and tsunami disaster in the district of Mentawai, West Sumatra Province, a technical report
- Boore DM, Atkinson GM (2008) Ground-motion prediction equations for the average horizontal component of PGA, PGV, and 5%-damped PSA at spectral periods between 0.01 s and 10.0 s. *Earthq Spectra* 24(1):99–138
- Campbell KW, Bozorgnia Y (2008) Ground motion model for the geometric mean horizontal component of PGA, PGV, PGD and 5%-damped linear elastic response spectra for periods ranging from 0.01 to 10.0 s. *Earthq Spectra* 24(1):139–171
- Chiou B, Youngs R (2008) A NGA model for the average horizontal component of peak ground motion and response spectra. *Earthq Spectra* 24(1):173–215
- Crouse CB (1992) Seismic hazard evaluation offshore Northwest Java-Indonesia-Maxus/ARII Offshore Area Indonesia
- Frankel A (1995) Mapping seismic hazard in the central and eastern United States. *Seismol Res Lett* 66(4):8–21
- Grundy P (2010) The Padang earthquake 2009 – lessons and recovery, Australian Earthquake Engineering Society 2010 conference, Perth, Western Australia
- International Federation of Red Cross and Red Crescent Societies (2005) Nias earthquake, information bulletin no. 03/2005
- Irsyam M, Asurifak M, Hendriyawan BB, Triyoso W, Firmanti A (2010) Development of spectral hazard maps for proposed revision of Indonesia seismic building code. *Geomech Geoenviron Int J* 5(1):35–47. doi:[10.1080/17486020903452725](https://doi.org/10.1080/17486020903452725)
- Kramer SL (1996) Geotechnical earthquake engineering. Prentice Hall, Upper Saddle River
- Natawijaya DH (2002) Neotectonics of Sumatran fault and paleogeodesy of the Sumatran subduction zone. Doctor of philosophy thesis. California Institute of Technology, Pasadena
- Sieh K, Natawidjaja D (2000) Neotectonics of the Sumatran fault, Indonesia. *J Geophys Res* 105:28295–28326
- Silver EA (1978) The Molucca Sea collision zone, Indonesia. *J Geophys Res* 83:1681–1691
- Standar Nasional Indonesia (2002) Tata cara perencanaan ketahanan gempa untuk bangunan gedung (SNI 03-1726-2002), Badan Standardisasi Nasional
- Wells DL, Coppersmith KJ (1994) New empirical relationships among magnitude, rupture length, rupture width, and surface displacements. *Bull Seismol Soc Am* 84:974–1002
- Youngs RR, Chiou SJ, Silva WJ, Humphrey JR (1997) Strong ground motion attenuation relationships for subduction zone earthquakes. *Seismol Res Lett* 68:58–73
- Zhao John X, Zhang J, Asano A, Ohno Y, Oouchi T, Takahashi T, Ogawa H, Irikura K, Thio H, Somerville P (2006) Attenuation relations of strong motion in Japan using site classification based on predominant period. *Bull Seismol Soc Am* 96:898

Chapter 4

Lessons Learned from the Recent Natural Disasters in Indonesia

Sri Prabandiyani Retno Wardani and Agus Setyo Muntohar

4.1 Introduction

Indonesia has 245 million people located in the world's largest archipelago on the Ring of Fire who are at risk from earthquakes, tsunamis, volcanoes, and landslides. Earthquakes, tsunamis, and volcanoes occur as a result of ongoing subduction of the Indo-Australian plate in the vicinity of Indonesia. It is one of the seismic sources in this area. High frictional stresses also cause medium earthquakes on the overriding plate that are often observed within and to the south of the island. The megathrust region to the west-northwest of Sumatera and Java has also caused colossal earthquakes, as the region is subject to medium, large, and massive earthquakes. Several major earthquakes recently occurred in Aceh in 2004, Nias in 2005, Yogyakarta, West Java and West Sumatra in 2006, Bengkulu and West Sumatra in 2007, and West Java and West Sumatra in 2009. Some of these were followed by large tsunamis that claimed the lives of hundreds of thousands of people and damaged half a million structures. The social and economic consequences of these earthquakes are tremendous.

Most of the islands in Indonesia form part of an active volcanic mountain chain. Geotectonic activities in the terrain consist of extremely complex morphostructural units within an uplifted sedimentary and frequently active volcanic mountain system. Weathered soils are commonly found in Indonesia as a result of volcanic activity. The soils predominantly consist of clay and sandy mixtures. The weathered soils are layered on the impermeable soil and rock. The geomorphologic

S.P.R. Wardani, Ph.D. (✉)
Department of Civil Engineering, Diponegoro University,
Jl. Hayam Wuruk, 5-7, 50241 Semarang, Indonesia
e-mail: wardani_spr@yahoo.com

A.S. Muntohar, Ph.D.
Department of Civil Engineering, Universitas Muhammadiyah, Yogyakarta, Indonesia
e-mail: muntohar@umy.ac.id

features of many slopes in Indonesia are similar in that they consist of folded marls or weathered volcanic deposits overlain by sequences of colluvium derived from volcanic breccia and ash. Massive deposits of these porous breccia and ash materials occur on the steeper sections of slopes to form huge collection areas of groundwater. Indonesia has a climate that provides one of the most active chemical-weathering environments to be found anywhere in the world. However, for tens of thousands of years, volcanic processes and tectonic uplift resulted in accretion rates that kept pace with denudation. Consequently, the terrain and particularly its slopes are in a constant phase of adjustment to the two processes. Periods of peak rainfall occur between January and February and again between March and early May. This corresponds to the times when the majority of landslides and high rainfalls occur.

4.2 Recent Earthquakes

Geologically, Indonesia lies on active tectonic plates. Hence, earthquakes occur daily in the region, and those with a 5-Mw magnitude or larger happen weekly. Figure 4.1 shows the epicenters of recorded earthquakes in Indonesia during 1992–2000 (BMKG, USGS 2009). Earthquakes struck West Java on September 2, 2009 and West Sumatera on September 30, 2009.

4.2.1 Padang Earthquake

A 7.6-Mw earthquake hit Padang on September 30, 2009. The epicenter was about 60 km northwest of Padang, at a depth of more than 120 km. The Mentawai Fault was responsible for this earthquake. This fault is parallel to the Sumatra Fault and situated between the trench and the Sumatera fault (Fig. 4.2) (Shieh 2009). Many aftershocks occurred, and more were expected in the days and months ahead. Most aftershocks are at least two degrees of magnitude smaller than the main shock, such as the first reported aftershock, which was 5.5 Mw. The 6.6-Mw earthquake on October 1 appears to not have been an aftershock strictly speaking. It occurred more than 200 km away from the September 30 earthquake rupture on a section of the Sumatran fault. That fault produced many large (7–7.5 Mw) earthquakes between 1892 and 1953, but had been mostly quiet for the past half-century. Figure 4.3 shows the relationship of the September 30, 2009 earthquake to the September 2007 ruptures (Konca et al. 2008). The earthquakes in September 2009 years ago were caused by fault ruptures farther to the south from Padang. The seismic intensity distribution of the earthquake was shown in Fig. 4.4 (BMKG, USGS 2009, USGS). In Padang and Pariaman, the reported earthquakes were greater than VII on the Mercalli scale. At those locations, there was heavy damage to both infrastructures and lives.

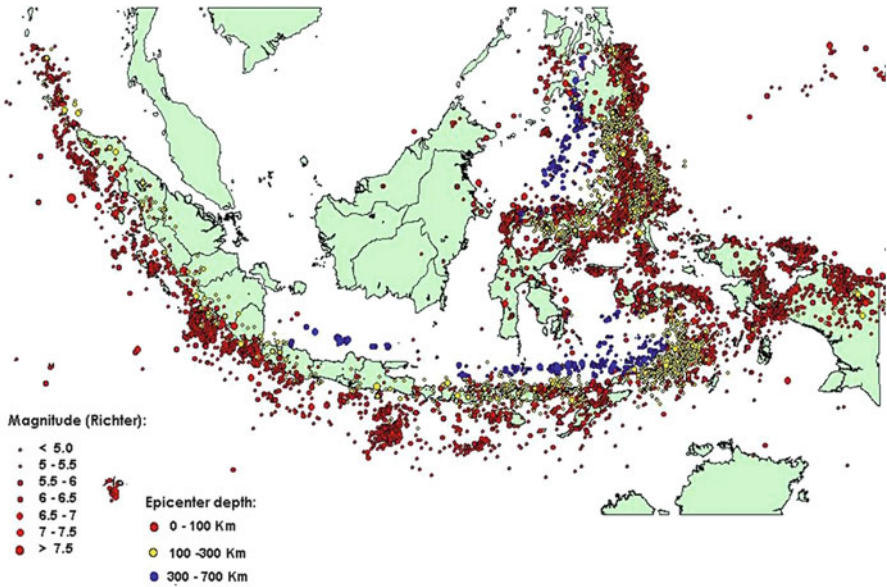


Fig. 4.1 Recorded earthquake in Indonesia during 1992–2000 (BMKG, USGS 2009)

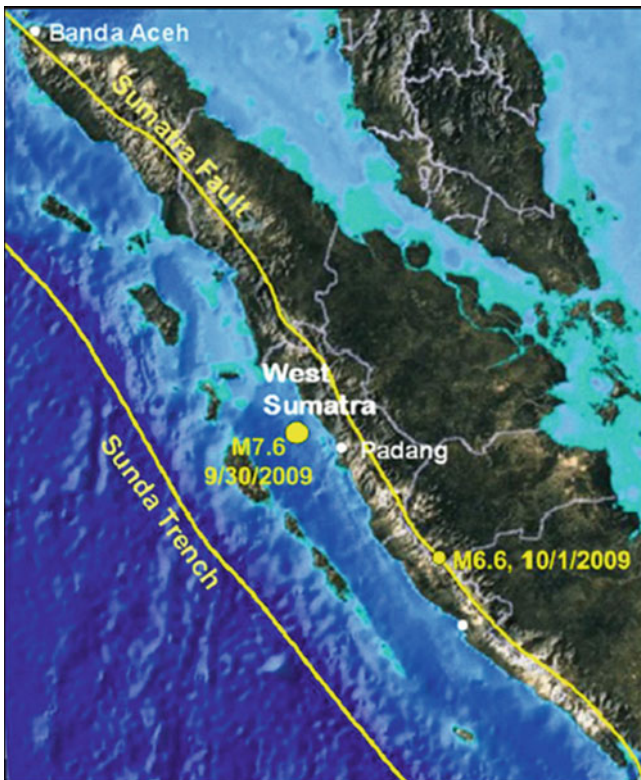


Fig. 4.2 Location of the September 30 and October 1 earthquake epicenters on the Sunda thrust fault and Sumatra strike-slip faults (Shieh 2009)

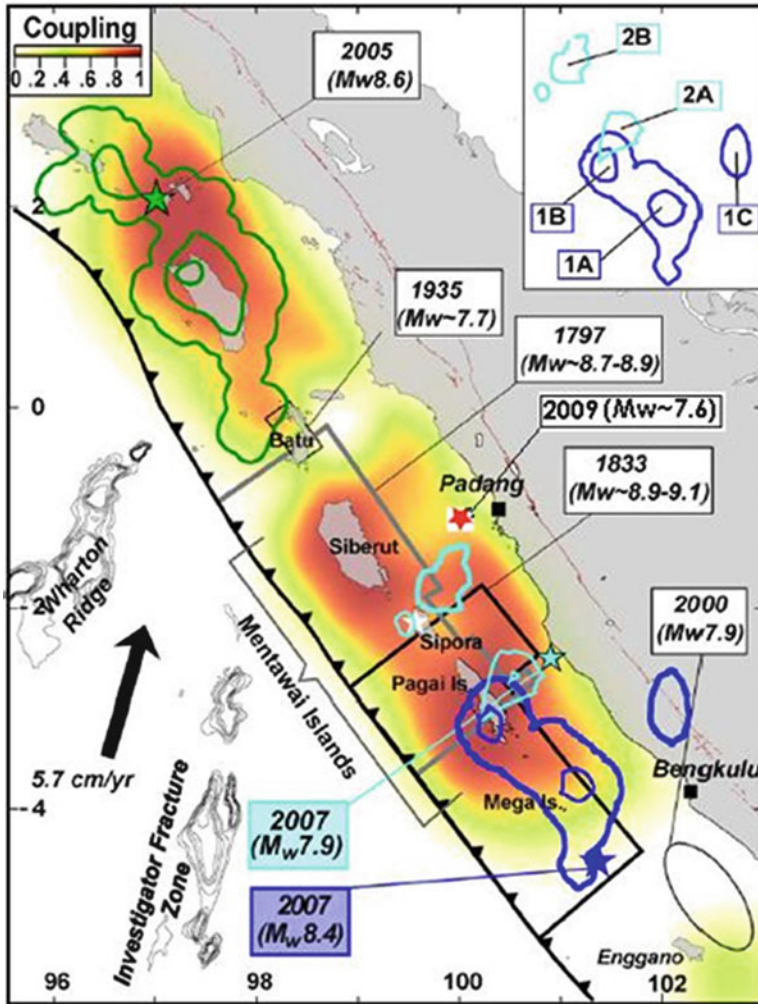


Fig. 4.3 Patches with strong interseismic coupling on the Sunda megathrust, offshore Sumatra, coincide with large seismic ruptures (Konca et al. 2008)

The shaking ground induced landslides and subsequently collapsed slopes at various spots in the mountain areas. As a result, many access roads were cut off, thus creating a significant amount of time to grasp the damage in the affected areas. Extensive landslides in Padang Pariaman resulted in high casualties; three small villages were buried (Fig. 4.5). Observations of the spoil site showed that the pumiceous tuff originating from late eruptions of the Maninjau caldera was light and porous and had little cohesion. Heavy rain over several days before the earthquake probably saturated the ground, increasing the driving force and

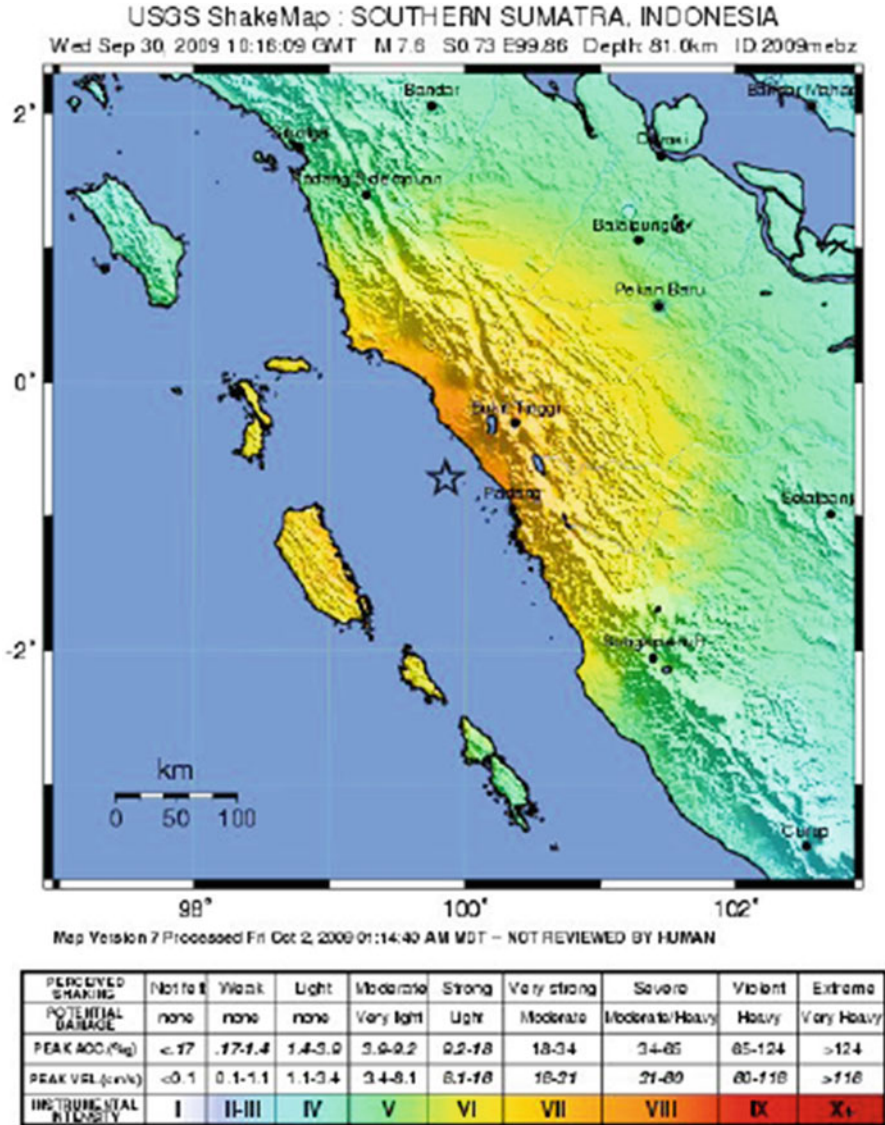


Fig. 4.4 Earthquake intensity map on September 30, 2009 (USGS)

weakening the soil resistance, causing the slope to be marginally stable. The flat lands below the hills at the toe of the hills, consisting mainly of loose silt, sand, and gravel mixtures, may have also lost lateral support and contributed to the massive landslides as well as debris and mud flows (Fig. 4.6). In highland areas, the heavy rain and earthquake caused near-surface loose colluvium to slide (EERI 2009).



Fig. 4.5 Massive landslides occurred in Pariaman: a village below this slide was buried



Fig. 4.6 Debris flows in rural areas northeast of Pariaman

Liquefaction occurred during the quake. Ground amplification of the seismic waves, which was particularly damaging to taller buildings, was reported with a longer natural period. Eyewitnesses described visible ground waves from the earthquake. Most liquefaction and lateral spreading were observed at the area near the coast (Fig. 4.7).



Fig. 4.7 Lateral spreading affecting the Seafront road (Jalan Samaudra) in Padang

4.2.2 West Java Earthquake

On September 2, 2009, a 7.3-Mw earthquake struck the Tasikmalaya District, West Java Province, at a depth of 30 km. A second 5.1-Mw earthquake followed at 3:15 p.m. at a depth of 38 km. A third 5.4-Mw earthquake struck at 4:28 p.m. at a depth of 15 km. A tsunami warning was issued but was withdrawn 1 h later. Affected districts and municipalities included Bogor, Cianjur, Sukabumi, the municipality of Sukabumi, West Bandung, Bandung, Garut, Banjar, Ciamis, the municipality of Tasikmalaya, and Purwakarta. The shaking was felt widely on Java, with maximum MMI intensities of VII at Tasikmalaya, VI at Cianjur and Sukabumi, V at Bandung, and IV at Jakarta. Figure 4.8 shows the earthquake intensity distribution and the damage level of the affected area; a historical earthquake in West Java is shown in Fig. 4.9 (USGS).

An earthquake induced a huge landslide at Cikangkareng; it buried 12 houses and killed 30 people (Fig. 4.10). The slopes of the region were very steep, about 80–90°, whereas the village was located near the slope. The geologic setting of the region was formed with sedimentary rock that consists of sandstone, tuff, and breccias (Koesmono et al. 1996). During the dry season, the rock weathered and

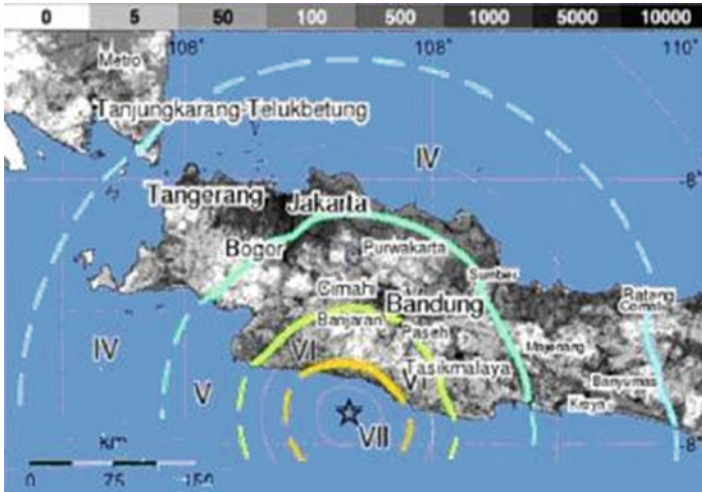


Fig. 4.8 Earthquake intensity distribution on September 2, 2009 quake off the south coast of West Java (USGS)

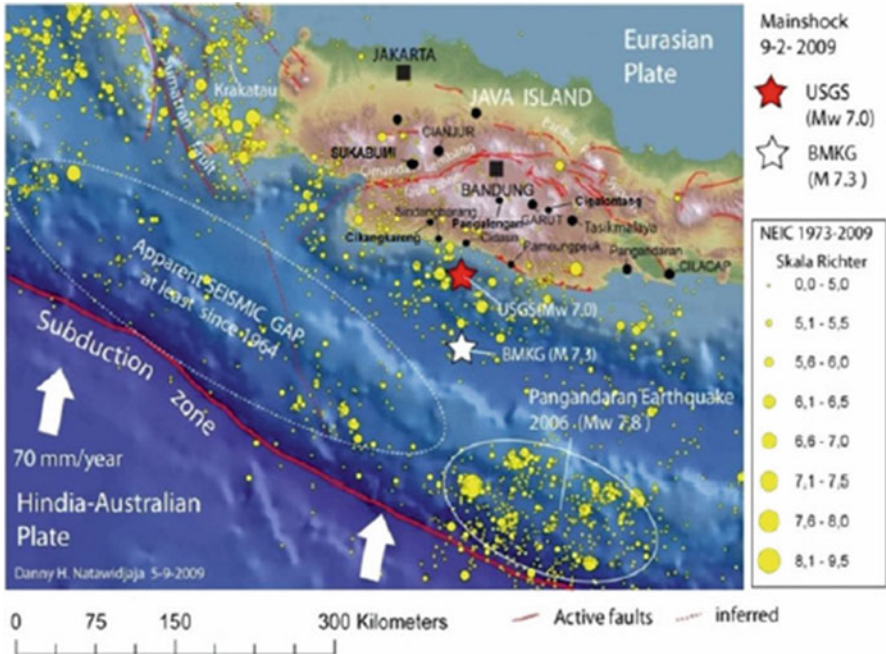


Fig. 4.9 General seismotectonic map of the West Java region (USGS)



Fig. 4.10 Landslide induced by earthquake at Cikangkareng, Cianjur: landslide source (*top*); rock debris materials covered village (*below*)

resulted in sandy silt and sandy clay. A joint was formed and a fissure was found near the ground surface. Consequently, the slopes collapsed easily during ground shaking when the earthquake occurred on September 2, 2009. Landslide materials such as rock and earth fall and flow quite fast and ruin villages (Fig. 4.10).

Liquefaction occurred during the earthquake. The ground shaking triggered mudflow at Pasir Gede, Sukahening village (Fig. 4.11). The area is located at $S07^{\circ}12'34,6''$ and $E108^{\circ}08'08,7''$. Based on interviews of local people, similar



Fig. 4.11 Sand boiling at Kp. Pasir gede, Sukahening village, Sukahening, Tasikmalaya

mud flows occurred in 1952 and 1982. According to the geology map (Budhitirina 1986), the mud flow location was laid on volcano sediment, breccia, lahar, and tuff underlain with andesite and basalt from the Talagabodas volcano. There was no fault observed in the mud flow region. However, the quake was possibly caused by a shear joint adjacent the aquifer layers. As a result, the gray color of mud flowed out with water because of pressure from the aquifer.

4.2.3 Lesson Learned

The two deadly earthquakes in September 2009 can act as a warning for the society and government to enhance disaster management preparedness. The disaster management law of the Republic of Indonesia No. 24/2007 contains paradigm shifting about the disaster, including preparedness, emergency response, and rehabilitation and reconstruction. Based on the recent earthquake overview, disaster preparedness was low. According to research on the preparedness index conducted by the Indonesian Institute of Science (LIPI 2007), disaster preparedness in the community was quite low. Household, government, and school communities must become aware of possible disasters and enhance their capacity to manage disaster risk.

It can be learned from the massive landslides in Pariaman and Cingkakareng that the community must be aware of and understand collateral disaster risk. The recent earthquake also pointed out the lack of an earthquake-induced landslide early

warning system (ELEWS). At the moment, the community and government focus on a rainfall-induced landslide early warning system. Hence, an integrated landslide warning system needs to be built.

4.3 Collapse of Situ Gintung Dam

4.3.1 Disaster Overview

On Friday morning, March 27, 2009, at 2:00 a.m., the Situ Gintung dam burst in Cirendeu, Ciputat, Tangerang, Banten Province (Fig. 4.12). The dam failure was triggered by torrential rains. The water in the reservoir, about 15-m wave of water, flushed into houses and villages downstream (Fig. 4.12). The dam was originally built by Dutch colonial authorities in 1933. It was made from earth compacted into a wall 16 m high, and the reservoir held at least two million cubic meters of water. The original imperative of the dam had been to retain water for irrigation of rice paddies, which were subsequently replaced by urban development.

Heavy rain was indicated as the triggering factor for the dam failure. On March 26, 2009 at 4.00–7.00 p.m., the nearest rainfall station in Ciputat (Balai II) recorded a rainfall duration of about 4 h, with accumulated rainfall of about 113 mm (BMKG 2009). The rainwater caused the water level in the reservoir suddenly rise. However, overflow of the water could not spill out through outlet tunnel because the spillway and outlet malfunctioned. Consequently, the water overtopped the crest of the earth dam. The overtopping caused some piping and cracks at the toe downstream of the dam. The piping allowed water to infiltrate the capillary breaks that caused the dam to collapse. Piping was also identified by eyewitnesses in December 2008.



Fig. 4.12 Collapse of the Situ Gintung dam on March 27, 2009

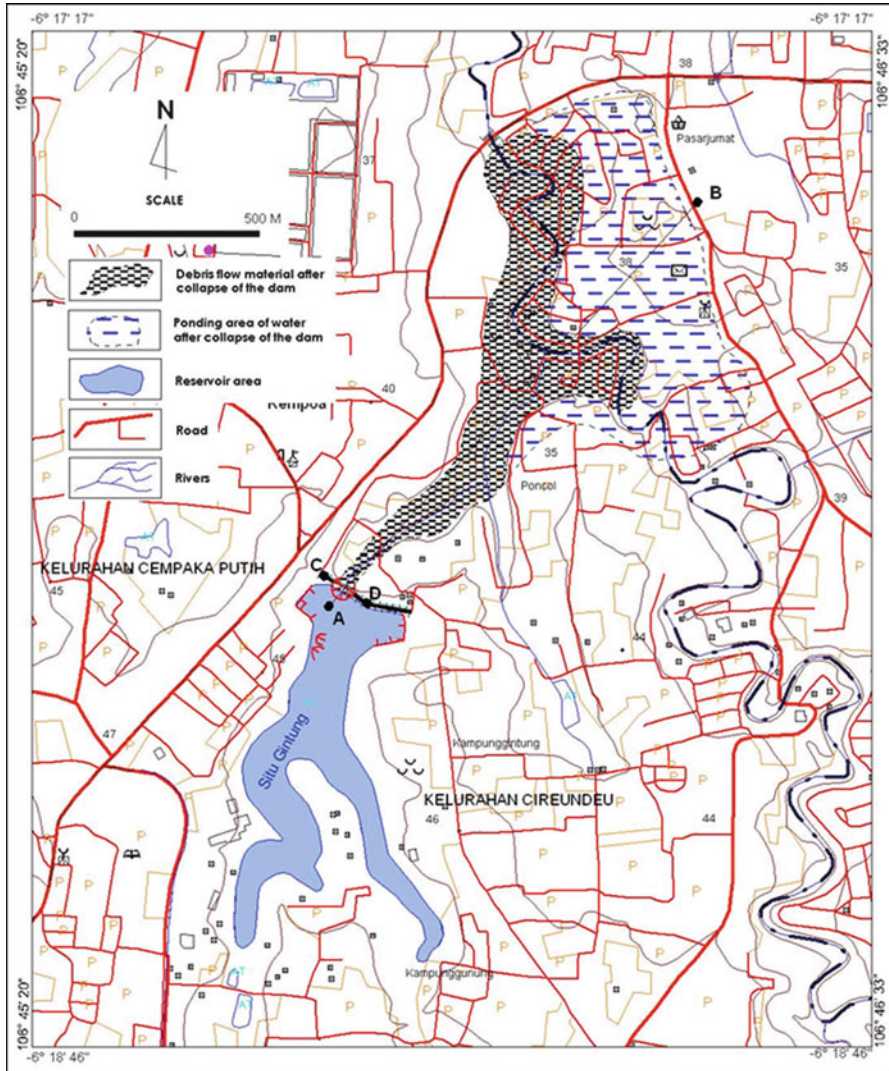


Fig. 4.13 Catchment area of Situ Gintang and the location of debris materials after the collapse of the dam

4.3.2 Lesson Learned

The area surround the Situ Gintang dam has developed into a populated settlement. According to the spatial planning law of the Republic of Indonesia No. 24/1992 or the current spatial planning law No. 26/2007, the Situ Gintang area is supposed to be a conservation area. Assigning the Situ Gintang area as a conservation area means only activities protecting the environmentally sensitive area of Situ Gintang

are allowed in the area. Residential buildings are certainly not allowed in conservation areas such as Situ Gintung.

To reduce disaster risk, mitigation has to be implemented continuously. Many dams in Jakarta and other regions are also located in heavily populated areas. An early warning system (EWS) has to be built to reduce the risk. An EWS includes routine maintenance of the dam, improving land use, and spatial planning, empowerment, and participation of the local society (Fig. 4.13).

4.4 Concluding Remarks

The location of Indonesia in the Ring of Fire puts the country at high risk of collateral disaster. The recent earthquakes in West Java and West Sumatera provide insight about collateral hazards. Damage and loss of some settlements and villages in Pariaman and Cingkangkareng caused by massive landslides resulting from earthquakes indicate that the early warning system, including the hazard map, was inadequate. To overcome this problem, establishing research collaboration among governments, universities, and research centers is needed to build an integrated early warning system in Indonesia. Also, when spatial planning, one has to consider the disaster risk area. Although constitutional law about spatial planning and settlement exists, enforcement must be strictly imposed and the rules must be obeyed.

References

- BMKG (2009) Analisis Curah Hujan Seputar Jebolnya Tanggul Situ Gintung. Stasiun Klimatologi Pondok Betung-Tangerang. Badan Meteorologi, Klimatologi dan Geofisika, Jakarta
- BMKG/USGS (2009) September 30, 2009 Strong ground motion record from Padang, Recorded by BMKG. <http://www.bmg.go.id/depan.bmg>. Accessed 2 Dec 2009
- Budhitrina T (1986) Peta Geologi Regional Lembar Tasikmalaya. Geology Survey of Indonesia
- EERI (2009) Learning from earthquakes the Mw 7.6 Western Sumatra earthquake of September 30. EERI special earthquake report
- Koesmono M, Kusnama, Suwarna N (1996) Peta Geologi Lembar Sindang Barang Dan Bandarwaru. Geology Survey of Indonesia, Bandung
- Konca AO, Avouac JP, Sladen A, Meltzner AJ, Shieh K, Fang P, Li ZH, Galetzka J, Genrich J, Chlieh M, Natawidjaja DH, Bock Y, Fielding EJ, Ji C, Helmberger DV (2008) Partial rupture of a locked patch of the Sumatra megathrust during the 2007 earthquake sequence. *Nature* 456:631–635
- LIPI (2007) Kajian Kesiapsiagaan Masyarakat Dalam Mengantisipasi Bencana Gempa Bumi & Tsunami. Research report. Indonesian Institute of Science, Jakarta
- Shieh K (2009) Padang earthquake struck at edge of zone where much bigger quake is expected. <http://www.earthobservatory.sg/news/2009/>, Accessed on 2 Dec 2009
- USGS. <http://www.usgs.gov>

Chapter 5

Behavior of Slope Protection and Retaining Structures During the Wenchuan Earthquake on May 12, 2008

Jianhui H. Deng, Fei Chen, Jinbing B. Wei, and Jiajia J. Tai

5.1 Introduction

At 14:28 on May 12, 2008, a strong earthquake measuring Ms 8.0 hit the Longmenshan mountain area in the west Sichuan province of China. The quake was induced by the thrust of the Longmenshan central fault, which resulted in approximately 50,000 rock avalanches and landslides (Xu Chong et al. 2009), destroying numerous villages and towns and causing nearly 90,000 people to die or go missing.

After the quake, the authors conducted an approximately 3-month field reconnaissance to the quake-hit area. This chapter mainly addresses the behaviors of commonly used slope-protecting or -retaining structures. Protecting structures refer to gravity retaining walls, protecting nets, and shotcrete, which does not add much force to reinforce a slope, but can protect the slope from further erosion, weathering, or local collapse. The term “retaining structures” refers to slide-resistant piles, anchored concrete frames, and cable bolts, whose basic function is to hold up a slope from deformation or slide through the interaction of structures and slope materials.

Geographic names cited in the chapter are illustrated in Fig. 5.1, along with epicenter and intensity contours. Most of the cases are located in the area of the Zipingpu reservoir, through which the national highway G213 and Dujiangyan-yingxiu expressway pass, and the earthquake intensity is IX–XI. Other cases are in Beichuan county, the Gucheng and Pubugou hydropower projects.

J.H. Deng, Ph.D. (✉) • F. Chen • J.B. Wei • J.J. Tai
Water Resources and Hydropower Engineering, Sichuan University, Chengdu, China
e-mail: jhdeng@scu.edu.cn

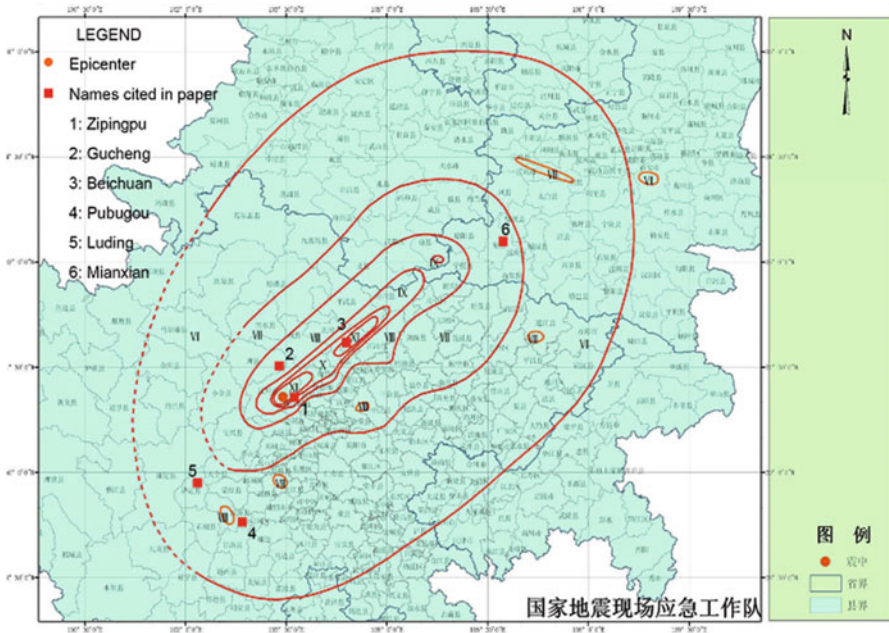


Fig. 5.1 Distribution of earthquake intensity and geographical names cited in the chapter

5.2 Geologic Background of the Longmenshan Fault Belt

As shown in Fig. 5.2, the Longmenshan fault belt extends approximately 500 km from the Luding county of the Sichuan Province in the southwest to the Mianxian county of the Sha'anxi Province in the northeast. The belt consists of four major faults—the back fault, the central fault, the front fault, and the buried fault in front of the mountain—and its total width is 30–40 km. The faults strike at 30–50° and dip to the northwest with a dip angle of 50–70°. The shattered fault zone is 10–100 m wide (Tang Rongchang and Han Weibin 1993).

The belt is famous for its nappe tectonic and klippe. It was first formed during Indo-China movement in the late Triassic period, then reactivated during Yanshan movement in the early Cenozoic era, and continuing into new tectonic movement; that is, Himalayan movement, making large-scale nappe tectonics to occur, the mountain to rise further, and the piedmont basin to relatively subside (Jin et al. 2008). Traditionally, the belt is divided into three segments, a north segment (north of Beichuan county), a middle segment (between Beichuan and Dujiangyan city), and a south segment (south of Dujiangyan city). The middle and south segments are considered to be more active than the north segment (Tang Rongchang et al. 1991), and the most recent research shows that the middle segment is the most active since the Pleistocene era and has the potential to create a strong earthquake, whereas the activity of the north segment weakened gradually in the Quaternary period and basically ceased after the Pleistocene (Chen Guoguang et al. 2007).

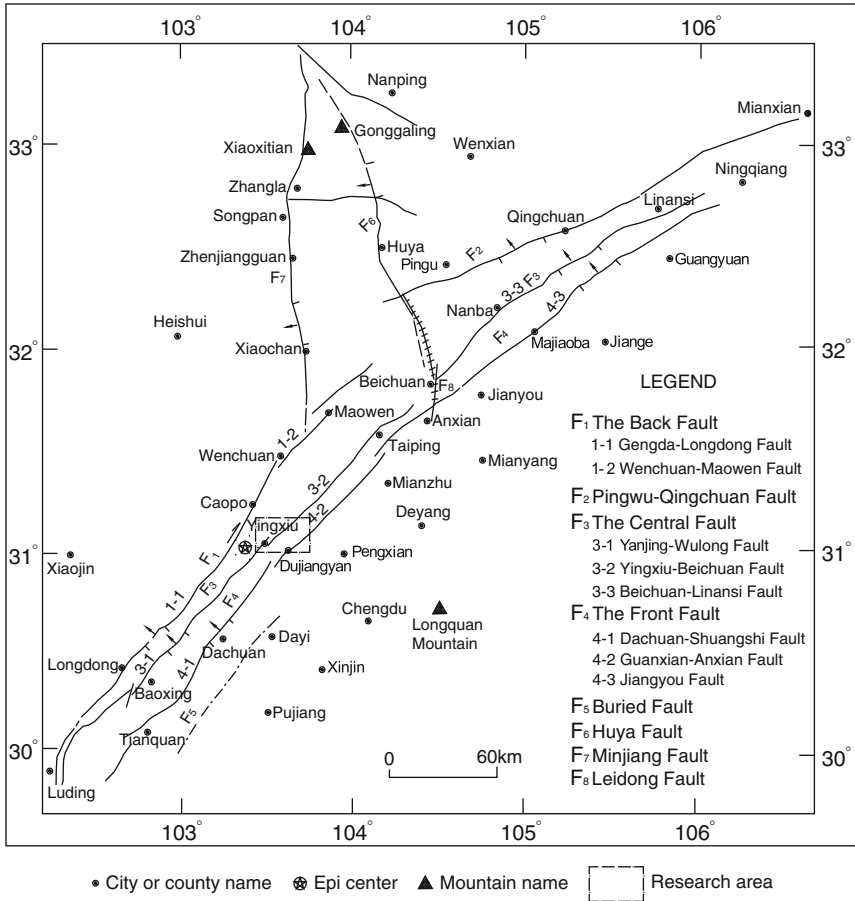


Fig. 5.2 Configuration of the Longmenshan fault belt (revised from Xie et al. 2008)

Rock types in the middle and south segments are also different from those in the north segment. In the middle and south segments, igneous rock, mainly granite and partly diorite and gabbro (Guanxian-Anxian Complex and Kangding Complex) from the middle to late Proterozoic period were distributed to the west of the central fault, whereas sedimentary, mainly clastic rocks of Triassic period, were distributed to the east and overlaid by limestone of the Devonian, Carboniferous, and Permian periods (klippe). In the north section, the metamorphosed limestone, sandstone, shale, and so on of the Sinian, Cambrian, and Silurian periods were distributed to the west of the central fault, and un-metamorphosed mudstone, sandstone, limestone, and dolomite of the Paleozoic to the Mesozoic era lay to the east.

5.3 Behavior of Protecting Structures

5.3.1 Gravity-Retaining Walls

Most of the retaining walls, both concrete and mason, along highway G213 from Dujiangyan to Yingxiu were well kept, although some failures did exist. The images in Fig. 5.3 show insufficient wall thickness and poor mortar quality in the mason retaining walls. Poor aggregates and unstable foundations are the main reasons for the failure of the concrete retaining walls (Fig. 5.4).

5.3.2 Protecting Nets

Protecting nets can be divided into active and negative nets. They are widely used in slope engineering with rockfall problems. This measure is effective when the rockfall is scarce and occasional. Along highway G213 and at the Zipingpu dam site, most of the active nets worked quite well (Fig. 5.5a); however, some failures occurred (Fig. 5.5b).

An earthquake causes a great amount of loosened rock blocks to fall, and negative nets are useless in this situation (Fig. 5.6). Although the Pubugou hydro-power project is approximately 210 km south of the epicenter and the quake's intensity was only VI, the failure caused a shepherd to die.

5.3.3 Shotcrete

Shotcrete is often used to protect a rock slope from rockfall and further weathering, or a soil slope from erosion and rainfall infiltration. As can be seen in Fig. 5.5b, the behavior of this structure was adequate during the earthquake. The major problem was cracking, and surface movement also existed within the soil slope (Fig. 5.7).

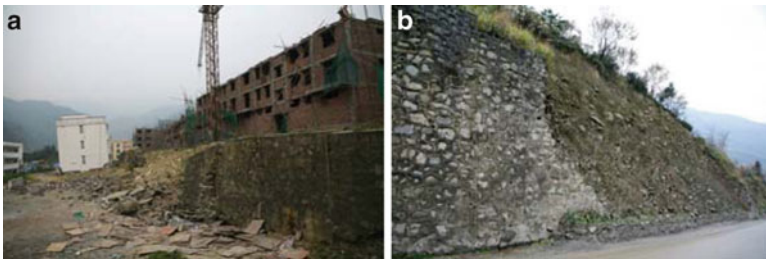


Fig. 5.3 Failures of mason retaining wall (a) Xuankou town. (b) Highway G213 near Yingxiu town

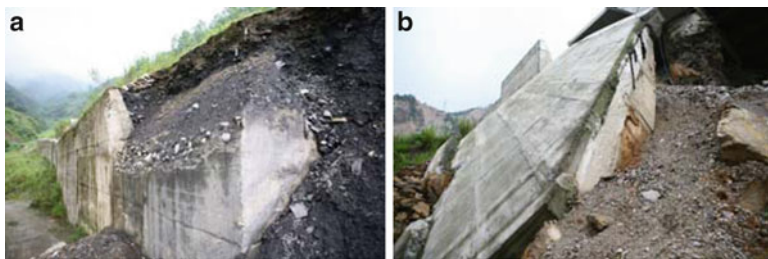


Fig. 5.4 Failures of concrete retaining wall along the Dujiangyan-Yingxiu expressway. (a) Poor aggregate. (b) Unstable foundation

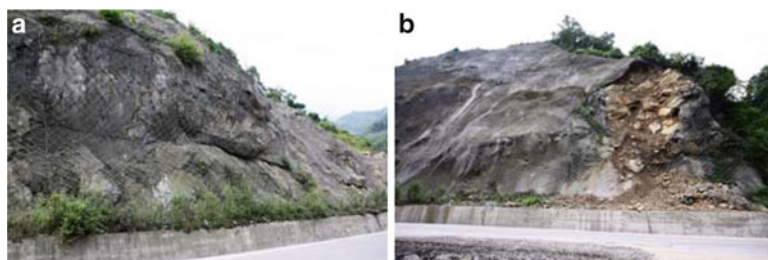


Fig. 5.5 Active nets along road G213



Fig. 5.6 Failure of a negative net at the Pubugou dam site



Fig. 5.7 Failure of shotcrete along highway G213



Fig. 5.8 Behavior of anchored concrete frame along the Dujiangyan-Yingxiu expressway

5.4 Behavior of Retaining Structures

5.4.1 *Anchored Concrete Frames*

The anchored concrete frames withstood the earthquake: Fig. 5.8 is a good example. Anchored concrete frames are suitable retaining structures for soil or fractured rock slopes.



Fig. 5.9 Wangjiayan landslide in Beichuan county

5.4.2 Slide-Resistant Piles

Piles have the advantage of good durability and are a widely used remedial measure for reinforcing landslides and unstable slopes. In addition, pile pits are usually excavated manually in mainland China, and their construction quality can be easily controlled, thus ensuring their performance during an earthquake. The Wangjiayan landslide in Beichuan County is a good example (Fig. 5.9). The slide destroyed half of the old town and caused more than 1,600 fatalities; however, the pile-reinforced part remained stable, thus protecting 600 lives. Other examples can also be found in the quake-hit area (Fig. 5.10), although the piles deformed or tilted to some extent. For this kind of structure, the problem may come from the landslides or collapse high above the piles (Fig. 5.11).

5.4.3 Cable Bolts

Cable bolts are mainly used to reinforce high slopes or potentially unstable landslide bodies. In hydropower engineering, almost every cut slope in the dam site is reinforced by cable bolts to ensure the safety of the structure at its toe. The experience of the Wenchuan earthquake proved that this type of structure is effective, as no failure was ever witnessed on slopes reinforced by cable bolts. The slopes at the Zipingpu dam site are good examples (Fig. 5.12). Only the unreinforced part experienced failure, whereas the reinforced part remained intact, although some permanent deformation did appear, as can be seen in Table 5.1 (Peng Shixiong and Song Shengwu 2009).



Fig. 5.10 Piles in Xuankou town along highway G213



Fig. 5.11 Buried piles in Yingxiu town along the Dujiangyan-Yingxiu expressway

Stress release or increase is observed in some projects. The outlet slope of the tailrace tunnels at the Pubugou hydropower project is an example (Table 5.2). The design capacity of the cables is 2,000 kN. Because of the slope deformation, the cables experienced fast stress increase before May 12, 2008 and their tonnage exceeded the design capacity of approximately 25%. The quake caused the tonnage to reduce 89.43 and 39.26%, respectively. The layout of instruments as well as their measurements are illustrated in Fig. 5.13. From these measurements it can be observed that no permanent deformation to the slope was induced by the quake. The stress loss was probably the result of a loosened cable anchor caused by the quake-induced high transient stress increase because the anchor was located near the fracture zone of Fault F1.

Another example is the back slope of the powerhouse in the Gucheng Hydropower project, Lixian County, Sichuan Province, as shown in Table 5.3. Except for



Fig. 5.12 The right bank slope at the Zipingpu dam site

Table 5.1 Earthquake-induced slope deformation at the Zipingpu dam site

Slope name	Height (m)	Maximum deformation (mm)	Protecting or retaining measure
Intake tunnel	90	11.52	Cable bolt
Outlet tunnel	100	4.15	Cable bolt
Spillway	250	Upper: 27 Lower: 6.68	Upper: anchored concrete frame; Lower: cable bolt, systematic rebar and shotcrete with steel mesh
Flood discharge tunnel	85	Upper: 22 Lower: 6.53	Upper: systematic rebar and shotcrete with steel mesh; Lower: cable bolt

Table 5.2 Stress loss of cable bolts at the Pubugou dam site

Date	PR13		PR15	
	Tonnage	Loss ratio	Tonnage	Loss ratio
2008-5-5	2,591.07		2,496.02	
2008-5-15	273.98	89.43	1,516.13	39.26

PR3, all the stresses in the other five cable bolts increased by 2.14–44.9 %, corresponding to the slope movement (Fig. 5.14); therefore, cable bolts play an important role in slope safety. However, from early September, only the stress of the PR1 was maintained, the stresses of the other five cable bolts began to lose, and by the end of 2008 the maximum lose rate was 95.12 % because the stresses exceeded the design capacity of the cables.

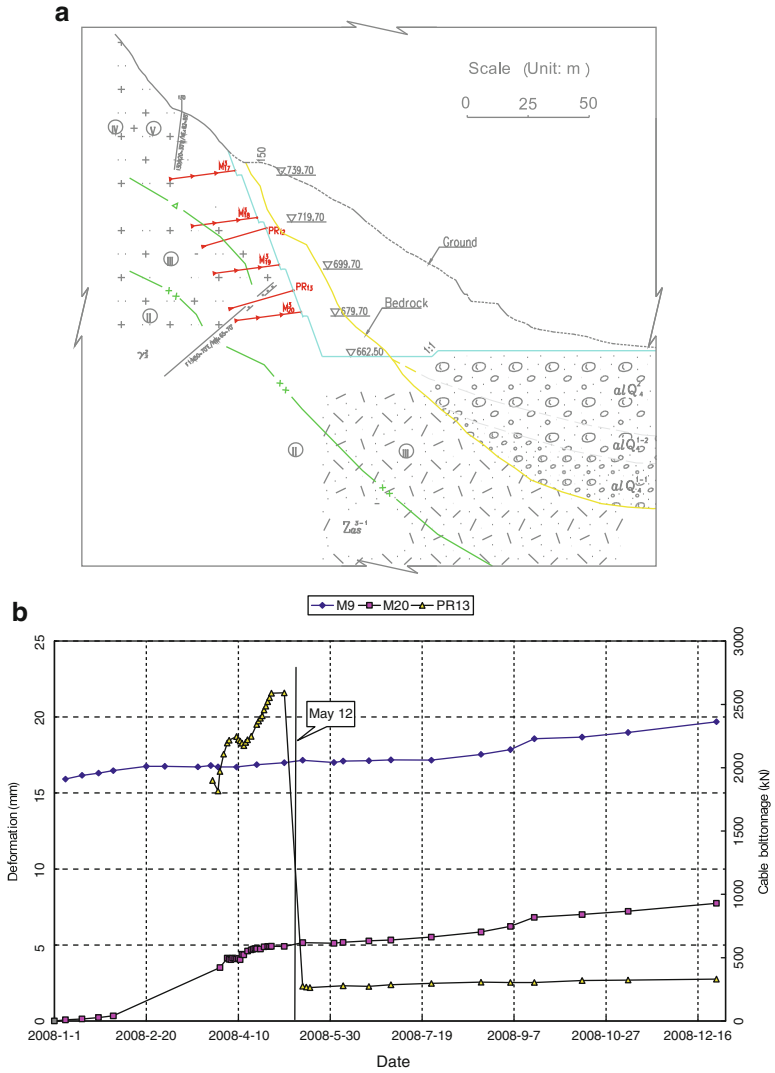


Fig. 5.13 Failure of cable bolts at the Pubugou hydropower project. (a) Layout of instruments. (b) Comparison between deformation and cable tonnage.

5.5 Conclusion

The lesson learned from the Wenchuan earthquake is that all cut slopes should be protected or retained in quake-prone areas, even when their geology is good. Compared with other roads in the quake-hit area, slope failures along the roads from Dajiangyan to Yingxiu were trivial, which saved many precious lives.

Table 5.3 Stress loss of cable bolts at the Gucheng dam site (unit: kN)

Date	PR1		PR2		PR3		PR4		PR5		PR6	
	Tonnage	Loss rate	Tonnage	Loss rate	Tonnage	Loss rate	Tonnage	Loss rate	Tonnage	Loss rate	Tonnage	Loss rate
2008-5-10	962.53		2,314.94		1,671.97		1,942.96		2,405.84		2,188.81	
2008-7-16	1,394.72	-44.90	2,941.76	-27.08	672.58	59.77	2,607.81	-34.22	2,457.39	-2.14	2,819.42	-28.81
2008-12-30	1,468.78	-52.60	300.83	87.01	81.52	95.12	139.79	92.81	500.68	79.19	1,609.78	26.45

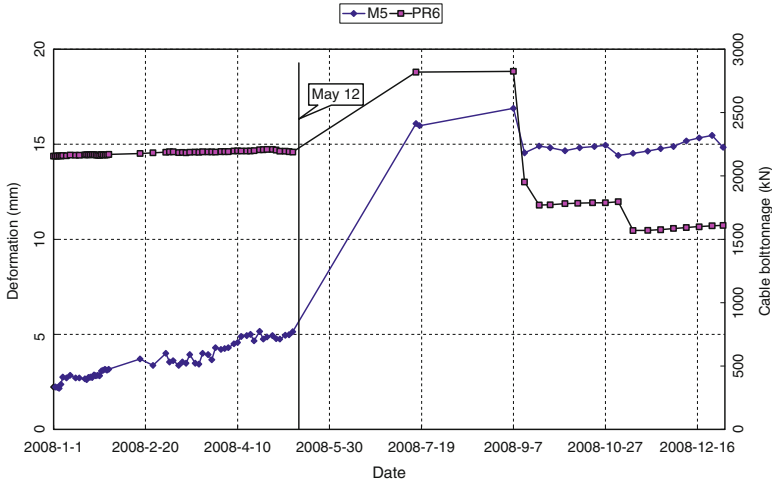


Fig. 5.14 Comparison between deformation and cable tonnage at the Gucheng dam site

Except for the negative net, all other protecting or retaining structures are effective if their construction quality is confirmed. For protecting structures, it is important to ensure that the slope is basically safe under an earthquake. Slide-resistant piles have sufficient redundancy to withstand earthquake surpassing their design intensity, whereas the design capacity of cable bolts should have some redundancy to resist the high transient stress induced by earthquakes.

Acknowledgment Field reconnaissance was financially supported by the Bureau of Science and Technology, Sichuan Province, under grant 2008SZ0156. Thanks should also be given to the instrumentation center of the Chengdu Hydropower Investigation and Design Institute (CHIDI) of the CHECC for kindly permitting the authors to publish data from the Gucheng hydropower project.

References

- Chen Guoguang, Ji Fengju, Zhou Rongjun et al (2007) Preliminary research of activity segmentation of Longmenshan fault zone since late quaternary. *Seismol Geol* 29(3):657–673 (in Chinese)
- Jin W, Tang L, Yang K, Wan G, Lu Z (2008) Progress and problem of study on characters of the Longmen Mountain Thrust Belt. *Geol Rev* 54:37–46 (in Chinese)
- Peng Shixiong, Song Shengwu (2009) Analysis of seismic damages and remedial design of Zipingpu hydraulic project. In: Sheng-wu Song et al (eds) *Analysis and investigation on seismic damages of projects subjected to Wenchuan earthquake*. Science Press, Beijing
- Tang Rongchang, Han Weibin (1993) *Active faults and earthquakes in Sichuan*. Earthquake Press, Beijing (in Chinese)

- Tang Rongchang, Wen Dehua, Huang Zuzhi et al (1991) The quaternary activity characteristics of several major active faults in the Songpan – Lonemenshan region. *Earthq Res China* 7 (3):64–71 (in Chinese)
- Xie Heping, Deng Jianhui, Tai Jijia et al (2008) Wenchuan large earthquake and post-earthquake reconstruction-related geotechnical problems. *Chin J Rock Mech Eng* 27(9):1781–1791 (in Chinese)
- Xu Chong, Dai Fuchu, Yao Xin (2009) Incidence number and affected area of Wenchuan Earthquake-induced landslides. *Sci Technol Rev* 27(11):79–81 (in Chinese)

Part II

Geotechnical Predictions

Chapter 6

Consolidation and Creep Settlement of Embankment on Soft Clay: Prediction Versus Observation

S. Robert Lo, M.R. Karim, and C.T. Gnanendran

6.1 Introduction

Embankments constructed in coastal areas are often founded on soft clay that are of low shear strength and high compressibility. These embankments often serve the dual function of elevating the road level and providing protection against flooding or storm surge. Embankments founded on soft soil present challenges in terms of both stability and settlement. The latter develops over a number of years; that is, it is time dependent.

Time-dependent behavior of a boundary value problem in geotechnical engineering can be classified into two different types. One is owing to the interaction between mechanical behavior (as governed by the effective stress principle) and seepage (driven by pore water pressure gradient). The other type is related to what is traditionally referred to as “secondary compression,” which is a characteristic of many soft clays.

Although a coupled finite element (FE) analysis; that is, the one that models the interaction between mechanical behavior (say with an elastic or elasto-plastic soil model) and seepage, can successfully predict the first type of time-dependent behavior, it cannot capture the second type. The Leneghans embankment foundation (see more details in the next section) is one such case. Lo et al. (2008) compared the computed results of a coupled analysis using the modified Cam clay (MCC) model for the foundation clay with long-term field measurements beneath the central zone of the embankment. Despite both the idealization and model parameters being conservative, the calculated settlement over 9 years was found to be about 20 % lower than the measured field value. This implies that the secondary compression is an important attribute of the Leneghans embankment foundation clay.

A number of elastic viscoplastic (EVP) models of have been proposed in the literature. Some of the EVP models are relatively complicated in their mathematical

S.R. Lo, Ph.D. (✉) • M.R. Karim, Ph.D. • C.T. Gnanendran, Ph.D.
University of New South Wales, Canberra, ACT 2600, Australia
e-mail: r.lo@adfa.edu.au

formulation and they present even more complex numerical issues when used in a coupled form. The main objective of this chapter is to investigate whether a relatively simple EVP model can be used to successfully predict the long-term multiple behavior characteristics of a geotechnical structure. It is also important that the input parameters can be objectively obtained from laboratory tests and that they have physical meanings for the engineer to relate it with other physical attributes of the soil.

In the field, during the construction and the early days after it, the settlement behavior is strongly influenced by the generation and dissipation of excess pore water pressure (pwp). Usually it takes more than a year, even with the use of prefabricated vertical drains (PVDs), for the excess pwp to mostly dissipate and the secondary compression to be unambiguously isolated. Thus to test the performance of an EVP model, longer duration field monitoring data are necessary. The case of the Leneghans embankment, for which we have up to 9 years of settlement monitoring data, is used here as a benchmark for assessing the predicting capability of the proposed methodology.

6.2 Field Case: The Leneghans Embankment

Detailed descriptions of the Leneghans embankment, its construction, soil properties, and instrumentation can be found in Lo et al. (2008). A brief description is presented here.

The Leneghans embankment was constructed as part of the Sydney-Newcastle freeway extension project by the Road and Traffic Authority (RTA), New South Wales, Australia, and is located about 150 km north of Sydney. The embankment is about 300 m long, ~60 m wide at the base, ~32 m wide at the crest, and was constructed to a reduced level (RL) of +5.5 m. The embankment was built parallel to an existing road embankment (the old Leneghans Drive), which acted as a berm for the new construction.

The natural ground level of the construction site was reported to vary from RL +0.5 to +0.9 m and the groundwater table fluctuated between RL +0.55 and +1.17 m. The subsoil consisted of very soft to soft alluvial clay of about 16.5 m thickness with a natural water content ranging between 72 to 99 % and a saturated unit weight of 14.8 to 16.2 kN/m³. The top 3 m of the clay layer was found to be firm and was reported to have higher permeability than the layers below. The liquid limit of the foundation soil was 82 to 94 % and the plastic limit was 28 to 31 % with a plasticity index of 54 to 63 %. Below the alluvial clay layers, the presence of highly to extremely weathered layers of shale bedrock were encountered.

A cross-section of the embankment with details of instrumentation at two transverse sections, namely, lines 1 and 2, are shown in Fig. 6.1. The construction of the embankment started in mid May 1995. A sand blanket was first placed up to RL +1.1 m to facilitate drainage as well as the placement of the geogrid reinforcements and other construction activities. Prefabricated vertical drains (100 × 5 mm) were installed

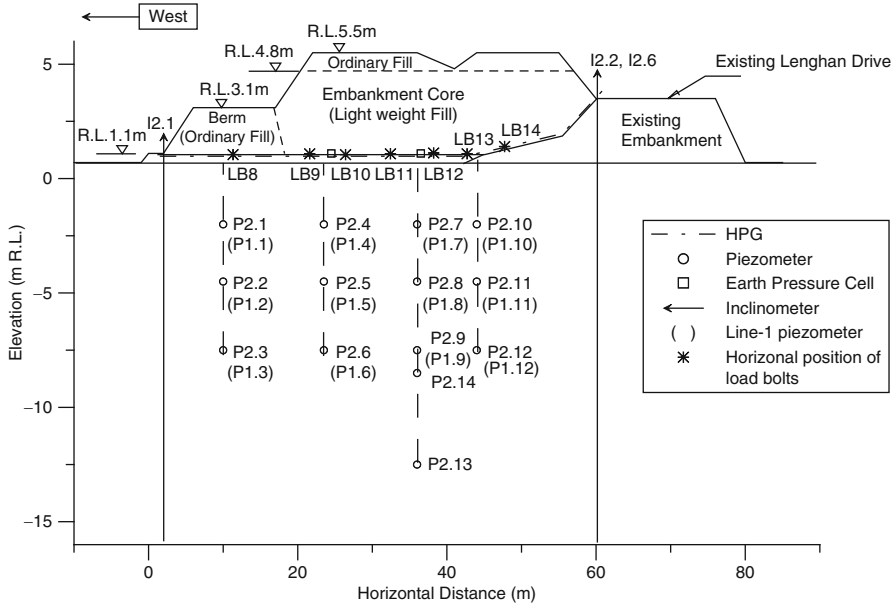
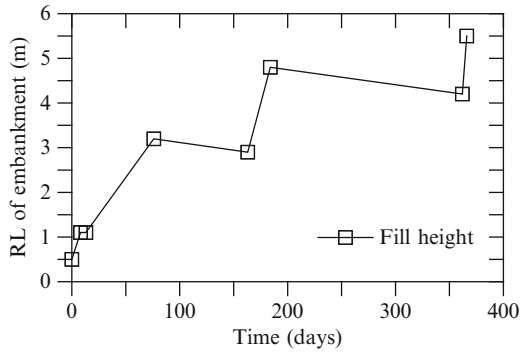


Fig. 6.1 Cross-section with instrumentation details (From Lo et al. 2008)

Fig. 6.2 Fill placement history of the Leneghans embankment (From Lo et al. 2008)



through the whole soft clay stratum at 1.5 m triangular spacing before placement of the embankment fill materials. The embankment fill was laid in three stages, allowing rest periods between the stages to ensure stability. Lightweight fill material was used for the core of the embankment. The fill placement history is shown in Fig. 6.2. The height of the embankment reached the specified RL of +5.5 m after about 1 year from the start of construction. After 578 days, it was surcharged by about 1 m of soil for about 7.5 months. After that, it was excavated back to the specified RL of +5.5 m.

The embankment was extensively instrumented with piezometers, earth pressure cells, inclinometers, horizontal profile gauges (HPGs), and also load bolts and strain gauges on the geosynthetics. The locations of these instrumentations can be found in Fig. 6.1.

6.3 Prediction Paradigm

This chapter takes the largely settled view that secondary compression is a material behavior that is associated with plastic deformation induced by effective stress, the so-called Hypothesis B. It can be modeled as creep. Therefore, both types of time-dependent behavior can be predicted with a coupled FE analysis provided that the occurrence of creep is captured using a suitable constitutive model. The paradigm adopted was to use a simple EVP model that uses input parameters determined from independent laboratory testing. This means the time-dependent behavior of the Leneghans embankment can be predicted without relying on elements of subjectivity in selecting input parameters.

The soil model proposed by Karim et al. (2011) was used for this study. The total strain rate in the formulation is divided into elastic and viscoplastic parts. The viscoplastic part is deduced based on Bjerrum's (1967) concept of secondary compression and pseudo-overconsolidation. It is characterized by the coefficient of secondary compression, C_α . However, the formulation does not require C_α to be a constant, as discussed later. The parameters used by this EVP model are:

- M – the slope of the critical state line in q - p space (where q is the deviator stress and p is the spherical pressure)
- λ – the virgin compression index, corresponding to a standard stress duration referred to as “reference time”, \bar{t}
- κ – the slope of the $e - \ln p$ plot in the recompression zone
- e_N – the void ratio of the in situ soil at the unit mean-normal effective stress on the normal consolidation line and corresponding to the reference time, \bar{t}
- ν – the elastic Poisson's ratio
- p_{c0} – the in situ preconsolidation pressure
- r_1, r_2 – two coefficients which controls the shape of the yield surface in q - p space, noting that the yield surface adopted is a distorted ellipse and r_1 and r_2 controls the distortion of the ellipse.
- C_α – the secondary compression coefficient taken as a variable as discussed later.

More details on the model can be found in Karim et al. (2011).

6.4 Modeling of Secondary Compression Coefficient

The void ratio, e , versus log-time plot during secondary compression is often assumed to be a straight line. Therefore, C_α , the slope of this plot, is commonly treated as a constant. Yin (1999), based on long duration testing (up to 33 days), reported that the plot was in fact nonlinear and he referred this to as “nonlinear creep.” He also presented a “creep parameter” function to fit this behavior. In Yin (1999), the creep parameter is defined as $C_{\alpha e}/\ln(10)$, where $C_{\alpha e}$ is the conventional secondary compression coefficient based on vertical strain definition.

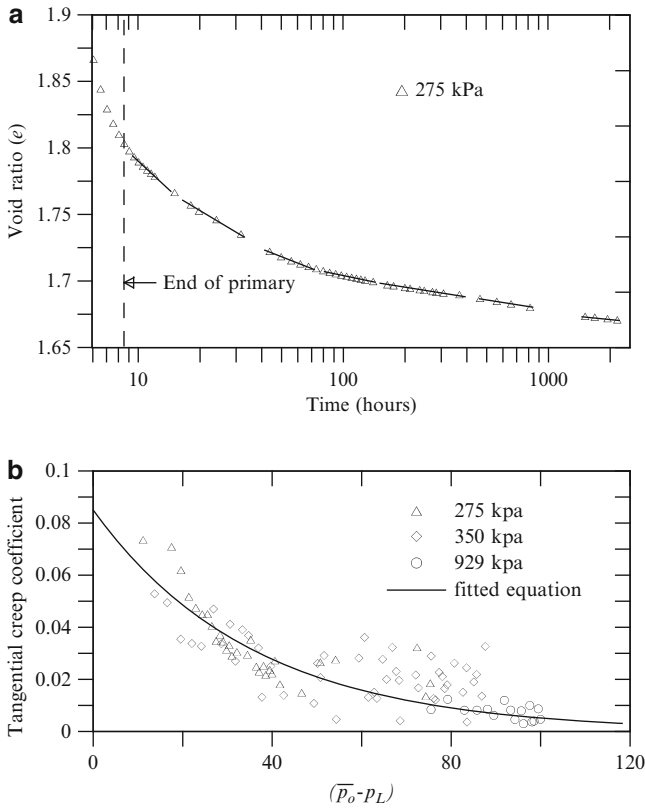


Fig. 6.3 Long duration odometer test results. (a) Void ratio plotted against log-time. (b) Determination of nonlinear creep function coefficients

The function related the “creep parameter” with “creep time” since the end of primary consolidation, t , an “initial creep rate,” ψ_0 , a reference time, t_0 and a “limit of creep strain,” $\Delta \epsilon_1$. The function could be used for direct estimation of creep strain or creep settlement or to derive a “specific” EVP model (Yin 1999). The use of time explicitly in the equation makes it difficult for more general application such as use in association with other EVP models, for example EVP models proposed by Kutter and Sathialingam (1992) or Karim and Gnanendran (2008). An alternative approach as proposed by Karim et al. (2010) to describe the nonlinear creep behavior is discussed next.

Long-duration odometer tests were conducted on undisturbed samples from the Leneghans embankment foundation clay and the relationship between C_α^* , defined as $de/d[\log(t)]$ and time was examined. C_α^* is referred to hereafter as creep coefficient and is the tangential slope of a void ratio versus $\log(\text{time})$ plot. Figure 6.3a presents the void ratio vs. time (log scale) plot for a long duration

creep test conducted under 275 kPa of stress. It can be seen from the figure that the tangential slope, C_α^* , changes with time. Although the slope of the line can be represented by an average “constant” value by linearizing over a shorter period of time, this average value is dependent on the duration over which the behavior is linearized. This makes the prediction of creep somewhat subjective.

Alternatively, if C_α^* can be established as a function of state and consolidation history, then C_α^* can be used in lieu of C_α in an incremental coupled analysis. It is desirable to have a creep coefficient function that has the following attributes:

- Its application is not tied to any specific EVP models
- The predicted creep (strain or void ratio) is bounded by the formulation
- The value of C_α^* reduces with the progression of creep

Karim et al. (2011) proposed the following equation for capturing the nonlinear nature of the creep coefficient.

$$C_\alpha^* = C_{\alpha\max} \exp(-N(\bar{p}_0 - p_L)) \quad (6.1)$$

Here, $C_{\alpha\max}$ and N are two positive constants, p_0 is the “creep-inclusive” preconsolidation pressure, as explained in Kutter and Sathialingam (1992). Assuming the λ and κ lines are straight in void ratio versus $\ln(p)$ space, it can be calculated using the following equation.

$$\bar{p}_0 = \exp((e_N - e - \kappa \ln p)/(\lambda - \kappa)) \quad (6.2)$$

p_L on the other hand, is the “creep-exclusive” preconsolidation pressure, and for most soils it can be calculated using the MCC yield surface (considering an elliptical yield surface with aspect ratio 2) equation:

$$p_L = p + \frac{q^2}{pM^2} \quad (6.3)$$

Equation 6.1 is not linked to any particular EVP model but is based on Bjerrum’s (1967) concept of the “quasi-preconsolidation.” $(\bar{p}_0 - p_L)$ is a measure of the extent of creep that has occurred. The soil will start creeping at a maximum rate, $C_{\alpha\max}$, once the state of the soil hits the λ -line, because, at that stage, $(\bar{p}_0 - p_L)$ is zero and thus $C_\alpha^* = C_{\alpha\max}$. As creep occurs, the difference between \bar{p}_0 and p_L increases and thus the value of C_α^* decreases. The exponential form of the function will ensure that creep is bounded. It is implicit in Eq. 6.1 that, the increments in \bar{p}_0 will be higher for the same amount of creep volumetric strain if the value of p is also higher, thereby implying that, the value of C_α^* will be smaller at higher stresses.

Table 6.1 Modified Cam clay parameters and permeability coefficients used for foundation clay

RL (m)	λ	κ	e_N	Vertical permeability parameters		
				K_{ref} (m/day)	e_{ref}	C_k
+0.3 to -2.8	0.33	0.066	2.877	3.0×10^{-5}	1.78	0.83
-2.8 to -7.8	0.38	0.076	3.291	1.5×10^{-5}	1.78	0.83
-7.8 to -10	0.38	0.076	3.291	1.5×10^{-5}	1.78	0.83
-10 to -16	0.33	0.066	2.877	1.5×10^{-5}	1.78	0.83

Note: $M = 1.113$, $\nu = 0.3$ for all layers

6.5 Material Parameters

6.5.1 Foundation Clay

The MCC material parameters used in this study have been determined from extensive laboratory experiments as presented by Lo et al. (2008) and are presented in Table 6.1. The two parameters, r_1 and r_2 , used for defining the yield surface were determined by matching the computed and experimental effective stress path in undrained triaxial tests and were found to be 1 and 2, respectively (Karim et al. 2011). The variation of p_{c0} with depth were inferred from the undrained shear strength data obtained from field vane shear tests as explained in Lo et al. (2008).

To determine $C_{a_{max}}$ and N required in Eq. 6.1, long duration (~3 months) odometer tests were conducted by Karim et al. (2010). The values of $C_{a_{max}}$ and N were determined by fitting Eq. 6.1 to test data as illustrated in Fig. 6.3b. This gives $N = 0.027$ and $C_{a_{max}} = 0.085$. An average “constant” creep coefficient was also determined by linearizing first 2 weeks of test results and was found to be 0.031. Two different EVP analyses were conducted. The first took into account the nonlinear nature of the creep coefficient and is referred to as creep-nonlinear analysis and the second using the “constant” C_α value and is referred to as “creep-simplified.” For comparison purpose, a third analysis was also conducted with the MCC model.

6.5.2 Embankment Fill

Two different types of materials were used as embankment fill during construction. They were lightweight bottom ash for the core of the embankment and ordinary fill materials for the berm section. The elastoplastic Mohr-Coulomb model was used for both materials. However, the Young’s modulus in the prefailure regime was allowed to vary with stress state in accordance with the Duncan-Chang equation. The angle of internal friction was taken as 40° for the bottom ash and 28° for the ordinary fill material (Huang 1990; Weng et al. 2010). The material parameters used for the modeling of the fill are presented in Table 6.2.

Table 6.2 Properties of embankment fill material

Parameter (unit)	Bottom ash	Ordinary fill
Cohesion (kPa)	5.0	5.0
Friction angle	40°	28°
Dilation angle	7°	4°
Unit wt. (kN/m ³)	14.0	20.0
Poisson's ratio	0.3	0.3
k	250	250
n	0.5	0.5
R_f	0.75	0.75

Note: k , n , and R_f are parameters for the Duncan-Chang equation

To ensure constructability, gabion units were placed at the western toe of the embankment. These gabion units were also modeled using Mohr-Coulomb material model. The material properties were similar to those used for the fill materials for the berm section, except that a cohesion of 100 kPa was assigned based on unconfined compression tests conducted on individual gabion units.

6.5.3 Foundation Soil–Embankment Fill Interface and Geogrid Reinforcement

The geogrid reinforcement was modeled as linear elastic–perfectly plastic one-dimensional bar elements. From the information provided by the manufacturer, the axial stiffness of the geogrid was taken to be 1,760 kN/m with a tensile strength of 125 kN/m. In all the analyses, interface elements were used between both the embankment fill and the foundation soil, and the reinforcement and the fill material to allow slip to occur independently either above or below the geogrid reinforcement. The parameters of the interface elements are listed in Table 6.3.

6.5.4 Permeability

The vertical permeability data as deduced from odometer tests were plotted in Fig. 6.4 and a semi-log function (Eq. 6.4) as first proposed by Taylor (1948) was used to describe the test data.

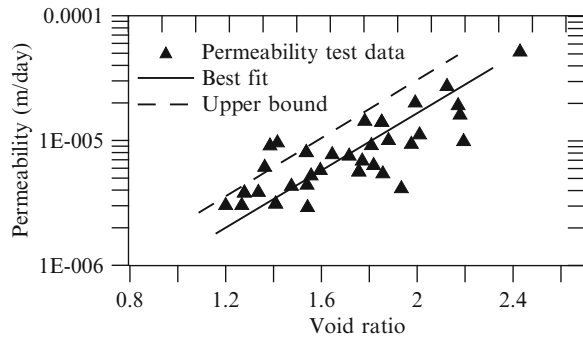
$$\log K = \log K_{\text{ref}} - (e_{\text{ref}} - e)/C_k \quad (6.4)$$

where K_{ref} and e_{ref} is the vertical permeability and void ratio at any reference point of the above equation. Because an odometer test tends to underestimate the actual permeability, the parameters were established from the upper bound limit shown as a dotted line (established by shifting the best fit line by one standard deviation of error). This gave, $C_k = 0.83$ and $K_{\text{ref}} = 1.5 \times 10^{-5}$ m/day for $e_{\text{ref}} = 1.78$.

Table 6.3 Properties of interface elements

Parameter (unit)	Foundation soil–geotextile interface	Embankment fill–geotextile interface
Cohesion (kPa)	3.0	3.0
Friction angle	28°	40°
Dilation angle	0°	0°

Fig. 6.4 Vertical permeability data plotted against void ratio



In determining the horizontal permeability, we have an additional complication: The installation of a PVD with a mandrel results in a smear zone around the PVD. Although the smear zone permeability of the soil may be approximated to be equal to the vertical permeability (Hansbo 1997; Indraratna and Redana 1998), the radius of the smear zone is dependent on the types and size of the mandrel and the shoes used.

To avoid such complications, an alternative approach was used. After Lo et al. (2008), the combined effects of horizontal permeability in an undisturbed zone and the annulus smear zone was represented by an equivalent horizontal permeability, K_h^* . The work of Indraratna et al. (2005) showed that the horizontal permeability can also be described by a semi-log equation. Thus, we expressed K_h^* as a multiple of K_v , that is,

$$K_h^* = \chi K_v \tag{6.5}$$

The multiplier χ can then be determined from back-analysis using the 1-year data during embankment construction and:

- idealizing the behavior around a PVD is as an axisymmetric unitcell using only settlement data beneath the center of the embankment
- modeling the PVD as free draining.

The last assumption is justified because the PVD had to satisfy a specification that ensures a minimum drainage capacity of 350 m³/year, well in excess of what is needed for drain resistance to be treat as negligible (Hansbo 1997; Chu et al. 2004).

The multiplier was varied systematically until a best match between the computed settlement (from a coupled FE analysis) and field data were obtained. It is pertinent to note that the permeability of the top 3 m of the soil were taken as

twice that of the layers, which is in line with the synthesis of field testing results by Lo et al. (2008).

The corresponding best match values of χ from the back analysis were: 1.97, 2.04, and 3.32 for “creep-nonlinear,” “creep-simplified,” and MCC analysis, respectively. Thus the back-estimated K_h^* values are dependent on the constitutive model used to model the foundation soil in the axisymmetric unitcell analysis. This is because both the permeability and the mechanical model affect the rate of settlement. If the constitutive model for the mechanical behavior of the soil is changed, then the permeability has to be adjusted to achieve a match with the field-measured settlement data. This implicates that we cannot use back analyzed permeability values reported in publications that used a different constitutive model.

6.6 Axisymmetric Unitcell Analysis Results

Although the axisymmetric unitcell analyses were conducted for the primary purpose of matching with field observation for the first year of construction so as to estimate horizontal permeability, time stepping was continued up to 9 years to predict time-dependent behavior beneath the center of the embankment.

6.6.1 Settlement Responses

Figure 6.5 compares the observed settlement beneath central zone of the embankment with the predictions. As expected, all three soil models gave predictions that are in close agreement with field data for the first year because the back-analyzed K_h^* for the respective soil model was used. However, the three different time-settlement curves diverged as time increased.

The prediction with the MCC analysis began to underestimate the settlement after 1 year, and the discrepancy increased with time and the computed

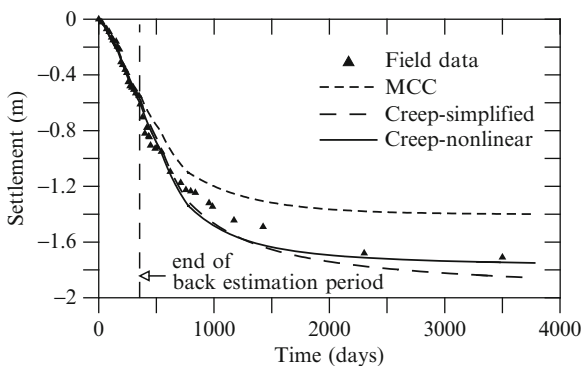


Fig. 6.5 Comparison of settlement from three different analyses and field values

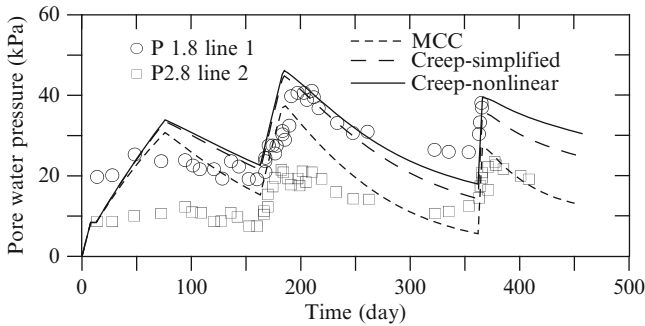


Fig. 6.6 Calculated and field excess pwp at RL -4.5 m

settlement essentially ceased after 4 years although the field data showed that the settlement continued with time. The MCC model led to under-estimation of the final settlement (at 9 years) by $\sim 20\%$.

Predicted settlements from both creep analyses closely followed the field values up to about 700 days and, after that, they began to exceed the field measurements. In the creep-nonlinear analysis, the use of a C_{α}^* function slowed down the process of creep, and toward the end of the sixth year, its prediction (rate and magnitude) closely followed the measured field values. The “creep-simplified” analysis, however, did not have this attribute and gave a 9-year settlement $\sim 8\%$ higher than the measured value. Furthermore, it predicted continued increase in settlement during the ninth year despite the field measurements showed that settlement essentially ceased after 6 years.

6.6.2 Excess pwp Responses: Calculation vs. Observation

The predicted pwp at the outside boundary of the unitcell for the first 425 days, at depths of RL of -4.5 m is plotted in Fig. 6.6 along with the measured values at the corresponding depths. It should be noted that the piezometers are the mid-point locations between the drains, which correspond to the outside boundary of the axisymmetric unitcell.

At this depth, the computed pwp responses for both the creep analyses were similar. The predicted evolution of excess pwp agreed well with the upper limit of the field data. This apparently conservative calculation was somewhat expected because the as-installed positions of the piezometers always tend to deviate from the mid-point locations between the drains. The deviation increases with depths, thus resulting in a lower excess pwp.

The MCC analysis on the other hand calculated significantly lower excess pwp than the other two analyses. At the RL -4.5 m, the calculated excess pwp response was closer to the “average” values of the field measurements. Taking into account the tendency of the as-installed piezometers to record lower excess pwp, the MCC

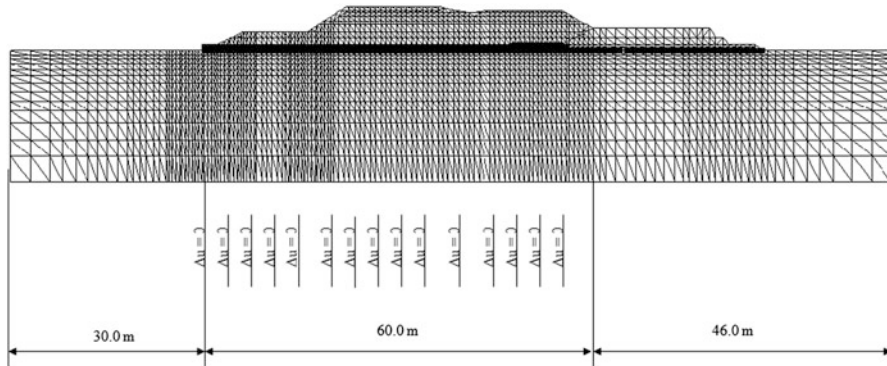


Fig. 6.7 Finite element geometry used for the 2-D plane strain analysis

analysis might have underpredicted. Similar responses were observed at RL -7.5 m. However, the figures are not presented here because of page limitations.

6.7 Full Embankment Analysis

6.7.1 Permeability Estimation

The use of PVDs makes plane strain modeling of an embankment problematic because the seepage condition around a drain is closer to axisymmetric. Thus, the “combined matching” procedure proposed by Hird et al. (1992) was used. The “combined matching” technique enables the use of an equivalent drain spacing for plain strain analysis, and thus helps to optimize the FE mesh. It is pertinent to note that to capture the dominantly horizontal pwp gradient, several elements between two free draining lines are needed. A plane strain unitcell width of 4.0 m was selected for the entire cross-section.

6.7.2 Plane Strain Modeling of the Embankment

The FE geometry used for the analyses is presented in Fig. 6.7. The new embankment was modeled along with the old one because of nonsymmetry. A total of 5,950 elements, with 11,328 nodes and 33 different material sets, were used to represent different parts of the FE idealization. The analyses were carried out using large-deformation formulations because of geometric nonlinearity. This allowed the updating of the nodal and Gauss point coordinates and their related material properties (if necessary).

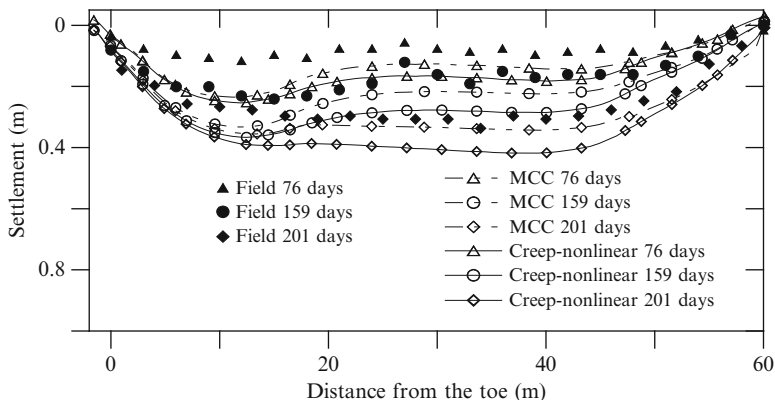


Fig. 6.8 Calculated and observed settlement profiles at 76, 159, and 201 days

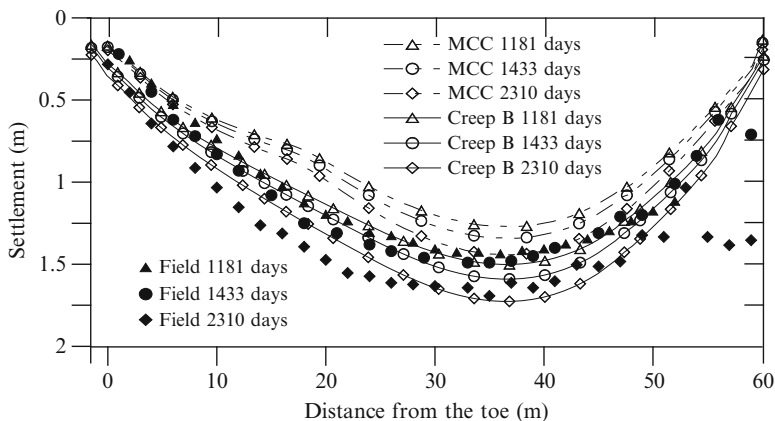


Fig. 6.9 Calculated and observed settlement profiles at 1,181, 1,433, and 2,310 days

6.8 Synthesis of Analysis Results

For the case of full embankment analyses, only the results from the MCC and Creep-nonlinear analyses are presented here because of length limitation.

6.8.1 Settlement Profiles

The measured settlement profiles (from HPGs) at sand blanket level are compared with the computed results in Figs. 6.8 and 6.9. It is observed in Fig. 6.8 that during the early days of construction, both the MCC and the creep-nonlinear

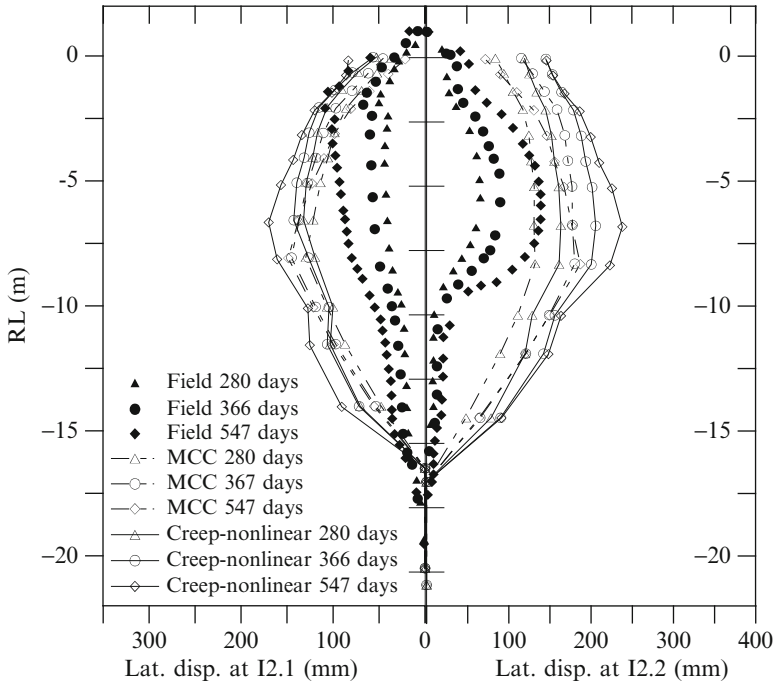


Fig. 6.10 Observed and measured lateral displacement profiles at I2.1 and I2.2

analyses overpredicted the settlement responses. However, the degree of overprediction reduced in the later days. The settlement profile computed with the MCC analysis was close to the field measurements at 201 days. The creep-nonlinear analysis, on the other hand, overpredicted the settlement at 201 days by a significant margin.

Figure 6.9 presents the calculated and observed settlement profiles at 1,181, 1,433, and 2,310 days after the start of construction. The effect of neglecting creep became evident as the MCC analysis shows significant under estimation of the settlement profiles. At the end of 2,310 days the MCC model underpredicted the maximum settlement by about 18 %, whereas the creep-nonlinear analysis predicted a settlement profile that matched well with the observed one.

It is interesting to note in Figs. 6.8 and 6.9 that the position of the maximum field settlement was not fixed at one location. Initially, it was below the berm; and time progressed, it moved toward the central zone.

6.8.2 Lateral Displacement Profiles

The lateral displacement profiles (at 280, 366, and 547 days) recorded by inclinometer I2.1 and I2.2 (see Fig. 6.1) are compared with the predicted results in Fig. 6.10.

For the case of I2.1, the shapes of the measured profiles for the top few meters appear to be slightly unusual, a maximum displacement occurred at about RL -3 m. The creep-nonlinear analysis gave the maximum lateral deflection occurred at around RL -6 m, whereas the MCC analysis predicted this to occur at around RL -7.5 m. The site report of RTA revealed that the gabion next to the inclinometer had been accidentally moved outward during construction and this may in turn pushed the inclinometer to deflect outward at a shallow depth (Mak 1996). The magnitudes of the displacements were overpredicted by both analyses, especially during the early days, although it reduced in later days. At 547 days, the difference between the calculated and field maximum displacements was about 37 % for the creep-nonlinear analysis and about 25 % for the MCC analysis.

In the case of I2.2, the location of the maximum displacement, which occurred at about RL -5 m, was well captured by both the creep-nonlinear and MCC analyses. However, its magnitude was overpredicted in both the cases. At the end of 547 days, the maximum displacement was overpredicted by about 58 % by creep-nonlinear analysis and about 35 % by the MCC analysis. Although it might be perplexing that the supposedly better creep analysis produced an inferior prediction, this could have been because of the compensating errors of neglecting creep in the MCC analysis.

6.8.3 Excess pwp Response

It should be noted that the “combined matching” procedure proposed by Hird et al. (1992) was adopted for these analyses to deduce the equivalent permeability for a plane strain idealization. One of the drawbacks of Hird et al.’s (1992) approach is that the, at the same location, the excess pwp predicted by the axisymmetric and plane strain unitcells may differ significantly (Hird et al. 1992, 1995). The analysis presented by them showed that the pwp response was significantly overpredicted at the periphery of the plane strain unitcell. To overcome this problem a correction factor was proposed by Karim (2011). This correction factor could be obtained by comparing the excess pwp responses in an axisymmetric unitcell with that of an equivalent plane strain unitcell. The presented excess pwp responses in this chapter correspond to the periphery of the plane strain unitcells after applying the correction.

In Fig. 6.11, the measured excess pwps from piezometers P2.7, P1.8, and P2.8 (located below the central zone of the main embankment) and the corresponding corrected predictions from the numerical analyses are presented. The shapes of the plots were well captured by both analyses: The MCC analysis traced the average field values, whereas the creep-nonlinear analysis overpredicted slightly. The uncorrected pwp computed using the creep-nonlinear model is also plotted (denoted by label PS) in the same figure to illustrate the importance of correction.

Overall, the shape of the time-excess pwp curves was well captured by both the analyses. Calculations from the MCC analysis were apparently better than those from the creep-nonlinear analysis. However, considering the tendency of the

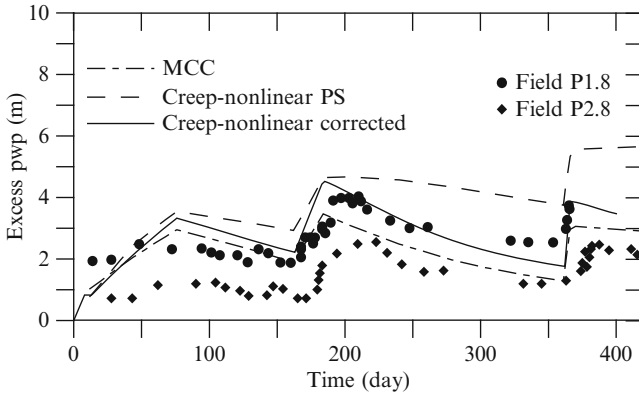


Fig. 6.11 Calculated and observed excess pwp at piezometer P2.7, P1.8, and P2.8

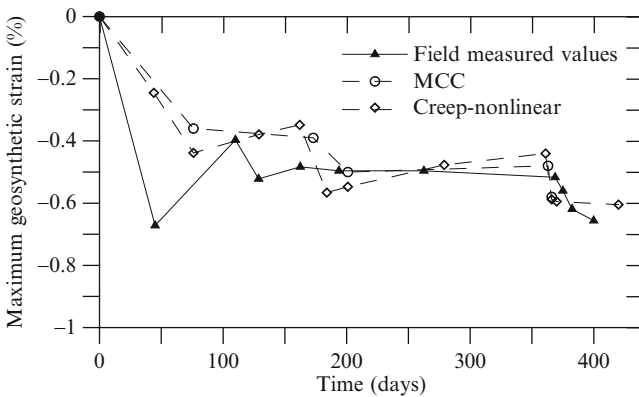


Fig. 6.12 Calculated and predicted maximum geotextile strains against time. *Note:* tension shown as negative

piezometers to deviate from their desired locations, it could be said that the excess pwp responses from the MCC analysis might have been under-predicted, and the prediction from the creep analysis was with reasonable accuracy.

6.8.4 Geotextile Strain

The measured and predicted maximum strains in the geogrid were plotted against time in Fig. 6.12. Both analyses essentially gave the same prediction throughout the period. In the early stage of construction, the measured strain was significantly higher than the predicted value. However, as construction progressed, the predicted and measured values were in reasonable agreement

6.9 Conclusions

This chapter demonstrates certain degree of success in predicting the long-term behavior of an embankment on soft clay using a relatively simple EVP model. The model allows nonlinear variation of creep coefficient and also uses a nonelliptical surface for the yield surface. Emphasis is given to objectively determining the material parameters used for the analysis. All the parameters that the models used were determined independently and mostly from conventional laboratory testing. A systematic approach was adopted to estimate the equivalent horizontal permeability of soil that takes into account the effects of PVD installation. Predictions using the modified cam clay model are also included for comparison purpose.

The analysis using the elastoplastic MCC model produced reasonable results, but the final settlement and the excess pwp responses were underpredicted. The EVP analysis with a constant creep coefficient produced very good agreement with field measured values both in terms of settlement and excess pwp. Better performance from the model was achieved when the creep coefficient was treated as nonlinear.

Acknowledgments The authors are grateful to RTA, New South Wales, Australia, for their generous support. The computational resource provided by the NCI National Facility, Australia, is also gratefully acknowledged. The opinions expressed in this chapter, however, are solely those of the authors.

References

- Bjerrum L (1967) Engineering geology of Norwegian normally consolidated marine clays as related to settlements of buildings. *Geotechnique* 17(2):81–118
- Chu J, Bo MW, Choa V (2004) Practical considerations for using vertical drains in soil improvement projects. *Geotext Geomembr* 22(2):101–117
- Hansbo S (1997) Aspects of vertical drain: Darcian or non-Darcian flow. *Geotechnique* 47(5):983–992
- Hird CC, Pyrah IC, Russel D (1992) Finite element modelling of vertical drains beneath embankments on soft ground. *Geotechnique* 42(3):499–511
- Hird CC, Pyrah IC, Russel D, Cinicioglu F (1995) Modelling the effect of vertical drains in two-dimensional finite element analyses of embankments on soft ground. *Can Geotech J* 32:795–807
- Huang W-H (1990) The use of bottom ash in highway embankments, subgrades, and subbases. Purdue University, West Lafayette
- Indraratna B, Redana IW (1998) Laboratory determination of smear zone due to vertical drain installation. *J Geotech Geoenviron Eng* 124(2):180–184
- Indraratna B, Rujikiatkamjorn C, Sathananthan I (2005) Radial consolidation of clay using compressibility indices and varying horizontal permeability. *Can Geotech J* 43(5):1330–1341
- Karim MR (2011) Modeling the long term behaviour of soft soils. Ph.D. thesis, University of New South Wales at Australian Defence Force Academy, Canberra

- Karim MR, Gnanendran CT (2008) A new elastic visco-plastic model for time dependent behaviour of normally consolidated and lightly over-consolidated clays. In: Proceedings of 61st Canadian geotechnical conference, GeoEdmonton'08, Edmonton, Canada, pp 394–401
- Karim MR, Gnanendran CT, Lo S-CR, Mak J (2010) Predicting the long-term performance of a wide embankment on soft soil using an elastic-visco-plastic model. *Can Geotech J* 47:244–257
- Karim MR, Manivannan G, Gnanendran CT, Lo S-CR (2011) Predicting the long-term performance of a geogrid-reinforced embankment on soft soil using two-dimensional finite element analysis. *Can Geotech J* 48(5):741–753
- Kutter BL, Sathialingam N (1992) Elastic-viscoplastic modelling of the rate-dependent behaviour of clays. *Geotechnique* 42:427–441
- Lo SR, Mak J, Gnanendran CT, Zhang R, Manivannan G (2008) Long-term performance of a wide embankment on soft clay improved with prefabricated vertical drains. *Can Geotech J* 45:1073–1091
- Mak J (1996) Prediction of trial pile responses based on winkler subgrade model. Geotechnical engineering section, RTA, Newcastle zone office, Newcastle, pp 1–7
- Taylor DW (1948) *Fundamentals of soil mechanics*. Wiley, New York
- Weng M-C, Lin C-L, Ho C-I (2010) Mechanical properties of incineration bottom ash: The influence of composite species. *Waste Manage* 30:1303–1309
- Yin JH (1999) Non-linear creep of soils in oedometer tests. *Geotechnique* 49(5):699–707

Chapter 7

Numerical Simulation of Soil Structures Reinforced by Geosynthetics

Masafumi Hirata, Atsushi Iizuka, Hideki Ohta, Takayuki Yamakami, Yoshihiro Yokota, and Koji Ohmori

7.1 Introduction

Geosynthetics-reinforcement is an engineering method intended to produce a reinforced composite ground with increased rigidity and supportive capability through the use of reinforcement grids placed in the ground. The tensile strength of soil is low. Geosynthetics-reinforcement was originally conceived as a measure for using reinforcement materials such as geosynthetics so as to supplement the

M. Hirata, D.Eng. (✉)

Technical Research Institute, Maeda Corporation, 1-39-16 Asahi-cho,
179-8914 Nerima-ku, Tokyo, Japan
e-mail: hirata.m@jcity.maeda.co.jp

A. Iizuka, D.Eng.

Research Center for Urban Safety and Security, Kobe University, 1-1 Rokkodai,
657-8501 Nada-ku, Kobe, Hyogo, Japan
e-mail: iizuka@kobe-u.ac.jp

H. Ohta, D.Eng.

Research and Development Initiative, Chuo University, 1-13-27 Kasuga,
112-8551 Bunkyo-ku, Tokyo, Japan
e-mail: ohta@tamacc.chuo-u.ac.jp

T. Yamakami

Information Media Center, Kanazawa University, Kakuma,
920-1192 Kanazawa, Ishikawa, Japan
e-mail: yama3364@staff.kanazawa-u.ac.jp

Y. Yokota, D.Eng.

Maeda Kohsen Corporation, 9-9 Hisamatsu-cho, 103-0005 Nihonbashi,
Chuo-ku, Tokyo, Japan
e-mail: yokota@mdk.co.jp

K. Ohmori, D.Eng.

Research Institute of Digital Geo-Environment, Ro 86-1 Kannondou-cho,
920-0352 Kanazawa, Ishikawa, Japan
e-mail: ohmori-10@safedraw.co.jp

low tensile strength of soil. The reinforcement effect produced by the use of geosynthetics is not a simple aggregate of the rigidity and strength of both geosynthetics and compacted soil. The effect is produced as a result of complex dynamic interactions between geosynthetics and compacted soil. Consequently, the effect of geosynthetics-reinforcement is generally higher than expected and therefore quite reliable when used against earthquakes and other geohazards.

Ohta et al. (1997, 2002) conducted four full-scale field tests in Kanazawa (Fig. 7.1) during the period from 1992 to 1996 so as to ascertain the reinforcement effects brought about by the use of geosynthetics. Their field tests revealed that geosynthetics and compacted soil behave as an integrated body. Assuming that the dynamic interactions between geosynthetics and compacted soil are the effects arising from geosynthetics restraining the dilatancy of compacted soil under shear, the authors conducted finite-element simulations of full-scale field tests (Hirata et al. 1999) and model tests (Iizuka et al. 2001). This chapter presents elasto-plastic constitutive models with the dilatancy of compacted soil under shear taken into consideration and an estimation method for constitutive properties of compacted soil. Furthermore, this chapter also presents finite-element simulations performed on the two full-scale field tests conducted in 1994 and 1996.

7.2 Outline of Full-Scale Field Model Tests

7.2.1 Full-Scale Field Model Test Conducted in 1994

Figure 7.2 shows a cross-sectional view of the full-scale field test embankment constructed in Yuhidera, Kanazawa in 1994. The embankment measured 5.0 m in height, 7.0 m in width, and 22.0 m in length, and had two vertical sides and a 30° overhanging slope. Soil in the site, known as “Omma sand,” was used to build the embankment. Table 7.1 shows physical test results for Omma sand. Geosynthetics (Adeam F-3, Maeda Kosen Co., Ltd.) made of a PVC plastic-coated, mixed-weave fabric of aramid and polyester fibers were used as reinforcements comprising ten layers at 0.5 m intervals. Figure 7.3 shows tensile test results for the geosynthetics. Table 7.2 shows material properties. In the field model test, the supporting fill was removed from top to bottom to create a cliff overhang of 5.0 m in height. After the supporting fill was removed under the overhanging portion, cutters installed in the portion to purposely bring the reinforced embankment to fail were used to cut the geosynthetics along a 60° plane and a 70° plane from top to bottom. Table 7.3 shows the test procedure.

In the test, the overhanging portion began to deform from the beginning of removal of the supporting fill. When the supporting fill was removed by 1.5 m in height (Step 2), the top geosynthetics layer yielded and the top edge collapsed, as shown in Fig. 7.4. As the supporting fill was removed further, the overhanging cliff face deformed further. When the supporting fill was removed by 4.1 m in height (Step 6), the overhanging cliff collapsed completely, as shown in Fig. 7.5. Probable

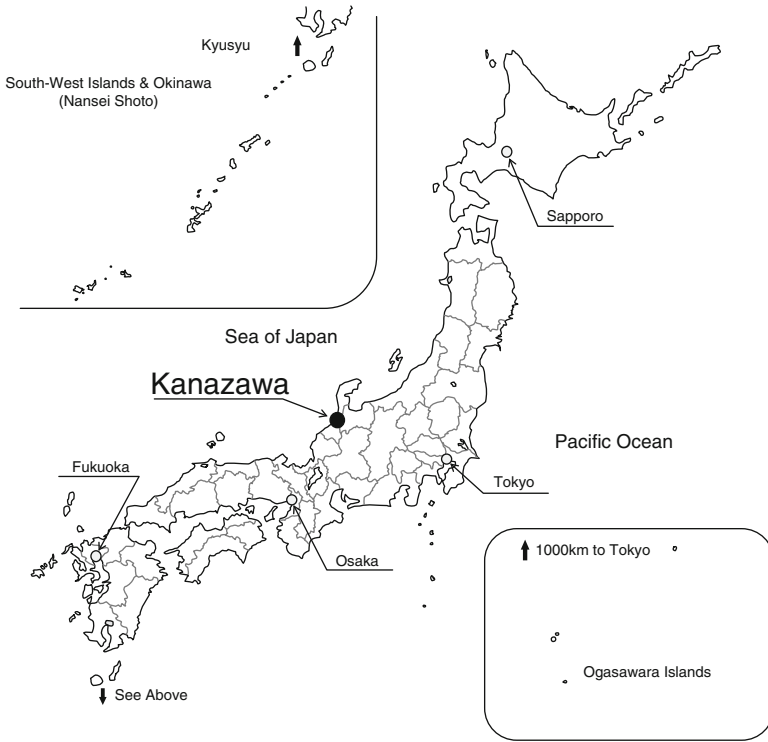


Fig. 7.1 Site of field experiments (Kanazawa, Japan)

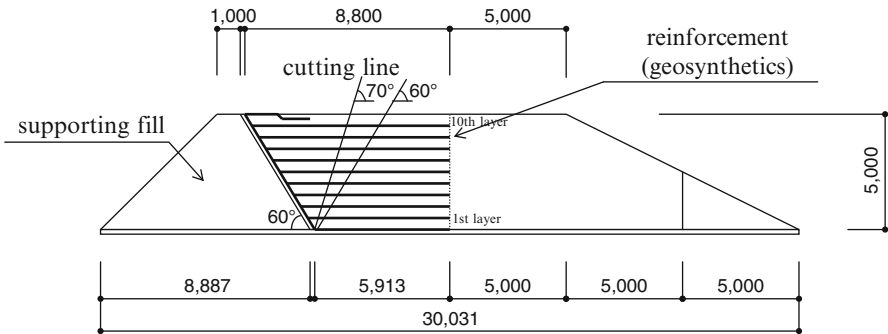


Fig. 7.2 Overview of geosynthetics-reinforced soil structure in 1994 (unit: mm)

causes of this collapse include: (1) the geosynthetics wrapping was too short, and (2) the geosynthetics happened to be loosely placed. After the supporting fill was removed, the reinforcement cutters were pulled by a backhoe to cut the geosynthetics one by one. No failure of the embankment occurred after all the geosynthetics were cut on the 60° plane. Subsequently, when on the 70° plane the seventh layer was cut

Table 7.1 Physical properties of Omma sand at Yuhidera in 1994

Specific gravity of soil particle	ρ_s (t/m ³)	2.714
<i>Grain size distribution</i>		
Gravel fraction	2–75 mm (%)	0.0
Sand fraction	75 μ m–2 mm (%)	69.8
Silt fraction	5–75 μ m (%)	30.2
Clay fraction	<5 μ m (%)	
Uniformity coefficient	U_c	–
Coefficient of curvature	U_c'	–
Maximum grain size	(mm)	2.0

Fig. 7.3 Uni-extension test of geosynthetics in 1994

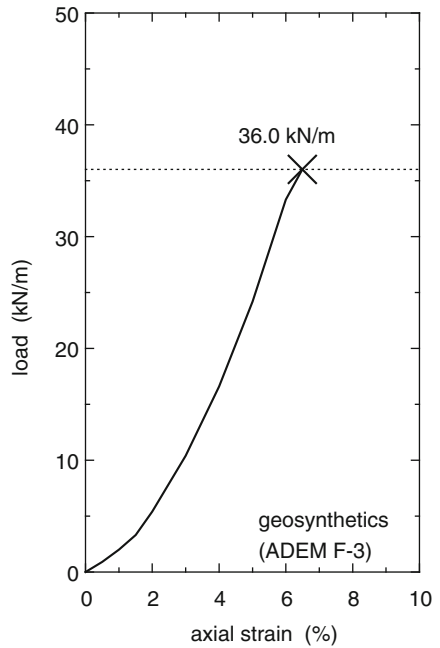


Table 7.2 Material properties of geosynthetics in 1994

Cross-section area	A	m ²	5.24×10^{-4}
Young's module	E	kN/m ²	1.06×10^6

Table 7.3 Steps of the 1994 experiment

Step	Content
1	Remove 0.7 m of supporting fill from the top
2	Remove 1.5 m of supporting fill from the top
3	Remove 2.4 m of supporting fill from the top
4	Leave as it is for 5 days
5	Remove 3.3 m of the supporting fill from the top
6	Remove 4.1 m of the supporting fill from the top
7	Remove 5.0 m of the supporting fill from the top
8	Cut geosynthetics of the tenth layer (top layer) along the 60-degree line
9	Cut geosynthetics of the ninth layer along the 60-degree line
10	Cut geosynthetics of the eighth layer along the 60-degree line
11	Cut geosynthetics of the seventh layer along the 60-degree line
12	Cut geosynthetics of the sixth layer along the 60-degree line
13	Cut geosynthetics of the fifth layer along the 60-degree line
14	Cut geosynthetics of the fourth layer along the 60-degree line
15	Cut geosynthetics of the third layer along the 60-degree line
16	Cut geosynthetics of the second layer along the 60-degree line
17	Leave as it is for 60 min
18	Cut geosynthetics of the tenth layer along the 70-degree line
19	Cut geosynthetics of the ninth layer along the 70-degree line
20	Cut geosynthetics of the eighth layer along the 70-degree line
21	Failure when cut geosynthetics of the seventh layer along the 70-degree line

**Fig. 7.4** Removing the fill supporting the overhanging cliff (Step 2)



Fig. 7.5 Overhanging cliff (Step 6), collapsed completely

(Step 21), the embankment collapsed, as shown in Fig. 7.6. Figure 7.7 shows how the marks moved during the collapse of the embankment, which, captured by video, clearly indicates that the overhanging portion and the embankment collapsed all at once.

7.2.2 Full-Scale Field Model Test Conducted in 1996

Figure 7.8 shows a cross-sectional view of the full-scale field test embankment built in Taiyogaoka, Kanazawa in 1996. The embankment was 5.0 m in height, 7.0 m in width, and 15.0 m in length and had two features, an overhanging cliff and a simple beam (soil bridge). The soil (Omma sand) in the site was used to build the embankment. The physical properties of the soil differed slightly from those of the soil used in the 1994 field model test, because the two soils were taken from different locations. Table 7.4 shows test results for the embankment material. Geosynthetics were used to wrap the soil in 10 layers at 0.5-m intervals. Figure 7.9 shows tensile test results for the geosynthetics, indicating that the material is about three times stronger than that use in the 1994 test. Table 7.5 shows their material properties. Simple beam and cantilever portions were prestressed to supplement the effect of embankment reinforcement. Prestress loads were 28.4 and 56.8 kN on the near and far portions, respectively, taking the weight of the embankment itself into account.

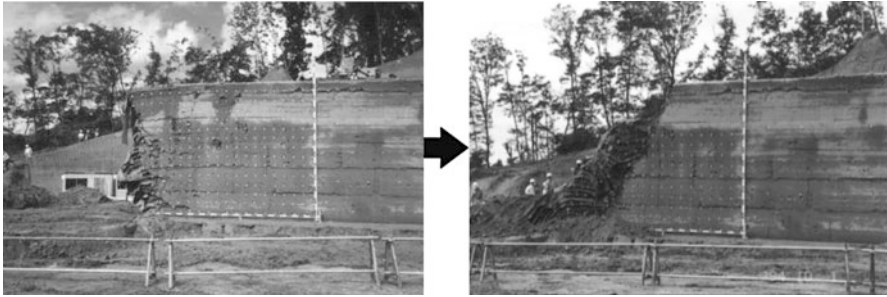


Fig. 7.6 When on the 70° plane the seventh geosynthetics was cut sequentially from the top (Step 21), the embankment was brought to failure

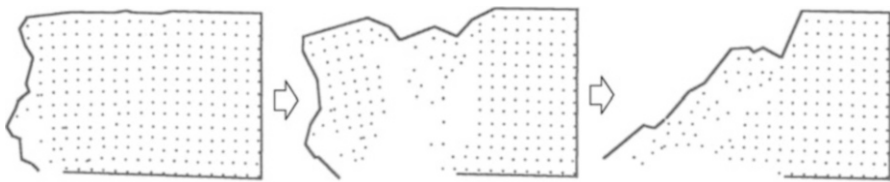


Fig. 7.7 Movement of the targets during the collapse of the embankment (Step 21)

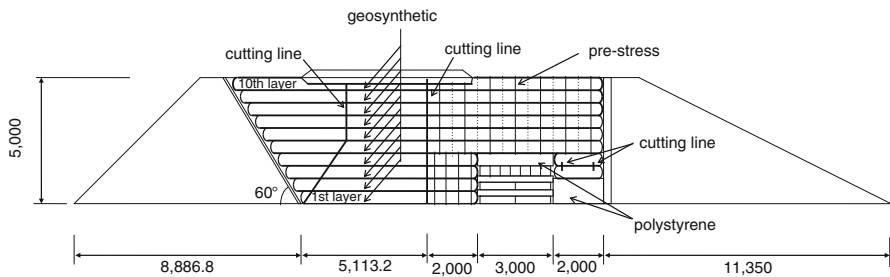


Fig. 7.8 Overview of geosynthetics-reinforced soil structure in 1996 (unit: mm)

Table 7.4 Physical properties of Omma sand at Tiyogaoka in 1996

Specific gravity of soil particle	ρ_s (t/m ³)	2.740
<i>Grain size distribution</i>		
Gravel fraction	2–75 mm (%)	2.0
Sand fraction	75 μ m–2 mm (%)	80.0
Silt fraction	5–75 μ m (%)	11.0
Clay fraction	<5 μ m (%)	7.0
Uniformity coefficient	U_c	21.8
Coefficient of curvature	U_c'	5.82
Maximum grain size	(mm)	9.5

Fig. 7.9 Uni-extension test of geosynthetics in 1996

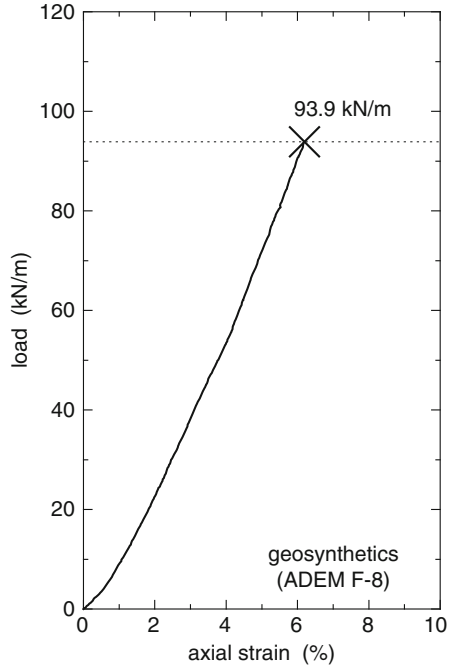


Table 7.5 Material properties of geosynthetics in 1996

Cross-section area	<i>A</i>	m ²	3.20×10^{-4}
Young's module	<i>E</i>	kN/m ²	4.86×10^6

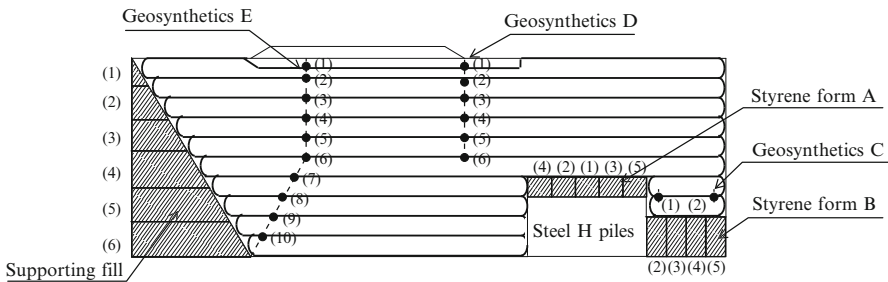


Fig. 7.10 Location of geosynthetics and styrene forms for experiment procedure in 1996

In the test, the embankment shape was altered three ways, from overhanging cliff to simple beam and to cantilever. In each of these shapes, changes in the embankment were observed. Moreover, reinforcement cutters were installed to allow the embankment to fail, as in the 1994 field test. Figure 7.10 shows where the cutters were installed. Table 7.6 shows test procedures. Figure 7.11 shows the embankment at the time the supporting fill was completely removed from under the overhang portion (Step 6). A 0.32-m sag occurred near the top edge of the overhang embankment. However, the overhanging cliff did not fail. Figure 7.12 shows the

Table 7.6 Steps of the 1996 experiment

Step	Content
1	Remove the supporting fill for overhanging cliff (1) (up to 0.670 m)
2	The same as above (2) (up to 1.536 m)
3	The same as above (3) (up to 2.402 m)
4	The same as above (4) (up to 3.268 m)
5	The same as above (5) (up to 4.134 m)
6	The same as above (6) (up to 5.000 m)
7	Remove styrene form A-(1) supporting soil bridge
8	The same as above A-(2)
9	The same as above A-(3)
10	The same as above A-(4)
11	The same as above A-(5)
12	Remove styrene form B-(1) supporting soil bridge
13	Cut geosynthetics C-(1)
14	Cut geosynthetics C-(2)
15	Remove styrene form B-(2) supporting soil bridge
16	The same as above B-(3)
17	The same as above B-(4)
18	Cut geosynthetics D-(1)
19	The same as above D-(2)
20	The same as above D-(3)
21	The same as above D-(4)
22	The same as above D-(5)
23	The same as above D-(6)
24	Cut geosynthetics E-(1)
25	The same as above E-(2)
26	The same as above E-(3)
27	The same as above E-(4)
28	Failure when cut geosynthetics E-(5)

embankment with the supporting fill removed from under the simple beam. The span reached 3.0 m long (Step 11). The simple beam retained its shape with its sag at beam center being approximately 0.1 m. The geosynthetics were subsequently cut one by one. When the sixth geosynthetics layer was cut in the overhanging portion (Step 28), the overhanging cliff collapsed forward. Figure 7.13 shows how the overhanging embankment collapsed. The soil and reinforcement of the overhang portion collapsed forward all together.

7.3 Model to Describe Dilatancy of Compacted Soils

In this investigation, the implementation of geosynthetics is assumed to have reinforcing effects, the result of which is that they work to restrain the dilatancy of compacted soil under shear. This section describes a constitutive model for representing the dilatancy of compacted soil and estimation of parameters required for constitutive modeling.

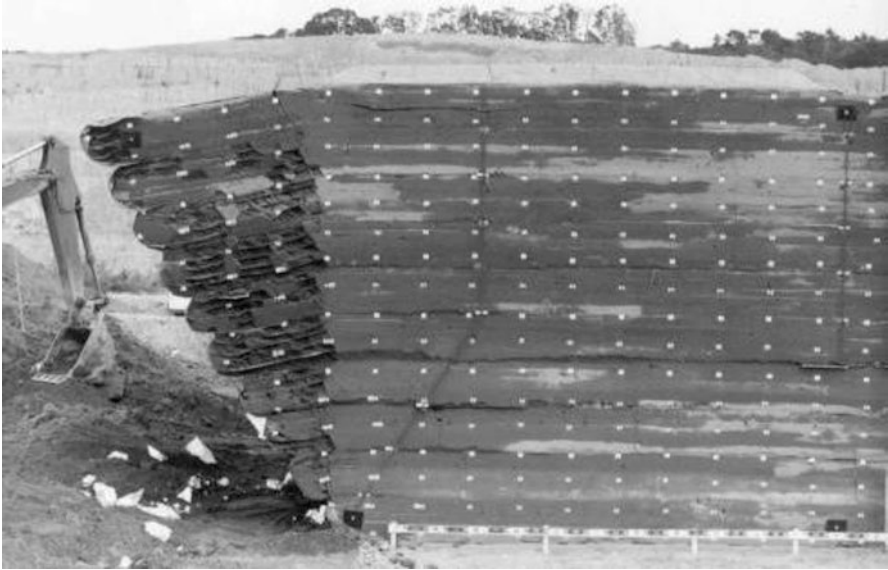


Fig. 7.11 Overhanging cliff (Step 6)



Fig. 7.12 Soil bridge (Step 11)

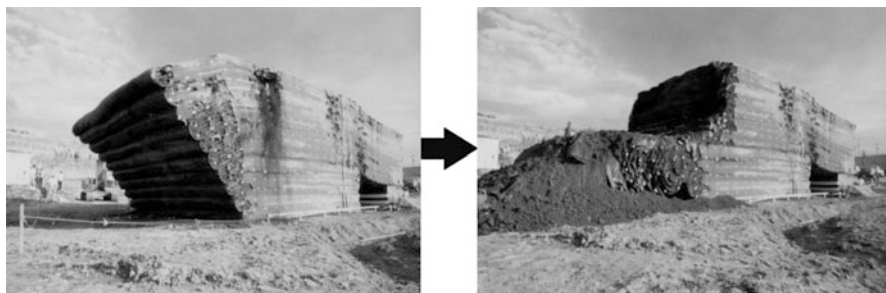


Fig. 7.13 When the sixth geosynthetic was cut sequentially from the top (Step 28), the embankment was brought to failure

7.3.1 Constitutive Model for Compacted Soils

The elasto-plastic constitutive model proposed by Sekiguchi and Ohta (1977) (the SO model) is originally intended to be used for natural sediment of saturated cohesive soils. However, because a similarity in shearing characteristics exists between unsaturated compacted soil and saturated overconsolidated clay, the SO model is used to represent unsaturated compacted soil in this chapter. The SO model is known to represent dilatancy, coupled with strain softening behaviors (positive dilatant responses). The conventional method proposed by Drucker (1950) to determine loading on elasto-plastic bodies, however, fails to draw a distinction between loading and unloading in the strain softening region. In our study, loading was determined for strain softening by applying to the SO model the determination method employed by Asaoka et al. (1994) for the Cam clay model (Hirata et al. 1999). The method is outlined as follows.

Plastic strain increment $\dot{\epsilon}^p$ is expressed by an associated flow rule:

$$\dot{\epsilon}^p = H \frac{\partial f}{\partial \sigma'} \quad (7.1)$$

Where, H is a plastic parameter determined according to continuous loading conditions, σ' is an effective stress tensor, and f is a yield function. The yield function for the SO model is shown as:

$$f = MD \ln \frac{p'}{p'_0} + D\eta^* - \epsilon_v^p = 0 \quad (7.2)$$

where M is a critical state parameter, D is a dilatancy coefficient (Shibata 1963), p' is the effective mean principal stress, ϵ_v^p is a volumetric plastic strain, and η^* is a generalized shear stress ratio. Using symbols X and L , plastic parameter H is expressed as:

$$H = \frac{L}{X} \quad (7.3)$$

In the case of the SO model, X and L are:

$$X = \frac{D}{p'}\beta^* + \frac{D^2}{p'^2}(\beta^{*2}K + 3G) \quad (7.4)$$

$$L = \frac{D}{p'} \left\{ \frac{3G}{2\eta^*}(\eta - \eta_0) + \beta^*K\mathbf{1} \right\} : \dot{\boldsymbol{\epsilon}} \quad (7.5)$$

where K is a volumetric elastic constant and G is a shearing elastic constant. β^* is expressed as:

$$\beta^* = M - \frac{3}{2\eta^*}\eta(\eta - \eta_0) \quad \eta = \frac{s}{p'}, \quad (7.6)$$

X takes a material-dependent value, as shown in Eq. (7.4). With the SO model, however, X practically takes a positive value. Therefore, the loading condition in strain softening can be determined according to whether L is positive or negative.

To look into geosynthetic reinforcement effects, simulations were conducted using the model shown in Fig. 7.14. In the simulation, compacted soil was wrapped around by geosynthetics and subjected to simple shear. The SO model and elastic bars (truss elements) were used to express the compacted soil and geosynthetics, respectively. Figure 7.15a shows simulation results of displacements and axial stress applied to the geosynthetics, assuming that the degree of compaction can be expressed by an overconsolidation ratio (OCR). The graph reveals that the axial stress applied to the geosynthetics increases with increasing OCR and the geosynthetics constrain the dilatancy of the compacted soil under shear. The simulation results shown in Fig. 7.15a are rearranged in Fig. 7.15b with OCR plotted on the horizontal axis. The results reveal a peak in the axial stress applied to the geosynthetics (in the case of $d = 3.0$ mm), suggesting the possibility that excessive compaction can reduce reinforcement effects.

7.3.2 Constitutive Properties of Compacted Soils

A series of constant volume shear tests was carried out to determine the constitutive parameters for the SO model, which was employed to simulate the mechanical behavior of the full-scale field model tests. Undisturbed soil samples were taken from each layer of the embankment body for the constant volume shear tests. However, it was found that the constant volume shear test apparatus used in the experiment does not have sufficient loading capacity to consolidate the undisturbed soil specimens up to a normally consolidated state. After consolidating the undisturbed soil specimens, they were sheared under, keeping their volume constant. But their effective stress paths obtained from shear tests indicated the characteristics of

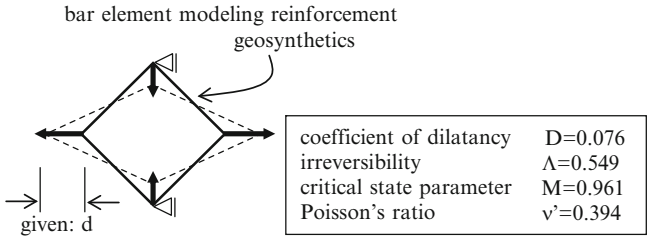


Fig. 7.14 Simulation model that examines the interaction of compacted soil and geosynthetics

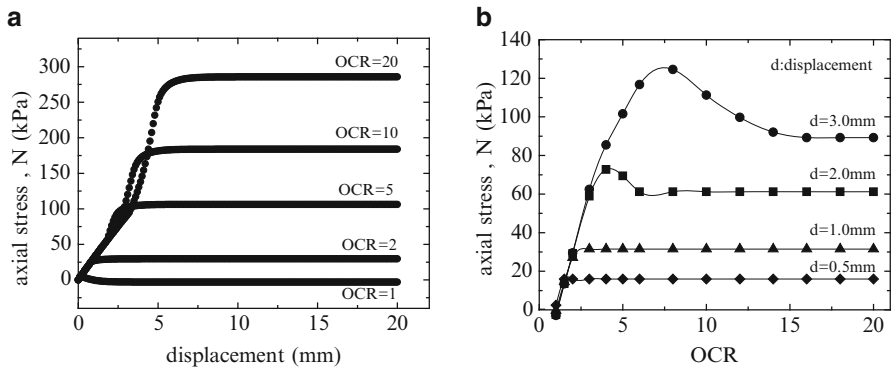


Fig. 7.15 Simulation results: (a) axial stress-displacement relationship; (b) axial stress-OCR relationship

overconsolidated soil specimens. Consequently, it was not possible to determine preconsolidation pressure. Therefore, it was decided to carry out a series of constant volume shear tests on the disturbed (remolded) samples with their water content adjusted, so as to estimate the preconsolidation pressure based on the relationships between the water content, the dry density and the shear strength following the technique proposed by Ohta et al. (1986). By collating the chart thus obtained against test results for undisturbed samples, preconsolidation pressure and other constitutive parameters could be specified for the undisturbed soil samples taken from the test site. Hereafter, the chart of relationships among the water content, dry density, and shear strength is referred to as a compaction control chart.

Figure 7.16 shows compaction control charts depicted based on the element test results. The upper part of Fig. 7.16 shows the relationship between dry density and consolidation pressure. Disturbed samples water contents of which were adjusted in five levels between 10 and 30 % were prepared. Consolidation test results for these samples are represented on the chart as thick solid lines corresponding to different water contents. Consolidation test results for undisturbed samples were also plotted on the chart. Lines were drawn from the plotted marks up to points where each line intersects with a constant water content curve that is closest to the water content of

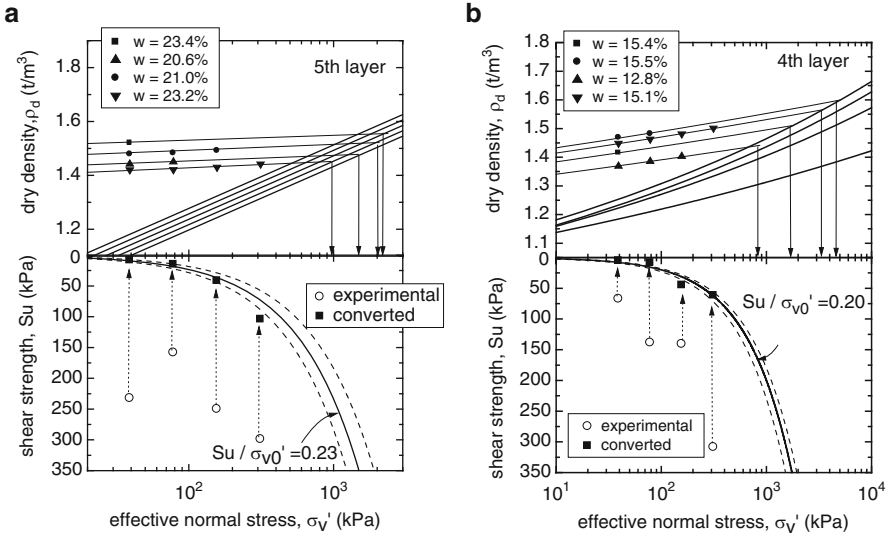


Fig. 7.16 Experimental relation of ρ_d , σ'_v , and S_u . (a) Omma sand at Yuhidera in 1994 (fifth layer). (b) Omma sand at Taiyogaoka in 1996 (fourth layer).

each undisturbed sample, as shown in Fig. 7.16. The value in the abscissa to the point of intersection was evaluated as the equivalent preconsolidation pressure of the undisturbed soil sample. The lower part of Fig. 7.16 shows the relationships between shear strength and consolidation pressure determined by constant volume shear tests conducted at different consolidation pressures. Test results for the disturbed samples revealed almost uniform shear strength for each of the different consolidation pressures, irrespective of differences in water content. This is represented by downward-sloping curves in the figure. As shown by the chart, strength increase rates for the disturbed samples were $S_u/\sigma'_{v0} = 0.23$ for the Yuhidera samples (sampled in 1994) and $S_u/\sigma'_{v0} = 0.20$ for the Taiyogaoka samples (sampled in 1996). Note that shear strengths of undisturbed samples are plotted on the chart as open circles.

The shear strength of an undisturbed sample is its overconsolidation strength, which depends on the preconsolidation equivalent pressure. Hence, the test results were checked by converting overconsolidation strength to normal consolidation strength. The following relationship holds for cohesive soils between overconsolidation strength and normal consolidation strength.

$$\left(\frac{S_u}{\sigma'_{v0}}\right)_{OC} = OCR^\Lambda \left(\frac{S_u}{\sigma'_{v0}}\right)_{NC} \tag{7.7}$$

This equation can be applied to compacted soils. In Eq. (7.7), OCR is an overconsolidation ratio expressed as $OCR = \sigma'_{v0}/\sigma'_{vi}$; Λ is an irreversible ratio:

$\Lambda = 1 - \kappa/\lambda$; and κ is the gradient of the expansion curve determined from the undisturbed samples shown in the upper part in Fig. 7.16. Results of conversion from overconsolidation strength determined for the undisturbed samples via Eq. (7.7) to normal consolidation strength are plotted as ■ in Fig. 7.16. After conversion, there was good agreement between the normal consolidation strength and the strength increase rate determined for the disturbed sample, which suggests the validity of estimated preconsolidation equivalent pressure.

Constitutive properties required for the SO model can be determined using the compaction control chart shown in Fig. 7.16. Regarding the SO model, a theoretical formula of constant volume shear strength for normal consolidation (Ohta et al. 1985) is expressed as:

$$\left(\frac{Su}{\sigma'_{v0}}\right)_{NC} = \frac{1 + 2K_0}{3\sqrt{3}} M \exp(-\Lambda) \quad (7.8)$$

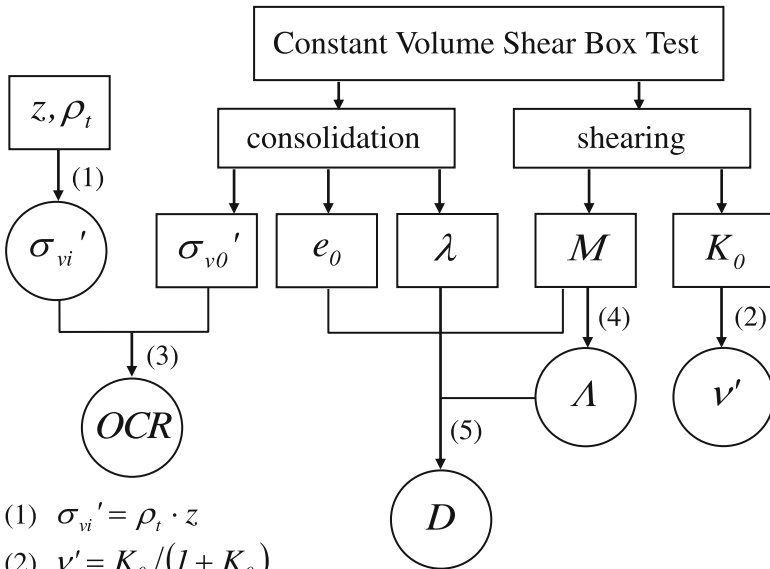
where K_0 is the coefficient of earth at rest, M is the critical state parameter ($= 6 \sin \phi' / (3 - \sin \phi')$, ϕ' : effective friction angle). Therefore, by employing the empiric relations: $M = 1.75\Lambda$ (Karube 1975) and $K_0 = 1 - \sin \phi'$ (Jaky 1944), Eq. (7.8) can be expressed as the function of only ϕ' . Now, because the strength increase rates Su/σ'_{v0} is given as 0.23 (Yuhidera) and 0.20 (Taiyogaoka), the effective friction angle is determined. Other constitutive properties were estimated after Iizuka and Ohta (1987) following the sequence shown in Fig. 7.17. Tables 7.7 and 7.8 list thus-obtained constitutive parameters.

7.4 Finite Element Method Simulations of Full-Scale Field Model Tests

7.4.1 Finite Element Method Simulation of Full-Scale Field Model Tests Conducted in 1994

Figure 7.18 shows the mesh formation used for the analysis. The SO model was used to represent embankment materials. For constitutive properties, estimates shown in Table 7.7 obtained via constant volume shear testing were used. Geosynthetics were modeled as elastic bars (truss elements) and used to provide ten layers at the same positions as in the field model test. For geosynthetics, the material properties are shown in Table 7.2. Analysis steps followed the sequence shown in Table 7.3 to be in accordance with the measurements conducted during the field model test. The cutting of geosynthetics was represented by removing trusses from the cutting locations in the actual test.

Figure 7.19 shows simulation results for removal of the supporting fill by 1.5 m in depth from under the overhanging portion (Step 2). Analysis results were in accord with the test results, with the top edge falling from the overhanging cliff, as shown in the figure. Figure 7.20 compares the test results and the simulation results



- (1) $\sigma_{vi}' = \rho_t \cdot z$
 (2) $v' = K_0 / (1 + K_0)$
 (3) $OCR = \sigma_{v0}' / \sigma_{vi}'$
 (4) $\Lambda = M / 1.75$: Karube (1975)
 (5) $D = \lambda \Lambda / \{M(1 + e_0)\}$: Ohta (1971)

Fig. 7.17 Constitutive parameter determination

Table 7.7 Constitutive parameters of Omma sand at Yuhidera in 1994

	1st layer	3rd layer	5th layer	7th layer	9th layer
Coefficient of earth pressure at rest: K_0	0.470	0.470	0.470	0.470	0.470
Critical state parameter: M	1.730	1.730	1.730	1.730	1.730
Effective Poisson's ratio: v'	0.320	0.320	0.320	0.320	0.320
Compression index: λ	0.195	0.195	0.195	0.195	0.195
Irreversibility ratio: Λ	0.850	0.850	0.850	0.850	0.850
Initial void ratio: e_0	0.920	0.920	0.870	0.900	0.860
Coefficient of dilatancy: D	0.050	0.050	0.051	0.050	0.051
Preconsolidation vertical pressure: σ_{v0}' (kPa)	598	686	980	882	774
Effective overburden pressure: σ_{vi}' (kPa)	78.1	60.9	43.7	26.3	8.9

Table 7.8 Constitutive parameters of Omma sand at Taiyogaoka in 1996

	2nd layer	4th layer	6th layer	8th layer	10th layer
Coefficient of earth pressure at rest: K_0	0.485	0.485	0.485	0.485	0.485
Critical state parameter: M	1.405	1.405	1.405	1.405	1.405
Effective Poisson's ratio: v'	0.327	0.327	0.327	0.327	0.327
Compression index: λ	0.097	0.097	0.097	0.097	0.097
Irreversibility ratio: Λ	0.803	0.803	0.803	0.803	0.803
Initial void ratio: e_0	0.980	0.968	1.010	0.934	0.799
Coefficient of dilatancy: D	0.028	0.028	0.028	0.029	0.031
Preconsolidation vertical pressure: σ_{v0}' (kPa)	330	371	275	532	2112
Effective overburden pressure: σ_{vi}' (kPa)	68.4	53.2	38.0	22.8	7.6

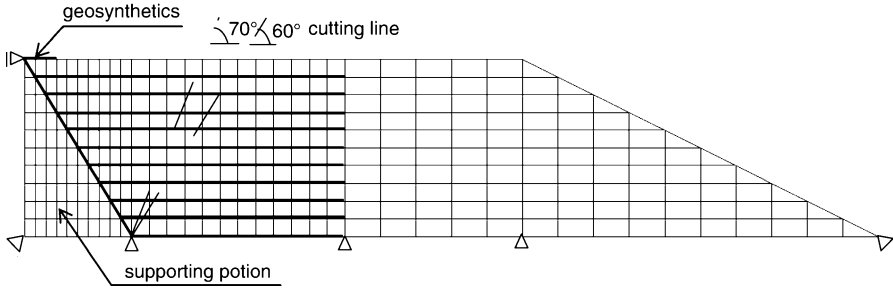


Fig. 7.18 Finite element model for trial embankment in 1994

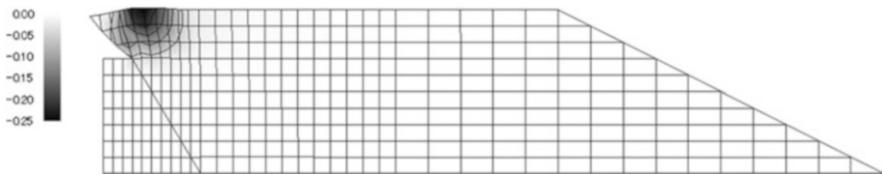


Fig. 7.19 Simulation results (contour of volumetric strain during Step 2)

for vertical displacements of the overhanging portion. The simulated embankment collapsed completely when 4.0 m of the supporting fill was removed (equivalent to Step 6) and the computation ended. This enabled comparison only up to Step 6; however, the simulation is believed to successfully reproduce the deformation behaviors of the overhanging portion observed in the model test.

7.4.2 *Finite Element Method Simulation of Full-Scale Field Model Tests Conducted in 1996*

Meshes used in the analysis are shown in Fig. 7.21. The embankment material was represented by the SO model. Constitutive parameters estimated are shown in Table 7.8. Geosynthetics were modeled as elastic bars (truss elements). Their constitutive properties are shown in Table 7.5. The simple beam and cantilever portions were subjected to prestressing at the same locations as in the field model test. Steel bars used to introduce the prestressing were modeled as elastic bars (truss elements) (Iizuka et al. 2004). Steps for analysis followed the sequence shown in Table 7.6 in accordance with the measurements performed during the field model test. Because it is impossible to simulate the removal of polystyrene foam from under the cantilever portion, Steps 12–17 are not included in the analysis.

Figure 7.22 shows computed results at the timing of cutting the sixth layer geosynthetics in the overhanging portion (Step 28). There was agreement between

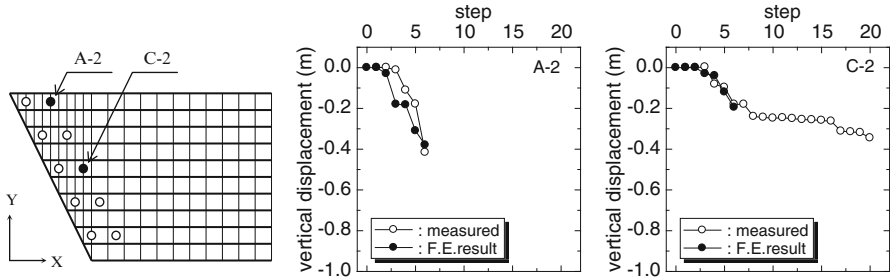


Fig. 7.20 Test results and simulation results for vertical displacements of the overhanging portion

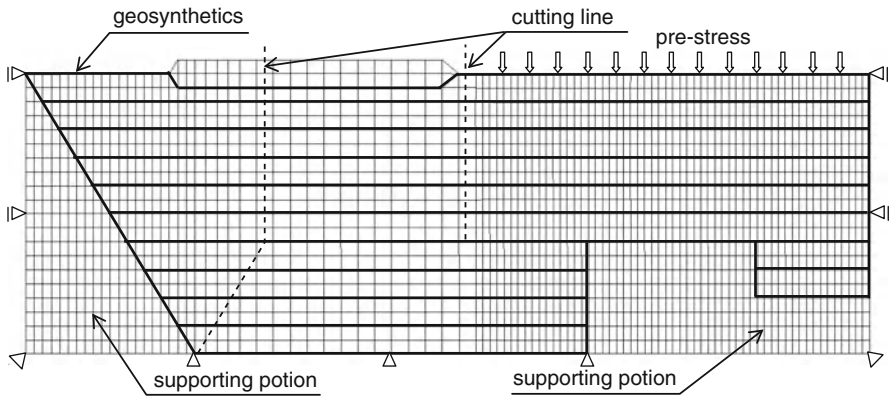


Fig. 7.21 Finite element model for trial embankment in 1996

the simulation results and the test results, with the embankment elements greatly deforming and failing at the location where the geosynthetics were cut, as shown in the figure. Figure 7.23 compares the monitored values in the model test to the computed results for vertical displacements of the overhang. Computed results showed slightly smaller displacements than monitored values in the model test. However, it is believed that the simulation successfully reproduced the deformation behaviors of the overhanging portion observed in the model test.

7.5 Conclusions

This chapter presents finite element simulations of two full-scale field model tests, assuming that a geosynthetic reinforcement effect is brought by constraining the dilatancy of compacted soil under shearing, in which the compacted soil is described by the elasto-plastic constitutive model proposed by Sekiguchi and Ohta. The simulation results are believed to successfully reproduce deformation and failure behavior observed in actual field model tests.

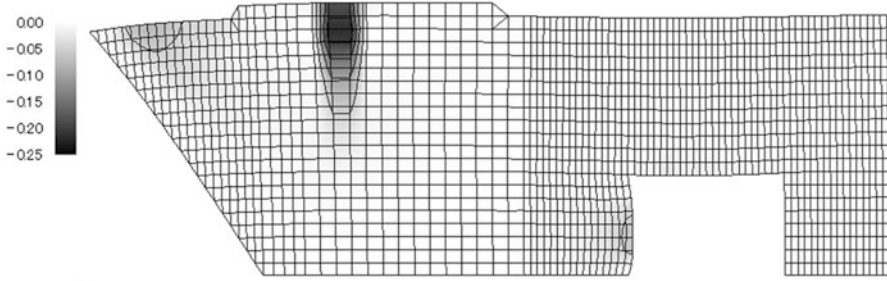


Fig. 7.22 Simulation results (contour of volumetric strain during Step 28)

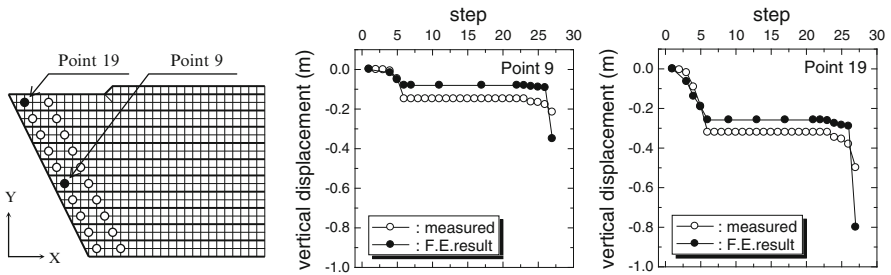


Fig. 7.23 Test results and simulation results for vertical displacements of the overhanging portion

References

Asaoka A, Nakano M, Noda T (1994) Soil-water coupled behaviour of saturated clay near/at critical state. *Soil Found* 34(1):91–105

Drucker DC (1950) Some implications of work hardening and ideal plasticity. *Q Appl Math* 7:411–418

Hirata M, Iizuka A, Ohta H, Yamakami T, Yokota Y, Ohmori K (1999) The numerical simulation of geosynthetics-reinforced soil structure using elasto-plastic dilatancy models. *J JSCE Geotechn Eng, Division*, No. 631/III-48, 179–192 (in Japanese)

Iizuka A, Ohta H (1987) A determination procedure of input parameters in elasto-viscoplastic finite element analysis. *Soil Found* 27(3):71–87

Iizuka A, Hirata M, Ohta H (2001) Reinforcement effect arising from confining dilatancy by geosynthetics. *J JSCE Geotechn Eng, Division*, No. 680/III-55, 15–28 (in Japanese)

Iizuka A, Hirata M, Ohta H, Kawai K, Yokota Y (2004) The role of numerical simulation for geosynthetics reinforced soil structure – from laboratory tests to full scale structures–, *GeoAsia 2004*. Invited Lecture at ISSMGE TC9 Sponsored Session. Proceedings of the 3rd Asian regional conference on Geosynthetics, Seoul, 2004, pp 153–172

Jaky J (1944) *Tarajmechanika*. *J Hung Archit Eng, Budapest*, vol 7, pp 355–358 (in Hungarian)

Karube D (1975) Unstandardized triaxial testing procedures and related subjects for inquiry. In: Proceedings of the 20th symposium on geotechnical engineering, Tokyo, 1975, pp 45–60 (in Japanese)

- Ohta H (1971) Analysis of deformation of soils based on the theory of plasticity and its application to settlement of embankment. Doctor thesis, Kyoto University, Kyoto
- Ohta H, Nishihara A, Morita Y (1985) Undrained stability of K_0 -consolidation clays. In: Proceedings of 11th ICSMFE, San Francisco, 1985, vol 2, pp 613–616
- Ohta H, Nishida Y, Kuniyasu I, Kaneko Y (1986) Soil compaction -quality and verification-. J JGS 'Tsuchi to Kiso' 34(5):43–48(in Japanese)
- Ohta H, Arai K, Asaoka A, Tatsuoka F, Moroto N, Iizuka A (1997) Progressive failure of slopes. Technical report for Grant-in-Aid from the Ministry of Education, Science and Culture, Science Research Project: Fundamental Research (A) (1), JSPS, Tokyo (in Japanese)
- Ohta H, Maeda Y, Nishimoto K, Yamakami T, Iizuka A, Kobayashi I (2002) A series of trial embankments of reinforced earth. In: Proceedings of 7th international conference on geosynthetics, Nice, 2002, vol 1, pp 307–312
- Sekiguchi H, Ohta H (1977) Induced anisotropy and time dependency in clays. In: Proceeding of the 9th ICSMFE, Specialty Session 9, Tokyo, 1977, pp 229–237
- Shibata T (1963) On the volume changes of normally consolidated clays. Annuals, disaster prevention research institute, Kyoto University, Kyoto, No. 6, pp 128–134 (in Japanese)

Chapter 8

Deformation Prediction of a Structure Placed on Soft Clay in Tokyo Bay Affected by Heavy Deep Well Pumping

Koki Matsumoto, Akira Kobayashi, and Hideki Ohta

8.1 Introduction

Many urban cities of Japan have experienced problems caused by the withdrawal of groundwater. Especially in the lowlands around Tokyo Bay, excessive withdrawal of groundwater caused the significant land subsidence well known to be a geohazard. The main reason for the serious withdrawal is large-scale industrial groundwater usage during a period of high economic growth in Japan.

The maximum value of groundwater head dropped in this area in about 1972 was approximately -60 m from the sea level of Tokyo Bay (T.P.; Tokyo Peil); the total land subsidence reached 4.5 m. The Tokyo metropolitan government has restricted groundwater pumping since 1956 to prevent further land subsidence. Sequentially, surface water has replaced groundwater for industrial use since 1961. As a result, the groundwater head rapidly recovered, and the subsidence experienced upheaval.

Many large developments were constructed in this coastal area between 1980 and 1990. The water pressure distribution in the ground was lower than the hydrostatic pressure distribution because the groundwater was in the process of recovering up to hydrostatic pressure in that decade.

K. Matsumoto, D.Eng. (✉)
Civil Engineering Division, Hazama Ando Corporation,
6-1-20 Akasaka, Minato-ku, Tokyo 107-8658, Japan
e-mail: matsumoto.koki@ad-hzm.co.jp

A. Kobayashi, D.Eng.
Faculty of Environmental and Urban Engineering, Kansai University,
3-3-35 Yamate-cho, Suita City, Osaka 564-8680, Japan
e-mail: koba5963@kansai-u.ac.jp

H. Ohta, D.Eng.
Research and Development Initiative, Chuo University, 1-13-27 Kasuga,
Bunkyo-ku, Tokyo 112-8551, Japan
e-mail: ohta@tamacc.chuo-u.ac.jp

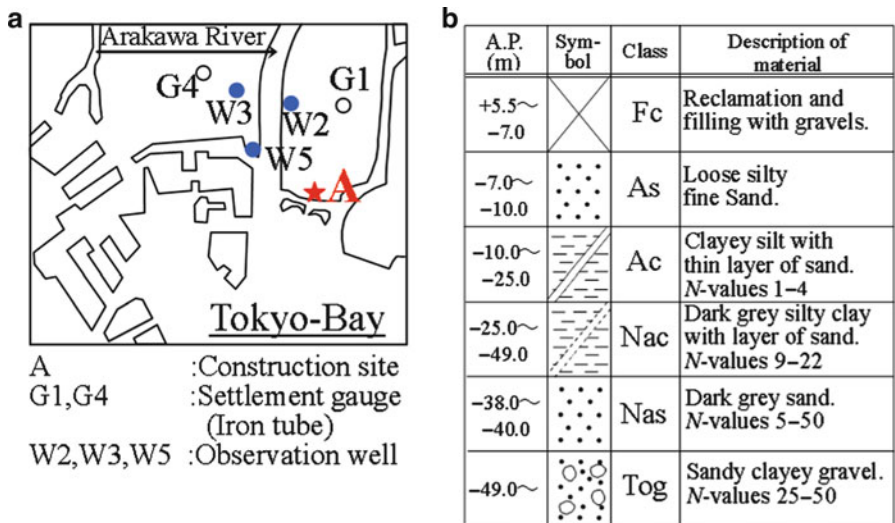


Fig. 8.1 (a) Observation well and settlement monitoring points around Tokyo Bay. (b) Soil profile

Such a remarkable fluctuation of groundwater table and reclamation works around the Bay area affected the initial stress state before new construction could begin. Unfortunately, in many cases the distribution of groundwater pressure was not measured before construction. In such cases, it was difficult to properly estimate initial stress conditions, such as the overconsolidation ratio, which is closely related to soil parameters. It should be emphasized that the initial effective stress state is definitely required.

This chapter presents a method to estimate the initial stress state before construction begins taking the heavy deep well pumping into account.

The construction work introduced in this chapter is on a public aquarium, the Tokyo Sea Life Park (Sea Museum) constructed on reclaimed land at the mouth of the Arakawa River in 1989 (Site-A in Fig. 8.1a). The three-story structure was reinforced concrete combined with about a 100-m diameter steel frame. The basement is supported by about 800 PHC piles ($\phi 600$ mm) driven into the Tokyo gravel layer at a depth of 55 m. A roof entrance located in the center of a concrete platform surrounded by fountains and pools is the architectural sales point. It can give the illusion that visitors dive into the waters of Tokyo Bay.

A large embankment was planned to be placed near the structure as an attractive landscape from the top of the hill approaching the museum. This large embankment immediately led to the possibility of severe damage to the piles resulting from a lateral displacement of the soft soil. It was necessary to ensure that deformation of the pile did not exceed the prescribed limits. It was suggested to reduce the height of the planned fill to minimize ground movement. Both ground movement and pile deformation adjacent to the embankment were monitored so as to watch the ground behavior during construction.

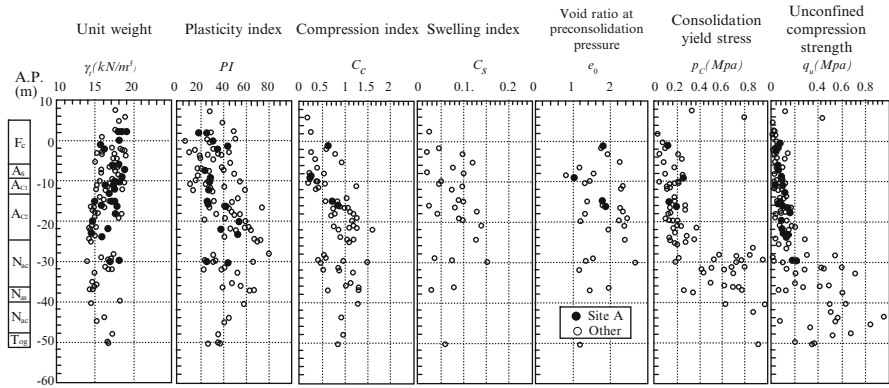


Fig. 8.2 Vertical profile of soil properties

The two-dimensional deformation process is analyzed by employing a soil–water coupling finite element program called Deformation Analysis Considering Stress Anisotropy and Reorientation (DACSAR) to predict the ground behavior resulting from proximity filling. The constitutive model used in the DACSAR program developed by Iizuka and Ohta (1987) is the one proposed by Sekiguchi and Ohta (1977). In analyzing the behavior of soft clay foundations, it is essential to estimate the in situ effective stress state before construction. But in this construction, no attempt was made to measure the groundwater pressure distribution.

Therefore, the authors used one-dimensional FEM soil–water coupling analysis to evaluate an initial stress state before construction. This technique estimates a stress state by following the groundwater table changes in the past and reclaiming history from 100 years ago when the hydrostatic pressure distribution did exist at the site. The estimated in situ initial condition was adopted into the two-dimensional FEM analysis, in anticipation that the prediction would be in agreement with the actual ground behavior.

Based on the results of prediction analysis, it was decided to employ a countermeasure to use 11,000 m³ of expanded poly-styrol (EPS) light fill to be placed in the vicinity of the fill to reduce the ground movement.

8.2 Description of the Site

8.2.1 Soil Profile

The sequence of soils revealed at Site-A is shown in Fig. 8.1b. The vertical distributions of soil properties are summarized in Fig. 8.2. Data obtained from more than 30 borings around Site-A were collected to create a reliable soil profile. The plotted solid circle indicates the results at Site-A, and plots of open circle

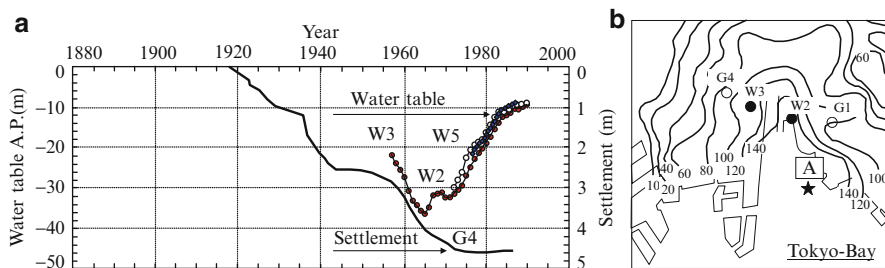


Fig. 8.3 (a) Water table fluctuation and ground settlement. (b) Subsidence contour from 1963 to 1973 (in cm)

indicate the results from the nearby area. The perspective of the ground profile became clear by collecting boring data around the construction site. Reclaimed and Filling ground (Fc), approximately 12.5 m thick, overlies alluvial soft clay (As,Ac) approximately 18 m in thickness, stiff silty clay of approximately 24 and 2 m of sand (Nac,Nas) and Tokyo Gravel (Tog), which is well known as bearing stratum in this area.

According to the distribution of consolidation yield stress and unconfined compression strength, the soil profile can roughly divide into two phases. The upper part is soft soil and lower part is stiff soil.

8.2.2 Groundwater and Reclamation Record

The ground of construction site was reclaimed during a period from 1972 to 1981, up to a height +5.5 m Arakawa peil (A.P.; T.P. = A.P. + 1.1344 m). Subsequently, 2.8 m height of preloading on the subsurface was placed for 4 years (1981–1985) and 4.0 m height of preloading was placed for 6 months (Nov. 1986–Apr. 1987) again.

According to the groundwater table measured at GL -70 m at the Site-W3 at 4 km distance from the construction site, the water table dropped to -36 m A.P. in 1965 and recovered to -10 m A.P. in 1990, and the ground subsidence reached 4.5 m, as shown in Fig. 8.3a. The land subsidence from 1963 to 1973 caused by heavy deep well pumping was 1.4 m, as shown in Fig. 8.3b.

8.2.3 Estimation of Initial Stress Condition by Using One-Dimensional Finite Element Method

We conducted one-dimensional analysis considering both the groundwater table changes from 100 years ago (1887) and the reclamation processes, which started in the early 1970s. Figure 8.4a shows a 1-D FEM mesh. The initial stress state of 1-D

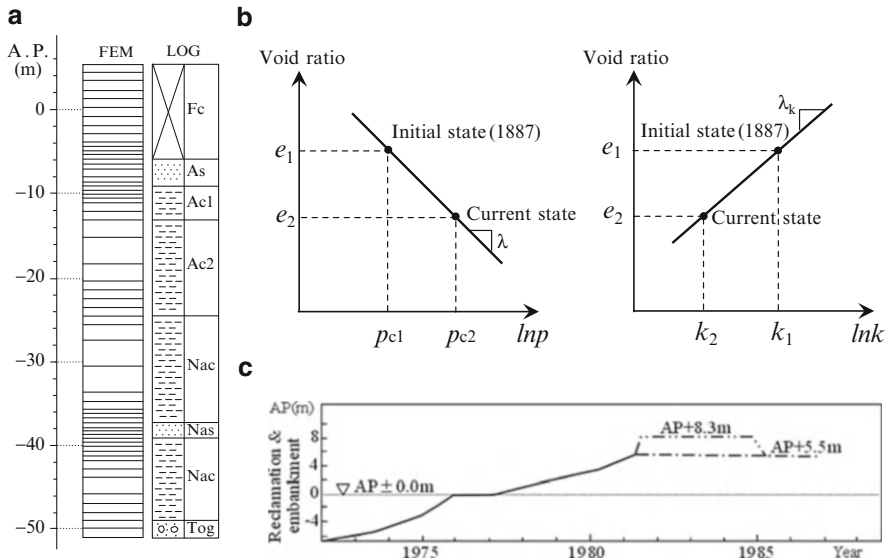


Fig. 8.4 (a) One-dimensional FEM mesh. (b) Initial condition in 1887 (permeability and void ratio). (c) Reclamation and embankment schedule

FEM was set as it used to be in 1887, when the distribution of groundwater pressure was supposed to be hydrostatic.

The sequence of analysis is as follows.

1. The initial effective stress of 1-D FEM (in 1887) is estimated assuming hydrostatic water pressure with water head at ± 0 m A.P.
2. It is assumed that in 1887, the alluvial clay layer (Ac-layer) was a normally consolidated condition. We assumed that the consolidation data yielded a stiff clay layer (Nac-layer) stress, as shown in Fig. 8.2, which remained from 1887, so the overconsolidated ratio of this layer is estimated in the range of 2–3.
3. Some material parameters used in 1-D FEM were determined based on the overconsolidated ratio. Some empiric procedures recommended by Iizuka and Ohta (1987) were also used.
4. In these parameters, the void ratio (e) and permeability (k) of clay material in 1887 were determined from the relationships of $e-\ln p$ and $e-\ln k$, considering the stress state at that time (see Fig. 8.4b).
5. The loading rate caused by reclamation was modeled by an addition of mesh following the reclamation procedure shown in Fig. 8.4c.
6. In the 1-D FEM analysis procedure, a hydraulic boundary condition at the Tog layer was given as the records of observation well (Site-W3), and for the no recorded period (1887–1955) a hydraulic boundary condition was assumed (broken line in Fig. 8.5).
7. The analytical results were compared with the actual ground compression (>GL-50 m) and distribution of groundwater pressure.

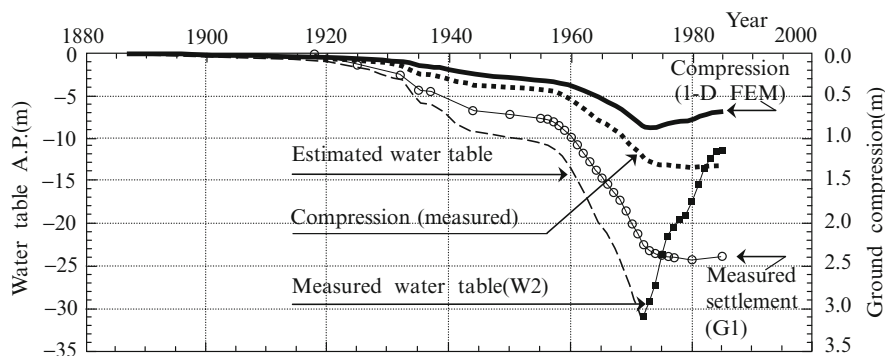


Fig. 8.5 Ground compression (measured vs. calculated)

8.3 The Results of One-Dimensional Finite Element Method Analysis

8.3.1 Ground Compression

Total land subsidence at Site-G1 (see Fig. 8.1a) reached around 2.4 m by 1986. The ground compression greater than GL-70 m is estimated to be approximately 55 % of the ground surface settlement based on the double tube observed record of 70 m length at Site-W2. According to Fig. 8.5, the calculated compression (*bold line*) by using 1-D FEM indicates approximately 50–70 % of the actual compression (*dotted line*). As shown in Fig. 8.3a and b, groundwater fluctuations are almost the same over a wide area, but ground subsidence is different from place to place. One of the reasons of the difference may be localization of soil profile.

8.3.2 Distribution of Groundwater Pressure

The distribution of groundwater pressure was not observed before construction began. However, fortunately, water pressure distribution was observed in another construction site at about 2 km from the same land reclaimed in 1984. The observed values were compared with the results of analysis. In 1972, the maximum lowering of water pressure distribution was computed as shown in Fig. 8.6a. In 1984, when the ground level was increased up to +2.5 m A.P. by additional filling, the distribution of groundwater had good agreement with actual values.

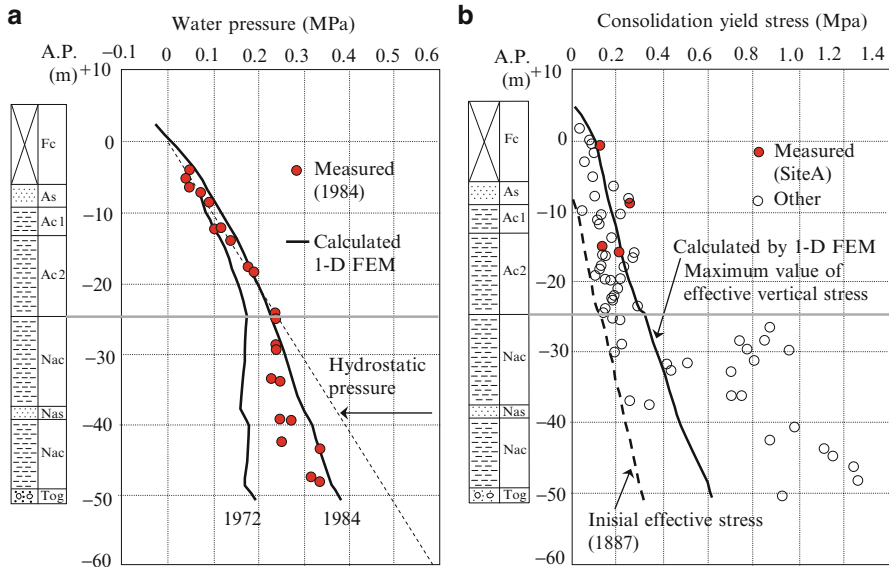


Fig. 8.6 (a) Distribution of ground water pressure. (b) Consolidation yield stress and maximum effective overburden pressure

8.3.3 Comparison Between Consolidation Yield Stress and Vertical Effective Stress

A vertical maximum effective stress in the Ac-layer affected by the large withdrawal of groundwater and reclamation was compared with consolidation yield stress. The results are shown in Fig. 8.6b. In the lower part of the As-layer at around -8 m A.P., the consolidation yield stress (red circle in Fig. 8.6b) is slightly bigger than the analyzed value. In the past, the water pressure dropped completely in the As-layer by pumping. Using the described method, the Ac-layer was supposed to be in the normal consolidation state, the Nac-layer with an overconsolidation state of $OCR = 2.3$.

8.4 Construction Sequence and Field Observations

8.4.1 Description of Construction and Planned Ground Monitoring

The construction sequence is shown in Figs. 8.7 and 8.8.

- (1) Preloading embankment of 4 m in height and its removal, (2) movement of preloading embankment, (3) pile driving, (4) excavation (3 m in depth) and surrounding embankment, (5) structure construction, and (6) landscape gardening.

No	Event	1986				1987				1988				1989			
		12	2	4	6	8	10	12	2	4	6	8	10	12	2		
(1)	Preload	[Hatched bar]															
(2)	Movement of the preload					[Hatched bar]											
(3)	Pile driving					[Hatched bar]											
(4)	Filling					[Hatched bar]											
	Excavation					[Hatched bar]											
(5)	Building	[Hatched bar]															
(6)	Garden around the structure															[Hatched bar]	

Fig. 8.7 Construction schedule

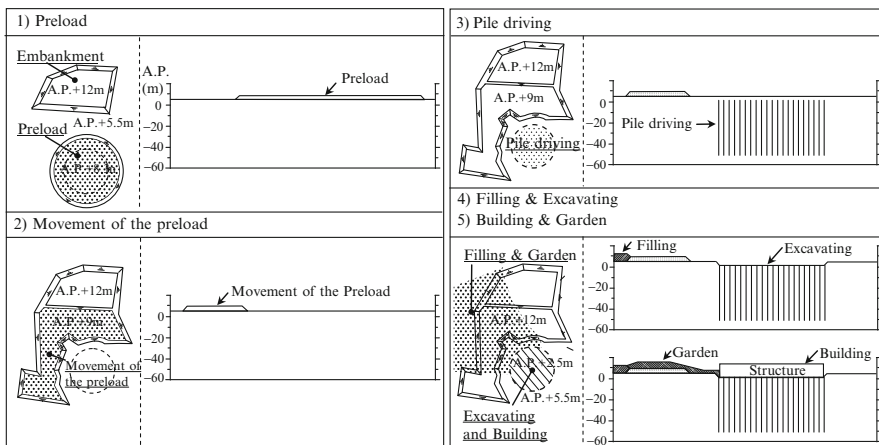


Fig. 8.8 Construction stage

The embankment in the vicinity of the structure resulted in a lateral movement, which could damage the piles of the structure. Therefore, monitoring of ground movement was carried out during the construction period. Ground settlement and lateral movement in the ground were measured by using settlement gages and inclinometers (*F* and *B*), as shown in Fig. 8.9a. After pile driving work, lateral movement of a pile was observed by an inclinometer set in a PHC pile (indicate *G*). The ground profile in Section X-X' is shown in Fig. 8.9b.

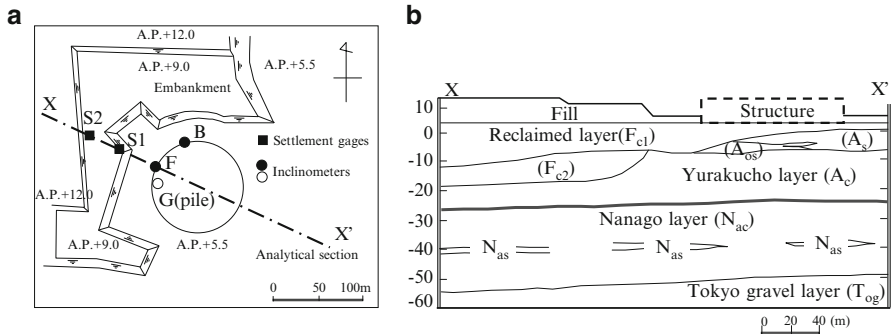


Fig. 8.9 (a) Monitoring points and 2-D analytical section. (b) Ground profile (X-X' section).

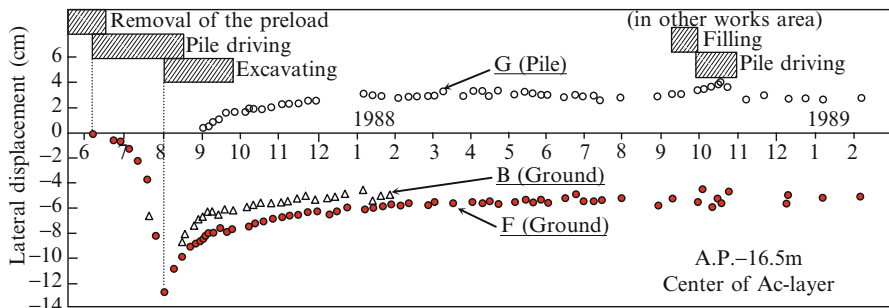


Fig. 8.10 Lateral displacement with elapsed times (at -16.5 m A.P.)

8.4.2 Field Observations

According to the monitoring results shown in Figs. 8.10 and 8.11, the pattern of ground displacement can be categorized as follows.

1. Pile driving stage, during which ground displacements were generated in a direction away from the pile driving area. Ground displacements varied linearly with depth.
2. The excavation and filling stage, during which the ground displacements occurred in the direction of the pile driving area. The largest ground displacement was observed in the soft clay Ac-layer.
3. Deformation of a pile (G) and ground deformation at a point F coincide with each other, even though point G and point F are 20 m apart.
4. It appears as if the pile deformed suddenly at the boundary between the soft clay Ac-layer and the stiff clay Nac-layer.

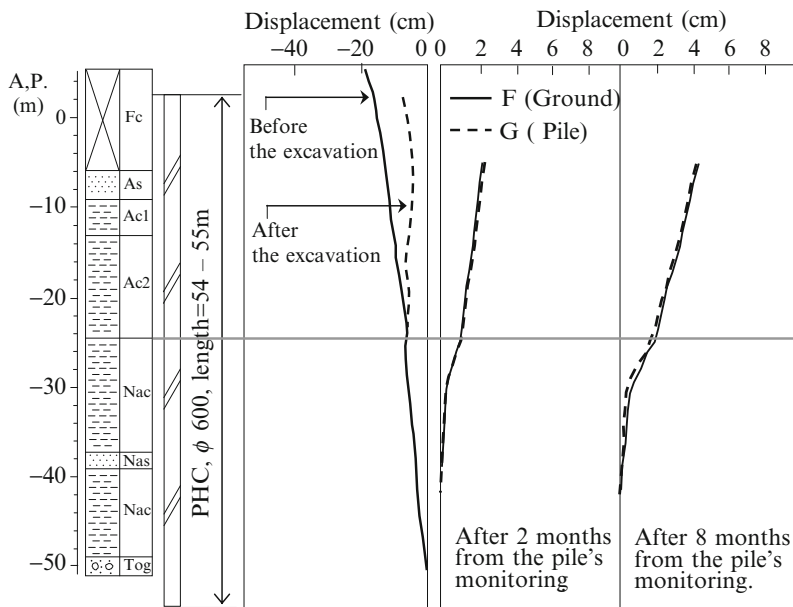


Fig. 8.11 Lateral deformation (Pile (G) and Ground (F))

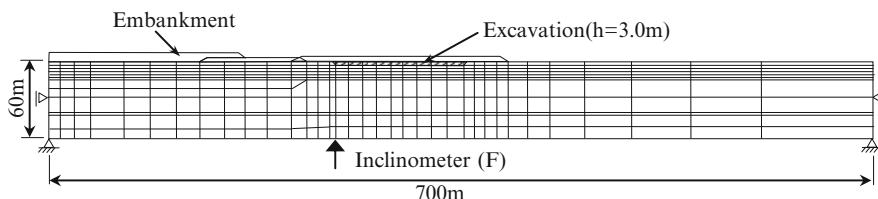


Fig. 8.12 Two-dimensional FEM mesh

8.5 Prediction of Ground Deformation by Using 2-D Finite Element Method

Prediction has been made of the ground deformation induced by further filling by using two-dimensional FEM analysis. A FEM mesh is shown in Fig. 8.12 and soil parameters are summarized in Table 8.1. The initial stress condition of 2-D FEM was estimated by taking account of a past stress history by using one-dimensional FEM analysis. To demonstrate the influence of the difference of initial stress states, two

Table 8.1 Soil parameters

D	Λ	M	ν'	k (cm/s)	K_0	K_i	α	$\dot{\nu}_0$	e_0	λ	λ_k	E (kPa)	ν	e_i
Crust				9.40E-07								40,000	0.353	2.025
Fc	0.076	0.875	1.08	9.40E-07	0.545	0.545	2.82E-03	3.10E-07	2.025	0.282	0.274			
Aoc	0.113	0.900	1.00	4.10E-08	0.629	0.629	3.76E-03	4.10E-07	1.275	0.282	0.435			
As				1.20E-06								21,000	0.361	1.275
Ac	0.191	0.900	1.00	6.40E-07	0.629	0.629	6.36E-03	6.90E-07	1.275	0.477	0.435			
Ac	0.126	0.900	1.04	6.40E-07	0.650	0.650	4.77E-03	5.20E-07	2.025	0.477	0.435			
Nac	0.128	0.930	1.45	5.90E-07	0.608	0.840	5.99E-03	6.50E-07	1.525	0.499	0.291			
Nas				3.60E-06								60,000	0.378	1.525
Tog				2.30E-03								150,000	0.300	2.000

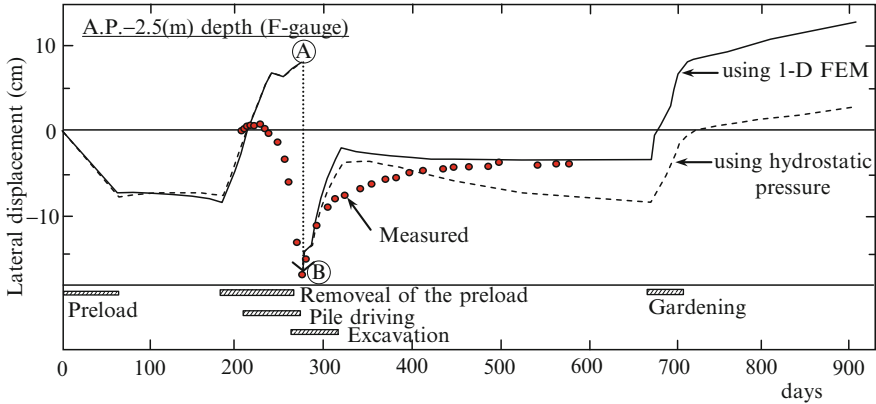


Fig. 8.13 Lateral displacement at -2.5 m A.P. (calculated vs. measured)

cases of groundwater pressure were compared. The first case is with hydraulic pressure distribution in which water head is assumed at ± 0 m A.P., and the other case is with the initial water pressure distribution estimated by one-dimensional FEM analysis.

8.5.1 Lateral Displacement of the Ground

Computed lateral displacement was compared with observed displacement of the ground (F). Figure 8.13 shows lateral displacement at a depth of AP -2.5 m. The effect of the piles was not taken into account; hence, the ground deformation was ignored during the pile driving period.

According to Fig. 8.14, lateral displacement (*solid line*) calculated that the one-dimensional FEM analysis was in good agreement with actually observed values (*solid circle*). It is confirmed that both lateral displacement of ground and pile changed suddenly near the border of the Ac- (soft clay) and Nac-layer (slightly stiff clay), as shown in Fig. 8.14. Using hydrostatic pressure as an initial state condition, it is seen that the lateral displacement was evaluated as slightly smaller, and the bending behavior in depth is not clearly recognized at the boundary of the Ac- and Nac-layer.

8.5.2 Ground Surface Settlement

The ground surface settlement around the structure with elapsed time is shown in Fig. 8.15. The prediction (*solid line*) is almost in good agreement with actually observed behavior (*solid circle*). On the other hand, the case (*dotted line*) using the hydraulic pressure distribution underestimates the ground settlement.

As mentioned, it is important to properly evaluate an initial groundwater distribution before construction.

Fig. 8.14 Lateral deformation (calculated vs. measured)

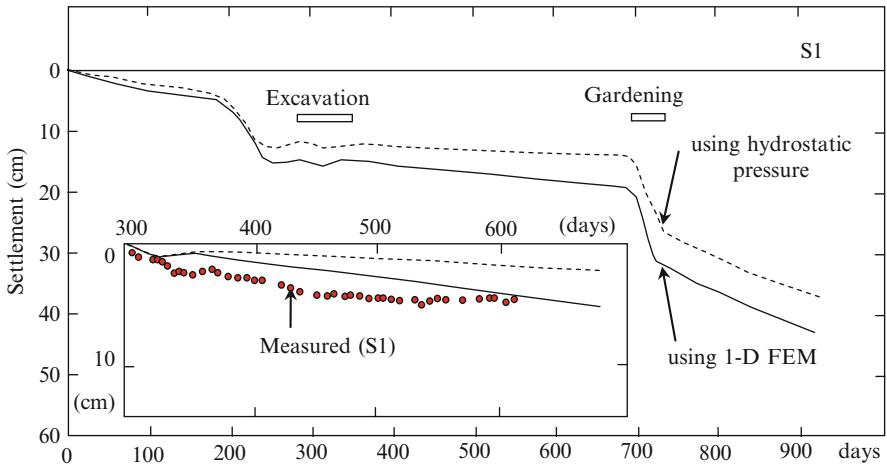
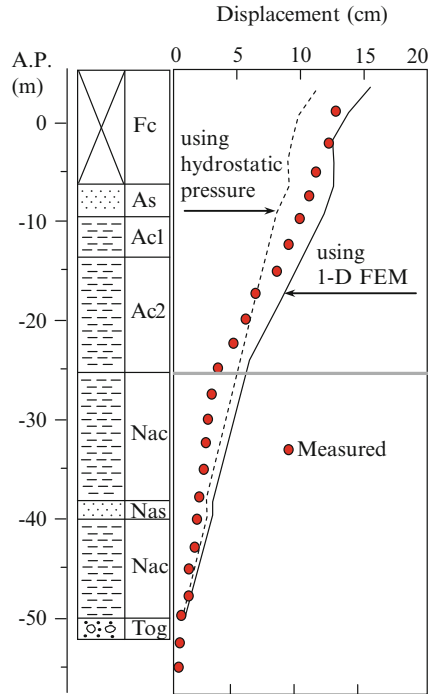


Fig. 8.15 Ground settlement (S1) (calculated vs. measured)

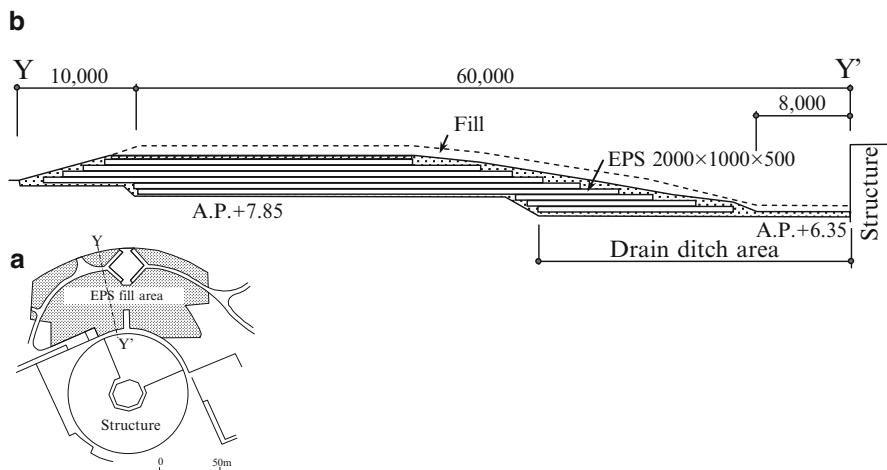


Fig. 8.16 EPS fill. (a) Plane. (b) Y–Y' section

8.6 Countermeasures

Countermeasures were considered to maintain the soundness of the piles. These countermeasures had to satisfy the following requirements:

1. The planned height of the hill had to remain at 7 m after completion of the construction.
2. The lateral movement of soft ground could not be increased by filling.
3. The period for embankment work could not be extended.

The most obvious solution to overload problems was to reduce the load. The EPS light-fill method was adopted based on a comparison of the effect, cost, and time to complete. Figure 8.16a shows the plan of EPS fill; the Y–Y' section is shown in Fig. 8.16b.

According to analytical results using FEM, it was expected that lateral displacement induced by further filling could be reduced to about one third, as shown in Fig. 8.17. It is confirmed that zero lateral displacement of the soft clay layer was observed during March 1989 to March 1991 after monitoring during construction.

8.7 Conclusions

1. In prediction of ground deformation by FEM analysis, it is essential to properly estimate the in situ initial stress state before construction begins. However, in the lowland around Tokyo Bay, distribution of groundwater pressure does not show the hydraulic state owing to large groundwater withdrawals and reclamation. Water pressure distribution before construction works was not monitored in

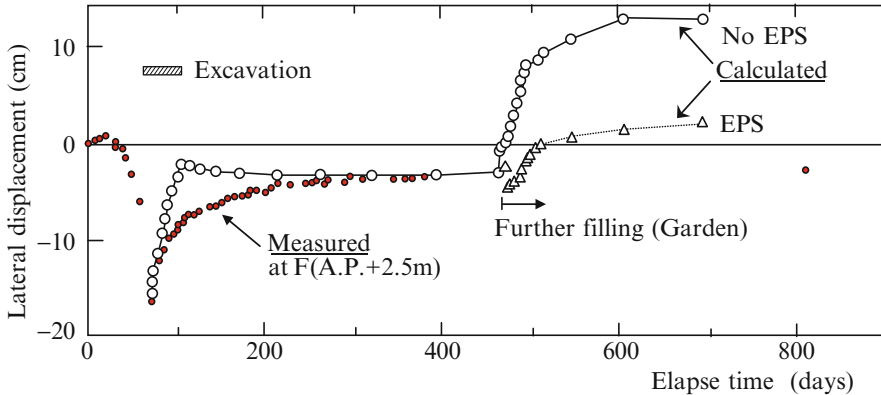


Fig. 8.17 Prediction of lateral displacement caused by further filling or EPS

many cases. In such cases, it is not easy to properly estimate an initial stress condition such as effective overburden pressure.

2. We used one-dimensional FEM of soil–water coupling analysis to evaluate an initial stress state before construction. This technique estimates the stress state altered by water table changes and reclamation history starting from the ground state 100 years ago. The long-term water table and compression records observed by the Tokyo metropolitan office were used in the computations. The distribution of water pressure estimated by 1-D FEM was in good agreement with the measured values before construction.
3. Lateral displacement of ground caused by further filling in the vicinity of the structure was predicted by two-dimensional FEM analysis using the initial stress state evaluated by 1-D analysis. The results accorded with the observed ground behavior well.
4. Countermeasures were considered to maintain the safety of the piles supporting the structure, and the EPS light-fill method (11,000 m³) was adopted. Zero lateral displacement of the soft clay layer was observed after the completion of construction.

Acknowledgments The authors gratefully acknowledge the support of the Tokyo Metropolitan Office, the Taniguchi Architectural Design Office, and the Kimura Structural Engineers' Office. The authors would also like to acknowledge Prof. Iizuka for giving valuable advice for performing FEM analysis.

References

- Iizuka A, Ohta H (1987) A determination procedure of input parameter in elasto-viscoplastic finite element analysis. *Soil Found* 27(3):71–87
- Sekiguchi H, Ohta H (1977) Induced anisotropy and time dependency in clay. In: *Proceedings of the specialty session 9, 9th ICSMFE, Tokyo*, pp 229–238

Chapter 9

Elasto-Plastic FEM Analysis and Safety Evaluation of Large Rockfill Dams During Reservoir Filling

Tetsuo Fujiyama, Takeshi Ishiguro, Yoshihisa Uchita, and Hideki Ohta

9.1 Introduction

Engineers specializing in rockfill dams must pay attention to uncertain factors contributing to hydraulic fracturing, estimate its probability, and confirm the stability of the actual dam body at the first reservoir filling. The failure of a large rockfill dam is one of the most tragic geohazards. There is as yet no established method, however, to evaluate dam stability against hydraulic fracturing that is accurate and practical enough to use in engineering practice. The authors have reported that the stress–deformation behavior of large rockfill dams during construction and first reservoir filling can be evaluated accurately enough using soil–water coupled elasto-plastic analysis (Ohta et al. 2001; Mori et al. 2001) and stability against hydraulic fracturing can be quantified by using the minor principal stress and pore water pressure thus computed (Ohta et al. 2005, 2006).

T. Fujiyama, D.Eng, (✉)

Technical Research Institute, Maeda Corporation, Nerima-ku, Tokyo, Japan

Science and Technology Department, Engineering Division, Nuclear Waste Management Organization of Japan (NUMO),

4-1-23 Shiba, Minato-ku, Tokyo 108-0014, Japan

e-mail: tfujiyama@numo.or.jp

T. Ishiguro, D.Eng,

CDS Project Section, Maeda Corporation, 3-11-18 Iidabashi, 102-0072 Chiyoda-ku, Tokyo, Japan

e-mail: isigurot@jcity.maeda.co.jp

Y. Uchita, D.Eng,

Construction Department, Tokyo Electric Power Company, 1-1-3 Uchisaiwai-cho, Chiyoda-ku, Tokyo 100-8560, Japan

e-mail: uchita.y@tepcoco.jp

H. Ohta, D.Eng,

Research and Development Initiative, Chuo University, 1-13-27 Kasuga, Bunkyo-ku, Tokyo 112-8551, Japan

e-mail: ohta@tamacc.chuo-u.ac.jp

This chapter provides an overview of the evaluation method for the stability of large rockfill dams against hydraulic fracturing. The stress–deformation behavior of a large rockfill dam during construction and first filling was simulated using soil–water coupled elasto-plastic analysis. The validity was confirmed by comparing with actual measurements during first filling and by the laboratory hydraulic fracturing tests using the embankment material. A tentative plan for the pre-estimation of the hydraulic stability of the embankment and first filling safety control was suggested and put into practice at an actual dam.

9.2 Mechanism of Hydraulic Fracturing and Current Evaluation Methods

Figure 9.1 was prepared by the Japanese Geotechnical Society’s Committee on the Mechanism of Hydraulic Fracturing and Evaluation Methods (Japanese Geotechnical 2002). The figure shows an approach to the evaluation of the mechanism of hydraulic fracturing. As shown, hydraulic fracturing is initiated by various uncertain factors. For example, differential settlement resulting from a highly irregular surface shape of the bedrock on which the dam is built, or considerable arching action during its construction because of the differences of the stiffness between each zones, results in extremely low effective stresses in the core zone of the completed dam and even cracking under certain conditions. As the first filling of the reservoir starts, infiltrating water is concentrated into hydraulically weak (low stress zones or cracks) areas so that fine grains in the core material flow out along them. This is how hydraulic fracturing is initiated and progresses. If the self-healing function of the core or the trapping function of the downstream filter against the fine-grained core material being washed out does not work, then hydraulic fracturing develops into piping that penetrates the dam in the transverse (upstream–downstream) direction, and the dam fails.

The related current design standard in Japan is shown on the right half of Fig. 9.1. The current Japanese standard merely touches on a method for checking on stresses in the dam by the total stress analysis method to evaluate the possibility of initiation of hydraulic fracturing. In the actual design, however, it is common practice to evaluate the possibility of the progress of hydraulic fracturing by checking on the critical flow velocity and critical hydraulic gradient. For the evaluation of inadequacy of trapping capability, what is being done is merely to apply filter criteria more or less as an alternative. Thus, the current evaluation method has a number of problems, including the following:

1. The consecutive mechanism of hydraulic fracturing is not evaluated comprehensively or in a unified way.
2. There is no established method of accurate evaluation that takes into account and reproduces the uncertain factors, initiation, and progress of the hydraulic fracturing.
3. Heterogeneity of a dam (because of various factors during construction and first filling) and concentrated seepage are not taken into account.

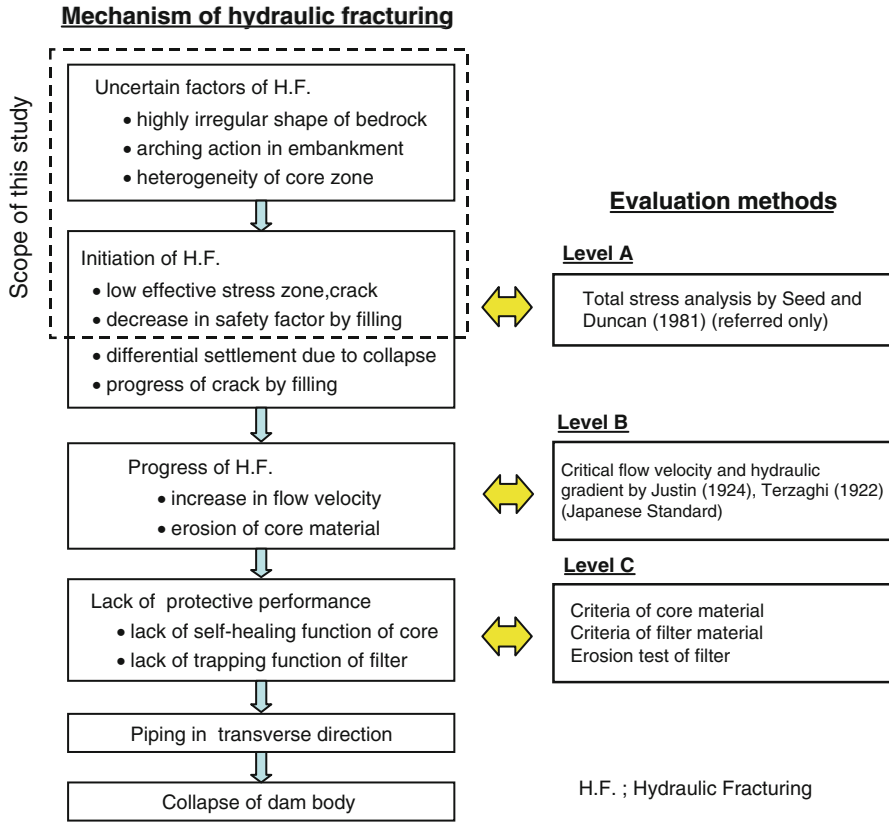


Fig. 9.1 Mechanism of hydraulic fracturing and the summary of its evaluation methods (Japanese Geotechnical 2002)

This study addresses the first and second issues listed in the preceding. In Fig. 9.1, the scope of this study is indicated as the rectangular area within the broken line. This study aims at investigating the initiation of hydraulic fracturing by a highly accurate, practical analysis technique that allows the consideration of various uncertain causes of hydraulic fracturing.

9.3 Evaluation of the Stability of Large Rock-Fill Dams During Reservoir Filling

9.3.1 An Overview Analysis of the Kamihikawa Dam

The results of construction and first reservoir filling analyses conducted by elasto-plastic effective stress analysis are used as the means of quantitative pre-evaluation

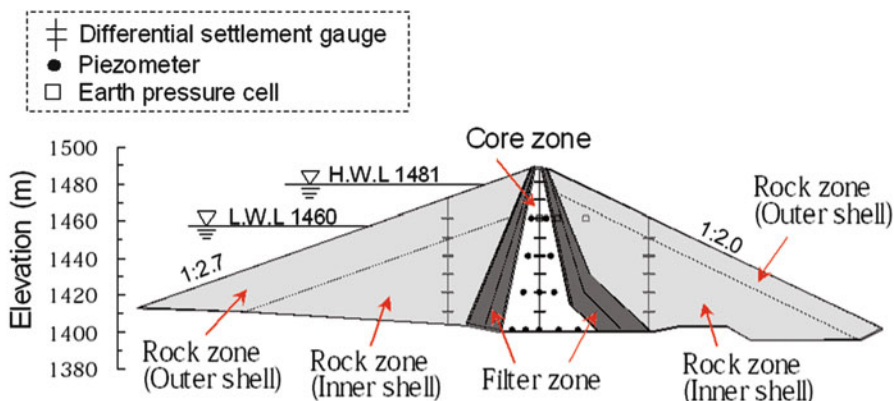


Fig. 9.2 Cross-section of the Kamihikawa Dam (After Ohta et al. 2001)

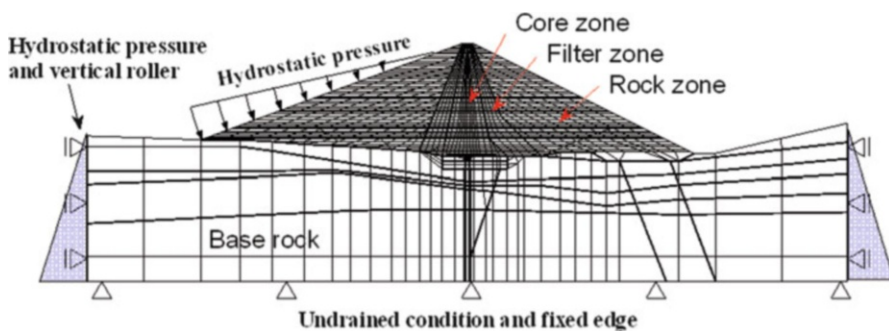


Fig. 9.3 Analytical model and boundary conditions (After Ohta et al. 2006)

of hydraulic fracturing potential. The embankment and reservoir filling process of a rockfill dam is reproduced by FEM, and the stress–deformation behavior of the core zone is traced with the aim of estimating the possibility of the occurrence of a hydraulically weak area and the initiation of hydraulic fracturing.

The Kamihikawa Dam analyzed in this study is an 87-m high, 94-m long center-core rockfill dam with a volume of 4,110,000 m³ (Ohta et al. 2001; Mori et al. 2001). The dam was completed in 1999 in Japan. Figure 9.2 shows a typical cross-section of the dam. In the typical cross-section, cross-arm settlement gauges, piezometers, and earth pressure cells were installed to measure dam behavior at the embankment construction and filling stages. Figure 9.3 shows the mesh diagram of the Kamihikawa Dam. In modeling the dam, the FEM model was zoned to express the initial heterogeneity of the dam materials. A soil–water coupled effective stress analysis that took into consideration the changes of pore water pressures in the core zone during construction and first reservoir filling in this analysis. An analysis code incorporating Sekiguchi and Ohta’s elasto-visco-plastic model (Sekiguchi and Ohta 1977) as the constitutive law was used. In the impoundment analysis conducted after the embankment analysis,

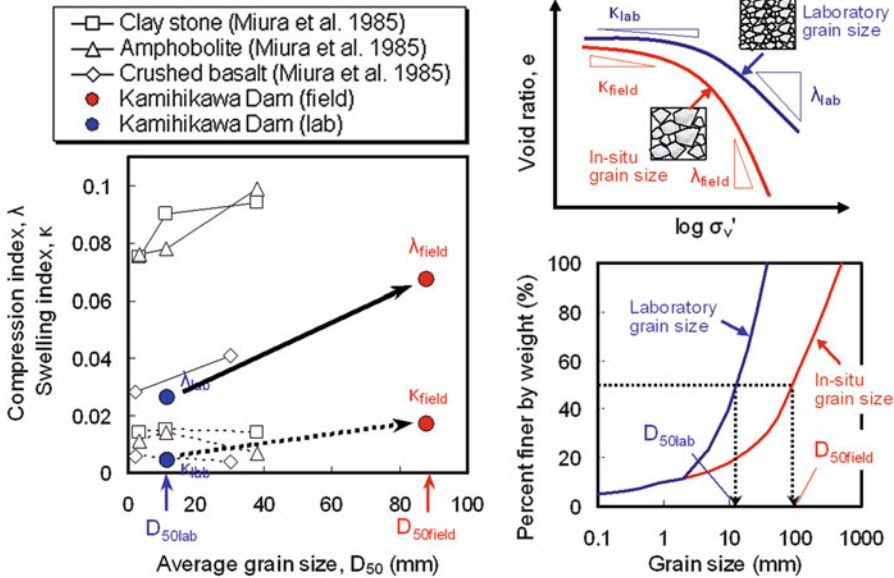


Fig. 9.4 Method of estimating the deformation parameters of in-situ rock zone by grain size correction (After Ohta et al. 2001)

a load equivalent to water pressure was given to the upstream rock surface as the total stress boundary condition, and hydrostatic head corresponding to the reservoir level was given to the same surface as the hydraulic boundary condition. Other details of the dam, including construction method, physical or mechanical properties, and the embankment and filling reservoir process are detailed in the references (Ohta et al. 2001; Mori et al. 2001).

Determining in situ characteristics of rock material is very difficult because coarse components are eliminated in laboratory tests. For this problem, the authors have presented a practical method to correct deformation parameters (λ , κ) equivalent to in situ characteristics using the average grain size D_{50} of in situ rock materials and laboratory specimens, as shown in Fig. 9.4. The comparison of measured and calculated settlements during construction adopting this method shown in Fig. 9.5 demonstrates that the grain size correction is quite satisfactory.

Figure 9.6 shows an example of a comparison of calculated and measured values of pore water pressure in the core zone during construction and first reservoir filling. The calculated and measured values are in considerably good agreement. These values indicate that the generation of pore water pressure caused by construction, the dissipation of water pressure after the finish of construction, and the rise of pore water pressure during the first reservoir filling have been accurately traced not only qualitatively but also quantitatively.

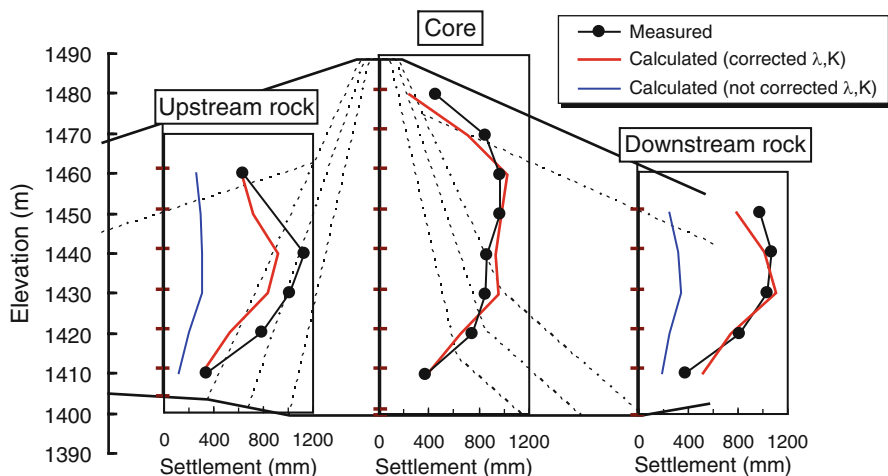


Fig. 9.5 Comparison of measured and calculated settlements of dam embankment during construction (the Kamihikawa Dam) (After Ohta et al. 2001)

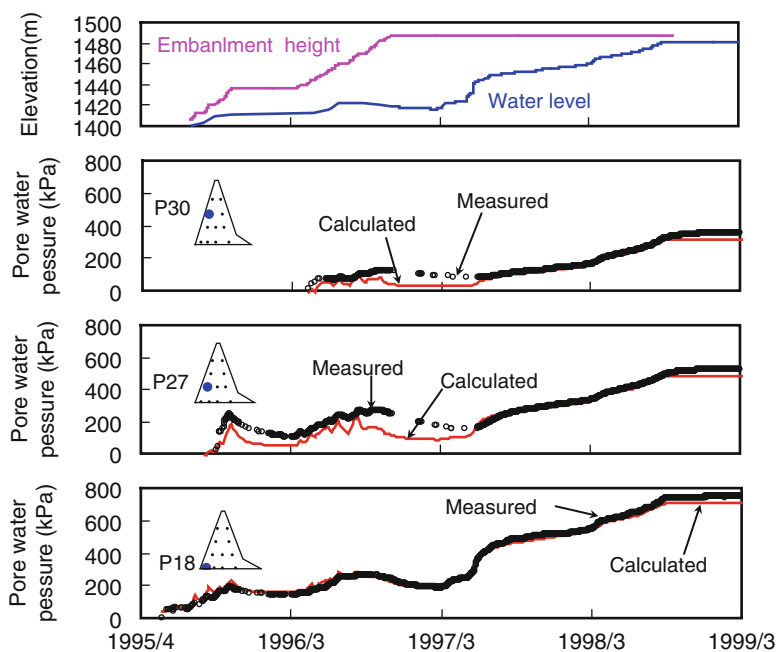


Fig. 9.6 Comparison of measured and calculated pore water pressures during construction and first filling (the Kamihikawa Dam) (After Ohta et al. 2006)

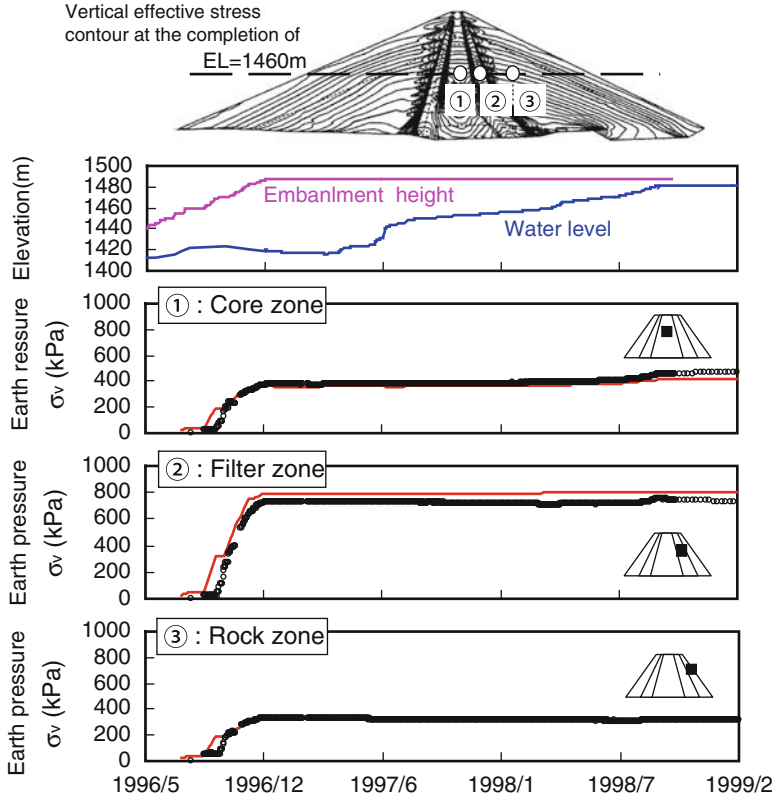


Fig. 9.7 Comparison of measured and calculated vertical earth pressures during construction and first filling (at an elevation 1,460 m at the Kamihikawa Dam) (After Ohta et al. 2006)

Figure 9.7 shows the data obtained from the earth pressure cells installed in the three (core, rock, filter) zones. The calculated and measured values also show good agreement.

9.4 Quantitative Evaluation of Stability Against Hydraulic Fracturing and Its Application to First Filling Management

9.4.1 Conditions for Hydraulic Fracturing of Impervious Materials

According to laboratory test results (Japanese Geotechnical 2002), hydraulic fracturing occurs when the relationship between the minor principal stress σ_3 acting on the soil and pore water pressure Δu satisfies the following condition.

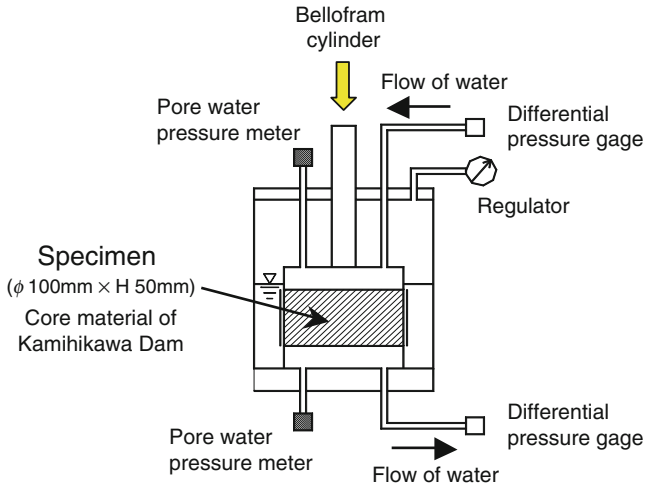


Fig. 9.8 Outline of hydraulic fracturing testing apparatus (After Ohta et al. 2005)

$$\Delta u \cdot \sigma_3 + n \quad (9.1)$$

m and n are test conditions.

The hydraulic fracturing criterion proposed by Seed and Duncan (1981) is

$$\Delta u > \sigma_3 + \sigma_t \quad (9.2)$$

in which σ_t is tensile strength of soil.

Equation (9.2) is equivalent to Eq. (9.1) in which $m = 1$ and $n = \sigma_t$, and it can be said that Eq. (9.2) corresponds to the state of the minor effective principal stress < 0 ; that is, the condition for the occurrence of cracking in the core zone. Murdoch (1992), who has proposed roughness values for core materials, gave $\Delta u > \sigma_3$ as the condition for the occurrence of hydraulic fracturing accompanied by complete cracking on the basis of laboratory test results. Kennard et al. (1967), who investigated the cause of the failure of the Balderhead Dam in the United Kingdom, and Alonso (1997), who collected and checked the values of earth pressure and pore water measurement data from several dams, has also concluded that hydraulic fracturing is initiated when the minor principal stress becomes smaller than pore water pressure and the minor effective principal stress becomes negative on the upstream side of the core zone. Thus, the value of minor effective principal stress of the core zone is directly related to the occurrence of cracking and the formation of hydraulically weak areas. Therefore, the minor effective principal stress may be one of the indicators for the hydraulic fracturing of a dam.

A test was conducted, therefore, to determine whether or not Eq. (9.2) holds true for the core material of the Kamihikawa Dam. In the test, a core material specimen was set in the test apparatus shown in Fig. 9.8. The density and water content of the

Fig. 9.9 Relationship between pore water pressure difference and flow rate (After Ohta et al. 2005)

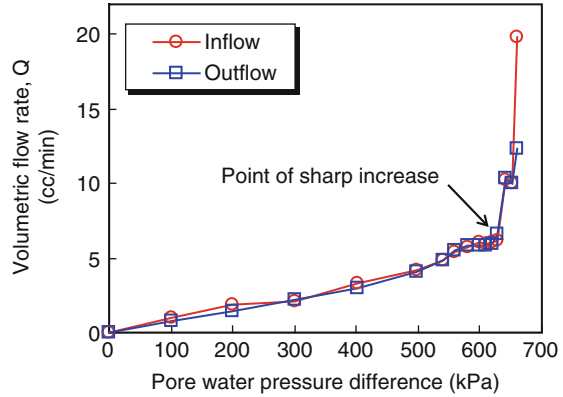
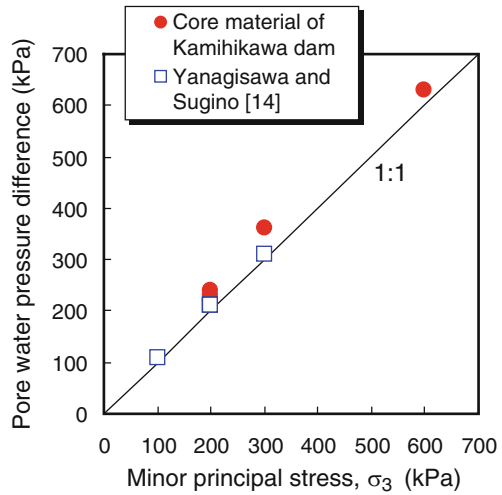


Fig. 9.10 Relationship between pore water pressure difference and minor principal stress (After Ohta et al. 2005)



test specimen were identical, with average values typically observed in field-compacted materials. After the specimen was consolidated by applying confining pressures in isotropic and/or anisotropic conditions, back pressure (pore water pressure) applied to the underside of the specimen was gradually increased, and the rate of seepage from the specimen and turbidity of the water were observed. Figure 9.9 shows an example of a test result. As shown, although pore water pressure was low, the rate of seepage was proportional to the pressure and the coefficient of permeability was more or less constant. However, as pore water pressure exceeded the confining pressure and continued to increase by a certain amount, the rate of seepage from the specimen began to increase sharply (*arrow* in the Fig. 9.9). This point was defined as the point of initiation of hydraulic fracturing. Figure 9.10 shows the relationship between the minor principal stress and pore water pressure at the initiation of hydraulic fracturing. The figure also shows the results of

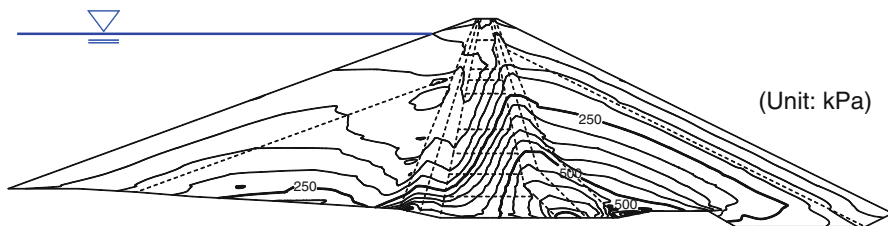


Fig. 9.11 Minor effective stress contour at the completion of first filling (After Ohta et al. 2006)

Yanagisawa and Sugano (1993), which experimentally verify that the Seed criterion of Eq. (9.2) is applicable to the core material of the Kamihikawa Dam.

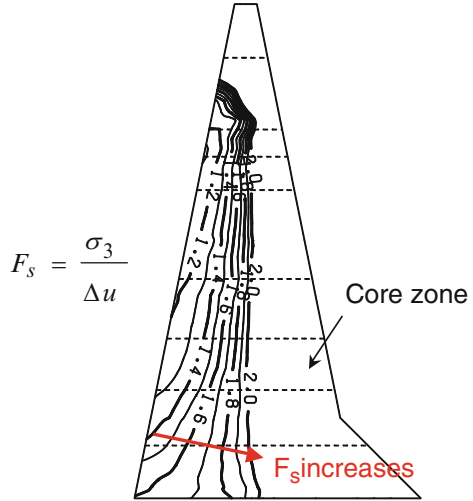
9.4.2 Quantitative Evaluation of Stability Against Hydraulic Fracturing

If the possibility of hydraulic fracturing of the core material can be estimated by Eq. (9.2), the safety factor against hydraulic fracturing is defined by the following expression:

$$F_{s3} = \frac{(\sigma_3 + \sigma_t)}{\Delta u} \quad (9.3)$$

In the construction and first filling analyses, the values of pore water pressure and minor principal total stress at a given location in the core zone at the full reservoir level were calculated. To be conservative, let us ignore the tensile strength σ_t of the core. It may be thought that if the minor effective principal stress obtained by subtracting pore water pressure is not negative (if cracking does not occur in the core), then local hydraulic fracturing does not occur. The phenomenon of piping, in which water penetrates a dam body in the transverse direction when hydraulic fracturing occurs, is believed to occur when the intermediate principal stress σ_2 in the direction of the dam axis becomes smaller than pore water pressure. For the purposes of this study, it is assumed that σ_2 is roughly equal to the minor principal stress σ_3 in the transverse direction, and σ_3 obtained in a two-dimensional analysis was used as a substitute. The validity of this assumption has been verified by the results of a three-dimensional effective stress analysis of the Kamihikawa Dam conducted separately (Ohta et al. 2006). Figure 9.11 shows the contours of the minor effective principal stress σ_3' of the dam when the full reservoir level is reached. There is no location at which the minor effective principal stress is negative. From this, it can be concluded that hydraulic fracturing is not likely to occur. Figure 9.12 shows the contours of the safety factor in the core zone calculated by Eq. (9.3) to evaluate the factor of safety against hydraulic fracturing in the core zone (although tensile strength is ignored). Figure 9.12 indicates that

Fig. 9.12 Safety factor contour of hydraulic fracturing of the core zone at the completion of first filling (After Ohta et al. 2006)



safety factor at the upstream location of the core zone is relatively lower (that agrees with the findings of Kennard et al. 1967 and Alonso 1997). Figure 9.12 also shows that the safety factor against hydraulic fracturing increases sharply at downstream locations in the core zone. This suggests that the possibility of full occurrence of piping in the transverse direction is very low.

9.4.3 Proposed Approach to the Management of Dam Stability During First Filling

During the first filling, pore water pressure, deformation, and rate of leakage are monitored continuously. At the Kamihikawa Dam, these measured data were used to establish a new approach to the management of dam stability during the first filling. The procedure and an example are as follows.

1. Conduct an elasto-plastic effective stress analysis to calculate pore water pressures u and principal total stresses (σ_1, σ_3) during the first filling at the locations of the piezometers installed in the core zone.
2. Prepare the values of $\sigma_1, \sigma_3,$ and u plotted against reservoir level at each piezometer location for use as a safety management chart. If the tensile strength of the core materials in a saturated condition is known, add the strength values to the total stress values and plot the lines showing the results thus obtained on the safety management chart.
3. Start filling the reservoir. Plot measured pore water pressures on the management chart and continue the filling, making sure that measured pore water pressures do not deviate substantially from the estimates and that the two limit lines (σ_1, σ_3) are not exceeded.

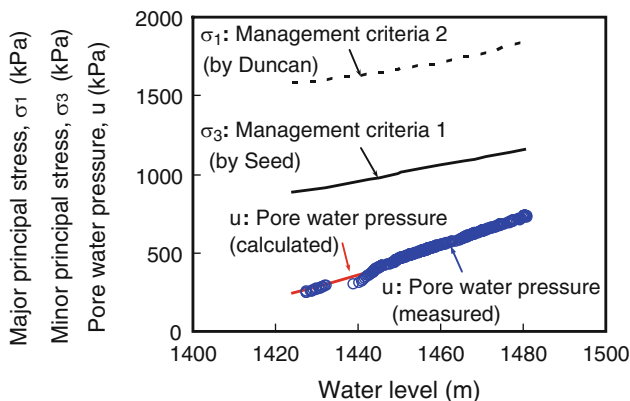


Fig. 9.13 An example of a safety management chart during the first filling (After Ohta et al. 2005)

Fig. 9.14 Relationship between water level and rate of leakage (After Ohta et al. 2005)

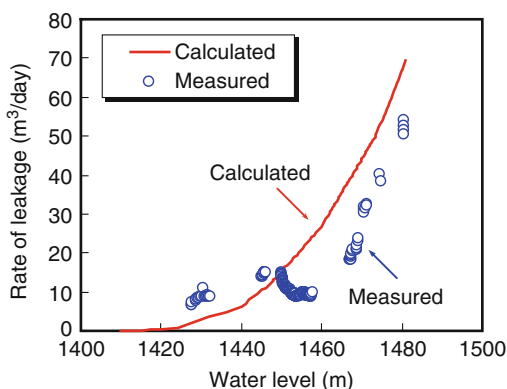


Figure 9.13 shows an example of a safety management chart actually used during the first filling of the Kamihikawa Dam. As shown, measured pore water pressure obtained during the first filling are plotted near the predicted line, and the plotted values are sufficiently lower than either of the two management criteria (Seed and Duncan 1981) for ensuring safety against hydraulic fracturing. By using a hydraulic fracturing evaluation chart such as this and measuring the rate of leakage from the dam and the turbidity of leaking water, the hydraulic stability of the dam can be evaluated and monitored quantitatively.

Figure 9.14 compares the measured rates of leakage from the dam obtained through the first filling analysis with the calculated values. Leakage management charts such as this, too, can be made available by conducting coupled analyses treating not only stress-deformation but also seepage flow. Measured leakage rates turned out to be close to the calculated values. The full reservoir level was reached in June, 1998, and the impoundment of the Kamihikawa Dam was successfully completed without causing anomalous behavior of the dam.

9.5 Simulations of the Past Hydraulic Fracturing Accidents of Large Rockfill Dams

9.5.1 Analysis to Reproduce Hydraulic Fracturing Events

A representative example of large-dam damage caused by hydraulic fracturing is found in the damage to the Balderhead Dam in the United Kingdom. Analysis was conducted to reproduce the hydraulic fracturing events at the dam. The approach was taken to not calculate directly from such details as cross-sectional details of the dam, construction process, and physical properties. Instead, the typical material parameters of the Kamihikawa Dam were used and the case of a dam with unique zoning (the Balderhead Dam) were analyzed. Thus, the case of the Kamihikawa Dam was calculated to compare with the case of the Balderhead Dam using the same set of material parameters. The difference caused by the geometric shape against hydraulic fracturing on the safety factor was investigated.

In the case of the Balderhead Dam, the width of the core zone changes abruptly at middle elevations so the core width is smaller than that of a typical dam. The hydraulic fracturing at the first filling occurred at the location where core width changed abruptly (Kennard et al. 1967). Figure 9.15 shows the cross-section of the Balderhead Dam (Kennard et al. 1967) and a contour diagram showing the minor effective principal stress σ_3' upon completion of the embankment. The upstream region is a high-stiffness filter zone, and the downstream region consists of a lower-stiffness core, a thin filter zone, and a rock zone. Considerable differential

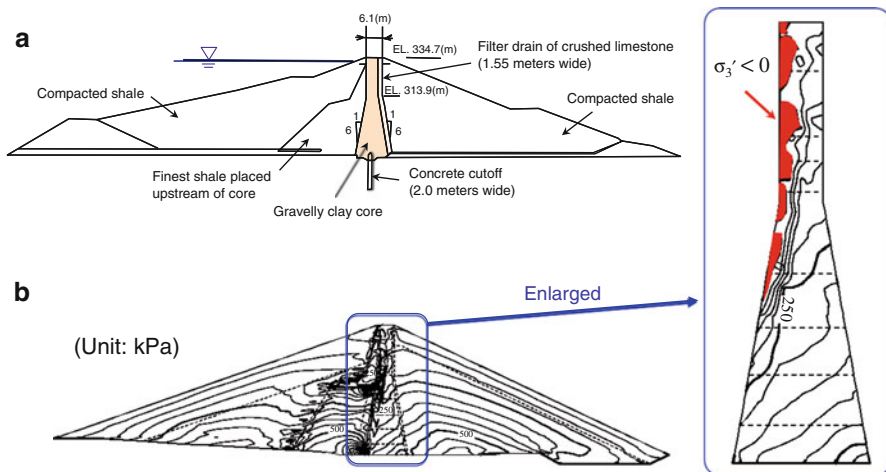


Fig. 9.15 Cross-section of the Balderhead dam and minor effective principal stress contour at the completion of construction simulating for a Balderhead-type dam. (a) Cross-section of the Balderhead Dam (After Kennard et al. 1967). (b) Minor effective principal stress contour at the completion of construction (After Ohta et al. 2006)

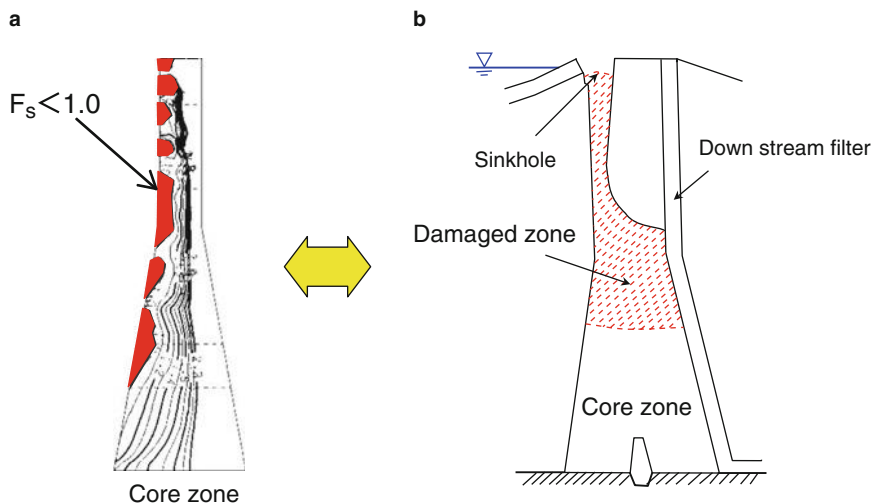


Fig. 9.16 Safety factor contour of hydraulic fracturing and damaged area ascertained by the field investigation of the Balderhead Dam. (a) Safety factor contour of H.F. (After Ohta et al. 2006). (b) Damaged areas ascertained by the field investigation (After Kennard et al. 1967)

settlement occurred between the upstream and downstream parts of the core zone during embankment construction in the analysis, and the minor principal stress decreased considerably in the upstream half of the core zone, which was relatively thin. The minor effective principal stress in the upstream half of the core zone upon completion of embankment was already negative (shown in black), indicating cracking.

Figure 9.16a is a contour diagram for the safety factor against hydraulic fracturing of the core zone at the high water level (the region in which the safety factor < 1.0 is shown in black). In the region in which the minor effective principal stress was negative when embankment construction was completed, the safety factor was lower than 1.0, and therefore the condition for the occurrence of hydraulic fracturing was satisfied. The investigation of the Balderhead Dam conducted after the accident revealed that the hatched area in Fig. 9.16b had eroded (Kennard et al. 1967). It is interesting to note that this erosion zone closely coincided with the zone in which the safety factor was lower than 1.0, as shown in Fig. 9.16a.

One more point is that the downstream filter zone may not have been fully defective at the Balderhead Dam. As mentioned in Sect. 9.2 once erosion of the core zone begins, the hydraulic stability of a dam is dependent on the downstream filter zone's ability to prevent or reduce the outflow of fine core material. If the downstream filter zone were fully functional, the damage of the dam might have been prevented. This indicates that giving consideration to the downstream filter zone is very important.

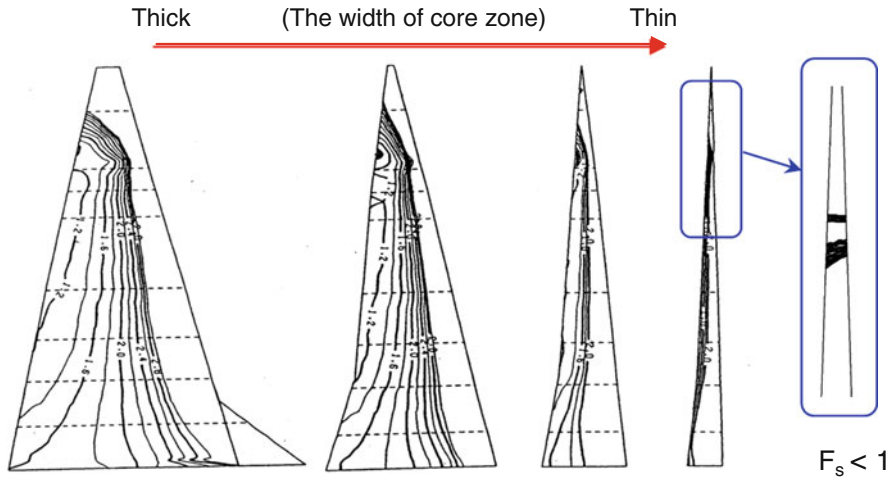


Fig. 9.17 Change of safety factor of hydraulic fracturing related to the width of core zone (After Ohta et al. 2006)

9.5.2 Analysis Concerning the Minimum Core Width Required

How thin can the core zone be? Figure 9.17 shows how the safety factor against hydraulic fracturing changes when the width of the core in the Kamihikawa Dam model is reduced gradually. As core width decreases, stability against hydraulic fracturing decreases, and in the narrowest-core-width case, the zone with insufficient safety (lower than 1) is penetrated by the water completely in the transverse direction. The safety factor against hydraulic fracturing defined in this chapter is on the safer side, because of ignoring the existence of prevention capability of filter zone and the constraint effect in the direction of the dam axis. However, in a case such as this, the probability of hydraulic fracturing during the first filling may be high.

Figure 9.18 summarizes the results of this analysis. The horizontal axis of the plot shows L/H (the ratio of core base width to dam height), and the vertical axis shows $L1$ (the length of the region in which the factor of safety against hydraulic fracturing at a higher elevation in the core zone is lower than 1)/ $L2$ (core width in the transverse direction at that elevation). As the L/H ratio decreases and the core width decreases, the $L1/L2$ ratio approaches 1, indicating that the possibility of occurrence of hydraulic fracturing, in which the core zone is penetrated in the transverse direction increases. The horizontal axis also shows the average values of the L/H ratio in the Hyttejuvet Dam (Japan Electric Power Civil Engineering 1981) and the Balderhead Dam, which are examples of hydraulic fracturing events involving a thin core zone. It is interesting that the L/H values for these dams show agreement with the region in which the penetration length $L/L2$ of hydraulic fracturing changes sharply.

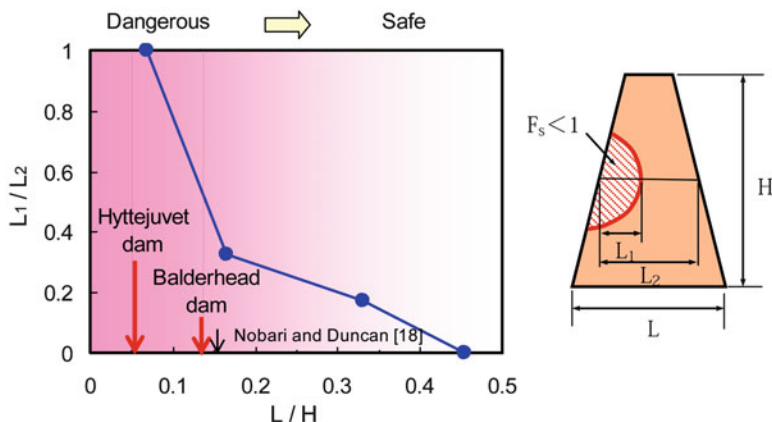


Fig. 9.18 Relationship between the ratio of core base width to dam height and the damaged zone (After Ohta et al. 2006)

Reporting on the results of an analysis of a thin-cored dam, Nobari and Duncan (1972) state that hydraulic fracturing occurred when the L/H ratio was 0.15. From all of these results, it can be concluded that to ensure stability of a dam against hydraulic fracturing, it is desirable to maintain a ratio of core base width to dam height (L/H) of at least 0.15–0.2, and that a dam with an L/H ratio of about 0.4–0.5 may be considered sufficiently stable.

9.6 Conclusions

Stability of rockfill dams against hydraulic fracturing during the first filling has been evaluated by using the results of embankment and impoundment analyses performed by elasto-plastic effective stress analysis. Based on the analysis, a method that is expected to be useful for dam stability management was proposed in this chapter. Validity of the proposed method was verified by applying it to actual dams. By this method, the influence of the various uncertain factors (e.g., core trench, zoning, core width, heterogeneity of permeability) affecting the hydraulic fracturing of large rockfill dams can be investigated in advance of the actual first filling of the reservoir.

References

- Alonso EE (1997) Flow and hydraulic fracture in earthfill dams. In: Proceedings of the 19th congress, Florence, 1997. International Commission on Large Dams, Q73-R34, pp 521–549
- Japan Electric Power Civil Engineering Association (1981) Advanced fill dam engineering. Behavior of dam (Chapter 8) and Accidents and response measures (Chapter 18), Tokyo, (in Japanese)

- Japanese Geotechnical Society (2002) Report of the committee on the mechanism of hydraulic fracturing of ground and evaluation methods. In: The proceedings of the symposium on the mechanism of hydraulic fracturing and its evaluation methods, Tokyo, 2002 (in Japanese)
- Justin JD (1924) The design of earth dams. *Trans Am Soc Civil Eng LXXXVIII(1)*:1–61
- Kennard MF, Penman ADM, Vauthan PR (1967) Stress and strain measurements in the clay core at Balder-head Dam. In: Proceedings of the 9th congress, Istanbul, 1967. International Commission on Large Dams, pp 129–150
- Miura N, Murata S, Yasufuku N, Akashi M (1985) Material constants and stress-strain characteristics of coarse materials. *Soil Found 33-6*:13–18 (in Japanese)
- Mori Y, Shimokawa Y, Uchita Y, Nakano Y (2001) Analysis of a zoned rockfill dam with center core. In: Proceedings of the 20th congress, Beijing, 2000, vol 3. International Commission on Large Dams, pp 1309–1336
- Murdoch LC (1992) Hydraulic fracturing of soil during laboratory experiments. Part(1)–(3). *Geotechnique 43(2)*:225–287
- Nobari ES, Duncan JM (1972) Effect of reservoir filling on stresses and movements in earth and rockfill dams. Geotechnique engineering report, No.TE72-1, University of California, Berkley, pp 1–198
- Ohta H, Yoshikoshi H, Mori Y, Yonetani S, Itoh M, Ishiguro T (2001) Behaviour of a rockfill dam during construction. In: Proceedings of the 15th international conference on soil mechanics and geotechnical engineering, Salt Lake City, 2001, pp 1227–1231
- Ohta H, Ishiguro T, Mori Y, Uchita Y, Tsuruta S, Takahashi A (2005) Uncertainty in safety evaluation of large rockfill dams during first filling. In: The 73th annual meeting of international commission on large dams, Tehran, 1–6 May 2005
- Ohta H, Takahashi A, Mori Y, Ishiguro T, Fujiyama T (2006) Safety of large rockfill dams during reservoir filling. In: Proceedings of the 22th congress, Barcelona, 2006. International Commission on Large Dams, Barcelona
- Seed B, Duncan JM (1981) The Teton dam failure – a retrospective review. In: Proceedings of the 10th international conference on soil mechanics and foundation engineering, Stockholm, 15–19 June 1981, pp 1–20
- Sekiguchi H, Ohta H (1977) Induced anisotropy and time dependency in clay. In: Proceedings of the 9th international conference on soil mechanics and geotechnical engineering, Tokyo, 1977, Speciality session 9, pp 229–239
- Terzaghi K (1922) *Der Grundbruch an Stauwerken und seine Verhütung. (The Failure of Dams by Piping and its Prevention.) Die Wasserkraft 17*:445–449. Reprinted in *From theory to practice in soil mechanics*. Wiley, New York, 1960, pp 114–118
- Yanagisawa E, Sugano T (1993) Study on hydraulic fracturing criteria for fill dam core material. *J Jpn Soc Dam Eng 12*:1–8 (in Japanese)

Chapter 10

Three Dimensional Soil/Water Coupled Analysis of Reverse Concreting Excavation Work

Shigehiko Sugie, Hideki Ohta, and Atsushi Iizuka

10.1 Introduction

In urban areas, construction projects are often conducted close to existing structures. Therefore, it is necessary to evaluate the influence on the surrounding structures and choose countermeasures for preventing geohazards based on the evaluation. The finite element method (FEM) has been generally used to predict the behavior of ground and structures. However, it is not necessarily easy to predict this behavior because various phenomena, such as those described in the following, are triggered by excavation works.

Release of ground stress induces the deformation of ground- and earth-retaining structures. When pumping up groundwater, consolidation accompanies the decrease in the groundwater level. There is also interaction between the ground- and earth-retaining structures being affected by the ground conditions. It depends on the construction method, sequences, and duration. For example, in case of excavating a rectangular pit, the three-dimensional effect is significant.

Thus, the phenomenon is quite complex, and there are many conditions that should be considered in prediction analysis. Authors have been pursuing the possibility of soil–water coupled FEM analysis by using three-dimensional models.

S. Sugie, D.Eng. (✉)

Technical Research Institute, Obayashi Corporation, 4-640 Shimokiyoto, Kiyose,
Tokyo 204-8558, Japan

e-mail: sugie.shigehiko@obayashi.co.jp

H. Ohta, D.Eng.

Research and Development Initiative, Chuo University, 1-13-27 Kasuga, Bunkyo-ku,
Tokyo 112-8551, Japan

e-mail: ohta@tamacc.chuo-u.ac.jp

A. Iizuka, D.Eng.

Research Center for Urban Safety and Security, Kobe University, 1-1 Rokkodai,
Nada-ku, Kobe, Hyogo 657-8501, Japan

e-mail: iizuka@kobe-u.ac.jp

This analysis method makes it possible to simulate the various ground and construction conditions such as those described in the preceding. The theoretical framework is based on the three-dimensional consolidation theory by Biot (1941).

This chapter first describes soil–water coupled FEM analysis (Ohta et al. 1991).

Then it introduces a large-scale ground excavation work by making use of the reverse concreting method constructed in Osaka, Japan (Sugie et al. 1999). Three-dimensional modeling of the ground, construction methods, and process to reproduce ground- and earth-retaining structure behaviors are described.

Finally it examines the performance of soil–water coupled FEM analysis based on the comparison between the analysis and data monitored at the site and reported in previous studies by Clough and O'Rourke (1990).

10.2 Tool of Analysis

The finite element program used in this investigation was proposed by Ohta et al. (1991) and is named GRASP3D (grasp real 3D action of subsoils and pore water). It is based on the three-dimensional consolidation theory by Biot (1941); namely, that saturated soil is regarded as a two-phase mixture consisting of soil skeleton and incompressible pore water.

The elasto-viscoplastic constitutive model for soil skeleton proposed by Sekiguchi and Ohta (1977) is used in this analysis to describe the time-dependent characteristics and stress-induced anisotropy.

The governing equations and mathematical formulation for such soil–water coupled problem can be summarized in Fig. 10.1. Here σ_{ij} and σ'_{ij} are components of total and effective stress tensors, respectively, p_w is the pore water pressure, ε_{ij} is the component of the strain tensor, ε_v is the volumetric strain, v_i is the component of the vector of the apparent pore water velocity vector, h is the total water head, and k_{ij} is the component of the material permeability coefficient tensor. These equations are discretized based on the weak forms of the equations of equilibrium and continuity.

By using the analysis method explained in the preceding, the change of ground-water environment and ground deformation induced by the construction can be estimated simultaneously.

10.3 Type of Construction Project

10.3.1 Ground Conditions

Material properties of the subsoil are summarized in Fig. 10.2. A thick layer of highly plastic clay is sandwiched by sand layers. This clay is normally consolidated with an N -value of 2–6 and unconfined compression strength q_u of approximately 0.1 MPa. The loose sand below the ground surface has an N -value of less than 10.

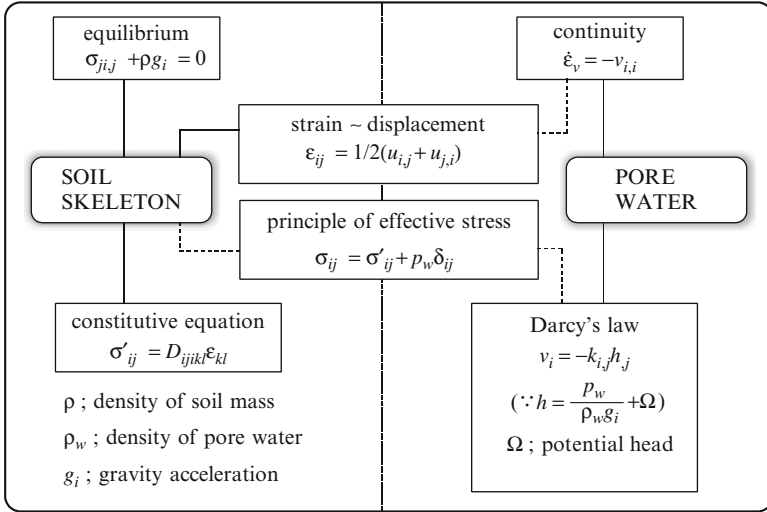
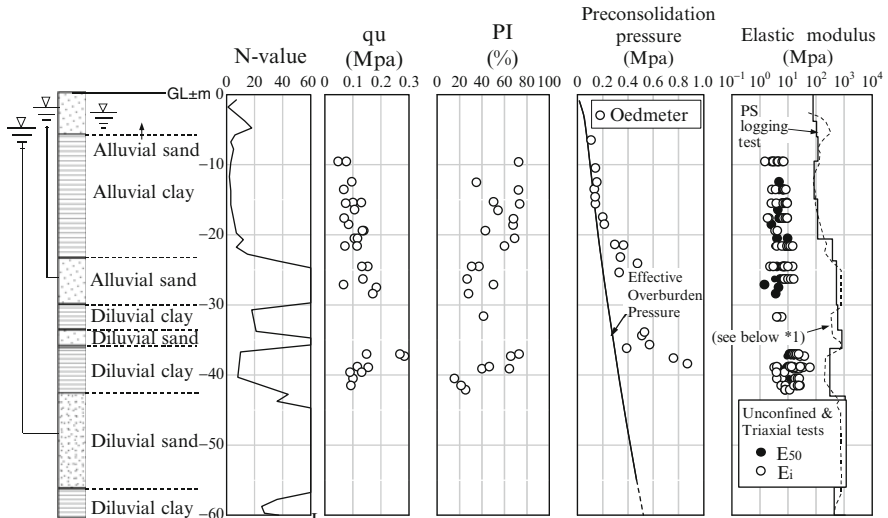


Fig. 10.1 Mathematical formulation for a soil–water coupled problem



*1) Broken line shows the value by using empirical relationship between S-wave velocity and N-value (Imai and Tonouchi, 1982)
 $V_s = 91 \cdot N^{0.337} \text{ m/sec} \implies E_{ps} = \rho \cdot V_s^2 \cdot 2(1+\nu)$

Fig. 10.2 Profile of subsoil

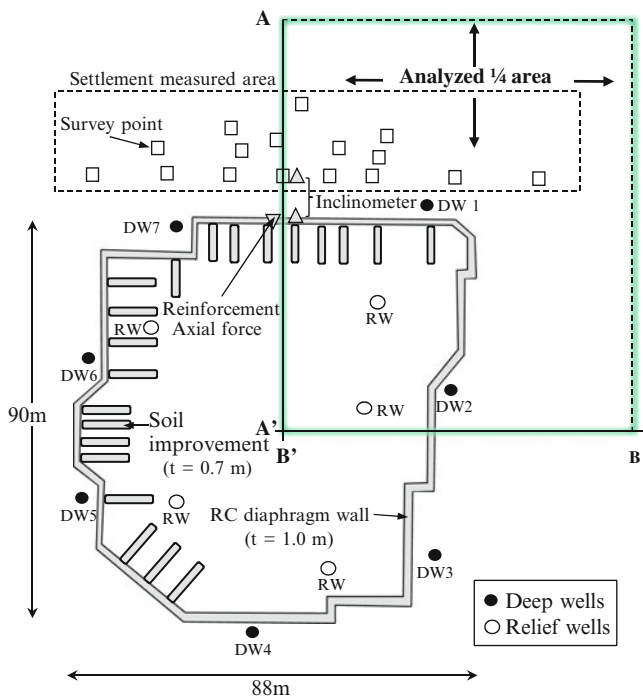


Fig. 10.3 Horizontal cross-section view of the construction site

The diluvial clay and sand layers are alternatively found underneath the alluvial layers. The diluvial clay is overconsolidated with an OCR of 2–2.5, and its strength is relatively small, with a q_u of approximately 0.1 MPa. The diluvial sand is dense, with an N -value of greater than 60.

10.3.2 Summary of Excavation Work

A wide and deep pit was excavated at the site of building construction by the reverse concreting excavation method. The plan and elevation of the excavated pit is shown in Figs. 10.3 and 10.4. The size of the excavated pit was 80 m \times 90 m, with a depth of 24 m. The excavation was divided into seven stages and finished within approximately 500 days, as shown in Fig. 10.4.

Because the highway and railroad were near the excavation area, the earth retaining wall made by reinforced concrete and ground improvement by soil-cement columns were adopted to reduce ground deformation. Various sensors were installed to monitor the movement of the ground and earth retaining walls.

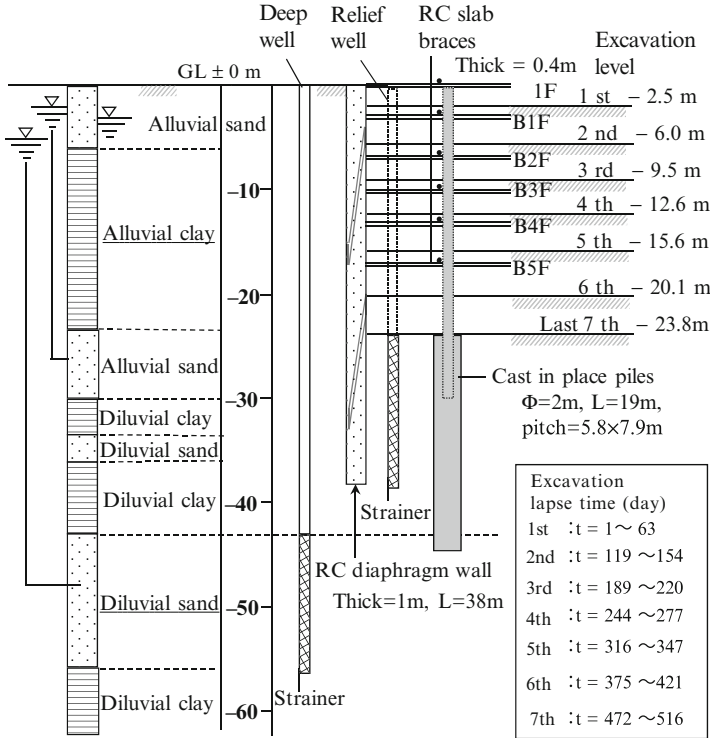


Fig. 10.4 Brace system of reverse concreting and pumping well installation for excavation work

At the final seventh stage of excavation, seven deep wells were installed around the outside of the earth retaining diaphragm wall to lower the pressure and thus prevent the ground heaving caused by groundwater pressure.

10.4 Finite Element Modeling of the Excavation Works

10.4.1 Finite Element Mesh and Geometric Boundary Condition

One fourth of the construction site was analyzed (see Fig. 10.3). The finite element mesh for the last seventh stage of the excavation (GL-24 m) is shown in Fig. 10.5.

The RC earth-retaining diaphragm wall and reverse concreting bracing slabs made of reinforced concrete were modeled by elastic shell (four-node square) elements. The cast-in-place piles installed in the ground at the excavation site were modeled by elastic truss (two-node) elements.

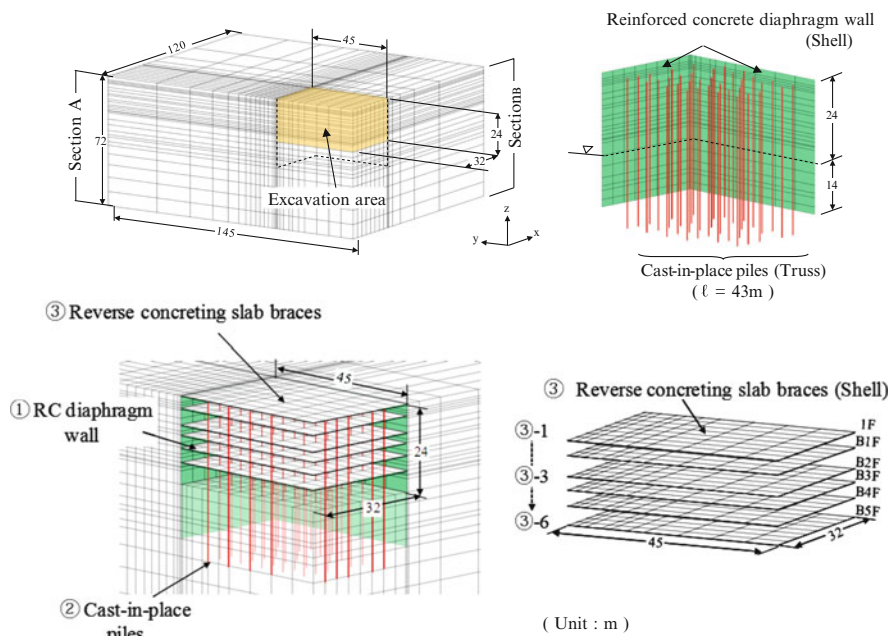


Fig. 10.5 Finite element modeling of the construction sequence (construction sequence: ①–③)

The boundaries of the finite element model allow only movement in the direction along the boundary plane. The vertical boundaries, Section A and Section B described in Fig. 10.5 allow no drainage of the water. The other vertical boundaries and the bottom boundary allow drainage.

10.4.2 Modeling of the Excavation Process

In the reverse concreting excavation method, excavation and reverse concreting slabs are constructed alternatively. In this site, the building was constructed simultaneously with the excavation work. Such process was simulated as shown in Fig. 10.5.

The process of excavation was represented by removing the elements in the place of excavation, as well as giving the nodal forces corresponding to the total stresses and body forces in the removed soil elements.

The construction of the reverse concreting slabs was represented by generating the shell elements corresponding to the stiffness and body force of the slab material. The dead load of the building was given on the nodes at the head of the cast-in-place piles represented by truss elements.

10.4.3 Modeling of the Measures to Groundwater

The water shielding of RC diaphragm wall was represented by installing the shell elements between the soil elements corresponding to the location of the wall with small permeability ($k = 1 \times 10^{-7}$ cm/s).

The groundwater level inside the diaphragm wall was kept lower than the bottom surface at every stage of excavation by relief wells (see Figs. 10.3 and 10.4). In addition to the relief wells, deep wells were introduced to prevent heaving of the bottom surface. During the last (seventh) excavation stage, the total water head at the points of these deep wells was kept 9 m below the ground surface.

To simulate these measures for groundwater, the total water head of the nodes on the bottom surface was fixed to 1 m lower than the level of the bottom surface at each excavation stage. At the last (seventh) stage of the excavation, the total water head of the nodes at the slits of the deep wells was fixed at GL-9 m. The groundwater head at the outer boundaries of the model was fixed at GL-3.2 m.

10.5 Soil Parameters

The elasto-plastic constitutive model proposed by Sekiguchi and Ohta (1977) was used to simulate the behavior of the clay layers except that at the bottom of the diluvial deposit below GL-56 m. The model parameters for the clay layers were determined as shown in Table 10.1, mainly from the oedometer tests with the aid of the empiric relationships between these parameters and the plasticity index of the soils (Iizuka and Ohta 1987).

The sand layers and the clay layer at the bottom of the diluvial deposit were simulated as elastic materials with elastic modulus obtained from the PS logging tests, and Poisson's ratio of 0.35. The coefficients of permeability of the sand layers were specified as $k = 2 \times 10^{-3}$ to 4×10^{-4} cm/s based on in situ permeability tests.

The model parameters for concrete members are given in Table 10.2. The elastic modulus of the reverse concreting slab before hardening was reduced to one half of the value in Table 10.2.

10.6 Behavior of Ground- and Earth-Retaining Diaphragm Walls

Calculated and measured values of the lateral displacement of the diaphragm wall, the settlement of ground surface behind the diaphragm wall, and the bending moment of the diaphragm wall are plotted in Figs. 10.6, 10.7, and 10.8, respectively. The calculation using the elastic modulus of sand layers obtained from PS

Table 10.1 Input parameters of clayey subsoil

	Depth (m)	C_c	e_0	ϕ' (deg)	ν'	K_0	OCR	k (cm/s)
Alluvial clay	6–8	0.40–1.01	1.20–1.65	23	0.36–0.38	0.57–0.62	1.0	$2 \times 10^{-7} \sim 8 \times 10^{-7}$
	18–24	0.52	1.21–1.25	25	0.36	0.57	1.7	$4 \times 10^{-7} \sim 7 \times 10^{-7}$
Diluvial clay	30–34	0.45	1.00	26	0.36	0.57	20	2×10^{-7}
	36–43	0.45–0.48	0.94–0.97	29	0.34–0.36	0.52–.57	2.5	$8 \times 10^{-7} \sim 2 \times 10^{-7}$

C_c compression index, e_0 void ratio at preconsolidation, ϕ' effective friction angle, ν' Poisson ratio, K_0 coefficient of earth pressure at rest, OCR overconsolidation ratio, k coefficient of permeability

Table 10.2 Input parameters of concrete structures

	E (MPa)	A (m ²)	I (m ⁴)	Type of element
Diaphragm wall	2.1×10^8	1.0	8.3×10^{-2}	Shell
Bracing slab	2.1×10^8	0.4	5.3×10^{-3}	Shell
Cast-in-place pile	2.1×10^8	2.73		Truss

A cross-section area (per unit width for wall and slab, per one for pile), E elastic modulus, I moment of inertia (per unit width for wall and slab)

Legend

Measured	FEM
○	Elastic modulus of sandy layers
	— $E=E_{ps}$ (PS logging test)
	- · - · $E=E_{ps} \times 0.5$
	- - - $E=E_{ps} \times 0.2$

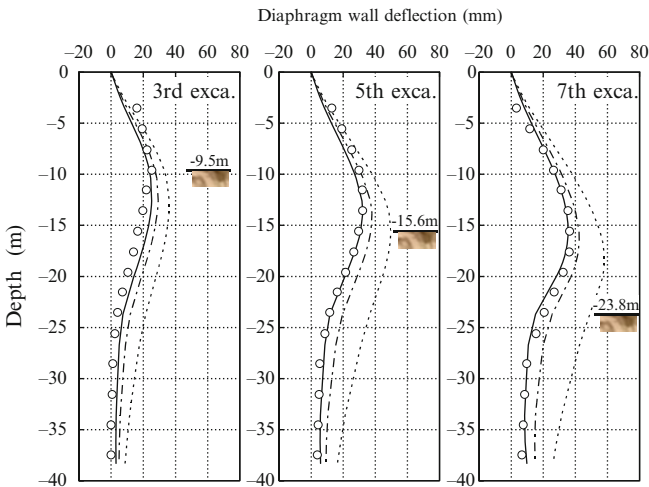


Fig. 10.6 Horizontal movement of the reinforced diaphragm wall

logging tests (E_{ps}) adequately simulates the measured behavior of the ground and the diaphragm wall. Akino (1990) and Tatsuoka et al. (1992) obtained 0.2–0.7 times the value of E_{ps} from back analysis on sandy soils at the excavated bottom ground.

It should be noted that the stiffness of soils obtained from triaxial tests or unconfined compression tests by conventional monitoring method using external dial gauge, was much smaller than that from obtained PS logging tests (see Fig. 10.2).

This fact indicates that the elastic modulus from the PS logging test, rather than conventional laboratory tests, should be used for analysis of this kind of excavation. In Fig. 10.2, the elastic modulus calculated from N -value using the equation of Imai and Tonouchi (1982) is also plotted by a broken line. It can be seen that such correlation between N -value and elastic modulus may be useful in the simulation.

Measured	FEM
○	Elastic modulus of sandy layers
	— E=Eps (PS logging test)
	- - - E=Eps × 0.5
	- - - - E=Eps × 0.2

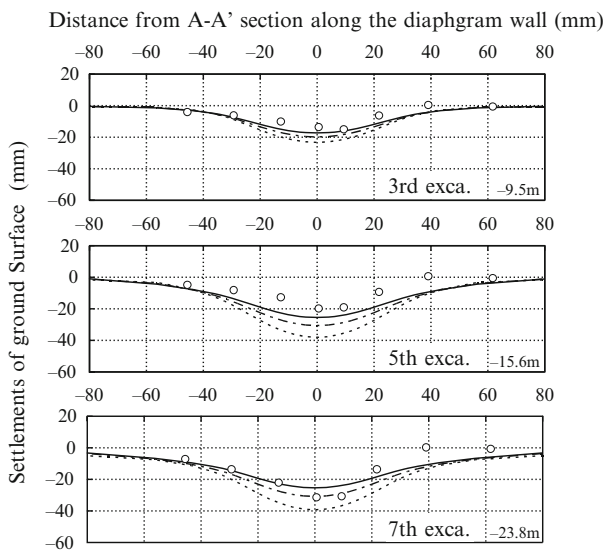


Fig. 10.7 Ground surface settlements behind the diaphragm wall

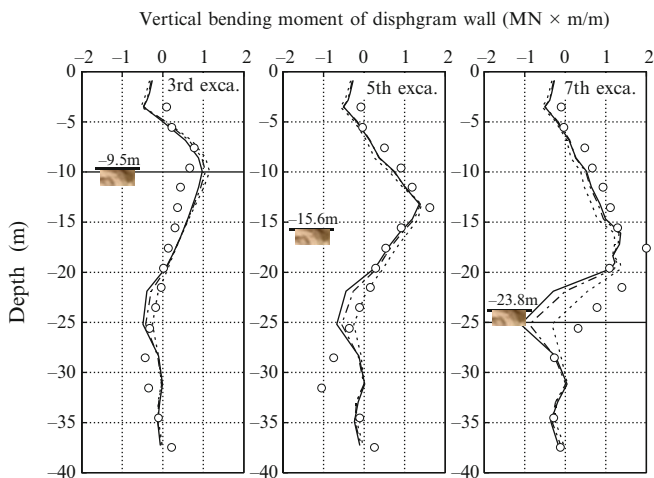


Fig. 10.8 Vertical bending moment at the reinforced concrete diaphragm wall

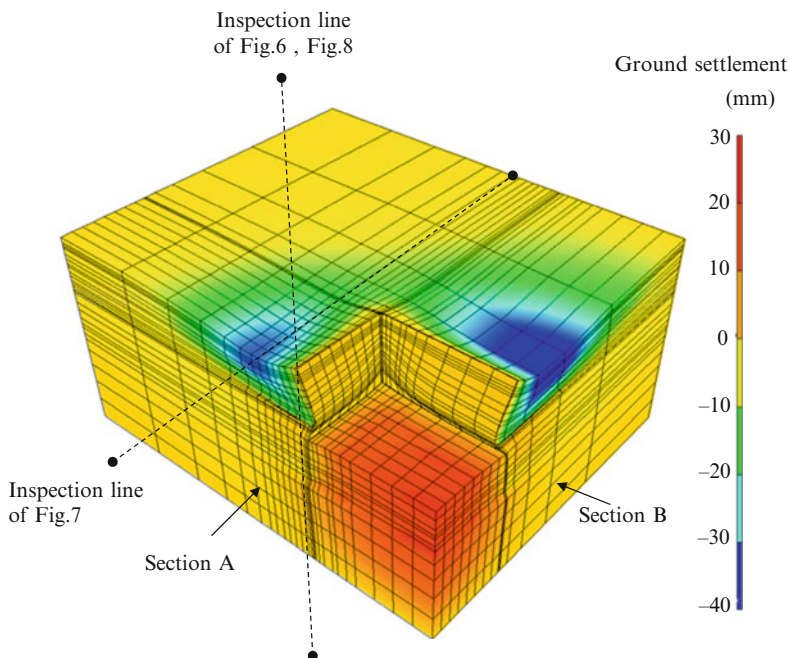


Fig. 10.9 Contour of ground settlement on deformed geometry

Figure 10.9 shows the three-dimensional view of the ground deformation and the calculated distribution of the ground settlement. To make it easy to verify, the amount of ground deformation is exaggerated by a factor of 150. It shows that the deformation around the corner of the excavation is smaller than in other parts. This is caused by the effect of three-dimensional constraint. This trend was also found in the measured values shown in Fig. 10.7.

In the transportation infrastructure, the inclination of the structure induced by ground settlement is the important parameter in addition to the amount of ground settlement. Especially in the case of excavation near a long structure, such as railroad tracks, it is difficult to evaluate the influence of construction only by using two-dimensional models. In addition, in case of the three-dimensional geometric conditions, one increasingly needs three-dimensional analysis.

Figure 10.10 shows the deformation of the diaphragm wall and the calculated distribution of the vertical and horizontal bending moment on the diaphragm wall. The vertical bending moment generated a smaller bending moment near the corner than the other part. Conversely, the higher horizontal bending moment generated at the corner. In general, measurement is typically carried out at the center of the diaphragm wall where the deformation is larger. Monitoring at the corner of the excavated pit rarely has been carried out. If the three-dimensionality of the member forces such as explained in the preceding is confirmed by measurement at several sites, the engineer engaged in ground excavation work will be able to propose a more economical policy.

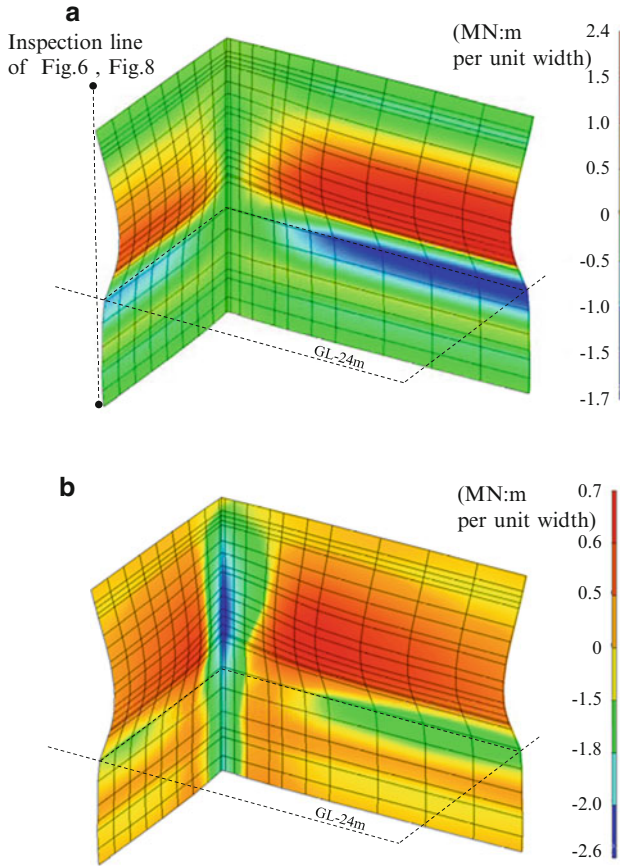


Fig. 10.10 Contour of the vending moment of the diaphragm wall on deformed geometry. (a) Vertical vending moment. (b) Horizontal vending moment

10.7 Comparison of the Analysis Results with the Measured Data Introduced by Clough and O'Rourke (1990)

Clough and O'Rourke (1990) examined the basic movement trends of ground settlements and the earth retaining wall resulting from excavation and support process. Figures 10.11 and 10.12 presented by them show maximum ground settlements δv and lateral movements of earth retaining wall δh , respectively, as a function of excavation depth H .

The authors added the range of the analysis results calculated at the each excavation step from the first to the last seventh step, as shown in Fig. 10.4.

Figure 10.11 shows that most of the measured settlements δv are less than 0.5% of H (line: $\delta v/H = 0.5\%$). There are some exceptional data beyond this line, in case of shallow excavation using soldier piles and lags or sheetpiles. The ground

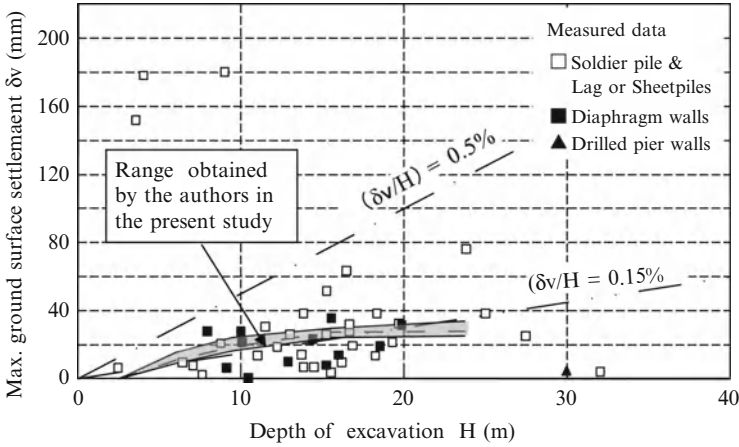


Fig. 10.11 Maximum ground surface settlements outside the diaphragm wall (Modified from Clough and O'Rourke 1990)

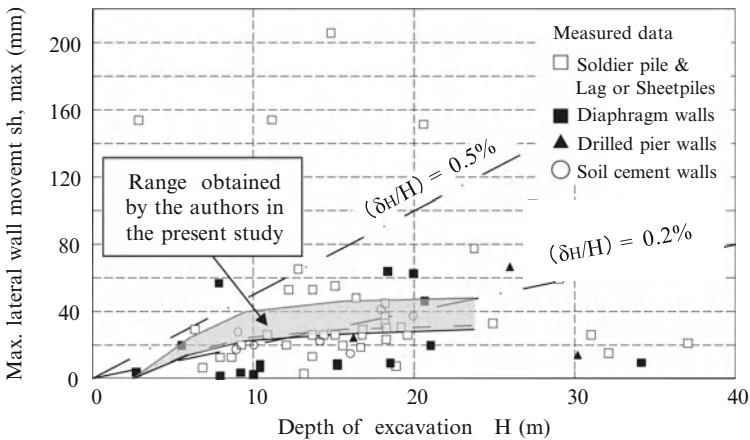


Fig. 10.12 Maximum lateral movements of the diaphragm wall (Modified from Clough and O'Rourke 1990)

settlements calculated in this study are in accordance with the trend of measured settlements typically shown by a line of 0.15 % of H (line: $\delta v/H = 0.15\%$).

Figure 10.12 shows that the measured wall movements δh are more widely scattered than measured settlements δv , especially in the case of soldier piles and lags or sheetpiles. The calculated wall movement in this study passes between the line of $\delta h/H = 0.5\%$ and the average line of $\delta v/H = 0.20\%$.

The increase of the ground settlement and wall movement calculated in the study has become slow with the increase of depth of excavation. This is owing to the effect of the restraint by the cast-in-place piles supporting the dead load of the building simultaneously constructed in the process of the reverse concreting excavation.

10.8 Conclusions

This chapter described three-dimensional soil–water coupled FEM analysis of a large-scale ground excavation by using reverse concreting excavation methods. In this analysis, the construction method, process, and nonlinearity of subsoil properties were taken into consideration.

The calculated movements of ground and the diaphragm wall were in good accordance with the measured data obtained from the construction site. The analysis results obtained from the present study are generally in good accordance with the data measured at the other excavation sites introduced by Clough and O'Rourke (1990).

From this, three-dimensional soil–water coupled FEM analysis was found to be reliable when used in engineering practice. And it was found that the elastic modulus of sandy soils obtained from PS logging test, rather than conventional laboratory tests, should be used for analysis of this kind of excavation.

References

- Akino N (1990) Estimation of rigidity of ground and prediction of settlement of building. *J Struct Constr Eng AIJ* 412:109–119 (in Japanese)
- Biot MA (1941) General theory of three dimensional consolidation. *J Appl Phys* 2:155–164
- Clough G, O'Rourke TD (1990) Construction induced movements of in-situ wall. In: Lambe PC, Hansen LA (eds) *Proceedings the conference on design and performance of earth retaining structures at New York, USA*. ASCE, New York, pp 439–479
- Iizuka A, Ohta H (1987) A determination procedure of input parameters in elasto-viscoplastic finite element analysis. *Soil Found* 27(3):71–86
- Imai T, Tonouchi K (1982) Relationship between N-value and S-wave velocity and its use. The foundation engineering and equipment. *Month J Kiso-Ko* 10:70–76 (in Japanese)
- Ohta H, Iizuka A, Omote Y, Sugie S (1991) 3D-analysis of soil/water coupling problems using elasto-viscoplastic constitutive relationships. In: Beer G, Booker JR, Carter JP (eds) *Proceeding 7th international conference of computer methods and advances in geomechanics at Cairns, Australia*. A.A. Balkema, Rotterdam, pp 1191–1196
- Sekiguchi H, Ohta H (1977) Induced anisotropy and time dependency in clay. In: *Proceedings 9th international conference on soil mechanics and foundation engineering, Tokyo, 1977, Specialty session 9*, pp 229–239
- Sugie S, Ueno T, Akino N, Sakimoto J (1999) Three-dimensional soil/water coupled FEM simulation of ground behavior adjacent to braced cuts. Report of Obayashi Corporation Technical Research Institute, Tokyo, No. 59, pp 69–74 (in Japanese)
- Tatsuoka F, Kohata Y, Kin Y, Shibuya S (1992) Deformation characteristics of soils and rocks from field and laboratory tests and back-analysis Part I – comparison of data from field tests, laboratory tests and back-analyses-. *Seisan-Kenkyu* 44(10):36–50 (in Japanese)

Chapter 11

Spatial Discretization of a Water Head in Soil–Water Coupled Finite Element Method Analysis Using the Hybrid-Type Penalty Method

Masafumi Hirata, Atsushi Iizuka, Hideki Ohta, Tetsuo Fujiyama, and Tomohide Takeyama

11.1 Introduction

In many cases, pore water flow and pore water pressure cause geohazards such as ground subsidence and slope failure. It is very important to take into account the pore water flow and pore water pressure as a soil–water coupled formulation in the analysis of ground behavior and slope stability.

M. Hirata, D.Eng. (✉)

Technical Research Institute, Maeda Corporation, 1-39-16 Asahi-cho, Nerima-ku, Tokyo 179-8914, Japan
e-mail: hirata.m@jcity.maeda.co.jp

A. Iizuka, D.Eng.

Research Center for Urban Safety and Security, Kobe University, 1-1 Rokkodai, Nada-ku, Kobe, Hyogo 657-8501, Japan
e-mail: iizuka@kobe-u.ac.jp

H. Ohta, D.Eng.

Research and Development Initiative, Chuo University, 1-13-27 Kasuga, Bunkyo-ku, Tokyo 112-8551, Japan
e-mail: ohta@tamacc.chuo-u.ac.jp

T. Fujiyama, D.Eng.

Technical Research Institute, Maeda Corporation, 1-39-16 Asahi-cho, Nerima-ku, Tokyo 179-8914, Japan

Science and Technology Department, Engineering Division, Nuclear Waste Management Organization of Japan (NUMO),
4-1-23 Shiba, Minato-ku, Tokyo 108-0014, Japan
e-mail: tfujiyama@numo.or.jp

T. Takeyama, D.Eng.

Department of Civil Engineering, Tokyo Institute of Technology, 2-12-1 O-okayama, Meguro-ku, Tokyo 152-8552, Japan
e-mail: takeyama.t.aa@m.titech.ac.jp

Two major methods are used to calculate pore water pressure in soil–water coupled finite element (FE) analysis. One is to represent the water head with a center of gravity element (Christian 1968), and the other is to represent the water head with a nodal point (Sandhu and Wilson 1969). These two methods are essentially the same, the only difference being in how the interpolation functions are selected. However, because pore water pressure is defined as a force constraining volumetric strains, it is more natural to represent the water head with a center of gravity element, which accordingly has been incorporated into many programs.

The soil–water coupled FEM analysis program deformation analysis considering stress anisotropy and reorientation (DACSAR; Iizuka and Ohta 1987) discussed in this chapter also uses the technique proposed by Christian, representing a water head with a center of gravity element. However, a problem has been identified in calculations using the original DACSAR: It fails to determine the correct water quantity flowing out from element boundaries depending on the manner of mesh generation (Takeyama et al. 2006). This chapter describes a new soil–water coupled FEM formulation using the hybrid-type penalty method (HPM) proposed by Takeuchi et al. (2000).

11.2 Spatial Discretization of Representing a Water Head with a Gravity Center of Element

11.2.1 Spatial Discretization of Continuity Equation in DACSAR

Figure 11.1 summarizes governing equations and boundary conditions for soil- and water-coupled problems. By multiplying the continuity equation shown in Fig. 11.1 by an arbitrary weighting function δh and integrating with respect to region V , we obtain the following weak form

$$\int_V \dot{\epsilon}_v \delta h dV - \int_{S_q} \bar{q} \delta h dV - \int_V \mathbf{k} \cdot \text{grad}(h) \text{grad}(\delta h) dV = \mathbf{0} \quad (11.1)$$

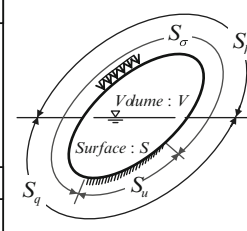
where $\dot{\epsilon}_v$ is a volumetric strain increment, \mathbf{k} is the hydraulic conductivity (coefficient of permeability) tensor, h is the total water head, and $\text{grad}(h)$ is the hydraulic gradient. Now assume that region V is divided into M elements. It is then assumed that for subregion V_e , the arbitrary total water head h is discretized by the interpolation function \mathbf{N}_h to the total water head vector \mathbf{h}^{me} ; and weighting function δh is also discretized by the same interpolation function \mathbf{N}_h (Galerkin method).

$$\begin{aligned} h &= \mathbf{N}_h \mathbf{h}^{me}, & \text{grad}(h) &= \mathbf{B}_h \mathbf{h}^{me} \\ \delta h &= \mathbf{N}_\delta \delta \mathbf{h}^{me}, & \text{grad}(\delta h) &= \mathbf{B}_h \delta \mathbf{h}^{me} \end{aligned} \quad (11.2)$$

Let \mathbf{h}^m be the total water head vector in region V . Then, the relationship between \mathbf{h}^m and the total water head \mathbf{h}^{me} in subregion V_e is expressed as follows:

$$\mathbf{h}^{me} = \mathbf{A}_{he} \mathbf{h}^m, \quad \delta \mathbf{h}^{me} = \mathbf{A}_{he} \delta \mathbf{h}^m \quad (11.3)$$

Governing Equations	
equilibrium equation	: $div \dot{\sigma} = \mathbf{0}, \quad \dot{\sigma} = \dot{\sigma}^T$
strain – displacement relation	: $\dot{\varepsilon} = -(\nabla \dot{\mathbf{u}})^S$
constitutive equation	: $\dot{\sigma}' = \mathbf{D}^{ep} : \dot{\varepsilon}$
effective stress principle	: $\dot{\sigma}' = \dot{\sigma} - \dot{p}_w \mathbf{1}$
Darcy's law	: $\mathbf{v} = -\mathbf{k} \cdot grad(h)$
total water head	: $h = p_w / \gamma_w + \Omega$
continuity condition	: $\dot{\varepsilon}_v = div \mathbf{v}$
Boundary Conditions	
stress boundary	: $\dot{\mathbf{t}} = \dot{\sigma}^T \cdot \mathbf{n}$ (on S_σ)
geometric boundary	: $\dot{\mathbf{u}} = \dot{\mathbf{u}}$ (on S_u)
velocity boundary	: $\bar{\mathbf{q}} = \mathbf{v} \cdot \mathbf{n}$ (on S_q)
head boundary	: $\bar{h} = h$ (on S_h)
Initial Value	
initial stress	: $\bar{\sigma} = \sigma _{t=0}$
initial total water head	: $\bar{h} = h _{t=0}$



$S = S_q + S_h = S_\sigma + S_u$

Fig. 11.1 Governing equations and boundary conditions for a soil–water coupled problem

where \mathbf{A}_{he} is a matrix that links degree of freedom m of the total water head vector \mathbf{h}^m in region V and degree of freedom me of the total water head vector \mathbf{h}^{me} in subregion V_e . Taking the arbitrariness of weighting function $\delta \mathbf{h}^m$ into account, Eq. (11.1) is expressed as follows:

$$\sum_{e=1}^M \mathbf{A}_{he}^T \left\{ \int_{V_e} \mathbf{N}_h^T \mathbf{B}_v dV \cdot \underline{\mathbf{u}}^{ne} - \int_{S_{qe}} \mathbf{N}_h^T \bar{\mathbf{q}} dS - \int_{V_e} \mathbf{B}_h^T \frac{\mathbf{k}}{\gamma_w} \mathbf{B}_h dV \cdot \gamma_w \mathbf{h}^{me} \right\} = \mathbf{0} \quad (11.4)$$

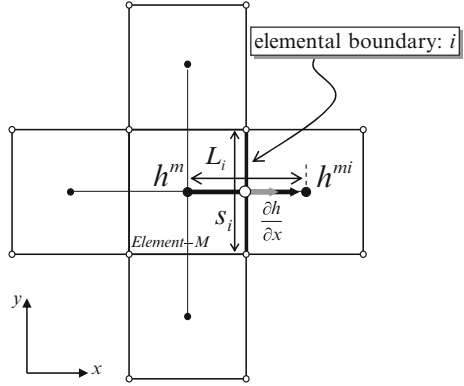
Equation (11.4) is a spatial discretization formula for the continuity equation obtained by the finite element method (FEM). Rearranging this equation yields:

$$\mathbf{K}_v \dot{\mathbf{u}}^n - \mathbf{K}_h \gamma_w \mathbf{h}^m = \dot{\mathbf{Q}} \quad (11.5)$$

where γ_w is the unit weight of pore water. Equation (11.5) contains matrices shown in the following:

$$\begin{aligned} \mathbf{K}_v &= \sum_{e=1}^M \mathbf{A}_{he}^T \int_{V_e} \mathbf{N}_h^T \mathbf{B}_v dV \mathbf{A}_e \\ \mathbf{K}_h &= \sum_{e=1}^M \mathbf{A}_{he}^T \int_{V_e} \mathbf{B}_h^T \frac{\mathbf{k}}{\gamma_w} \mathbf{B}_h dV \mathbf{A}_{he} \\ \dot{\mathbf{Q}} &= \sum_{e=1}^M \mathbf{A}_{he}^T \int_{S_q} \mathbf{N}_h^T \bar{\mathbf{q}} dS \end{aligned} \quad (11.6)$$

Fig. 11.2 Calculation of hydraulic gradient by Akai and Tamura



When the method proposed by Christian, representing the water head at the center of the element, is applied to Eq. (11.4), it is found that the total water head is unique over an element and then the interpolation function \mathbf{N}_h given in Eq. (11.4) becomes a constant. Moreover, because the \mathbf{B}_h matrix calculated by differentiation of interpolation function becomes zero, the spatial discretization formula given as Eq. (11.4) is simplified as follows:

$$\sum_{e=1}^M \mathbf{A}_{he}^T \left\{ \int_{V_e} \mathbf{B}_v dV \dot{\mathbf{u}}^{ne} - \int_{S_{qe}} \mathbf{v} \cdot \mathbf{ndS} \right\} = \mathbf{0} \tag{11.7}$$

Note that Eq. (11.7) is the same as the spatial discretization formula determined by the finite volume method (FVM) with non-Galerkin weighting. In other words, Christian’s method representing the total water head at the element center of gravity is a special case of FEM conforming to FVM. The second term on the left-hand side of Eq. (11.7) indicates the balance of pore water flowing in or out at elementary boundaries and is defined as follows:

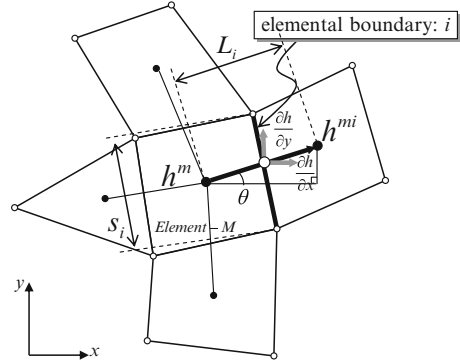
$$\int_{S_{qe}} \mathbf{v} \cdot \mathbf{ndS} = - \int_{S_{qe}} \mathbf{k} \cdot \text{grad}(h) \cdot \mathbf{ndS} \tag{11.8}$$

Akai and Tamura (1978) assumed orthogonal meshes, shown in Fig. 11.2, as concrete measures to determine the hydraulic gradient contained in Eq. (11.8). In this case, the gradient $\text{grad}(h)$ at element boundary i shown in Fig. 11.2 is expressed as follows, using distance L_i between neighboring element centers of gravity and the differential water head:

$$\text{grad}(h) = \frac{\partial h}{\partial L_i} = \frac{h^{mi} - h^m}{L_i} \tag{11.9}$$

Because hydraulic gradients can be determined for other element boundaries, as by Eq. (11.9), Eq. (11.8) is rearranged, as follows:

Fig. 11.3 Calculation of hydraulic gradient by deformation analysis considering stress anisotropy and reorientation (DAC SAR)



$$-\int_{S_{qe}} \mathbf{k} \cdot \text{grad}(h) \cdot \mathbf{ndS} = \alpha \gamma_w h^m - \sum_{i=1}^4 \alpha_i \gamma_w h^{mi} \quad (11.10)$$

where coefficients α_i and α are defined, as follows:

$$\alpha_i = \frac{k}{\gamma_w} \frac{s_i}{L_i}, \quad \alpha = \sum_{i=1}^4 \alpha_i \quad (11.11)$$

The spatial discretization formula presented by Akai and Tamura fails to express shapes of complex strata or soil structures because it assumes the orthogonal meshes shown in Fig. 11.2. Therefore, DAC SAR assumes meshes as shown in Fig. 11.3 to extend Eq. (11.9), as follows, using distance L_i between neighboring element centers of gravity and angle θ .

$$\text{grad}(h) = \left\{ \begin{array}{l} \frac{\partial h}{\partial x} \\ \frac{\partial h}{\partial y} \end{array} \right\} = \left\{ \begin{array}{l} \frac{h^{mi} - h^m}{L_i} \cdot \sin \theta \\ \frac{h^{mi} - h^m}{L_i} \cdot \cos \theta \end{array} \right\} \quad (11.12)$$

However, Eq. (11.12) happens to result in incorrect calculations. This is evident when the following derivation method incorporating the FVM is examined.

11.2.2 Calculation of the Hydraulic Gradient Using the Finite Volume Method

Because Christian’s method of representing the total water head at the element center of gravity is a special case of FEM conforming to FVM, formulation of FVM can be applied to hydraulic gradient calculation for general meshes. In the case of FVM, for a partial area formed by an element center of gravity and nodal points on

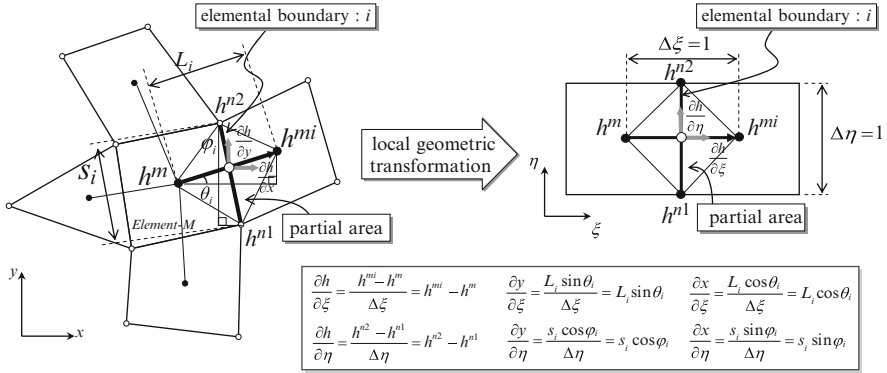


Fig. 11.4 Local geometric transformation of partial area for general mesh using the finite volume method

an element boundary, the hydraulic gradient at the element boundary is determined as follows:

$$\text{grad}(\mathbf{h}) = \left\{ \begin{matrix} \frac{\partial \mathbf{h}}{\partial x} \\ \frac{\partial \mathbf{h}}{\partial y} \end{matrix} \right\} = \frac{1}{\det[\mathbf{J}]} \left\{ \begin{matrix} \frac{\partial \mathbf{h}}{\partial \xi} \frac{\partial y}{\partial \eta} - \frac{\partial \mathbf{h}}{\partial \eta} \frac{\partial y}{\partial \xi} \\ -\frac{\partial \mathbf{h}}{\partial \xi} \frac{\partial x}{\partial \eta} + \frac{\partial \mathbf{h}}{\partial \eta} \frac{\partial x}{\partial \xi} \end{matrix} \right\} \quad (11.13)$$

where $\det[\mathbf{J}]$ is a Jacobian, defined in the following:

$$\det[\mathbf{J}] = \frac{\partial x}{\partial \xi} \frac{\partial y}{\partial \eta} - \frac{\partial y}{\partial \xi} \frac{\partial x}{\partial \eta} \quad (11.14)$$

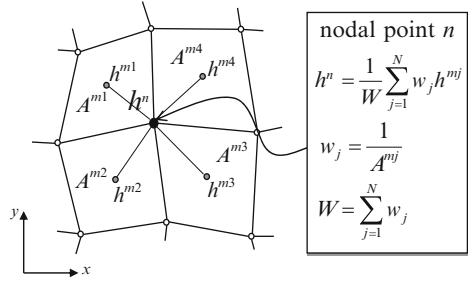
Now assume that the total water head values are h^{n1} and h^{n2} at nodal points on element boundary i , as shown in Fig. 11.4. Then the hydraulic gradient at element boundary i is determined as follows:

$$\text{grad}(\mathbf{h}) = \left\{ \begin{matrix} \frac{\partial \mathbf{h}}{\partial x} \\ \frac{\partial \mathbf{h}}{\partial y} \end{matrix} \right\} = \left\{ \begin{matrix} \frac{(h^{mi} - h^m) \cos \varphi_i}{L_i \cos(\varphi_i - \theta_i)} - \frac{(h^{n2} - h^{n1}) \sin \theta_i}{s_i \cos(\varphi_i - \theta_i)} \\ -\frac{(h^{mi} - h^m) \sin \varphi_i}{L_i \cos(\varphi_i - \theta_i)} + \frac{(h^{n2} - h^{n1}) \cos \theta_i}{s_i \cos(\varphi_i - \theta_i)} \end{matrix} \right\} \quad (11.15)$$

where φ_i is the angle of the element boundary with respect to the y -axis and θ_i is the angle of the line connecting the neighboring centers of gravity with respect to the x -axis. Because it is possible to determine hydraulic gradients for other element boundaries, as by Eq. (11.15), the water quantity flowing out at the element boundary calculated by Eq. (11.8) is rearranged as follows:

$$-\int_{S_{qe}} \mathbf{k} \cdot \text{grad}(\mathbf{h}) \cdot \mathbf{ndS} = \alpha \gamma_w h^m - \sum_{i=1}^4 \alpha_i \gamma_w h^{mi} + \sum_{i=1}^4 \beta_i \gamma_w (h^{ni+1} - h^{ni}) \quad (11.16)$$

Fig. 11.5 Approximation method of the water head value on a nodal point



Coefficients α_i , α , and β_i are defined in the following:

$$\alpha_i = \frac{k_x}{\gamma_w} \frac{s_i}{L_i} \frac{\cos^2 \varphi_i}{\cos(\varphi_i - \theta_i)} + \frac{k_y}{\gamma_w} \frac{s_i}{L_i} \frac{\sin^2 \varphi_i}{\cos(\varphi_i - \theta_i)}, \quad \alpha = \sum_{i=1}^4 \alpha_i \tag{11.17}$$

$$\beta_i = \frac{k_x}{\gamma_w} \frac{\sin \theta_i \cos \varphi_i}{\cos(\varphi_i - \theta_i)} + \frac{k_y}{\gamma_w} \frac{\cos \theta_i \sin \varphi_i}{\cos(\varphi_i - \theta_i)}$$

The values of the total water head at nodal points are needed in calculating hydraulic gradients for general meshes, as given by Eq. (11.16), even with Christian’s method of representing the total water head at the element center of gravity. DACSAR fails to calculate the correct quantity of water flowing out at an element boundary, depending on the manner of mesh generation. This problem arises from Eq. (11.12), which determines hydraulic gradients simply by two water head values at neighboring element centers of gravity. When orthogonal meshes ($\varphi_i = \theta_i = 0$), such as those shown in Fig. 11.2, are assumed for Eqs. (11.16) and (11.17) when hydraulic-conductivity anisotropy is ignored ($k_x = k_y = k$), perfect conformity is yielded between Eqs. (11.16) and (11.17) and the spatial discretization formula proposed by Akai and Tamura given by Eqs. (11.10) and (11.11). This eliminates the need for the values of the total water head at the nodal points.

We have made program corrections by applying the aforementioned FVM-based extension to DACSAR. The values of the total water head at nodal points were determined by approximation using weighted averages, as shown in Fig. 11.5.

$$h^n = \frac{1}{W} \sum_{j=1}^N w_j h^{mj}, \quad w_j = \frac{1}{A^{mj}}, \quad W = \sum_{j=1}^n w_j \tag{11.18}$$

where N is the number of elements surrounding nodal point n and w_j is a weighting factor, which is the multiplicative inverse for element area A^{mj} .

Fig. 11.6 Analytical conditions of a one-dimensional consolidation

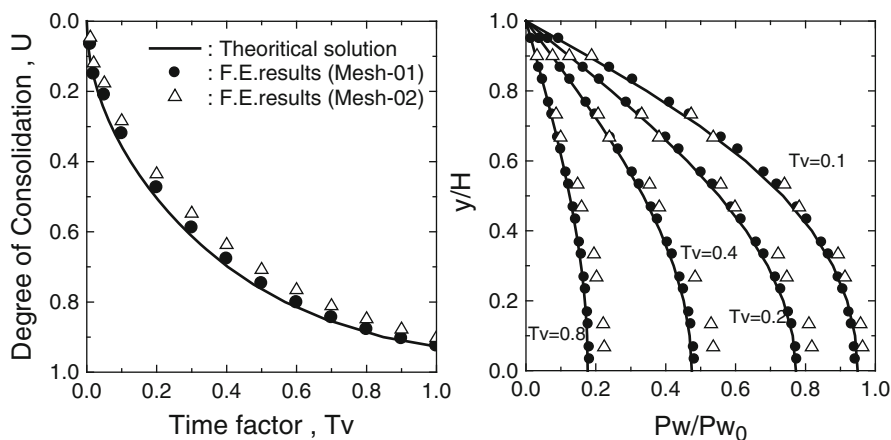
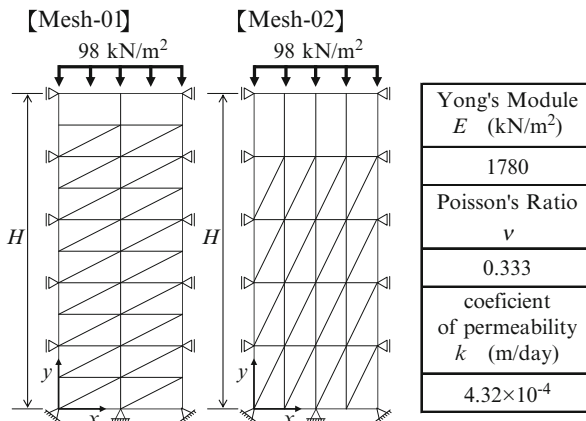


Fig. 11.7 Comparison of theoretical solution and simulation results using the finite volume method (difference in the mesh)

11.2.3 Simulation of One-Dimensional Consolidation Using the Finite Volume Method

Simulation of one-dimensional consolidation was performed under conditions shown in Fig. 11.6 (drained from upper boundary) and the results were compared with Terzaghi's theoretical solution to examine the FVM-based program. Figure 11.7 shows computed results for different manners of mesh generation. The figure reveals that computed results for Mesh-01 are in good agreement with the theoretical solution, whereas in the case of Mesh-02, which employs coarse meshes in draining direction, the computed results are not in agreement with the theoretical solution. Figure 11.8 shows computed results for Mesh-02 obtained by setting the hydraulic conductivity in the x-direction to two or five times larger

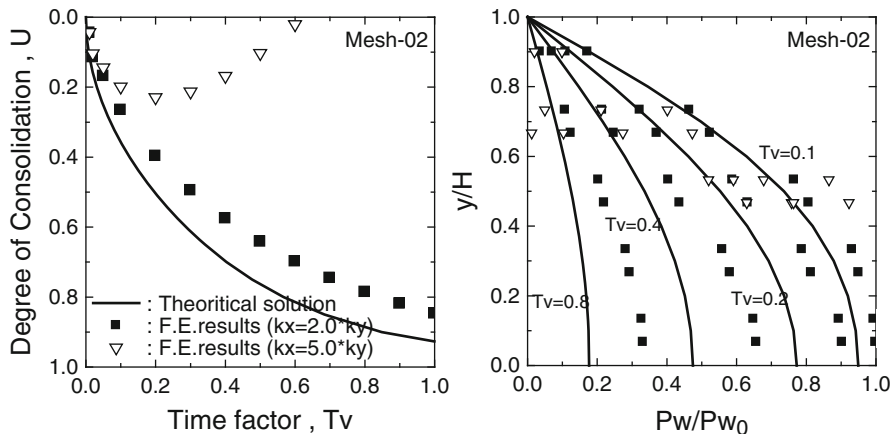


Fig. 11.8 Comparison of theoretical solution and simulation results using the finite volume method (difference in the coefficient of permeability)

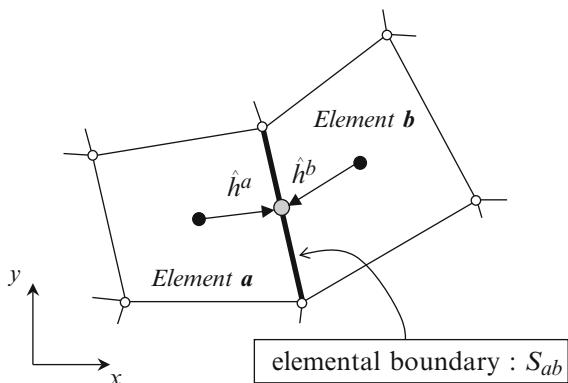
than that in the y-direction. Hydraulic conductivity in the x-direction should have no effects, by nature, on calculation in one-dimensional consolidation. However, increasing hydraulic conductivity in the x-direction caused calculation results that are not in agreement with the theoretical solution. Moreover, when hydraulic conductivity was increased to five times larger than that in the y-direction, the calculation diverged. One probable cause of disagreement between the computed results and the theoretical solution is approximation errors of values of the total water head at nodal points. Because total water head distributions are nonlinear, approximation errors become substantial when meshes in the draining direction are coarse. Furthermore, approximation errors are magnified when hydraulic-conductivity anisotropy is taken into consideration. To avoid this problem, it is necessary to use some other technique that requires values of the total water head at nodal points.

11.3 Soil-Water Coupled Finite Element Method Analysis Using the Hybrid-Type Penalty Method

11.3.1 Spatial Discretization of the Continuity Equation Using the Hybrid-Type Penalty Method

The hybrid-type penalty method (HPM) is a technique that employs the idea of the hybrid variation principle in a continuity equation and introduces penalty approximation to Lagrange’s undetermined multiplier λ contained in the element boundary conditional equation. This technique assumes an independent total water head value and a hydraulic gradient for each element and therefore requires no value of the

Fig. 11.9 Water head value on the element boundary



total water head at the nodal point and avoids the aforementioned approximation errors.

Let \hat{h}^a and \hat{h}^b be the total water head at boundary face S_{ab} of neighboring elements a and b , as shown in Fig. 11.9. Now, based on the hybrid variation principle, continuity can be relaxed by using Lagrange's undetermined multiplier λ , which is common on boundary face S_{ab} and expressing condition $\hat{h}^a = \hat{h}^b$ set on boundary face S_{ab} by the following equation:

$$H_{ab} = \delta \int_{S_{ab}} \lambda (\hat{h}^a - \hat{h}^b) dS \quad (11.19)$$

Because Lagrange's undetermined multiplier λ in Eq. (11.19) denotes flow rate at the boundary face, the undetermined multiplier can be expressed by the following equation using penalty P and relative differential water head ϕ_{ab} at boundary face S_{ab} .

$$\lambda = P \cdot (\hat{h}^a - \hat{h}^b) = P \cdot \phi_{ab} \quad (11.20)$$

Although penalty P can take an arbitrary value, this chapter uses a value defined as hydraulic conductivity $k \times 10^8$, as used by Takeuchi et al. (2000). Divide region V into M elements, and number of the boundaries between neighboring element is assumed to be N . Then the weak form of the continuity equation expressed by Eq. (11.1) becomes the following hybrid residual equation:

$$\sum_{e=1}^M \left\{ \int_{V_e} \dot{\epsilon}_v \delta h dV - \int_{S_{sqe}} \bar{q} \delta h dS - \int_{V_e} \mathbf{k} \cdot \text{grad}(h) \text{grad}(\delta h) dV \right\} + \sum_{ab=1}^N \left\{ \delta \int_{S_{ab}} \phi_{ab} \cdot P \cdot \phi_{ab} dS \right\} = \mathbf{0} \quad (11.21)$$

Because it is assumed that a constant hydraulic gradient occurs within each element, in the case of a two-dimensional model, the water head h within a given element is expressed as follows, using the total water head h_G represented at the element center of gravity and hydraulic gradients i_x and i_y :

$$h = h_G + (x - x_G) \cdot i_x + (y - y_G) \cdot i_y \quad (11.22)$$

The water head h set independently for each element is expressed by the following equation:

$$h = \mathbf{N}_h \mathbf{H}^{me} \quad (11.23)$$

Matrices in Eq. (11.23) are defined as follows:

$$\begin{aligned} \mathbf{N}_h &= \begin{bmatrix} 1 & (x - x_G) & (y - y_G) \end{bmatrix} \\ \mathbf{H}^{me} &= \begin{bmatrix} h_G & i_x & i_y \end{bmatrix} \end{aligned} \quad (11.24)$$

where \mathbf{H}^{me} is the degree-of-freedom vector for each element. According to Eq. (11.23), the hydraulic gradient in an element is determined as follows:

$$\text{grad}(h) = \mathbf{B}_h \mathbf{H}^{me} \quad (11.25)$$

The differential water head ϕ_{ab} at boundary face expressed by Eq. (11.20) is expressed by the following equation using vector \mathbf{H}^{mab} , which has degree of freedom mab at each boundary.

$$\phi_{ab} = \mathbf{N}_h \mathbf{H}^{me} \Big|_a - \mathbf{N}_h \mathbf{H}^{me} \Big|_b = \mathbf{N}_{hab} \mathbf{H}^{mab} \quad (11.26)$$

By rearranging the residual equation given as Eq. (11.21) using Eqs. (11.23), (11.25), and (11.26), we obtain:

$$\begin{aligned} \sum_{e=1}^M \delta \mathbf{H}^{meT} \left\{ \int_{V_e} \mathbf{N}_h^T \mathbf{B}_V \dot{\mathbf{u}}^{ne} dV - \int_{S_e} \mathbf{N}_h^T \bar{q} dS - \int_{V_e} \mathbf{B}_h^T \frac{\mathbf{k}}{\gamma_w} \mathbf{B}_h \cdot \gamma_w \mathbf{H}^{me} dV \right\} \\ + \sum_{ab=1}^N \delta \mathbf{H}^{mabT} \left\{ \int_{S_{ab}} \mathbf{N}_{hab}^T P \mathbf{N}_{hab} \mathbf{H}^{mab} dS \right\} = \mathbf{0} \end{aligned} \quad (11.27)$$

Furthermore, when \mathbf{H}^m is a vector with degree of freedom m for the entire region, vector \mathbf{H}^{me} of each element and vector \mathbf{H}^{mab} at each element boundary can be expressed by the following equation, using constant matrices \mathbf{A}_{he} and \mathbf{M}_{he} :

$$\begin{aligned} \mathbf{H}^{me} &= \mathbf{A}_{he} \mathbf{H}^m, & \mathbf{H}^{mab} &= \mathbf{M}_{he} \mathbf{H}^m \\ \delta \mathbf{H}^{me} &= \mathbf{A}_{he} \delta \mathbf{H}^m, & \delta \mathbf{H}^{mab} &= \mathbf{M}_{he} \delta \mathbf{H}^m \end{aligned} \quad (11.28)$$

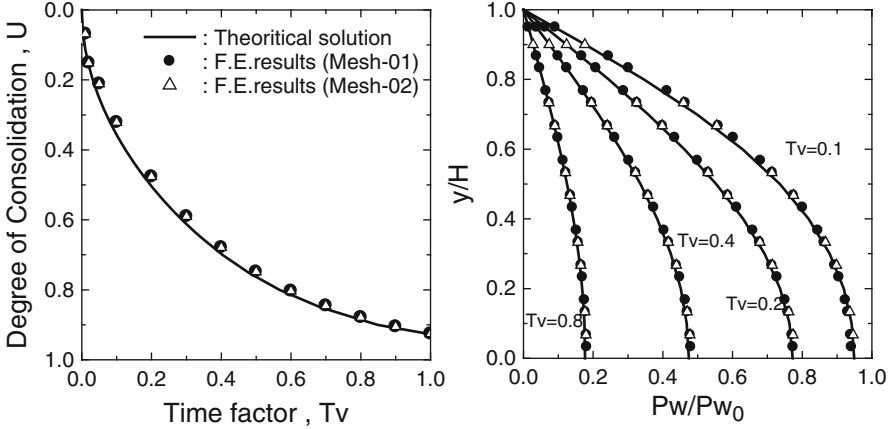


Fig. 11.10 Comparison of theoretical solution and simulation results using the hybrid-type penalty method (difference in the mesh)

By substituting Eq. (11.28) for Eq. (11.27) and taking the arbitrariness of weighting function $\delta \mathbf{H}^m$ into consideration, the following spatial discretization formula of continuity equation is finally obtained:

$$\mathbf{K}_v \dot{\mathbf{u}}^n - (\mathbf{K}_h - \mathbf{K}_{hs}) \gamma_w \mathbf{H}^m = \dot{\mathbf{Q}} \tag{11.29}$$

Compared with the spatial discretization formula expressed as Eq. (11.5), this equation additionally has a \mathbf{K}_{hs} matrix term as a result of using HPM. The \mathbf{K}_{hs} matrix is defined in the following:

$$\mathbf{K}_{hs} = \sum_{ab=1}^N \mathbf{M}_{he}^T \int_{S_{ab}} \mathbf{N}_{hab}^T \mathbf{P} \mathbf{N}_{hab} dS \mathbf{M}_{he} \tag{11.30}$$

The authors achieved program improvements by applying the spatial discretization formula given as Eq. (11.29) to DACSAR.

11.3.2 Simulation of One-Dimensional Consolidation Using the Hybrid-Type Penalty Method

The program incorporating HPM was verified via one-dimensional consolidation simulations. Calculations were performed under conditions shown in Fig. 11.6 to compare with the FVM-based program.

Figure 11.10 shows computed results for different manners of mesh generation. Although the computed results obtained by FVM (as shown in Fig. 11.7) were not in agreement with the theoretical solution, the computed results shown in Fig. 11.10,

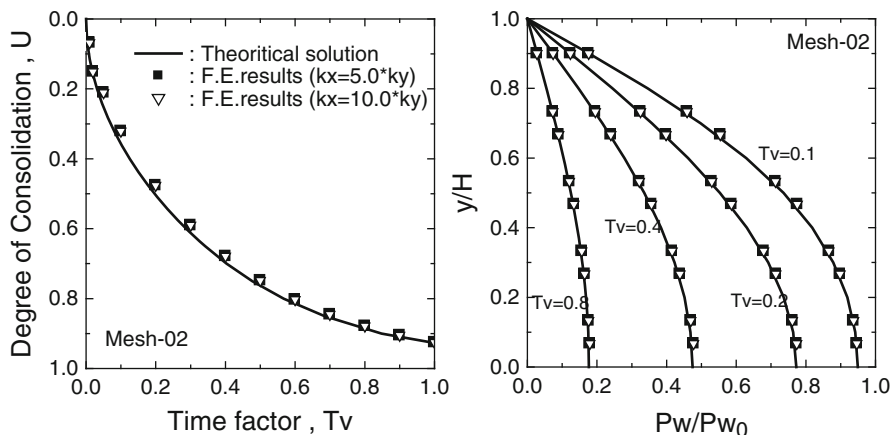


Fig. 11.11 Comparison of theoretical solution and simulation results using the hybrid-type penalty method (difference in the coefficient of permeability)

obtained by the program incorporating HPM, are in good agreement with the theoretical solution. Figure 11.11 shows computed results for Mesh-02 shown in Fig. 11.6 obtained by setting the hydraulic conductivity in the x-direction to five or ten times larger than that in the y-direction. In contrast with the results shown in Fig. 11.8 obtained via FVM, in which the solution diverged when the hydraulic conductivity was fivefold in the x-direction, the computed results shown in Fig. 11.11, obtained by HPM, were in good agreement with the theoretical solution even when the hydraulic conductivity was tenfold. This reveals the absence of influence from the hydraulic conductivity in the x-direction. It is believed that, as discussed in the preceding, the use of HPM fixed the problem of dependence on the manner of mesh generation.

11.4 Example of Finite Element Model Simulation for Actual Site

The efficacy of the program incorporating HPM was verified through analysis of an actual site. The site had a test embankment approximately 35 m in height that was built during the Note Airport site development (Nagahara et al. 2002). A high-moisture content cohesive soil was used as the material for the test embankment. Horizontal artificial drainage was employed in the embankment to facilitate consolidation. Figure 11.12 shows the mesh used for the analysis. The mesh was complex, containing triangular elements as a result of the inclined base and the gradient of the installed drainage. Horizontal hydraulic conductivity was calculated by taking the effects of the staggered arrangement of artificial drainage, drain resistance, and compression of artificial drainage resulting from overburden stress into account. This is a case in

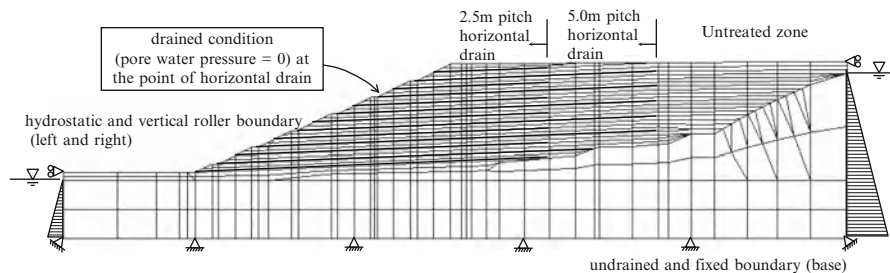


Fig. 11.12 Mesh figure and boundary conditions

Table 11.1 Material parameters of embankment

Unit weight	γ_t	15.5	kN/m^3
Initial void ratio	e_0	2.208	
Compression index	λ	0.271	
Irreversibility ratio	Λ	0.821	
Preconsolidation vertical pressure	σ_{v0}'	200.0	kN/m^2
Effective overburden pressure	σ_{vi}'	38.7	kN/m^2
Coefficient of earth pressure at rest	K_0	0.59	
Coefficient of in situ earth pressure at rest	K_i	1.00	
Effective Poisson ratio	ν'	0.37	
Critical state parameter	M	1.21	
Subloading parameter	m	0.50	
Coefficient of permeability	k	1.95×10^{-5}	cm/s

which a program incorporating FVM would present noticeable effects concerning the manner of mesh generation and hydraulic-conductivity anisotropy.

Table 11.1 shows embankment material parameters used for the analysis. The embankment material, in computation, was described by a modified Cam-clay model taking subloading surfaces (Hashiguchi 1989) into consideration. The computed results were compared with results of additional analyses conducted using FVM and the Sandhu and Wilson method, which represents the total water head at the nodal point.

Figure 11.13 shows excess pore water pressure distribution immediately after the embankment was completed. Compared with the computed results by the Sandhu and Wilson method, computed results obtained by HPM present a gentler distribution. One probable cause for this is the difference associated with discrete points. Nevertheless, both are virtually identical in their distribution trend. Figure 11.14 shows the results computed by an FVM-based program. In the computation using FVM, excess pore water pressure locally concentrated and the calculation diverged in the middle of the process. Figure 11.15 compares field observation and FEM computation results. Although computed results by the Sandhu and Wilson method and by HPM present a slight disparity resulting from a difference associated with discrete points, both analysis results successfully reproduced the field observation outcomes and presented no major difference in calculation accuracy.

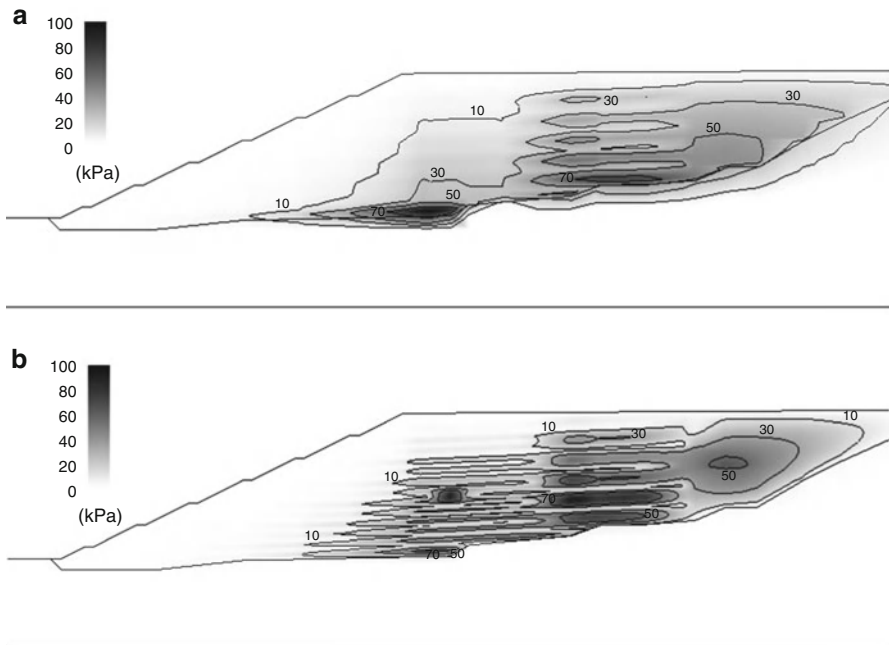


Fig. 11.13 Contour of the excess pore water pressure at the time of completion of embankment. (a) Simulation results using the hybrid-type penalty method. (b) Simulation results of the Sandhu and Wilson method

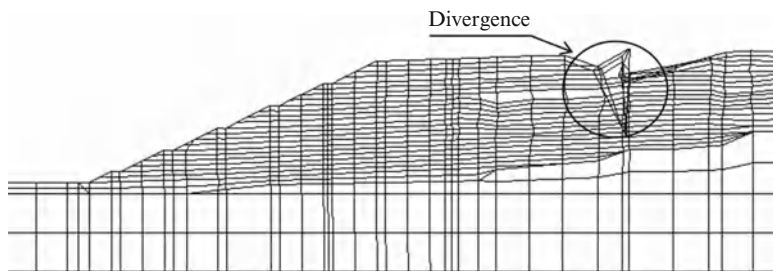


Fig. 11.14 Deformation figure by the calculation using the finite volume method

11.5 Conclusions

This chapter presents a correct extension incorporating the finite volume method (FVM) for spatial discretization formula of the total water head used in the soil–water coupled FEM analysis program DACSAR. Use of FVM, however, fails to present a perfect solution to the problem of dependence on the manner of mesh generation. Then, this chapter describes an analysis technique that

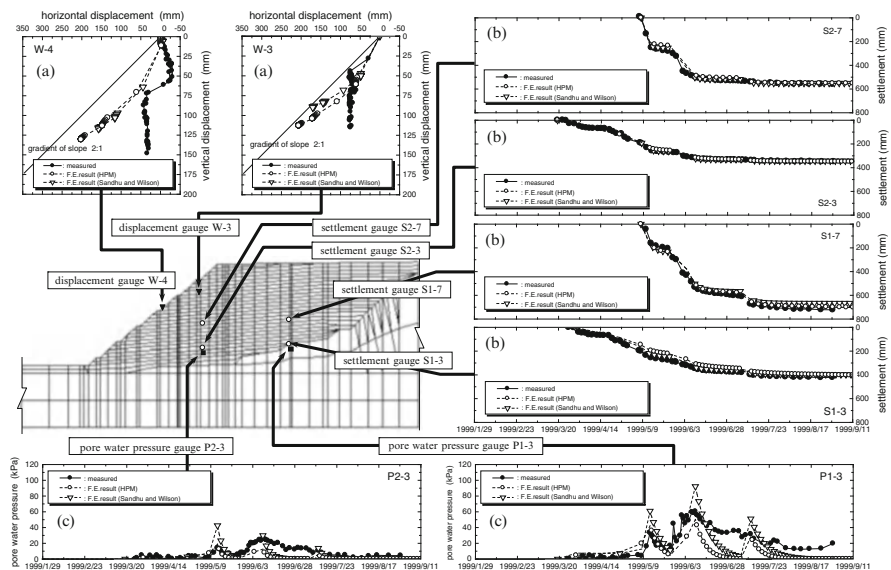


Fig. 11.15 Comparison of observation results and simulation results; (a) Displacement of the bankment slope. (b) Settlement. (c) Excess pore water pressure

incorporates the hybrid-type penalty method proposed by Takeuchi et al. and requires no value of the total water head at the nodal point. An HPM-based program was used to analyze one-dimensional consolidation and an actual embankment construction. Results reveal that the HPM-based computational technique was able to overcome problems such as incorrect computation and numerical errors depending on the manner of mesh generation and hydraulic-conductivity anisotropy. The efficacy of the HPM-based computation technique was also verified in a comparison with the Sandhu and Wilson method, which represents the total water head at the nodal point.

The spatial discretization technique representing the total water head at the element center of gravity is still widely employed in the soil–water coupled FEM programs, as well as in DACSAR, and they are used in geotechnical engineering practice. These programs may have a problem similar to that of DACSAR. It is expected that the problem will become increasingly noticeable as analyses using complex mesh and boundary conditions have increased because of the rapid development of computers in recent years. Accordingly, care should be exercised when conducting such an analysis.

References

Akai K, Tamura T (1978) Numerical analysis of multi-dimensional consolidation accompanied with elasto-plastic constitutive equation. *J JSCE* 269:95–104 (in Japanese)
 Christian JT (1968) Undrained stress distribution by numerical method. *Proc ASCE* 96(SM6):1333–1345

- Hashiguchi K (1989) Subloading surface model with unconventional plasticity. *Int J Solid Struct* 25:917–945
- Iizuka A, Ohta H (1987) A deformation procedure of input parameters in elasto-viscoplastic finite element analysis. *Soil Found* 27(3):71–87
- Nagahara H, Takeda H, Tsuruoka N, Imai T, Ishiguro T, Fujiyama T, Itoh M, Ohta H (2002) Behavior of high airport embankment with geotextile horizontal drain. In: *Proceedings of 7th international conference on geosynthetics, Nice, 2002*, vol 2, pp 1051–1054
- Sandhu R, Wilson EL (1969) Finite element analysis of flow in saturated porous media. *Proc ASCE* 95(EM3):641–652
- Takeuchi N, Yada K, Kusabuka M, Takeda H (2000) Development of numerical method for seepage flow problems using penalty. *Trans JSCES* 2000, Paper No. 20000023 (in Japanese)
- Takeyama T, Iizuka A, Ohta H (2006) Spatial discretization of water head using approximation by linear function. In: *Proceedings of the 41st JNCGE, Kagoshima, 2006*, pp 321–322 (in Japanese)

Chapter 12

Theoretical Analysis for Noncoaxiality of Toyoura Sand

Shinya Tachibana and Jiro Kuwano

12.1 Introduction

It has been recognized that to predict more precise deformation in design of soil structure, experimental investigations and model developments for the mechanical characteristics of soil materials are desired. Noncoaxiality between directions of principal stress and those of inelastic stretching (or strain increment) is an essential property of soil materials and has received considerable attention both in experimental and theoretical works. Through the experiment tests using advanced devices such as a hollow cylindrical apparatus that makes possible the control of test conditions under the rotation of the principal stress axes, it has been revealed that the direction of inelastic strain increment is dependent on that of the stress increment (e.g., Ishihara and Towhata 1983; Miura et al. 1986; Gutierrez et al. 1991; Ohkawa et al. 2011). These facts support the necessity of the stress rate effect in constitutive modeling. As for the stress rate effect, Yatomi et al. (1989) incorporated the noncoaxial term induced by the stress rate into the Cam-clay model (Schofield and Wroth 1968) in the manner of Rudnicki and Rice (1975). They showed the introduction of noncoaxiality induced by the stress rate effect made it easier for shear bands to occur and reduced the instantaneous shear modulus with shearing. Hashiguchi and Tsutsumi (2001) also proposed a sophisticated constitutive model considering the tangential stress rate effect in a more general description.

On the other hand, as a mechanical property of soil material, anisotropy is caused by the sedimentation process of soil, which is also observed in laboratory tests. Experimental facts show the anisotropy of sand samples as a dilatancy characteristic, strength, and stiffness because of the horizontal alignment of subelongated sand

S. Tachibana, D.Eng. (✉) • J. Kuwano, D.Eng.
Geosphere Research Institute, Saitama University, 255 O-kubo,
338-8570 Sakura-ku, Saitama, Japan
e-mail: stachi@mail.saitama-u.ac.jp; jkuwano@mail.saitama-u.ac.jp

particles (Oda 1972). The anisotropy can be described by taking account of the rotation of the loading surface into elasto-plastic constitutive modeling (Sekiguchi and Ohta 1977). Introduction of anisotropy also leads to noncoaxiality even when the associated flow rule is adopted (Iizuka et al. 1992). Therefore, to discuss the inelastic strain increments obtained from laboratory tests, one needs to distinguish the noncoaxiality caused by anisotropy induced by rotation of the loading surface from that caused by the stress rate effect quantitatively.

In this study, the anisotropy in the loading surface and the effect of the stress rate tangent to the loading surface, both of which cause noncoaxiality, were taken into consideration in the constitutive modeling. Then, focusing on the dilatancy characteristics of the test results, the parameters in the model associated with the anisotropy were first estimated because the stress rate effect does not contribute to the behavior of volume change. By using these parameters, the noncoaxiality between measured in experiment and predicted by model may be compared.

12.2 General Description of the Model

The constitutive model applied in this study is summarized briefly. It is noted that, here and in what follows, the signs of stress, stress rate, strain, and stretching components are chosen to be positive for tension, and stress refers to effective stress. As for notations and symbols, boldface letters denote tensors; the symbol ‘:’ denotes an inner product of two second-order tensors (e.g., $\mathbf{a} : \mathbf{b} = a_{ij}b_{ij}$), or a double contraction of adjacent indices of tensors of rank two and higher (e.g., $\mathbf{A} : \mathbf{b} = A_{ijkl}b_{kl}$); and the symbol ‘ \otimes ’ indicates an tensor product (e.g., $\mathbf{a} \otimes \mathbf{b} = a_{ij}b_{kl}$).

Consider the current configuration of the material point by \mathbf{x} and the current velocity by \mathbf{v} , and then denote the velocity gradient by $\mathbf{l} = \partial\mathbf{v}/\partial\mathbf{x}$. The velocity gradient \mathbf{l} can be decomposed additively into symmetric and skew-symmetric parts as

$$\mathbf{l} = \mathbf{d} + \mathbf{w}; \quad \mathbf{d} = \frac{\mathbf{l} + \mathbf{l}^T}{2} \quad \text{and} \quad \mathbf{w} = \frac{\mathbf{l} - \mathbf{l}^T}{2} \quad (12.1)$$

where \mathbf{d} is called a deformation rate, or stretching, \mathbf{w} is called a spin, or vorticity, and symbol $(\)^T$ stands for the transpose.

An additive decomposition of stretching \mathbf{d} is introduced in the manner of Hashiguchi and Tsutsumi (2001) as

$$\mathbf{d} = \mathbf{d}^e + \mathbf{d}^i \quad (12.2)$$

where \mathbf{d}^e and \mathbf{d}^i are the elastic and inelastic stretching, respectively. Further, let the inelastic stretching \mathbf{d}^i be additively decomposed into the plastic stretching \mathbf{d}^p and the tangential stretching \mathbf{d}^t as

$$\mathbf{d}^i = \mathbf{d}^p + \mathbf{d}^t \quad (12.3)$$

Each rate type of constitutive equation based on this kind of decomposition does not involve the material time derivative, but represents an objective rate of stress to fulfill the objectivity. Therefore, the elastic response is characterized by a hypoelastic rate constitutive equation as

$$\mathbf{d}^e = \mathbf{c}^{e-1} : \overset{\circ}{\boldsymbol{\sigma}} \quad (12.4)$$

where $\boldsymbol{\sigma}$ is the effective Cauchy stress, and $\overset{\circ}{\boldsymbol{\sigma}}$ is the co-rotational objective rate of stress. Adopting Hooke's law, the fourth-order elastic tensor \mathbf{c}^e is the given by

$$\mathbf{c}^e = KI \otimes \mathbf{I} + 2GA \quad (12.5)$$

where K , G are the elastic bulk and shear moduli, respectively.

In this study, to evaluate the plastic stretching \mathbf{d}^p , the anisotropic EC model proposed by Ohno et al. (2006) with a subloading surface model by Hashiguchi and Chen (1998) is applied. Thus, the function of the subloading surface is expressed as

$$f = (\lambda - \kappa) \ln \frac{p}{p_0} + \frac{\lambda - \kappa}{n_E} \left(\frac{\eta^*}{M} \right)^{n_E} + \int \text{tr} \mathbf{d}^p dt - (\lambda - \kappa) \ln R = 0 \quad (12.6)$$

where, M is the critical state parameter. λ and κ are the compression and swelling indices, which describe the slopes of the normal-consolidation and the swelling line, respectively, in the $\ln v - \ln p$ space (v : specific volume; Hashiguchi 1995). The material parameter n_E determines the shape of the normal-yield and subloading surfaces and prescribes the dilatancy characteristics of the model. η^* is the generalized stress ratio defined by Sekiguchi and Ohta (1977):

$$\eta^* = \sqrt{\frac{3}{2}} \|\boldsymbol{\eta} - \boldsymbol{\eta}_0\| \quad (12.7)$$

The second-order tensor $\boldsymbol{\eta}$ is the stress deviator \mathbf{s} divided by p , called the stress ratio tensor. The subscript 0 indicates the state of preconsolidation. R is the similarity ratio of the subloading surface to the normal-yield surface. The elastic bulk and shear moduli are given by

$$K = \frac{p}{\kappa}, \quad G = \frac{3(1 - 2\nu)}{2(1 + \nu)} K \quad (12.8)$$

where ν is the Poisson ratio. For the progress of the subloading surface, the following evolution law is assumed (Hashiguchi and Chen 1998):

$$\dot{R} = -u_R \ln R \|\mathbf{d}^p\| \quad (12.9)$$

The plastic stretching \mathbf{d}^p is evaluated by using associated flow rule as

$$\mathbf{d}^p = \gamma \frac{\partial f}{\partial \boldsymbol{\sigma}} \quad (12.10)$$

Plastic multiplier γ is determined from the consistency condition subjected to subloading surface ($\dot{f} = 0$) under plastic loading conditions. Then one can derive

$$\gamma = - \frac{\frac{\partial f}{\partial \boldsymbol{\sigma}} : \dot{\boldsymbol{\sigma}}}{\text{tr} \frac{\partial f}{\partial \boldsymbol{\sigma}} + u_R \ln R \frac{\partial f}{\partial R} \left\| \frac{\partial f}{\partial \boldsymbol{\sigma}} \right\|} \quad (12.11)$$

Equations (12.4), (12.10), and (12.11) provide the plastic stretching of the model expressed by

$$\mathbf{d}^p = \frac{1}{h} \left[\frac{3\xi}{2\eta^*} (\boldsymbol{\eta} - \boldsymbol{\eta}_0) : \dot{\boldsymbol{\sigma}} - \frac{1}{3} \beta^* \text{tr} \dot{\boldsymbol{\sigma}} \right] \left[\frac{3\xi}{2\eta^*} (\boldsymbol{\eta} - \boldsymbol{\eta}_0) - \frac{1}{3} \beta^* \mathbf{I} \right] \quad (12.12)$$

with

$$h = \frac{pM}{\lambda - \kappa} \left[\beta^* - u_R (\lambda - \kappa) \frac{\ln R}{R} \sqrt{\frac{3}{2} \xi^2 + \frac{1}{3} \beta^{*2}} \right] \quad (12.13)$$

$$\beta^* = M - \frac{3}{2\eta^*} \left(\frac{\eta^*}{M} \right)^{n_E - 1} (\boldsymbol{\eta} - \boldsymbol{\eta}_0) : \boldsymbol{\eta} \quad \text{and} \quad \xi = \left(\frac{\eta^*}{M} \right)^{n_E - 1} \quad (12.14)$$

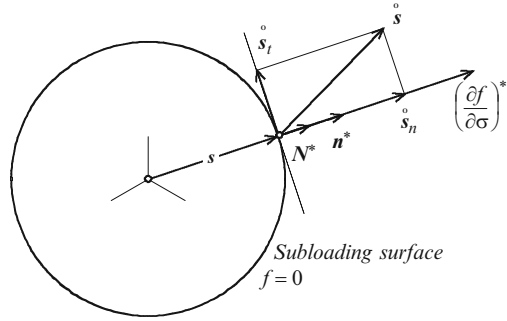
It is promised that the plastic stretching \mathbf{d}^p is induced by the stress-rate component normal to the subloading surface because of applying the associated flow rule.

On the other hand, the tangential stretching \mathbf{d}^t is induced by the stress-rate component tangent to the subloading surface and given by Hashiguchi and Tsutsumi (2001):

$$\mathbf{d}^t = \frac{1}{T} \dot{\mathbf{s}}_t \quad (12.15)$$

where the deviatoric-tangential stress rate $\dot{\mathbf{s}}_t$ is given by

Fig. 12.1 Illustration of directions of deviatoric tensors on the deviatoric stress plane



$$\begin{aligned} \hat{s}_t &= \hat{s} - \hat{s}_n; & \hat{s}_n &= \hat{s} : \frac{N^*}{\|N^*\|} n^* \quad \text{and} \\ n^* &= \frac{N^*}{\|N^*\|} = \left(\frac{\partial f}{\partial \sigma} \right)^* / \left\| \left(\frac{\partial f}{\partial \sigma} \right)^* \right\| \end{aligned} \tag{12.16}$$

The symbol $()^*$ denotes the deviatoric component. The directions of each tensor in Eq. (12.6) on deviatoric stress plane are illustrated in Fig. 12.1. Next, one can derive the deviatoric-tangential stress rate of the form

$$d^t = \frac{1}{T} \left[\hat{s} - \frac{3}{2} \frac{(\eta - \eta_0) \otimes (\eta - \eta_0)}{\eta^{*2}} : \hat{s} \right] \tag{12.17}$$

Hashiguchi and Tsutsumi (2001) proposed the function T as a monotonically decreasing function of R and assumed as

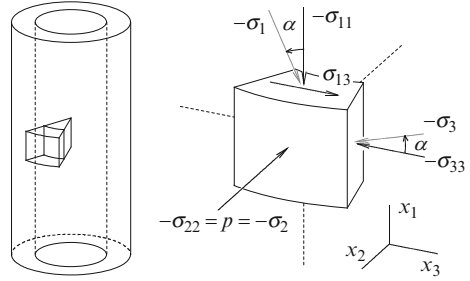
$$T = \frac{p}{\alpha \chi^c R^b}; \quad \chi = \frac{\eta^*}{M} \tag{12.18}$$

where a, b, c are material constants.

12.3 Verification of the Model

The model ability to simulate shear behavior of dense Toyoura sand under the conditions of constant effective mean stress p and constant intermediate principal stress coefficient b is examined in this section. Some model parameters are also determined taking into account the theoretical conditions.

Fig. 12.2 The hollow cylindrical specimen and stresses acting on an element



12.3.1 p Constant and b Constant Shear Conditions

If a hollow cylindrical specimen is subjected to torsional loading (as shown in Fig. 12.2), the stress state of an infinitesimal small element in the sample is given by

$$\sigma = \begin{bmatrix} \sigma_{11} & 0 & \sigma_{13} \\ 0 & \sigma_{22} & 0 \\ \sigma_{13} & 0 & \sigma_{33} \end{bmatrix} \tag{12.19}$$

where σ_{11} is the axial stress, σ_{22} is the radial stress, σ_{33} is the peripheral stress, and σ_{13} is the torsional shear stress. Under the condition that $p = \text{const.}$ and $b = (\sigma_2 - \sigma_3)/(\sigma_1 - \sigma_3) = 0.5$, the stresses are controlled so as to fulfill the following relation:

$$\sigma_{22} = \sigma_2 = \frac{1}{2}(\sigma_1 + \sigma_3) = \text{const.} \tag{12.20}$$

where $\sigma_1, \sigma_2, \sigma_3$ are the major, intermediate and minor principal stress, respectively. The relationships between stress components and the principal stresses with the angle of principal stress axes rotation α are

$$\left. \begin{matrix} \sigma_{11} \\ \sigma_{33} \end{matrix} \right\} = \frac{\sigma_1 + \sigma_3}{2} \pm \frac{\sigma_1 - \sigma_3}{2} \cos 2\alpha \tag{12.21}$$

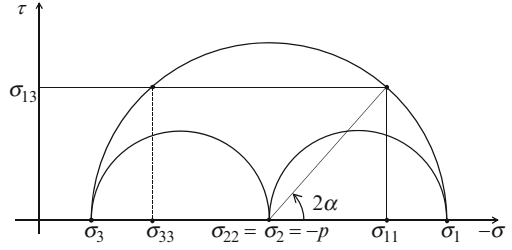
$$\sigma_{22} = \sigma_2 = -p \tag{12.22}$$

$$\sigma_{13} = \frac{\sigma_1 - \sigma_3}{2} \sin 2\alpha \tag{12.23}$$

Figure 12.3 illustrates the Mohr's circle for this condition. The stress state induced for this condition can also be given by

$$X = \sigma_{33} - \sigma_{11} \quad \text{and} \quad Y = 2\sigma_{13} \tag{12.24}$$

Fig. 12.3 Mohr's stress circle for the principal stress axes rotation



The angle between the current stress vector and the positive direction of X -axis in the $X - Y$ plane makes twice the angle α , which can be written as

$$2\alpha = \tan^{-1}\left(\frac{Y}{X}\right) \quad (12.25)$$

Therefore, the stress parameters X and Y can be also written as functions of r , the magnitude of current stress in $X - Y$ plane; that is,

$$X = r \cos(2\alpha) \quad \text{and} \quad Y = r \sin(2\alpha) \quad \text{with} \quad r = \frac{2\sqrt{3}}{3} p \dot{\eta} \quad (12.26)$$

The rate form of Eq. (12.24) gives

$$\dot{X} = \dot{\sigma}_{33} - \dot{\sigma}_{11} \quad \text{and} \quad \dot{Y} = 2\dot{\sigma}_{13} \quad (12.27)$$

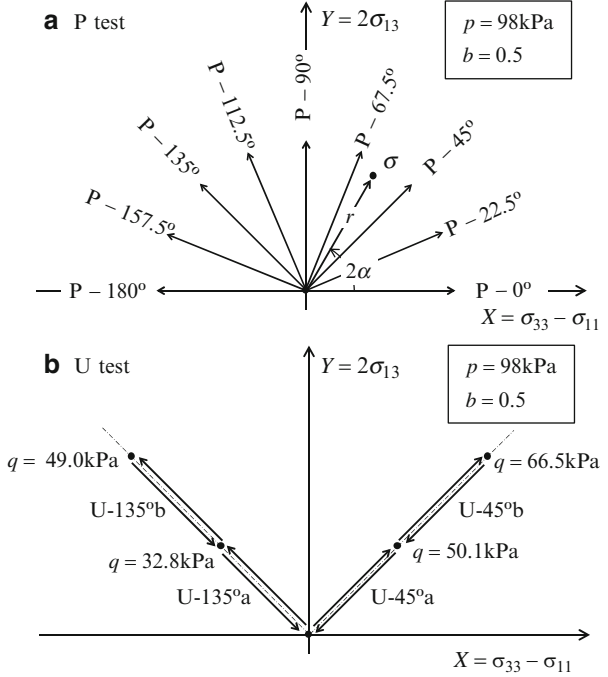
Thus, for the proportional loading such that $\dot{\alpha} = 0$, Eq. (12.27) can be rewritten as

$$\dot{X} = \dot{r} \cos(2\alpha) \quad \text{and} \quad \dot{Y} = \dot{r} \sin(2\alpha) \quad \text{with} \quad \dot{r} = \frac{2\sqrt{3}}{3} p \dot{\eta} \quad (12.28)$$

Hereafter, the model will be verified comparing with the test results of Ohkawa et al. (2011) for drained shear at $p = 98$ kPa from the isotropic stress state as shown in Fig. 12.4. For P tests, the sand samples are monotonously sheared while keeping the angle 2α constant from the isotropic consolidation state, whereas the unloading shear was conducted from the prescribed stress level for U tests. It is noted that the axial stress is also controlled in all tests so as to satisfy the following relation:

$$\dot{\sigma}_{11} = -\frac{\dot{r}}{2} \cos(2\alpha) \quad (12.29)$$

Fig. 12.4 Prescribed stress paths on X - Y plane for (a) P test and (b) U test



12.3.2 Subloading Surface in X - Y Plane

Let the axi-symmetric anisotropy be assumed to be

$$\eta_0 = \begin{bmatrix} -\frac{2}{3}\eta_0 & 0 & 0 \\ 0 & \frac{1}{3}\eta_0 & 0 \\ 0 & 0 & \frac{1}{3}\eta_0 \end{bmatrix} \tag{12.30}$$

where the positive parameter η_0 represents the slope of the central axis of both subloading and normal-yield surface in the $p - q$ plane. Then, by substituting Eqs. (12.26) and (12.30) into Eq. (12.6), the following expression of subloading surface in terms of X and Y can be obtained:

$$(X - p\eta_0)^2 + Y^2 = \frac{4}{3}p^2M^2 \left(n_E \ln \frac{Rp_c}{p} \right)^{\frac{2}{n_E}} - \frac{1}{3}p^2\eta_0^2 \tag{12.31}$$

If an isotropic stress state is set to be an initial condition for the shear, the initial radius of subloading surface coincides with the distance between the center of the surface and the origin because the current stress always locates on the surface. Thus, the initial value of pre-consolidation pressure $p_{c,i}$ can be calculated from Eq. (12.31) as

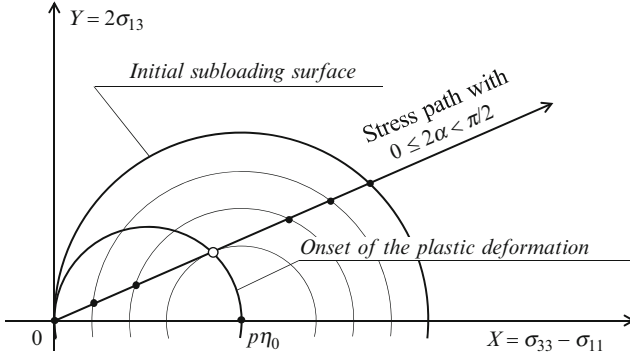


Fig. 12.5 Onset of the plastic deformation with progress of subloading surface for $0 \leq 2\alpha < \pi/2$ monotonic shearing

$$p_{c,i} = \frac{p}{R_i} \exp \left[\frac{1}{n_E} \left(\frac{\eta_0}{M} \right)^{n_E} \right] \tag{12.32}$$

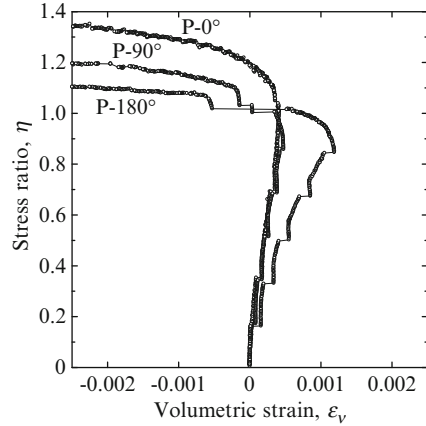
where R_i indicates the initial value of the similarity ratio R .

The subloading surface changes its size because of shearing while keeping the location of its center under the assumption of isotropic hardening. When stress path traces toward inner side of the subloading surface, the surface simultaneously shrinks and the deformation behavior becomes an elastic state. On the other hand, the situation such that the surface expands because of the stress path toward the outer side of the surface results in an elasto-plastic deformation. Therefore, the early stage of shear with the principal stress angles $0 \leq 2\alpha < \pi/2$ from the isotropic stress condition can be regarded as an elastic state, whereas plastic deformation occurs from the beginning of shear with the angles $\pi/2 \leq 2\alpha \leq \pi$. In cases of shear with the angles $0 \leq 2\alpha < \pi/2$, plastic deformation occurs when the stress reaches the point at which the stress path and the surface come in contact with each other (as shown in Fig. 12.5). Therefore, the condition for plastic deformation onset for the proportional loading such that $\dot{\alpha} = 0$ can be given by

$$\eta = \begin{cases} \frac{\sqrt{3}}{2} \eta_0 \cos(2\alpha) & \text{for } 0 \leq 2\alpha < \frac{\pi}{2} \\ 0 & \text{for } \frac{\pi}{2} \leq 2\alpha \leq \pi \end{cases} \tag{12.33}$$

This condition provides a basis for estimation of parameter η_0 from the test results. Figure 12.6 shows the dilatancy characteristics obtained from test cases $P-0^\circ$, $P-90^\circ$, and $P-180^\circ$. Apparent anisotropy can be recognized both in contract and dilation behaviors, whereas these tests involve the creep stage at the prescribed stress level. A similar tendency can be seen in the tests of Miura et al. (1986). Although the differences in the amount of the volume contraction at the early stage of shear among these tests are quite small, it seems that the stress ratio at the onset of volume change in the $P-0^\circ$ test is higher than that in other tests.

Fig. 12.6 Dilatancy behavior during monotonic shearing for tests $P - 0^\circ$, $P - 90^\circ$ and $P - 180^\circ$



An approximate estimate from the onset of volume change in the $P - 0^\circ$ test gives a value of stress ratio η of 0.2. This stress ratio can be regarded as the onset of plastic deformation for $2\alpha = 0$ because both elastic and tangential parts of stretching have no contribution to the volume change. Therefore, by using the condition of Eq. (12.33), the value of η_0 can be determined as $\eta_0 = 0.23$.

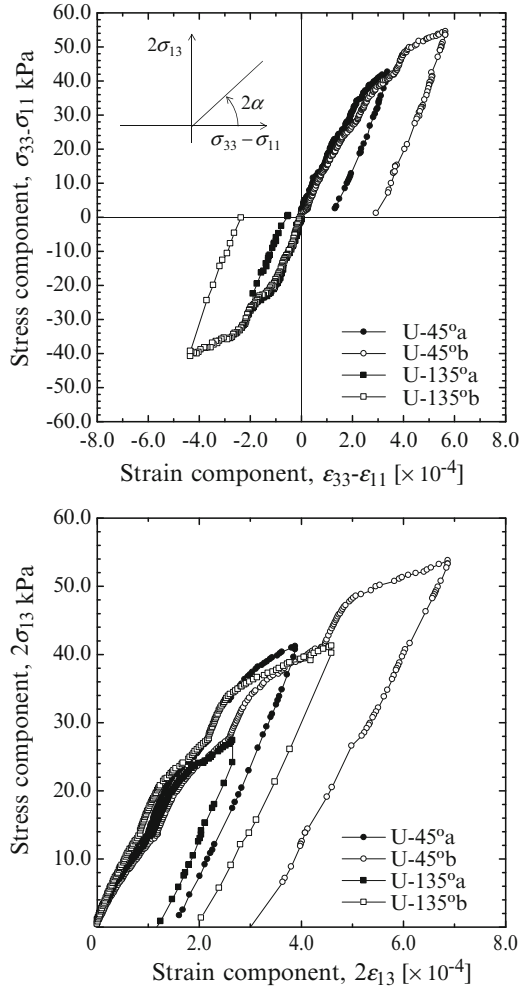
12.3.3 Elastic Response

By using Eq. (12.4), one can get an elastic modulus G in the X - Y plane as

$$2G = \frac{\overset{\circ}{\sigma}_{11} - \overset{\circ}{\sigma}_{33}}{d_{11}^e - d_{33}^e} \quad \text{or} \quad 2G = \frac{\overset{\circ}{\sigma}_{13}}{d_{13}^e} \quad (12.34)$$

Therefore, the elastic shear modulus G can be estimated by taking a tangent of the stress-strain relationship at the elastic states. Figure 12.7 shows the stress-strain relationships for U tests. The unloading paths can be regarded as an elastic state when the subloading surface has once expanded because of loading to the prescribed stress level, and then shrinks because of unloading. Assuming that co-rotational stress rate is identified to stress rate and stretching to strain rate, elastic shear modulus G is estimated by using Eq. (12.34) and plotted against the stress ratio in Fig. 12.8. The estimated elastic shear modulus G shows a slight increasing tendency with an increasing stress ratio and ranges from 50 to 120 MPa. Moreover, it seems that the modulus estimated from the first equation in Eq. (12.34) is larger at the same stress level than that from the second. Although these tendencies suggest that the elastic response is also characterized as anisotropy and the value of G varies with an increase of stress ratio without any changes in effective mean stress p , the constant value of

Fig. 12.7 Stress-strain relationships for U tests



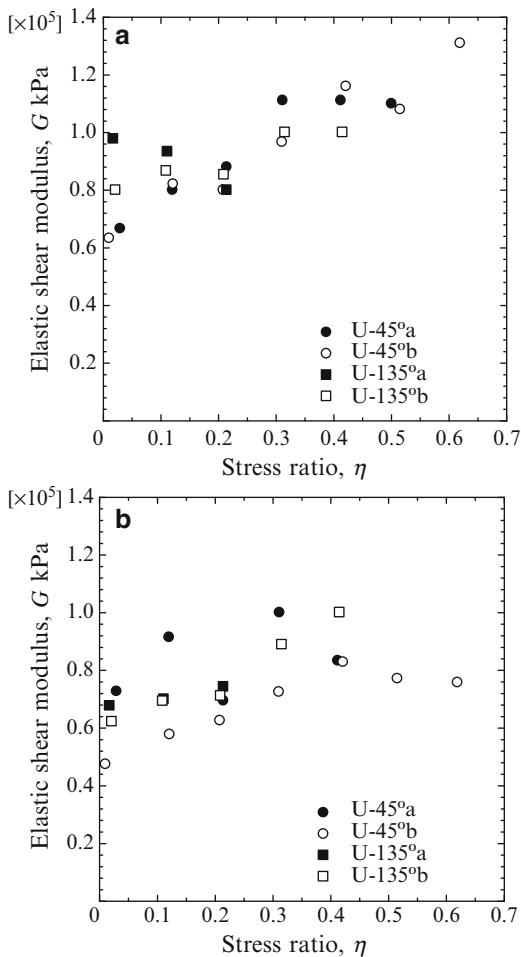
elastic shear modulus can be approximately determined as $G = 80$ MPa from test results to comply with the definition of the model.

By using Eq. (12.8), Poisson's ratio can be given by

$$\nu = \frac{3p - 2\kappa G}{6p + 2\kappa G} \quad (12.35)$$

The relationship between Poisson's ratio ν and swelling index κ is shown in Fig. 12.9 with the values of $G = 80$ MPa and $p = 98$ kPa. Tsutsumi and Hashiguchi (2005) determined the value of the swelling index for Toyoura sand from the test results of Gutierrez et al. (1991) as $\kappa = 0.00057$. Therefore, this value is also applied in this study, which leads to $\nu = 0.299$ and $K = p/\kappa = 172$ MPa.

Fig. 12.8 Estimated shear modulus against the stress ratio for monotonic unloading shear by the (a) by the first and (b) by the second equations in Eq. (12.34)



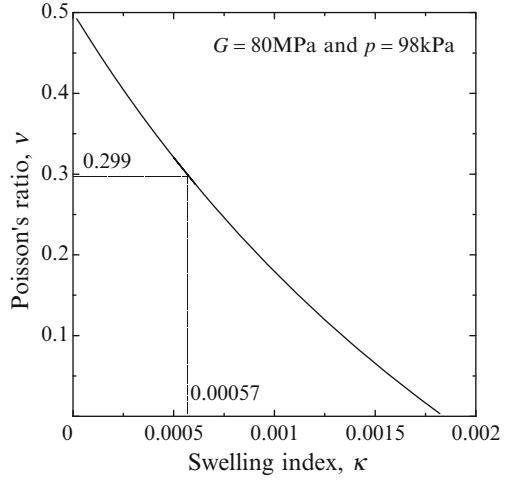
12.3.4 Transition from Contract to Dilate Volume Change

As shown in Fig. 12.6 and also discussed by Miura et al. (1986), transition from contract to dilate in volume change owing to shear can be seen in the test results. In this section, the condition of the transition point is examined.

Under an effective mean stress constant condition, each part of stretching can be reduced to

$$d^e = \frac{1}{2G} s^{\circ} \tag{12.36}$$

Fig. 12.9 Relationship between Poisson's ratio and the swelling index



$$\mathbf{d}^p = \frac{1}{h} \frac{3\xi}{2\eta^*} (\boldsymbol{\eta} - \boldsymbol{\eta}_0) : \overset{\circ}{\mathbf{s}} \left[\frac{3\xi}{2\eta^*} (\boldsymbol{\eta} - \boldsymbol{\eta}_0) - \frac{1}{3}\beta^* \mathbf{I} \right] \quad (12.37)$$

$$\mathbf{d}^t = \frac{1}{T} \left[\overset{\circ}{\mathbf{s}} - \frac{3}{2} \frac{(\boldsymbol{\eta} - \boldsymbol{\eta}_0) \otimes (\boldsymbol{\eta} - \boldsymbol{\eta}_0)}{\eta^{*2}} : \overset{\circ}{\mathbf{s}} \right] \quad (12.38)$$

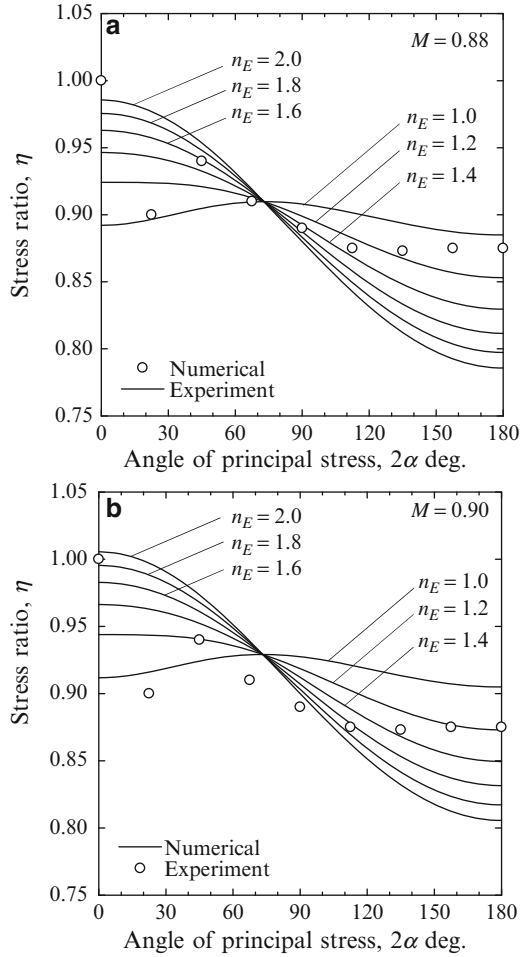
Because a trace of elastic and tangential parts of stretching becomes zero, volume change under the condition is given by

$$\text{tr} \mathbf{d} = \text{tr} \mathbf{d}^p = -\frac{1}{h} \frac{3\xi}{2\eta^*} \beta^* (\boldsymbol{\eta} - \boldsymbol{\eta}_0) : \overset{\circ}{\mathbf{s}} \quad (12.39)$$

To discuss the transition condition such that $\text{tr} \mathbf{d} = 0$ during plastic shear, it is necessary to clarify the characteristics of each parameter in Eq. (12.39). Stress parameter η^* is non-negative and becomes zero only when the stress state locates on the axisymmetric anisotropic axis in p - q plane. Because the stress under the condition that $p = \text{const.}$ and $b = 0.5$ never reaches the axi-symmetric anisotropic axis, stress parameter η^* is always positive. As is evident from Eq. (12.14), therefore, the stress parameter ξ also takes a positive value during shearing. The states $h > 0$, $h = 0$, and $h < 0$ correspond to the hardening, perfect-plastic and the softening states, respectively, because the plastic multiplier γ is positive during plastic loading (e.g., Hashiguchi and Tsutsumi 2003). Therefore, the state $h = 0$ can be defined as the failure state such that a stress–strain curve for monotonic loading usually exhibits a peak. By substituting Eqs. (12.24), (12.26), (12.27), and (12.28) into the final term of Eq. (12.39), one can derive the following equation:

$$(\boldsymbol{\eta} - \boldsymbol{\eta}_0) : \overset{\circ}{\mathbf{s}} = \frac{1}{\sqrt{3}} \dot{\gamma} \left[\eta - \frac{\sqrt{3}}{2} \eta_0 \cos(2\alpha) \right] \quad (12.40)$$

Fig. 12.10 Stress ratio at the transition point against the angle of principal stress 2α with (a) with $M = 0.88$ and (b) with $M = 0.90$

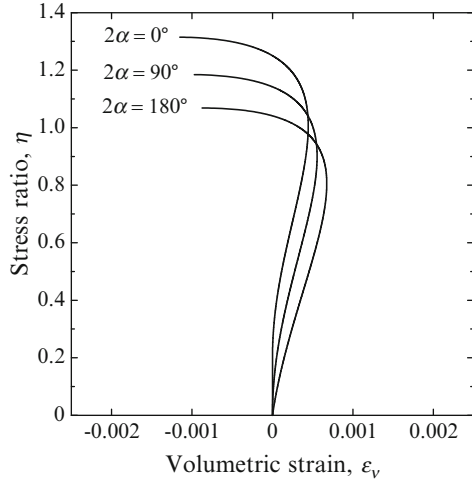


Thus, this term is taken to be positive during plastic loading except for the onset of plastic deformation as recognized from Eq. (12.33). Conclusively, the transition condition is given by

$$\beta^* = M - \frac{3}{2\eta^*} \left(\frac{\eta^*}{M}\right)^{n_E-1} \quad \boldsymbol{\eta} : (\boldsymbol{\eta} - \boldsymbol{\eta}_0) = 0 \quad (12.41)$$

The stress ratio η satisfying transition condition $\text{tr} \boldsymbol{d} = 0$ can be calculated by solving Eq. (12.41) with Newton's method. Numerical solutions are depicted against the angle of principal stress 2α as shown in Fig. 12.10, together with the results of the P test of Ohkawa et al. (2011). Herein, the anisotropic parameter η_0 is set to be 0.23 as determined in Sect. 12.3.2 and the critical state parameter M is assumed to be 0.88 and 0.90. The stress ratio at transition point obtained from

Fig. 12.11 Numerical simulations in the volumetric change for monotonic shear loading



experiment tests shows a decreasing tendency with increasing the angle of principal stress, although only the data of $2\alpha = 22.5^\circ$ stray out of this trend. Predictions of the model can express such decreases with 2α except for the case of $n_E = 1.0$. However, it is difficult to find the combination of M and n_E that can express test results quantitatively. In this study, therefore, the values of these parameters are assumed to be $M = 0.90$ and $n_E = 2.0$ so as to fit the stress ratio at the transition when $2\alpha = 0^\circ$.

To illustrate the model performance in the simulation of anisotropic behavior of sand for monotonic loading under conditions that $b = 0.5$ and $p = 98$ kPa, the model is used to predict the dilatancy behavior for the tests $P = 0^\circ$, $P = 90^\circ$, and $P = 180^\circ$. The following material parameters and initial condition are used in calculations: $\lambda = 0.0057$, $\kappa = 0.00057$, $M = 0.90$, $\eta_0 = 0.23$, $n_E = 2.0$, $\nu = 0.299$, $u_R = 18.0$, and $R_i = 0.1$. Among these parameters, the values of λ , u_R and R_i are set so as to well simulate the volume changes in three tests, whereas the aforementioned values are used for other parameters. The calculated results are shown in Fig. 12.11, which can be compared with experimental results in Fig. 12.6.

12.3.5 Noncoaxiality

Finally, noncoaxiality; that is, the noncoincidence of the principal directions of inelastic stretching and those of stress, is focused on in this section. To compare the noncoaxiality between the experiment and numeric results, the noncoaxial angle is defined as

$$2\omega = \tan^{-1} \frac{2d_{13}^i}{d_{33}^i - d_{11}^i} \quad (12.42)$$

In the model applied in this study, inelastic stretching constitute parts of plastic and tangential stretching as $\mathbf{d}^i = \mathbf{d}^p + \mathbf{d}^t$. Therefore, by substituting Eqs. (12.37) and (12.38), the noncoaxial angle of the model is given by

$$2\omega = \tan^{-1} \left[\frac{\frac{1}{T} \overset{\circ}{s}_{13} + \frac{3}{2} \frac{s:(\eta-\eta_0)}{\eta^2} \frac{Y}{p} \left(\frac{3}{2} \frac{\xi^2}{h} - \frac{1}{T} \right)}{\frac{1}{T} \left(\overset{\circ}{s}_{33} - \overset{\circ}{s}_{11} \right) + \frac{3}{2} \frac{s:(\eta-\eta_0)}{\eta^2} \left(\frac{X}{p} - \eta_0 \right) \left(\frac{3}{2} \frac{\xi^2}{h} - \frac{1}{T} \right)} \right] \quad (12.43)$$

If we consider the model with anisotropy caused by the rotation of the yield surface but without the tangent effect; that is, $T \rightarrow 0$ and $\mathbf{d}^t = 0$, the inelastic stretching \mathbf{d}^i constitutes only plastic stretching \mathbf{d}^p and Eq. (12.43) reduces to

$$2\omega = \tan^{-1} \frac{Y}{X - p\eta_0} \quad (12.44)$$

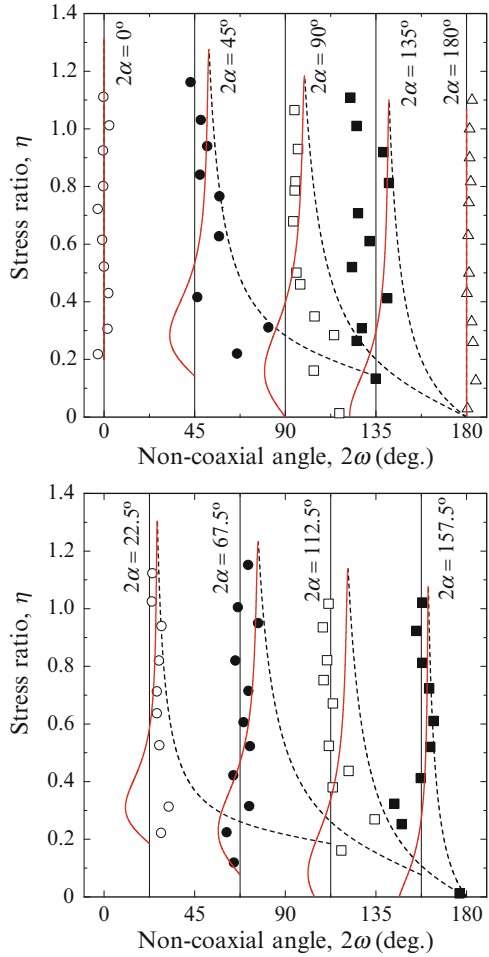
It is natural that this direction represents the normal to the subloading surface because the associated flow rule is adopted for the plastic stretching \mathbf{d}^p . Furthermore, in an isotropic case ($\eta_0 = 0$), this angle coincide with the direction of principal stress, which gives a coaxial prediction.

In Fig. 12.12, comparisons of the model prediction for noncoaxial angles with experiments of Ohkawa et al. (2011) are presented. In the predictions, the material parameters mentioned in the preceding are also used. Solid lines indicate the prediction from the model with both anisotropy and tangent effect with material constants $a = 0.002$, $b = c = 1.0$ for function T in Eq. (12.18). On the other hand, dashed lines indicate the normal direction of the subloading surface, which is predicted by the model with anisotropy but without the tangent effect. Although variations of the noncoaxial angle in the test results appear, it seems that test results mostly locate between the direction of principal stress 2α and the angle normal to the subloading surface, and approach the direction of principal stress with increases of stress ratio. Therefore, not only anisotropy with the associated flow rule but also the tangential stress rate effect should be introduced in the modeling so as to well predict the noncoaxiality. However, there is still room for argument about more accurate prediction of noncoaxial angle in the description of function T .

12.4 Conclusions

The capability of the model in which both the anisotropy and the tangential effect are examined comparing the experimental results of drained shear under conditions in which the effective mean stress and the intermediate principal stress coefficients are kept constant.

Fig. 12.12 Comparisons between measured and predicted angles of noncoaxiality



The model can express the anisotropic responses in the volume change caused by shearing. Focusing attention on the contract–dilute transition in volume change, the stress ratio at transition obtained from experiments shows a decreasing tendency with an increase in the angle of principal stress. The theoretical condition well predicts this tendency and provides the determination of the contractancy parameter n_E and the critical state parameter M .

The noncoaxiality angle estimated from experiments seems to locate between the principal stress angle and the normal to loading surface. Therefore, not only the anisotropy with associated flow rule, but also the tangential stress rate effects are required in the modeling of sand material.

References

- Gutierrez M, Ishihara K, Towhata I (1991) Flow theory for sand during rotation of principal stress directions. *Soil Found* 31(4):121–132
- Hashiguchi K (1995) On the linear relations of $V\text{-ln}p$ and $\ln v\text{-ln}p$ for isotropic consolidation of soils. *Int J Numer Anal Method Geomech* 11:347–365
- Hashiguchi K, Chen ZP (1998) Elastoplastic constitutive equation of soils with the subloading surface and rotational hardening. *Int J Numer Anal Method Geomech* 22:197–227
- Hashiguchi K, Tsutsumi S (2001) Elasto-plastic constitutive equation with tangential stress rate effect. *Int J Plast* 17:117–145
- Hashiguchi K, Tsutsumi S (2003) Shear band formation analysis in soils by the subloading surface model with tangential stress rate effect. *Int J Plast* 19:1651–1677
- Iizuka A, Yatomi C, Yashima A, Sano I, Ohta H (1992) The effect of stress induced anisotropy on shear band formation. *Arch Appl Mech* 62:104–114
- Ishihara K, Towhata I (1983) Sand response to cyclic rotation of principal stress directions as induced by wave loadings. *Soil Found* 24(4):105–117
- Miura K, Miura S, Toki S (1986) Deformation behavior of anisotropic dense sand under principal stress axes rotation. *Soil Found* 26(1):36–52
- Oda M (1972) Initial fabrics and their relations to mechanical properties of granular materials. *Int J Plast Soil Found* 12(1):17–36
- Ohkawa H, Kuwano J, Nakada T, Tachibana S (2011) Yielding characteristics and non-coaxiality of Toyoura sand on p' -constant shear stress plane. *Soil Found* 51(1):179–190
- Ohno S, Iizuka A, Ohta H (2006) Two categories of new constitutive model derived from non-linear description of soil contractancy. *J Appl Mecha JSCE* 9:407–414 (in Japanese)
- Rudnicki JW, Rice JR (1975) Conditions for the localization of the deformation in pressure-sensitive dilatant material. *J Mech Phys Solid* 23:371–394
- Schofield AN, Wroth CP (1968) *Critical state soil mechanics*. McGraw-Hill, London
- Sekiguchi H, Ohta H (1977) Induced anisotropy and time dependency in clays, constitutive equation of soils. In: *Proceedings of specialty session 9, 9th international conference soil mechanics and foundation engineering, Tokyo, 1977*, pp 306–315
- Tsutsumi S, Hashiguchi K (2005) General non-proportional loading behavior of soils. *Int J Plast* 21:1941–1969
- Yatomi C, Yashima A, Iizuka A, Sano I (1989) General theory of shear bands formation by a non-coaxial cam-clay model. *Soil Found* 29(3):41–53

Chapter 13

Threshold of Friction Stabilizes Self-Weight Transmission in Gravitating Loose Sand Heaps

Thirapong Pipatpongsa and Hideki Ohta

13.1 Introduction

The angle of repose is the maximum angle that granular materials can be piled up without lateral supports or confining pressure applied to the surfaces. Therefore, containers are not required for the storage of mining and mineral ores, agricultural grains, pharmaceutical and chemical products, and so on. Stockpile of these materials in loose conditions is frequently in wedge-shaped (see Fig. 13.1) and conical heaps.

Conical and prismatic shapes are two common geometries of granular heaps that have been extensively examined in both theories and experiments. Load transfer mechanisms in both geometries are a fundamental research that have been investigated by broad and various disciplines (Hummel and Finnan 1921; Trollope 1956, 1957; Jotaki 1979; Bouchaud et al. 1995; Šmíd and Novosad 1981; Wittmer et al. 1996, 1997; Cantelaube and Goddard 1997; Vanel et al. 1999; Didwania et al. 2000; Wiesner 2000). Despite being a seemingly simple problem, there is no unique stress solution because the challenge involves both deposition method and construction history. Self-weight transmission can be viewed as a state of equilibrium in which compressive forces are connected in networks of both major and minor directions. Therefore, columns of lines or curves dominantly transfer a weight toward a supporting rigid and rough base with a certain confining pressure to prevent a buckled configuration.

This chapter concentrates on load transmission of sand heaps in prismatic shapes. The geometry of a prismatic sand heap reduces the problem from three

T. Pipatpongsa, D.Eng. (✉)

Global Scientific Information and Computing Center, Tokyo Institute of Technology,
2-12-1 O-okayama, 152-8550 Meguro-ku, Tokyo, Japan
e-mail: pthira@gsic.titech.ac.jp

H. Ohta, D.Eng.

Research and Development Initiative, Chuo University,
1-13-27 Kasuga, 112-8551 Bunkyo-ku, Tokyo, Japan
e-mail: ohta@tamacc.chuo-u.ac.jp



Fig. 13.1 Storage of lignite piled up by belt-conveyor at the Mae Moh mine under operation of the Electricity Generating Authority of Thailand

dimensions to two because the stress condition along the longitudinal direction is out of interest in practice. Therefore, this chapter focuses on a system of stresses in triangular cross-section. Nadai (1963b) idealized the planar sand heap problem by hypothesizing that the major principal stress adjusts itself during the growth of a sand heap by aligning the angle of major compression away from the vertical direction in a half angle measured from the apex. However, the derivation of stress fields was not rigorous (Marais 1969; Nadai 1963b); therefore, Pipatpongsa et al. (2010) derived a rigorous stress field solution based on Nadai's hypothesis, which was later called a stress closure of polarized principal axes (PPA) by the author.

The present chapter reviews basic concepts used in Pipatpongsa et al. (2010) with an insightful explanation of the basic assumptions and closure of the PPA. Many graphic illustrations and step-by-step interpretation processes are added to explain the basic idea of how to obtain principal stress axes. In addition, the same stress solutions are provided with different derivation techniques. Finally, the stability of a static sand heap is discussed.

13.2 State of Stress in a Sand Heap

For loose and cohesionless earth, the angle of repose is equivalent to the constant-volume friction angle (Cornforth 1973); therefore, friction is mobilized in a loose sand heap along both sides of slope surface inclined at the angle of repose ϕ . Because of geometric symmetry, consider the sliding plane on the left-hand side of

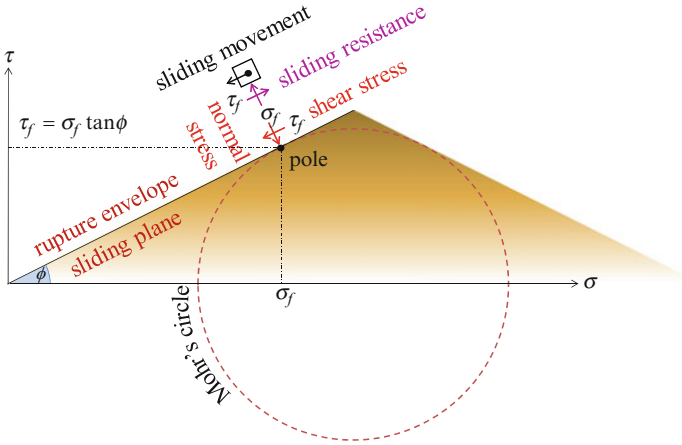


Fig. 13.2 Small traction induced by sliding movement of thin sand layers along the sliding plane of a sand heap

the sand heap where the frictional resistance is mobilized as shown in Fig. 13.2. The right-hand side can be viewed in a similar way by viewing a sand heap at the opposite side.

Hereafter, the subscript “f” denotes variables at a failure. From the physical space, it is clear that shear stress τ_f acting along the sliding plane rotates counter-clockwise around a point just inside the slope because it cascades down a thin sand layer; so τ_f is considered to be a positive shear in Mohr space according to the sign convention of soil mechanics. The normal stress, σ_f , acting normally to the sliding plane because of the weight of a thin sand layer gives little traction (σ_f, τ_f), exerting on the slope with a limiting stress ratio $\tau_f/\sigma_f = \tan \phi$, although values of both σ_f and τ_f are almost zero. A Mohr’s stress circle representing this limiting stress condition can be obtained by drawing a circle that is tangent to the failure envelope, $\tan \phi$, and in contact with a point (σ_f, τ_f) , as shown in Fig. 13.3.

The pole of a Mohr’s circle is typically located by the intersection of Mohr’s circle with a line extending from given traction in Mohr’s circle parallel to a plane of action. One can find that a traction (σ_f, τ_f) located on a sliding plane, which also inclines at angle ϕ , is the pole of a Mohr’s circle because the intersecting point is coincided with the tangent point for this case. The pole of Mohr’s circle is helpful to define the directions of major and minor principal stresses. As a result, the major principal stress σ_{1f} and minor principal stress σ_{3f} can be determined from a Mohr’s circle as shown in Fig. 13.3.

The directions of σ_{1f} and σ_{3f} can be presented by drawing lines from the pole to a point $(\sigma_{3f}, 0)$ and a point $(\sigma_{1f}, 0)$, respectively. These two directions are normal to each other. Herein, the direction of σ_{1f} inclines at an angle ω_f measured from the vertical, whereas the direction of σ_{3f} inclines at an angle ω_f measured from the horizontal. A particular relation between an angle ω_f and a friction angle ϕ is obtained by introducing a line extending from the pole to the center of Mohr’s

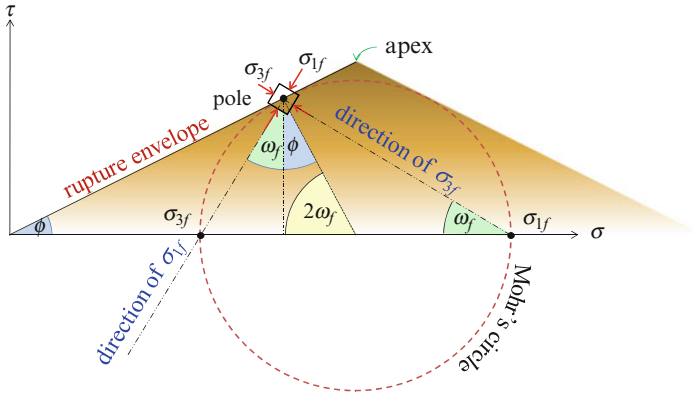


Fig. 13.3 State of stress in Mohr space at the limit state superimposed with a physical space of a sand heap in which the angle of major compressive stress $\omega_f = \pi/4 - \phi/2$ can be geometrically derived

circle. According to Fig. 13.3, the limiting stress along the sliding slope in the left hand side of a sand heap in both physical space and Mohr space indicates that the angle ω_f can be geometrically derived by setting an equation $2\omega_f + \phi = \pi/2$ for a right triangle with a hypotenuse representing a radius of Mohr's circle; hence, the expression of ω_f is obtained.

$$\omega_f = \frac{\pi}{4} - \frac{\phi}{2} \tag{13.1}$$

By mirroring the principal stress axes at the sliding plane on the left-hand side along the central plane, lying through the apex, to the right-hand side (see Fig. 13.4), one could find out that the axis of σ_1 represented by an angle ω is not constant in the bulk of a sand heap, but is gradually rotated from its limit ω_f of each side, showing by points A and D, around the apex of a sand heap, indicated by point C. Point B, lying along the central plane below point C, is the intersecting point of two minor principal directions extending from points A and D; whereas point E, lying along the central plane above point C is the intersecting point of two major principal directions extending from points A and D.

Although the base of the sand heap is stiff and is not settled, each half tends to spread away from the central plane because of body force. The spreading mechanism is referred to as an active condition (Michalowski and Park 2004; Savage 1998), thus revealing that the direction of major compressive stress along the central plane σ_{1c} acts parallel to the direction of gravity; in other words, the direction of minor compressive stress along the central plane σ_{3c} acts in accord with the direction of gravity (see Fig. 13.4). Because the angle of the major principal axis measured from the vertical axis is zero, the expression ω_c is expressed in Eq. (13.2), where a subscript “c” denotes the variables at the central plane.

$$\omega_c = 0 \tag{13.2}$$

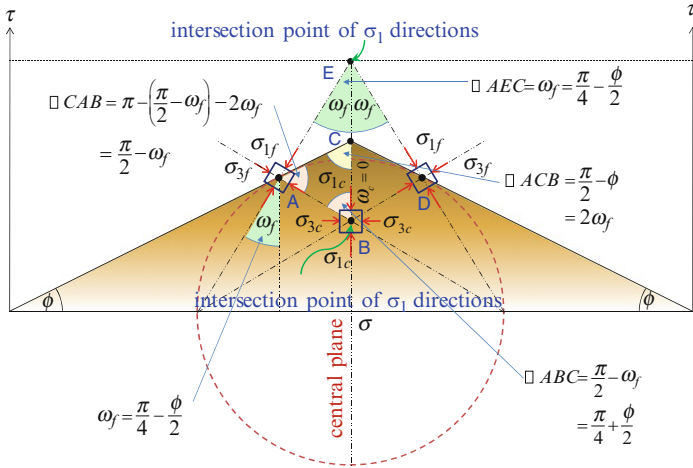


Fig. 13.4 Symmetric conditions along the central plane of a sand heap with the apex at point C where the direction of major principal axes passing points A , D , and B join one another at a point E

According to Fig. 13.4, $\angle AEC = \omega_f$, $\angle ACB = 2 \times \angle AEC = 2\omega_f$ and $\angle CAB = \angle ABC = \pi/2 - \omega_f$; hence, a circle with its center at a point C tracing points A , B , D , and E exists, as depicted in Fig. 13.5. It appears that the axes of major principal stress of three representative points merge at the top of a circle that has its center on the apex of a sand heap.

It is known that a physical interpretation of the von Mises yield criterion was made by Arpad L. Nadai (1937), who introduced the concept of octahedral stresses, which aids viewing the yielding condition on the octahedral plane. Moreover, Nadai’s sand hill analogy, which is a visual interpretation of a stress function for a fully plasticized structural member under ultimate torque as the surface of a sand heap accommodated on that cross-sectional area is also introduced by Nadai (1963a). Therefore, it is not a surprise that Nadai (1963b) can visualize that the orientations of major principal axes in sand heaps along any circle traces about its apex (as explained in Fig. 13.5) follows the simple rule that all directions of σ_1 converge toward the top of that circle (as depicted in Fig. 13.6).

The graphic interpretation of directions of σ_1 viewed in Fig. 13.6 can be algebraically expressed in relation with angular coordinate θ , which is measured from the vertical. Nadai (1963b) observed that $\omega = \omega_f = \pi/4 - \phi/2$ at $\theta = \pi/2 - \phi$ and $\omega = \omega_c = 0$ at $\theta = 0$; therefore, he postulated the description of ω as a linear relation with θ . Also, Eq. (13.3) can be geometrically obtained from Fig. 13.6 because an inscribed angle ω is always half of the corresponding central angle θ .

$$\frac{\omega - \omega_c}{\theta - 0} = \frac{\omega_f - \omega_c}{(\pi/2 - \phi) - 0} \Rightarrow \omega = \frac{\theta}{2} \tag{13.3}$$

The rule given by Eq. (13.3) is assumed to be effective throughout a sand heap for any given radius of a circle with the center fixed at the apex of a sand heap. The

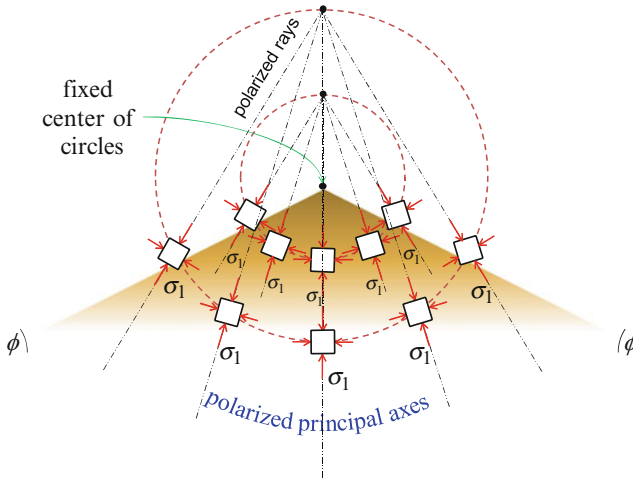
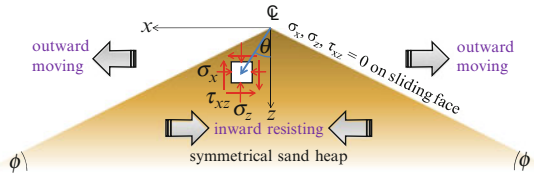


Fig. 13.7 Schematization of Nadai's (1963) hypothesis on the directions of major principal axes in a sand heap

Fig. 13.8 Geometry of a symmetric sand heap in a rectangular coordinate system



A heuristic assumption is required before drawing a typical Mohr's circle whether a body is in active or passive condition. As explained, a sand heap is in active condition because of the outward movement away from the central plane; therefore, $\sigma_z > \sigma_x$ is thoroughly realized. Inward resisting shear acting toward the central plane prevents a sand heap from sloughing. Therefore, a typical state of stress delineated in Fig. 13.8 can be represented by a Mohr's circle drawn in Fig. 13.9. A point (σ_z, τ_{xz}) denotes a compressive normal stress σ_z with counter-clockwise shear stress τ_{xz} acting along a horizontal plane, whereas a point $(\sigma_x, -\tau_{xz})$ denotes a compressive normal stress σ_x with clockwise shear stress τ_{xz} acting along a vertical plane. The pole is determined by the intersection with a Mohr's circle by a straight line either extending from point (σ_z, τ_{xz}) in parallel to a horizontal plane or a straight line extending from point $(\sigma_x, -\tau_{xz})$ in parallel to a vertical plane. Consequently, the major and minor principal stresses σ_1 and σ_3 can be determined together with an angle ω of the major principal axis measured from the vertical. A typical state of stress on the right-hand side is readily available by mirroring the state of stress in the left-hand side of a sand heap.

By definition, p and q denote in-plane stress invariants that directly correspond to a center distant from the origin and radius of a Mohr's circle, respectively.

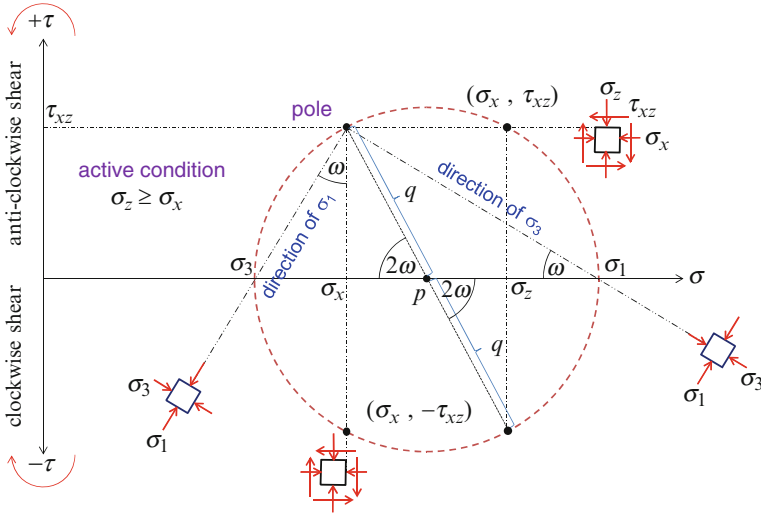


Fig. 13.9 Relation between principal stresses and stress components via a Mohr's circle

$$p = \frac{(\sigma_1 + \sigma_3)}{2} = \frac{(\sigma_x + \sigma_z)}{2} \tag{13.5}$$

$$q = \frac{(\sigma_1 - \sigma_3)}{2} = \sqrt{\left(\frac{(\sigma_x - \sigma_z)}{2}\right)^2 + \tau_{xz}^2} \tag{13.6}$$

According to the geometry of Fig. 13.9, we can express three stress components in terms of p , q , and ω .

$$\sigma_x = p - q \cos 2\omega \tag{13.7}$$

$$\sigma_z = p + q \cos 2\omega \tag{13.8}$$

$$\tau_{xz} = q \sin 2\omega \tag{13.9}$$

By removing p and q from Eqs. (13.7), (13.8), and (13.9), we obtain the following relation between θ and stress components.

$$\tan 2\omega = \frac{2\tau_{xz}}{(\sigma_z - \sigma_x)} \tag{13.10}$$

Substituting a particular relation between θ and ω given by Eq. (13.3) and a geometric relation between θ and x/z expressed in Eq. (13.4) into Eq. (13.10), we

obtain the stress closure, namely, the closure of polarized principal axes (Pipatpongsa et al. 2010) that physically relate stress components with a local coordinate. Therefore, Eq. (13.11) is not considered a generalized constitutive equation but is an ad hoc equation limited only to a sand heap problem (Savage 1998).

$$\sigma_x = \sigma_z - 2\left(\frac{z}{x}\right)\tau_{xz} \quad (13.11)$$

The static equilibrium conditions in a plane rectangular coordinate system, as shown in Eqs. (13.12) and (13.13), must be satisfied under the gravity field directing along the z -axis, where γ is the bulk unit weight of a sand heap that is assumed to be constant.

$$E_x(x, z) = \frac{\partial\sigma_x}{\partial x} + \frac{\partial\tau_{xz}}{\partial z} = 0 \quad (13.12)$$

$$E_z(x, z) = \frac{\partial\tau_{xz}}{\partial x} + \frac{\partial\sigma_z}{\partial z} - \gamma = 0 \quad (13.13)$$

We can remove σ_x from Eqs. (13.12) and (13.13) by substituting Eq. (13.11). Again, we can remove σ_z by making a further derivation with some rearrangements using $\partial E_x/\partial z - \partial E_z/\partial x$ to obtain Eq. (13.14), which is freed from σ_x and σ_z .

$$\underbrace{-\frac{\partial^2\tau_{xz}}{\partial x^2} - \frac{2z}{x}\frac{\partial^2\tau_{xz}}{\partial x\partial z} + \frac{\partial^2\tau_{xz}}{\partial z^2}}_{A=-1, \quad B=-2z/x, \quad C=1} - \frac{2}{x}\frac{\partial\tau_{xz}}{\partial x} + \frac{2z}{x^2}\frac{\partial\tau_{xz}}{\partial z} + \frac{2}{x^2}\tau_{xz} = 0 \quad (13.14)$$

The preceding partial derivative equation (PDE) of τ_{xz} can be formulated and is ready to be solved if the providing boundary conditions are sufficient. Because a strategy to solve PDE is dependent on the characteristics of its equation system, we shall characterize the type of this PDE whether it is elliptic, parabolic, or hyperbolic. Let us consider coefficients of $\partial^2\tau_{xz}/\partial x^2$, $\partial^2\tau_{xz}/\partial x\partial z$, and $\partial^2\tau_{xz}/\partial z^2$ (i.e., A , B , and C , respectively).

$$B^2 - 4AC = 4\left(\frac{z}{x}\right)^2 + 4 > 0 \quad (13.15)$$

By determining a discriminant of PDE, as indicated in Eq. (13.15), we found that our problem is a hyperbolic PDE because an expression of discriminant is clearly greater than zero. Equation (13.14) can be written in more compacted form as shown in the following equation:

$$\left(\partial_{zz}^2 - 2\partial_{xz}^2\frac{z}{x} - \partial_{xx}^2\right)\tau_{xz}(x, z) = 0 \quad (13.16)$$

13.4 Self-Similar Solution in a Sand Heap

The exact solution of Eq. (13.16) might contain many possible forms. All past studies (Cantelaube and Goddard 1997; Cates et al. 1998; Didwania et al. 2000; Marais 1969; Michalowski and Park 2004; Nadai 1963b; Sokolovskii 1965; Wittmer et al. 1997), including this study, adopt the assumption of self-similarity for uniquely solving a particular solution for Eq. (13.16) because the characteristics of the problem have no inherent length scale for a semi-infinite geometry. Therefore, stress distributions appear in the similar geometric shape at all depths from the apex of a sand heap. Moreover, self-similarity can be achieved with its immediate consequence that the stress solutions can be expressed in the separated-variable form between its depth z and gradient $t = x/z$.

$$t = \frac{x}{z} \quad (13.17)$$

$$\sigma_x(x, z) = \gamma z \chi_x(t) \quad (13.18)$$

$$\sigma_z(x, z) = \gamma z \chi_z(t) \quad (13.19)$$

$$\tau_{xz}(x, z) = \gamma z \chi_{xz}(t) \quad (13.20)$$

Consequently, the reduced forms of Eq. (13.16) are expressible as equations of t only because z is cancelled out. Now, we can reduce a problem form PDE to a linear derivative equation.

$$\left(\frac{d^2}{dt^2} - \frac{4}{t(1+t^2)} \frac{d}{dt} + \frac{4}{t^2(1+t^2)} \right) \chi_{xz}(t) = 0 \quad (13.21)$$

Further compacted form of Eq. (13.21) can be expressed as a derivative of a function of $\chi_{xz}(t)/t$.

$$\left(\frac{d^2}{dt^2} - \frac{2}{t} \frac{1-t^2}{1+t^2} \frac{d}{dt} \right) \left(\frac{\chi_{xz}(t)}{t} \right) = 0 \quad (13.22)$$

By the order-reduction technique, Eq. (13.22) can be simply written by the following double derivation:

$$\frac{d}{dt} \left(\ln \frac{d}{dt} \left(\frac{\chi_{xz}(t)}{t} \right) \right) = \frac{2}{t} \frac{1-t^2}{1+t^2} \quad (13.23)$$

Double integration of Eq. (13.23) leads to a general solution with unknown constants c_1 and c_2 . Characteristics of hyperbolic equation system give us a hint that this equation requires Cauchy boundary condition for a stable and unique solution; therefore, known values of χ_{xz} and its gradient $d\chi_{xz}/dt$ at a given t are necessary.

$$\chi_{xz}(t) = \left(\left(\tan^{-1}t - \frac{t}{1+t^2} \right) c_1 + c_2 \right) t \quad (13.24)$$

Because of the condition of traction-free on the sliding plane given by Eq. (13.25), where $t = \cot \phi$, a value of χ_{xz} is available; but a magnitude of $d\chi_{xz}/dt$ at the sliding plane is not available.

$$\chi_x|_{t=\cot \phi} = 0 \quad (13.25)$$

$$\chi_z|_{t=\cot \phi} = 0 \quad (13.26)$$

$$\chi_{xz}|_{t=\cot \phi} = 0 \quad (13.27)$$

Let us obtain self-similar forms of Eqs. (13.12), (13.13), and (13.11), using Eqs. (13.17), (13.18), (13.19) and (13.20). In addition, the derivation of Eq. (13.30) with respect to t is determined to express the PPA stress closure in form of first order differential equation.

$$E_x(t) = \frac{d\chi_x}{dt} - \frac{d\chi_{xz}}{dt}t + \chi_{xz} = 0 \quad (13.28)$$

$$E_z(t) = \frac{d\chi_{xz}}{dt} - \frac{d\chi_z}{dt}t + \chi_z - 1 = 0 \quad (13.29)$$

$$\chi_x = \chi_z - 2\chi_{xz}/t \quad (13.30)$$

$$\frac{d\chi_x}{dt} = \frac{d\chi_z}{dt} - \frac{2}{t} \frac{d\chi_{xz}}{dt} + \frac{2}{t^2}\chi_{xz} \quad (13.31)$$

By manipulation of the above equations, we can evaluate χ_{xz}/dt at $t = \cot \phi$, using Eqs. (13.25), (13.26), (13.27), (13.28), (13.29), (13.30) and (13.31).

$$\left. \frac{d\chi_{xz}}{dt} \right|_{t=\cos \phi} = -\sin^2 \phi \quad (13.32)$$

Two conditions provided by Eqs. (13.27) and (13.32) provide us sufficient requirement to solve unknown c_1 and c_2 ; therefore, a particular solution for χ_{xz} as well as τ_{xz} is obtained:

$$\begin{aligned} \chi_{xz} &= \frac{\tau_{xz}}{\gamma z} \\ &= \frac{\sin \phi}{2 \cos^3 \phi} \frac{x}{z} \left(-\tan^{-1} \left(\frac{x}{z} \right) + \frac{x/z}{1 + (x/z)^2} + \left(\frac{\pi}{2} - \phi \right) - \sin \phi \cos \phi \right) \quad (13.33) \end{aligned}$$

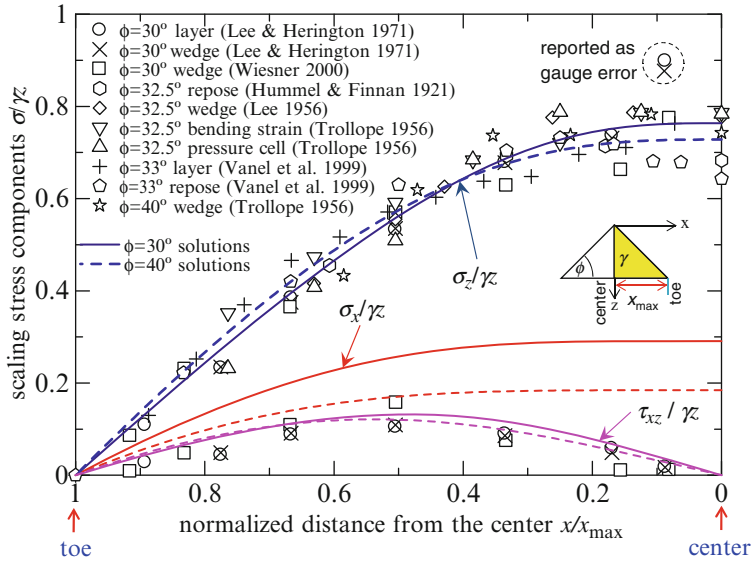


Fig. 13.10 Comparison with past experimental data through normalized stress distribution along the normalized half-width base obtained from the theoretic and experimental data

Now, we can derive χ_x from Eq. (13.28) using Eq. (13.33), with the initial condition provided by Eq. (13.25). By knowing both solutions of τ_{xz} and χ_x , a solution of χ_z is directly retrieved from Eq. (13.30). Finally, solving fundamental equation using zero-traction boundary along the slope face results in closed-form solutions for stress field scaling with a typical overburden pressure γz :

$$\chi_x = \frac{\sigma_x}{\gamma z} = \frac{\sin \phi}{2 \cos^3 \phi} \left(3 \tan^{-1} \left(\frac{x}{z} \right) - \left(3 - \frac{(x/z)^2}{1 + (x/z)^2} \right) \frac{x}{z} - 3 \left(\frac{\pi}{2} - \phi \right) + \frac{3 - \cos^2 \phi}{\tan \phi} \right) \tag{13.34}$$

$$\chi_z = \frac{\sigma_z}{\gamma z} = \frac{\sin \phi}{2 \cos^3 \phi} \left(\tan^{-1} \left(\frac{x}{z} \right) - \left(1 + \frac{(x/z)^2}{1 + (x/z)^2} \right) \frac{x}{z} - \left(\frac{\pi}{2} - \phi \right) + \frac{1 + \cos^2 \phi}{\tan \phi} \right) \tag{13.35}$$

Validation of the derived equations with the past experimental data on sand heaps was reported in Pipatpongsa et al. (2010) by comparing the theoretical results with the published experiments reported during 1921–2000 for granular materials whose friction angles are ranged from 30° to 40°. Despite different sand deposition methods, measure techniques and types of granular material, the derived equations show a good agreement with the measured vertical and shear stresses featuring in terms of scaling stresses as shown in Fig. 13.10. As discussed by Savage (1998), there is no clear central pressure drop in prismatic sand heaps and our theoretical results also matches

Fig. 13.11 Distribution of the safety factor in a two-dimensional heap body with $\phi = 30^\circ$



with this observation. We also observe that there is no much difference in profiles of vertical pressure as well as shear stress for a typical range of friction angle of sand. Though none of the horizontal pressure existed, our theoretical results predict that in contrast to profiles of vertical and shear stresses, one would observe much difference in measured profile of horizontal stress, depending on friction angles, whereas fine sand gives higher horizontal pressure than rough sand.

13.5 Evaluation of Factor of Safety in a Sand Heap

A sand heap is statically stable with variation of factor of safety. Regions located along the sliding planes are on the verge of failure, while region located along the central plane stands on the most stable side. Theoretical evaluation of factor of safety is possible because the solutions for stress field are at our hand. Based on the Mohr-Coulomb failure criterion, a ratio of q/p must be less than its limit given by $\sin \phi$, which can be determined from a trigonometry delineated in Fig. 13.3.

$$\frac{q}{p} = \frac{\sqrt{(\sigma_z - \sigma_x)^2 + 4\tau_{xz}^2}}{\sigma_z + \sigma_x} \leq \sin \phi \tag{13.36}$$

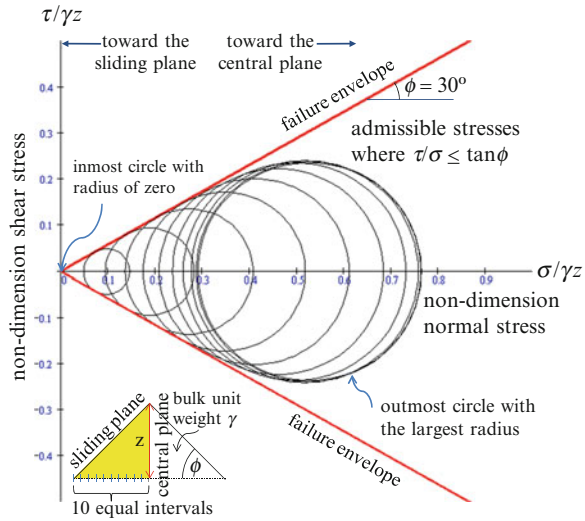
Safety factor, SF, is defined as the ratio of resistance to load, using the following expression where $SF \geq 1$ represents the state of admissible stress, including the failure state when $SF = 1$.

$$SF = \frac{\sin \phi}{q/p} = \frac{(\sigma_z + \sigma_x) \sin \phi}{\sqrt{(\sigma_z - \sigma_x)^2 + 4\tau_{xz}^2}} \tag{13.37}$$

The graphic representation of the safety factor in a sand heap with $\phi = 30^\circ$ is shown by a color contour of Fig. 13.11. We can observe that most volume of a sand heap nearly undergoes yielding and reaches incipient failure, especially for outer regions covering a stable inner region.

Mohr's circle is another way of graphic representation. Figure 13.12 shows stress states in a sand heap with $\phi = 30^\circ$ at the same height for various locations

Fig. 13.12 Nondimensional state of stresses in Mohr space for 10 equal intervals across the horizontal plane of a sand heap with $\phi = 30^\circ$



starting from the sliding plane to the central plane with 10 equal intervals. We can observe from the similar result with safety factor evaluation that a sand heap is stable with a threshold of safety factor. Therefore, a small disturbance can easily destabilize the stable shape of a sand heap.

13.6 Conclusions

Nadai's idealization of gravitating loose earth appears in his classical textbook, but it was unnoticed until the author found that his idealization provides a particular stress closure that can lead to the rigorous stress states of sand heaps. The closed-form stress field solution for a prismatic shape derived by the authors is in good agreement with many experimental data, which is important and makes a convincing result. For the benefit of those who are interested in this fundamental problem, this chapter provides detailed explanations about Nadai's assumption by adding many graphic diagrams and Mohr's circle in an effort to supplement his original few pages of explanation. Mathematical derivations of self-similar stress field equations from a hyperbolic type partial differential equation are clarified. Based on stability analysis, a sand heap is resting on a threshold of resistance; therefore, it indicates that the load-bearing structure of a sand heap can be promptly destabilized by a small disturbance.

References

- Bouchaud JP, Cates ME, Claudin P (1995) Stress-distribution in granular media and nonlinear-wave equation. *J De Phys I* 5(6):639–656
- Cantelaube F, Goddard JD (1997) Elastoplastic arching in 2D granular heaps. In: Proceedings of the third international conference on powders and grains, Balkema, Durham, 1997, pp 231–234
- Cates ME, Wittmer JP, Bouchaud JP, Claudin P (1998) Development of stresses in cohesionless poured sand. *Philos Trans R S Lond Ser A-Math Phys Eng Sci* 356(1747):2535–2560
- Cornforth DH (1973) Prediction of drained strength of sands from relative density measurements. ASTM special technical publication 523: evaluation of relative density and its role in geotechnical projects involving cohesionless soils. American Society for Testing and Materials, Baltimore, Md. pp 281–303
- Didwania AK, Cantelaube F, Goddard JD (2000) Static multiplicity of stress states in granular heaps. *Proc R Soc Lond Ser A Math Phys Eng Sci* 456(2003):2569–2588
- Hummel FH, Finnan EJ (1921) The distribution of pressure on surfaces supporting a mass of granular material. In: Minutes of the proceedings of the Institution of Civil Engineers 212 (session 1920–1921 – Part 2), London, pp 369–392
- Jotaki T (1979) On the bottom pressure distribution of the bulk materials piled with the angle of repose. *J Soc Power Technol, Japan*, pp 184–191
- Marais GR (1969) Stresses in wedges of cohesionless materials formed by free discharge at the apex. *Trans ASME Ser B J Eng Ind* 91:345–352
- Michalowski RL, Park N (2004) Admissible stress fields and arching in piles of sand. *Geotechnique* 54(8):529–538
- Nadai A (1937) Plastic behavior of metals in the strain – hardening range. Part I. *J Appl Phys* 8(3):205–213
- Nadai A (1963a) Theory of flow and fracture of solids, vol I. McGraw-Hill, New York
- Nadai A (1963b) Theory of flow and fracture of solids, vol II. McGraw-Hill, New York
- Pipatpongsa T, Heng S, Iizuka A, Ohta H (2010) Statics of loose triangular embankment under Nadai's sand hill analogy. *J Mech Phys Solid* 58(10):1506–1523
- Savage SB (1998) Modeling and granular material boundary values problems. *Physics of dry granular media*. Kluwer Academic, Cargese, pp 25–95
- Šmíd J, Novosad J (1981) Pressure distribution under heaped bulk solids. In: Proceedings of the 1981 Powtech conference, Institution of Chemical Engineers, Birmingham, 1981, pp 1–12
- Sokolovskii VV (1965) Statics of granular materials. Pergamon Press, Oxford
- Trollope DH (1956) The stability of wedges of granular materials. Ph.D. thesis, University of Melbourne, Melbourne
- Trollope DH (1957) The systematic arching theory applied to the stability analysis of embankments. In: Proceedings of the 4th international conference on soil mechanics and foundation engineering, vol 2, London, pp 382–388
- Vanel L, Howell D, Clark D, Behringer RP, Clement E (1999) Memories in sand: experimental tests of construction history on stress distributions under sandpiles. *Phys Rev E* 60(5):R5040–R5043
- Wiesner TJ (2000) Failure stresses beneath granular embankments. *Development in theoretical geomechanics*. A.A. Balkema, Sydney, pp 33–41
- Wittmer JP, Claudin P, Cates ME, Bouchaud JP (1996) An explanation for the central stress minimum in sand piles. *Nature* 382(6589):336–338
- Wittmer JP, Cates ME, Claudin P (1997) Stress propagation and arching in static sandpiles. *J De Phys I* 7(1):39–80

Chapter 14

Elasto-Plastic Constitutive Model for Unsaturated Soils with Subloading Surface Concept

Shintaro Ohno, Katsuyuki Kawai, Atsushi Iizuka, Shinya Tachibana, Shin-ichi Kanazawa, and Hideki Ohta

14.1 Introduction

An elasto-plastic constitutive model for unsaturated soils is expected to predict the rainfall induced slope instability and the long-term behavior of earth structures, such as rock-fill dams and embankments. The typical mechanical behavior of unsaturated soils are as follows: shrinkage and increase of stiffness upon drying

S. Ohno (✉)

Civil Engineering Design Division, Kajima Corporation, 6-5-30 Akasaka,
107-8502 Minato-ku, Tokyo, Japan
e-mail: onoshi@kajima.com

K. Kawai • A. Iizuka

Research Center for Urban Safety and Security, Kobe University, 1-1 Rokkodai,
Nada-ku, 657-8501 Kobe, Hyogo, Japan
e-mail: kkawai@kobe-u.ac.jp; iizuka@kobe-u.ac.jp

S. Tachibana

Geosphere Research Institute, Saitama University, 255 O-kubo,
338-8570 Sakura-ku, Saitama, Japan
e-mail: stachi@mail.saitama-u.ac.jp

S.-i. Kanazawa

Department of Civil and Environmental Engineering, Faculty of Science and Engineering,
Chuo University, 1-13-27 Kasuga, 112-8551 Bunkyo-ku, Tokyo, Japan
e-mail: kanazawa@civil.chuo-u.ac.jp

H. Ohta

Research and Development Initiative, Chuo University, 1-13-27 Kasuga,
112-8551 Bunkyo-ku, Tokyo, Japan
e-mail: ohta@tamacc.chuo-u.ac.jp

(i.e., suction increase), collapse with reduction of stiffness upon wetting (i.e., suction decrease), and the influences of suction history related to the hysteresis of soil-water retention characteristics. Ohno et al. (2007) proposed a new elasto-plastic constitutive model, in which the effective degree of saturation is used as a parameter relating to stiffness, to describe the typical mechanical behavior of unsaturated soils. The model proposed by Ohno et al. (2007) is called the S_e hardening model.

Although the S_e hardening model can describe the typical mechanical behavior of unsaturated soils, two problems remain to be solved.

1. Singular point on yield surface: The shape of the S_e hardening model's yield surface is identical to the original Cam clay model. Therefore, the model has difficulty in conducting numerical calculation as indicated by Takeyama et al. (2006). When a stress point exists on the singular point, plastic strain rate cannot be derived by the associated flow rule because the tangent of the yield surface at the singular point is not uniquely defined.
2. Description of overconsolidated (or elastic state) soils: In conventional elasto-plastic theory, the interior of the yield surface is a purely elastic domain. Therefore, a conventional elasto-plastic constitutive model cannot predict smooth stress-strain curves observed in overconsolidated soil tests. In the case of the S_e hardening model, the stress point tends to be in an elastic state because a smaller degree of saturation brings a larger yield surface (hardening parameter). This problem affects the S_e hardening model greatly, compared with constitutive models for saturated soils.

The authors introduce the exponential contractancy model (EC model) by Ohno et al. (2006) to the S_e hardening model to realize a numerical stability of computations at the singular point on the yield surface. The EC model was derived from the nonlinear function capable of describing contractancy (negative dilatancy) characteristics of soils. This model has no singular point on the yield surface by specifying a proper value of the parameter that controls the shape of the yield surface, as mentioned later.

The authors also introduce the subloading surface model by Hashiguchi and Chen (1998) to the S_e hardening model to realize an accurate prediction of the mechanical behavior of overconsolidated (or elastic state) soils. The subloading surface is defined as the inside of the yield surface. It is assumed that current stress always exists on subloading surface. Plastic strain is induced by expansion of the subloading surface, even when the stress point is inside of the yield surface.

In this chapter, the authors summarize the S_e hardening model proposed by Ohno et al. (2007). After brief explanations of the EC model by Ohno et al. (2006) and the subloading surface model by Hashiguchi and Chen (1998), the authors introduce those models to the S_e hardening model. Finally, triaxial shear tests under constant net stress undrained conditions are simulated to verify the applicability of the constitutive model.

14.2 S_e Hardening Model

14.2.1 Yield Function of S_e Hardening Model

Some constitutive models for unsaturated soils (Alonso et al. 1990; Kohgo et al. 1993; Karube and Kawai 2001) have been developed since Bishop (1960) first proposed effective stress for unsaturated soils. Ohno et al. (2007) showed that these constitutive models were equivalent in their capability of describing yield function with effective stress and parameters associated with stiffness.

Effective stress for unsaturated soils applied by Ohno et al. (2007) is shown as

$$\sigma' = \sigma^{\text{net}} + p_s \mathbf{1} \quad (14.1)$$

where,

$$\sigma^{\text{net}} = \sigma - p_a \mathbf{1}, \quad p_s = S_e s \quad (14.2)$$

$$s = p_a - p_w, \quad S_e = \frac{S_r - S_{rc}}{1 - S_{rc}} \quad (14.3)$$

where σ' is the effective stress tensor, σ^{net} is the net stress tensor, $\mathbf{1}$ is the second order identity tensor, σ is the total stress tensor, S is the suction, p_s is the suction stress, p_a is the pore air pressure, p_w is the pore water pressure, S_r is the degree of saturation, S_e is the effective degree of saturation, and S_{rc} is the degree of saturation at $s \rightarrow \infty$.

A general form of yield function for unsaturated soils proposed by Ohno et al. (2007) is shown as

$$f(\sigma', \xi, e_v^p) = MD \ln \frac{p'}{\xi p'_{\text{sat}}} + D \frac{q}{p'} - e_v^p = 0 \quad (14.4)$$

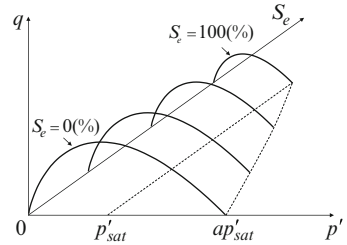
where,

$$MD = \frac{\lambda - \kappa}{1 + e_0} \quad (14.5)$$

$$p' = \frac{1}{3} \sigma' : \mathbf{1}, \quad q = \sqrt{\frac{3}{2}} s : \mathbf{s}, \quad \mathbf{s} = \sigma' - p' \mathbf{1} = \mathbf{A} : \sigma', \quad \mathbf{A} = \mathbf{I} - \frac{1}{3} \mathbf{1} \otimes \mathbf{1} \quad (14.6)$$

where M is the critical state parameter, D is the coefficient of dilatancy after Shibata (1963), e_v^p is the plastic volumetric strain, p' is the effective mean principal stress, q is the shear stress, λ is the compression index, κ is the swelling index, and e_0 is the initial void ratio, \mathbf{I} is the fourth-order identity tensor, p'_{sat} is the yield stress in the

Fig. 14.1 Yield surface of the S_e hardening model



saturated state, and ξ is the function to describe increase of yield stress caused by desaturation. The operational notations used in the paper are as follows,

$$\mathbf{a} : \mathbf{b} = a_{ij}b_{ij}, \quad \mathbf{B} : \mathbf{b} = B_{ijkl}b_{kl}, \quad (\mathbf{a} \otimes \mathbf{b})_{ijkl} = a_{ij}b_{kl} \tag{14.7}$$

where \mathbf{a} , \mathbf{b} are the second-order tensors and \mathbf{B} is the fourth-order tensor.

Ohno et al. (2007) proposed a new functional form of ξ , where the effective degree of saturation is used as a parameter relating to stiffness to describe the typical mechanical behavior of unsaturated soils as

$$\xi = \exp[(1 - S_e)^n \ln a] \tag{14.8}$$

Where a and n are fitting parameters to control the shape of the yield line at $p' - q$ plane (see Fig. 14.1).

Substituting Eq. (14.8) into Eq. (14.4), the yield function proposed by Ohno et al. (2007) is obtained as

$$f(\sigma', S_e, \epsilon_v^p) = MD \ln \frac{p'}{p'_{sat} \exp[(1 - S_e)^n \ln a]} + D \frac{q}{p'} - \epsilon_v^p = 0. \tag{14.9}$$

Equation (14.8) is called the S_e hardening model. This model corresponds to the original Cam clay model in the saturated state ($S_e = 1$ and $\xi = 1$). Figure 14.1 shows the yield surface of the S_e hardening model. In this model, the yield surface expands and/or contracts with not only the plastic volumetric strain but also the effective degree of saturation.

14.2.2 Application of S_e Hardening Model

Ohno et al. (2007) demonstrated the appropriateness of the S_e hardening model by simulating experiments for unsaturated soils by Kato (1998). Kato (1998) applied suction and confining stress to a compacted specimen, shown in Fig. 14.2. Table 14.1 shows the initial conditions of specimens (void ratio e , water content w , and degree of saturation S_r).

Fig. 14.2 Stress paths of experiments

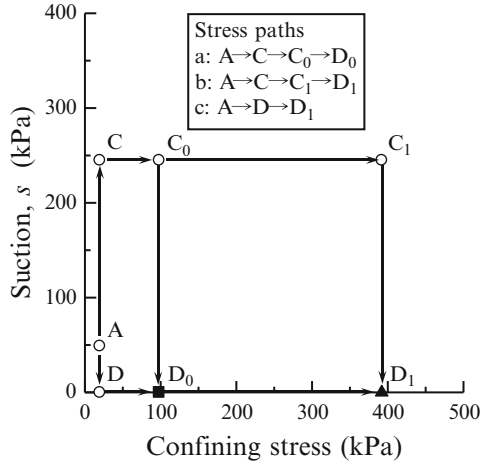


Table 14.1 Initial conditions of specimens

Test	e	w (%)	S_r (%)
a	1.303	25.2	52.3
b	1.257	25.4	54.8
c	1.327	25.4	51.9

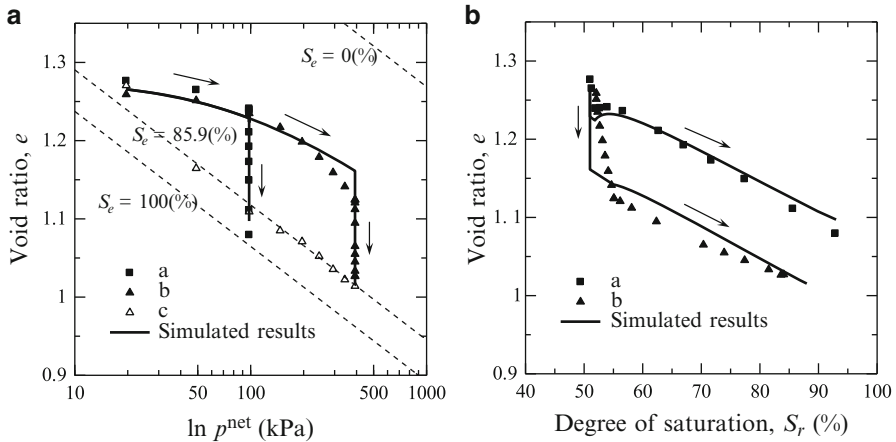


Fig. 14.3 Comparison of simulated results with experimental results. (a) Relationship between void ratio and net stress. (b) Relationship between void ratio and degree of saturation

Figure 14.3 shows the simulated results compared with the experimental results. It is seen from Fig. 14.3 that the simulated results have a good agreement with the experimental results. Tests a and b finally reach to the compression line of the initially saturated specimen, test c, regardless of their stress path (see Fig. 14.3a). Broken lines in Fig. 14.3a indicate the constant S_e line predicted by the S_e hardening model. The soil parameters used for the S_e hardening model are listed in Table 14.2.

Table 14.2 Parameters used in simulations

e_0	λ	p'_{sat} (kPa)	S_{re} (%)	a	n
1.187	0.075	19.6	15.0	150.0	1.0

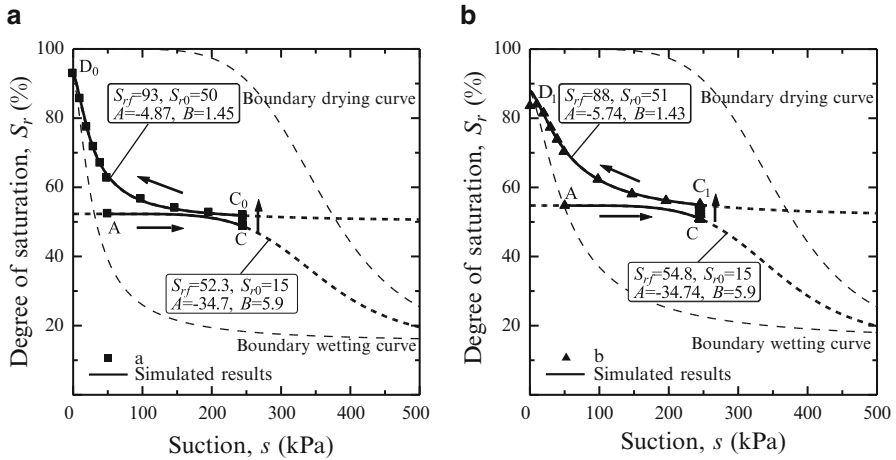


Fig. 14.4 Soil-water retention characteristics. (a) Test a. (b) Test b

In this simulation, the soil-water retention characteristic curve (WRC) model proposed by Kawai et al. (2007) is applied as

$$S_r = \frac{S_{\text{rf}} - S_{\text{r0}}}{1 + s^B \exp(A)} + S_{\text{r0}} \tag{14.10}$$

where S_{rf} , S_{r0} , A , B are the fitting parameters to describe the soil-water retention characteristic curve.

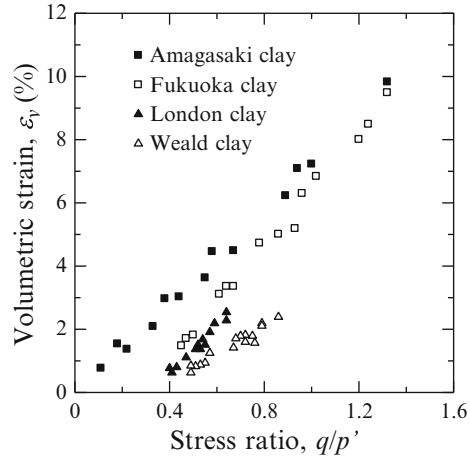
Figure 14.4 shows soil-water retention characteristics and the relationship between suction and the degree of saturation. Broken lines in Fig. 14.4 are drawn with the soil-water retention characteristic curve (WRC) model proposed by Kawai et al. (2007). Fitting parameters for WRC are appended in Fig. 14.4. It is seen that the WRC model expresses the experimental results well. It is found through these comparisons that the S_e hardening model can satisfactorily describe the behavior of unsaturated soil under loading and wetting.

14.3 S_e Hardening Model with Nonlinear Contractancy Description and Subloading Surface

14.3.1 Exponential Contractancy Model

Elasto-plastic constitutive models for clays are based on following two experimental results. (1) Volume change of saturated clays is independent of effective

Fig. 14.5 Experimental data on contractancy after Shibata (1963)



stress path (Henkel 1960). (2) Volume change of saturated clays consists of two components, consolidation and contractancy (Shibata 1963). Ohta and Hata (1971) derived the yield function of clays under axisymmetric stress condition by modeling consolidation and contractancy. The description of contractancy by using a linear (or a bilinear) relation between the volumetric strain ϵ_v and stress ratio q/p' under conditions of constant effective mean principal stress p' is the essence of the elasto-plastic constitutive model proposed by Ohta and Hata (1971). This assumption is acceptable and gives the clear physical meaning, because it is the simple interpretation of the experimental data on contractancy. However, the interpretation of the experimental data on contractancy of soils isn't restricted to linear or bilinear relations (see Fig. 14.5). It is worth considering nonlinear function in describing contractancy characteristics of soils.

Ohno et al. (2006) developed the following nonlinear function capable of describing contractancy of clays of a wide variety:

$$\epsilon_v = \frac{MD}{n_E} \left(\frac{q}{p'M} \right)^{n_E} \quad (14.11)$$

where n_E is the fitting parameter.

Ohno et al. (2006) fitted the experimental data after Shibata (1963) by using Eq. (14.11) (see Fig. 14.6). Table 14.3 shows the parameters used by Ohno et al. (2006). Equation (14.11) has a good capacity for fitting experimental data. Then, Ohno et al. (2006) derived the yield function from Eq. (14.11) as

$$f(\sigma', \epsilon_v^p) = MD \ln \frac{p'}{p'_0} + \frac{MD}{n_E} \left(\frac{q}{p'M} \right)^{n_E} - \epsilon_v^p = 0 \quad (14.12)$$

where p'_0 is the preconsolidation pressure.

Fig. 14.6 Experimental data fitted by nonlinear function

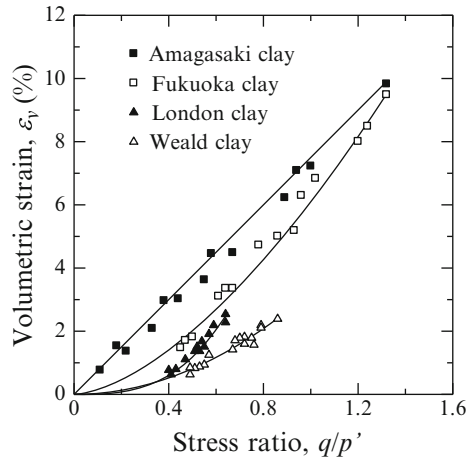
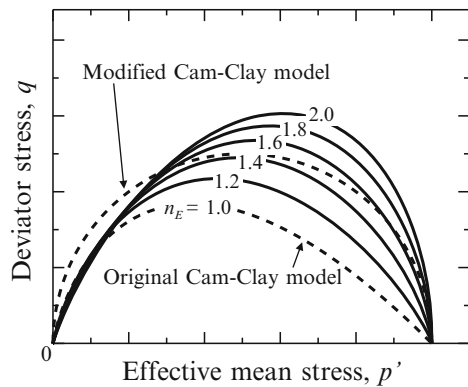


Table 14.3 Parameters after Ohno et al. (2006)

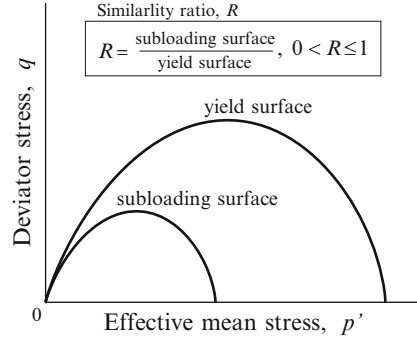
Names of clays	M	n_E
Amagasaki clay	1.32	1.0
Fukuoka clay	1.32	1.6
London clay	0.65	3.0
Weald clay	0.86	2.0

Fig. 14.7 Shapes of yield surfaces of the exponential contractancy model



Equation (14.12) is called the Exponential Contractancy model (EC model). It is noted that the authors restrict the model to the isotropically consolidated state, although Ohno et al. (2006) take the anisotropically consolidated state into consideration. Substitution of $n_E = 1.0$ into Eq. (14.12) yields the yield function of the original Cam clay model. Figure 14.7 shows the shape of the yield surfaces of the EC model. The fitting parameter n_E is selected as 1.0, 1.2, 1.4, 1.6, 1.8 and 2.0. It is seen in Fig. 14.7 that the selection of the fitting parameter n_E results in the various shapes of the yield surface.

Fig. 14.8 Yield and subloading surfaces



Although the exponential contractancy model is originally derived to describe nonlinear contractancy behavior of soils, this model also realizes a numerical stability of computations at the singular point on the yield surface, because this model has no singular point on the yield surface when the fitting parameter n_E is specified larger than 1.0. In this chapter, the authors introduce the exponential contractancy model to the S_c hardening model to realize a numerical stability of computations at the singular point on the yield surface.

14.3.2 Subloading Surface Model

In conventional elasto-plastic theory, the interior of the yield surface is a purely elastic domain. Therefore, a conventional elasto-plastic constitutive model cannot predict smooth stress-strain curves observed in overconsolidated soil tests. Hashiguchi and Chen (1998) proposed the subloading surface model to describe a mechanical behavior of overconsolidated soil. The subloading surface is defined inside of the yield surface. Figure 14.8 shows the positions of yield and subloading surfaces relative to each other. The subloading surface retains a similarity to the yield surface. Hashiguchi and Chen (1998) defined the similarity ratio R of subloading surface to yield surface, and proposed the evolution law of R , which controls plastic strain ϵ^p induced by expansion of subloading surface, as

$$\dot{R} = -\frac{m}{D} \ln R \|\dot{\epsilon}^p\| \tag{14.13}$$

where m is the parameter that controls the degree of plastic strain occurrence by subloading surface.

In this modeling of constitutive relation for soils, the current stress always exists on the subloading surface, and a plastic yielding occurs even when the current stress is inside the yield surface. In this chapter, the authors introduce the subloading surface model to the S_c hardening model to realize an accurate prediction of the mechanical behavior of overconsolidated (or elastic state) soils.

14.3.3 Derivation of Stress–Strain Relationship of the S_e Hardening Model with Nonlinear Contractancy Description and Subloading Surface

The authors apply the function ξ (see, Eq. (14.8)), which describes increase of yield stress caused by desaturation to the yield function of the exponential contractancy model shown in Eq. (14.12) as

$$f(\sigma', S_e, e_v^p) = MD \ln \frac{p'}{p'_{\text{sat}} \exp[(1 - S_e)^n \ln a]} + \frac{MD}{n_E} \left(\frac{\eta}{M}\right)^{n_E} - e_v^p = 0. \quad (14.14)$$

Then, the authors assume that subloading surface is located inside of yield surface. The functional form of subloading surface is described by using similarity ratio R as follows:

$$\begin{aligned} f(\sigma', S_e, e_v^p, R) &= MD \ln \frac{p'}{p'_{\text{sat}} \exp[(1 - S_e)^n \ln a]} \\ &+ \frac{MD}{n_E} \left(\frac{\eta}{M}\right)^{n_E} - e_v^p - MD \ln R = 0 \end{aligned} \quad (14.15)$$

The current stress is assumed to be on the subloading surface. Consistency condition for subloading surface leads to

$$\dot{f}(\sigma', e_v^p, S_e, R) = \frac{\partial f}{\partial \sigma'} \dot{\underline{\sigma}}' + \frac{\partial f}{\partial S_e} \dot{S}_e + \frac{\partial f}{\partial e_v^p} \dot{e}_v^p + \frac{\partial f}{\partial R} \dot{R} = 0 \quad (14.16)$$

The strain rate $\dot{\epsilon}$ is a summation of the elastic and plastic strain rates $\dot{\epsilon}^e$, $\dot{\epsilon}^p$:

$$\dot{\epsilon} = \dot{\epsilon}^e + \dot{\epsilon}^p. \quad (14.17)$$

The elastic constitutive model for unsaturated soils is given by

$$\underline{\sigma}' = \mathbf{C}^e : \dot{\epsilon}^e + K_{S_e} \dot{S}_e \mathbf{1} \quad (14.18)$$

$$\mathbf{C}^e = K \mathbf{1} \otimes \mathbf{1} + 2G \mathbf{A}, \quad K = \frac{1 + e_0}{\kappa} p' = \frac{\Lambda}{MD(1 - \Lambda)} p', \quad \Lambda = 1 - \frac{\kappa}{\lambda} \quad (14.19)$$

$$G = \frac{3(1 - 2\nu')}{2(1 + \nu')} K, \quad K_{S_e} = -p' n \left[(1 - S_e)^{n-1} \ln a \right] \quad (14.20)$$

where K is the bulk modulus, and G is the shear modulus ν' is the effective Poisson's ratio.

The associated flow rule is adopted as

$$\dot{\epsilon}^p = \gamma \frac{\partial f}{\partial \sigma'} \quad (14.21)$$

where γ is the positive proportionality factor.

Substituting the consistency condition shown in Eq. (14.16) into Eqs. (14.13), (14.17), (14.18) and (14.21), the positive proportionality factor γ is obtained as

$$\gamma = \frac{\frac{\partial f}{\partial \sigma'} : \mathbf{C}^e : \underline{\sigma}' + \left(\frac{\partial f}{\partial p'} K_{S_e} + \frac{\partial f}{\partial S_e} \right) \dot{S}_e}{\frac{\partial f}{\partial \sigma'} : \mathbf{C}^e : \frac{\partial f}{\partial \sigma'} - \frac{\partial f}{\partial e_v^p} \frac{\partial f}{\partial p'} + \frac{\partial f}{\partial R} \frac{m}{D} (\ln R) \left\| \frac{\partial f}{\partial \sigma'} \right\|}}. \quad (14.22)$$

Finally, substituting the elastic constitutive model shown in Eq. (14.18) into Eqs. (14.17), (14.21) and (14.22), the stress–strain relationship of the S_e hardening model with nonlinear contractancy description and subloading surface is derived as

$$\begin{aligned} \underline{\sigma}' = & \left(\mathbf{C}^e - \frac{\mathbf{C}^e : \frac{\partial f}{\partial \sigma'} \otimes \frac{\partial f}{\partial \sigma'} : \mathbf{C}^e}{\frac{\partial f}{\partial \sigma'} : \mathbf{C}^e : \frac{\partial f}{\partial \sigma'} - \frac{\partial f}{\partial e_v^p} \frac{\partial f}{\partial p'} + \frac{\partial f}{\partial R} \frac{m}{D} (\ln R) \left\| \frac{\partial f}{\partial \sigma'} \right\|}} \right) : \dot{\epsilon} \\ & - \left[\frac{\mathbf{C}^e : \frac{\partial f}{\partial \sigma'} \left(\frac{\partial f}{\partial p'} K_{S_e} + \frac{\partial f}{\partial S_e} \right)}{\frac{\partial f}{\partial \sigma'} : \mathbf{C}^e : \frac{\partial f}{\partial \sigma'} - \frac{\partial f}{\partial e_v^p} \frac{\partial f}{\partial p'} + \frac{\partial f}{\partial R} \frac{m}{D} (\ln R) \left\| \frac{\partial f}{\partial \sigma'} \right\|}} + K_{S_e} \mathbf{1} \right] \dot{S}_e \end{aligned} \quad (14.23)$$

where,

$$\frac{\partial f}{\partial \sigma'} = \frac{D}{3p'} \left[M - \left(\frac{q}{p'M} \right)^{n_E-1} \frac{q}{p'} \right] \mathbf{1} + \frac{3D}{2p'q} \left(\frac{q}{p'M} \right)^{n_E-1} \mathbf{s} \quad (14.24)$$

$$\frac{\partial f}{\partial p'} = MD \frac{1}{p'} - D \left(\frac{q}{p'M} \right)^{n_E-1} \frac{q}{p'^2}, \quad \frac{\partial f}{\partial S_e} = MDn(1 - S_{re})^{n-1} \ln a \quad (14.25)$$

$$\left\| \frac{\partial f}{\partial \sigma'} \right\| = \sqrt{\frac{1}{3} \left(\frac{\partial f}{\partial p'} \right)^2 + \frac{3}{2} \left(\frac{\partial f}{\partial q} \right)^2}, \quad \frac{\partial f}{\partial e_v^p} = -1, \quad \frac{\partial f}{\partial R} = -\frac{MD}{R}. \quad (14.26)$$

14.4 Triaxial Shear Simulation Under Constant Net Stress Undrained Condition

Triaxial shear tests under constant net stress p^{net} undrained conditions are simulated to verify the applicability of the proposed constitutive model, by using the stress–strain relationship shown in Eq. (14.22). In these simulations, initial values

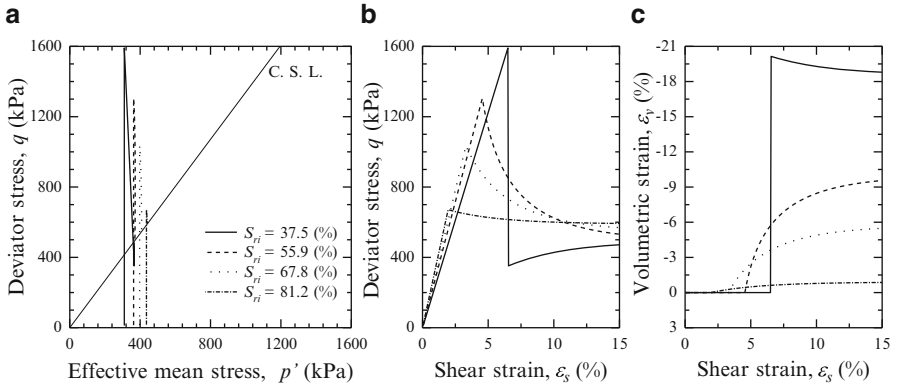


Fig. 14.9 Simulated results without subloading surface concept. (a) Effective stress paths. (b) Relationship between shear stress and shear strain. (c) Relationship between volumetric strain and shear strain

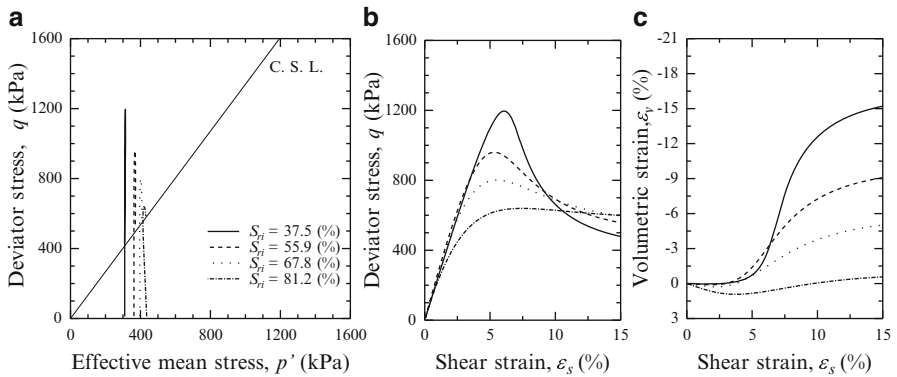


Fig. 14.10 Simulated results with subloading surface concept. (a) Effective stress paths. (b) Relationship between shear stress and shear strain. (c) Relationship between volumetric strain and shear strain

Table 14.4 Parameters for the S_e hardening model

M	D	Λ	v'	n_E
1.340	0.040	0.765	0.312	1.5
m	a	n	p'_{sat} (kPa)	S_{rc} (%)
1.0	90.0	1.0	490.0	15.0

of degree of saturation S_{ri} are assumed to be 37.5, 55.9, 67.8 and 81.2 (%). Constant net stress p^{net} is specified to be 245.0 (kPa). Figure 14.9 shows the simulated results without the subloading surface concept. Figure 14.10 shows the simulated results with the subloading surface concept. All simulations are conducted with nonlinear contractancy description (the exponential contractancy model). Tables 14.4 and 14.5 show the parameters for the S_e hardening model and the soil-water retention characteristic curve used in the simulations.

Table 14.5 Parameters for the soil–water retention characteristic curve

S_{rf} (%)	S_{r0} (%)	A	B
94.0	15.0	−32.0	5.35

Compared with the simulated results without the subloading surface concept (Fig. 14.9), the simulated results with the subloading surface concept (Fig. 14.10) show smooth stress–strain curves observed in experiments of soils. Moreover, the subloading surface concept (Fig. 14.9) tends to overestimate the peak strength of unsaturated soils.

14.5 Conclusions

In this chapter, the authors proposed the elasto-plastic constitutive model for unsaturated soils to realize a numerical stability of computations at the singular point on the yield surface and an accurate prediction of the mechanical behavior of overconsolidated (or elastic state) soils. The exponential contractancy model (EC model) by Ohno et al. (2006) and the subloading surface model by Hashiguchi and Chen (1998) were introduced to the S_c hardening model by Ohno et al. (2007). Then, the authors derived the stress–strain relationship of the proposed constitutive model. The applicability of the proposed constitutive model was verified by simulating triaxial shear tests under constant net stress undrained conditions.

References

- Alonso EE, Gens A, Josa A (1990) A constitutive model for partially saturated soils. *Geotechnique* 40(3):405–430
- Bishop AW (1960) The principal of effective stress. *Norwegian Geotech Inst* 32:1–5
- Hashiguchi K, Chen ZP (1998) Elastoplastic constitutive equation of soils with the subloading surface and rotational hardening. *Int J Numer Anal Method Geomech* 22:197–227
- Henkel DJ (1960) The shear strength of saturated remoulded clays. In: *Proceedings of research conference on shear strength of cohesive soils, Boulder, Colorado*, pp 533–554
- Karube D, Kawai K (2001) The role of pore water in the mechanical behavior of unsaturated soils. *Geotech Geol Eng* 19(3):211–241
- Kato S (1998) Deformation characteristics of a compacted clay in collapse under isotropic stress state and its shear deformation after collapse. *J JSCE* 596(43):271–281 (in Japanese)
- Kawai K, Iizuka A, Hayakawa E, Wang W (2007) Non-uniform settlement of compacted earth structures caused by the deformation characteristics of unsaturated soil on wetting. *Soil Found* 47(2):195–206
- Kohgo Y, Nakano M, Miyazaki T (1993) Theoretical aspects of constitutive modeling for unsaturated soils. *Soil Found* 33(4):49–63
- Ohno S, Iizuka A, Ohta H (2006) Two categories of new constitutive model derived from non-linear description of soil contractancy. *J Appl Mech JSCE* 9:407–414 (in Japanese)

- Ohno S, Kawai K, Tachibana S (2007) Elasto-plastic constitutive model for unsaturated soil applied effective degree of saturation as a parameter expressing stiffness. *J JSCE* 63(4): 1132–1141 (in Japanese)
- Ohta H, Hata S (1971) A theoretical study of the stress-strain relations for clays. *Soil Found* 11(3):195–219
- Shibata T (1963) On the volume changes of normally consolidated clays. In: *Annuals, Disaster Prevention Research Institute, Kyoto University, Kyoto, No. 6*, pp 128–134 (in Japanese)
- Takeyama T, Ohta H, Iizuka A, Pipatpongsa T, Ohno S (2006) Method to cope with the singular point of yield surface in Sekiguchi-Ohta model. In: *Proceedings of Geo-Kanto 2006, Yokohama*, pp 313–317 (in Japanese)

Chapter 15

Stress–Strain Relationship for the Singular Point on the Yield Surface of the Elasto-Plastic Constitutive Model and Quantification of Metastability

Tomohide Takeyama, Thirapong Pipatpongsa, Atsushi Iizuka, and Hideki Ohta

15.1 Introduction

When we try to predict deformation of the ground caused by external action such as construction of an airport or highway or an earthquake, etc. by using numerical analysis, the constitutive model representing the stress–strain relationship of soil is of primary importance. The original Cam clay model (Roscoe et al. 1963) is one of the typical elasto-plastic constitutive models. The original Cam clay model was extended and generalized for anisotropically consolidated clay (Sekiguchi and Ohta 1977). These two constitutive models have the singular point on the yield surface. The isotropically consolidated state in the original Cam clay model and the anisotropically consolidated (K_0 -consolidated) state in the Sekiguchi-Ohta's model correspond to the singular point on the yield surface. On the singular point, the stress–strain relationship cannot be calculated in the usual manner

T. Takeyama (✉)
Department of Civil Engineering, Tokyo Institute of Technology,
2-12-1 O-okayama, 152-8552 Meguro-ku, Tokyo, Japan
e-mail: takeyama.t.aa@m.titech.ac.jp

T. Pipatpongsa
Global Scientific Information and Computer Center, Tokyo Institute of Technology,
2-12-1 O-okayama, 152-8550 Meguro-ku, Tokyo, Japan
e-mail: pthira@gsic.titech.ac.jp

A. Iizuka
Research Center for Urban Safety and Security, Kobe University, 1-1 Rokkodai,
657-8501 Nada-ku, Kobe, Hyogo, Japan
e-mail: iizuka@kobe-u.ac.jp

H. Ohta
Research and Development Initiative, Chuo University, 1-13-27 Kasuga,
112-8551 Bunkyo-ku, Tokyo, Japan
e-mail: ohta@tamacc.chuo-u.ac.jp

because the derivative of yield function with respect to the effective stress at the singular point is not uniquely defined. The stress–strain relationship can be calculated when the effective stress is in the vicinity of the singular point. However, the volume change computed by employing such technique is smaller than the theoretical value. Therefore, a special treatment is needed to describe the stress–strain relationship on the singular point of yield surface. In this research, the method of deriving the stress–strain relationship on the singular point using Koiter’s flow rule (1953) is proposed. We performed the simulation by giving the strain in various directions in the strain space by employing the Sekiguchi-Ohta’s model. As a result, it was found that the simulated effective stress does not get away from the singular point of the yield surface if the strain paths are given within a certain range in the strain space. This range of incremental strain is called “metastable space” (Roscoe et al. 1963). We derived the metastable space analytically in this chapter.

15.2 Singular Point of the Sekiguchi and Ohta’s Model

The yield function of the Sekiguchi and Ohta’s model is

$$f = MD \ln \frac{p'}{p'_0} + D\eta^* - \epsilon_v^p = 0. \quad (15.1)$$

where M is the critical state parameter, D is the coefficient of dilatancy proposed by Shibata (1963), p' is the effective mean stress, and η^* is the generalized stress ratio (Sekiguchi and Ohta 1977).

$$\eta^* = \sqrt{\frac{3}{2}} \|\eta - \eta_0\|. \quad (15.2)$$

where η is the stress deviator \mathbf{s} divided by p' and is called stress ratio tensor. The subscript 0 indicates the preconsolidated state. The superscript e and p indicates the elastic state and plastic state, respectively. The yield surface described by Eq. (15.1) in the axisymmetric stress plane is shown in Fig. 15.1. The singular point of the yield surface is indicated by a circle in the figure.

Figure 15.2 shows the simulated effective stress path and $e - \ln p'$ relationship of the normalized relative stress K_0 -consolidation. In the simulation, initial stress was set very close to the singular point. If the stress is right on the singular point, the simulation cannot be performed without a special treatment. The parameters used in the simulation are listed in Table 15.1. Two sets of strain increment are given: one is $\Delta\epsilon_v = 0.200\%$, $\Delta\epsilon_s = 0.133\%$ and the other is $\Delta\epsilon_v = 0.020\%$, $\Delta\epsilon_s = 0.013\%$. The stress path resulting from the simulation proceeds along the

Fig. 15.1 Yield surface of the Sekiguchi-Ohta’s model in axisymmetric stress plane

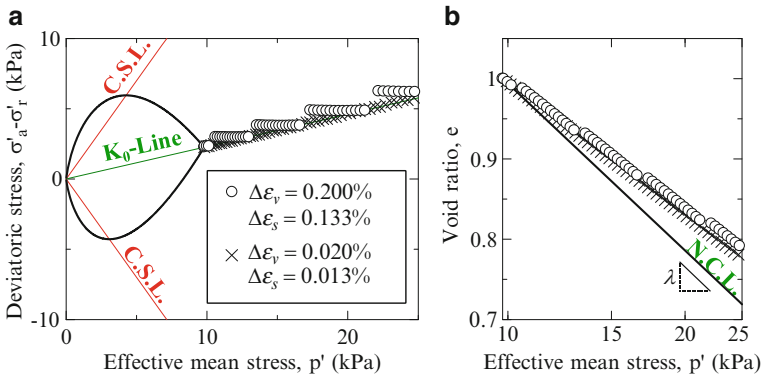
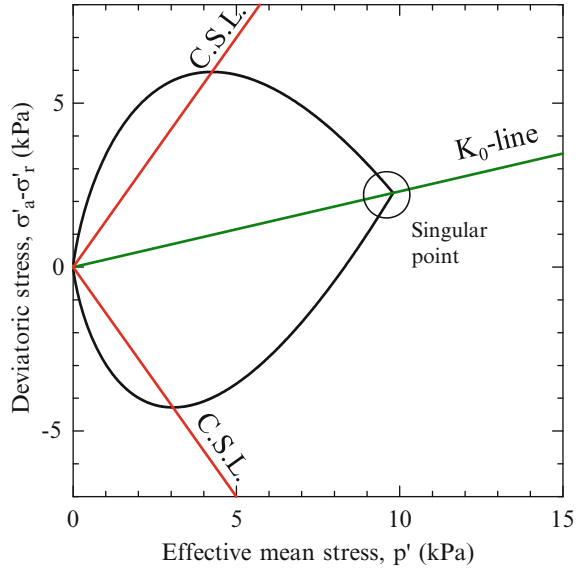


Fig. 15.2 Simulation result of K_0 -consolidation. (a) Stress path. (b) $e - \ln p'$ relationship

Table 15.1 Parameters used in the simulation

M	D	Λ	ν'	σ'_{vi} (kPa)	K_i	σ'_{v0} (kPa)	K_0	λ
1.4	0.086	0.8	0.33	11.3	0.799	11.3	0.8	0.3

K_0 -line (i.e., the stress ratio is almost constant); the volume, therefore, should change along the normal consolidation line (NCL) in the $e - \ln p'$ relationship according with the theory. However, the result of simulation did not coincide with the NCL and was calculated smaller than the theoretical value as shown in Fig. 15.2.

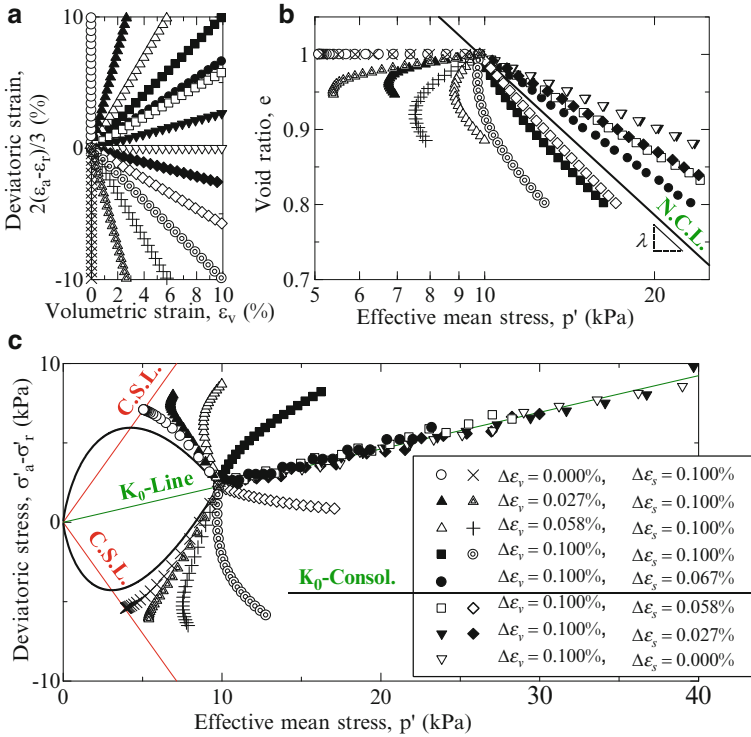


Fig. 15.3 Result of simulation in which the various directions of strain paths are given. (a) Given strain paths. (b) $e - \ln p'$ relationship. (c) Stress paths

Because the simulated volumetric change is smaller than that expected by the theory even in the case that the finer strain increment is given, it can be concluded that this error is not caused by the magnitude of the given strain increment. Additional series of simulation were carried out by giving the various directions of strain path in addition to $\Delta\epsilon_r = 0$, which is K_0 -consolidation. The given strain paths, the resulting void ratio change, and resulted stress paths are shown in Fig. 15.3. The parameters used in the simulation are the same in the simulation of K_0 -consolidation (Table 15.1). The simulated stress paths also proceed along K_0 -line not only in the case of K_0 -consolidation but also in the cases that the increment of the deviatoric strain is smaller than the increment of the volumetric strain. In these cases, the calculated volumetric change does not follow the theory. This result indicates that there is a certain range in the direction of strain path for which the stress paths cannot get away from the singular point. The volumetric change cannot be correctly calculated by using the Sekiguchi-Ohta's model or the original Cam clay model in the simulation. This is a very serious problem.

15.3 Special Treatment for Singular Point of the Sekiguchi and Ohta's Model

In order to resolve the problem related to the singular point of yield surface, we need the correct stress–strain relationship in the case that the stress is right on the singular point. The derivation of stress–strain relationship on the singular point is introduced in this chapter by applying the Koiter's associated flow rule (1953). Koiter's associated flow rule is widely used to handle plastic flow at the intersection of multiple yield surfaces. In the Koiter's associated flow rule, the direction of the plastic strain rate at the intersecting edges or vertices of the multiple yield surfaces f_1, f_2, \dots, f_n is assumed to be a summation of the normal vectors of the yield surfaces. The plastic strain rate can be described as

$$\dot{\epsilon}^p = \sum_{i=1}^n \dot{\gamma}_i \frac{\partial f_i}{\partial \boldsymbol{\sigma}}. \quad (15.3)$$

Two yield functions f_1, f_2 are considered and applied to Koiter's associated flow rule in this chapter. The first derivative of yield function of the Sekiguchi-Ohta's model Eq. (15.1) with respect to the effective stress is

$$\frac{\partial f}{\partial \sigma'} = \frac{D\beta}{3p'} \mathbf{1} + \sqrt{\frac{3}{2}} \frac{D}{p'} \bar{\mathbf{n}}, \quad \beta = M - \eta^* - \sqrt{\frac{3}{2}}(\eta_0 - \eta). \quad (15.4)$$

$\mathbf{1}$ is the Cronecker's delta. $\bar{\mathbf{n}}$ is the normalized relative stress deviator:

$$\bar{\mathbf{n}} = \frac{\bar{\mathbf{s}}}{\|\bar{\mathbf{s}}\|} \quad (15.5)$$

where $\bar{\mathbf{s}}$ is the relative stress deviator defined as

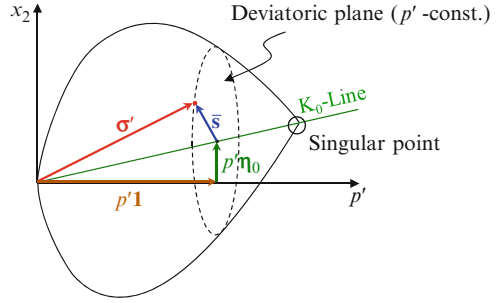
$$\bar{\mathbf{s}} = \mathbf{s} - p' \boldsymbol{\eta}_0. \quad (15.6)$$

The effective stress is divided into the isotropic and deviatoric components $\boldsymbol{\sigma}' = p' \mathbf{1} + \mathbf{s}$. Thus, substituting Eq. (15.6), the effective stress can be described as

$$\boldsymbol{\sigma}' = p' \mathbf{1} + p' \boldsymbol{\eta}_0 + \bar{\mathbf{s}}. \quad (15.7)$$

The relationship among three components in Eq. (15.7) can be schematically drawn as shown in Fig. 15.4. The vertical axis x_2 in Fig. 15.4 represents the major principal axis projected to the deviatoric stress plane. On the singular point, the normalized relative stress deviator $\bar{\mathbf{n}}$ cannot be determined because the relative stress deviator $\bar{\mathbf{s}}$ becomes 0.

Fig. 15.4 Schematic relationship among three components in Eq. (15.7)



Therefore, it is clearly found that the first derivative Eq. (15.4) of yield function with respect to effective stress is not uniquely defined on the singular point. However, by assuming $\bar{\mathbf{n}}$ tentatively, the derivative of yield function can be calculated even in the case that the stress is right on the singular point. Here, $\pm \bar{\mathbf{n}}_v$ are assumed as imaginary tensors on the singular point. Two yield surfaces f_1 and f_2 corresponding to $\bar{\mathbf{n}}_v$ and $-\bar{\mathbf{n}}_v$ are defined respectively as

$$f_1 = MD \ln \frac{p'}{p'_0} + D \sqrt{\frac{3}{2}} \frac{\bar{\mathbf{s}} : \bar{\mathbf{n}}_v}{p'} - \epsilon_v^p = 0 \tag{15.8}$$

$$f_2 = MD \ln \frac{p'}{p'_0} - D \sqrt{\frac{3}{2}} \frac{\bar{\mathbf{s}} : \bar{\mathbf{n}}_v}{p'} - \epsilon_v^p = 0. \tag{15.9}$$

The derivative of f_1 and f_2 are

$$\frac{\partial f_1}{\partial \sigma'} = \frac{D\beta_1}{3p'} \mathbf{1} + \sqrt{\frac{3}{2}} \frac{D}{2p'} \bar{\mathbf{n}}_v, \quad \beta_1 = M - \sqrt{\frac{3}{2}} (\eta_0 : \bar{\mathbf{n}}_v) \tag{15.10}$$

$$\frac{\partial f_2}{\partial \sigma'} = \frac{D\beta_2}{3p'} \mathbf{1} - \sqrt{\frac{3}{2}} \frac{D}{2p'} \bar{\mathbf{n}}_v, \quad \beta_2 = M + \sqrt{\frac{3}{2}} (\eta_0 : \bar{\mathbf{n}}_v). \tag{15.11}$$

The first terms of Eqs. (15.10)₁ and (15.11)₁ are the isotropic part of the derivative of yield function and the second terms are the deviatoric part. Figure 15.5 show the yield surface of the Sekiguchi-Ohta's model and the derivative of f_1 and f_2 in (a) the axisymmetric stress plane and (b) the deviatoric stress plane. Curves f_1 and f_2 are the intersections that appear when cutting the yield surface by a plane passing through both the origin and the singular point. $\bar{\mathbf{n}}_v$ is the imaginary tensor tentatively determining the direction of the plane.

The equations needed in deriving the stress–strain relationship on the singular point are as follows,

$$\dot{\epsilon} = \dot{\epsilon}^e + \dot{\epsilon}^p \tag{15.12}$$

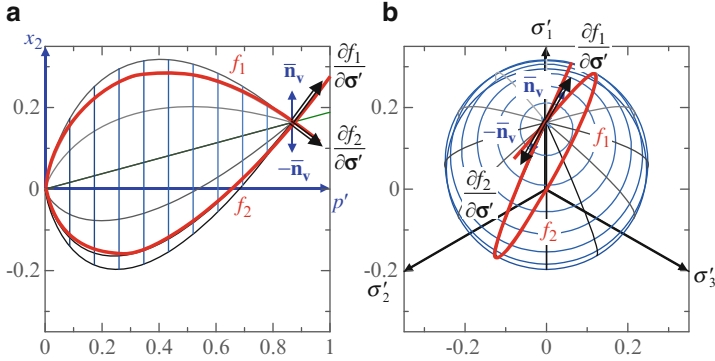


Fig. 15.5 Yield surface of Sekiguchi-Ohta's model and the derivative of the yield functions f_1 and f_2 in (a) the axisymmetric stress plane, and (b) the deviatoric stress plane

$$\underline{\sigma}' = \mathbf{C}^e : \dot{\epsilon}^e, \quad \mathbf{C}^e = K\mathbf{1} \otimes \mathbf{1} + 2GA \quad (15.13)$$

$$\dot{\epsilon}^p = \dot{\gamma}_1 \frac{\partial f_1}{\partial \sigma'} + \dot{\gamma}_2 \frac{\partial f_2}{\partial \sigma'} \quad (15.14)$$

$$\dot{f}_1 = \dot{f}_2 = 0 \quad (15.15)$$

Equation (15.12) represents the elasto-plastic decomposition of strain in rate form. Equation (15.13) is the constitutive equation for the hypo-elastic body where K and G is the elastic bulk modulus and the elastic shear modulus. $\mathbf{A} = \mathbf{I} - (\mathbf{1} \otimes \mathbf{1})/3$ is the fourth order tensor, which converts a second order tensor into the deviatoric tensor applying double dot product. \mathbf{I} is the fourth order isotropic tensor. Equation (15.14) is the Koiter's associated flow rule. Equation (15.15) is the condition that the stress is always on the yield surface (i.e., the state is elasto-plastic).

From Eqs. (15.12), (15.13), (15.14) and (15.15), an equation

$$\left\{ \begin{array}{l} \frac{\partial f_1}{\partial \sigma'} : \mathbf{C}^e : \dot{\epsilon} \\ \frac{\partial f_2}{\partial \sigma'} : \mathbf{C}^e : \dot{\epsilon} \end{array} \right\} = \left[\begin{array}{ll} \frac{\partial f_1}{\partial \sigma'} : \mathbf{C}^e : \frac{\partial f_1}{\partial \sigma'} + \mathbf{1} : \frac{\partial f_1}{\partial \sigma'} & \frac{\partial f_1}{\partial \sigma'} : \mathbf{C}^e : \frac{\partial f_2}{\partial \sigma'} + \mathbf{1} : \frac{\partial f_2}{\partial \sigma'} \\ \frac{\partial f_2}{\partial \sigma'} : \mathbf{C}^e : \frac{\partial f_1}{\partial \sigma'} + \mathbf{1} : \frac{\partial f_1}{\partial \sigma'} & \frac{\partial f_2}{\partial \sigma'} : \mathbf{C}^e : \frac{\partial f_2}{\partial \sigma'} + \mathbf{1} : \frac{\partial f_2}{\partial \sigma'} \end{array} \right] \left\{ \begin{array}{l} \dot{\gamma}_1 \\ \dot{\gamma}_2 \end{array} \right\} \quad (15.16)$$

is obtained. Replacing Eq. (15.16) as

$$\left\{ \begin{array}{l} L_1 \\ L_2 \end{array} \right\} = \begin{bmatrix} X_{11} & X_{12} \\ X_{21} & X_{22} \end{bmatrix} \left\{ \begin{array}{l} \dot{\gamma}_1 \\ \dot{\gamma}_2 \end{array} \right\}, \quad (15.17)$$

the consistent parameters used in the Koiter's associated flow rule $\dot{\gamma}_1$ and $\dot{\gamma}_2$ are

$$\left\{ \begin{array}{l} \dot{\gamma}_1 \\ \dot{\gamma}_2 \end{array} \right\} = \frac{1}{\det \mathbf{X}} \begin{bmatrix} X_{22} & -X_{12} \\ -X_{21} & X_{11} \end{bmatrix} \left\{ \begin{array}{l} L_1 \\ L_2 \end{array} \right\}. \quad (15.18)$$

By substituting Eq. (15.18) to the equation that is obtained from Eqs. (15.12), 15.13 and (15.14):

$$\underline{\sigma}' = \mathbf{C}^e : \left(\dot{\epsilon} - \dot{\gamma}_1 \frac{\partial f_1}{\partial \underline{\sigma}'} + \dot{\gamma}_2 \frac{\partial f_2}{\partial \underline{\sigma}'} \right), \quad (15.19)$$

the stress–strain relationship on the singular point is finally derived as

$$\underline{\sigma}' = [\mathbf{C}^e - \Lambda K \mathbf{1} \otimes \mathbf{1} + (1 - \Lambda) K (\eta_0 : \bar{\mathbf{n}}_v) \bar{\mathbf{n}}_v \otimes \mathbf{1} - 2G \bar{\mathbf{n}}_v \otimes \bar{\mathbf{n}}_v] : \dot{\epsilon} \quad (15.20)$$

where $\Lambda = 1 - \kappa/\lambda$ is the so-called irreversible ratio. However, it still remains unknown how $\bar{\mathbf{n}}_v$ should be assumed. The strain rate tensor is divided into the isotropic and deviatoric parts, $\dot{\epsilon} = \dot{\epsilon}_v \mathbf{1}/3 + \dot{\epsilon}_d$ where $\dot{\epsilon}_v$ is the volumetric strain and $\dot{\epsilon}_d$ is the deviatoric strain tensor. Thus Eq. (15.20) takes the form

$$\underline{\sigma}' = (1 - \Lambda) K \dot{\epsilon}_v \mathbf{1} + (1 - \Lambda) K \dot{\epsilon}_v (\eta_0 : \bar{\mathbf{n}}_v) \bar{\mathbf{n}}_v + 2G \dot{\epsilon}_d - 2G (\dot{\epsilon}_d : \bar{\mathbf{n}}_v) \bar{\mathbf{n}}_v. \quad (15.21)$$

Because the relative stress deviator never changed in the case that the stress point is on the singular point, $\dot{\bar{\mathbf{s}}} = 0$, the decomposition form of the increment stress is

$$\underline{\sigma}' = \dot{p}' \mathbf{1} + \dot{p}' \eta_0. \quad (15.22)$$

By equalizing the isotropic and the deviatoric part of the right hand side both of Eqs. (15.21) and (15.22), the following equations are obtained.

$$\dot{p}' = (1 - \Lambda) K \dot{\epsilon}_v \quad (15.23)$$

$$\dot{p}' \eta_0 = (1 - \Lambda) K \dot{\epsilon}_v (\eta_0 : \bar{\mathbf{n}}_v) \bar{\mathbf{n}}_v + 2G \dot{\epsilon}_d - 2G (\dot{\epsilon}_d : \bar{\mathbf{n}}_v) \bar{\mathbf{n}}_v \quad (15.24)$$

Eq. (15.23) represents the normal consolidation line. From Eqs. (15.23) and (15.24), $\bar{\mathbf{n}}_v$ takes the form,

$$\bar{\mathbf{n}}_v = \frac{(1 - \Lambda) K \dot{\epsilon}_v \eta_0 - 2G \dot{\epsilon}_d}{\|(1 - \Lambda) K \dot{\epsilon}_v \eta_0 - 2G \dot{\epsilon}_d\|}. \quad (15.25)$$

The stress–strain relationship mentioned above can only be applied to the situation that the stress is on the singular point. If the stress is not on the singular point, the usual stress–strain relationship should be applied. Therefore, it is necessary to judge whether the stress point proceeds right on the singular point or not. This judgment is enabled based on the sign of the consistent parameters $\dot{\gamma}_1$ and $\dot{\gamma}_2$. When one of the consistent parameters is negative, the usual stress–strain relationship should be applied and when both of the consistent parameters are positive, the stress–strain relationship proposed in this chapter is needed.

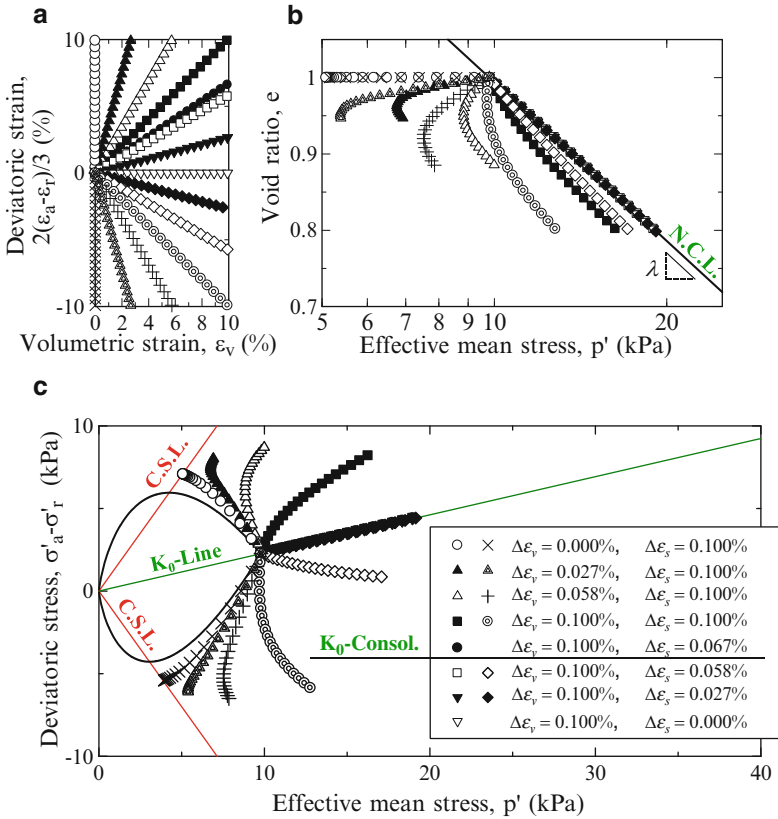


Fig. 15.6 Result of simulation with the special treatment for the singular point of yield surface in which the various directions of strain paths are given. (a) Given strain paths; (b) $e - \ln p'$ relationship. (c) Stress paths

Figure 15.6 show the result of simulation in which the various strain paths are given by applying the special treatment for the singular point of the yield surface. The simulated volumetric change is consistent with the theory even when the stress point proceeds along the K_0 -line. Comparison of Figs. 15.3 and 15.6 indicating whether the stress point proceeds on the singular point or not is properly judged based on the sign of the consistent parameters $\dot{\gamma}_1$ and $\dot{\gamma}_2$.

15.4 Metastability

Roscoe et al. (1963) who proposed the original Cam clay model mentioned in their paper that a clay sample may contain local regions in which plastic distortion occurs in different directions in such a manner that the whole sample does not exhibit any

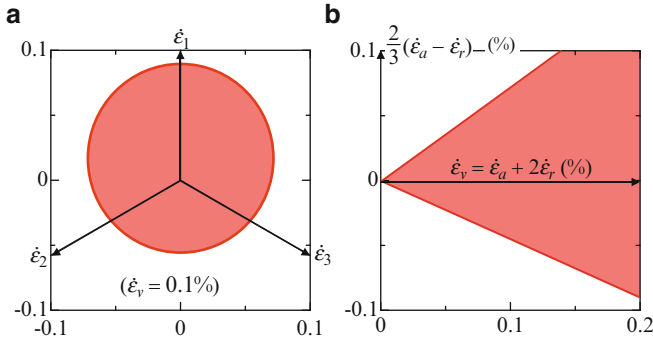


Fig. 15.7 Metastable space: the range of incremental strain in which the stress cannot get away from the singular point in (a) the deviatoric strain plane, and (b) the axi-symmetric strain plane.

overall distortion during isotropic consolidation. They also noted that a clay sample in a state of isotropic virgin consolidation is sensitive to shear stress of the slightest magnitude and that quite substantial shear distortion can take place without any shear stress being applied. They called a state of isotropic virgin-consolidation as “metastable state.”

As well as the original Cam clay model, the shear distortion can occur without any change in stress ratio in the Sekiguchi-Ohta’s model as shown in Fig. 15.6. Therefore, the metastable state for the Sekiguchi-Ohta’s model is a state of anisotropic virgin consolidation. The effective stress point always proceeds on the singular point when the strain increment within a certain range is given. In other words, there is a certain range in direction of the strain increment vector (see Figs. 15.3a and 15.6b) that makes a clay sample to remain in the metastable state. This nature of elasto-plastic constitutive model is called “Metastability” after Roscoe et al.

The condition under which the stress cannot get away from the singular point is that both of the consistent parameters $\dot{\gamma}_1$ and $\dot{\gamma}_2$ are positive. Taking this into the constitutive equations on the singular point, the condition is described by

$$2\frac{G}{K}\Lambda\dot{\epsilon}_v - (\eta_0 : \mathbf{b}) \pm \sqrt{\frac{2}{3}}M\|\mathbf{b}\| > 0, \tag{15.26}$$

where $\mathbf{b} = (1 - \Lambda)K\dot{\epsilon}_v\eta_0 - 2G\dot{\epsilon}_d$.

Figure 15.7 show the condition described by Eq. (15.26) in (a) the deviatoric strain plane and (b) the axi-symmetric strain plane. When strain increment vectors shown in Figs. 15.3a and 15.6a are in the shaded zone shown in Fig. 15.7b, the stress states associated with the given strain increment vectors will follow the K_0 -line shown in Figs. 15.3c and 15.6c. In incremental principal strain space, the right hand side of Eq. (15.26) is drawn as a surface of a cone. The space inside of this cone is named “metastable space.” When the strain increment within the “metastable space” is applied, a clay sample keeps a metastable state and the effective stress cannot get away from the singular point.

15.5 Conclusions

By performing the simulation in which the various direction of strain paths were given employing the Sekiguchi-Ohta's model, it was found that the stress proceeds on the singular point of the yield surface and the volumetric change cannot be calculated correctly in the case that the given strain path is within the metastable space. This error might be caused by the fact that the stress jumps when the generalized stress ratio becomes almost 0 (i.e., the stress is very close to the singular point). In order to obtain correct solution even in the case that the stress is on or very close to the singular point, the stress–strain relationship on the singular point was derived and the method to judge whether the stress got away from the singular point or not is proposed in this chapter. The metastable space, the range in which the stress cannot get away from the singular point, is also derived analytically.

References

- Koiter WT (1953) Stress-strain relations, uniqueness and variational theorems for elastic-plastic materials with a singular yield surface. *Q Appl Math* 11:350–354
- Roscoe KH, Schofield AN, Thurairajah A (1963) Yielding of clays in states wetter than critical. *Geotechnique* 13(3):211–240
- Sekiguchi H, Ohta H (1977) Induced anisotropy and time dependency in clays, constitutive equation of soils. In: *Proceedings of specialty session 9, 9th international conference on soil mechanics and foundation engineering, Tokyo, 1977*, pp 306–315
- Shibata T (1963) On the volume changes of normally consolidated clays. *Annals of Disaster Prevention Research Institute, Kyoto University, Kyoto, No. 6*, pp 128–134

Chapter 16

Analysis of Earth Pressure Problems by Upper and Lower Equilibrium Methods

Akira Nishihara, Shinji Shimamoto, and Hideki Ohta

16.1 Introduction

Most practical solutions of the failure of soil structures are based on the classical plastic theory in which soil mass is assumed to be a rigid plastic body. These solutions are categorized into three, the limit equilibrium method, the slip line method, and limit analysis.

The problem of active and passive earth pressure acting on a rigid retaining wall was first studied by Coulomb with the limit equilibrium method, assuming a simple straight failure line and the equilibrium of forces acting on soil mass. However, the solution of the limit equilibrium method has been recognized to overestimate the passive earth pressure acting on a rigid retaining wall.

The slip line method proposed Sokolovski (1960) is a more complicated and numerical solution based on the formulation of Kotter's curvilinear equilibrium equations. Although the solution of the slip line method has been considered to be most accurate, this method has been used less in practice because of the complicated numerical calculation.

A. Nishihara, D.Eng.

Department of Architecture and Civil Engineering, Faculty of Engineering, Fukuyama University,
1 Gakuencho, 729-0292 Fukuyama, Hiroshima, Japan

e-mail: nishihara@fucc.fukuyama-u.ac.jp

S. Shimamoto

Load and Traffic Design Division, CTI Engineering Co., Ltd., 1-6-7 Dosyou-machi, Chuo-ku,
541-0045 Osaka-shi, Osaka, Japan

e-mail: shimamoto@ctie.co.jp

H. Ohta, D.Eng. (✉)

Research and Development Initiative, Chuo University, 1-13-27 Kasuga, 112-8551 Bunkyo-ku,
Tokyo, Japan

e-mail: ohtaoffice@kib.biglobe.ne.jp

With the development of the plastic limit theorems of perfect plasticity, many problems have been solved on a much more logical basis. The limit analysis based on the principle of maximum plastic work theory of plasticity gives both of the upper bound and the lower bound of correct solutions (Chen and Rosenfarb 1973; Chen 1975).

This chapter examines the logical basis of the plastic limit theorems of perfect plasticity and proposes a set of new methods called upper and lower equilibrium methods (ULEM) of obtaining both the upper and the lower bound solutions.

16.2 Plastic Limit Theorems of Perfect Plasticity

Let us consider a soil mass, such as shown in Fig. 16.1, in the state of static equilibrium. The soil mass is assumed to be a perfectly plastic body.

Conditions that should be satisfied by stresses and deformations in the body of perfectly plastic state are as follows (Hill 1948).

1. Stress equilibrium equations

$$\sigma_{ij,j} + \rho_i = 0 \quad (16.1)$$

where σ_{ij} is the stress tensor and ρ_i is the body force vector.

2. Boundary condition on stress

$$\sigma_{ij} \cdot n_j = \bar{T}_i \quad (16.2)$$

where n_j is a unit normal vector and \bar{T}_i is the boundary value of surface traction vector on the stress boundary surface S_T .

3. Failure conditions

$$f(\sigma_{ij}) = 0 \quad (16.3)$$

4. Compatibility condition

$$\dot{\epsilon}_{ij} = \frac{1}{2}(v_{i,j} + v_{j,i}) \quad (16.4)$$

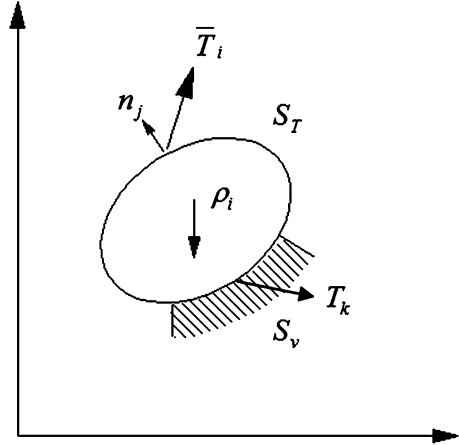
where $\dot{\epsilon}_{ij}$ is the strain rate tensor and v_i is the velocity vector.

5. Boundary condition on velocity

$$v_i = \bar{v}_i \quad (16.5)$$

where \bar{v}_i is the boundary value of velocity on the velocity boundary surface S_v .

Fig. 16.1 System in the state of static equilibrium



6. Flow rule

$$\epsilon_{ij} = \Lambda \frac{\partial f}{\partial \sigma_{ij}} \quad (16.6)$$

where f is a failure function given by Eq. (16.3) and Λ is a constant.

When all of above conditions are satisfied, the calculated value of surface traction T_k on the velocity boundary surface should be a correct solution. However, because it is very difficult to obtain a correct solution, approximate solutions satisfying some of these conditions are obtained. For example, solutions of the limit equilibrium method, the slip line method, and the lower bound solutions of the limit analysis are obtained considering only the conditions of stress without considering the conditions concerning velocity.

In this chapter, the system of stress and surface traction satisfying stress equilibrium equations and boundary condition on stress is called the equilibrium stress system. The statically admissible stress system is one of the equilibrium stress systems that does not violate the failure condition. The lower bound theorem of limit analysis guarantees that solutions derived from the statically admissible stress system is not greater than the correct solution.

On the other hand, the system of strain rate and velocity satisfying compatibility condition and boundary condition on velocity is called the compatible velocity system. When the stress system related to the compatible velocity system by flow rule satisfies failure condition, the stress system such as this is called the compatible stress system. The upper bound theorem of limit analysis guarantees that solutions derived from the compatible stress system is not smaller than the correct solution. However, it should be noted that the compatible stress system is not requested to satisfy the equilibrium condition. The upper bound theorem is based on the principle of plastic work, which includes the equilibrium condition. Therefore, the principle of plastic work cannot be applied to the compatible stress system, and it is not guaranteed that the compatible stress system gives the upper bound solution.

16.3 Upper and Lower Equilibrium Methods

Davis (1968) and Collins (1973) showed that Coulomb's solution, a typical stress equilibrium solution, is the same as the upper bound solution. Also, Drescher and Detoumay (1993) showed that for a general case consisting of a number of blocks, considering the continuity of the motion of rigid blocks, the numerical calculation in the upper bound solution is logically equivalent with the limit equilibrium method. These results indicate that the upper bound solutions can be obtained from the equilibrium stress system.

In the analysis of the failure of soil structures based on the rigid plastic theory, soil mass is divided into some rigid blocks. When the equilibrium stress system in a rigid block is considered, there are two cases of the equilibrium stress state. One is the case in which the stress state in the block is presented by a single stress circle as shown in Fig. 16.2. The stress state in this case clearly violates the failure condition. In this chapter, the stress state such as this is called post-failure stress system. In Fig. 16.2b, the direction of the lines connecting the pole P and each point (i, j, k) on the failure line shows directions of block surfaces shown in Fig. 16.2a. In this case, each surface of the block is a slip surface.

Another case is the statically admissible stress system described by Fig. 16.3. In the statically admissible stress system, it is required that the stress state in the block does not violate the failure condition. To consider this stress state in a block, we must divide a block into two areas by the stress discontinuity line as shown in Fig. 16.3a. In this case, the stress circle in each area does not violate the failure condition. The stress represented by the intersection of two stress circles, "s", gives the stress on the stress discontinuity line. Through this stress discontinuity line, the stresses in each area and on block surfaces satisfy the stress equilibrium. It should be noted that block surface "j" and "k" are not slip surfaces.

In upper and lower equilibrium methods (ULEM), the soil mass is divided into some rigid blocks. Figure 16.4 shows the case of the passive earth pressure on the rigid retaining wall. In this case, the ground surface is the stress boundary surface and the face of a wall is the velocity boundary surface. In this chapter,

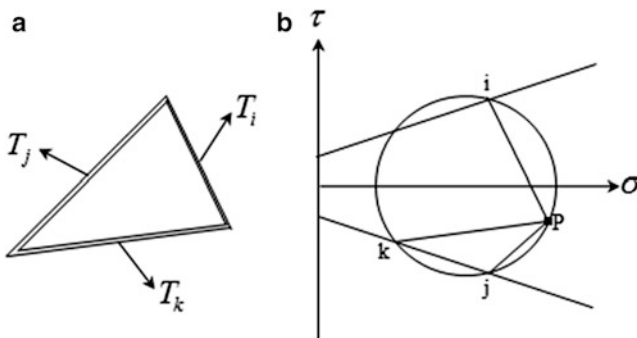


Fig. 16.2 Postfailure stress system. (a) Rigid block and (b) stress circle

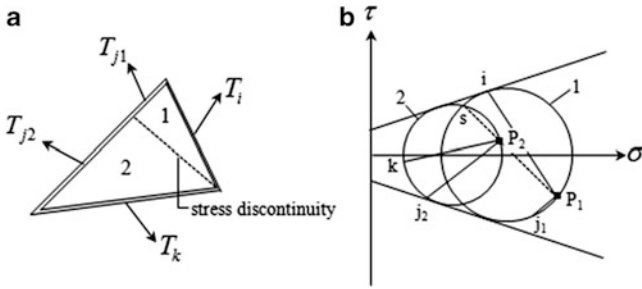


Fig. 16.3 Statically admissible stress system. (a) Rigid block and (b) stress circle

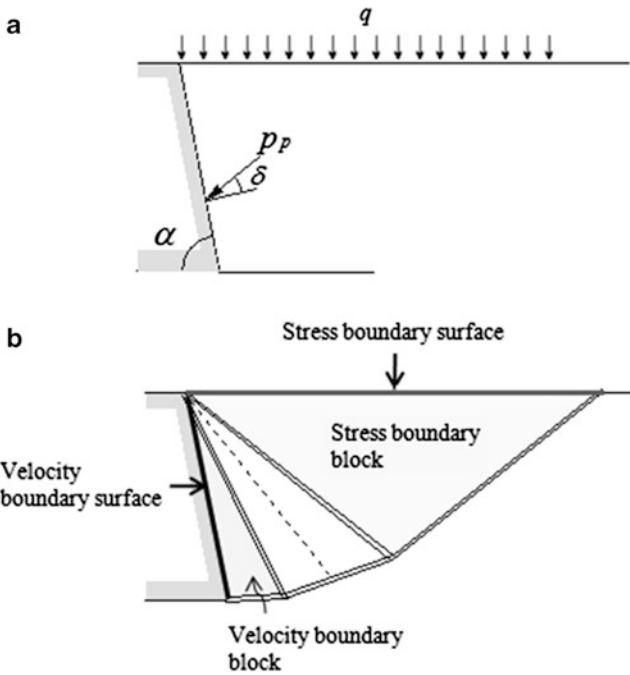
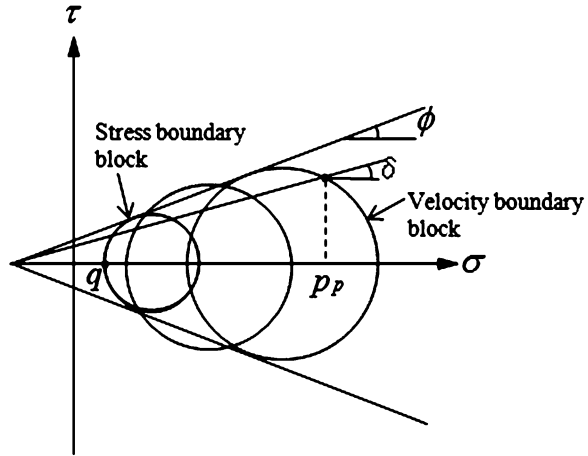


Fig. 16.4 Schematic view of the analysis of the earth pressure problem. (a) Passive earth pressure acting on rigid block with a friction angle δ . (b) Division of soil mass into blocks

a block adjacent to the stress boundary surface is called the stress boundary block and a block adjacent to the velocity boundary surface is called the velocity boundary block.

Figure 16.5 shows stress circles of each block. The stress circle for the stress boundary block can be determined by the stress boundary condition. Then the stress circle in the next block is determined by considering stress continuity and failure condition. In the same manner, a series of stress circles are determined throughout the region. The earth pressure acting on the retaining wall is calculated from the

Fig. 16.5 Stress circles of each block



stress state in the velocity boundary block. In ULEM, the lower bound solution and the upper bound solution are obtained from thus determined statically admissible stress system and the postfailure stress system respectively.

16.4 Solutions of the Earth Pressure Problems by Upper and Lower Equilibrium Methods

16.4.1 Passive Earth Pressure

Figure 16.6a shows an example of the statically admissible stress system in the case of the passive earth pressure problem. In this example, the soil mass is divided into four blocks and the shape of blocks is indicated in Fig. 16.6b. Each of the intermediate blocks II and III is divided in two areas by the stress discontinuity line.

On the other hand, the postfailure stress system and shape of blocks are given in Fig. 16.7a and b respectively. The block surfaces are velocity discontinuities (i.e., slip lines).

The passive earth pressure acting on the wall is calculated from the geometrical relationships of stress circles shown in Figs. 16.6a and 16.7a. The statically admissible stress system gives the lower bound solution and the postfailure system gives the upper bound solution of the passive earth pressure respectively.

Table 16.1 shows the results of the calculated passive earth pressure coefficient. The case in which the solution is not obtained is the case of the stress boundary block overlaying the velocity boundary block. In this case, there exists theoretically no stress state satisfying the condition of equilibrium. In Table 16.1, the solutions both of the slip line method (Sokolovski 1960) and the limit equilibrium method are shown for comparison. The solutions of the limit equilibrium method are so-called Coulomb's earth pressure. In the case of passive earth pressure, it has long been

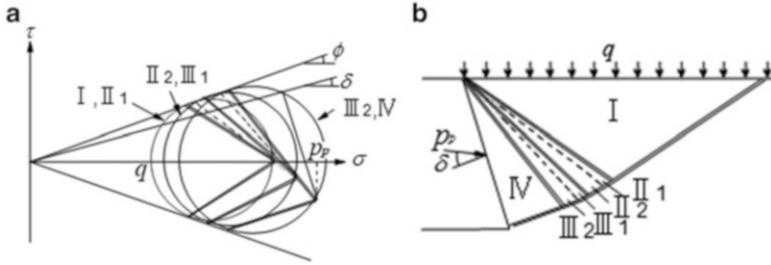


Fig. 16.6 Statically admissible stress system. (a) Stress circles. (b) Shape of blocks

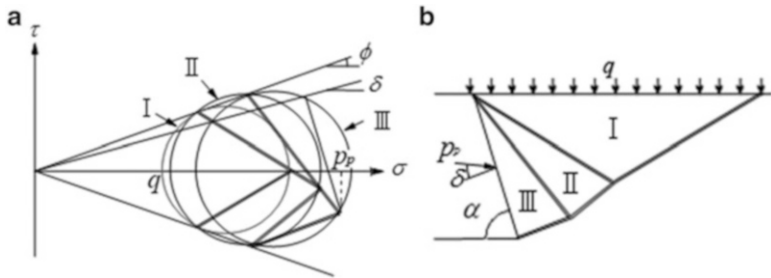


Fig. 16.7 Postfailure stress system. (a) Stress circles. (b) Shape of blocks

recognized that the solution of the limit equilibrium method is the upper bound solution and greatly over estimate the passive earth pressure. However, as shown in Table 16.1, the solution of the limit equilibrium method is smaller than the lower bound solution in some cases. The limit equilibrium method considers only forces on the surface of blocks, not the stress state in the blocks. Therefore, the solution of the limit equilibrium method is not guaranteed to be the upper bound solution from the viewpoint of the theory of plasticity.

The solution of the slip line method has been considered to be a most accurate solution. As shown in Table 16.1, most of the solutions of the slip line method are between the lower solutions and the upper solutions or beyond the upper bound solutions. In the slip line method, the stresses along the slip lines satisfy both the failure condition and equilibrium condition. These stress states meet the postfailure stress system. Therefore, the slip line method can be considered to be a kind of the Upper Equilibrium Method. There are some solutions slightly smaller than the lower solutions; these are the result of numerical errors in calculations.

16.4.2 Active Earth Pressure

In the case of the active earth pressure problem, the statically admissible stress system and the postfailure stress system are given as shown in Figs. 16.8 and 16.9, respectively. It should be noted that, in the active earth pressure problem, the

Table 16.1 Passive earth pressure coefficient

ϕ	δ	α	ULEM		Slip line method	Limit equilibrium method
			Lower solution	Upper solution		
10	0	70	–	–	1.34	1.36
		90	1.42	1.42	1.42	1.42
		110	1.71	1.71	1.74	1.76
	5	70	–	–	1.46	1.455
		90	1.54	1.55	1.56	1.57
		110	1.85	1.87	1.95	2.04
	10	70	1.52	1.53	1.53	1.55
		90	1.61	1.66	1.67	1.73
		110	1.9	2.08	2.1	2.38
20	0	70	–	–	1.71	1.748
		90	2.04	2.04	2.04	2.04
		110	2.79	2.81	2.9	2.98
	5	70	2.08	2.08	2.08	1.905
		90	2.51	2.52	2.55	2.31
		110	3.41	3.54	3.8	3.61
	10	70	2.35	2.41	2.42	2.08
		90	2.79	3.08	3.04	2.635
		110	3.66	4.79	4.62	4.46
30	0	70	–	–	2.16	2.27
		90	3	3	3	3
		110	4.76	4.8	5.06	5.34
	5	70	3.16	3.16	3.16	2.53
		90	4.42	4.48	4.62	3.505
		110	6.88	7.5	8.45	6.88
	10	70	4.07	4.33	4.3	2.82
		90	5.41	6.93	6.55	4.14
		110	7.88	15.28	12.3	9.19

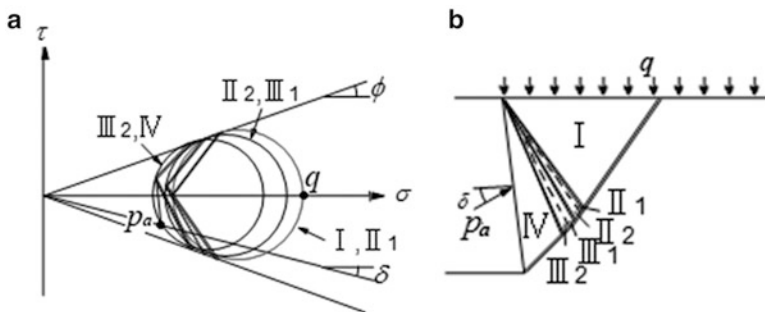


Fig. 16.8 Statically admissible stress system. (a) Stress circles. (b) Shape of blocks

statically admissible stress system gives the upper bound solution and the post-failure stress system gives the lower bound solution.

Table 16.2 shows the result of the calculated active earth pressure coefficient. In the case of active earth pressure problem, the limit equilibrium solution has been

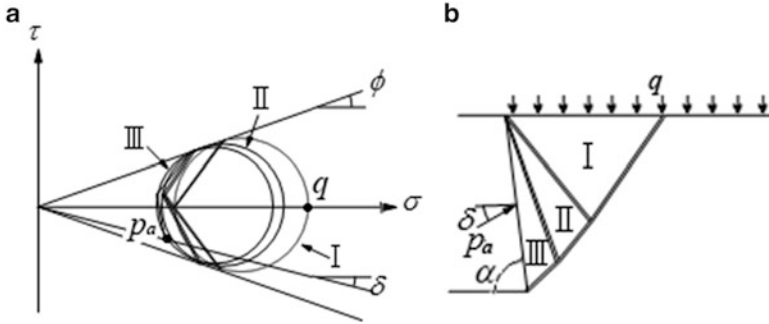


Fig. 16.9 Postfailure stress system. (a) Stress circles. (b) Shape of blocks

Table 16.2 Active earth pressure coefficient

ϕ	δ	α	ULEM		Slip line method	Limit equilibrium method
			Lower solution	Upper solution		
10	0	70	—	—	0.826	0.833
		90	0.704	0.704	0.7	0.704
		110	0.662	0.663	0.665	0.644
	5	70	—	—	0.794	0.801
		90	0.667	0.667	0.67	0.662
		110	0.624	0.63	0.62	0.588
	10	70	0.788	0.79	0.794	0.786
		90	0.649	0.659	0.65	0.635
		110	0.593	0.628	0.596	0.549
20	0	70	—	—	0.656	0.648
		90	0.49	0.49	0.49	0.49
		110	0.403	0.405	0.482	0.38
	5	70	—	—	0.612	0.615
		90	0.451	0.452	0.45	0.465
		110	0.369	0.374	0.356	0.351
	10	70	0.615	0.616	0.612	0.615
		90	0.442	0.452	0.44	0.447
		110	0.346	0.382	0.344	0.33
30	0	70	—	—	0.521	0.498
		90	0.333	0.333	0.33	0.333
		110	0.236	0.238	0.229	0.212
	5	70	—	—	0.487	0.485
		90	0.305	0.305	0.3	0.319
		110	0.213	0.218	0.206	0.199
	10	70	0.502	0.502	0.51	0.478
		90	0.309	0.318	0.31	0.308
		110	0.204	0.234	0.195	0.188

thought to be the lower bound solution. As shown in Table 16.2, some of the limit equilibrium solutions are larger than the upper bound solution. Therefore, the limit equilibrium solution is not guaranteed to be the lower bound solution.

As mentioned earlier, the slip line solution that meets the postfailure stress system gives the lower bound solution. As shown in Table 16.2, most of the solutions of the slip line method are between the lower solutions and the upper solutions or slightly smaller than the lower bound solutions.

16.5 Conclusions

In this chapter, the authors proposed a set of new methods called upper and lower equilibrium methods (ULEM) of obtaining both the upper and lower bound solutions of collapse load. The logical basis of the plastic limit theorems of perfect plasticity was first examined, and it was shown that there are two stress states, the statically admissible stress system and the postfailure stress system in the stability problems. In the ULEM, both of the upper and lower solutions of collapse load can be obtained by considering these two stress systems. The ULEM give not only the stress state but also the shape of slip lines.

Validity of the ULEM is confirmed by applying it to the analysis of the earth pressure acting on a rigid retaining wall. The solutions of the ULEM give good estimates of the passive and active earth pressure. It was shown that the limit equilibrium solution is not guaranteed to be the upper or lower bound solution. It was also shown that the slip line method is a kind of ULEM considering the postfailure stress system.

References

- Chen WF (1975) *Limit analysis and soil plasticity*. Elsevier, Amsterdam
- Chen WF, Rosenfarb JL (1973) Limit analysis solutions of earth pressure problems. *Soil Found* 13(4):45–60
- Collins LF (1973) A note on the interpretation of Coulomb's analysis of the thrust on rough retaining wall in terms of the limit theorems of plasticity theory. *Geotechnique* 23(3):442–447
- Davis EH (1968) Theories of plasticity and the failure of soil masses. In: *Soil mechanics: selected topics*. Butterworth, London, pp 341–380
- Drescher A, Detoumay E (1993) Limit load in translational failure mechanism for associative and non-associative. *Geotechnique* 43(3):443–456
- Hill R (1948) A variational principle of maximum plastic work in classical plasticity. *Q J Mech Appl Math* 1:18–28
- Sokolovski VV (1960) *Statics of soil media*. Butterworth, London

Part III
Geotechnical Practices in Dealing
with Geo-hazards

Chapter 17

Rehabilitation of the Old Rossio Railway Station Building: Enlargement and Underpinning

Pedro Simão Sêco e Pinto, João Barradas, and Arlindo Sousa

17.1 Introduction

This chapter describes the enlargement and underpinning of the old Rossio railway station building (1886). This work included the construction of new underground walls and mechanical stairways for the connection with a nearby underground metro station and also the construction of a new underground metro gallery for a new line, under some old, huge retaining walls that sustain the embankment of the railway platforms. A careful study was performed for this station in order to avoid unacceptable damages. Some of the system and suitability tests that were performed for the anchors are presented.

It was necessary to perform the underpinning of an east–west wall and the principal retaining walls, with 15 m in height and a thickness around 2.5 m, and Bairro Alto wall.

These walls were later reinforced in order to ensure their long-term safety against rotational failure. The main geological conditions are described. The field and laboratory tests are referred, as well as the geotechnical characteristics. The methodology to design the retaining walls, based on Eurocode 7, is introduced. The seismic design is based on Eurocode 8. The monitoring results of the anchor loads and ground displacements resulting from the excavation are presented. Some final considerations are presented.

P.S.S. e Pinto, Ph.D. (✉)

Geotechnical Department, University of Coimbra, Coimbra, Portugal

Geotechnical Department, National Laboratory of Civil Engineering (LNEC), Lisbon, Portugal

e-mail: pspinto@lnec.pt

J. Barradas, Ph.D.

Geotechnical Department, National Laboratory of Civil Engineering (LNEC), Lisbon, Portugal

A. Sousa

Engineer, Geotechnical Department, National Laboratory of Civil Engineering (LNEC),
Lisbon, Portugal

17.2 Background

Because of the crossing of the Rossio railway station building (1886) by an underground gallery (for the Lisbon Metro), a careful study was performed for this station in order to avoid unacceptable damages. The building originally had three levels: ground floor (+11.86 m), second floor (+19.93 m), and third floor (+25.96 m). For the installation of a commercial center two new floors were built: intermediate second floor (+15.21 m) and intermediate third floor (+22.79 m). For the construction of the underground it was necessary to perform the underpinning of east–west and a north–south retaining walls, with 13 m in height and a thickness around 3 m. Both walls sustain an embankment on which the railways platforms were built.

The underground gallery was built underneath the whole extension of the north–south retaining wall and part of the east–west retaining wall.

The enlargement of the station includes two new underground halls connected by mechanical and fixed stairways with each other.

A cross-section of one of the tied back walls is shown in Fig. 17.1.

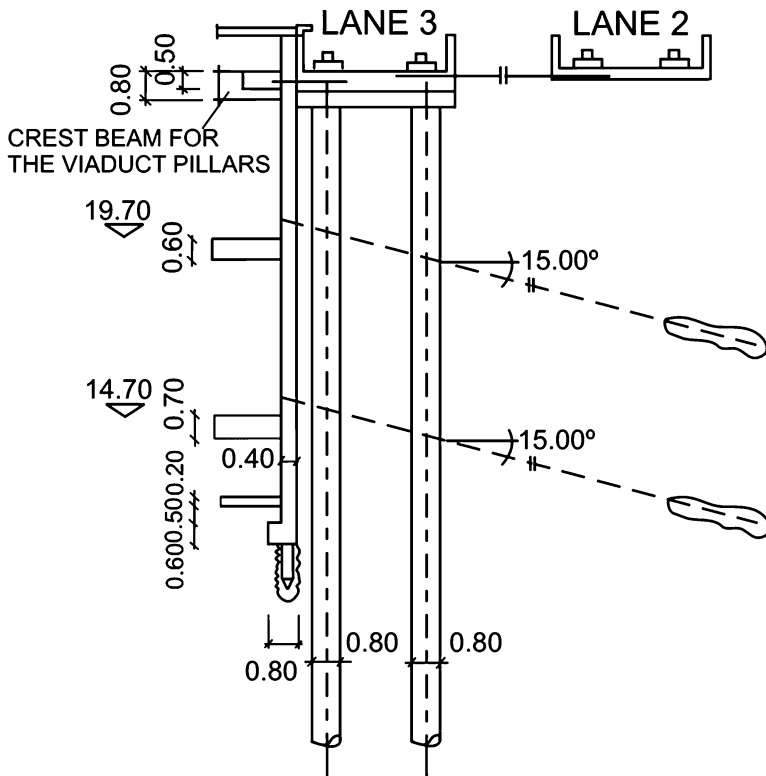


Fig. 17.1 Cross-section of the tied back wall

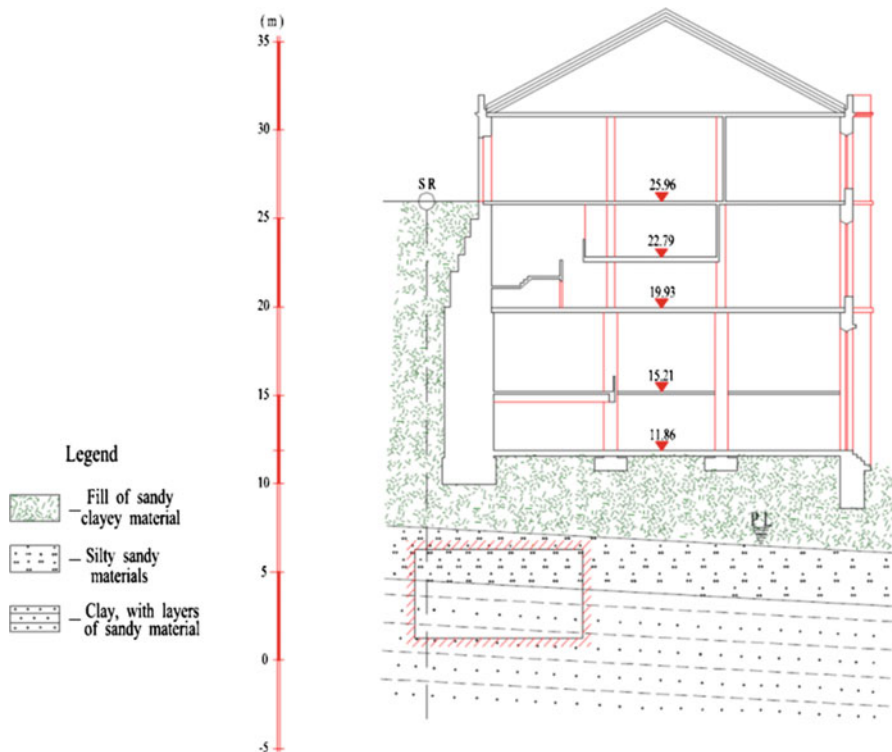


Fig. 17.2 Geological profile (Adapted from Consortium 1996a)

For the underpinning of the retaining walls, more than a dozen large reinforced concrete (RC) frames were erected, side by side, under the base of the walls (Consortium 1996b). These simple but massive structures allowed the excavation of the space for the installation of the Metro gallery (Fig. 17.2) under the beam of each frame.

Other parts of the station building also had to be underpinned, by means of RC frames, micropiles, and jet-grout columns.

In the design phase of the underpinning of the retaining walls, it was recognized that the walls didn't meet the safety conditions required by Eurocodes 7 and 8 and Portuguese Actions Code, especially concerning the rotational failure scenario for both static and seismic actions.

Therefore it was decided to reinforce both walls by:

1. Definitive anchorages and a grid of RC beams, in the case of the north-south wall
2. Micropiles going through the body of the wall and into the ground behind and under it, in the case of the east-west wall (Sêco e Pinto et al. 2008)

17.3 Main Geological Characteristics

In this section the main geological characteristics of each layer are presented.

Based in the results collected from borings executed at Rossio site, the following units were considered as shown in Fig. 17.2 (Consortium 1996a).

Landfill: composed of sandy-clayey material with a thickness varying from 3.5 to 20 m.

“Estefânia Areolas”: composed of sandy materials or silty-sandy materials with thickness around 3 m.

Clays and calcareous rocks from “Prazeres”: composed of dark grey to dark brown clay, with layers of sandy material, up to the depth that is significant to the design of the structures of the Rossio station.

17.4 Geotechnical Characteristics

After an evaluation of the results of the field investigation (boreholes, trenches, vane shear tests, pressurometer tests, penetrometer tests, and Lefranc tests) and the laboratory tests (chemical tests, oedometer tests, triaxial tests), the geotechnical characteristics adopted are shown in Table 17.1 (Consortium 1996a).

17.5 Design of Retaining Walls

17.5.1 Static Conditions

The gravity type retaining structures were designed taking into consideration limit states (Eurocode 0 1990; Eurocode 7 1997).

Table 17.1 Geotechnical properties

Properties	Landfill	Estefânia Areolas	Clays and calcareous rocks	Masonry retaining wall
United classification:	CL, CH	–	CL, CH	–
% passing sieve # 200 (ASTM)	28–100	–	32–75	–
Liquid limit (%)	18–47	–	28.3–43.4	–
Plastic index (%)	3.4–26.7	–	4.3–21	–
Unit weight (kN/m ³)	17.6	–	–	22
Strength (c_u) (kPa)	32.7–169.7	–	–	–
Cohesion c' (kPa)	0	0	33	1,000
Friction angle ϕ' (°)	30	33	35	45
k (m/s)	10^{-9}	10^{-5}	10^{-6} to 10^{-7}	–
Poisson ratio	0.35	–	0.25	0.2
SPT values	4–18	6–39	10–60	–
CPT values (MPa)	0.2–5	–	–	–

Table 17.2 Partial factors—ultimate limit states in persistent and transient situations (Eurocode 7 1997)

Case	Actions			Ground properties			
	Permanent		Variable	$\tan \phi'$	c'	c_u	q_u^a
	Unfavorable	Favorable	Unfavorable				
Case A	1.00	0.95	1.50	1.10	1.30	1.20	1.20
Case B	1.35	1.00	1.50	1.00	1.10	1.00	1.00
Case C	1.00	1.00	1.30	1.25	1.60	1.40	1.40

^aCompressive strength of soil

The following ultimate limit states (with severe consequences) can occur:

1. Loss of overall stability
2. Failure of a structural element such as a retaining wall, an anchorage, a micropile, etc.
3. Foundation failure
4. Unacceptable leakage through or beneath the wall
5. Rotational failure
6. Movements of the retaining structure that may cause collapse of other structures
7. Unacceptable change to the flow of groundwater
8. Failure by sliding at the base of the wall

The following serviceability limit states (with less severe consequences) can occur:

1. Movements of the retaining structure that may affect the appearance or efficient use of the building and other structures
2. Excessive vibrations

The values of partial factors for permanent and variable actions given in Table 17.2 were used for verification of ultimate limit states situations. For accidental situations, all numerical values of partial factors for actions were taken equal to 1.0 (Eurocode 1 1991).

Cases A, B, and C have been introduced in order to ensure stability and adequate strength in the structure and in the ground.

Case A is only relevant to buoyancy problems, where hydrostatic forces are included in the main unfavorable action.

Case B is often critical to the design of the strength of structural elements involved in foundations or retaining structures. Where there is no strength of structural materials involved, Case B is irrelevant.

Case C is generally critical in cases, such as slope stability problems, where there is no strength of structural elements involved. Case C is often critical to the sizing of structural elements involved in foundations or retaining structures, and sometimes to the strength of structural elements. Where there is no strength of ground involved in the verification, Case C is irrelevant.

Permanent actions include self-weight of structural and non-structural components and those actions caused by ground, groundwater and free water.

In calculation of design earth pressures for Case B, the partial factors given in Table 17.2 are applied to characteristic earth pressures. Characteristic earth pressures comprise characteristic water pressures together with stresses that are admissible in relation to the characteristic ground properties and characteristic surface loads.

All permanent characteristic earth pressures on both sides of a wall are multiplied by 1.35 if the total resulting action is unfavorable and by 1.00 if the total resulting action effect is favorable. Thus, all characteristic earth pressures are treated as being derived from a single source.

For the verification of serviceability limit states, partial safety factors are used for all permanent and variable actions except where specified otherwise.

For the anchored structures the following additional ultimate limit states are considered (Eurocode 7 1997):

1. Failure of the ground anchorage by tension
2. Structural failure of the ground anchorage caused by shear forces, distortion at anchorage head or corrosion
3. Loss of anchorage load caused by excessive displacements of the anchorage head or by creep and relaxation
4. Failure or excessive deformation of parts of the structure caused by the applied anchorage force.

For permanent ground anchorages (those with a service life greater than 2 years) protective corrosion barriers must be provided.

Design values of ground properties, X_d , are derived from characteristic values, X_k , using the equation:

$$X_d = \frac{X_k}{Y_m} \quad (17.1)$$

where Y_m is the safety factor for the ground property, or shall be assessed directly.

The characteristic value of a soil or rock parameter is selected as a cautious estimate of the value affecting the occurrence of the limit state.

For serviceability limit states all values of Y_m are equal to 1.0.

17.5.2 Analysis of the Principal Retaining Wall

For the design and behavior evaluation of the principal retaining wall with 15 m height and 2.5 m thickness, numerical analyses were performed using the FLAC code (Consortium 1996b) with the following purposes:

1. Identification of plastic zones

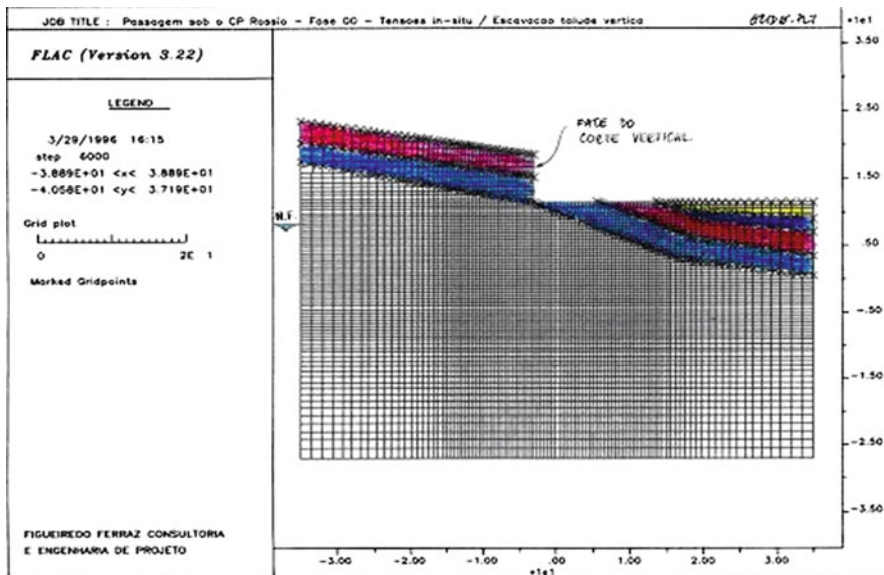


Fig. 17.3 Phase 1 (Adapted from Consortium 1996b)

2. Computation of displacements distribution
3. Distribution of stresses and strains in the retaining walls

The analysis of the principal wall was performed with the following phases:

1. Calculation of the ground initial stresses
2. Introduction of the effect of masonry retaining wall
3. Remotion of the material near Rossio station structure
4. Introduction of the linear elements of the building
5. Introduction of the effect of the retaining wall

The results obtained for the different phases are presented in Figs. 17.3, 17.4, 17.5, and 17.6.

17.5.3 Seismic Analysis

The seismic action was based on the Portuguese Code (RSA 1983) and defined by a stochastic gaussian stationary vectorial process (two horizontal orthogonal components and one vertical component). The Portuguese territory is affected by two seismotectonic sources: (1) near source, which represents a moderate magnitude earthquake at a short focal distance with a duration of 10 s; and (2) far source, which represents a higher magnitude earthquake at a longer focal distance with a duration of 30 s.

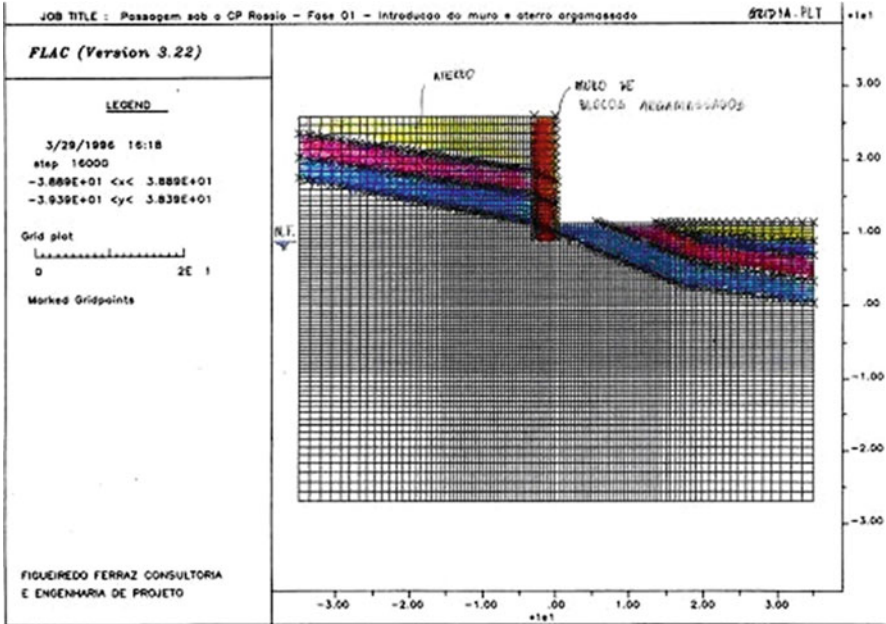


Fig. 17.4 Phase 2 (Adapted from Consortium 1996b)

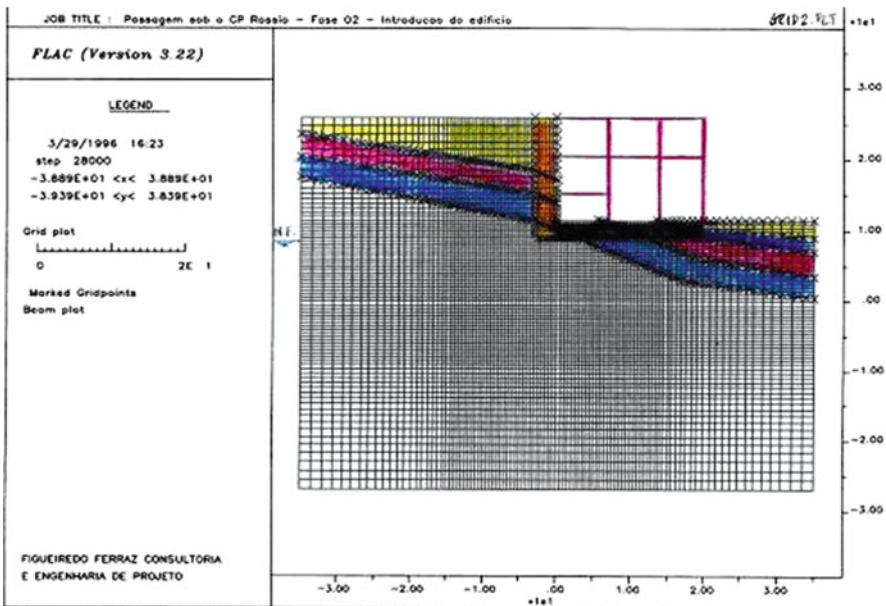


Fig. 17.5 Phase 4 (Adapted from Consortium 1996b)

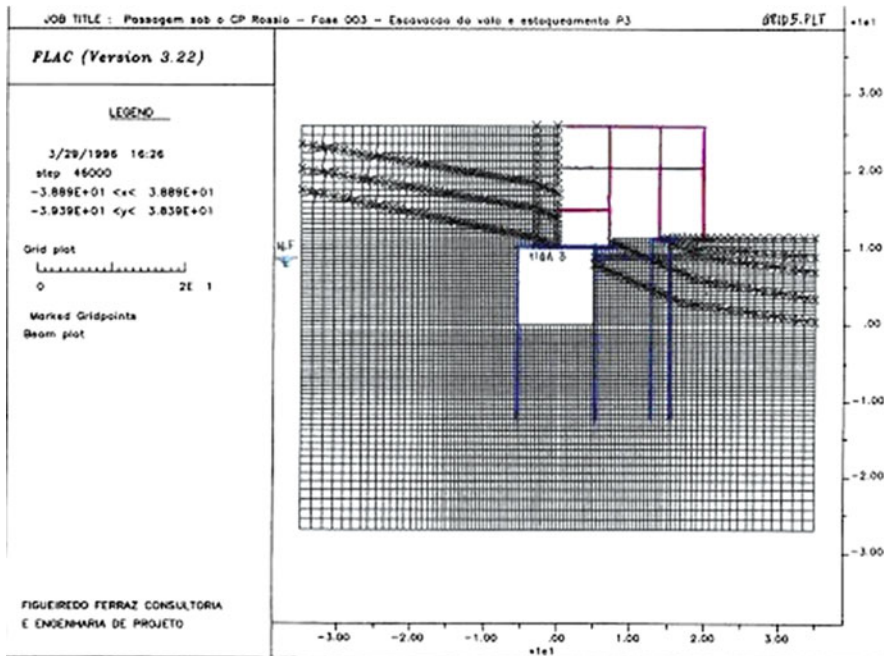


Fig. 17.6 Phase 5 (Adapted from Consortium 1996b)

In Eurocode 8 (1998) the seismic hazard is described in terms of a single parameter, that is, the value a_g of the effective peak ground acceleration in rock or firm soil called “design ground acceleration” expressed in terms of:

1. The reference seismic action associated with a probability of exceeding (PNCR) of 10 % in 50 years;
2. A reference return period (TNCR) = 475 years. These recommended values may be changed by the National Annex of each country.

The earthquake motion in EC 8 is represented by the elastic response spectrum defined by three components. The following factors can be listed to explain the behavior of gravity retaining structures during an earthquake:

1. Increase of dynamic earth pressures
2. Variation of hydrodynamic pressure of the backfill
3. Decrease of stabilizing forces related to the weight of the structure
4. Increase of pore pressures and consequently reduction of effective pressures
5. Soil liquefaction of backfill and/or foundation material

The stability of soil foundation shall be assessed for the following two conditions: overall stability and local soil failure.

For the pseudostatic analysis of rotating structures the seismic coefficients can be taken as (Eurocode 8 1998):

Table 17.3 Factor affecting the horizontal seismic coefficient (Eurocode 8 1998)

Type of retaining structure	r
Free gravity walls that can accept a displacement $d_r \leq 300\alpha$ S(mm)	2
As above with $d_r \leq 200\alpha$ S(mm)	1.5
Flexural RC walls, anchored or braced walls, RC walls founded on vertical piles, restrained basement walls and bridge abutments	1.0

$$k_h = \frac{\alpha_{gr}\gamma_f S}{gr} \quad (17.2)$$

$$k_v = \pm 0.5k_h \quad (17.3)$$

when the ratio α_{vg}/α_{gr} is greater than 0.6. Otherwise,

$$k_v = \pm 0.33k_h \quad (17.4)$$

where α_{gr} is the peak ground acceleration, α_{vg} is the vertical component of acceleration, S is the soil parameter, γ_f is the importance factor of the structure, and factor r takes the values listed in Table 17.3.

In Rossio station, the following values were adopted: for the near source, $k_h = 0.27$ and $k_v = 0.135$; for the far source, $k_h = 0.16$ and $k_v = 0.08$.

The earth pressure coefficients were computed by the Mononobe and Okabe method.

17.5.4 Experimental Tests

Three types of on-site anchorage tests are usually considered:

1. Investigation tests
2. Suitability tests
3. Acceptance tests

The lack of results of system tests to evaluate the long-term behavior of anchorages of the type that was intended to be used in Rossio station also required a test of this type to be performed in one anchorage. According to standard EN 1537, "Execution of special geotechnical work – Ground Anchorages," a test of this type requires the excavation of the anchorage after the load protocol has been carried out, and so this anchorage had to be built outside the station.

Investigation tests were needed to establish for the designer, in advance of the installation of the working ground anchorages, the ultimate load resistance in relation to the ground conditions and materials used.

Suitability tests were carried out to confirm the acceptable creep and load characteristics at proof and lock-off load levels, following the procedure recommended in the above mentioned EN 1537 (1994).

Table 17.4 Coefficient ξ for determination of R_{ak} (Eurocode 7 1997)

Number of suitability tests	1	2	>2
(a) coefficient ξ applied to the mean value R_{am}	1.5	1.35	1.3
(b) coefficient ξ applied to the minimum value R_{am}	1.5	1.25	1.1

For the determination of the anchorage characteristic load value R_{ak} , from R_{am} values measured in one or more suitability tests, a reduction factor was used to take into account the variability of ground and the constructive procedure. As minimum both conditions (a) and (b) from Table 17.4 were satisfied using equation:

$$R_{ak} = \frac{R_a}{\xi} \quad (17.5)$$

The calculation of the anchorage strength R_{am} , obtained from suitability tests considers the two modes of failure and the creep limit load.

The design value R_a , is given by equation:

$$R_a = \frac{R_{ak}}{\gamma_m} \quad (17.6)$$

where $\gamma_m = 1.25$ for temporary ground anchorages and $\gamma_m = 1.5$ for permanent ground anchorages.

The total length of the permanent anchorages is 18 m with a tendon free length of 9 m and a fixed tendon length bonded to the ground by grout of 9 m measured in one or more suitability tests. The six steel cables tendon has a cross-sectional area of 592.2 mm².

For each load test the anchorages were loaded in four incremental cycles from a datum load to a maximum test load, with measurement of displacements of the anchorage head. Displacement values caused by creep were also determined.

Figures 17.7, 17.8, 17.9, and 17.10 related to the anchor A02 show the applied loads versus anchorage head displacements, the applied loads versus elastic and permanent displacements, the displacement values versus time, and the ks values for the evaluation of creep, for the suitability test of an anchorage of the principal wall.

Measurement of electrical resistance between an anchorage and the surrounding soil or structure to determine the effectiveness of the applied corrosion protection system was also performed.

17.6 Retaining Wall of Bairro Alto

The results of some of the anchor tests are summarized in Table 17.5.

The total length of the permanent anchorages is 18 m with a tendon free length of 9 m and a fixed tendon length bonded to the ground by grout of 9 m. The 6 steel cables tendon has a cross-sectional area of 592.2 mm².

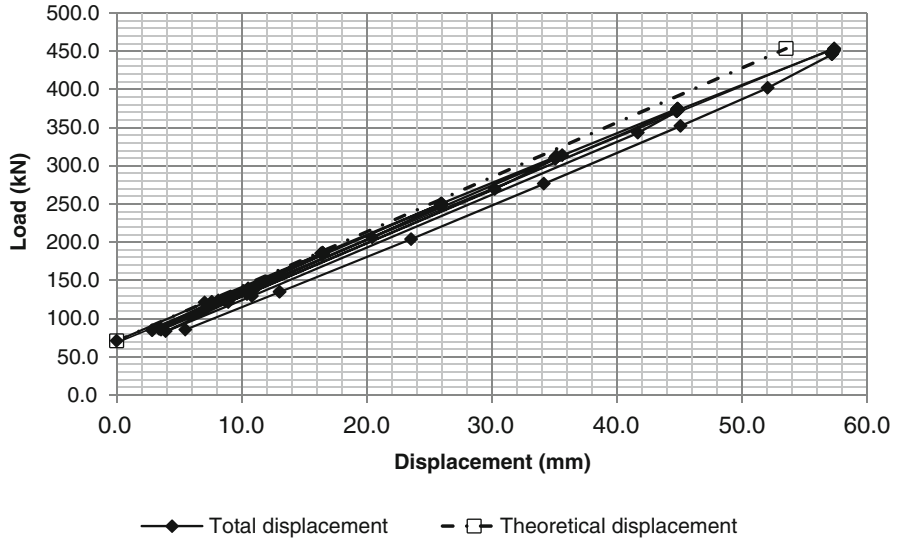


Fig. 17.7 Applied loads versus displacement for Principal Wall anchor A02

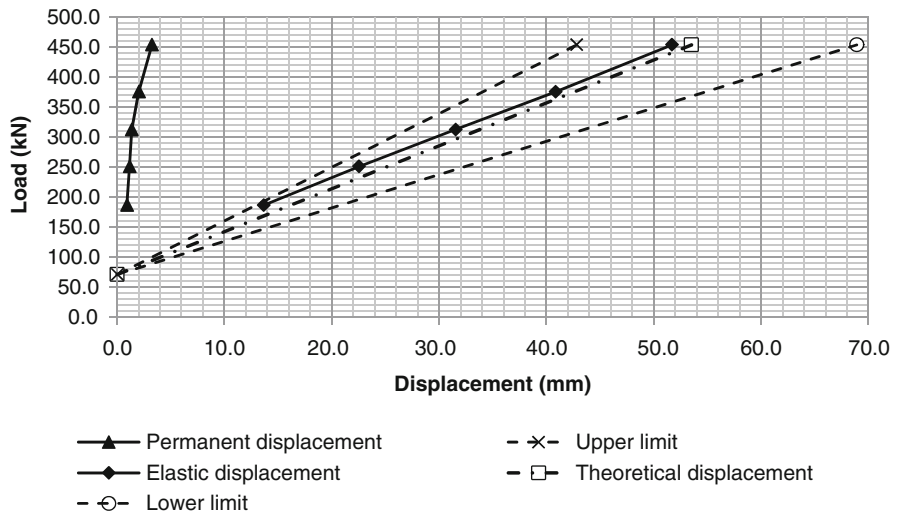


Fig. 17.8 Applied loads versus elastic and permanent displacements for Principal Wall anchor A02

The results of investigation testing of anchor A19F3 are shown in Figs. 17.11, 17.12, 17.13, and 17.14. The results of suitability testing of anchor A6F2 are shown in Figs. 17.15, 17.16, 17.17, and 17.18.

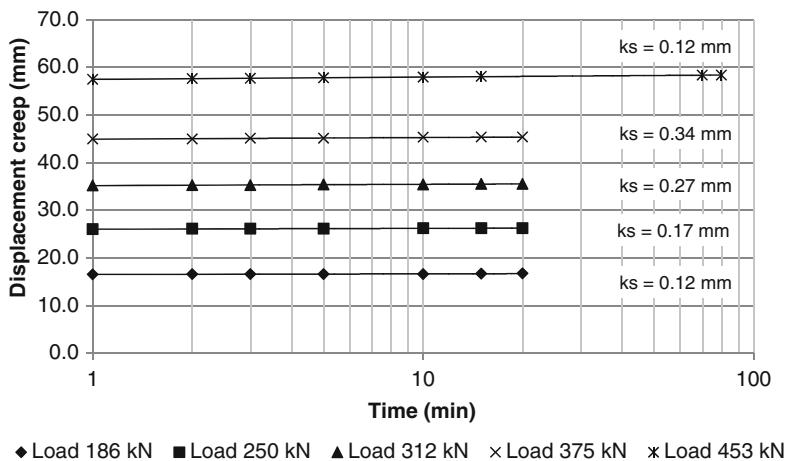


Fig. 17.9 Displacements versus time for Principal Wall anchor A02

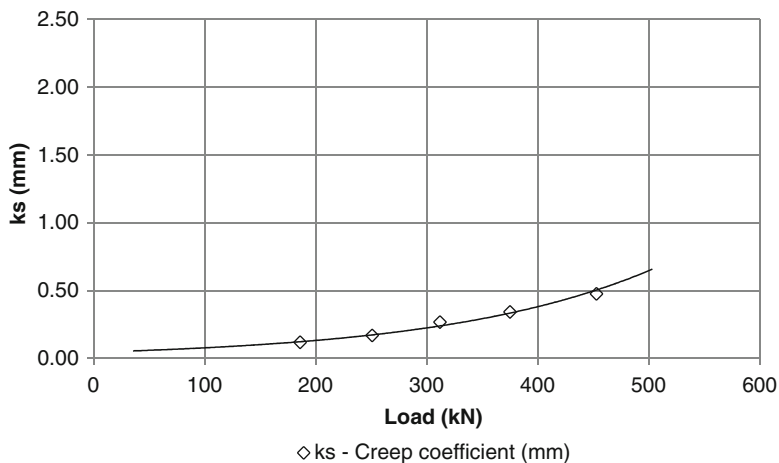


Fig. 17.10 Values of ks for Principal Wall anchor A02

17.7 Corrosion Protection Tests

In permanent anchors the integrity of the pregrouted encapsulation shall be proven in order to detect:

1. The existence of voids
2. The existence of longitudinal fissures
3. The existence of transverse fissures
4. Following EN 1537 (1994): (1) in the encapsulation zone a minimum cover of 5 mm shall be provided; (2) exterior to corrugated duct, a minimum cover of 20 mm shall be provided; (3) anticorrosive protection of tendons shall be provided.

Table 17.5 Anchorage tests

Anchor	Max. force (kN)	Max. disp. (mm)	Permanent disp. (mm)	Test method	Initial free length (m)	Calculated free length (m)	Max. <i>k_s</i> (mm)
A02	453.3	57.38	3.25	Accep. T	15.6	16.0	0.34
A14	453.0	89.19	14.05	Accep. T	21.3	21.2	0.60
A21	459.0	86.27	14.97	Accep. T	21.3	20.3	0.91
A35	456.0	77.33	16.16	Accep. T	21.3	17.9	0.70
A2F3	619.8	127.50	19.18	Accep. T	21.0	20.8	0.64
A6F2	623.3	110.35	5.36	Suitab. T	21.4	20.7	0.63
A8V	728.1	130.33	16.87	Accep. T	21.0	17.6	0.58
A13F1	581.7	189.50	65.52	Accep. T	25.6	25.6	0.53
A16F1	673.9	149.49	32.89	Inv. T	21.0	20.0	0.32
A18V	642.5	122.27	5.79	Accep. T	21.0	20.8	1.07
MBA19F3	629.3	119.14	5.5	Inv. T	21.4	17.9	0.63

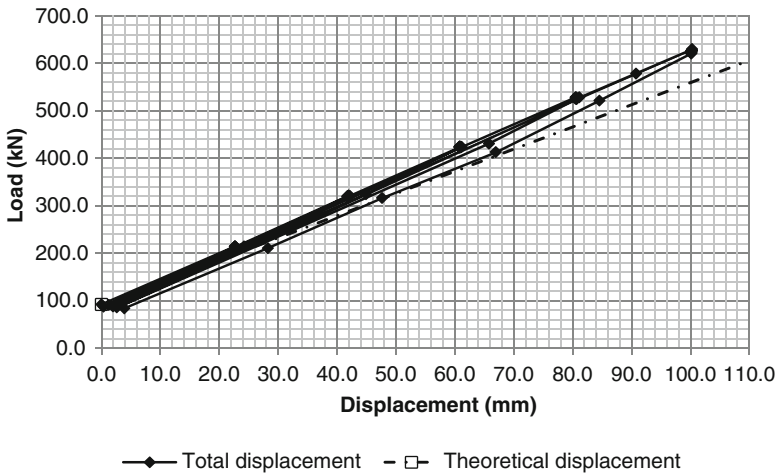


Fig. 17.11 Applied loads versus displacement for Bairro Alto Wall anchor A19F3

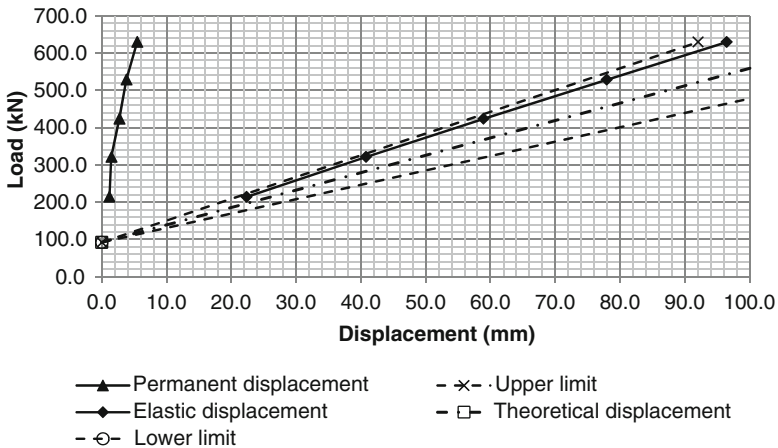


Fig. 17.12 Applied loads versus elastic and permanent displacements for Bairro Alto Wall anchor A19F3

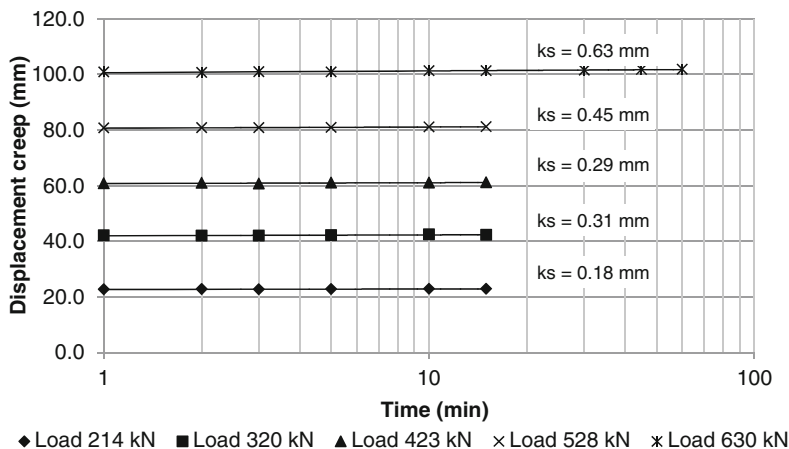


Fig. 17.13 Displacements versus time for Bairro Alto Wall anchor A19F3

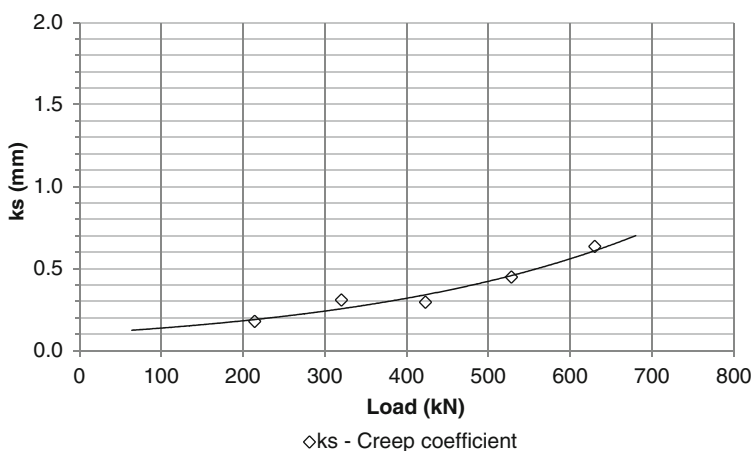


Fig. 17.14 Values of k_s for Bairro Alto Wall anchor A19F3

- In addition, electrical resistivity tests shall provide a minimum value of 100 kΩ between tendon and ground.

Water samples shall be taken for the determination of pH value and concentration of ionic sodium, magnesium, and potassium.

In summary, the corrosion protection systems tests aim to test the corrugated duct and the internal and external protections.

A detailed suitability test shall also be performed. The check list includes:

- Thickness of the grout and behavior of the spacers
- Position of the tendon

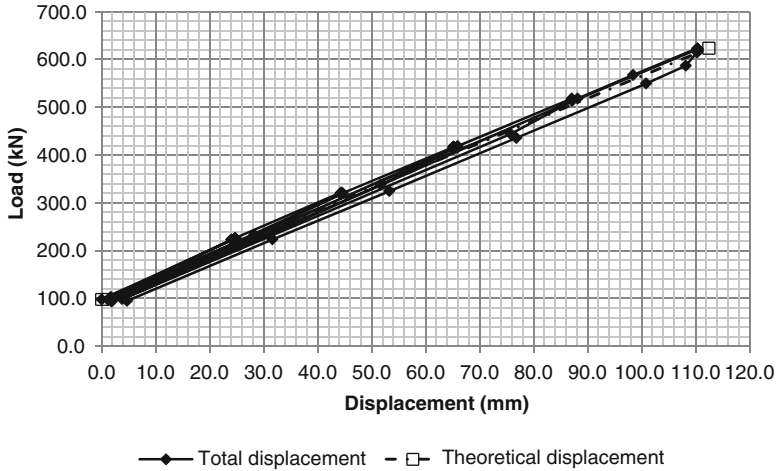


Fig. 17.15 Applied loads versus displacement for Bairro Alto Wall anchor A6F2

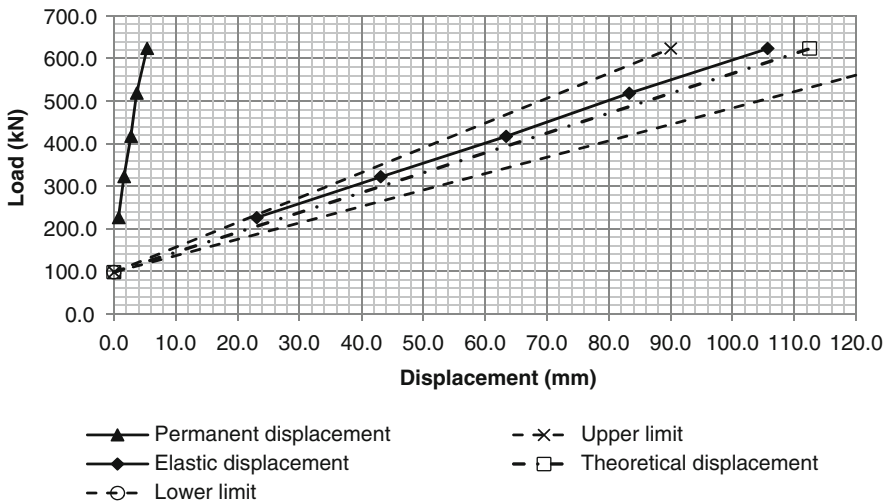


Fig. 17.16 Applied loads versus elastic and permanent displacements for Bairro Alto Wall anchor A6F2

The properties of grouts such as density, viscosity, exudation, and setting time shall be verified.

During grouting, grouting pressure and grouting volume shall be controlled.

The results of the investigation test are shown in Figs. 17.19, 17.20, 17.21, and 17.22.

After the anchor load test the anchor shall be excavated and the different anchor elements, namely head, tendon, and grout body, shall be observed.

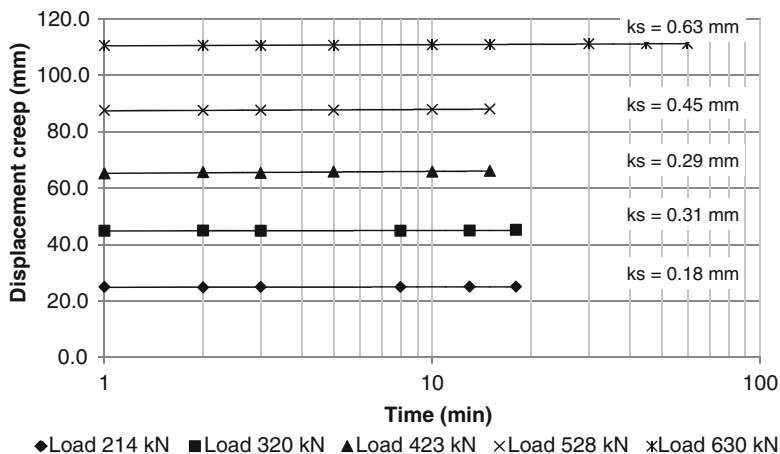


Fig. 17.17 Displacements versus time for Bairro Alto Wall anchor A6F2

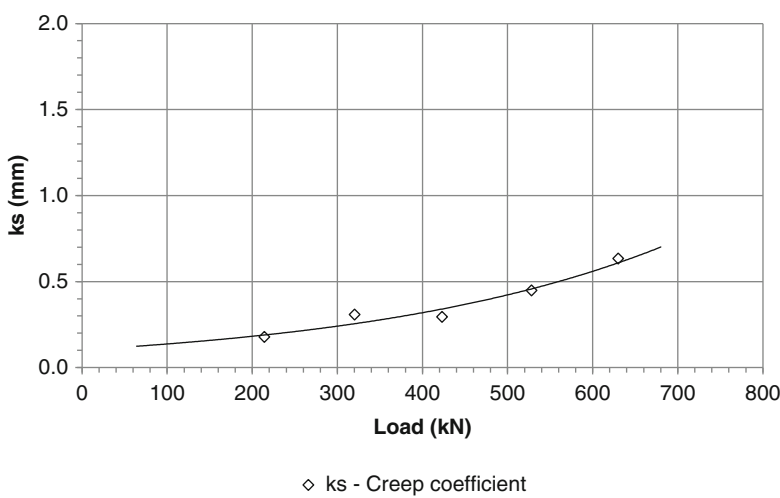


Fig. 17.18 Values of ks for Bairro Alto Wall anchor A6F2

The measurements of electrical resistivity allow the checking of the protective barrier of the steel tendon from the ground and the protection of the anchor head.

Figures 17.23, 17.24, 17.25, and 17.26 show photos representative of the steel tendon protection at different phases of the test.

The visual inspections have shown:

1. A good encapsulation
2. No direct contact between anchor head and reinforcement steel of the anchored structure

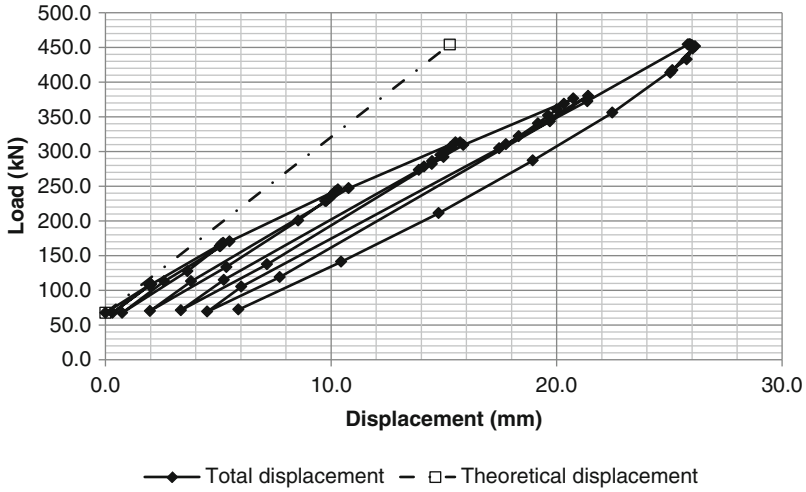


Fig. 17.19 Applied loads versus displacement

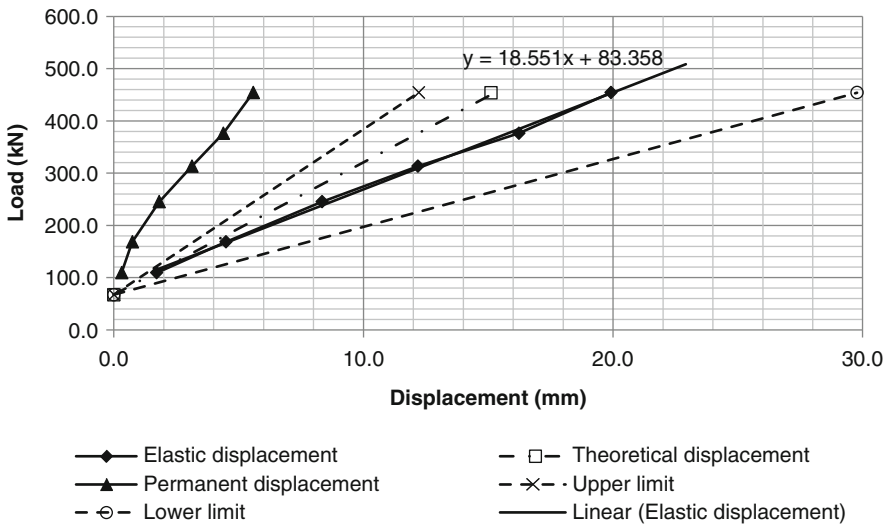
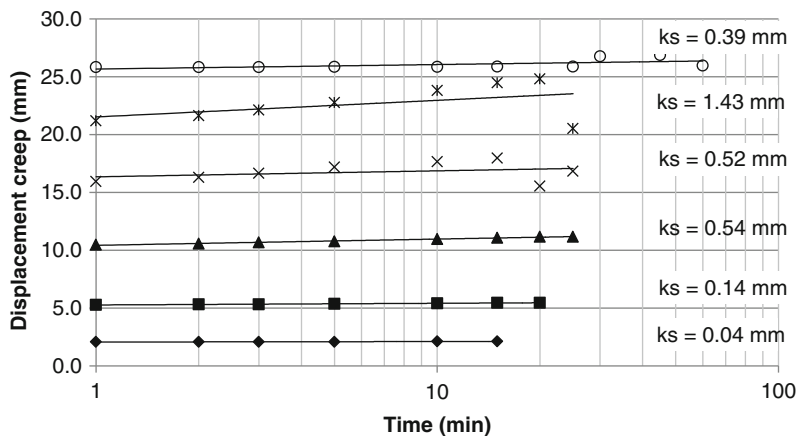


Fig. 17.20 Applied loads versus elastic and permanent displacements

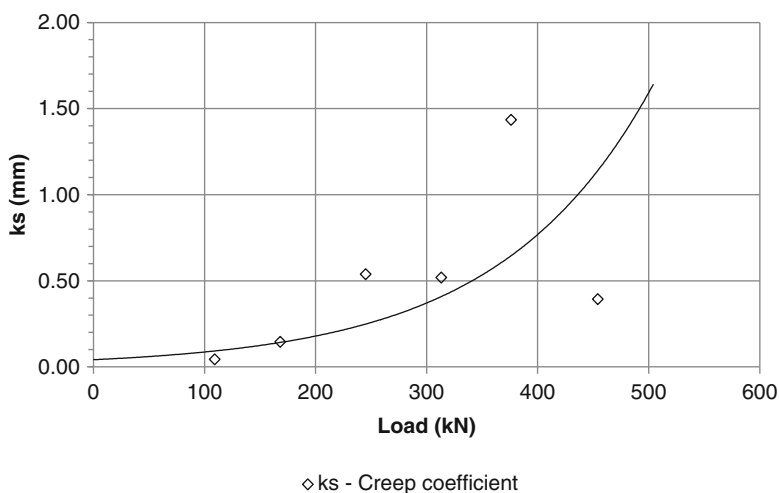
- 3. In some sections there was no minimum cover of 5 mm between the duct and bar
- 4. No cracks were observed in the grout body exterior to the manchette tube

The tests have shown a good overall electrical isolation of the anchor from ground and structure.



◆ Load 109 kN ■ Load 168 kN ▲ Load 245 kN × Load 313 kN * Load 376 kN ○ Load 454 kN

Fig. 17.21 Displacements versus time



◇ ks - Creep coefficient

Fig. 17.22 Values of ks

17.8 Evaluation of the Station Building Behavior

To study the effects of interaction of the underpinning works (including the already mentioned retaining walls) with the Rossio station building, a 3D linear finite element analysis, using SAP 90 code, to predict the maximum stresses and strain values, was performed (Consortium 1996c).



Fig. 17.23 Anchor excavation



Fig. 17.24 Close view of anchor excavation



Fig. 17.25 Transverse section of the anchor



Fig. 17.26 Longitudinal section of the anchor

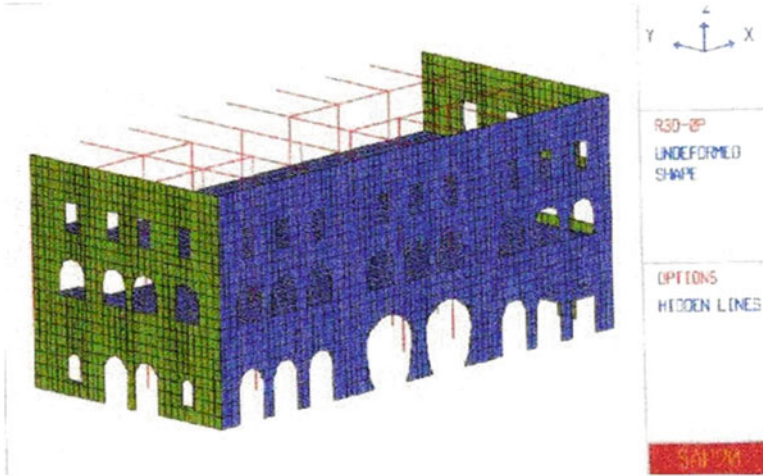


Fig. 17.27 3D model (Adapted from Consortium 1996c)

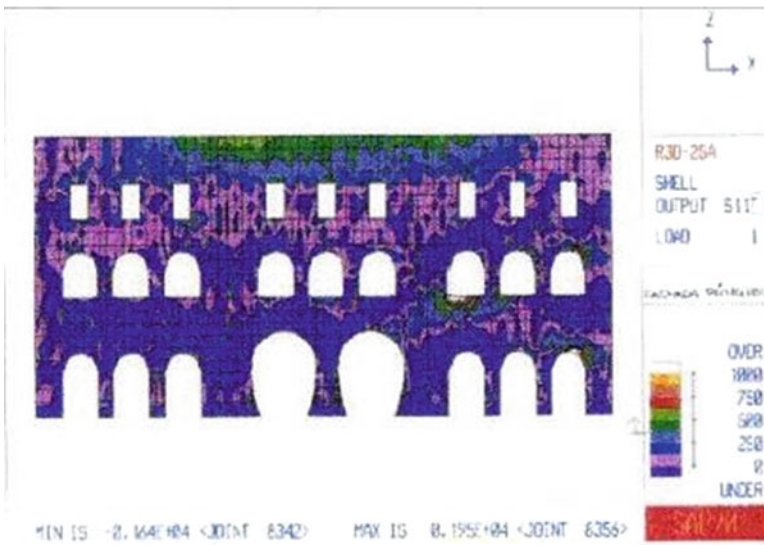


Fig. 17.28 Horizontal stress distributions of principal façade (Adapted from Consortium 1996c)

For the calcareous stone of the façade the following parameters were adopted: unit weight: 25 kN/m³; elasticity modulus: 30 GPa; poisson ratio: 0.26; and tension failure stress 1,000 kPa.

Two numerical analyses were performed:

1. The first analysis simulated the former situation of the building and can be considered as a reference.



Fig. 17.29 Vertical stress distribution of principal façade (Adapted from Consortium 1996c)

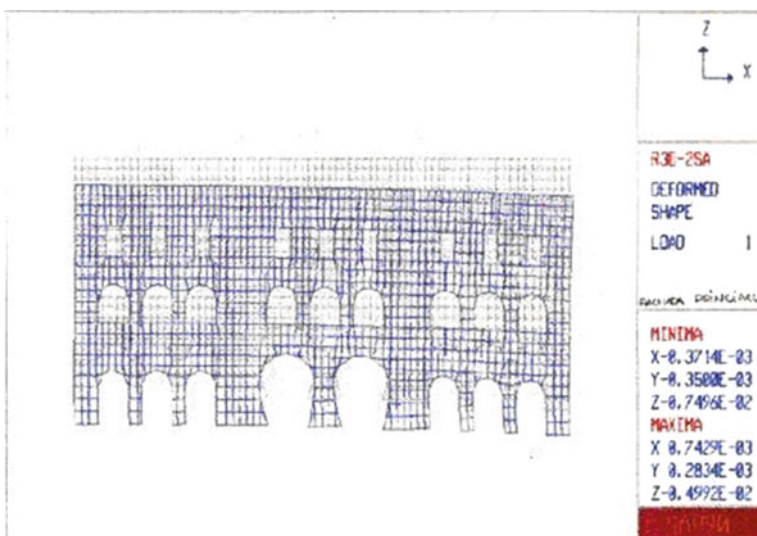


Fig. 17.30 Deformations of principal façade (Adapted from Consortium 1996c)

2. The second analysis simulated the final phase after the reinforcement.

Figure 17.27 shows the finite element mesh. Figure 17.28 shows the horizontal stress distribution of principal façade. Figure 17.29 shows the vertical stress distribution of principal façade. Figure 17.30 shows the deformations of the principal façade.

It is important to remark that:

1. The Rossio station building has a historical and patrimonial value.
2. One important purpose was to minimize the damages, even the nonstructural ones.
3. The predictable damages were extensive cracks on façades of stonework.
4. The rehabilitation work in these kinds of cases is delicate and costly.
5. The negative impact on population caused by the damages related to underground work is relevant.

17.9 Monitoring and Environmental Impacts

To control the structure behavior a monitoring system was installed, including the following types of instruments: clinometers, extensometers, surface movement points, and inclinometers. Some anchorages were also instrumented with load cells.

To minimize the environmental impacts the following actions were taken:

1. Protection of anchorage tendons and micropile reinforcements against electric currents
2. Control of vibrations caused by drilling work

As an example of the monitoring readings, obtained to build the tied back walls referred in Fig. 17.1, some results are presented in Figs. 17.31, 17.32, 17.33, and 17.34.

Figure 17.31 describes the evolution of horizontal displacements measured in one inclinometer tube. For the monitoring of anchors the instrumentation included a logger. Details of the logger are shown in Figs. 17.32 and 17.33. The results measured by the logger are shown in Fig. 17.34.

17.10 Conclusions

The following conclusions can be drawn:

1. The selected enlargement and underpinning solutions allowed the construction of the underground gallery for the Lisbon Metro and excessive damages in the station building and in other structures were avoided. This solution enabled the use of the railway platforms of the station without any major constraints.
2. The numerical analyses with simulation of the construction phases allowed the calculation of the stresses and strains distributions and also the identification of

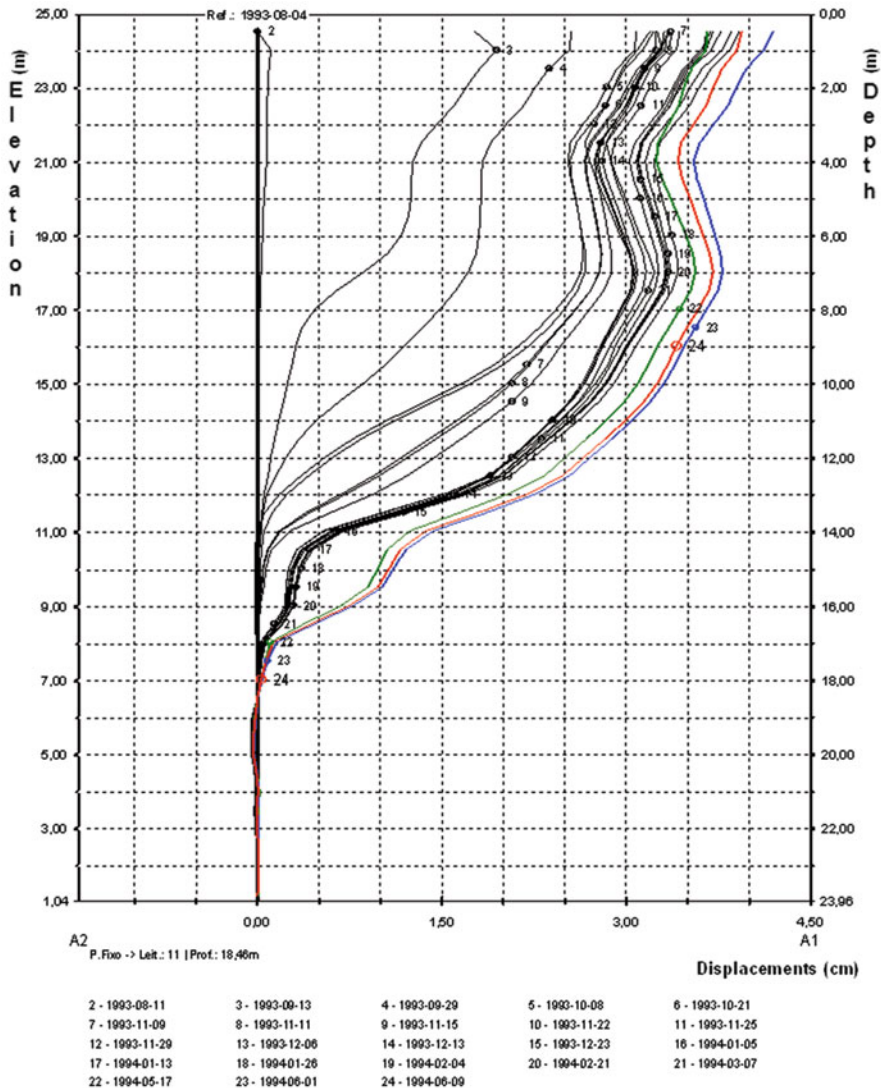


Fig. 17.31 Evolution of horizontal displacements in one inclinometer tube

the plastic zones. The analyses of the alternative solutions were of great importance to select the one that was retained in each zone.

3. The need to reinforce both main retaining walls against rotational failure arose from the lack of safety conditions for this scenario, which was identified during the design analyses for the underpinning of the station.

Fig. 17.32 Logger**Fig. 17.33** General view of equipment

4. The tests performed for the anchorages of the reinforcement works of the two main walls supported the design of these works and allowed an adequate quality control.
5. The corrosion tests to assess the behavior of permanent anchors have shown a good overall electrical isolation of the anchor from ground and structure.
6. The 3D finite element linear analyses to predict the maximum stresses and strain distributions of the Rossio station building were important to analyze the damages and to guide the rehabilitation work.
7. The monitoring of the structures during construction allowed the safe implementation of the solutions including the purpose of maintaining most of the station functionality.

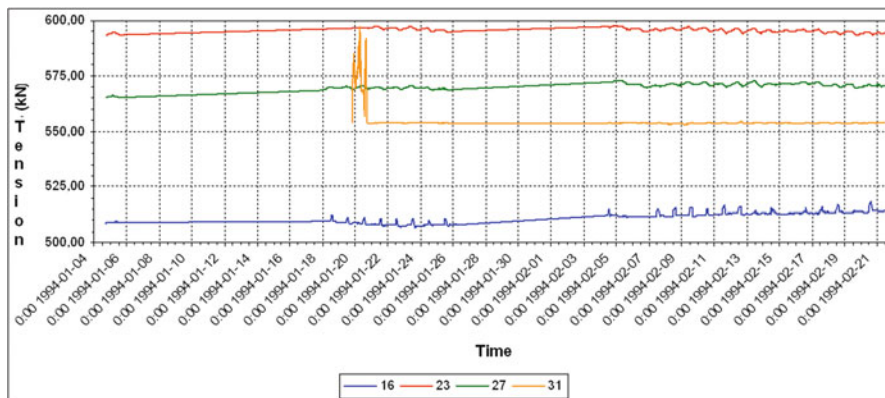


Fig. 17.34 Values of anchor loads measured by the logger

Acknowledgments Special thanks are due to REFER, EPE, and to LNEC for the permission to publish the results of old Rossio railway station. The support of Consortium and Metropolitano de Lisboa is acknowledged.

References

- Consortium (1996a) Section 60 – Restauradores-Baixa/Chiado. Geological and geotechnical report (in Portuguese). Doc. RT – 02.3-0238
- Consortium (1996b) Section 60 – Restauradores-Baixa/Chiado. Crossing under CP-Rossio. Numerical analysis of the principal retaining wall (in Portuguese). Doc. RT – 02.3-0168
- Consortium (1996c) Section 60 – Restauradores-Baixa/Chiado. Crossing under CP-Rossio. 3-D Analysis of the station building (in Portuguese). Doc. RT-02.3-0242, 31.12.96
- EN 1537 Execution of special geotechnical work – ground anchors
- Eurocode 0 (1990) Basis of structural design
- Eurocode 1 (1991) Actions on structures
- Eurocode 7 (1997) Geotechnical design-part 1. ENV
- Eurocode 8 (1998) Design of structures for earthquake resistance of structures. ENV
- European Standard EN 1537 (1994) Execution of special geotechnical work – ground anchors
- RSA (1983) Regulamento de Segurança e Acções para Estruturas de Edifícios e Pontes. Decreto-Lei nº 235/83 de 31 de Maio
- Seco e Pinto PS, Barradas J, Sousa A (2008) Lessons learned from two case histories of retaining structures. In: 5th international conference on case histories in geotechnical engineering, Arlington, 2008

Chapter 18

Analysis of Slope Stability and Landslide in Seismic Active Regions

Askar Zhussupbekov, Rauan Ermagambetovich Lukpanov,
Serik Beisengalievich Yenkebayev, and Vitaliy Analolievich Khomyakov

18.1 Introduction

Almaty is the previous capital of Kazakhstan, located in the foothills of Zailiyskogo AlaTau Mountain in a seismically active region. It has a steepness of mountain slope more than 15° , and the degree of seismic activity of the region is 10 by the MSK-64 scale. The whole Almaty territory is covered by a thick network of tectonic breaches in northeasterly and northwest directions that predestines greater danger of possible earthquakes. Depending on engineering-seismological conditions, two zones stand out in the territory of the city: Zone I seismic magnitude is 9° . There are industrial and civil buildings with reinforced bearing construction. Zone II seismic magnitude is more than 9° . Zone II concerns a recreational area with different light type buildings (Khomyakov and Pustogachev 2006).

Distribution of soil is up to 40 m from the ground surface. Most of the construction of Almaty city is located on the roots of the mountains in problematic geological conditions. Soil condition present in Almaty is alluvial soil, therefore in cases of condensed construction conditions it is necessary to carefully research the physical and mechanical properties of the soil to develop recommendations for reliable construction design. The absence of areas free for construction inside of Almaty city and the attractive natural condition of the suburbs result in cutting the slopes for individual construction (private houses) near the mountain. This action provokes disturbance of water conditions of soil forming the slopes and necessitates shear

A. Zhussupbekov Ph.D. (✉) • R.E. Lukpanov Ph.D. • S.B. Yenkebayev Ph.D.
Department Civil Engineering, Eurasian National University of L.N. Gumilyov,
106 room, 5 Munaitpasov str., Astana 080010, Kazakhstan
e-mail: astana-geostroi@mail.ru; rauan_82@mail.ru; yenkebayev-serik@mail.ru

V.A. Khomyakov
Department Civil Engineering, The Kazakh Leading Academy of Architecture and Civil
Engineering (KazGASA), KazGASA, 210a room, 28 Ryskulbekov str., Kazakhstan
e-mail: khomyakov57@list.ru

strength research while taking into account natural state and mineralogical consist. The aforementioned conditions explain the urgency of this research.

Principal causes of landslide formation are the following: outflow of water from engineering communications; soil humidifying as a result of thawing and atmospheric precipitation; changes of durability parameters φ and C caused by changes in physical condition of the ground; changes of parameters φ and C by the dynamics of seismic activities; loading from buildings and structures; and vertical cracks in the structure of the soil forming a slope (Zhussupbekov and Khomyakov 2010).

18.2 Geological Condition of Almaty

Fluvioglacial deposits (fQI) are generally spread through the inclined flatlands and consist of coherent soil and on the depth of 120–150 m fluvial deposits presented by gravel sand soil. The principal feature of coherent soil is uniformity in both vertical and horizontal direction. Deposits commonly present in clay loam and sandy loam.

Proluvial deposits (apQII) usually spread through most parts of the territory. Proluvial deposits are present in clay loam and sandy loam with glasses of sandy soil and gravel. The principal feature of coherent soil is the presence of carbonate inclusions. In mineralogical consistence the following inclusions dominate: calcium, quarts, feldspar, mica, chlorites, kaolin, and hydrate iron.

Alluvial deposits usually are spread through terraces of rivers. The deposits are characterized by an assortment of lithologic composites and are present in sand, gravel sand, sandy loam, and loam. The thickness of the stratum varies from 2–5 m up to 30 m.

Clay soil is the most widespread type of soil. It is possible to define qualitative changes of clay depending on its age. Comparison diagrams of physical and mechanical properties of Almaty region soil are presented in Fig. 18.1.

The aforementioned information shows that clay soil is difficult to mark out definite and concrete values of friction angle and cohesion parameters. For example values of friction angle for proluvial-alluvial soil vary in range of 7° up to 58° . However, more generalized data show a range from 22° to 26° . Cohesion also has a big range from 4 to 180 kPa.

The typical exogenous processes of the region are follows:

- Erosion subsidence
- Deflationary process
- Salification process
- Bogging process

The geological profile of the Alatau slopes is presented in Fig. 18.2.

The deposited soil may present as one stratum as well as interlaced rows of layers. The placement and extension of the stratum is defined by the genesis process of the slope during a long time. The main purpose is determination of the

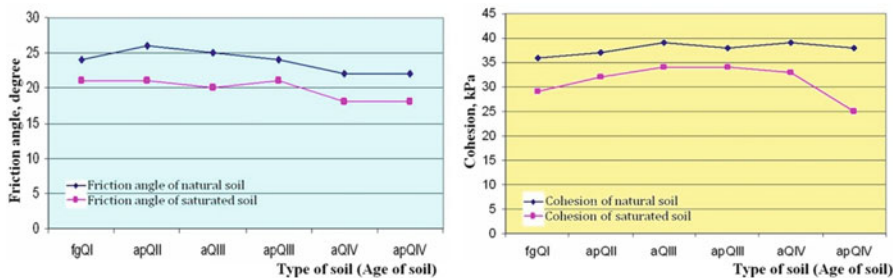


Fig. 18.1 Comparison diagrams of friction angle and cohesion

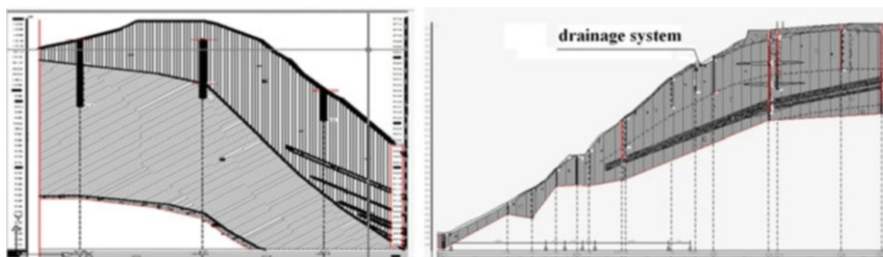


Fig. 18.2 Geological profile of AlaTau slope

placement, extension, and physical and mechanical properties of slope soil Malyshevsky and Khomyakov (2009) and Khomyakov et al. (2010).

Research of the physical and mechanical properties has shown changing of construction properties of slopes soil during exploitation. The general causes are: avalanches, presented by zone of accumulation; ravine formation on the slopes, especially for loose soil (river area); suffusion processes for soil periodically saturating; flooding of city territory; the local flooding of inclined areas caused by engineering communications leakage and other cases of flooding by surface or ground water; the stress condition alteration of slopes caused by erection of different types of structures and buildings, and incorrect performance (construction) of retaining structures; and probable land sliding during Almaty subway construction (Khomyakov 2010a, b).

The problem of design in such soil conditions is: when designing soil constructions formed by coarse crushed stones, designers mainly use strength parameters that correspond to fine crushed stones instead of coarse. These parameters do not take into account insufficient characteristics of stones soil as a whole and the particularities of their work in construction.

The existing directions of research: strength of soil increases with growing fraction; strength of soil decreases with increase of fraction; strength is independent from fractions of soil.

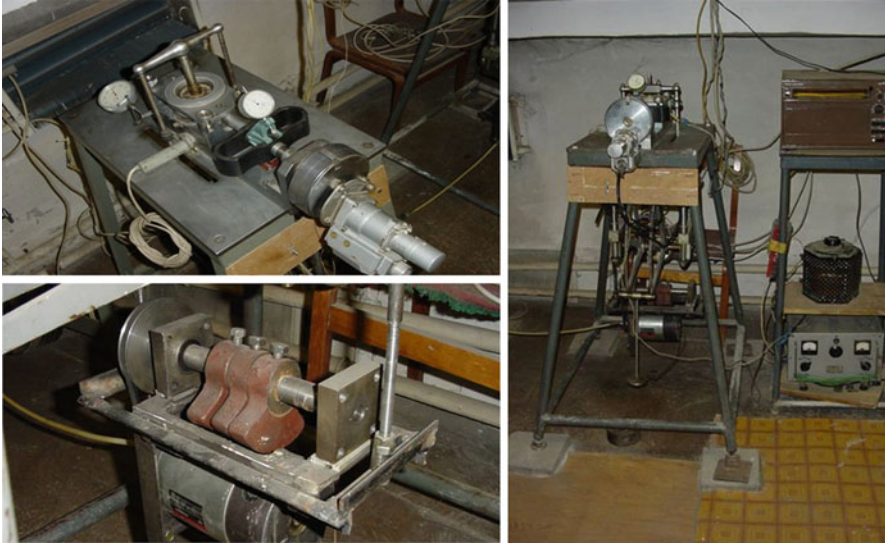


Fig. 18.3 General view of shear test equipment

18.3 Description of Experimental Equipment

Shear test equipment was used for analysis of strength parameters of soil (Fig. 18.3). The equipment used is a modified direct shear tester VCV-25 (40 cm²) and a device developed by MISI (100 cm²).

Some modification of test equipment allowed:

- Control of normal stress by dynamometer, located in lower shifted to cartridge clip
- The possibility of undertaking the test with constant, but controlled velocity of deformation
- The value of shear strain under one move of the cartridge clip of the equipment up to 15 mm
- The possibility of checking normal, tangent stress and strain at one time in the whole test process
- The possibility of repeating the test by returning the cartridge clip to the initial position

The movement of the cartridge is put into action by an electric motor with a planetary train and is constant during the test. The movement speed varies from 0.5 to 0.01 mm/min. The cartridge of the shear test equipment was changed in order to achieve a strain of 20–25 %.

The Baranov dynamometer was installed into the lower part of the stamp. The strain gages were installed for automatically recording the horizontal strain. The signal transferred constantly and was recorded by automatic system. Two

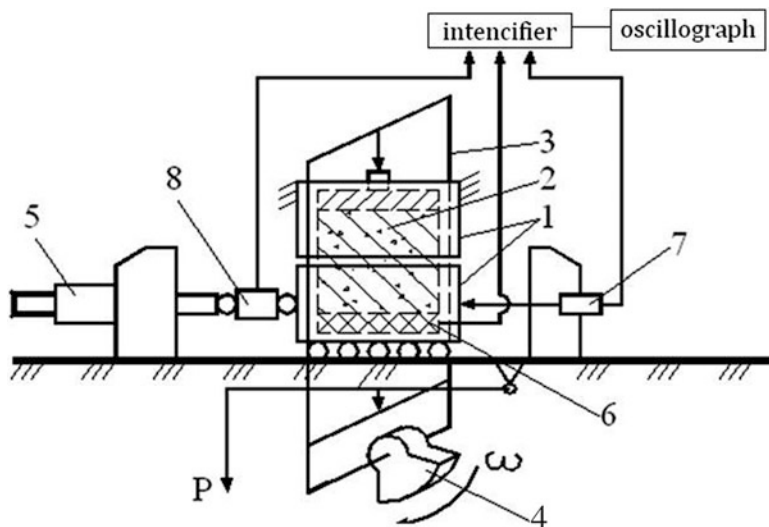


Fig. 18.4 Scheme of modified shear test equipment

transducers of ICH type were installed to monitor vertical deformation of the sample. The scheme of modified shear test equipment is presented in Fig. 18.4.

A special eccentricity rotary vibrator was constructed to create a vibrodynamic effect to the sample, working from direct current of the electromotor PJK-25/3. The general view of the eccentricity rotary vibrator is presented in Fig. 18.3. The variety of eccentricity rotary vibrator positions allows changing amplitude of impact loads. The frequency of the impact load is controlling by the automatic transformer, LATR. The magnitude of frequency is indicated by tachometer. The tachometer actuator is carried out through the cable socket of the speedometer, connected to the eccentricity rotary vibrator. Construction of the device allows creating frequency in range of 0–30 Hz (Khomyakov 2009).

One other piece of modified direct shear test equipment was used for testing coherent, sandy and gravel soil with a fraction less than 20 mm—SP-100. The general view and scheme of modified direct shear test equipment is presented in Fig. 18.5.

This equipment provides more uniform distribution of stresses, acting in shear plane by symmetrical action of normal N and tangent T stresses. Increasing the thickness of the equipment wall up to 20 mm has allowed raising the values to shear strain up to 20 %. The general parts of this equipment are the lower and upper parts of the cartridge clip. The dimension of a soil specimen is 100 cm² in cross-section and 10 cm in height. The specimen is placed inside the cartridge clip.

Construction of the equipment provides uniform normal pressures to the specimen of soil and thereby provides homogeneity of the stress condition of the soil in shear plane. Equipment allows testing of the soil with fraction up to 20 mm.

Fig. 18.5 General view and scheme of modified shear test equipment SP-100

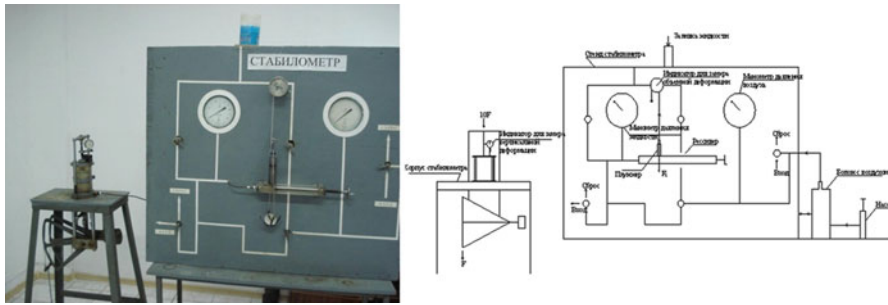


Fig. 18.6 General view and scheme of developed triaxial test equipment

The shear moving of soil specimen comes at constant velocity, but might be controlled at times and might be changed from 0.5 to 0.01 mm/min.

Triaxial test equipment, developed at KazGASA, is presented in Fig. 18.6. The general difference from traditional triaxial equipment is a compensator of the piston type with built-in plunger for checking the three-dimensional deformation change, Khomyakov (2010a, b).

18.4 Results of Laboratory Testing

The purpose of the laboratory test is to analyze how mineralogic contents influence the strength parameters of soil corresponding to the residual effects. Minerals forming clay and sand soil of Almaty were extracted for testing. It was found by petrographic analysis that the basic mineral forming the Almaty soil is quartz (SiO₂), ranging up to 90–99 %. From the aforementioned it follows that quartz has a big influence for the residual strength parameters of sand soil and kaolin, montmorillonite, and mica for the clay soil. It was chosen to test the following

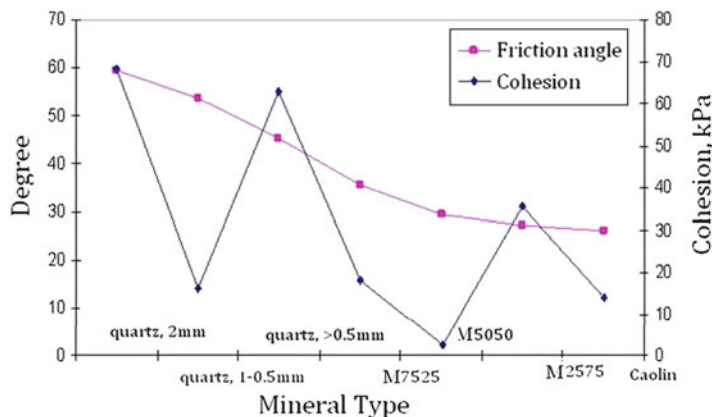


Fig. 18.7 Dependence strength parameters from mineralogical contents (peak values)

mixture of soil: crushed minerals of quartz by fraction of 2–1 mm, 1–0.5 mm, and less than 0.5 mm; kaolin powder in dry condition; three mixtures made from quartz, by fraction less the 0.5 mm and kaolin (mixture 1—sand 75 % and kaolin 25 %—M75-25, mixture 2—sand 50 % and kaolin 50 %—M50-50, mixture 3—sand 25 % and kaolin 75 %—M25-75). The peak friction angle according to results of tests equal 30.5° for kaolin and residual friction angle equals 26.7° . After many tests were performed, it was found that decreasing the sand fraction from coarse to fine, from sand to kaolin resulted in smooth, stepped decreasing of friction angle from 60° to 30° . Cohesion changed spasmodically in discrete steps but tendency of decrease is reviewed (Fig. 18.7). The residual resistance was characterized by insignificant range of friction angle changing (Fig. 18.8).

For different fractions, quartz changed only 4° . The fluent stepped decreasing of friction angle is reviewed for the mixtures depending on the quartz contents. For mixture 2—sand 50 % and kaolin 50 %—friction angle is changed only $4\text{--}5^\circ$, but cohesion is extremely changed. Results obtained show that mineralogical content has a big influence on the strength parameters of soil.

For analysis of dynamic loading to the peak and residual strength parameters it was decided to use typical region clay sediment on the construction site, “Complex of the ski jumps in Remizovka canyon, Almaty.” The clay is placed to a depth up to 40 m.

Tested soil is subjected to static and dynamic loads. Static load is organized under the normal stress of 100, 200, and 300 kPa. Dynamic load is organized under the normal stress of 100, 200, and 300 kPa. The dynamic value has formed accordingly 20, 15, and 10 % from static value. The exact value of the vertical load increment was defined by records obtained by measuring equipment. Results of dynamic and static tests are presented in Figs. 18.9 and 18.10.

Consider that action of vibrations superimposes additional influence on the stress condition of a soil specimen. During the processing of data for the base, an accepted condition is that determination of stress–strain conditions is produced

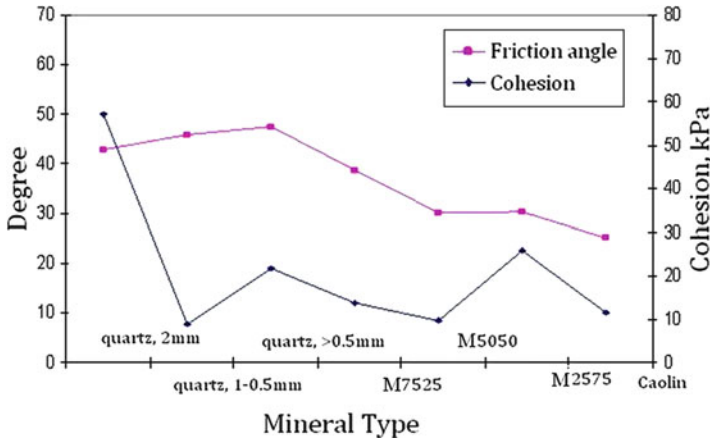


Fig. 18.8 Dependence strength parameters from mineralogical contents (residual values)

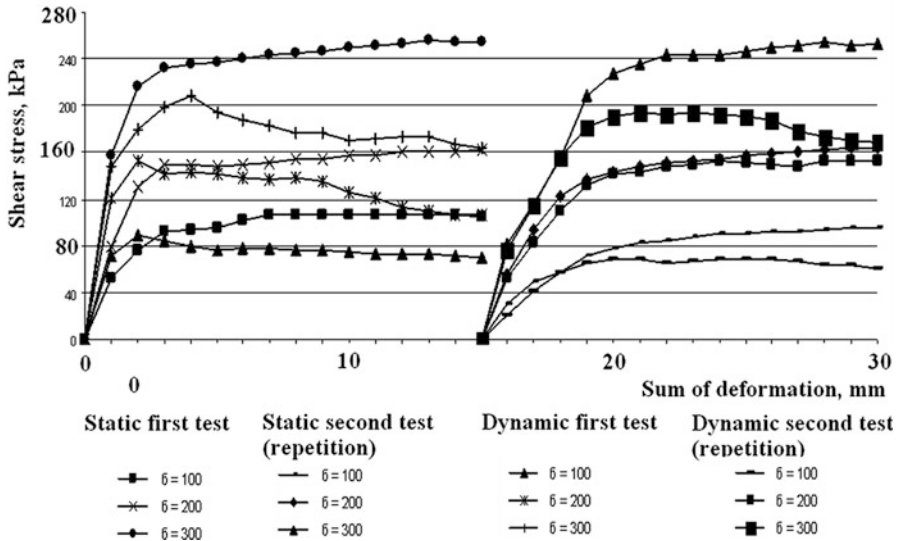


Fig. 18.9 Dependence between deformation and shear stress

with provision for amplitude change of the normal stress. The equation of ultimate equilibrium:

$$\tau_{ult} = (\sigma_{avg} - \alpha \cdot \Delta\sigma_n) \operatorname{tg}\varphi_k + c_k, \tag{18.1}$$

where σ_{avg} —an average for period value of normal stress; $\Delta\sigma_n$ —the amplitude change of normal stress; φ_k и C_k —parameters of strength corresponding to condition of dry friction of the Coulomb; α —the factor characterizing change in the internal relationships of the soil by dynamic, which can change from -1 up to $+1$.

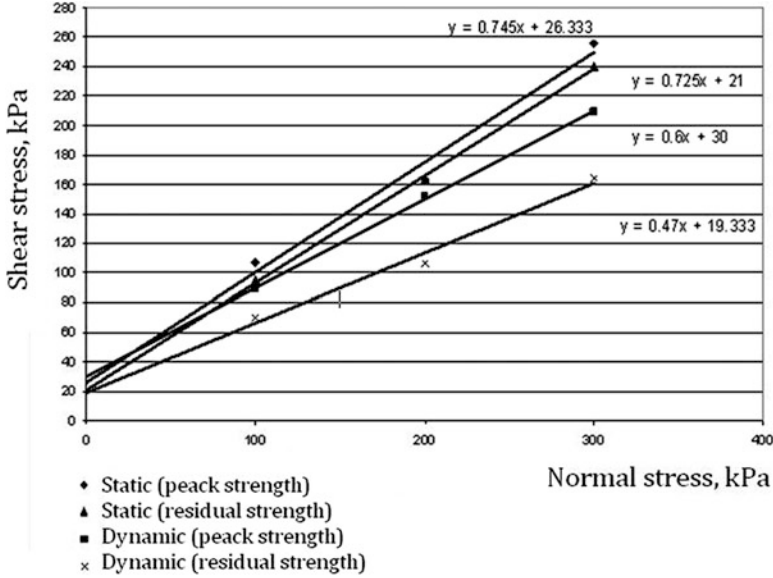


Fig. 18.10 Diagram of critical state

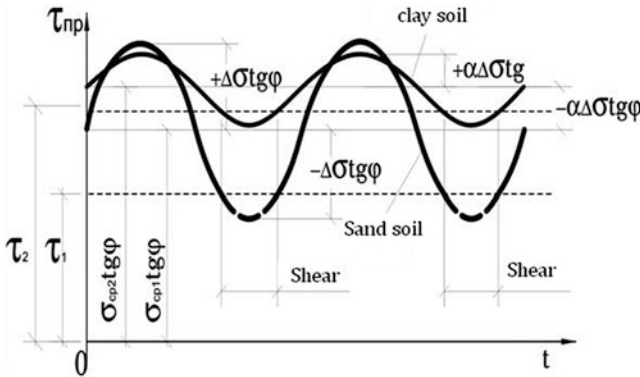


Fig. 18.11 Normal and shear stresses changing under dynamic loads

The physical meaning of this coefficient is the influence of vibration, which inflicts additional stress to the soil specimen and results in changes of stress through the vertical direction. The values of coefficient α depend on type of soil and its condition and may vary from -1 to $+1$, Fig. 18.11.

The vibration action leads to change in the shear strength of soil; the change is connected with influence of the vibrations on the stress–strain condition of a soil specimen. Shear deformation occurs most often when the average stress changes, aside from reduction. The vibration in clay soil not only can reduce, but also increase shear strength by means of inertia of internal relationships.

18.5 Modified Method of Slope Stability Analysis

According to well-known concepts, the decrease of bearing capacity of soil ground corresponds to destruction of soil structure under the load. The soil structure is disturbed much faster under dynamic loads. Therefore, the main idea is considering the soil model as an elasto-plastic model with residual parameters of strength owing to high seismic activity. This is allowed to make some correction to the values of friction angle and cohesion. The classical method of analysis assumes subdivision of the slipping section into the slides.

After that, effective total weight of the slices, G , is defined. Multiplying G of each slice into the distances (to the center of circle) r presents moment. The forces from the right side of the lines are increasing this moment (active moment) whereas forces from the left side quite the contrary are decreasing the moment (resisting moment), SNiP RK 5.01-01-2002. Therefore, from Fig. 18.12:

$$M_a = \sum_5^9 G \cdot r - \sum_1^4 G \cdot r \quad (18.2)$$

Resisting moment M_r depends on the sum of friction and cohesion forces, acting along the critical slip surface and assuming uniformity along the whole length of the circle. However, deformation is already developed in sections 8 and 9 because of cracking. This leads to decreasing strength parameters— c and φ .

The resisting moment, using concepts of peak and residual strength, might be expressed by the following equation:

$$M_r = R \left[\sum_1^n c_a l_i \right] + R \left[\sum_1^n G \cos \beta_i \operatorname{tg} \varphi_a \right] \quad (18.3)$$

where c_a and φ_a are adjusted values of strength parameters defined by peak and residual strength values of soil:

$$c_a = \frac{c_p l_r + c_{\text{res}} l_{\text{def}}}{l_r + l_{\text{def}}} \quad (18.4)$$

$$\varphi_a = \frac{\varphi_p l_r + \varphi_{\text{res}} l_{\text{def}}}{l_r + l_{\text{def}}} \quad (18.5)$$

where c_p and φ_p are strength parameters corresponding to peak strength of soil and applicable for nondeformed segments of the slope, and c_{res} and φ_{res} are strength parameters corresponding to residual strength of soil and applicable for deformed segments of the slope.

Safety factor might be determined by following equation:

$$\gamma_s = \frac{M_a}{M_r} \quad (18.6)$$

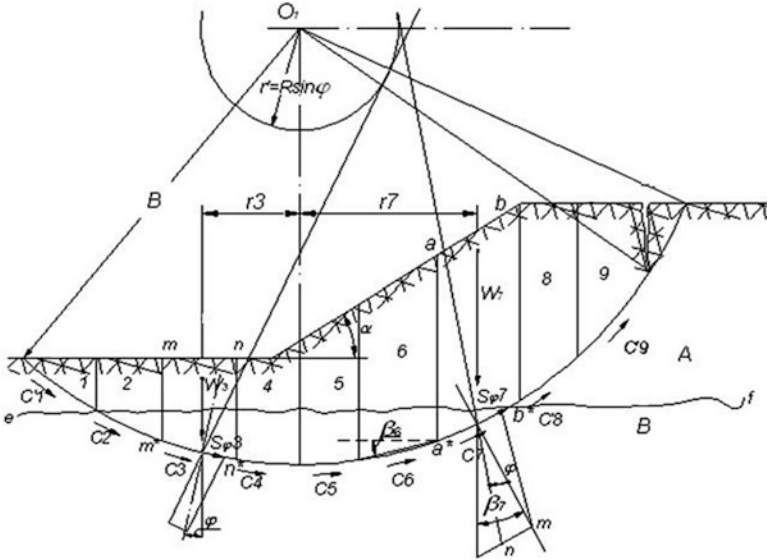


Fig. 18.12 Design diagram of stability analysis of the slope with a crack developing

It has been suggested that the initial critical state of soil forms only in the upper part of the slip surface. At the same time the slope starts to move not along the whole length of slip surface and only on zone equal 1/3–1/5 of the height of the moving zone wherein maximum tensile strength has a place.

The seismic influence within the considered soil slope is taken into account by calculation of additional horizontal forces, which are defined by multiplying the weight of the soil into the dynamic coefficient k_{hf} . The values of the coefficient take into account seismic influence, and according to the standard this coefficient is variable from 0.05 to 0.3 depending on seismic activity. As long as the magnitude of Almaty seismic activity is 10° , the dynamic coefficient k_{hf} is assume as 0.3. Horizontal seismic force is equal to:

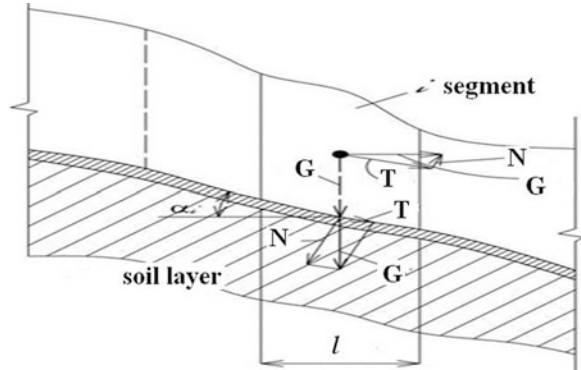
$$G_{si} = G_i \sqrt{1 + k_{hf}^2} \tag{18.7}$$

After that, horizontal seismic force is divided on the following components: normal N_{is} and tangent G_{is} . The calculation of acting and resisting forces with seismic allowance in a range of segments (see Fig. 18.13) is recommended using the following equations:

$$T_a = G_i \sin \alpha + G_{si} \cos \alpha \tag{18.8}$$

$$T_r = (G_i \cos \alpha + G_{si} \sin \alpha) \operatorname{tg} \varphi + c_i l_i \tag{18.9}$$

Fig. 18.13 Diagram of vectors interaction in soil segment for seismic loads



18.6 Analysis of Stress–Strain Condition of Foundation Pit Wall on Construction Site of “Almaty”

The foundation pit was made by steps with miscellaneous depths varying from 2.5 m up to 14.0 m. Maximum depth of the pit is 14.0 m. Design depth is 21.5 m. The wall of the pit is retained by Rabitz net, average thickness 5–7 cm.

The soil at a construction site is created by filling with clay soil and inclusion of crushed stone. The contractors researched only filling with clay soil and not taking into account crushed stone influence. However, the soil contains more than 25 % of inclusions. During experimental research more correct strength parameters of filling soil were obtained. Numerical analysis was done using a computer program—Lira 9.4 (see Fig. 18.14). Numerical analysis results were compared with results of proposed slope stability analysis method. Both were used for design of retaining construction. Some variants of retaining construction are presented in Fig. 18.15.

Finally, on the basis of efficiency analysis it was suggested to use variant 2. The general view and features of anchorage are presented in Fig. 18.16.

18.7 Conclusion

The main scientific and practical results of research are the following:

Study of lithological and geological processes of the territory of Almaty and adjacent areas revealed the most typical types of geological elements forming most areas under intensive construction. This study gave an estimation of changing of physical and mechanical properties of elements from geological, climatic, and some technical factors. The archive material analysis and experiences of past years showed that soil parameters in general are defined by the history of the formation of soil mass.

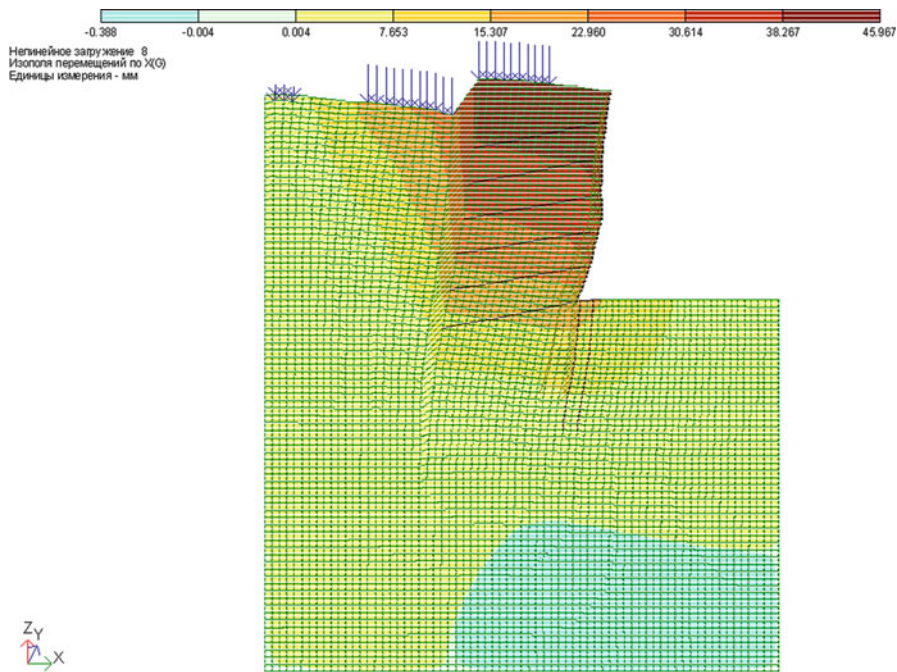


Fig. 18.14 Deformation mesh of foundation pit

Number of variation	Scheme of slope reinforcement	Volumes of earthwork, m3	Concrete expense m3	Percent of reinf-t, m3	Quantity of anchor	Remarks
1		0,00	9,12	2,83	4	Reinforcement of ditch by stepless slope height of 21m
2		94,5	0,283	4,87	3	Reinforcement ditch by three stepped vertical slopes with distances from each other in horizontal direction - 4.5m
3		94,5	0,225	5,16	4	Reinforcement of ditch by four stepped vertical slopes with distance from each other-3m

Fig. 18.15 Variants of retaining construction foundation pit

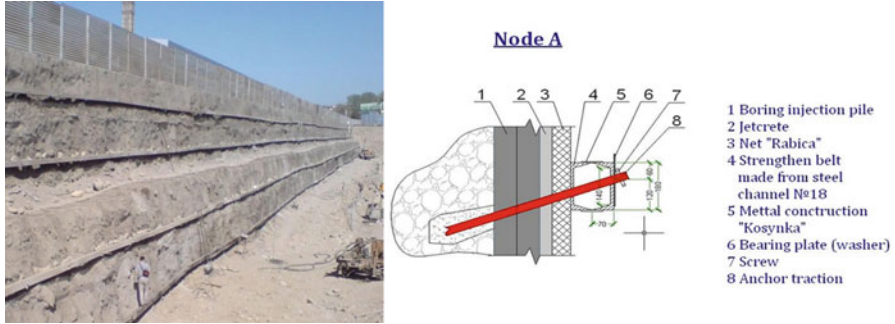


Fig. 18.16 Retaining construction foundation pit

Analysis of the well-known methods of the calculation of slope stability showed that one of the main reasons for the distinctions of degree between strict mathematical methods and practical data is a problematical geological condition. To resolve the problem, an incremental method for determination of the factor for stability slopes and boards of deep foundation pits was developed, taking into account kinematics of the particles moving and formation of the critical slip surface.

It was found that dynamic influence changes shear strength of soil in contrast to the static loads. For loose soil in dry conditions, the shear strength undergoes a small reduction. Dynamic influence has more effect on cohesion than angle of friction. For loamy soil, dynamic influence changes stress condition and general shear strength. Herewith, dynamic influence can bring both reduction and increase of shear strength that is defined by type of the soil.

A method was developed to determine the stability factor, taking into account deformation developments of slope or initial movement of the board of the foundation pit and formation of landslide pressure. Regularities of stress–strain and ultimate condition of formation under the shear are taken into account in this method.

It was found that increased fractions diameter in composition of the soil increases angle of internal friction.

The proposed method of slope and board foundation pit stability analysis can be used under seismic activity up to magnitude of 10^0 . This method allows determination of the correct strength parameters of coarse soil depending on percentage of contents of fine and coarse fraction and takes into account their work during landslide pressure formation from coarse fraction up to 20 mm.

Recommendations were made to determine the seismic load and possible variants of the calculation against deformation action, allowing increased stability of board foundation pits and slopes in seismic conditions.

References

- Khomyakov VA (2009) Direct shear test of coherent soil under dynamic load. In: Proceedings of ENU of L.N.Gumilyov, Astana, 2009, pp 336–339
- Khomyakov VA (2010a) Features of shear stress formation of soil ground. In: Proceedings of international conference dedicated to 75th anniversary of Aitaliyev Sh.M, Almaty, 2010, pp 57–59
- Khomyakov VA (2010b) Research of strength and stability of soil grounds. ScD thesis, Department of Civil Engineering, ENU of L.N.Gumilyov, Astana, 2010, 232 p
- Khomyakov VA, Pustogachev VA (2006) Modern construction in seismic condition. In: Proceedings of tresses and reports of young geotechnical specialists. KazNISSA, Almaty, 2006, pp 90–93
- Khomyakov VA, Abakanov AT, Almabekova SM (2010) Research of defomative properties of soil by using triaxial test equipment for design in high seismic condition. In: Proceedings of ENU of L.N.Gumilyov, Astana, 2010, pp 339–342
- Malyshevsky AA, Khomyakov VA (2009) Shear resistance of coarse soil. In: Proceedings of Kazakhstan-China international symposium, Almaty, 2009, pp 237–239
- SNiP RK 5.01-01-2002 Soil basement and foundations
- Zhussupbekov AZh, Khomyakov VA (2010) Features of slope stability analysis under construction of Alatau territory. In: Proceedings of international conference, Volgograd, 2010, pp 15–23

Chapter 19

Recent Developments of PVD Soft Ground Improvement: Laboratory Test Results and Simulations

Dennes T. Bergado, Suthasinee Artidteang, Jaturonk Saowapakpiboon, and Yip Poon Lai

19.1 Introduction

One of the cheapest soft ground improvement techniques is prefabricated vertical drains (PVDs). In this method, pore water squeezed out during the consolidation of the clay caused by the hydraulic gradients created by preloading can flow faster in the horizontal direction toward the drain, and then flow freely along the drain vertically toward the permeable drainage layers. Thus, the installation of the PVDs in the clay reduces the length of the drainage paths and, thereby, reduces the time to complete the consolidation process. Consequently, the higher horizontal permeability of the clay is also utilized (Hansbo 1979, 1981, 1987, 1997; Bergado et al. 1991, 2002). The vacuum consolidation was proposed in the early 1950s by Kjellmann (1952), the developer of the prefabricated vertical wick drain. The studies of vacuum-induced consolidation continued up to the present (Holtz 1975; Choa 1989; Cognon et al. 1994; Bergado et al. 1996, 2006; Tang and Shang 2000; Chai et al. 2006a, b; Saowapakpiboon et al. 2008a, b, 2009). Vacuum consolidation works by reducing the pore water pressure while maintaining constant total stress. The effective stress is increased owing to the reduced atmospheric pressure in the soil mass. The net effect is an additional surcharge ensuring early attainment of the required settlement and an increased shear strength resulting in increased embankment stability. Abuel-Naga et al. (2005) and Abuel-Naga and Bergado (2005) have

D.T. Bergado, Ph.D. (✉) • S. Artidteang, Ph.D.
6TE Program School of Engineering and Technology, Asian Institute of Technology,
P.O. Box 4, Klong Luang, Pathumthani, Bangkok, Thailand
e-mail: bergado@ait.ac.th; kwangce@gmail.com

J. Saowapakpiboon
Department of Highways, Sri Ayuthaya Road, Bangkok, Thailand
e-mail: jtrsnum@gmail.com

Y.P. Lai, Ph.D.
AnchorSol Co Ltd., Kuala Lumpur, Malaysia
e-mail: yypplai@gmail.com

studied the thermal behavior of soft Bangkok clay. The effect of temperature on the coefficient of the hydraulic permeability was also studied previously (e.g., Towhata et al. 1993; Morinl and Silva 1984; Houston and Lin 1987; Burghignoli et al. 1995; Delage et al. 2000); it was reported that the hydraulic conductivity of soil increased with increasing the temperature. The applicability of using the thermal treatment up to 90 °C combining with PVD called Thermo-PVD as a ground improvement technique was first proposed by Abuel-Naga et al. (2006a, b). The Thermo-PVD works by the removal of the smear zone and, consequently, faster rate of consolidation was achieved because of the elevated temperature. Thermally induced increase in permeability of soils around a heat source in the smear zone can offset the effect of disturbance caused by the PVD installation.

19.2 PVD Improved with Vacuum and Heat Preloading in Laboratory Tests

19.2.1 Large-Scale Consolidometer

The large-scale consolidometer as shown in Fig. 19.1 consisted of a cylinder cell of 0.45 m in inner diameter and 0.95 m in height made of polyvinyl chloride, with a thickness of 10 mm which can resist pressure less than 500 kPa. The upper and lower pedestal with a thickness 40 mm were connected by eight steel rods of 12 mm. The piston system consists of a piston with 40 mm in thickness and a hollow shaft with outside diameter of 100 mm. To prevent the tilting of the piston, a guide was installed on the upper pedestal around the shaft and was fixed with the

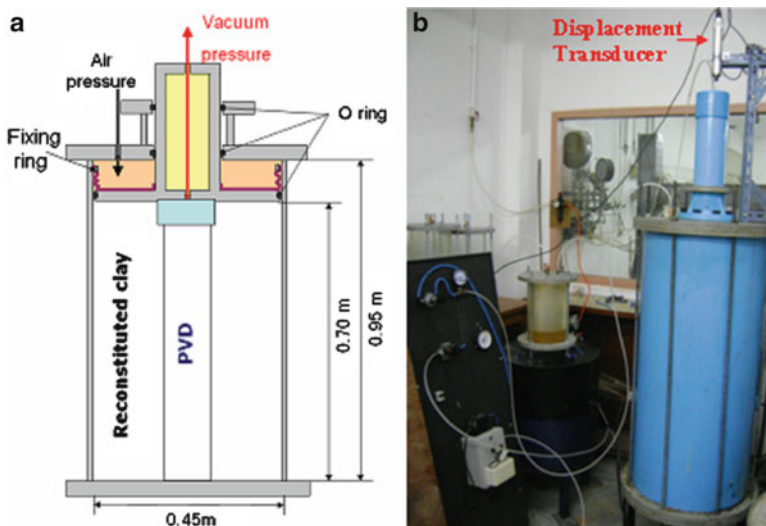


Fig. 19.1 Large-scale consolidometer. (a) Sketch and (b) Real photograph

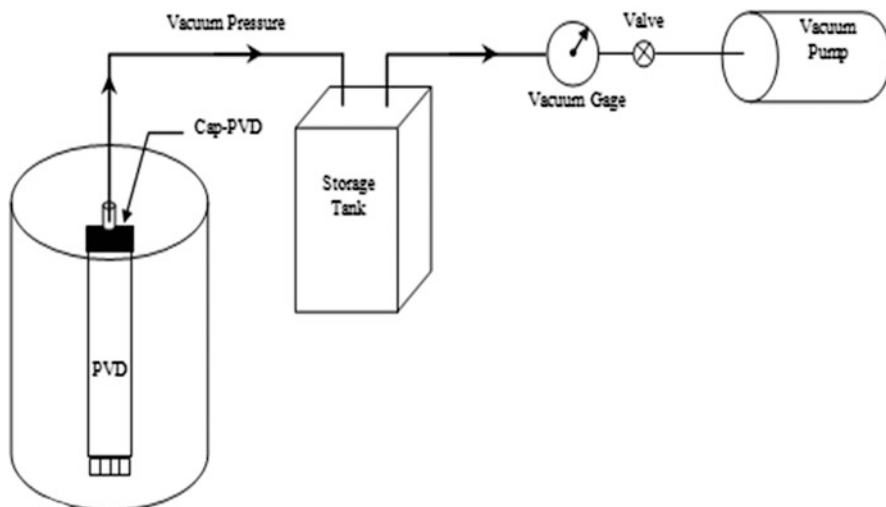


Fig. 19.2 Schematic diagram of Vacuum-PVD

upper pedestal with eight steel bolts of 15 mm in diameter. Silicon grease-lubricated “O” rings were used to seal the spaces between the upper pedestal and the cylinder cell, between the lower pedestal and the cylinder cell, between the piston and the cylinder cell, between the shaft and the upper pedestal, as well as between the guide and the shaft. The air pressure was applied through the upper pedestal to the top of the piston and the vacuum pressure was applied through the shaft of the piston to the bottom of piston and the PVD cap, respectively. Air pressure was transformed to vacuum pressure by a vacuum generator, which was connected directly to the air pump during consolidation test. A natural rubber membrane with a thickness of 3 mm was installed in the chamber above the piston to prevent the leakage of the air pressure and/or vacuum pressure through the piston. The natural rubber membrane was folded in a vertical direction initially to allow for vertical displacement of the piston during consolidation. Geotextiles were placed on top and bottom of the soil specimens to prevent clogging of the loading piston. The dial gauge was placed on top of the shaft for settlement measurement. A KPD-200 kPa excess pore water pressure transducer was connected to a data logger to monitor the pore water pressure in the specimen during consolidation.

19.2.2 Vacuum Generator

The schematic diagram for Vacuum-PVD is shown in Fig. 19.2. For the large consolidometers, the vacuum generator was utilized to transform the air pressure to vacuum pressure as shown in Fig. 19.3. This apparatus was connected directly with an air pump during the consolidation test. The water generated from suction by vacuum pressure was stored in a closed container.



Fig. 19.3 Vacuum generator

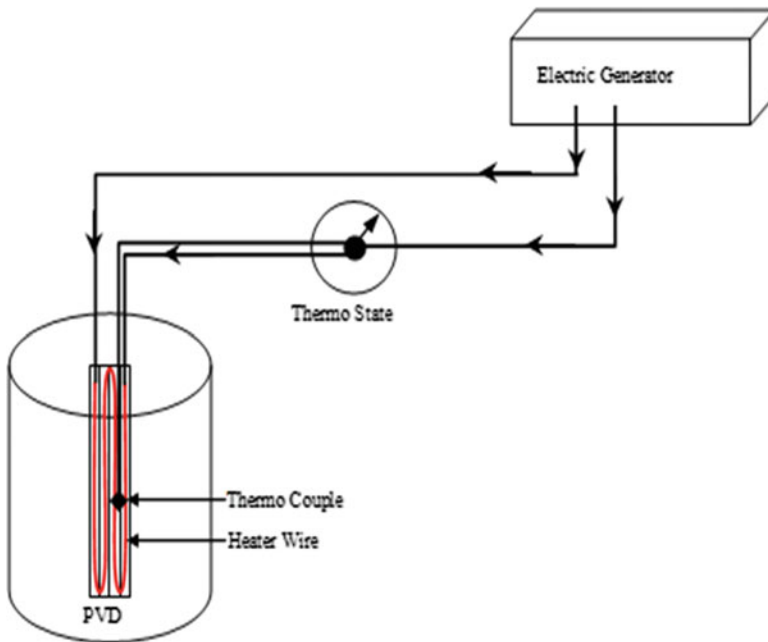


Fig. 19.4 Schematic diagram of Thermo-PVD

19.2.3 Heat Source

For the laboratory tests, the flexible wire heater was used as a heat source that was connected to the PVD to transfer the heat throughout PVD length. A thermocouple was connected to the thermostat that can record the temperature up to 120 °C at the center of the sample. The thermostat was used to maintain the supply of heat and automatically shut down upon reaching the specified amount of heat. Both heater wire and thermocouple were connected to the thermostat, which was programmed with two functions, namely: to transfer heat to the heaters at the desired temperature and to keep that temperature constant, as monitored by the readings taken by the thermocouple with an accuracy of ± 0.1 °C. The schematic diagram for Thermo-PVD is shown in Fig. 19.4.



Fig. 19.5 Flexible heater wire combined with PVD

Table 19.1 Physical properties of soft Bangkok clay

Physical properties	
Liquid limit (%)	102.24
Plastic limit (%)	39.55
Water content (%)	112.69
Plasticity index	62.69
Total unit weight (kN/m^3)	14.70
Specific gravity	2.66

For a large consolidometer, the PVD was attached to a flexible heater wire with a capacity of 120°C and power of 6 W/m , as shown in Fig. 19.5, for the reconstituted specimen improved with Thermo-PVD and Thermo-Vacuum-PVD. Thermocouples were installed at required radial distances and were connected to the digital data logger to monitor the temperature and heat transfer during the consolidation test. Before and after the laboratory tests, the water contents and shear strengths were also measured at the aforementioned locations; the temperature sensor boxes were used to maintain the temperature at the heat source and shut down automatically upon reaching the controlled heat of 90°C , at the heat source.

19.2.4 Laboratory Vane Shear Apparatus

A laboratory vane shear apparatus, capable of measuring shear strengths at different locations and depths, was used to determine the undrained shear strengths before and after the tests. The vane blades, made of stainless steel, were 20 mm in diameter and 40 mm in height. The apparatus was attached to an adjustable stainless steel rod and could be adjusted to locate measurement points within the specimen. The maximum torque was determined electronically.

19.2.5 Physical Properties and Testing Procedures

The soil samples were obtained from the site of the Second Bangkok International Airport, which is located 30 km southeast of Bangkok. The soft clay samples were collected from 3.0 to 4.0 m depths below a weathered crust layer. Table 19.1 shows

Table 19.2 Summary of CeTeau drain properties (CT-D911)

Drain body	Configuration	++++++
	Material	Polypropylene
	Channels	44
Filter jacket	Material	Polypropylene
	Colour	Grey
Weight (g/m)		78
Width (mm)		100
Thickness (mm)		3.5

the physical properties of the soft Bangkok clay. The PVD material used was CeTeau drain CT-D911, which is summarized in Table 19.2.

The disturbed samples were remolded by adding a sufficient amount of water until its water content was greater than its liquid limit. The samples were then thoroughly mixed in a mechanical mixer and transferred in layers into the consolidometer. At each layer, the air bubbles were eliminated by using a vibrator. For reconstitution using the large consolidometer, a 50 kPa pressure was applied. Drainage was allowed at the top and bottom of the apparatus. Silicone grease was applied to the insides of the large consolidometer to reduce the friction. Throughout the whole process the settlements were monitored until 90 % consolidation, by the Asaoka (1978) method. After reconstitution, the water content, shear strength, and specimen height were determined.

19.2.6 Consolidometer Test Program

For large consolidometer tests, the vertical pressure of 50 kPa was increased to 100 kPa after reconstitution under the applied vertical pressure in the specimen improved with PVD. For the specimen improved with PVD and vacuum pressure (Vacuum-PVD), a vertical pressure of 50 kPa and vacuum pressure of -50 kPa were applied. For the Thermo-PVD, the specimen was improved with PVD combined with vertical pressure of 100 kPa together with application of heat up to 90 °C. For the Thermo-Vacuum-PVD, the specimen was improved with PVD combined with heat up to 90 °C, together with vertical pressure of 50 kPa and vacuum pressure of -50 kPa. The temperatures were controlled by an electronic thermal control unit that received the signal from thermocouples. Drainage was allowed to flow only one way. Settlement was monitored during the test until the soil specimen reached 90 % consolidation. The Asaoka (1978) method was used to estimate the degree of consolidation and the magnitude of final settlement. The large-scale consolidometer test of specimens improved with PVD, Vacuum-PVD, Thermo-PVD and Thermo-Vacuum-PVD are shown in Fig. 19.6.

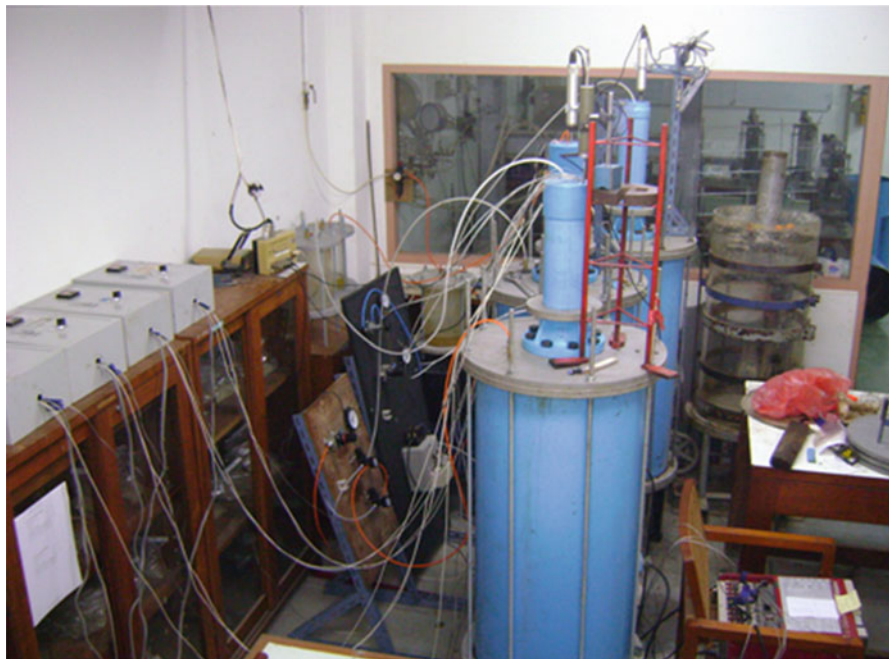


Fig. 19.6 Large-scale consolidometer tests for PVD, Vacuum-PVD, Thermo-PVD, and Thermo-Vacuum-PVD

19.3 Back Calculation of Compressibility Parameters

From the settlement observation, the final settlement S_f is determined by the Asaoka (1978) method. The coefficient of consolidation is back calculated by the Hansbo (1979) method, C_h is back calculated from the following relationships when $U_h = 90\%$.

$$U_h = 1 - \exp\left(\frac{-8T_h}{F}\right) \quad (19.1)$$

where U_h is the degree of consolidation for horizontal drainage; T_h is the time factor for horizontal drainage; F is the factor that expresses the additive effect caused by the spacing of the drains, $F(n)$, smear effect, F_s , and well-resistance, F_r . The values of $F(n)$, F_s , and F_r are given by the following equations:

$$F(n) = \ln\left[\frac{D_c}{d_w}\right] - \frac{3}{4} \quad (19.2)$$

$$F_s = \left[\frac{K_h}{K_s} - 1 \right] \ln \left[\frac{d_s}{d_w} \right] \quad (19.3)$$

$$F_r = \frac{2}{3} \pi L^2 \frac{K_h}{q_w} \quad (\text{Average one way drainage}) \quad (19.4)$$

$$F = F(n) + F_s + F_r \quad (19.5)$$

where D_e is the diameter of the equivalent soil cylinder, d_w , is the equivalent diameter of the drain, K_h is the coefficient of horizontal permeability, K_s is the horizontal permeability of the smear zone, d_s is the diameter of the smear zone, L is the length of the drain for double drainage and twice the length of the drain for single drainage, and q_w is the discharge capacity of the drain at hydraulic gradient of 1 (one). The time factor, T_h , for horizontal drainage can be calculated using:

$$T_h = \frac{C_h t}{D_e^2} \quad (19.6)$$

where C_h is the coefficient of horizontal consolidation and t is the time elapsed after the application of the load.

In PVDCON, finite element formulation considers the effects of PVDs by modifying 1D continuity equation of consolidation as follows (Chai and Miura 2000):

$$\frac{K_v}{\gamma_w} \frac{\partial^2 (u - p_{\text{vac}})}{\partial z^2} - \frac{8K_h(u - p_{\text{vac}})}{\gamma_w D_e^2 \mu} + \frac{\partial \epsilon_v}{\partial t} = 0 \quad (19.7)$$

$$\mu = \ln \frac{n}{s} + \frac{K_h}{K_s} \ln s - \frac{3}{4} + \pi \frac{2l^2 K_h}{3q_w} \quad (19.8)$$

where γ_w is the unit weight of water, z is depth, t is time ϵ_v is volumetric strain, u is excess pore water pressure, p_{vac} is the final vacuum pressures, K_v is hydraulic conductivity in the vertical direction, K_h is hydraulic conductivity in the horizontal direction, l is drainage length, D is the diameter of unit cell, q_w is discharge capacity of PVD, $n = D/d_w$ (d_w is the equivalent diameter of PVD, see Abuel-Naga and Bouazza 2009), and $s = d_s/d_w$, K_h , K_s , and d_s are defined previously.

A computer program, PVDCON, has been developed for calculating 1-D consolidation of soft clay improved with prefabricated drain (PVD) and sand drain (SD). The program can consider the following: (1) multilayer improved ground; (2) the effect of both vertical permeability of natural ground and PVD or SD; (3) both full and partial penetration of PVD or SD; (4) effect of surface vacuum pressure; (5) either one-way or two-way drainage; and (6) undrained shear strength variation during the consolidation process.

19.4 Laboratory Test Results and Simulations

19.4.1 Consolidation Behavior of Tested Samples

The comparison of settlement of specimens improved with and without vacuum and heat in the new large-scale consolidometer test are shown in Fig. 19.7. The specimen improved with Vacuum-PVD has a higher rate of settlement than the specimen improved with PVD, but the final settlement magnitudes are the same. In contrast, much faster and higher settlements were achieved from Thermo-PVD and Thermo-Vacuum-PVD. However, the performance of Thermo-PVD is slightly lower than Thermo-Vacuum-PVD. Among the tests, the Thermo-Vacuum-PVD combination achieved the fastest rate of settlement and the largest final settlement. There is a 25 % increase in final settlement in Thermo-PVD with almost the same settlement magnitude with the Thermo-Vacuum-PVD because of the application of heat in addition to surcharge loads.

Similar results were obtained in experiments by Pothiraksanon et al. (2008a, b) in which the use of the Thermo-PVD resulted in increased settlements by about 30 %. In addition, Saowapakpiboon et al. (2009) showed that the Thermo-PVD has highest volume contraction and rate of consolidation because of thermal effects. These results demonstrated that at higher the temperature, higher volume contraction and higher rate of consolidation resulted from the increased hydraulic conductivity. The compressibility increased because of thermally induced irreversible contraction

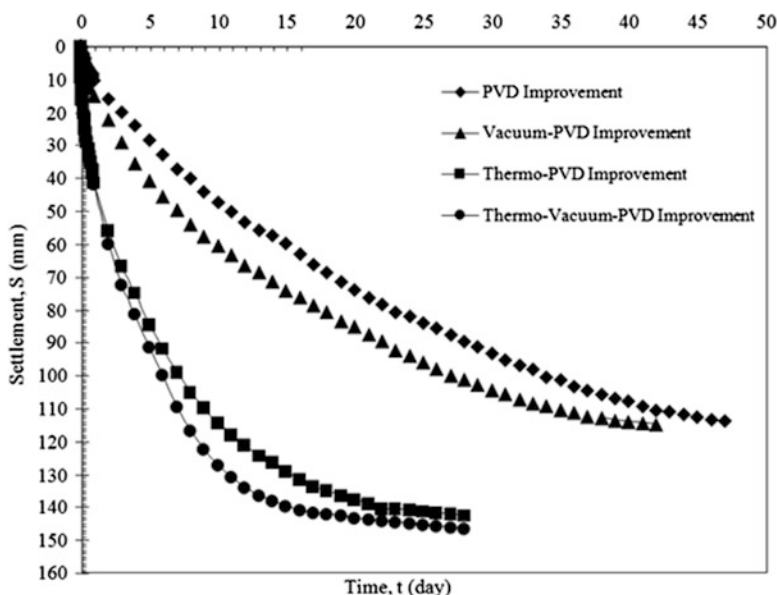


Fig. 19.7 Comparison of all settlement behavior using large consolidometers with reconstituted specimens

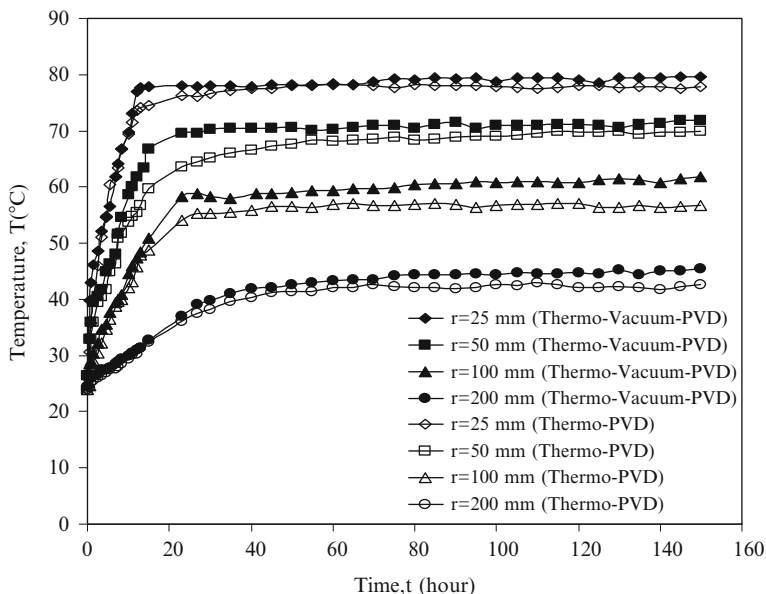


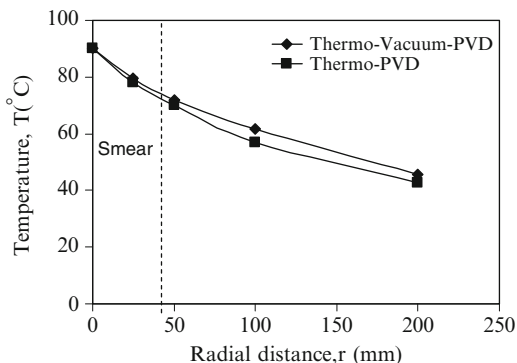
Fig. 19.8 Comparison of heat transfer in Thermo-PVD and Thermo-Vacuum-PVD

of saturated normally consolidated soft Bangkok clay. Furthermore, Abuel-Naga et al. (2006a) showed that the Thermo-PVD indicated a substantial amount of settlement of about five times using an undisturbed specimen of soft Bangkok clay in the laboratory model test. Moreover, the compression line of soft Bangkok clay shifts to the left with approximately similar slope upon heating when the thermal loading is applied at the normally consolidated state. Thus, heating the clay specimen combined with vacuum pressure (Thermo-Vacuum-PVD) has achieved the highest settlement and also faster rate of consolidation than Thermo-PVD, Vacuum-PVD, and PVD, respectively.

19.4.2 Heat Transfer

The heat transfers in the soil specimens at specific temperatures with respect to the specific distances from PVD were observed. Flexible wire heaters attached to the core of PVD were used as heat source to increase the temperature up to 90 °C. Temperatures of the heat source were measured by thermocouples, which were embedded at 150 mm depth and at radial distances of 25, 50, 100, and 200 mm from the center of the specimen. The temperature variations with time in the Thermo-PVD specimen and Thermo-Vacuum-PVD specimens in the large consolidometer are plotted in Fig. 19.8. The temperature decreased with increasing distances from the heat source. The Thermo-Vacuum-PVD has heat transfer characteristics similar to the Thermo-PVD. The radius, r , of 25 mm corresponds to the location of the

Fig. 19.9 Comparison of temperature in Thermo-PVD and Thermo-Vacuum-PVD at radial distances



smear zone with a mandrel dimension of 18.2 mm × 81.90 mm, and the diameter of the disturbed zone can be calculated as 87 mm. Figure 19.9 shows the average temperature of 80 °C in the smear zone and decreased with distance from the heat source. It took 40 h for the temperature to reach equilibrium in the large consolidometer as shown in Fig. 19.8. The result is consistent with the previous work of Abuel-Naga et al. (2006a) wherein the temperature around the PVD decreased as the radial distance from the PVD increased.

19.4.3 Vacuum and Thermal Effects on Water Content

The reduction in water content was measured before and after consolidation tests at the radial distances of 25, 50, 100, and 200 mm from the center of the specimens at depths of 10 and 40 mm. Lower water contents were observed nearer to the heat source with significant reduction in water contents. The levels of water content reduction decreased with the distance from the heat source. Figure 19.10 shows the comparison of percent decrease in water contents before and after consolidation tests at radial distances of 25, 50, 100, and 200 mm from the center of the specimen. The percent decrease of water contents after consolidation tests at the smear zone of Vacuum-PVD was slightly higher than that with PVD only. The Thermo-PVD had much higher percent decrease of water contents than the Vacuum-PVD, whereas the Thermo-Vacuum-PVD had the highest percent decrease of water contents but nearly similar to that of Thermo-PVD.

19.4.4 Effect of Vacuum and Heat on Shear Strength of Clay

A comparison of the increase in the shear strength in all four tests after improvement in the reconstituted specimens is plotted in Fig. 19.11. For the smear zone, the normal PVD and Vacuum-PVD were not much different in the increase of shear

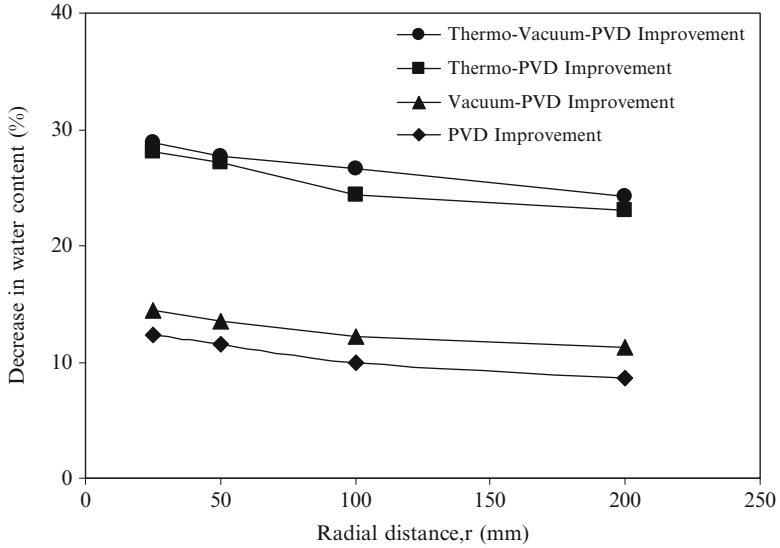


Fig. 19.10 Comparison of decrease in water content after consolidation test of large consolidometers at radial distances

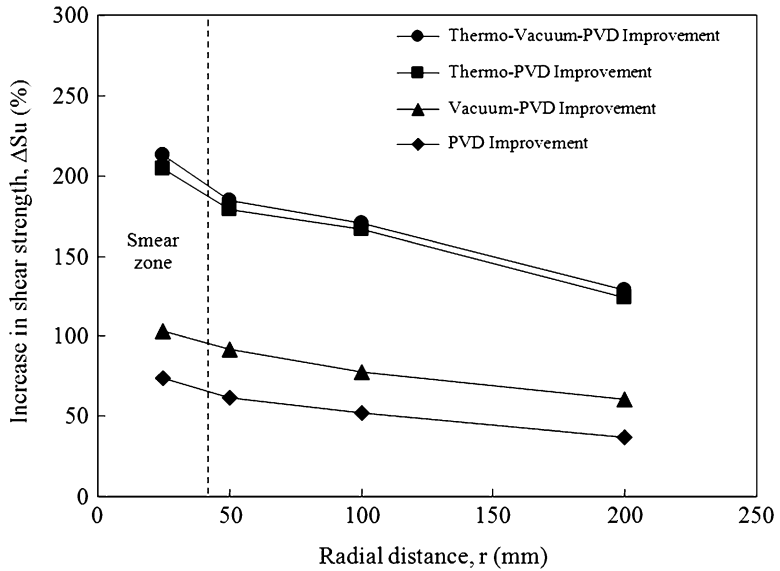


Fig. 19.11 Comparison of increase in shear strength after consolidation test of large consolidometers with radial distances

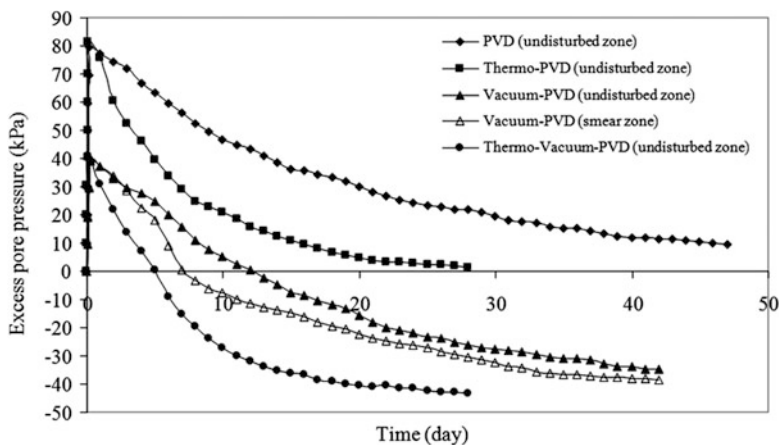


Fig. 19.12 Comparison of excess pore water pressure during consolidation in large consolidometer using reconstituted specimens

strengths. For Thermo-PVD, the shear strength had increased but slightly less than the Thermo-Vacuum-PVD around the smear zone. The results demonstrated that much higher shear strength developed in the smear zone using Thermo-PVD and Thermo-Vacuum-PVD. The clay particles led to flocculated structure or higher in volume contraction as the soil porosity decreased because of increased temperature so that the shear strength increased (Abuel-Naga et al. 2008).

19.4.5 Vacuum and Thermal Effects on Excess Pore Pressure

The excess pore water pressures were measured at the large-scale consolidometer tests during consolidation by using excess pore water pressure transducers, which were inserted through the wall at 350 mm height from the bottom of the cylinder cell into the smeared and undisturbed zone and monitored by digital data logger. The measured data are plotted in Fig. 19.12. For the specimen with PVD only, the excess pore water pressure had increased to a maximum of 80 kPa and decreased to about 10 kPa after 47 days in the undisturbed zone. For Thermo-PVD, the specimen at the undisturbed zone had demonstrated higher excess pore water pressures to 80 kPa and then rapidly reduced to 1 kPa after 28 days because of the effects of thermally induced pore water pressures and volume changes. This behavior can be explained by the increase in permeability in the smear zone at higher temperature, consequently, the excess pore water pressures dissipated more rapidly (Pothiraksanon et al. 2008a, b). The thermally induced excess pore water pressure and volume change occurred because the thermal expansion coefficient of the pore water is approximately 15 times larger than the thermal expansion of the clay solid skeleton (Abuel-Naga et al. 2007).

In the case of the Vacuum-PVD specimen, the maximum excess pore water pressure in the smear zone had increased about 40 kPa and dissipated rapidly after 8 days and decreased to about -40 kPa after 40 days. The excess pore water pressures in the undisturbed zone increased to maximum of 40 kPa and transformed to minus excess pore water pressure after 13 days and decreased to about -40 kPa after 40 days. The excess pore water pressure had reduced faster at the smear zone than in the undisturbed zone owing to the proximity to vacuum source. The excess pore water pressure of the Thermo-Vacuum-PVD specimen in the undisturbed zone increased to 40 kPa and reduced very fast to -9.1 kPa after only 6 days and then decreased to about -43 kPa after 28 days. The vacuum preloading generated negative (suction) excess pore water pressure equivalent to the applied vacuum pressure. This behavior is similar to the results obtained by Indraratna et al. (2005) wherein the assumption of constant vacuum pressure distribution over the soil surface and linearly decreasing vacuum pressure along the drain length were indicated. Moreover, Chai et al. (2007) showed that the measured and simulated excess pore water pressures and vacuum pressures varied with time.

19.4.6 Back-Calculated Compressibility Parameters

The test results from reconstituted specimens in the new large-scale consolidometer are back-calculated to determine the values of C_h and K_h/K_s by using the method from Hansbo (1987). The back-calculated values of a reconstituted specimen improved with PVD is demonstrated in Fig. 19.13a, where C_h value was 1.93 m²/year with K_h/K_s of 3.0. Figure 19.13b shows the results of the reconstituted specimen improved with Vacuum-PVD; the back-calculated C_h value was 2.23 m²/year with K_h/K_s of 2.7. This behavior was observed by Mohamedelhassan and Shang (2002), that the vacuum and surcharge preloading of the same magnitude produces similar coefficients of consolidation. For the reconstituted sample in the large consolidometer with heat (Thermo-PVD), the corresponding back-calculated C_h and K_h/K_s were 4.17 m²/year and 1.4, respectively (Fig. 19.14a). These values show that the thermal effects increased the permeability of the smear zone, which resulted in decreased K_h/K_s values and increased C_h values. The result indicated the increase in soil permeability in the smear zone as temperature increased Abuel-Naga and Bergado (2005). Moreover, for the reconstituted specimen improved with Thermo-Vacuum-PVD, the C_h and K_h/K_s were 4.38 m²/year and 1.1, respectively (Fig. 19.14b). The predicted curve agreed well with the observed values of reconstituted specimens in large-scale consolidometer tests. The values of the C_h and K_h/K_s for all the specimens are also summarized in Table 19.3.

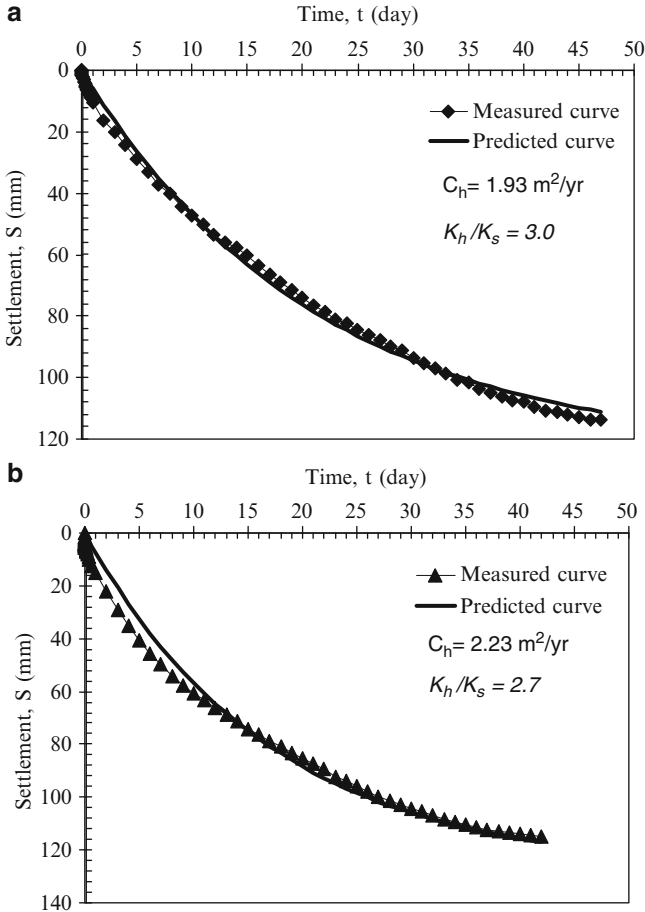


Fig. 19.13 The observed and predicted curves for settlements to determine C_h values for the reconstituted specimen improved with (a) PVD and (b) Vacuum-PVD

The percent increases in C_h of the reconstituted specimen improved with Vacuum-PVD, Thermo-PVD, and Thermo-Vacuum-PVD consisted of 15.54, 116.06, and 126.42 %, respectively. The reductions in K_h/K_s were 10.00, 53.33, and 63.33 %, respectively. Thus, the vacuum pressure can increase the horizontal coefficient of consolidation, C_h , because applying vacuum pressure generated negative pore water pressure along the drain so the effective stress of soil increased, which resulted in faster rate of settlement with the same magnitudes of settlement compared to PVD only. Whereas the high temperature can increase the coefficient of horizontal consolidation, C_h , with the reduction of K_h/K_s that means permeability increased by reducing the drainage retardation effects in the smear zone around the PVD.

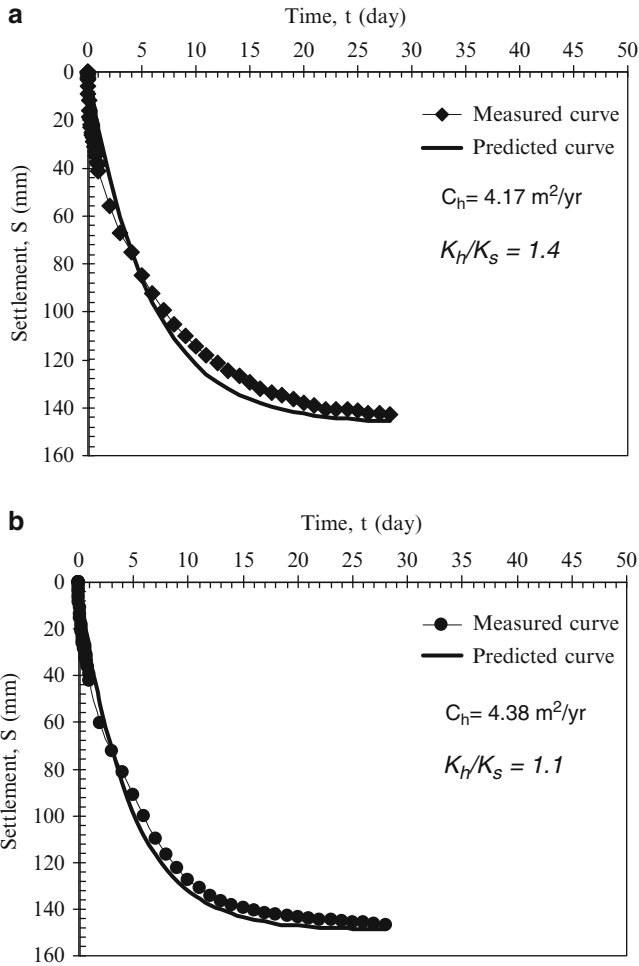


Fig. 19.14 The observed and predicted curves for settlements to determine C_h values for the reconstituted specimen improved with (a) Thermo-PVD and (b) Thermo-Vacuum-PVD

Table 19.3 Summary of changes in flow parameters for specimens in large-scale consolidometer

Flow parameters	PVD	Vacuum-PVD	Thermo-PVD	Thermo-Vacuum-PVD
C_h (m^2/year)	1.93	2.23	4.17	4.38
K_h/K_s	3.00	2.70	1.40	1.10

19.4.7 Numerical Simulations

ABAQUS software is a finite element program coupled with Biot consolidation theory and employed to simulate the 2D drain analysis (Hibbitt et al. 2006). The cylinder of PVD-improved reconstituted specimens with and without vacuum

Table 19.4 PVD type and parameters used in laboratory test

<i>PVD size</i>			
Width	W	m	0.0500
Thickness	T	m	0.0035
Diameter	d_w	m	0.0268
Discharge capacity	q_w	m ³ /year	100
<i>Mandrel</i>			
Width	T	m	0.0182
Thickness	W	m	0.0819
Diameter	d_m	m	0.044
<i>Smear zone</i>			
Diameter	d_s	m	0.0871

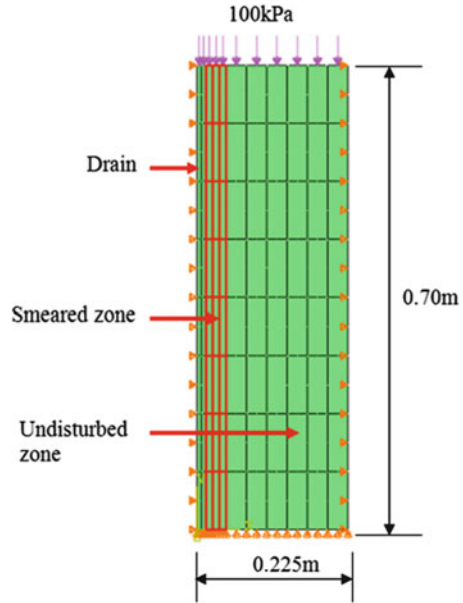
Table 19.5 Simulation parameters of reconstituted soil in laboratory test

H (m)	e_0	k (m/day)	κ	ν	λ	M	e_{cs}
0.70	2.29	6.3E-05	0.055	0.3	0.569	0.8	4.51

was modeled and simulated by the finite element program. The PVD was installed at the center and simulated as a drain with equivalent diameter of 26.8 mm (equivalent to one-half of the width) and length of the band-shaped drain (Chai and Miura 1999). The well resistance was taken into account by the simulated discharge capacity of 100 m³/year (Bergado et al. 1996) because the discharge capacity of equal or greater than 100 m³/year has little effect on the settlement behavior (Shen et al. 2005). The smeared zone was modeled with equivalent diameter of 87.2 mm corresponding to two times the equivalent mandrel diameter 43.6 mm (Hansbo 1987; Bergado et al. 1991). Table 19.4 shows the parameters of PVD used in the experiment. In the simulation model, water flowed to the drain radially and to the top vertically similar to the laboratory model test. The effect of smear is very important for calculation of consolidation with PVD because the consolidation process is mainly affected by radial drainage. In this study, the FEM simulation was used to analyze the performance of PVD improvement with and without vacuum preloading combined with surcharge preloading and the ratio of horizontal permeability in the undisturbed area to smeared zone, K_h/K_s . The modified Cam clay model and CAX8RP (eight-node biquadratic displacement, bilinear pore water pressure, reduced integration) elements in axisymmetry were used in the simulation. Parameters of reconstituted specimens were investigated by standard oedometer test as tabulated in Table 19.5.

In the simulation model, a two-dimensional axisymmetric mesh was used, with 11 elements in the x -direction (0.225 m wide) and 8 elements in the z -direction (total height of 0.70 m) as shown in Fig. 19.15, which consisted of three parts, namely: drained zone, smeared zone, and undisturbed zone, respectively. The drained zone, smeared zone, and undisturbed zone were provided with eight elements in the z -direction and two elements, three elements, and six elements, respectively, in

Fig. 19.15 Geometry and mesh of reconstituted specimen improved with PVD only



the x -direction. The element chosen was a four-node axisymmetric quadrilateral element with bilinear displacement and bilinear pore water pressure variations. For the specimen improved with PVD only, a surcharge of 100 kPa was applied at the top and simulated as surface pressure. Full drainage was allowed at the top by setting the pore water pressure to zero at the surface (Fig. 19.15). For the specimen improved with Vacuum-PVD, a surcharge of 50 kPa and vacuum pressure of -50 kPa were applied at the top and simulated using a finite element program in axisymmetric condition (Fig. 19.16).

At the bottom, the vertical and horizontal components of displacements were fixed ($u_x = u_z = 0$), and on the right-hand side, the horizontal component of displacement was fixed ($u_x = 0$) to simulate the frictionless interface between the soil and the rigid cell. The left hand of the mesh was a symmetry line (no horizontal displacement). Flow of pore water through the walls of the cell was not allowed. At the top, a uniform downward pressure of 100 kPa was applied instantaneously in the case of PVD only and two uniform downward and upward pressures of 50 kPa each were applied in the same manner in the case of Vacuum-PVD. The top surface was open and permeable but the bottom surface was made impervious. The purpose of the analysis was to predict the time dependency of the settlements and pore water pressures in the soil mass after load application and compare with the predicted values from the Hansbo (1979) method.

Fig. 19.16 Geometry and mesh of reconstituted specimen improved with vacuum-PVD

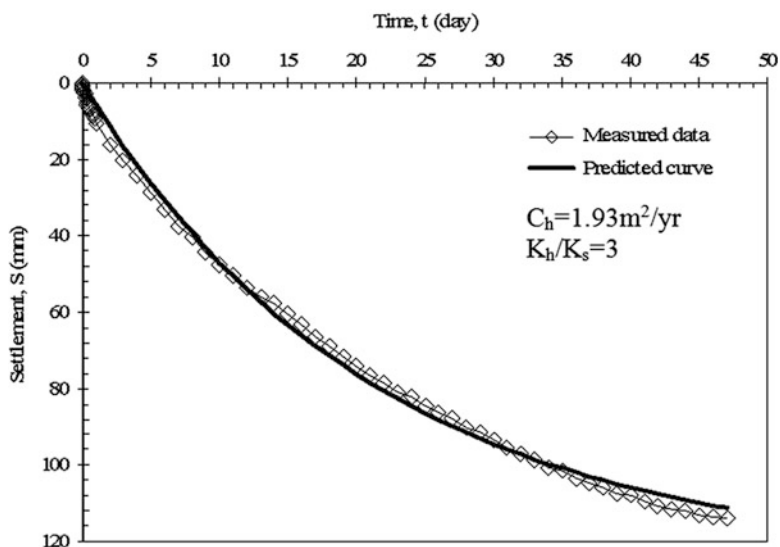
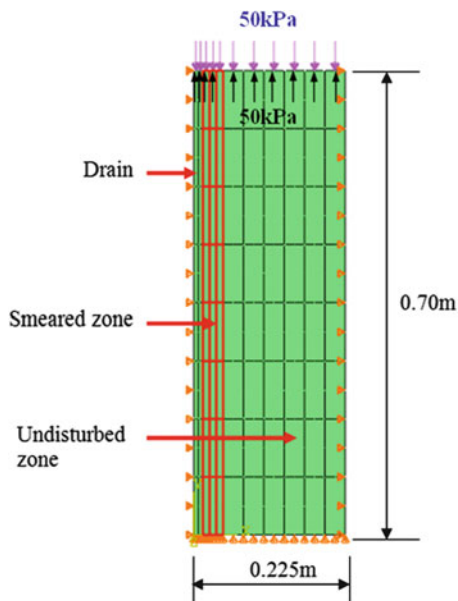


Fig. 19.17 The measured and predicted curves for settlements to determine C_h values for the reconstituted specimen improved with PVD only

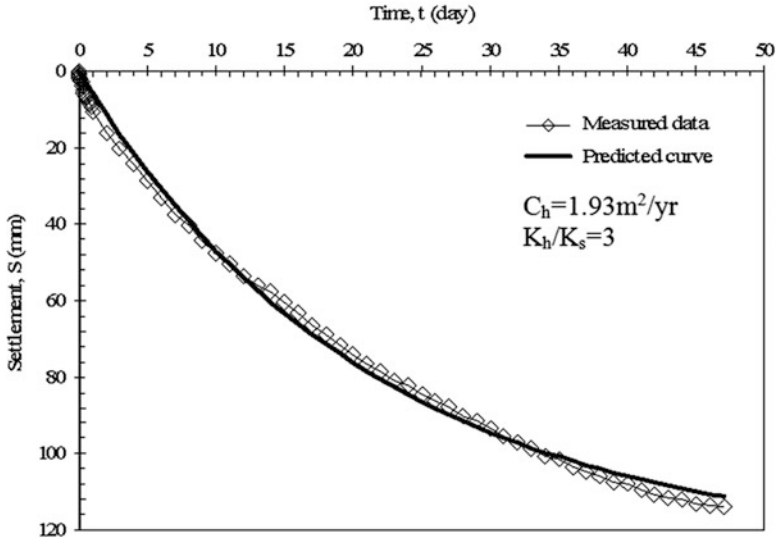


Fig. 19.18 The measured and predicted curves for settlements to determine C_h values for the reconstituted specimen improved with vacuum-PVD

Table 19.6 Back-calculated flow parameters of PVD-improved reconstituted specimens with and without vacuum preloading combined with surcharge preloading

Type of improved reconstituted specimen	C_h (m^2/year)	K_h/K_s
PVD with surcharge preloading	1.93	3.0
PVD with surcharge and vacuum preloading	2.23	2.7
Percent change	16 %	10 %

19.4.8 Simulation Results and Discussions

The measured and theoretical time settlement curves of the large consolidometer for the reconstituted specimens are presented in Figs. 19.17 and 19.18 for PVD only and Vacuum-PVD and tabulated in Table 19.6. The values of C_h and K_h/K_s for the specimen improved with PVD only are $1.93 \text{ m}^2/\text{year}$ and 3.0, respectively, as shown in Fig. 19.17. The final settlement predicted by the Asaoka (1978) method was 124.9 mm. For the specimen improved with Vacuum-PVD, the corresponding values are 2.23 and 2.7 m^2/year , respectively, as demonstrated in Fig. 19.18, and the final settlement predicted by Asaoka (1978) method was 124.7 mm. Consequently, the use of Vacuum-PVD increased the hydraulic conductivity of the smear zone resulting in the decrease in K_h/K_s by 10 % and an increase in C_h by 16 % as tabulated in Table 19.6.

The measured and simulated excess pore water pressure and/or vacuum pressure variation with time of the specimens improved with PVD only and Vacuum-PVD

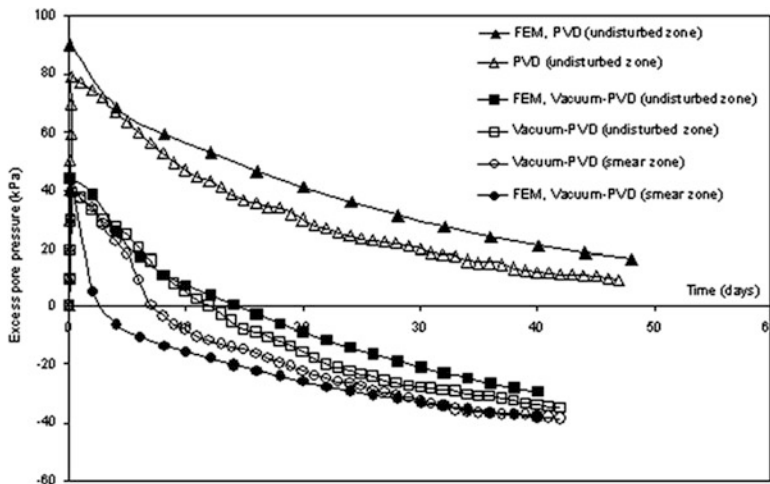


Fig. 19.19 The measured and simulated curves of excess pore water pressure for reconstituted specimens improved with PVD only and Vacuum-PVD

are compared as shown in Fig. 19.19. The simulated maximum excess pore water pressure values and dissipation rates are higher than the measured data of both specimens with PVD only and Vacuum-PVD. The measured excess pore water pressure has increased to a maximum of 80 kPa and after 47 days decreased to about 10 kPa but the FEM excess pore water pressure has increased to a maximum of 90 kPa and after 47 days decreased to about 15 kPa. The excess pore water pressure was slightly overestimated by FEM simulation with K_h and K_v in which the dissipation of measured data is faster than FEM analysis. For Vacuum-PVD, the maximum measured excess pore water pressure in the smear zone increased about 40 kPa, dissipated gradually after 7 days, and decreased to about -35 kPa after 40 days but the FEM excess pore water pressure in the smear zone increased to a maximum of 44 kPa, dissipated rapidly after 3 days, and decreased to about -38 kPa after 40 days. Moreover, the maximum measured excess pore water pressure in the undisturbed zone increased to about 39 kPa, dissipated gradually after 12 days, and decreased to about -35 kPa after 40 days. As well, the FEM excess pore water pressure in the undisturbed zone increased to maximum of 44 kPa, dissipated gradually after 14 days, and decreased to about -30 kPa after 40 days. Thus, the vacuum preloading generated negative (suction) excess pore water pressure equivalent to the applied vacuum pressure. This behavior is similar to the results obtained by Indraratna et al. (2005) in which the assumption of constant vacuum pressure distribution over the soil surface and linearly decreasing vacuum pressure along the drain length were indicated. Moreover, Chai et al. (2007) showed that the measured and simulated excess pore water pressure and vacuum pressure varied with time.

19.5 Conclusions

Based on the data and results of the analyses, the following conclusions can be made:

1. For the Thermo-PVD improvement, the consolidation rate was faster and the settlements were larger compared with the Vacuum-PVD improvement. The sample with PVD only had the lowest settlement rate with magnitude of final settlement equal with the Vacuum-PVD.
2. The C_h and K_h/K_s values for reconstituted sample with PVD were 1.93 and 3 m²/year, respectively. Upon preloading with vacuum pressure, the corresponding values were 2.23 and 2.7 m²/year. The corresponding values were 4.17 and 1.4 m²/year, respectively, for Thermo-PVD. For the specimen with combined vacuum and heat preloading, the C_h and K_h/K_s values were 4.38 and 1.1 m²/year, respectively. The permeability of the smear zone increased due largely to heat and vacuum pressure effects.
3. The reduction of water content occurred with the increase in temperature and vacuum pressure around the PVD core.
4. The shear strengths increased with increasing temperatures and decreasing water contents. The largest increase in the shear strength was within the smear zone at distances up to two times the equivalent radius of the mandrel.
5. The hydraulic conductivity of the smear zone increased because of heat and vacuum effects. For the specimen with Thermo-PVD and Vacuum-PVD, K_h/K_s values slightly decreased whereas the coefficient of horizontal consolidation, C_h , increased.
6. The excess pore water pressure simulated by the finite element method yielded quite good simulations of excess pore water pressure at the final loading stage but the simulated excess pore water pressure at the early stage was higher than the actual excess pore water pressure.
7. The settlement simulated by the finite element method yielded quite good simulations of settlement both at the early stage and final loading stage.
8. The finite element software, ABAQUS, was found to be very useful to predict settlements of ground improvement using PVD with and without vacuum preloading.
9. The permeability of the smear zone increased because of the increase in temperature, which caused the reduction of viscosity in the pore water. Consequently, the K_h/K_s values slightly decreased whereas the coefficient of horizontal consolidation, C_h , increased.

References

- Abuel-Naga HM, Bergado DT (2005) Thermal conductivity and fabric anisotropy of saturated clays. *Geotech Eng J* 36(2):99–108

- Abuel-Naga HM, Bergado DT, Rujivipat P (2005) Thermal consolidation of soft Bangkok clay. *Int J Lowland Technol* 7(1):13–22
- Abuel-Naga HM, Bergado DT, Chaiprakaikeow S (2006a) Innovative thermal technique for enhancing the performance of prefabricated vertical drain system. *Geotext Geomembr* 24(6):359–370
- Abuel-Naga HM, Bergado DT, Grino L, Rujivipat P, Thet Y (2006b) Experimental evaluation of engineering behavior of soft Bangkok clay under elevated temperature. *J Geotech Geoenviron Eng ASCE* 132(7):902–910
- Abuel-Naga HM, Bergado DT, Bouazza A (2007) Thermally induced volume change and excess pore water pressure of soft Bangkok clay. *Eng Geol* 89(1–2):144–154
- Abuel-Naga HM, Bergado DT, Bouazza A (2008) Thermal conductivity evolution of saturated clay under consolidation process. *Int J Geomech ASCE* 8(2):114–122
- Abuel-Naga HM, Bouazza A (2009) Equivalent diameter of a prefabricated vertical drain. *Geotext Geomembr* 27:227–231
- Asaoka A (1978) Observational procedure of settlement prediction. *Soils Found* 18(4):87–101
- Bergado DT, Asakami H, Alfaro M, Balasubramaniam AS (1991) Smear effects of vertical drains on soft Bangkok clay. *J Geotech Eng ASCE* 117(10):1509–1529
- Bergado DT, Manivannan R, Balasubramaniam AS (1996) Filtration criteria for prefabricated vertical drain geotextile filter jacket in soft Bangkok clay. *J Geotech Eng* 3(1):63–83
- Bergado DT, Balasubramaniam AS, Fannin RJ, Holtz RD (2002) Prefabricated vertical drain (PVD) in soft Bangkok clay: a case of NBIA project. *Can Geotech J* 39(2):304–315
- Bergado DT, Saowapakpiboon J, Kovittayanon N, De Zwart TP (2006) Ceteau-S PVD vacuum system in soft Bangkok clay: a case study of the Suvarnabhumi Airport project. *The 6th Symposium on soft ground improvement and geosynthetics, Bangkok, 2006*, pp 18–27
- Burghignoli A, Desideri A, Miliziano S (1995) Discussion of volume change of clays induced by heating as observed in consolidation tests by Towhata, I., Kuntiwattanakul P., Seko, I. and Ohishi, K. *Soils Found* 35(1):125–127
- Chai JC, Miura N (1999) Investigation of factors affecting vertical drain behavior. *J Geotech Geoenviron Eng* 125(3):216–226
- Chai JC, Miura N (2000) A design method for soft subsoil improvement with prefabricated vertical drain. In: *Proceeding of the international seminar on geotechnics in Kochi, Japan, 2000*, pp 161–166
- Chai JC, Carter JP, Hayashi S (2006a) Vacuum consolidation and its combination with embankment loading. *Can Geotech J* 43:985–996
- Chai JC, Miura N, Bergado DT (2006b) Preloading clayey deposit by vacuum pressure with cap-drain. In: *Proceeding of the 21st Japanese geosynthetic symposium, Aomori, 2006*, pp 45–52
- Chai JC, Miura N, Nomura T (2007) Experimental investigation on optimum installation depth of PVD under vacuum consolidation. *The 3rd China-Japan joint, geotechnical symposium, Chongqing, 2007*, pp 87–92
- Choa V (1989) Drains and vacuum preloading pilot test. In: *Proceeding of the 12th international conference on soil mechanics and foundation engineering, Rio de Janeiro, 1989*, pp 1347–1350
- Cognon JM, Juran I, Thevanayagam S (1994) Vacuum consolidation technology: principles and field experience. In: *Proceedings of the vertical and horizontal deformations of embankments (Settlement'94)*. ASCE Special Publication 40(2):1237–1248
- Delage P, Sultan N, Cui YJ (2000) On the thermal consolidation of Boom clay. *Can Geotech J* 37:343–354
- Hansbo S (1979) Consolidation of clay by band shaped prefabricated drains. *Ground Eng* 12(5):16–25
- Hansbo S (1981) Consolidation of fine-grained soils by prefabricated drains. In: *Proceedings of the 10th international conference on soil mechanics and foundation engineering, Stockholm, 1981*, pp 677–682
- Hansbo S (1987) Design aspects of vertical drains and lime column installation. In: *Proceedings of the 9th Southeast Asian geotechnical conference, Bangkok, 1987*, pp 1–12

- Hansbo S (1997) Aspects of vertical drain design: Darcian or non-Darcian flow. *Geotechnique* 47(5):983–992
- Hibbitt, Karlsson, Sorensen (2006) ABAQUS/standard user's manual. HKS Inc
- Holtz RD (1975) Preloading by vacuum: current prospects. *Transp Res Rec* 548:26–69
- Houston SL, Lin HD (1987) A thermal consolidation model for pelagic clays. *Mar Geotech* 7:79–98
- Indraratna B, Sathanathan I, Rujikiatkamjorn C, Balasudramaniam AS (2005) Analytical and numerical modelling of soft soil stabilized by PVD incorporating vacuum preloading. *Int J Geomech* 5(2):114–124
- Kjellmann W (1952) Consolidation of clay soil by means of atmospheric pressure. In: *Proceedings on soil stabilization conference, Boston, 1952*, pp 258–263
- Mohamedelhassan E, Shang JQ (2002) Vacuum and surcharge combined one-dimensional consolidation of clay soils. *Can Geotech J* 39:1126–1138
- Morin R, Silva AJ (1984) The effect of high pressure and high temperature on some physical properties of ocean sediments. *J Geophys Res* 89(1):511–526
- Pothiraksanon C, Bergado DT, Abuel-Naga HM, Hayashi S, Du YJ (2008a) Reduction of smear effects around PVD using Thermo-PVD. *Lowland Technol Int* 9(2):38–48
- Pothiraksanon C, Saowapakpiboon J, Bergado DT, Thann NM (2008b) Reduction of smear effects around PVD using Thermo-PVD. *Ground Improv* 161:179–187
- Saowapakpiboon J, Bergado DT, Chai JC, Kovittayanon N, De Zwart TP (2008a) Vacuum-PVD combination with embankment loading consolidation in soft Bangkok clay: a case study of the Suvarnabhumi Airport project. In: *Proceeding of the 4th Asian regional conference on geosynthetics, Shanghai, 2008*, pp 440–449
- Saowapakpiboon J, Bergado DT, Hayashi S, Chai JC, Kovittayanon N, De Zwart TP (2008b) CeTeau PVD vacuum system in soft Bangkok clay: a case study of the Suvarnabhumi Airport project. *Lowland Technol Int* 10(1):42–53
- Saowapakpiboon J, Bergado DT, Thann YM, Voottipruex P (2009) Assessing the performance of prefabricated vertical drain (PVD) with vacuum and heat preloading. *Geosynth Int* 16(1):384–392
- Shen SL, Chai JC, Hong ZC, Cai FX (2005) Analysis of field performance of embankments on soft clay deposit with and without PVD-improvement. *Geotext Geomembr* 23(6):463–485
- Tang M, Shang JQ (2000) Vacuum preloading consolidation of Yaogiang airport runway. *Geotechnique* 50(6):613–653
- Towhata I, Kuntiwattanakul P, Seko I, Ohishi K (1993) Volume change of clays induced by heating as observed in consolidation tests. *Soils Found* 33(4):170–183

Chapter 20

Study on Regional Ground Upheaval Phenomenon Caused by the Rising of Groundwater Level and Its Effect on Underground Infrastructure

Sokkheang Sreng, Hiroshi Tanaka, Tejiro Saito, Takuya Kusaka, Tamio Ito, and Atsushi Koizumi

20.1 Introduction

As an important geoenvironmental issue, it is known that ground settlement caused by the change of groundwater level strongly affects the underground infrastructure such as subway, sewer system, irrigation system, deep foundations, etc. Ground settlement caused by the lowering of groundwater level had been a serious social problem in Japan since the middle of the twentieth century. This problem was alleviated since the establishment of regulations for environmental pollution prevention to control the use of underground water from 1970. Subsequently, groundwater level has been recovered in the recent few decades, with a rising trend being found in the urban areas of the

S. Sreng, D.Eng. (✉) • H. Tanaka • T. Kusaka, D.Eng.
Research and Development Center, Nippon Koei Co., Ltd., 2304 Inarihara, Tsukuba-shi,
Ibaraki 300-1259, Japan
e-mail: sokkheang-sr@n-koei.jp; tanaka-hr@n-koei.jp; kusaka-tk@n-koei.jp

T. Saito, D.Eng.
Civil Engineering Division, Nishimatsu Construction Co., Ltd., 1-20-10 Toranomon,
Minato-ku, 105-8501 Tokyo, Japan
e-mail: tejiro_saito@nishimatsu.co.jp

T. Ito
Watershed Management Division, Geology and Geotechnology Department, Nippon Koei Co.,
Ltd., 2, Kojimachi 4-chome, Chiyoda-ku, 102-0083 Tokyo, Japan
e-mail: a3895@n-koei.co.jp

A. Koizumi, D.Eng.
Faculty of Creative Science and Engineering, Waseda University, 3-4-1 O-kubo, Shinjyuku,
169-8555 Tokyo, Japan
e-mail: koizumi@waseda.jp

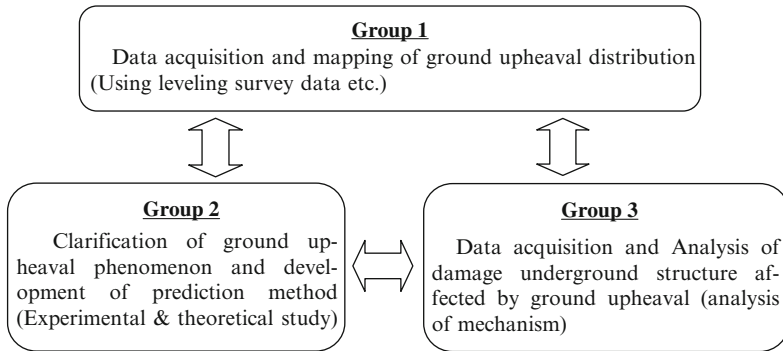


Fig. 20.1 Activities of the ground upheaval study committee

major cities in Japan. In contrast to the lowering of groundwater level, the rising of groundwater level always leads to ground upheaval caused by rebound of the clay layer. This phenomenon also affects the underground infrastructure, and sometimes leads to unexpected deformation and serious damage in such structures.

In order to solve this problem, the Kanto branch of the Japanese Geotechnical Society has established a study committee on the ground deformation caused by the change of groundwater level for 3 years from 2010 to 2012. The authors belong to the study committee and have already presented some related papers (Sreng et al. 2009).

This chapter aims to introduce the activities of the study committee and its recent study results. This study introduces the ground deformation distribution of Tokyo city, and the results of centrifuge model tests of ground deformation caused by the change of groundwater level. The phenomenon of the clay ground deformation also will be simulated by theoretical analysis.

20.2 Activities of the Study Committee

Our study activities are divided into three groups as shown in Fig. 20.1. In order to investigate the situation of ground upheaval, Group 1 is working on data acquisition and mapping of ground upheaval distribution using levelling survey data published by the Japanese Government. Based on the situation of ground upheaval investigated by Group 1, Group 2 is working on experimental and theoretical study in order to clarify and predict the ground upheaval phenomenon caused by the rising of groundwater level. Group 3 is mainly working on investigation of the damage mechanism of underground structures that might be affected by the ground upheaval phenomenon. In order to investigate the damaged condition of underground structures, Group 3 is also working on analysis of underground structures

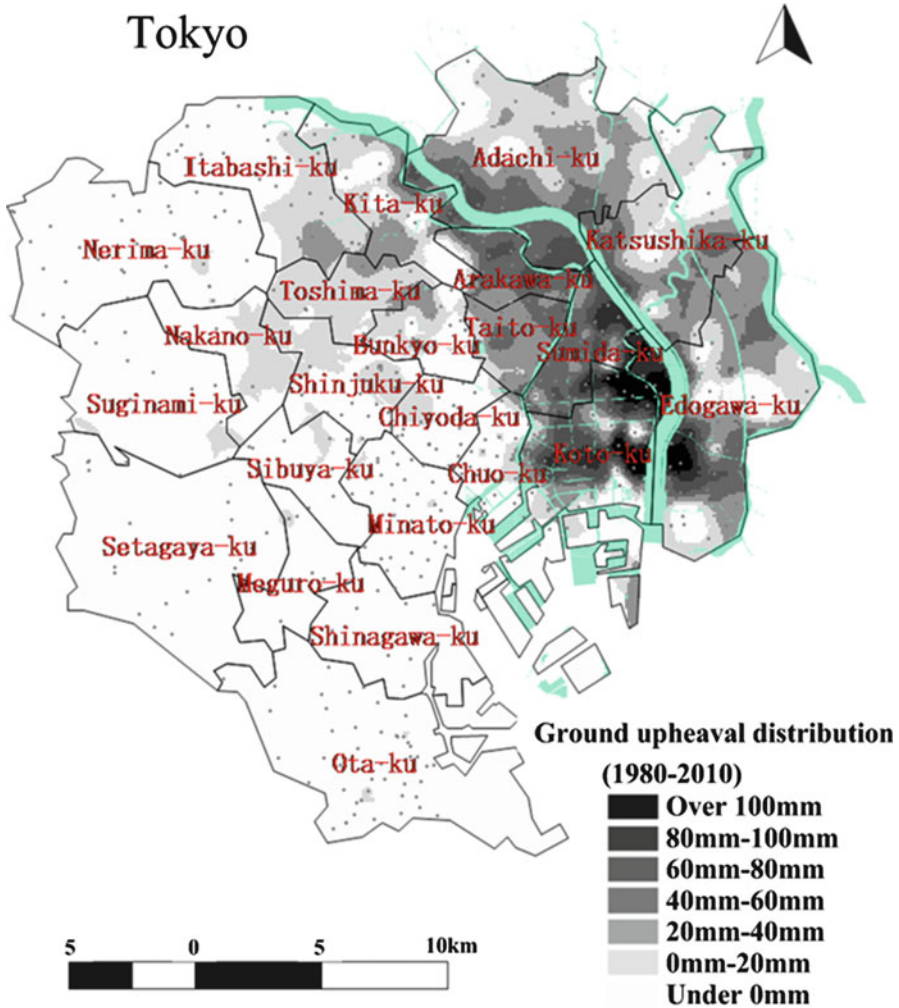


Fig. 20.2 Ground upheaval distribution of Tokyo area (30 years: 1980–2010)

using monitoring data and the map of ground upheaval distribution developed by Group 1. The final goal of the study committee is to propose a countermeasure method to protect the underground infrastructure from damage.

20.3 Mapping of Ground Upheaval Distribution

Figure 20.2 shows the ground upheaval distribution of the Tokyo area mapped from leveling data of the Annual Report of Civil Engineering Support & Training Center, Tokyo Metropolitan Government (1952–2010). In this figure, the black shaded area

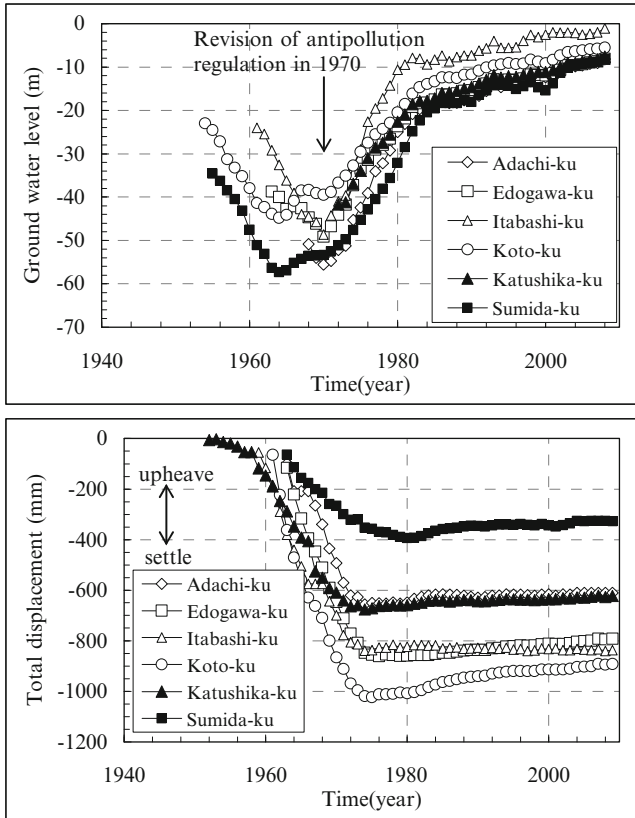


Fig. 20.3 Relation between ground water and ground displacement (Tokyo)

represents upheaval distribution and the white area shows settlement distribution. It shows that ground upheaval occurred in most areas of Tokyo as well as other cities in Japan. It is considered that differential deformation of ground (upheaval and settlement), as shown in the figure, may influence all underground structures constructed in those areas.

Figure 20.3 shows an example of the relation between groundwater level and ground displacement plotted against time. It can be seen that after the revision of antipollution regulation for controlling the use of groundwater from 1970 on in Japan, groundwater level has risen year by year. As a result, ground upheaval occurred in a wide area of Japan in accordance with the rising of groundwater level. It was noted that the ground upheaval phenomenon did not immediately occur when the groundwater level began rising in 1970, but after 10 years, in 1980, the ground upheaval phenomenon has appeared year by year.

Table 20.1 Material properties

Soil particle density ρ_s (g/cm ³)	2.758
Liquid limit (%)	59.7
Plastic limit (%)	28.4
Plastic index	31.3
Compression index C_c	0.342
Swelling index C_s	0.015–0.035

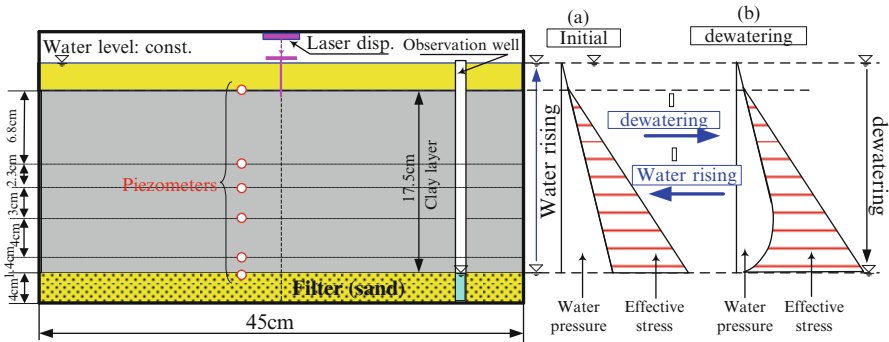


Fig. 20.4 Configuration and instrumentation of the test model

20.4 Centrifuge Model Test

Material used in the centrifuge model test was alluvial clay that was taken from Tachibana Bay in Tokushima Prefecture. The clay material used for the model test was slurry material by adjusting 90 % of the initial water content. The physical properties of the clay material used in the tests are shown in Table 20.1.

The configuration and instrumentation of the test model is presented in Fig. 20.4. The test was conducted under 50 G of centrifugal acceleration to simulate the 8.75-mthick clay layer prototype (model scale is 17.5 cm in thick). Clay material was prepared with normally consolidated clay, which was done by conducting self-weight consolidation in a 50-G centrifugal force field. As shown in Fig. 20.4, at the bottom of the clay layer a 4-cm filter layer using sandy material was placed to simulate drainage. In the clay layer, six piezometers were installed to measure pore water pressure induced inside the clay soil. Ground surface displacement occurred during test was measured by a laser type displacement transducer installed on the top of the model container. The initial condition of ground water level (total head of the filter layer) was raised from the filter layer to 18 cm in height, which is 5 mm higher than the level of the ground surface as shown in Fig. 20.4a. Test procedures are as follows:

1. At the initial condition as shown in Fig. 20.4a, the self-weight consolidation process was conducted at the 50-G level for about 10 h to complete the self-weight consolidation process. The completion of self-weight consolidation was determined using the “3t” method.
2. Groundwater level was lowered at the rate of 2 mm/s from the initial condition to filter layer surface. When groundwater level reached filter layer, groundwater level was paused and kept at this condition until the completion of consolidation (see process (a) to (b) in Fig. 20.4).

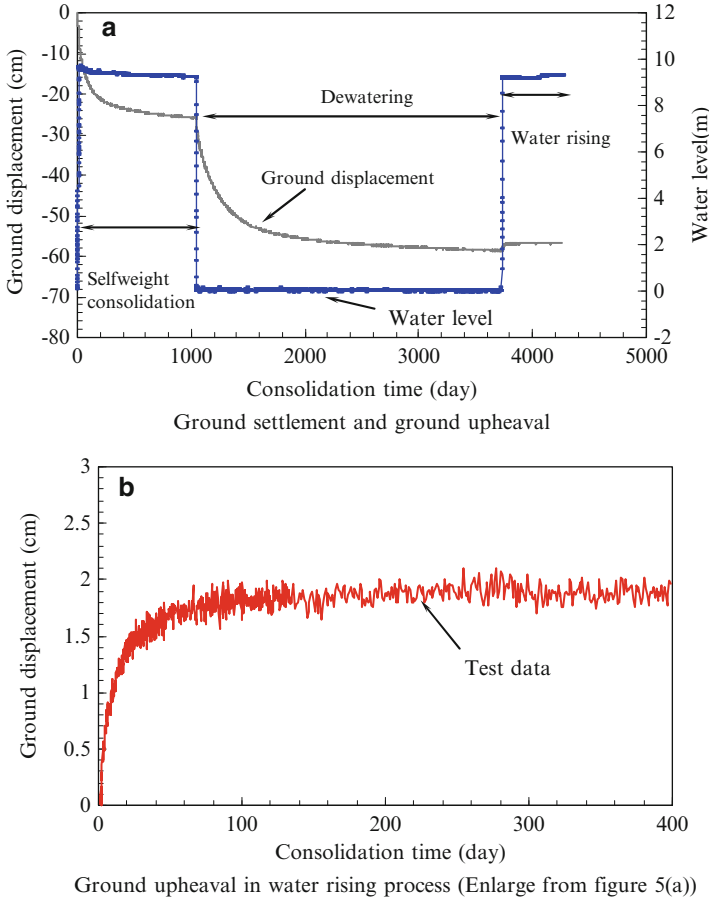


Fig. 20.5 Groundwater level, settlement and consolidation time relation. (a) Ground settlement and ground upheaval. (b) Ground upheaval in water rising process (Enlarge from Fig. 20.5a)

3. Groundwater level was raised back to the initial condition in the rate of 2 mm/s. Self-weight consolidation of the clay ground in this process was also kept until the completion of consolidation (see process (b) to (a) in Fig. 20.4).

During the test, water level on the ground surface was controlled to be constant by supplying water from a water tank mounted on the top of the model container.

20.5 Experimental Results

Figure 20.5a shows the relationships between groundwater level, ground displacement, and consolidation time in prototype scale. Figure 20.5b shows ground upheaval in the water rising process enlarged from Fig. 20.5a. As shown in Fig. 20.5a, ground settlement and ground upheaval occur in accordance with lowering and

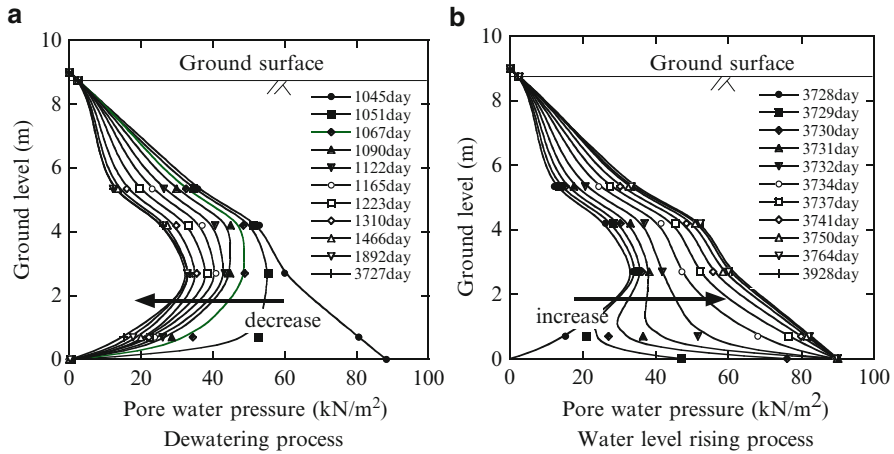


Fig. 20.6 Pore water pressure distribution. (a) Dewatering process. (b) Water level rising process

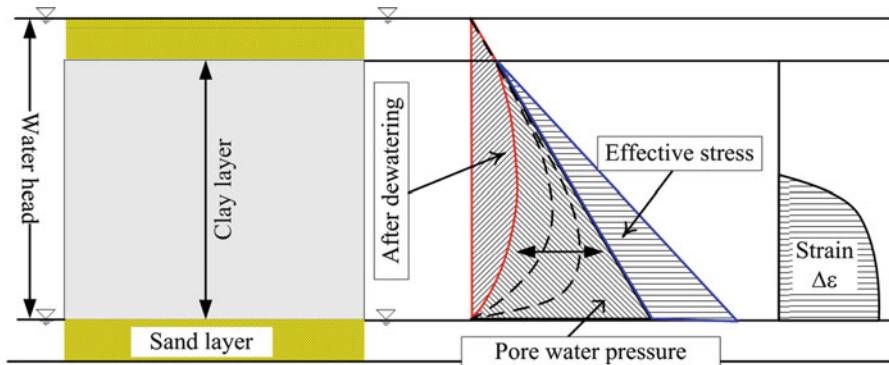


Fig. 20.7 Relationship of σ'_z , u_z and related ground strain $\Delta\epsilon$

rising of the water level. Ground upheaval caused by the rising of the ground-water level was successfully verified by the centrifuge model test. This result shows the same tendency as measurement data on file, as presented in Fig. 20.3.

Figure 20.6 shows pore water pressure distribution induced in a clay layer during lowering and rising of the water level. In the dewatering process, pore water pressure distribution dissipates from hydrostatic pressure condition (before dewatering) to the final stage (after dewatering) as shown in Fig. 20.6a. It is noted that pore water pressure distribution at the final stage of the dewatering process does not become zero. In the process of water level rising, pore water pressure distribution increases in accordance with the rising of the water level. It is revealed that pore water pressure distribution in a vertical direction of clay ground presents curves shaped similar to curves in consolidation theory as shown in Fig. 20.7.

Figure 20.7 illustrates a schematic view of the relationship of effective stress, pore water pressure and seepage pressure as given in Eq. (20.1), and the related ground strain.

$$\sigma'_z = \sigma_z - u_z \quad (20.1)$$

where σ'_z is effective stress of soil, u_z is pore water pressure, and σ_z is total stress of soil.

20.6 Theoretical Study

20.6.1 One Dimensional Consolidation Theory

In order to clarify the phenomenon of ground settlement and ground upheaval caused by the lowering and rising of groundwater level, a modified theoretical model based on one-dimensional consolidation theory proposed by Mikasa and Takada (1995) was used.

In this consolidation theory, the following equation was adopted as the governing equation for soft clay by consideration of self-weight and the variable of coefficient of consolidation C_v .

$$\begin{aligned} \frac{\partial \epsilon}{\partial t} = c_{vr} \left[\left(\frac{f_0}{f} \right)^2 \left\{ \frac{\partial^2 \epsilon_r}{\partial z_0^2} + \frac{f - f_2}{f} \left(\frac{\partial \epsilon_r}{\partial z_0} \right)^2 \right\} - \left(\frac{f_0}{f} \right) \frac{d}{d \epsilon_r} (m_{vr} \cdot \gamma') \frac{\partial \epsilon_r}{\partial z_0} \right] \\ + \left(\frac{f_0}{f} \right) \frac{\partial c_{vr}}{\partial z_0} \left\{ \left(\frac{f_0}{f} \right) \frac{\partial \epsilon_r}{\partial z_0} - m_{vr} \cdot \gamma' \right\} \end{aligned} \quad (20.2)$$

where ϵ_r is relative strain, m_{vr} is relative coefficient of volume compressibility, and c_{vr} is relative coefficient of consolidation presented by Eqs. (20.3), (20.4), and (20.5), respectively.

$$\epsilon_{vr} = \ln \left(\frac{f_1 - f_2}{f - f_2} \right) \quad (20.3)$$

$$m_{vr} = \frac{f}{f - f_2} m_v \quad (20.4)$$

$$c_{vr} = \frac{f - f_2}{f} c_v \quad (20.5)$$

where f_1, f_2 is arbitrary volume ratio, m_v is coefficient of volume compressibility, and C_v is coefficient of consolidation presented by Eq. (20.6).

$$c_v = \frac{k}{m_v \gamma_w} \quad (20.6)$$

Fig. 20.8 f -log P relation

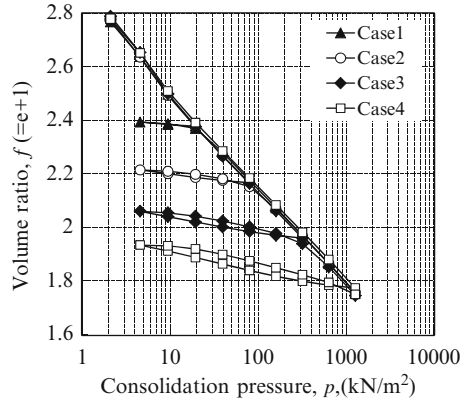
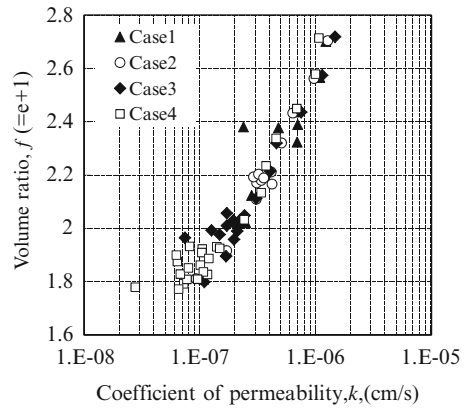


Fig. 20.9 f -log k relation



c_v is a variable value that can be calculated from coefficient of volume compressibility m_v and coefficient of permeability k . Here, coefficient of volume compressibility m_v and coefficient of permeability k is determined from f -log p relation (Fig. 20.8) and f -log k relation (Fig. 20.9) obtained from the standard consolidation test as shown in Eqs. (20.7), (20.8), and (20.9).

$$m_v = \frac{0.4343C_c}{fp_i} \cdot 10^{\frac{f-f_i}{C_c}} \quad (\text{for normally consolidated region}) \quad (20.7)$$

$$m_v = \frac{0.4343C_s}{fp_i} \cdot 10^{\frac{f-f_i-(C_s-C_c)\log\frac{p_c}{p_i}}{C_s}} \quad (\text{for over-consolidated region}) \quad (20.8)$$

where C_c is compression index, C_s is swelling index, p_c is consolidation yield stress, and f_i, p_i is experimental constants.

$$k = k_i 10^{\frac{f-f_{ik}}{C_k}} \quad (20.9)$$

where k_i, C_k, f_{ik} are experimental constants (Table 20.2).

Table 20.2 List of the parameters for one-dimensional analysis

$G_s(=\rho_s/\rho_w)$	2.758
$p_i(\text{kN/m}^2)$	1
C_c	0.341
C_s	0.015–0.035
f_i	2.827
$k_i(\text{cm/s})$	1
C_k	0.722
f_{ik}	6.891

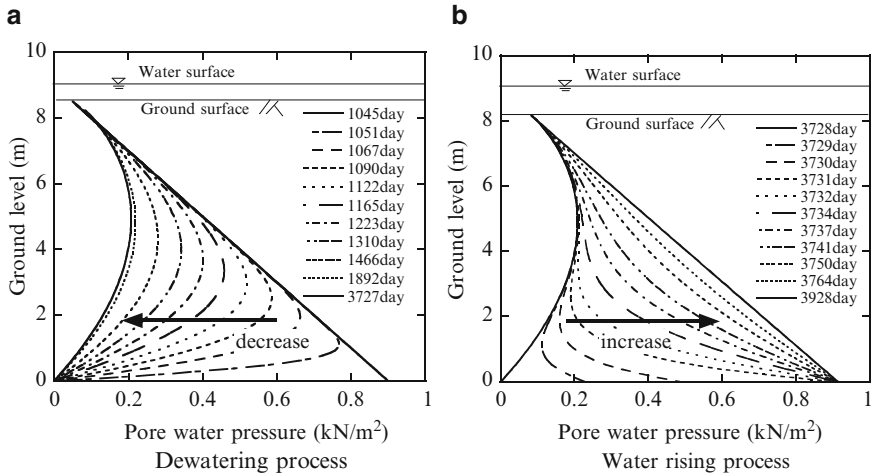


Fig. 20.10 Pore water pressure distribution of analysis. (a) Dewatering process. (b) Water rising process

20.6.2 Comparison of Test and Analysis Results

Results of centrifuge model tests were calculated using the proposed analytical model. Figure 20.10 shows pore water pressure distribution of dewatering and water rising process calculated from the one-dimensional consolidation theory. Calculated pore water pressure in both processes shows the same tendency as results of the centrifuge model test shown in Fig. 20.5.

Figure 20.11a shows ground displacement obtained from calculation compared with test results of all processes. Settlement obtained from analytical results is slightly larger than that of test results. However, the phenomenon of ground settlement and ground upheaval in dewatering and water rising processes obtained from test results is simulated well by analytical results. Figure 20.11b shows the comparison of ground upheaval processes obtained from tests and analysis results. It reveals that the phenomenon of ground upheaval of the test result was simulated well by the analysis result.

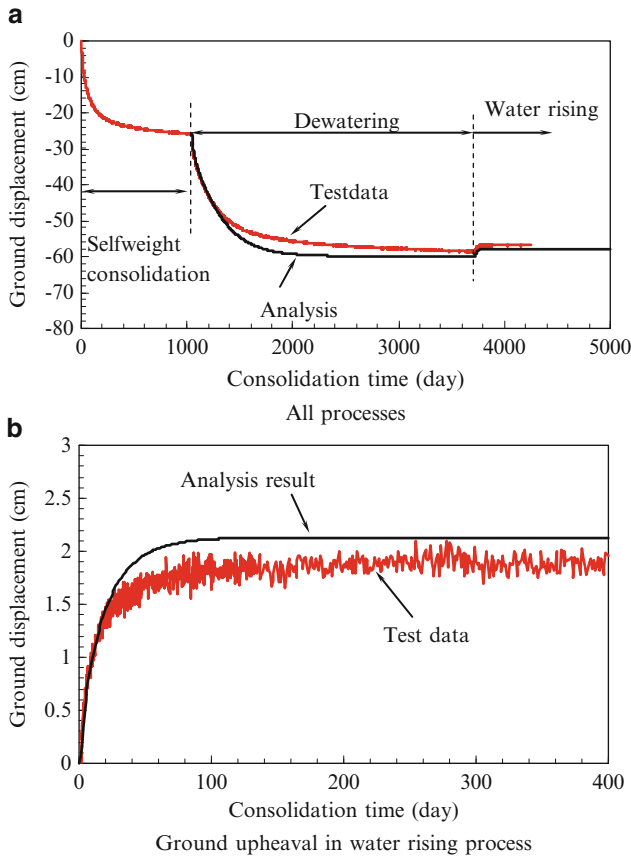


Fig. 20.11 Comparison of ground settlement between test and analysis results. (a) All processes. (b) Ground upheaval in water rising process

Figure 20.12 shows the calculated strain distribution obtained from one-dimensional theory. Note that because of the change of effective stress caused by the change of groundwater level, the change of strain distribution concentrated from the bottom of the clay layer up to the middle of clay ground layer. This phenomenon might affect the underground structure constructed in lower part of the clay ground layer.

20.6.3 Two Dimensional FE Analysis

One case of two-dimensional analysis was carried out as an example in order to observe the effect of uplift caused by the restoration of the water table to the underground structure.

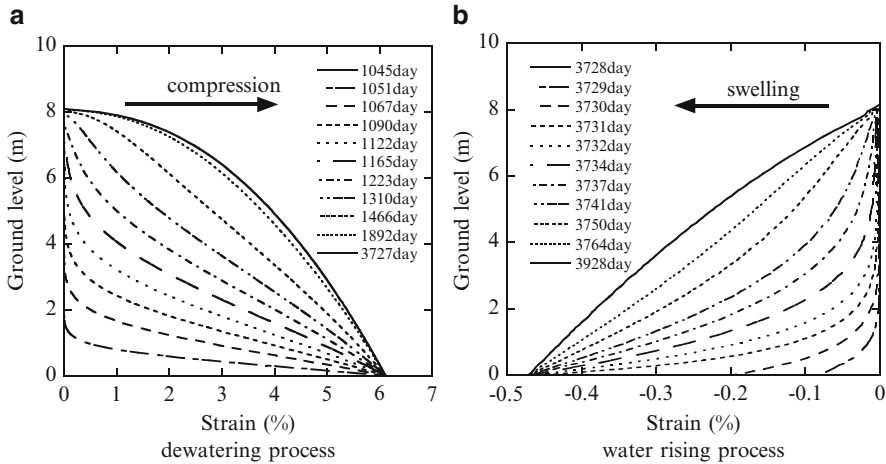


Fig. 20.12 Strain distribution obtained from analysis. (a) Dewatering process. (b) Water rising process

The analysis was carried out under some imaginary conditions. The condition was set so that the location is assumed to be a coastal area like Tokyo. Therefore, the results shown in this section might not be a general tendency but it could be one of the possible cases that may occur in real life.

The code used for the simulation is 'Dif,' which is commercial coupled deformation-seepage flow analysis software based on the original DACSAR coded by Iizuka and Ohta (1987). The Sekiguchi-Ohta model is used as the constitutive equation for clay material in this analysis. Figure 20.13 shows the dimension of the analysis model and boundary condition. Table 20.3 shows the list of the parameters used for the analysis.

Table 20.4 shows the analysis schedule. The underground structure is assumed to be a shield tunnel with diameter of 10 m. The thickness of the reinforced concrete (RC) segment is assumed to be 45 cm.

Note that excavation for the tunneling is not taken into account in order to see especially the effect of the water table restoration.

Figure 20.14 shows the vertical distribution of the pore pressure during the analysis. Figure 20.15 shows the vertical displacement of both top and bottom of the tunnel after the restoration of the water level.

Heave at the top of the tunnel is larger than the bottom. Therefore the tunnel stretches vertically and shrinks horizontally in this analysis. Figure 20.16 shows the bending moment of the tunnel at the final analysis stage (5 years after restoration).

Note that the effect of the heave after restoration of the water level to the tunnel is not the same depending on the timing of the construction. In this analysis there might be a possibility of cracking inside and outside because of the additional tension caused by the restoration of the water table.

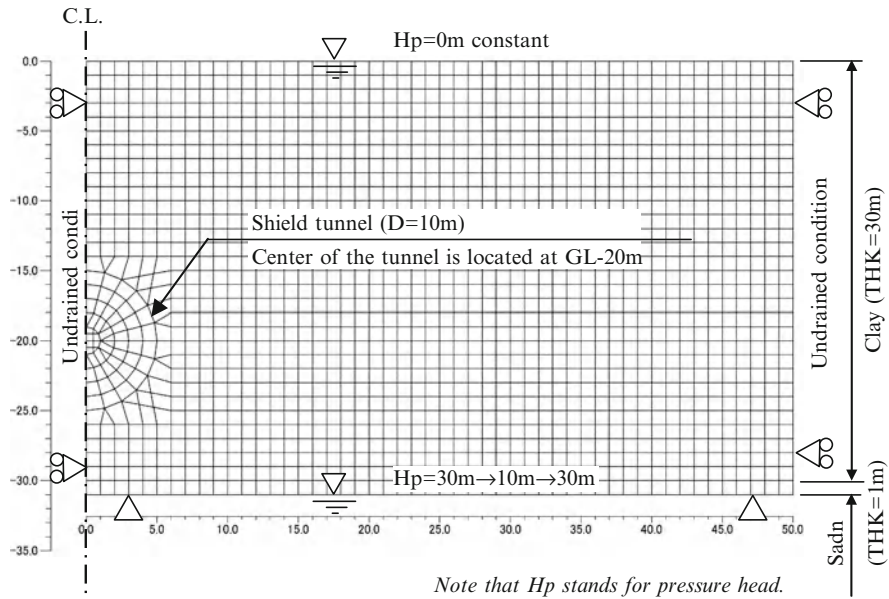


Fig. 20.13 FE mesh and boundary condition

Table 20.3 List of the parameters for analysis

Parameters for clay with plastic index = 50 and over consolidation ratio = 1			
γ_t (kN/m ³): Unit weight			17.0
D : Coefficient of Dilatancy proposed by Shibata (1963)			0.089
Λ : Irreversibility ratio expressed by $\Lambda = 1 - \kappa/\lambda$			0.800
M : Critical state parameter			0.963
ν' : Effective Poisson's ratio			0.369
k_x (m/s): Coefficient of permeability in x direction			1.00E-6
k_y (m/s): Coefficient of permeability in y direction			1.00E-7
K_0 : Coefficient of Earth Pressure at rest immediately after K_0 -normal consolidation			0.585
λ : Compression index in the $e-\ln(p'/p_0')$ relation			0.365
e_0 : Void ratio corresponding to σ_{vo}' at reference state			1.35
Parameters for sand			
γ_t (kN/m ³): Unit weight	20.0	ν' : Effective Poisson's ratio	0.300
E (kN/m ²): Young's modulus	$8.4E + 4$	k (m/s): Coefficient of permeability	1.00E-5
Parameter of RC segment	$E = 3.70E+7$ (kN/m ²), $I = 6.08E-3$ (m ⁴ /m), $A = 0.450$ (m ² /m)		

20.7 Conclusions

This study aimed to clarify the mechanism of ground upheaval caused by the rising of the water level. Investigation of ground upheaval distribution, centrifuge model test, and numerical analysis were conducted. The main concluding remarks drawn from this study are summarized as follows.

Table 20.4 Analysis schedule

Stage	Incremental days	Control of the pressure head at the bottom
1	100	Initial stress calculation H_p at the bottom = 30 m
3–12	100	H_p is decreased from 30 to 10 m in 100 days
13–32	3,560	Keep H_p = 10 m for 10 years
33–43	100	H_p is restored from 10 to 30 m in 100 days. Before restoration of the water level shield tunnel is modeled as beam element
44–54	1,825	Keep H_p = 30 m for 5 years

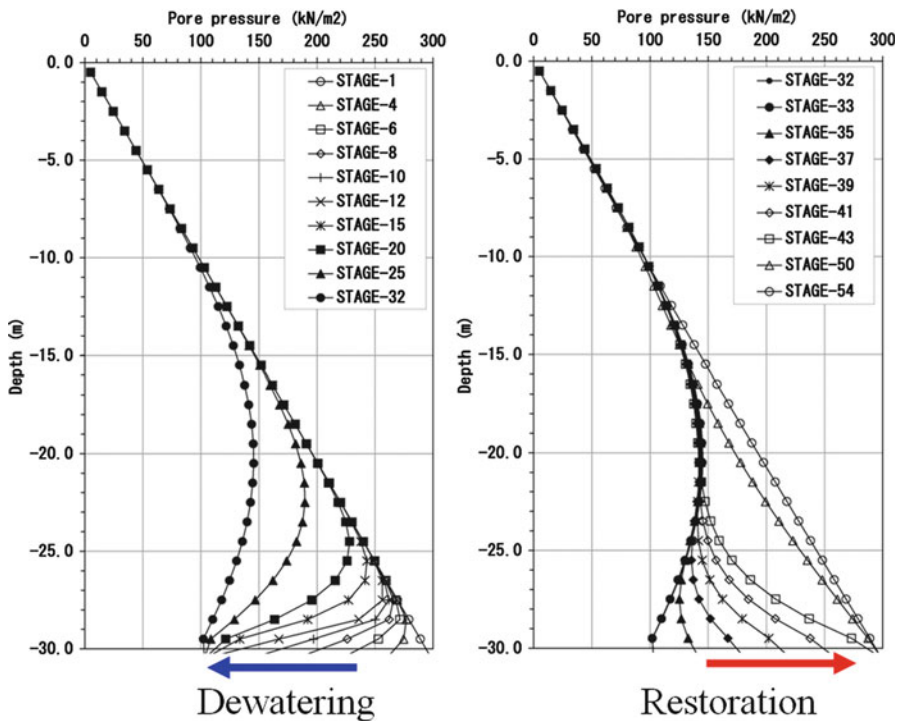


Fig. 20.14 Pore pressure distribution obtained by the FE analysis. (a) Dewatering. (b) Restoration

- Using leveling survey data provided by the Japanese government, a map of ground upheaval distribution of Tokyo city in Japan was created to clarify the situation of ground upheaval. It is found that because of the rising water level, ground upheaval occurred in a wide area, especially in large cities such as Tokyo. Ground upheaval might influence all underground structures constructed in such upheaval areas.
- Centrifuge model test successfully simulated the relationship between underground water level and ground movement obtained from field measurement data. Furthermore, change in pore water pressure distribution caused by rising

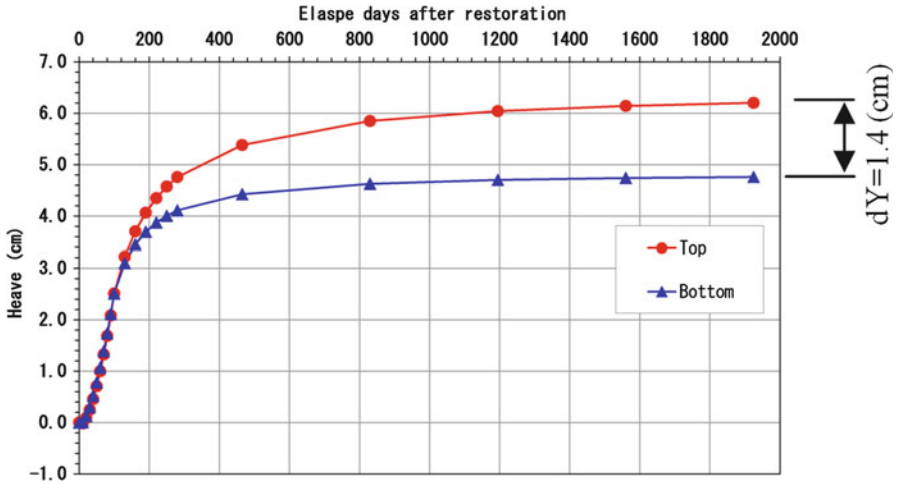
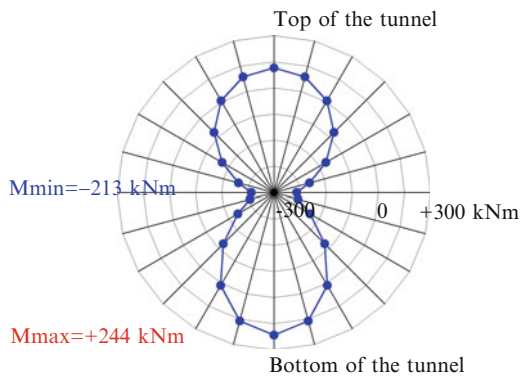


Fig. 20.15 Heave of the top and bottom of the tunnel after restoration

Fig. 20.16 Bending moment of RC segment caused by restoration of water table



and lowering of water level was clearly observed by piezometers. It was seen that pore water pressure is greatly changed at the lower part of a clay layer. Therefore, it can be said that observed pore water pressure is an important datum for verifying the numerical analysis.

3. Numerical theory based on the one-dimensional consolidation theory proposed by Mikasa was used to verify the results of the centrifuge model test. By comparing the results of experimental and analytical study, it was shown that the proposed numerical model can be used to predict ground upheaval as well as ground settlement.
4. One case of two-dimensional FE analysis was carried out as an example to simulate the effect of the ground upheaval to the underground structure. The deformation of the structure (i.e., stretches vertically and shrinks horizontally) is likely to follow the upheaval of the soil according to the analysis. Further study on the interaction between structure and the ground upheaval is to be

carried out and the effect of the three-dimensional structural stiffness in this phenomenon also is to be examined.

In order to investigate and estimate the influence of ground upheaval on underground structures, further studies by both numerical and experimental approaches are necessary.

References

- Civil Engineering Support & Training Center, Tokyo Metropolitan Government (1952–2010). Annual report on leveling data
- Iizuka A, Ohta H (1987) A determination procedure of input parameters in elasto-viscoplastic finite element analysis. *Soil Found* 27(3):71–87
- Mikasa M, Takada N (1995) Nonlinear consolidation theory for nonhomogeneous soil layers. In: Proceedings of the international symposium on compression and consolidation of clayey soils, IS-Hiroshima, pp 447–452
- Shibata T (1963) On the volume change of normally consolidated clays. *Disaster Prevention Research Institute Annuals*, No. 6, Kyoto University (in Japanese)
- Sreng S, Li L, Sugiyama H, Kusaka T, Saito M (2009) Upheaval phenomenon in clay ground induced by rising groundwater level. In: Proceedings of the fourth biot conference on poromechanics. Columbia University, New York, pp 106–203

Chapter 21

A Robust Control Approach for Decision Making and Reliability Design of Soil Structures

Takeshi Sato, Takeshi Nagae, and Hirofumi Nishida

21.1 Introduction

In the design and construction method selection on soil structure, when the ground is vast and characterized by irregularities, it is desirable that the problem be formulated in a stochastic (and not deterministic) manner (The Japanese Geotechnical Society 1999). Reliability design is a potential method that takes the probability characteristics of ground properties into account. In reliability design, site investigations are first carried out at multiple locations on the site. Next, the probability distribution of ground characteristics (e.g., soil strength and soil density) are defined based on these investigations. Finally, from the probability distribution obtained in this way, the soil structure is designed based on some desired criteria (e.g., minimization of the expected value of the life cycle cost of the soil structure). It is essential that the probability distribution of the ground properties is accurately estimated in the reliability design.

However, because of vastness and irregularities in the ground, the site investigations, even when measured a number of times and at differing places,

T. Sato, D.Eng. (✉)

Civil Design and Service Department of Osaka Head Office, Toyo Construction Co., Ltd, 4-1-1 Koraihashi, Chuo-ku, Osaka 541-0043, Japan
e-mail: sato-takeshi@toyo-const.co.jp

T. Nagae, D.Eng.

Department of Management Science and Technology, Tohoku University, 6-6 Aoba, Aramaki, Aoba-ku, Sendai, Miyagi 980-8579, Japan

Graduate School of Engineering, Tohoku University 6-6-11 Aoba, Aramaki, Aoba, Miyagi 980-8579, Sendai
e-mail: nagae@m.tohoku.ac.jp

H. Nishida, D.Eng.

Kanagawa Water Supply Authority, 1194 Yasashicho, Asahi-ku, Yokohama, Kanagawa 241-8525, Japan
e-mail: nishida.6u@kwsa.or.jp

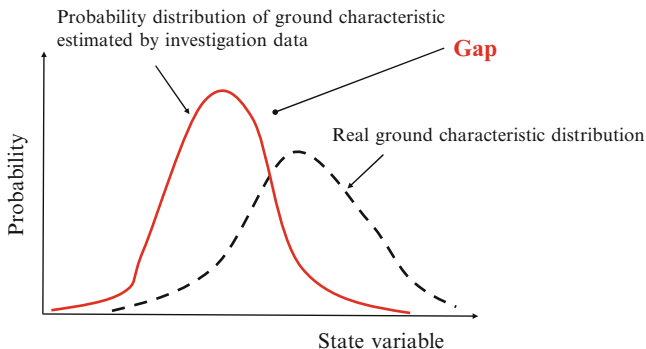


Fig. 21.1 Concept of gap between a probability distribution on design and real ground

may not be enough to grasp the true distribution of ground characteristics. Therefore, the probability distribution that is estimated from ground investigations may not necessarily correspond with the true distribution of ground characteristics; in some cases there might be significant divergence (gap) between the probability distribution and the true distribution. In reliability design, the designer aims to identify any unnecessary construction methods and estimate the associated unnecessary cost by evaluating the incorrectness of the estimated stability of the soil structure. If the designer is unable to amply carry out an investigation to estimate the probability distribution of the ground characteristics as described, it is important that a generalized theory of reliability design is made available (Fig. 21.1).

A robust control approach is one approach for rational decision making in cases where sufficient information to estimate the probability distribution is unavailable. In this approach, the “most undesirable to the extent that it does not deviate to the extreme” is adopted for the probability distribution obtained from the investigation results. In this study, we try to generalize conventional reliability design, based on the idea of robust control approach for a given soil structure. More specifically, the probability distribution of ground characteristics is first estimated from investigative results, and is considered to be the “reference distribution.” Subsequently, artificial probability distributions are generated at a certain “distance” from the reference. In these artificial distributions, the distribution to the most undesirable result (i.e., to maximize the expected value of life-cycle cost) is a “model distribution,” and the design is based on this model distribution. In addition, in robust control, the aim is to grasp the specifications for soil structure using the minimum cost based on design results. By using this approach, while making the best use of the information obtained from ground investigations, it becomes possible to incorporate robust design for any possible distribution. In addition, “distance” between the reference distribution and artificial distribution, model distribution, and the design based on it are all uniquely determined in this approach. In other words, the parameters that are required to determine the model distribution and design can be aggregated into only one scalar as “distance” from the reference distribution. For this reason, in the robust control approach, the information underlying the design can be easily shared between the designer (contractor) and the client, and a rational consensus is possible.

The purpose of this chapter is to generalize the concept of robust control approach, which can be applied to reliability design on soil structures, and to construct methods required for concrete calculations. This chapter is organized as follows: First, the basic idea of robust control approach is presented. Next, the design method using robust control approach is proposed. Then, an application example is shown, as applied to the imaginary construction of embankments on soft ground. Finally, the applicability of the reliability design for robust control approach is confirmed.

21.2 Robust Control Approach for Reliability Design on Soil Structures

Specification design and reliability design are two aspects of soil structure design. Specification design takes into consideration factors associated with known events wherein a particular situation is clearly defined. Reliability design, on the other hand, is a probabilistic model that considers the probability of the occurrence of an event. However, when the soil structure is designed, there is a possibility that situations not defined initially may occur. We define such unforeseen situations using a model-risk situation and estimate the probability of unknown situations. The probability of unknown situations means that the chance of an event occurring can be enumerated but it is not possible for probability models to be made. The probability of these events can never be estimated. A model risk situation means that the probable models can be made, but it is not possible for the occurrence probability of these models to be accurately estimated.

The problem addressed in this chapter is the model-risk situation. In this situation, probability distribution of the design parameters used for the reliability design might include a gap parameter in order to include distribution of the real ground characteristics. In this chapter, the gap between probability distribution of the design parameters and distribution of the real ground characteristics is assumed to be the distance between the two probability distributions. The magnitude of the gap is represented as an estimate from relative entropy, as used in information theory. Second, we propose a robust control approach that can estimate the relationship between the life cycle cost (hereafter referred to as LCC) on soil structure and the risk-sensitivity variation for the gap.

21.2.1 Formulation of the Gap Between Two Probability Distributions by Relative Entropy

Probability distribution gap is a divergence between two probability distributions. In information theory, the gap is often represented as relative entropy (Cover and Thomas 1991) or Kullback–Leibler divergence (Kapur 1989; Stutzer 1995).

The gap between the distribution of real ground characteristics and probability distribution of the state variable in reliability design can be represented by discretized relative entropy as follows:

$$D = \sum_i^n q_j(i) \ln \frac{q_j(i)}{p_j(i)} \quad (21.1)$$

Where D is the probability distribution gap, $q_j(i)$ and $p_j(i)$ are the true probability distribution that represents the real ground characteristics and the objective probability distribution, obtained from the investigation data, respectively.

21.2.2 Robust Control Approach Incorporating Risk Sensitivity

The gap between the two aforementioned probability distributions can be represented in terms of relative entropy (Eq. 21.1). In reality, however, it is not possible to quantify the gap because the true probability distribution cannot be definitely known. Therefore, in this chapter true probability distribution is forecasted by multiplying a risk coefficient to the relative entropy. Because Eq. (21.1) is composed of true probability distribution $q_j(i)$ and objective probability distribution $p_j(i)$, the risk coefficient is able to estimate the range of gap uncertainty between $q_j(i)$ and $p_j(i)$. In this chapter this coefficient is defined as the risk sensitivity coefficient θ ($\theta \geq 0$). If the risk sensitivity coefficient θ is zero, the uncertain gap is zero, $p_j(i)$ is trusted completely and $p_j(i)$ is fully identical with $q_j(i)$. Conversely, when $p_j(i)$ is not trusted, θ increases. But in case of excessively large θ , $q_j(i)$ is estimated by choosing a completely different probability distribution against $p_j(i)$, and investigation data-based substantial design becomes meaningless. For this reason, θ , as given in the design stage, should be set within certain limits.

Meanwhile, the initial cost for the soil structure (including the construction costs and construction methods for soil structure stability) and LCC are affected by the probability distribution of the state variables associated with investigation data and tests results. Contractors and clients should select the design results that minimize the sum of these costs in the final design stage. In this decision-making process, it is important to choose options that will minimize the final total cost, under conditions for which maximum gap occurs between each probability distribution. In this chapter, total cost is taken into consideration in the design, and the risk θ must choose as the maximum; H is defined as the maximum risk in this chapter. Therefore the range of H is $H \geq 0$, where $H = 0$ means that the objective probability distribution can be completely trusted. The range of θ is $0 \leq \theta \leq H$. In Fig. 21.2, these processes are represented as the relationship between the maximum gap H and the contour of LCC , including the initial cost. As mentioned before, it is impossible to know the true probability distribution. Therefore, the probability distribution $q_a(i)$ against $p_j(i)$ is considered as a substitute to the true probability distribution,

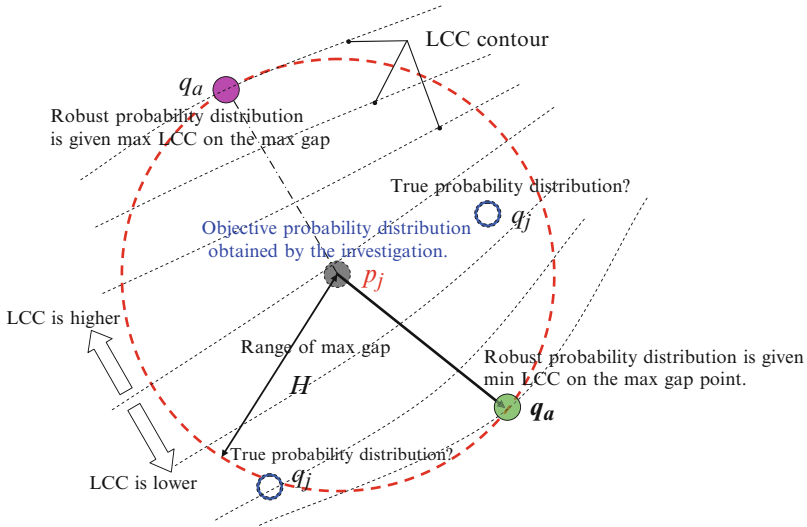


Fig. 21.2 Concept of the relationship between an objective probability distribution $p_j(i)$ and a robust probability distribution $q_a(i)$ and a range of max gap H

and we assumed LCC and risk as the circle where the center point is $p_j(i)$ estimated by the investigation data, and the radius is the maximum gap H . From Fig. 21.2, the intersection points of the probability distribution $q_a(i)$ with the maximum gap H and the LCC contour line added include the maximum LCC and the minimum LCC . The considerable probability distribution should choose the q_a that intersects on the minimum LCC contour line because it is important to choose the minimum total cost under the maximum gap. In this chapter, we refer to this decision making as the robust control approach (Zhou et al. 1995; Ben-Tal and Nemirovski 1998, 2002; Lim and Shanthikumar 2007; Petersen et al. 2000). The probability distribution (or probability) located at the maximum of divergence is referred to as the robust probability distribution (or robust probability) q_a .

21.3 Decision-Making Framework Used in Robust Control Approach

21.3.1 Calculation of Robust Probability Distribution (Using One Variable)

This section presents a discretized robust probability distribution $q_a(i)$ involving one state variable (Nishida et al. 2011). As mentioned before, it is important to

choose $q_a(i)$ under the maximum gap. The robust probability distribution $q_a(i)$ can therefore be described as:

$$\{q_a(i)\} = \arg \max_{q_a} \left\{ \sum_{i=1}^{N_a} q_a(i) \cdot \pi_a(i) - \frac{1}{\theta} \sum_{i=1}^{N_a} q_a(i) \ln \frac{q_a(i)}{p_j(i)} \right\} \quad (21.2)$$

where $p_j(i)$ is the objective probability distribution representing the ground characteristics based on investigation data and soil test results. Furthermore, $i = 1, 2, \dots, N_a$ denotes the index of data representing the probability distribution, and the objective function $\pi_a(i)$ is decision factors on design, where each i represents a specific value of the $\pi_a(i)$. Since $q_a(i)$ is a probability distribution

$$\sum_{i=1}^{N_a} q_a(i) = 1 \quad (21.3)$$

Using Lagrange multiplier λ_L and Eqs. (21.2) and (21.3),

$$L(q_a(i), \lambda_L) = \sum_{i=1}^{N_a} q_a(i) \cdot \pi_a(i) - \frac{1}{\theta} \sum_{i=1}^{N_a} q_a(i) \ln \frac{q_a(i)}{p_j(i)} - \lambda_L \left\{ \sum_{i=1}^{N_a} q_a(i) - 1 \right\} \quad (21.4)$$

The condition that Eq. (21.4) is to have the extreme value is

$$\frac{\partial L}{\partial q_a(i)} = \pi_a(i) - \frac{1}{\theta} (1 + \ln q_a(i) - \ln p_j(i)) - \lambda_L = 0 \quad (21.5)$$

As a solution to Eq. (21.5) for $q_a(i)$,

$$q_a(i) = \frac{\exp(\pi_a(i) \cdot \theta)}{\exp(1 + \lambda_L \cdot \theta)} p_j(i) \quad (21.6)$$

Furthermore, from constraints of Eqs. (21.6) and (21.3)

$$\exp(1 + \lambda_L \cdot \theta) = \exp(\pi_a \cdot \theta) \sum_{i=1}^{N_a} p_j(i) \quad (21.7)$$

By substituting Eq. (21.7) into Eq. (21.6), $q_a(i)$ is

$$q_a(i) = \frac{\exp(\pi_a(i) \cdot \theta)}{\sum_{i=1}^{N_a} p_j(i) \cdot \exp(\pi_a(i) \cdot \theta)} p_j(i) \quad (21.8)$$

Using $q_a(i)$ the contractor can design and select construction methods that take the gap of each probability distribution into consideration. In a similar fashion, robust probability distribution can also be calculated for multiple state variables.

21.3.2 Decision-Making Framework Incorporating Robust Control Approach

This section describes a decision-making framework for reliability design using a robust control approach. This decision-making framework consists of three stages:

21.3.2.1 Stage 1: Estimation of Soil Structure Stability Under All Possible Events

First, the contractor obtains the design parameter variation (state variables) \tilde{X} through investigations and testing. Next, the contractor performs design calculations for the soil structure with regard to each state variable \tilde{X} . The soil structures corresponding to each of the calculations are confirmed whether or not they are out of the specified stability range. At the same time, the contractor must ensure that the construction methods, the countermeasures, the specifications, etc. have been taken into consideration from the design perspective. b_i is represented as the construction methods or the construction-method specifications, and the design-calculation taking account of each b_i is represented as performance function $g(\tilde{X}, b_i)$. The contractor assesses whether the soil structure is out of the specified stability range according to results obtained by $g(\tilde{X}, b_i)$. The objective function $\pi_a(i)$ is calculated, and the expected value π shows whether the soil structure is within the specified stability range. For instance, when the performance function is $g(\tilde{X}, b_i) > 0$ and $g(\tilde{X}, b_i) \leq 0$, π is set to 1 and 0 as a flag number. Incidentally design calculation techniques are conceivably varied. For instance, in the next section (Application Example), ground deformation analysis is performed by FEM.

21.3.2.2 Stage 2: Calculation of Robust Probability Distribution, Failure Probability, and the Expected Total Cost for Risk Sensitivity

The robust probability $q_a(i)$ is calculated using Eq. (21.8), $\pi, p_j(i)$ at all ranges of the risk sensitivity coefficient θ . The failure probability p_f is calculated by using $q_a(i)$ and π at each θ :

$$p_f = \sum \cdots \sum q_a(i) \cdot \pi \quad (21.9)$$

Furthermore, the expected total cost (hereafter referred to as *ETC*) is calculated for each θ as:

$$ETC = C_1(b_i) + C_2 \cdot p_f \quad (21.10)$$

where $C_1(b_i)$ is the initial cost associated with the construction method and countermeasures C_2 is the compensation cost. In the robust control approach, the *ETC* calculated for each risk sensitivity coefficient plays a key role in decision making. In the robust control approach, *ETC* is calculated at the assumed range for θ and C_2 .

21.3.2.3 Stage 3: Construction of the Relationship Table

A relationship table is constructed in order to compare θ , C_2 , and C_1 of the selected construction method, as well as *ETC*. The contractor and the client can confirm the relationship between θ and *ETC* along $\theta \geq 0$ by using this table. Using this framework, the contractor and the client can understand the magnitude of the risk associated with the designed soil structure to be chosen.

21.4 Application Example of Framework Incorporating Robust Control Approach

21.4.1 Application Example Settings for Deep-Mixing Method on Land

In this chapter, the applicability of the robust control approach framework is demonstrated using an application example. Figure 21.3 shows the application example analyzed in this section. This application example is not a real case. The soil structure is defined as a 5-m high embankment constructed on soft clay ground with a uniform thickness layer of 20 m. The filling speed is 50 mm/day. The building, 10 m in width and 20 m in length, is located 10 m away from the toe of the embankment slope. The specified item on the performance function of the framework is the tilt angle of the building foundation. The building failure criterion (limited angle) is set to a maximum tilt angle of $\delta_{\max} = 3 \times 10^3$ for the two ends of the building foundation, as reference of the allowable tilt angle of the small building foundation (Architectural Institute of Japan 2008). Namely, the soil structure stability defined that the tilt angle is less than the regulation angle during the 50 years after filling the embankment. To prevent building displacement caused by filling the embankment, a block type improvement of the deep-mixing method (hereafter referred to as DMM) is made to the soft clay ground below the embankment.

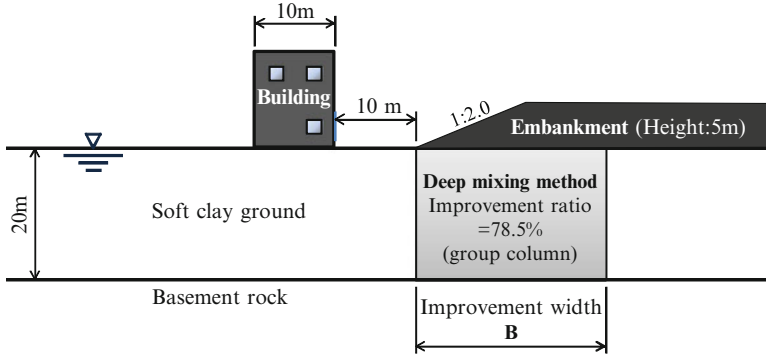


Fig. 21.3 Schematic cross-section of the application example

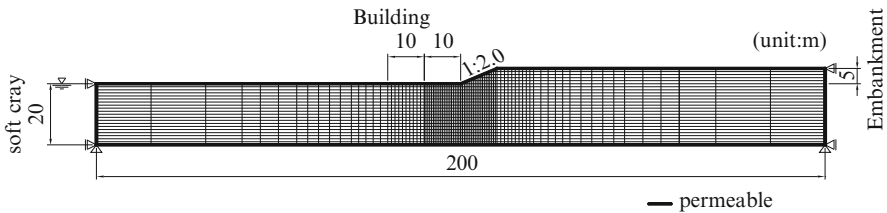


Fig. 21.4 FEM mesh used for the analysis in this application example

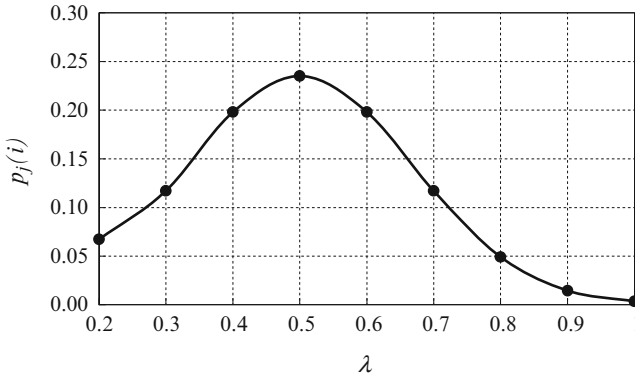
The deformation analysis was conducted by FEM. The FEM program used for the analysis was the water-soil coupled elasto-plastic finite element method code DACSAR (Iizuka and Ohta 1987). The FEM mesh is shown in Fig. 21.4. The embankment and the improvement block were linear elastic bodies. The Young modulus for the embankment was set to 2,800 kN/m² from N value = 4 and $E = 700 N$ (kN/m²) (Nishida et al. 2011). The Young modulus E for the improvement block was calculated from the following relational equation between unconfined compression strength and modulus of deformation E is

$$E = 200q_u \cdot a_p \tag{21.11}$$

where q_u is unconfined compression strength of the DMM block and a_p is improvement ratio, which were set to 500 kN/m² and 78.5 % respectively. Table 21.1 lists input parameters for the embankment and DMM block. In this table, γ is the wet unit weight, ν' is effective Poisson's ratio, and κ is the permeability coefficient. The elasto-plastic constitutive model developed by Sekiguchi and Ohta (1977) was used on the soft clay layer.

Table 21.1 Input parameter lists for the embankment and the improvement body

Material	γ (kN/m ³)	E (kN/m ²)	ν'	K_i	κ (m/day)
Embankment	16	2,800	0.33	0.5	1.0×10^{-2}
Improvement ground	16	78,500	0.33	0.5	1.0×10^{-5}

**Fig. 21.5** Objective probability distribution p_j of λ

21.4.2 Framework of Robust Control Approach for the Application Example

This framework is based on the decision-making framework in Sect. 21.3. In this application example, FEM analysis uses the compression index λ as the only state variable because the amount of ground deformation caused by embankment depends substantially on λ . In this chapter, λ is restricted to a range of 0.2–1.0 considering the deformation characteristics of general soft clay ground. Figure 21.5 shows the dependence of objective probability distribution $p_j(i)$ on λ . The relationship depicted in Fig. 21.5 assumes that the probability distribution of λ is obtained from a soil testing. Figure 21.6 shows the framework of this application example. The three stages of this framework are described below.

21.4.2.1 Stage 1

FEM analysis is performed for all combinations (λ, B) between the DMM block width B and the range of state variable λ . The maximum tilt angle of the building foundation (δ_{\max}) for every combination is selected from the analysis results. Using the calculated δ_{\max} for all combinations (λ, B) , π_i is set as

$$\pi_i = \begin{cases} 1 : \delta_{\max} \geq 3 \times 10^{-3} \\ 0 : \delta_{\max} \leq 3 \times 10^{-3} \end{cases} \quad (21.12)$$

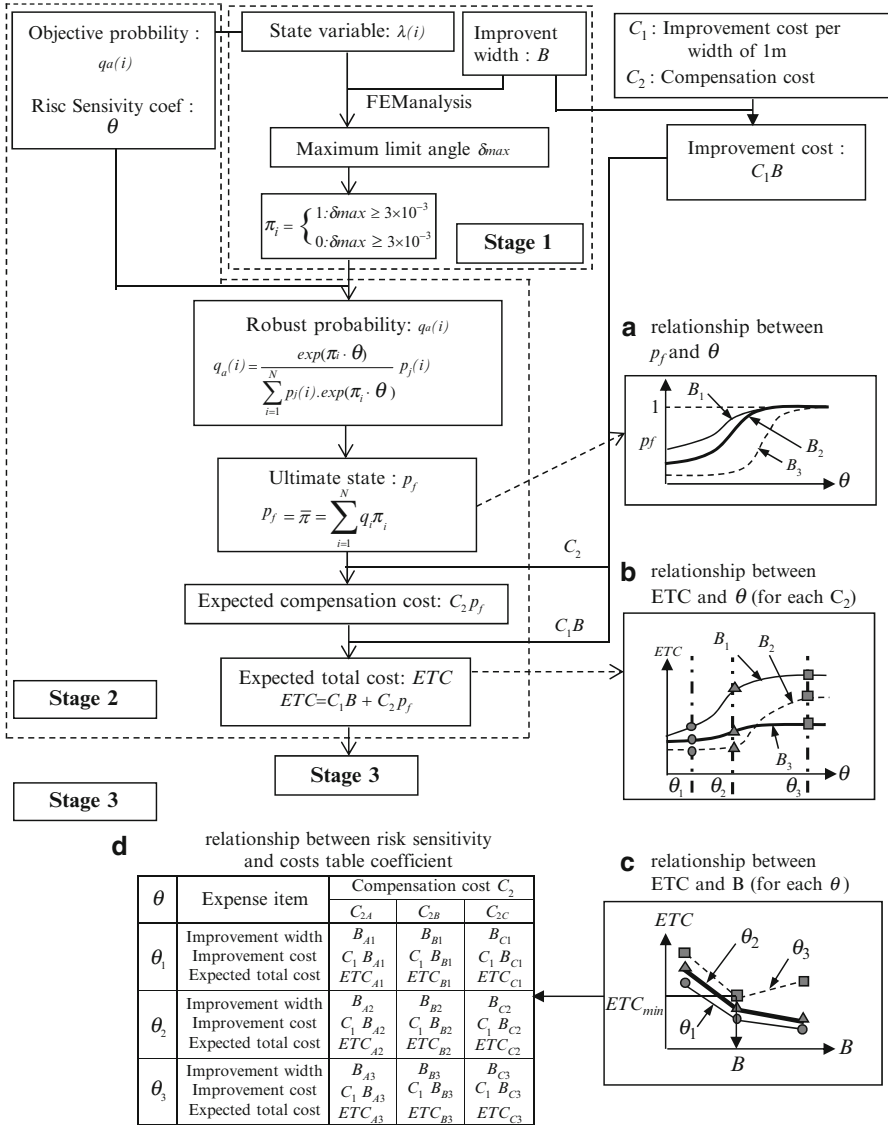


Fig. 21.6 Framework for the application example

21.4.2.2 Stage 2

The robust probability $q_a(i)$ is calculated using the objective probability $p_j(i)$ of λ, π_i, θ and Eq. (21.8). The failure probability p_f is calculated using π_i (flags number; 0 or 1), and $q_a(i)$ is then:

$$p_f = \bar{\pi} = \sum_{i=1}^N q_i(i) \pi_i \tag{21.13}$$

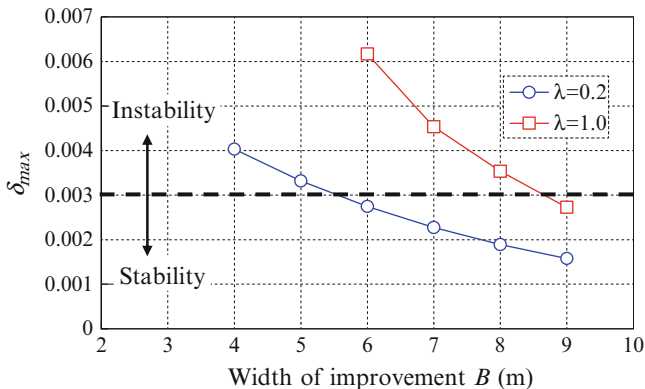


Fig. 21.7 Maximum angle of ground-level inclination δ_{max} as a result of varying the improvement width on $\lambda = 0.2$ and $\lambda = 1.0$

For each B , the p_f versus θ relationship is drawn, as shown in Fig. 21.6a. In this step, the range of θ may be set up from $p_f = 0$ to $p_f = 1$. The *ETC* is calculated by:

$$ETC = C_1B + C_2p_f \tag{21.14}$$

where C_1 is DMM cost per meter and C_2 is the compensation cost. For each B , the *ETC* versus θ relationship is shown in Fig. 21.6b.

21.4.2.3 Stage 3

The value of *ETC* and B on θ , which is to be noticed, is read by using Fig. 21.6b. The relationship between *ETC* and B on each θ is shown in Fig. 21.6c. The DMM block width B at the minimized *ETC* is read on each θ , which is to be calculated using Fig. 21.6c. The θ , C_1 , and C_2 relationship table is made as shown in Fig. 21.6d. The contractor and the client can choose the DMM width B corresponding to the reliability of the objective probability by using this relationship table.

21.4.3 Sensitivity Analysis Results

21.4.3.1 Range of Improvement-Block Width Settings

Figure 21.7 shows the maximum tilt angle of the building foundation δ_{max} with each DMM block width B on $\lambda = 0.2$ and $\lambda = 0.1$. This figure shows that the minimum B on $\delta_{max} = 3 \times 10^3$ is 6.0 m at $\lambda = 0.2$ and is 9.0 m at $\lambda = 0.1$. Hence, the selecting range to calculate δ_{max} is set at B is 0.6–0.9 m and λ is 0.1–0.2. The robust probability $q_a(i)$ and the failure probability p_f are calculated by

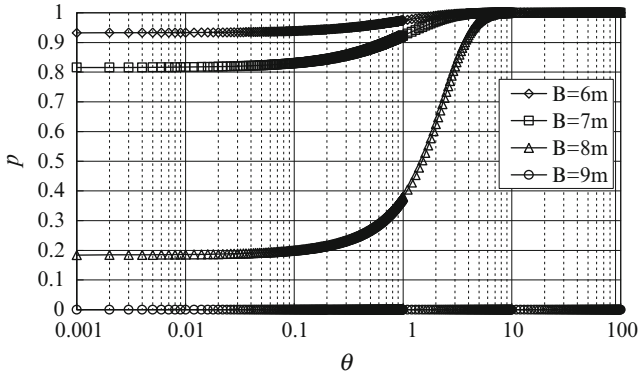


Fig. 21.8 Relationship between θ and failure probability p_f under improvement width conditions of $B = 6-9$ m

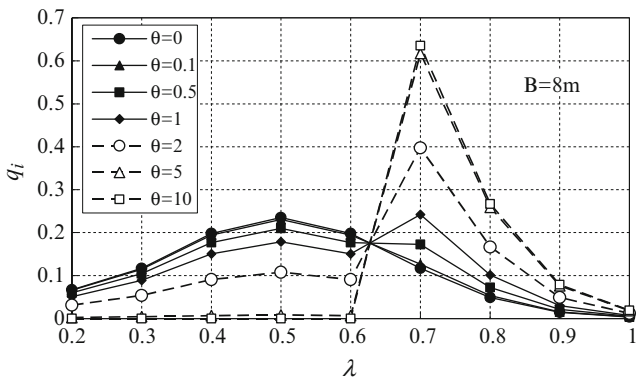


Fig. 21.9 Robust probability $q_a(i)$ with the risk sensitivity θ at $B = 8$ m

substituting $p_j(i)$, π_i , and θ for Eqs. (21.8) and (21.13). Figure 21.8 shows the relationship between θ and p_f under the $B = 6-9$ m. From this figure, in the case that B is not 9 m, p_f converge to 1 at about $\theta = 10$, but in case of $B = 9$ m, p_f is 0 irrespective of θ . The reason for this result is that the large DMM width $B = 9$ m is sufficiently stable against the ground deformation caused by construction of the embankment. Figure 21.9 shows the $q_a(i)$ on each θ at $B = 8$ m. This figure shows that the robust probability increasingly deviates from the $p_j(i)$ in λ with θ increasing, and $q_a(i)$ do not almost vary in $5 < \theta < 10$. Consequently, in the study, it is sufficient to analyze up to $\theta < 10$.

21.4.3.2 Decision Making for Improvement Width

Table 21.2 shows the DMM cost per 1 m length (C_1) and compensation cost for the building (C_2) in this application example. In calculating DMM cost, the DMM

Table 21.2 C_1 and C_2 used in this application example

Item	Cost (million yen)	Remark
Soil improvement cost		5,500 yen/m ³
C_1	172.7	Soil improvement ratio
per improvement width 1 m		Improvement depth and length
Compensation cost	100	CASE-1
C_2	10	CASE-2
	5	CASE-3

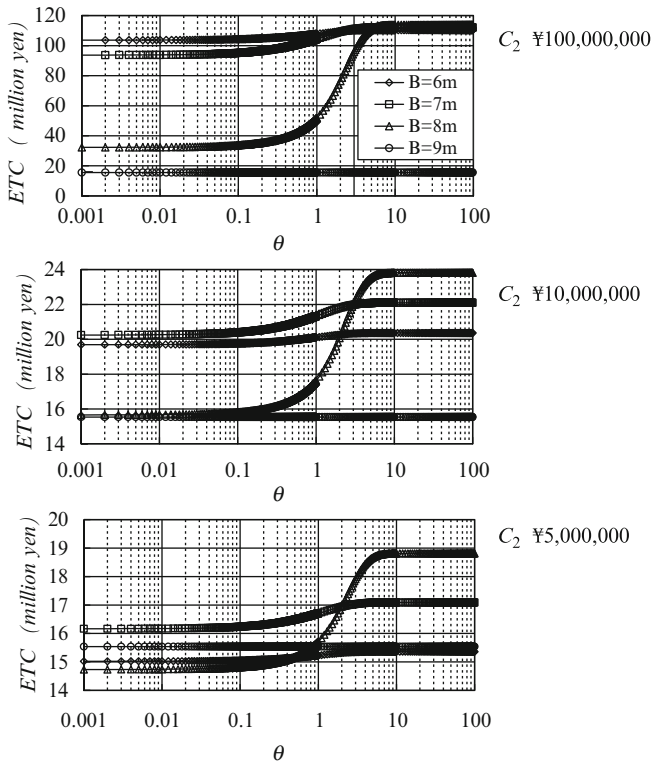


Fig. 21.10 Relationship between θ and ETC for each compensation cost C_2

length (the cross direction at Fig. 21.3) is set to 20 m to correspond to the length of the building. For compensation cost, three cases of costing are assumed: ¥100,000,000/¥10,000,000/¥5,000,000. The ETC was calculated by substituting the p_f and θ relationship (Fig. 21.6) and C_1 and C_2 (Table 21.2), into Eq. (21.14). If C_2 is ¥100,000,000 or ¥10,000,000, ETC is minimized at $B = 9$ m, irrespective of the θ value as shown (Fig. 21.10). It can be seen that if C_2 is ¥5,000,000, the DMM width B that is minimized ETC depends on the value of θ . Furthermore, the optimum

Table 21.3 Relationship with θ , B , ETC and compensation costs C_2

θ	Item	C_2 (million yen)		
		100	10	5
0	B (m)	9	9	8
	C_1B (million yen)	15.54	15.54	13.82
	ETC (million yen)	15.54	15.54	14.74
0.1	B (m)	9	9	8
	C_1B (million yen)	15.54	15.54	13.82
	ETC (million yen)	15.54	15.54	14.74
0.5	B (m)	9	9	6
	C_1B (million yen)	15.54	15.54	10.36
	ETC (million yen)	15.54	15.54	15.15
1	B (m)	9	9	6
	C_1B (million yen)	15.54	15.54	10.36
	ETC (million yen)	15.54	15.54	15.33
2	B (m)	9	9	6
	C_1B (million yen)	15.54	15.54	10.36
	ETC (million yen)	15.54	15.54	15.33
5	B (m)	9	9	6
	C_1B (million yen)	15.54	15.54	10.36
	ETC (million yen)	15.54	15.54	15.36
10	B (m)	9	9	6
	C_1B (million yen)	15.54	15.54	10.36
	ETC (million yen))	15.54	15.54	15.36

B for minimizing ETC has been shown in Table 21.3. This table shows that decision making with regard to the DMM width can be as follows:

1. If the compensation cost is ¥100,000,000 or ¥10,000,000, the ETC of $B = 9$ m is minimum irrespective of the reliability about the $p_j(i)$ at λ . Therefore, the optimal decision should be selected $B = 9$ m to reduce the failure probability to zero.
2. If the compensation cost is ¥5,000,000 and the reliability of the objective probability at λ is sufficiently high, the ETC can be minimized by adopting $B = 8$ m.

We can understand intuitively that the best decision making for minimizing the ETC should be selected to the narrow DMM block width under the low compensation cost. In general, however, even if the compensation cost is low, reducing the DMM width is not a readily made option. The reason for this is that ambiguity remains in the relationship between design parameters and reliability. The robust control approach, however, will enable contractors to have a clear idea of how to make optimal decisions regarding matters that seem ambiguous, as they are always aware of the variance between probability distribution and actuality. The contractor and clients can also share this important relationship between the risk sensitivity coefficients, the ETC , significance of the soil structure, and acceptable risks.

21.5 Conclusions

In this chapter we have applied the robust control approach to the problem of construction of imaginary embankments on soft clay ground. Using our approach we were able to establish the relevance between ground improvement width and compensation costs, and the relationship between the risk sensitivity coefficient and the expected total cost. By clarifying the relationship between the expected total cost of soil structure and reliability of the probability distribution of the ground characteristics, it is demonstrated that the specification of the soil structure can be chosen in a more reasonable manner. In cases where sufficient information for estimating the probability distribution cannot be obtained, it is found that the robust control approach can be an effective decision-making tool for rational reliability design. Following our approach, information underlying the design can be easily shared between the designer (contractor) and the client, and a rational consensus is possible.

References

- Architectural Institute of Japan (2008) Recommendations for design of small building foundations. Architectural Institute of Japan, Tokyo, pp 86–87 (in Japanese)
- Ben-Tal A, Nemirovski A (1998) Robust convex optimization. *Math Oper Res* 23:769–805
- Ben-Tal A, Nemirovski A (2002) Robust optimization: methodological and applications. *Math Program Ser B* 92:453–480
- Cover TM, Thomas JA (1991) Elements of information theory. Wiley, New York
- Kapur KN (1989) Maximum-entropy models in science and engineering. Wiley Eastern Ltd., New York
- Lim AEB, Shanthikumar G (2007) Relative entropy, exponential utility, and robust dynamic pricing. *Oper Res* 55(2):198–214
- Nishida H, Nagae T, Satoh T, Hayashi K (2011) A method of ground the improvement design based on the robust approach. *J Geotech Eng* 67(1):16–25 (in Japanese)
- Iizuka A, Ohta H (1987) A determination procedure of input parameters in elasto-viscoplastic finite element analysis. *Soils Found* 27(3):71–87
- Petersen IR, James MR, Dupuis P (2000) Minimax optimal control of stochastic uncertain systems with relative entropy constraints. *IEEE Trans Automat Contr* 45(3):398–412
- Sekiguchi H, Ohta H (1977) Induced anisotropy and time dependency of clay. In: Proceedings of specialty session 9th ICSMFE, Tokyo, pp 229–239
- Stutzer M (1995) A Bayesian approach to diagnosis of asset pricing models. *J Econom* 68:367–397
- The Japanese Geotechnical Society (1999) Geotechnical engineering handbook. The Japanese Geotechnical Society, Tokyo, pp 441 (in Japanese)
- Zhou L, Doyle J, Glover K (1995) Robust and optimal control. Prentice Hall, Upper Saddle River

Chapter 22

Development of a Portable Triaxial Testing Apparatus—*Smart Triaxial*

Eiki Nakayama, Ichizo Kobayashi, Atsushi Iizuka, Moriyuki Taya,
and Hideki Ohta

22.1 Introduction

In classical field theories, a body in motion has been traditionally described by a set of differential equations accompanied by a set of initial conditions and a set of boundary conditions. The ground in motion should also be analyzed basically in the same manner. For this, we need the K_0 -value and material parameters of the geo-material existing at certain depths in the ground. These parameters are available from triaxial tests on undisturbed samples provided by our traditional techniques of soil sampling. The specimen placed on the pedestal in the triaxial chamber should be first brought back to the in situ effective stress state it experienced in the ground and then be subjected to controlled loading simulating the external

E. Nakayama

Core Laboratory, OYO Corporation, 1-66-2 Miyahara-cho, 330-0812 Kita-ku, Saitama, Japan
e-mail: nakayama-eiki@oyonet.oyo.co.jp

I. Kobayashi, D.Eng.

Technical Research Institute, Kajima Corporation, 2-19-1 Tobitakyu,
182-0036 Chofu, Tokyo, Japan
e-mail: koba13@kajima.com

A. Iizuka, D.Eng.

Research Center for Urban Safety and Security, Kobe University, 1-1 Rokkodai,
657-8501 Nada-ku, Kobe, Hyogo, Japan
e-mail: iizuka@kobe-u.ac.jp

M. Taya

Head Office, OYO Corporation, 2-6 Kudan-kita 4-chome, 102-0073 Chiyoda-ku, Tokyo, Japan
e-mail: taya-moriyuki@oyonet.oyo.co.jp

H. Ohta, D.Eng. (✉)

Research and Development Initiative, Chuo University, 1-13-27 Kasuga,
112-8551 Bunkyo-ku, Tokyo, Japan
e-mail: ohtaoffice@kib.biglobe.ne.jp

agency the ground is expected to undergo during construction work or earthquakes, flooding etc.

The initial state of in situ effective stress is typically described by a parameter K_0 defined as a ratio of horizontal to vertical components of in situ effective stress, assuming that the principal stresses are horizontal and vertical. In the laboratory, K_0 -values are usually specified as a ratio of effective radial stress to effective axial stress subjected to a specimen being consolidated with no radial strain. We usually ignore the effect of lateral expansion or compression of samples that might have taken place during processes of drilling, sampling, and sample preparation including extrusion of samples from sampling tubes and trimming of samples.

K_0 -consolidation with no lateral strain usually requires time- and labor-consuming feedback processes of stress controlling and therefore is often replaced by isotropic consolidation in which samples are subjected to all-round pressure in triaxial chambers. More frequent use of isotropic consolidation in engineering practice resulted in relatively rare performance of K_0 -consolidation in the past research on mechanical behavior of soils. The authors have tried to develop a portable triaxial testing apparatus, *Smart Triaxial*, aiming at making it easier to perform not only K_0 -consolidation but also various other testing programs not available in traditional triaxial testing apparatuses.

Except in the case that the rate of K -consolidation is extremely slow in which no appreciable hydraulic gradient is observed in the specimen, K_0 -consolidation (with no lateral strain throughout the whole specimen) cannot be performed in a triaxial chamber in a rigorous sense, because the existence of hydraulic gradient in the specimen inevitably results in the nonuniform effective stress state and the associated nonuniform distribution of strain in the specimen. K_0 -consolidation in a triaxial chamber can only be carried out with “no overall radial strain,” which is merely an approximation of “no radial strain at any point in the specimen.”

Possible differences between the effective stress paths during CU (Consolidated Undrained) tests on isotropically consolidated and K_0 -consolidated clays were clearly demonstrated by Henkel and Sowa (1963). Two Japanese groups with Mitachi (Hokkaido University) and Watabe (Port and Airport Research Institute) as the central figures have actively investigated the mechanical behavior (including the effective stress paths) of K_0 -consolidated clays (Oda and Mitachi 1992; Hwang et al. 1998; Watabe et al. 2002, 2003; Li et al. 2003). A new type of triaxial apparatus for K_0 -consolidated clays was proposed by Ohta et al. (1979) and Ohta et al. (1981). Others have also described automatic controlled loading triaxial testing systems, for example Dasenbrock and Hankour (2006).

22.2 Design Concept of the *Smart Triaxial*

Smart Triaxial is a compact triaxial apparatus such as shown in Fig. 22.1. Specifications are summarized in Table 22.1. It works with the power supplied through AC 100 V or DC 24 V and is portable, being packed in carrying bags. It is

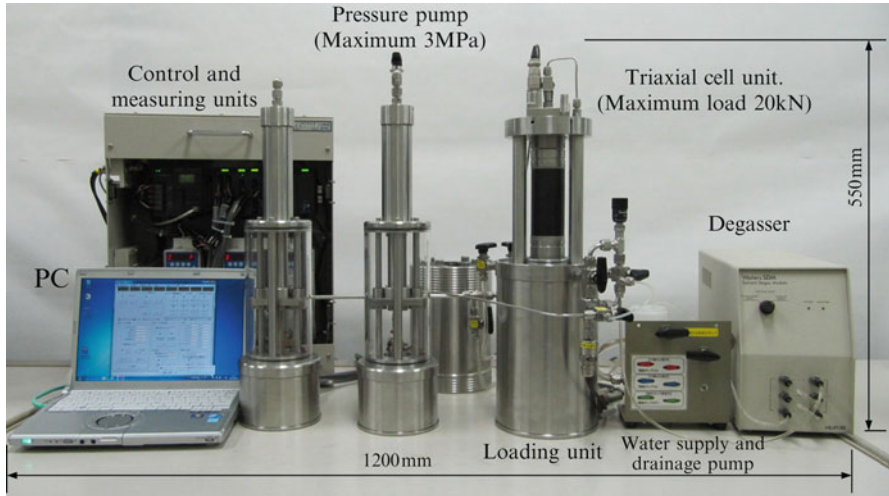


Fig. 22.1 Picture of the *Smart Triaxial* apparatus

Table 22.1 Summary of the *Smart Triaxial* apparatus

Specifications	
Specimen	Diameter: 50 mm Height: 100 mm
Axial load	Max compression force: 20 kN (A/D converter: 16 bit) Max displacement: 30 mm Resolution: 4.085×10^{-7} mm/pulse Max compression speed: 0.2 mm/s
Cell and back	Max pressure: 3.0 MPa (A/D converter: 16 bit)
Pressure	Max output volume: 100 cc Resolution: 1.767×10^{-6} cc/pulse Max output speed: 0.884 cc/s
Test type	Consolidation test: Isotropic, anisotropic, K_0 Compression and extension tests: CU (a) constant cell pressure, (b) constant volume (excess pore pressure = 0) CD (a) constant cell pressure, (b) constant mean principal stress Cyclic test: Sine, sawtooth, and random waves

small in its appearance but the size of specimens is as big as 50 mm in diameter and 100 mm in height. The test program is fully automatic and needs no manual adjustment after a test start. The apparatus consists of (1) triaxial chamber combined with a loading system, (2) piston pumps supplying cell pressure and back pressure, (3) control and measuring units connected with a personal computer, and (4) degasser.

Fig. 22.2 Lines connected to triaxial chamber of the *Smart Triaxial*

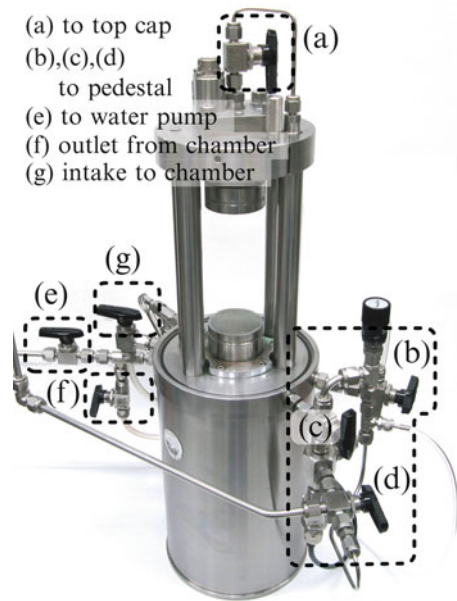


Figure 22.2 shows the triaxial chamber connected to the outside (two pressure pumps, water supply and drainage pump, control and measuring units, and degasser) through seven valves/connectors, which are :

- (a) Drainage line to and from the top cap. (It is connectable to (1) the degasser, which starts working to de-air the line of the pore pressure transducer, and (2) one of the pressure pumps.)
- (b–d) Drainage line to and from the pedestal. (These three valves control (1) drainage to and from the pedestal, (2) the pore pressure transducer, and (3) the pressure pump mentioned in (a), which controls the back pressure.)
- (e) Water tank, which is not shown in Fig. 22.1 or 22.2.
- (f) Outlet from triaxial chamber
- (g) Intake to triaxial chamber

Top plate of the triaxial chamber is supported by four cylindrical hollow pillars standing vertically at an angle of 90° to the bottom plate. These hollow pillars play the role of the drainage paths for the water and air to and from the specimen and the chamber. This makes it possible to have no drainage (usually coiled) tube from the top cap of the specimen (see Fig. 22.3). The axial loading system located at the bottom part of the triaxial chamber consists of a stepper motor (800,000 pulse/rotation), speed controller, and precision ball screw (5-mm pitch) forming a jack for raising or lowering the pedestal to compress or extend the specimen. The accuracy of the loading jack is 12,240,000 pulses per 5 mm (4.085×10^{-4} $\mu\text{m}/\text{pulse}$). The maximum compression force is 20 kN and maximum moving speed of the pedestal is 0.2 mm/s.

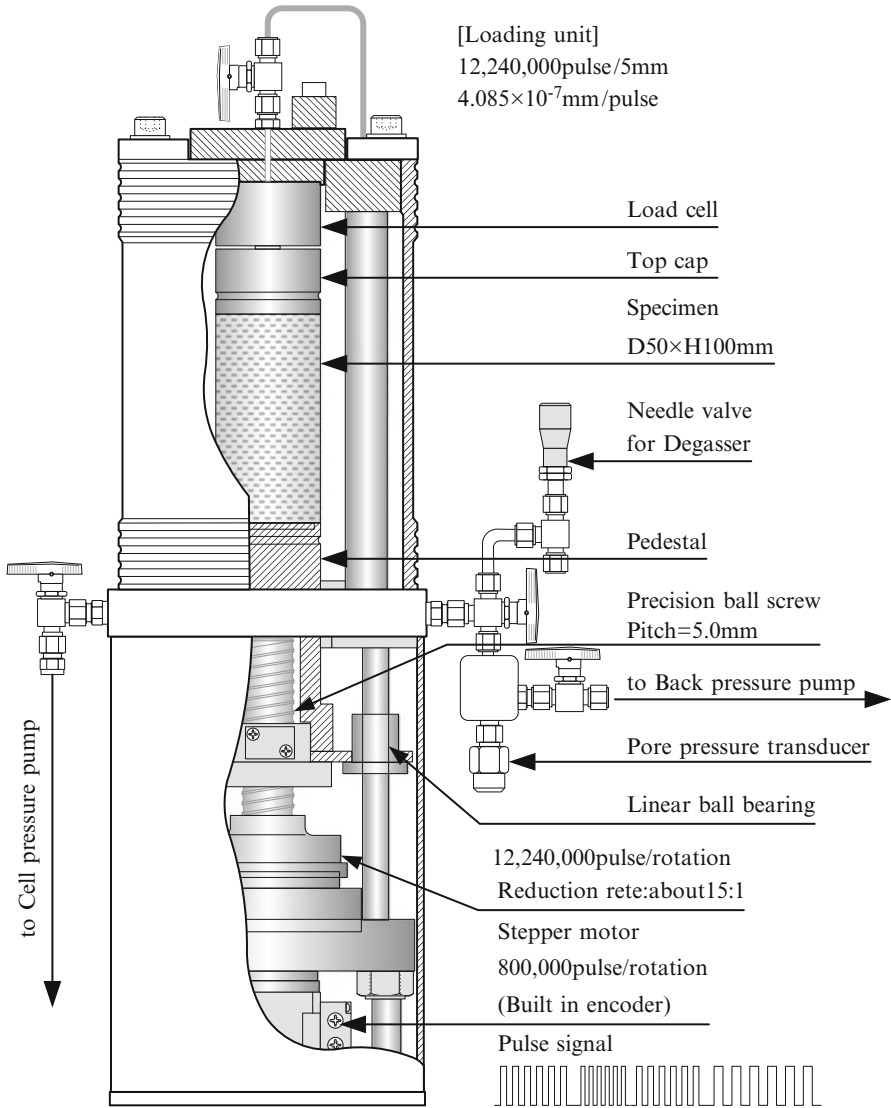


Fig. 22.3 Reduction rate in axial loading system located at the bottom of the triaxial chamber

The cell pressure and the back pressure are controlled by the outflow pressure of the pressure pump (Fig. 22.4) consisting of a piston (30 mm diameter), a cylinder, a pulse-controlled motor (800,000 pulse/rotation), and precision ball screw (lead of 2 mm). The accuracy of the actuator piston pump is 1.767×10^{-6} cc/pulse and the maximum outflow and maximum outflow pressure are 100 cc and 3.0 MPa, respectively.

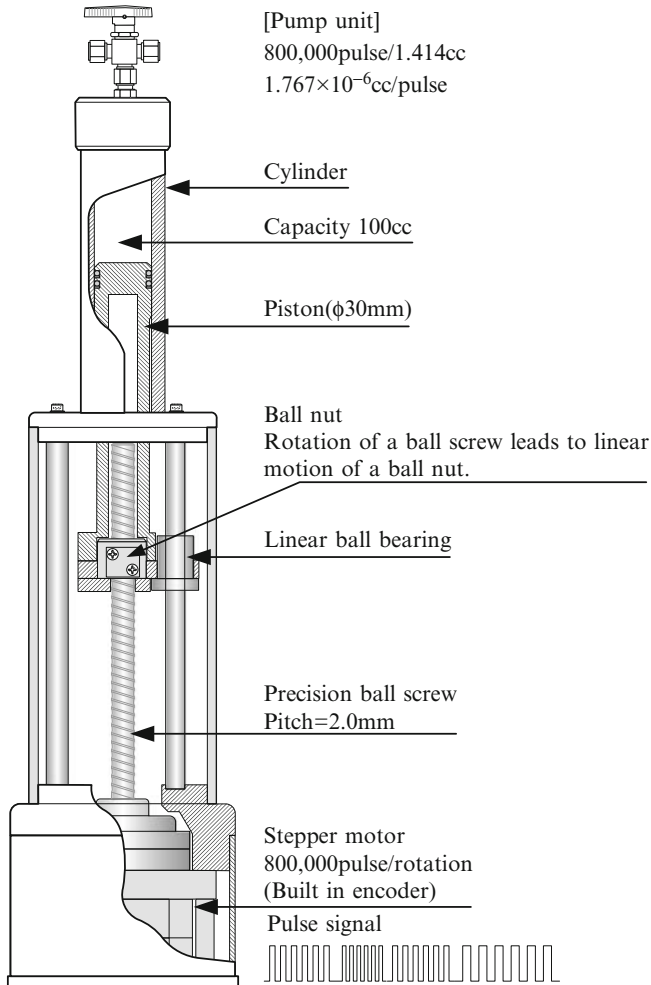


Fig. 22.4 Pressure pump for cell pressure and back pressure

The control and measuring units of the *Smart Triaxial* apparatus consist of a programmable logic controller (PLC), monitoring sensors, an amplifier unit, and a motor driver as shown in Fig. 22.5. Based on the data monitored during an ongoing test, the PLC performs the feedback control of the test and keeps the specimen in the intended states of stresses and strains. The PLC reduces the working load of the personal computer and enables stable long-term testing. It is possible to control the PLC remotely through a LAN.

Monitoring sensors are (1) a load cell to measure the axial load, (2) pressure transducers, (3) axial strain indicator, and (4) specimen volume change. The load cell is located just above the top cap for the specimen and attached to the top plate of the triaxial chamber as shown in Fig. 22.3. The pore water expelled from the

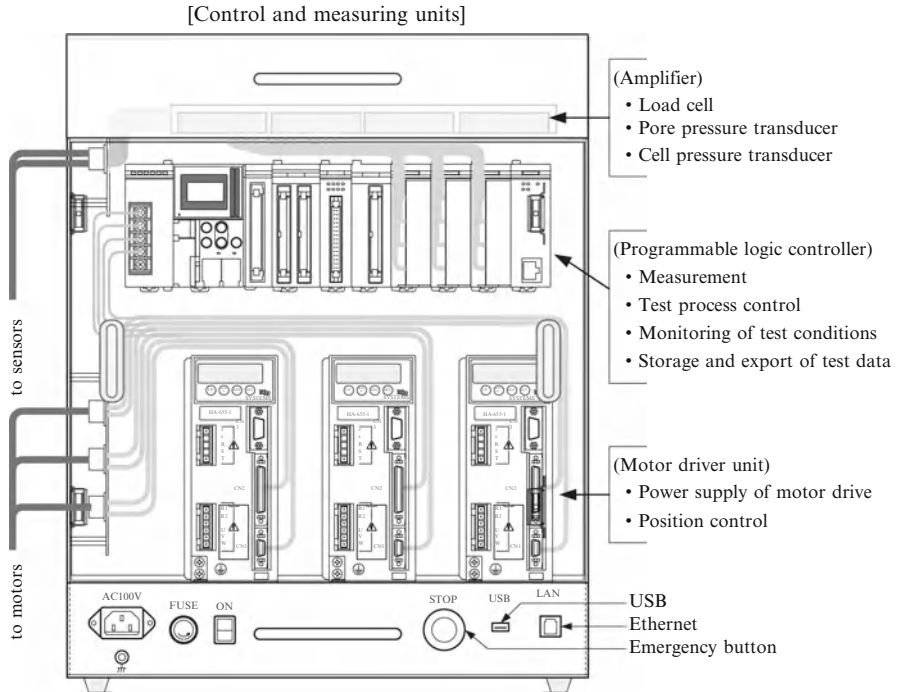


Fig. 22.5 Control and measuring units

specimen flows through a hole at the center of the load cell. Because the load cell is inside the chamber, it is designed as a shear type load cell that is hardly affected by the change in the cell pressure. Depending on the strength of the specimen, we should choose either of the load cells with maximum capacity of 5.0 or 20.0 kN. Similarly, we should choose either of the pressure gauges with maximum capacity of 1.0 or 3.0 MPa, depending on the level of cell pressure applied during testing. The pressure transducers are a high accuracy type with a diaphragm made of monocrystalline sapphire, having very little drift with time.

The change in the length of the specimen is calculated from the displacement of the pedestal. The displacement of the pedestal is calculated from the encoder counts of the loading jack with the correction caused by the change in the height (with the accuracy of the order of 0.1 μm) of the triaxial chamber pressurized inside. The change in the volume of the specimen is calculated from the amount of water flow controlled by the pressure actuator for the back pressure. In a similar way, a correction is made for the change in the volume of the cylinder of the pressure pump and pipes forming the back pressure system.

An electric pump supplies water to the triaxial chamber from a water tank. The *Smart Triaxial* apparatus needs about 4 L to perform a test. A device called a degasser (far right in Fig. 22.1) eliminates the gas dissolved in the water and enables

Table 22.2 Performance of degasser compared with other deaeration methods

Water treatment	Dissolved oxygen (mg/L)	Ratio to VD
Tap water	7.28	7.9
Ion exchanged water (IEW)	6.20	6.7
IEW + degasser (DG)	1.86	2.0
IEW + vacuum de-aeration (VD)	0.92	1.0

de-aired water to circulate through the specimen with the help of the back pressure pump. Table 22.2 shows the performance of the degasser in comparison with other de-aeration methods indicating that the dissolved oxygen in the water treated by the degasser is less than 1/3 of that in ion-exchanged water (IEW) and about double in the water treated by IEW and vacuum de-aeration method. The use of the degasser may not be the best method but seems to be acceptably effective.

The *Smart Triaxial* is operated only by software, no manual adjustment is available. The *Smart Triaxial* is activated by input of the parameters to control the test procedures, testing conditions, monitoring processes, and the online display of the output data.

22.3 Testing Procedures

A wide variety of software is developed to make it possible to carry out various kinds of testing programs. After the manual handling of trimming the soil specimen, placement of the soil specimen, and jacketing the soil specimen with a cylindrical rubber membrane, all the testing procedures are automatically controlled by the software until the final stage of removal of the specimen from the *Smart Triaxial*.

Before the setting up of the specimen in the triaxial chamber, the piping systems of cell pressure and pore water pressure are subjected to flushing. At this preliminary stage of testing, the pressure transducers for the cell pressure and pore water pressure are respectively subjected to the water level at a height of the base plate of the triaxial chamber and a height of the top surface of the pedestal as shown in Fig. 22.6. The software of the *Smart Triaxial* recognizes the water pressure at this stage as the reference pressure and calculates the water pressure at the midheight of the specimen during the ongoing testing. The effective stress in the specimen is calculated by using the water pressure at the level of mid-height of the specimen.

The placement of the specimen is performed manually, basically following the usual process: (1) put the O-ring setter with rings temporarily in place over the bottom of the pedestal; (2) put filter paper drainage strips around the side surface of the specimen and place a porous stone with filter paper on the top of the specimen; (3) set the rubber membrane around the specimen over the filter paper strips using a membrane stretcher; (4) turn the top part of the membrane downward and bottom part of the membrane upward so that top and bottom parts of the specimen remain unjacketed; (5) place the specimen on a circular filter paper placed on the porous stone embedded in the pedestal; (6) fold the lower end of the membrane downwards

Fig. 22.6 Reference of cell pressure and pore water pressure measurement

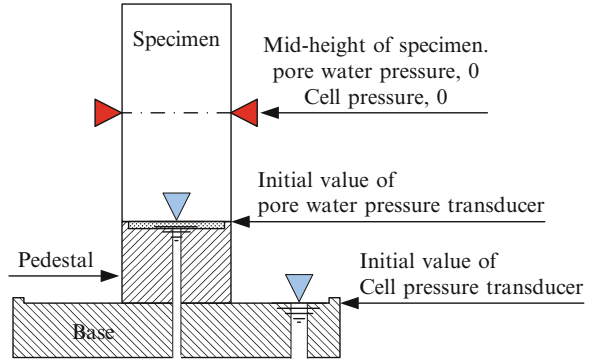
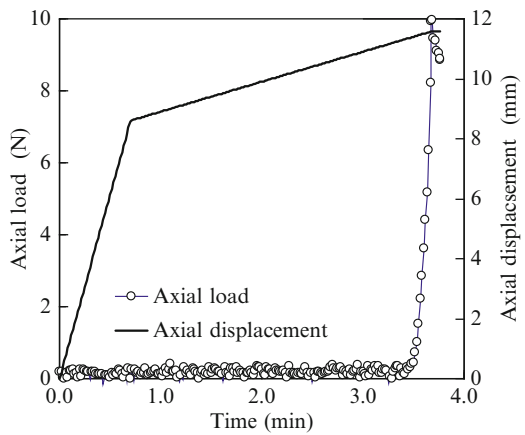


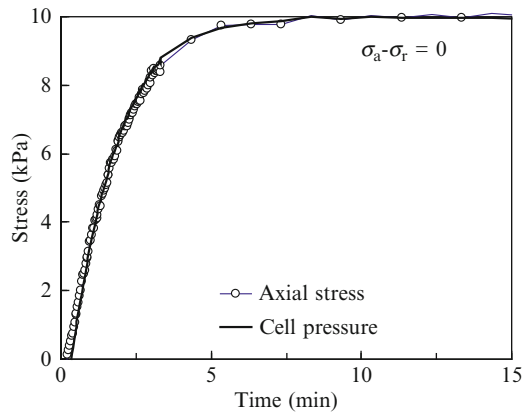
Fig. 22.7 An example of “Specimen set up” process



onto the pedestal; (7) slide an O-ring from the setter to seal the membrane against the pedestal; (8) when the specimen has been moved upwards, so that the porous stone on top is just in contact with the top cap, fold the top end of the membrane upward onto the top cap and slide an O-ring from the setter to seal the membrane; and (9) remove the O-ring setter.

After manual placement of the specimen on the pedestal, the pedestal is moved upward, step (8) above, until the porous stone on the specimen just touches the top cap. Upward movement of the pedestal stops when the load transmitted from the specimen to the top cap reaches a certain threshold contact load specified as an input parameter before the test starts. This process is performed automatically by activating the software “Specimen set up.” Speed of the upward movement of the pedestal consists of two stages, the second stage of which is specified by an input parameter arbitrarily chosen by the experimenter. Figure 22.7 shows an example of a “Specimen set up” record in which the pedestal had to move upward 11.6 mm before the porous stone on the top surface of the specimen touched the top cap with a contact load of 10 N. The effect of the bedding error has not yet been systematically investigated using the *Smart Triaxial* and remains as a subject for the future study.

Fig. 22.8 An example of “Preliminary consolidation” process



Prior to the application of the back pressure, “Preliminary consolidation” may be performed in case an effective confining stress at a very low level is preferable to apply to the specimen. During the process of “Preliminary consolidation,” cell pressure can be arbitrarily chosen by the experimenter while the axial and radial stresses are kept equal to each other (i.e., an isotropic stress condition is maintained). When necessary, it is possible to increase the cell pressure keeping the pore water pressure at zero. Figure 22.8 shows an example of the “Preliminary consolidation” process in which 15 min were spent to raise the cell pressure up to 10 kPa.

After the “Preliminary consolidation” has been completed, “Flushing and saturation” should be carried out aiming at eliminating air bubbles existing not only in any gaps between the specimen and the rubber membrane but also in the specimen itself. Flushing can be performed in two ways: (1) by the constant flow rate method and (2) by the double suction method. When the constant flow rate method is used, the water comes up through the pedestal and tends to go up passing through the gap between the specimen and the rubber membrane to the top cap. A low effective confining stress is applied so that the rubber membrane is held in close contact with the specimen and excessive water cannot accumulate between the membrane and the specimen. The left part of Fig. 22.9 shows an example of the constant flow rate method in which the water flows at a rate of 0.5 cc/min with cell pressure of up to 31 kPa.

The double suction method introduced by Rad and Clough (1984) as “Vacuum procedure” and by Tatsuoka (1986) as “Double suction method” is also applicable as shown in the right part of Fig. 22.9 in which 38 cc of the water is used in 120 min with an applied cell pressure of -40 kPa while the pore pressure (back pressure) is kept at -50 kPa, resulting in 10 kPa of the effective confining stress in the specimen. In this example, water de-aired in the degasser goes up to the specimen through the pedestal and is sucked by the back pressure pump that is connected to the top cap. The de-aired water flows upward from the pedestal to the top cap capturing air bubbles not only in the gap between the specimen and the rubber membrane but also in the specimen to a certain degree.

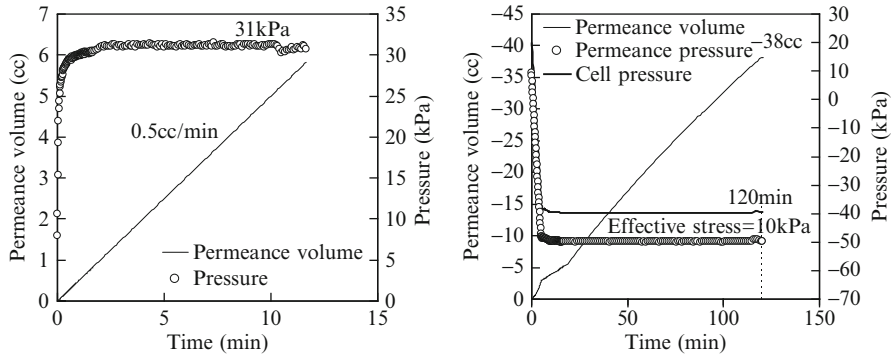
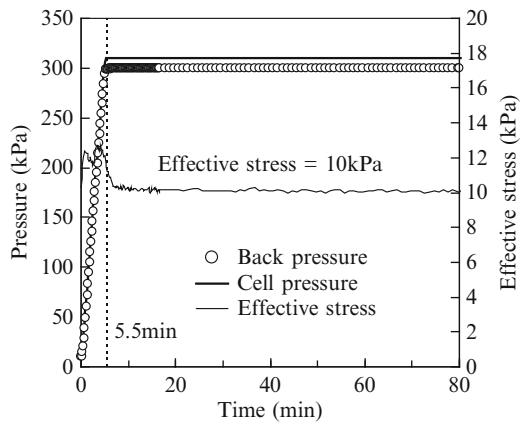


Fig. 22.9 Examples of “Flushing and saturation” process (*Left*: Constant flow rate method, *right*: Double suction method)

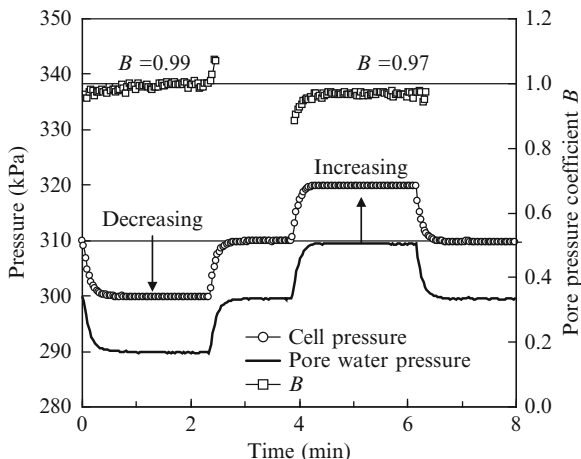
Fig. 22.10 An example of “Back pressure set up” process



The software “Back pressure set up” is activated to apply the back pressure by inputting (1) intended back pressure, (2) intended effective stress in the specimen, and (3) time needed in the back pressure application. During the process of back pressure application, the axial stress is kept controlled to be equal to the cell pressure, resulting in the isotropic stress state in the specimen. An example is shown in Fig. 22.10 in which back pressure of 300 kPa is applied in 5.5 min, keeping the effective stress in the specimen as 10 kPa.

A process of “*B*-value measurement” is activated by inputting (1) increment of the cell pressure and (2) time duration required for measurement. In case that *B*-value happens to be considerably less than unity, the stress increases during the process of *B*-value measurement could result in volume decrease and additional consolidation. To prevent such unintended consolidation, it is possible to input a negative increment of the cell pressure. Figure 22.11 is an example of *B*-value measurement in which is measured change in the pore water pressure caused by adding the cell pressure increments of plus and minus 10 kPa. The initial values of the cell and pore water pressure prior to *B*-value measurement are 310 and 300 kPa,

Fig. 22.11 An example of “*B*-value measurement” process



respectively. Time duration for measurement is 2 min in this example and obtained *B*-value is 0.98 on average ($B = 0.99$ for minus increment of cell pressure and $B = 0.97$ for plus increment).

In the *Smart Triaxial*, a piston pump is employed to produce the back pressure, that is, the pump pressure is identical with the pore water pressure and amount of out-going or in-coming water is the volume change of the specimen. Three types of consolidation can be carried out: (1) isotropic consolidation ($\sigma'_a = \sigma'_r$), (2) anisotropic consolidation ($\sigma'_r = K\sigma'_a$), and (3) Ko-consolidation ($\varepsilon_r = 0$). It should be noted that these three definitions of consolidation are not rigorously satisfied in *Smart Triaxial* tests because of the inevitable nonuniform distribution of the pore water pressure in the specimen, but are only satisfied as overall approximations.

Isotropic consolidation is carried out by controlling the back pressure pump in such a way that the excess pore water pressure is kept at zero and by controlling the axial stress in such a way that $\sigma_a = \sigma_r$. Figure 22.12 shows an example of isotropic consolidation in which the cell pressure is 400 kPa, whereas the back pressure is 300 kPa and therefore the effective stress in the specimen is 100 kPa.

Anisotropic consolidation is carried out by inputting target values of (1) axial stress, (2) radial stress (cell pressure), and (3) time duration to be needed in reaching the target values of (1) and (2). A sufficiently slow loading duration should be chosen by the experimenter. During the consolidation process, the excess pore water pressure is controlled to be zero. The volume change of the specimen is measured by the piston pump shown in Fig. 22.13.

Ko-consolidation, in which overall radial strain is kept zero during the whole process of consolidation, is automatically performed in the following manner:

1. Apply the cell pressure and back pressure and keep the cell pressure constant during the consolidation process.
2. Raise the pedestal giving the axial strain to the specimen at a constant rate, which should be slow enough to allow the excess pore water pressure to dissipate (to obtain relatively uniform distribution of pore water pressure throughout the specimen).

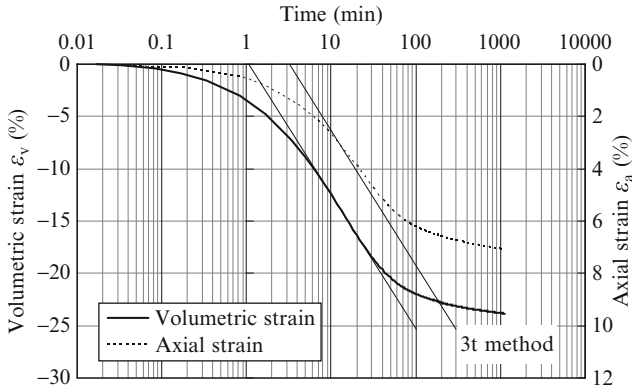
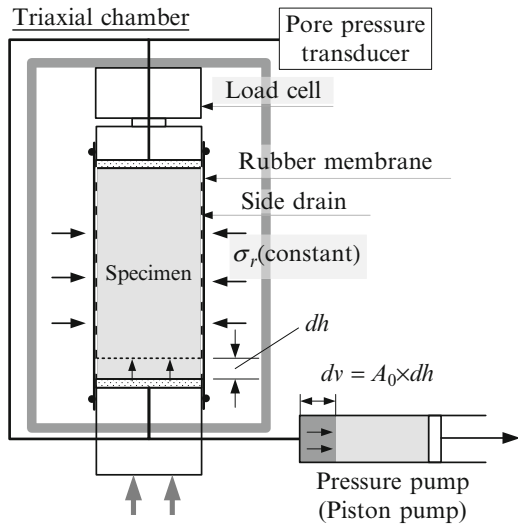


Fig. 22.12 An example of “Isotropic consolidation” process

Fig. 22.13 Mechanism of K_o -consolidation in the *Smart Triaxial*



3. During the process (2), pore water flows from the top cap and the pedestal to the piston pump as shown in Fig. 22.13 so that the amount of expelled water corresponds to the volume obtained as the increment of axial displacement of the pedestal multiplied by the original cross-sectional area of the specimen, resulting in the overall K_o -condition.

Figure 22.14 shows an example of the K_o -consolidation process preceded by isotropic consolidation with cell pressure of 310 kPa and back pressure of 300 kPa. The K -value, which is initially unity, changes during the following K_o -consolidation and eventually becomes $K_o = 0.47$. The rate of loading during anisotropic and K_o -consolidation should be chosen to be slow enough. How slow should it be? This is still open to question and is subjected to future investigation. The specimen used in the example shown in Fig. 22.14 is then subjected to an

Fig. 22.14 An example of Ko-consolidation in the *Smart Triaxial*

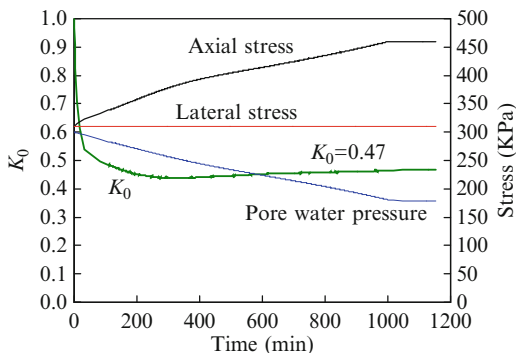
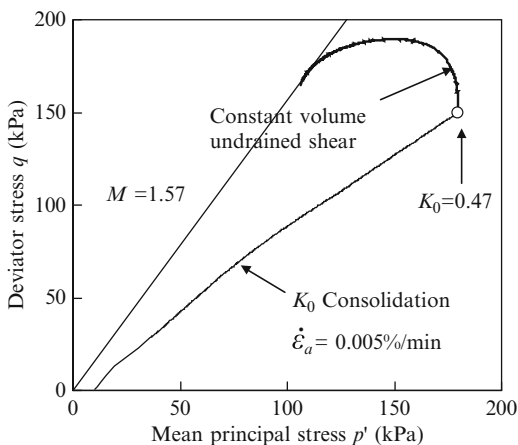


Fig. 22.15 An example of Ko-consolidated constant volume undrained compression test



undrained compression test. Figure 22.15 shows the effective stress path during shear with a constant rate of axial strain of 0.005 %/min.

The *Smart Triaxial* is furnished with software for shear tests such as compression and extension tests, p' – constant tests, stress path tests, constant volume shear, stress relaxation tests, cyclic loading tests, etc. as follows:

- (a) The usual undrained compression and extension tests are carried out with pore pressure measurement under conditions of constant cell pressure.
- (b) Drained tests are performed, freely allowing the pore water to be expelled from and/or sucked into the specimen.
- (c) During “undrained” tests of the constant volume type, the cell pressure is controlled in such a way that the excess pore water pressure is kept at zero, resulting in no water flow from and/or into the specimen and hence no volume change taking place (see Taylor 1948). Because the excess pore water pressure is kept at zero, the effective stress in the specimen is calculated as the difference between the cell pressure and the back pressure. This constant volume type of undrained shear test produces reasonably accurate data of effective stress changes during shear even in case that B -value is not high enough.

Figure 22.16 show an example of stress relaxation test in which an isotropically consolidated specimen is subjected to constant volume undrained compression with

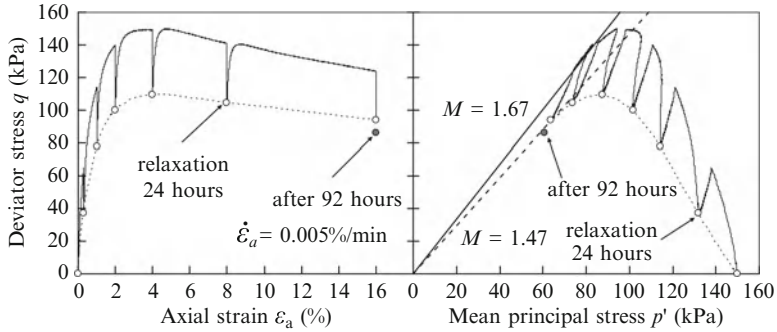


Fig. 22.16 Stress relaxation of constant volume undrained compression test on an isotropically consolidated, undisturbed sample (*Left*: stress-strain relations, *right*: effective stress paths)

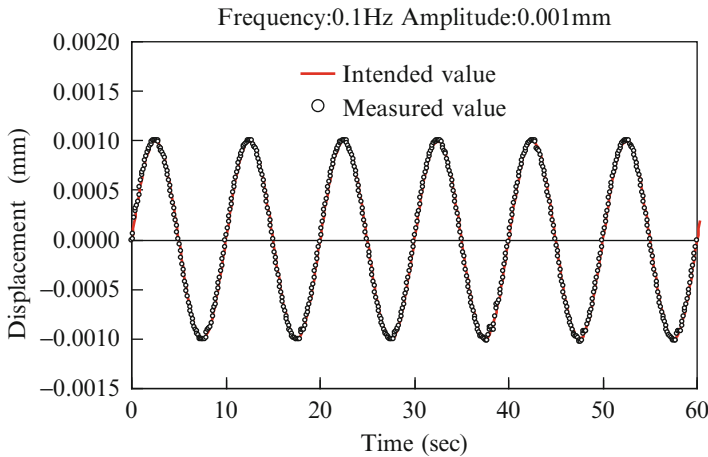


Fig. 22.17 Calibration with sine wave displacement control

a rate of axial strain of 0.005 %/min. At six stages on the process of undrained shear, upward movement of the pedestal is stopped and stress relaxation (decrease in effective axial and radial stresses) is measured for 24 h. Very small changes in dimensions of the triaxial chamber caused by the change in axial and radial stresses during the relaxation process are taken into correction, which requires slight movement of the pedestal to keep the axial strain constant during stress relaxation. In the preceding stress relaxation during a constant volume undrained test, it was found that the change in the room temperature gives a nonignorable effect on the measured test results. Therefore, the test shown in Fig. 22.16 is carried out in a constant temperature room of 20 °C ± 0.2 °C.

Software for three types of cyclic loading is available in the *Smart Triaxial*: (1) sine wave, (2) sawtooth wave, and (3) random wave. Either strain-controlled or stress-controlled tests are possible by inputting (1) frequency, (2) strain amplitude, (3) stress amplitude, and (4) number of cycles. Figures 22.17, 22.18, and 22.19 show the results of calibration of three types of cyclic loadings.

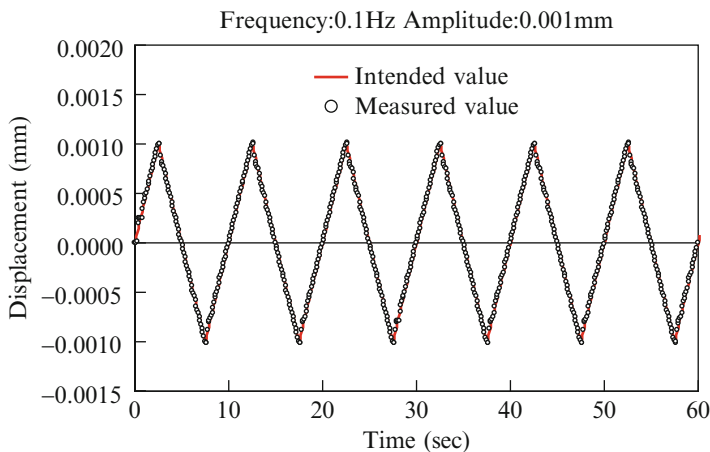


Fig. 22.18 Calibration with sawtooth wave displacement control

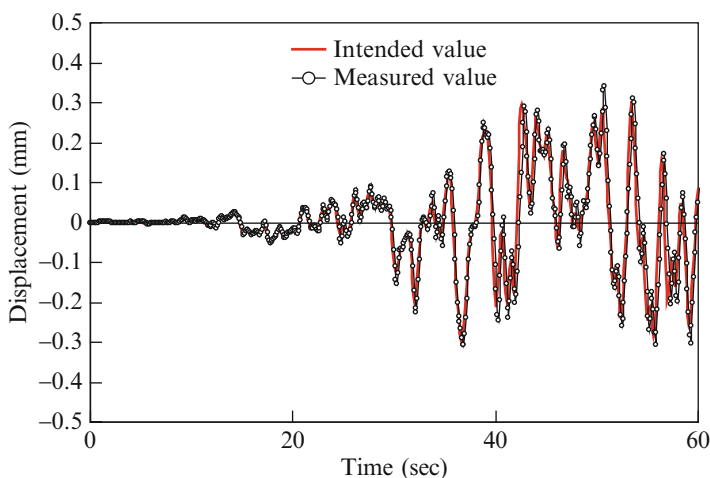


Fig. 22.19 Calibration with random wave displacement control

22.4 Undrained Behavior of Osaka Bay Clay

Aiming at checking the overall performance of the *Smart Triaxial*, a series of CU were carried out on five undisturbed samples taken from the sea bed of Osaka Bay at the site of Kansai International Airport. Because only five samples are available, as seen in Table 22.3, comparison of compression and extension tests is made on isotropically and anisotropically consolidated clay specimens. All the undrained

Table 22.3 Properties of Osaka Bay Clay

No.	①	②	③	④	⑤
Site	Osaka Bay	Osaka Bay	Osaka Bay	Osaka Bay	Osaka Bay
Depth (m)	GL-24.00~ -24.80	GL-26.00~ -26.80	GL-30.00~ -30.80	GL-32.00~ -32.80	GL-33.00~ -33.80
Critical state parameter, M	1.49	1.57	1.08	1.18	1.54
Effective angle of internal friction, ϕ' ($^\circ$)	36.6	38.6	41.1	47.2	37.9
Natural water content, w_n (%)	79.5	87.0	74.8	69.5	68.2
Liquid limit, w_L (%)	102.5	101.2	95.6	95.9	89.7
Plastic limit, w_p (%)	30.2	30.6	29.7	30.3	30.5
Plasticity index, I_p	72.3	70.6	65.9	65.6	59.2
Wet density, ρ_t (g/cm 3)	1.523	1.528	1.545	1.581	1.580
Clay fraction under 2 μm (%)	59	50	45	41	49
Stratigraphic classification	Ma13	Ma13	Ma13	Ma13	Ma13

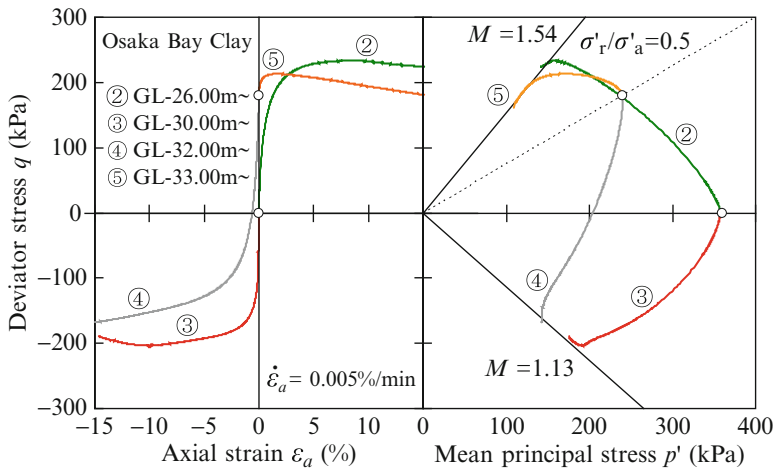
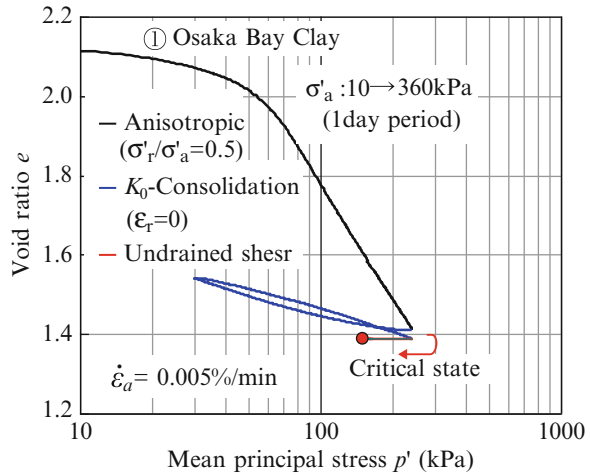


Fig. 22.20 Constant volume undrained tests on isotropically and anisotropically consolidated undisturbed samples of Osaka Bay clay (*Left*: stress–strain relations, *right*: effective stress paths)

tests are carried out by employing constant volume tests in which the cell pressure is controlled during the whole process of shearing in such a way that the excess pore water pressure is kept at zero.

Samples No. 2 and 3 (see Table 22.3) taken from depths of 26.00–26.80 m to 30.00–30.80 m were isotropically consolidated and subjected to compression (No. 2) and extension (No. 3) tests. Samples No. 4 (32.00–32.80 m) and No.5 (33.00–33.80 m) were anisotropically consolidated with a value of σ'_r/σ'_a of 0.5 and then subjected to extension and compression tests. The effective stress paths (shown in Fig. 22.20) for these two tests start from an identical stress point

Fig. 22.21 Plot of e -log p' during (1) anisotropic consolidation, (2) Ko-rebound with zero overall radial strain $\epsilon_r = 0$, (3) Ko-reloading ($\epsilon_r = 0$), and (4) undrained constant volume compression of Sample No. 1 in Table 22.3



in the figure. The reason why anisotropic consolidation ($K = 0.5$) is applied to these two undisturbed samples rather than Ko-consolidation is that Ko-values of each sample may not be identical and therefore the effective stress paths of samples No. 4 and No. 5 may not start from an identical stress point, and so the figure becomes complicated disguising the difference in the effective stress paths for isotropically and anisotropically consolidated clays. Figure 22.20 shows the stress–strain curves and effective stress paths of the specimens isotropically and anisotropically consolidated at pressures well beyond the preconsolidation pressure.

In addition to four CU tests plotted in Fig. 22.20, sample No. 1 in Table 22.3 was subjected to (1) anisotropic consolidation, (2) Ko-rebound with zero overall radial strain $\epsilon_r = 0$, (3) Ko-reloading ($\epsilon_r = 0$), and (4) undrained constant volume compression. Step (1) was carried out by increasing the effective axial stress from 10 to 360 kPa within 1 day. The following steps (2), (3), and (4) were performed at an axial strain rate of 0.005 %/min. The appropriate rate of loading during these four steps should be investigated in future study, but for the time being the authors have chosen the above mentioned rate of loading. Void ratio plotted against logarithm of the effective mean principal stress p' is shown in Fig. 22.21, indicating the preconsolidation pressure of the specimen is well below 360 kPa. The combination of Fig. 22.21 and the effective stress path during steps (1) through (4) is given in Fig. 22.22.

The results of a series of CU tests on undisturbed samples of Osaka Bay clay listed in Table 22.3 are summarized in Fig. 22.23, indicating that the performance of the portable *Smart Triaxial* is good enough for use in engineering practice even at sites remote from well-equipped geotechnical laboratories.

Fig. 22.22 Plot of e - p' and effective stress path during (1) anisotropic consolidation, (2) K_0 -rebound with zero overall radial strain $\epsilon_r = 0$, (3) K_0 -reloading ($\epsilon_r = 0$), and (4) undrained constant volume compression of Sample No. 1 in Table 22.3

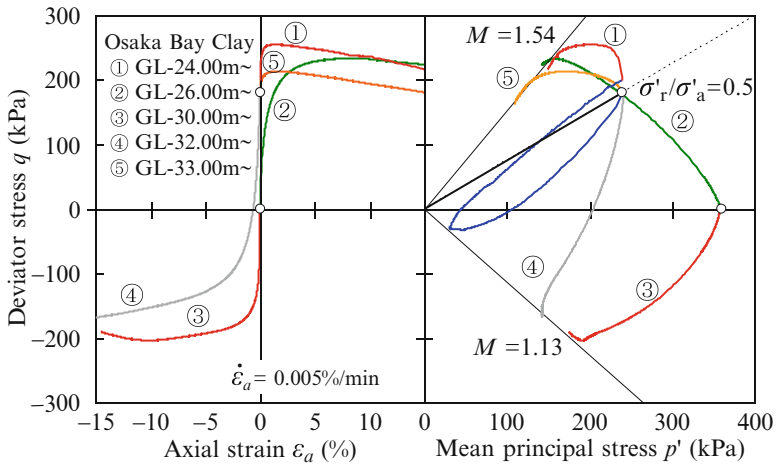
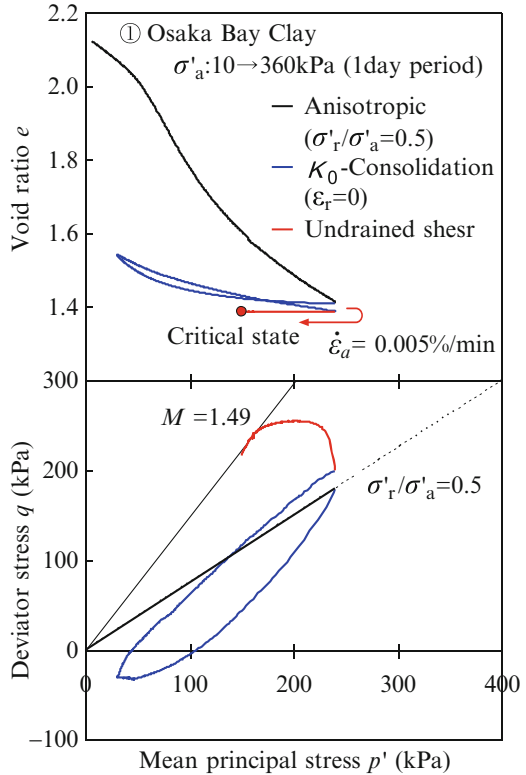


Fig. 22.23 Stress–strain relations and effective stress paths obtained by CU tests on undisturbed samples of Osaka Bay clay listed in Table 22.3

22.5 Summary and Conclusions

As pointed out by Henkel and Sowa (1963), the rate dependency of the triaxial test results is not negligible. However, it was not practical to carry out the tests with very slow rates of loading (which correspond to the loading rate at many of the sites and fields), because many steps of triaxial testing need manual adjustment making slow loading tests very expensive. The authors developed the automatic *Smart Triaxial* testing equipment as one of the possible ways to solve this problem. In this paper, the design concept and testing procedures are proposed together with a set of results of CU tests on undisturbed Osaka Bay clay taken from the sea bed at the site of Kansai International Airport. The results of the experimental investigation of the usefulness of the apparatus lead to the following conclusions:

1. The new triaxial apparatus is small enough to be packed in carrying bags yet the size of the specimen is 50 mm in diameter and 100 mm in height. The maximum compression force is 20 kN and the maximum cell pressure is 3 MPa.
2. The test program is fully automatic and needs no manual adjustment after the manual handling of trimming, placing, and jacketing of the soil specimen until the final stage of the removal of the specimen. The apparatus is controlled only by software; no manual adjustment is available.
3. The apparatus is activated by inputting the parameters to control the testing procedures, testing conditions, monitoring process, and online display of output data.
4. The testing procedure consists of (a) Specimen set up, (b) Preliminary consolidation, (c) Flushing and saturation, (d) Back pressure set up, (e) B -value measurement, (f) Consolidation (isotropic, anisotropic, and K_0), and (g) Compression, extension, p' -constant shear, stress path tests, constant volume shear, stress relaxation tests, and cyclic loading (sine, sawtooth, and random waves).
5. A series of CU tests on undisturbed samples of Osaka Bay clay showed that the new portable triaxial apparatus is good enough for the use in engineering practice.

Acknowledgement The authors are grateful to Dr. Teruaki Hurudoi, then Senior Vice President of Kansai International Airport Land Development Co., Ltd for providing undisturbed Osaka Bay clay sampled from the site of Kansai International Airport. The authors wish to express their sincere gratitude to Professor M. J. Pender, University of Auckland, for his valuable suggestions, comments, and editing of the manuscript. This work was supported by JSPS Grant-in-Aid for Scientific Research (No. 23310119, 23560594).

References

- Dasenbrock DD, Hankour R (2006) Improved soil property classification through automated triaxial stress path testing. In: GeoCongress 2006, Atlanta, 2006
- Henkel DJ, Sowa VA (1963) The influence of stress history on stress paths in underdrained triaxial tests on clay. Laboratory Shear Testing of Soils, ASTM Special Technical Publication No. 361, Philadelphia, pp 280–291

- Hwang SC, Mitachi T, Shibuya S, Tateichi K (1998) Stress-deformation characteristics in the wide range from small strain to failure state and undrained shear strength of natural clays. *J Geotech Eng (Japan Society of Civil Engineers)* 589/III-42:305–319 (in Japanese)
- Li D, Shibuya S, Mitachi T (2003) Mechanical characteristics and aging effects of Osaka Bay Clay. *J Geotech Eng (Japan Society of Civil Engineers)* 736/III-63:273–285 (in Japanese)
- Oda Y, Mitachi T (1992) Triaxial Ko-consolidation test on saturated clay. *J Geotech Eng (Japan Society of Civil Engineers)* 448/III-19:45–52 (in Japanese)
- Ohta H, Wroth CP, Shibata T (1979) Triaxial apparatus to preserve the in-situ effective stress state. In: *Proceedings of 24th symposium on geotechnical engineering, Tokyo, 1979*, pp 165–172 (in Japanese)
- Ohta H, Hata S, Fukagawa R, Onoue K, Yasuda S, Morita Y (1981) Estimation of in-situ deformability of soils. In: *Proceedings of 10th international conference on soil mechanics and foundation engineering, Stockholm, 1981*, vol 2, pp 533–536
- Rad NS, Clough GW (1984) New procedure for saturating sand specimens. *J Geotech Eng ASCE* 110(9):1205–1218
- Tatsuoka F (1986) Design and production of soil shear testing apparatus – testing methods. *Chishitsu Chosa* 3:53–58 (in Japanese)
- Taylor DW (1948) *Fundamentals of soil mechanics*. Wiley, New York
- Watabe Y, Tsuchida T, Adachi K (2002) Undrained shear strength of Pleistocene clay in Osaka Bay. *J Geotech Geoenviron Eng ASCE* 128(3):216–226
- Watabe Y, Tanaka M, Tanaka H, Tsuchida T (2003) Ko-consolidation in a triaxial cell and evaluation of in-situ Ko for marine clays with various characteristics. *Soils Found* 43(1):1–20

Chapter 23

Innovation in Disaster Mitigation Technologies

Jian Chu

23.1 Introduction

There has been an increasing trend in both the frequency and intensity of natural disasters such as flooding and earthquake in recent years. There is an urgent need to enhance our disaster mitigation and rehabilitation capabilities so our infrastructures and constructed facilities can be better protected. We also need more cost-effective solutions to allow disaster mitigation measures to be applied to a larger area within the limited budget. For example, liquefaction has long been identified as one of the major hazards. However, ground treatment for liquefaction can only be carried out for the ground where important infrastructures such as ports and airports are constructed because of the high cost involved in ground treatment for liquefaction. If a much cheaper liquefaction mitigation method can be developed, ground treatment for liquefaction can then be applied over a wider range. Then the disaster associated with liquefaction can be greatly reduced. In this paper, the areas in which innovation may play a role are identified. A few examples are given to illustrate how innovative ideas or technologies can be adopted to improve our technical abilities for disaster prevention and mitigation. These include (1) the use of geotextile tubes and geotextile mats to construct dikes; (2) the use of biogas technology to reduce liquefaction potential of sand; (3) the use of bioclogging technology to reduce riverbank or coastal erosion or make temporary water ponds on a beach or in a desert; (4) the use of quick setting materials, and (5) the use of quick construction technologies. Some of the ideas presented are still new and needed to be developed further before they can be used in practice. Nevertheless, any great technology starts from immature ideas. As long as the idea is good, we

J. Chu, Ph.D. (✉)

Department of Civil, Construction and Environmental Engineering,

Iowa State University, 328 Town Engineering Building, Ames, IA 50010-3232, USA

e-mail: jchu@iastate.edu

have a chance to turn the idea into a technology and make a positive social and economic impact.

Geotechnical construction involves mainly the materials used for the construction and the construction process itself. Therefore, the areas in which innovations will play an important part are likely to be the use of new materials and the use of alternative construction processes. For disaster mitigation or rehabilitation projects, costs of the materials and speed of construction become important consideration factors. We need to use inexpensive materials as much as possible to bring down the cost and at the same time to complete the project as quickly as possible to save lives or reduce the suffering or inconvenience to the people affected by disasters. Another consideration is to use as little heavy equipment as possible because mobilization of heavy machines may be difficult in disaster affected areas. To be innovative in materials and construction processes, one needs to draw ideas from other disciplines. Examples will show how new construction materials can be adopted and how technologies developed for other disciplines can be applied to geotechnical problems.

23.2 Use of Geosynthetic Mats

Dike or embankment constructions are an important part of flood or coastal defense systems. In the past, dikes were constructed using earth, rock, or concrete. The dike constructed using earth alone may encounter more problems such as erosion or breaching. The slopes of dikes made of earth alone also have to be very gentle to provide stability for the dike. One way to overcome the shortcomings associated with dikes built by earth is to use geosynthetics. There are already many examples in the use of geosynthetic materials for dike construction or disaster mitigation Guo et al. (2009); Yan et al. (2009). One of them is to use geotextiles or geomembrane to form tubes or bags that are filled by soil or water. These so-called geosynthetic tube or geosynthetic bag methods have been adopted in coastal projects as shown in Fig. 23.1 as examples. The use of geosynthetics has greatly enhanced the stability of the dikes. It has also reduced the amount of soil used because the slope of the dike can be steeper. The use of geosynthetics has also provided better resistance against erosion and breaching.

However, when the sausage shaped geosynthetic tubes are stacked in several layers to form a dike, the system can be weak in lateral stability. This is particularly the case when the ground is soft. One approach to solve this problem is to use geosynthetic mattresses or geosynthetic mats instead of geosynthetic tubes. The term geosynthetic mat is used to describe a geosynthetic bag with a mattress-like geometry, that is, the height is much smaller than its lateral dimension as shown in Fig. 23.2. A geosynthetic mat can be as long as the whole cross-section of the dike. Thus, the geosynthetic mat is very stable laterally. When a dike is constructed, geosynthetic mats can be stacked one on top of another to reach the required height as shown in Fig. 23.3a. Those geosynthetic mats can be filled using sand, although clay has also been used. One case study has been provided by Yan and Chu (2010).

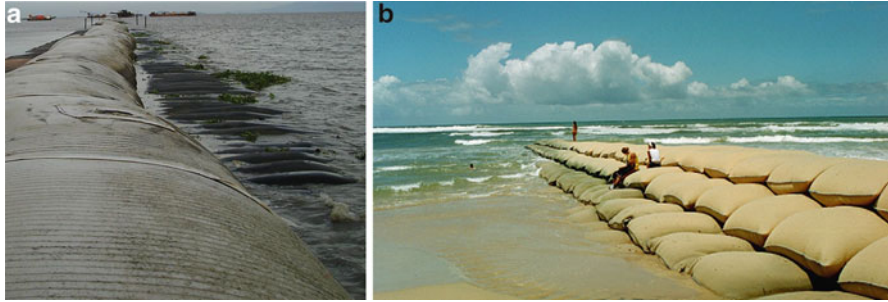


Fig. 23.1 Examples of applications of (a) geotextile tubes for coastal protection (After Lee 2009) and (b) geotextile bags as breakwater (After Saathoff et al. 2007)



Fig. 23.2 Example of a geosynthetic mats

The designed cross-section of the dike is shown in Fig. 23.3a. Geosynthetic mats across the whole cross-section of the dike were stacked together to form the dike. The height of each mat was about 0.5 m. A picture of the dike constructed using this method is shown in Fig. 23.3b.

In addition to providing good lateral stability, another advantage of using geotextile mats is that the dikes constructed can tolerate greater settlement or differential settlement so that the soil below the geosynthetic mats may not need to be treated intensively or even treated at all. One practical example is provided by Yan and Chu (2010).

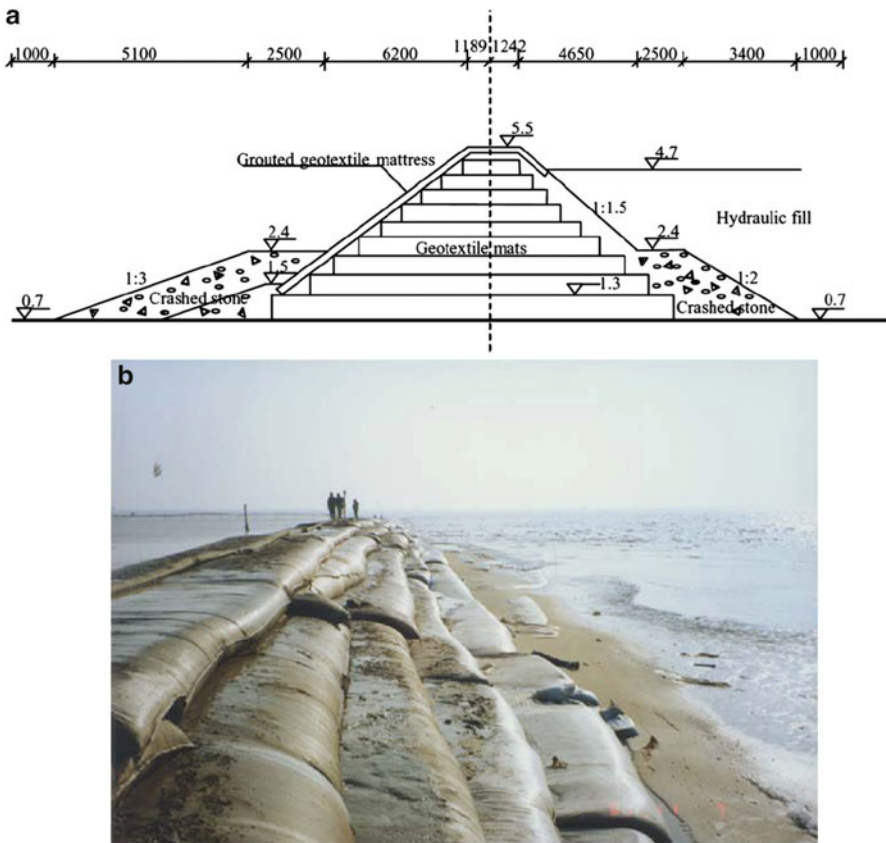


Fig. 23.3 Dike built of geosynthetic mat (a) design and (b) dike constructed (After Yan and Chu 2010)

23.3 Use of Biogas for Mitigation of Liquefaction

Soil liquefaction often occurs in sandy soil during an earthquake. It is one of the major causes for earthquake-related disasters. More recently liquefaction was largely responsible for extensive damage to residential properties in the eastern suburbs and satellite townships of Christchurch, New Zealand during the 2010 Canterbury earthquake and more extensively again following the Christchurch earthquakes that followed in early and middle 2011. The common methods that can be adopted for mitigation of liquefaction include the following four broad categories: (1) replacement or physical modification; (2) densification; (3) pore water pressure relief; and (4) foundation reinforcement, as summarized by Chu et al. (2009). However, it is difficult to treat ground for the purpose of mitigation of liquefaction because the scale of the ground to be treated is normally huge and thus

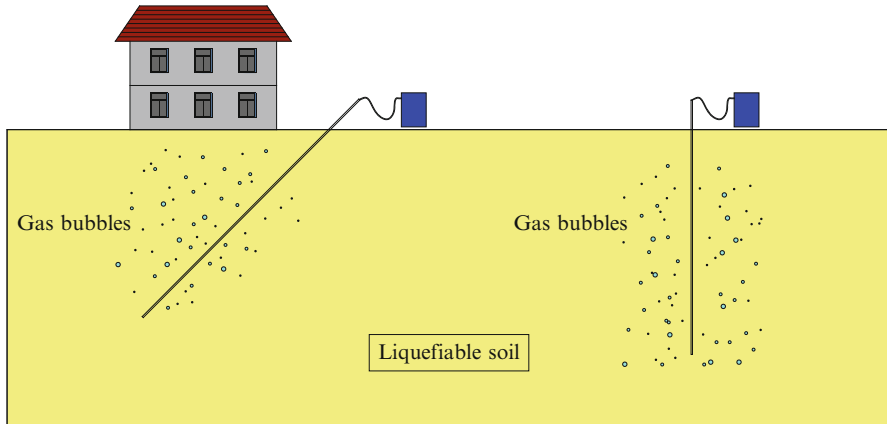


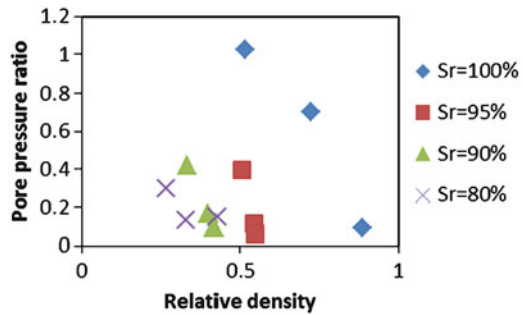
Fig. 23.4 Injection of gas bubbles in saturated sand for the prevention of liquefaction

too expensive to be implemented. Therefore, there is a need for more cost-effective solutions for liquefaction treatment.

A new approach for mitigation of the liquefaction potential of sand is to introduce gas bubbles into potentially liquefiable, saturated sand. The main cause of liquefaction is the generation of pore water pressure. Several studies (e.g., Okamura et al. 2006; Yegian et al. 2007) have shown that when saturated sand is made slightly unsaturated (with a degree of saturation between 85 and 95 %) by inclusion of gas bubbles, the excess pore water pressure generated in soil under a dynamic load will be greatly reduced.

However, it is difficult to introduce gas into ground to maintain the sand desaturated for a long time. This is because the gas bubbles tend to dissolve in water or escape from the ground over time. Pumping can be used as illustrated conceptually in Fig. 23.4. However, the distribution of gas bubbles introduced by pumping will not be even. Furthermore, the gas pumped into ground tends to present in the form of aggregated gas pockets rather than individual bubbles. As a result, the sizes of the gas bubbles or aggregates are not small enough to be kept in the ground for a long period of time. One innovative way to overcome the above problems is to generate tiny gas bubbles in situ using microorganisms. This method is promising because it has the following three advantages: (1) It consumes the least energy because the low viscosity bacteria and nutrient fluid can be delivered easily into sand; (2) The gas generated by bacteria can be distributed more evenly than other means; (3) The gas bubbles generated by bacteria are tiny so the gas bubbles are less prone to escape from the ground. This so-called biogas method for mitigation of liquefaction is being developed by our research group. To verify the effectiveness of the biogas method, shaking table tests using a laminate box were carried out on saturated sand and sand desaturated to a degree of saturation of 95, 90, and 80 % using biogas. Some of the results are presented in Fig. 23.5, where the pore water pressure ratio is plotted against the relative density of sand for soil with

Fig. 23.5 Pore water pressure ratios measured from model tests on bacteria desaturated sand (After He 2012)



different degree of saturation S_r . The pore water pressure ratio is defined as the ratio of maximum excess pore water pressure to the initial effective overburden stress. When the pore water pressure ratio is close to 1, liquefaction becomes possible. The normal design requirement is to control the pore pressure ratio to be less than 0.5. The samples with the degree of saturation less than 100 % in these tests were created using nitrogen gas produced by denitrifying bacteria. The ground acceleration applied was 1.5 m/s^2 . It can be seen from Fig. 23.5 that the pore water pressure ratio for the saturated sand with a relatively density of 50 % is as high as 1 and thus the sand liquefied under the applied ground acceleration. One of the conventional ways to prevent liquefaction from happening is to increase the relative density of sand. This requires energy-intensive soil improvement methods such as dynamic compaction to be used. However, if the degree of saturation of the sand is lowered down to 95 %, the pore pressure ratio would reduce to 0.4 for sand with the same density (Fig. 23.5). The cost and energy required to lower the degree of saturation from 100 to 95 % is much less. If we lower the degree of saturation to 90 %, the pore water pressure ratio can be controlled to be even less than 0.2. Therefore, the biogas method can be very effective for liquefaction mitigation. It is also less expensive compared with any conventional methods.

23.4 Use of Bioclogging for Erosion Control or Cutoff of Seepage

Bacteria can also be used to reduce the permeability of sand through the so called bioclogging approach. One of the methods that has been developed by our research group is to use urease producing bacteria to precipitate a layer of calcium carbonate on top of sand, as shown in Fig. 23.6. This hard layer of crust has a permeability of less than 10^{-7} m/s and thus can be used as an impervious layer for building a water pond in the desert or on the beach for emergency water storage or for erosion control for beach or riverbank. A detailed description of this bioclogging method is given in Chu et al. (2012).

Fig. 23.6 Formation of an impervious layer on top of sand



23.5 Use of Quick Setting Materials

Construction speed is one of the important considerations in disaster mitigation and rehabilitation projects. For this reason, construction materials that allow construction to be carried out quickly should be adopted. Unfortunately, when the conventional construction material cement is used, it requires 28 days to gain full strength. Sometimes, an immediate repair such as for a runway or highway is required. Then we will need to use other quick setting materials. One such a material is plastic waste. Every year, millions of tons of plastic waste are generated. Plastic can be melted under a temperature ranging from 70 to 170 °C and mixed with soil, either sand or clay, to form strong construction materials such as bricks and blocks or porous drain materials as shown in Fig. 23.7. The major advantage of using plastic is that the plastic treated soil can gain strength almost immediately. When 10 % (by weight) plastic is used, the uniaxial strength obtained can be in the range of 19–42 MPa depending on the types of soil. This strength is sufficient for most of the geotechnical problems. Thus, the use of plastic provides a good alternative to conventional construction materials for quick repair of runways or roads.

23.6 Use of Quick Construction Technologies

Assuming we have to construct a sea dike or river dike on soft seabed or riverbed quickly for a disaster mitigation project without the use of heavy machines, then the geotextile mattress method discussed before may not be applicable because it may not be quick enough. If the seabed or riverbed is soft, we will have to treat the ground before the construction of the dike. The convention soil replacement method (such as sand key) or fill surcharge or vacuum preloading method using vertical drains are slow too. We can also install deep cement mixing columns, stone columns. However, special equipment that can operate above water is required. After the foundation soil is improved, we also need a way to place the earth to form a dike. Then rip rap or other shore protection methods may need to be applied too.



Fig. 23.7 Use of plastic to make instant strong construction materials on site

An alternative method to speed up the construction using rocks as shell and sandy/clayey soil as core materials can be proposed as follows. Rock columns can be installed by replacement method using simply a cone type of hammer dropping from a barge. The cradles created by the hammer are filled with rocks and is further compacted to form columns as shown in Fig. 23.8a. Two examples are given in Chu et al. (2009). After this, rock filled gabion boxes can be used to form the outer boundary of the first layer of the dike as shown in Fig. 23.8a. Then earth can be filled in between as shown in Fig. 23.8b. If clayey soil is used, drains should be placed along the gabion and soil interface as shown in Fig. 23.8a and b. Once the first layer of dike is constructed, the process can be repeated to construct the second and third layer until the design height is achieved.

23.7 Conclusions

More cost-effective methods are required to cope with the increasing demand for more extensive disaster prevention and mitigation measures. This can only be achieved by developing more innovative solutions. The areas in which innovation may play a major role are the use of new construction materials and the use of innovative approaches. A few examples have been given in this paper. The methods that use new or innovative materials include the use of geotextile mats for dike construction and the use of quick setting materials such as plastic. The new approaches introduced include the use of biogas to reduce the liquefaction potential of sand and the use of bioclogging technology to reduce riverbank or coastal erosion or make temporary water ponds on a beach or in dessert. A quick construction method for dike construction is also introduced. Some of the examples were introduced with the intention to stimulate more new ideas and interests in the development of innovative approaches for disaster mitigations. It is only a matter of time for some of the ideas to be fully developed into practical solutions.

Acknowledgements The contributions of V. Ivanov, V. Stabnikov, H. Jia, W. Guo, and N.H. Cao to the research projects presented are greatly acknowledged.

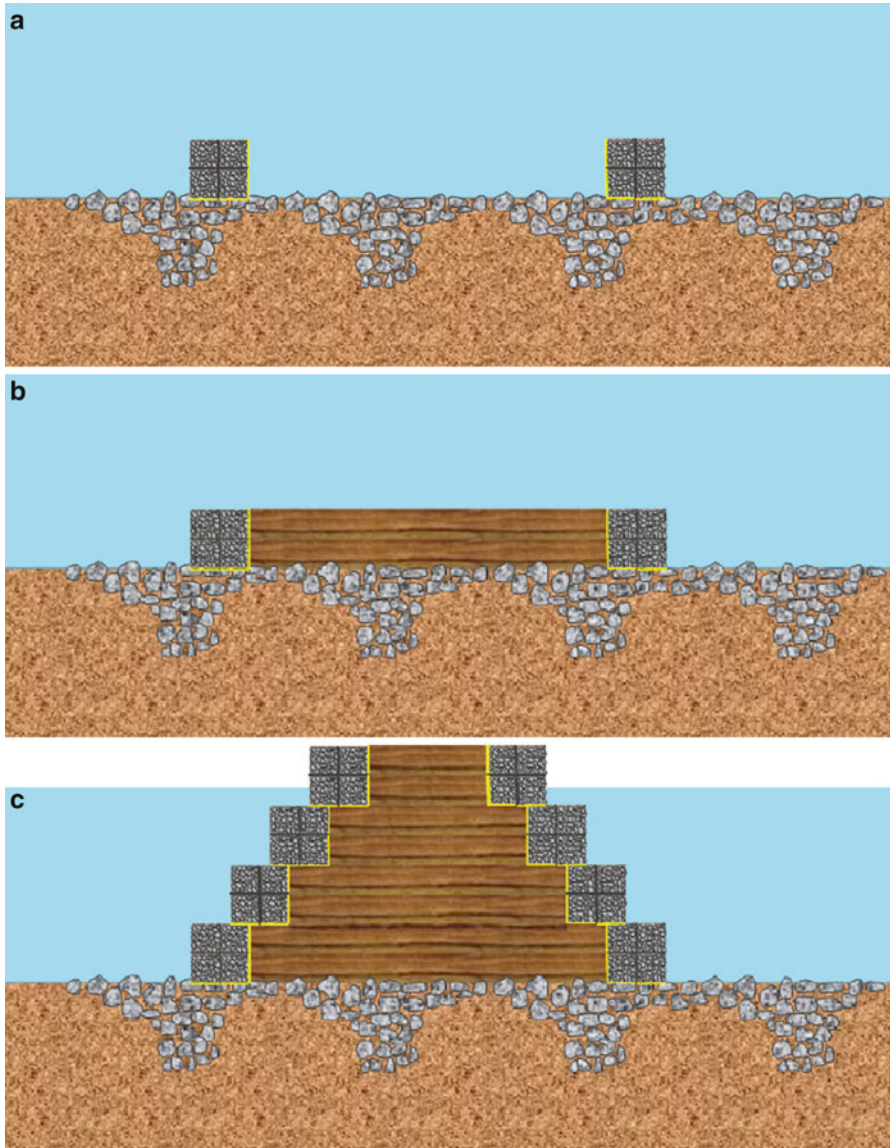


Fig. 23.8 Schematic illustration of proposed quick dike construction method. (a) Installation of rock columns by replacement method and rock filled gabion boxes. (b) Placement of soil in between the gabions for the first layer. (c) Repeat the process in (a) and (b) until the required height is achieved

References

- Chu J, Varaksin S, Klotz U, Menge P (2009) Construction processes, State-of-the-art report. In: Proceedings of 17th international conference on soil mechanics and geotechnical engineering, Alexandria, 5–9 Oct, vol 4, pp 3006–3135
- Chu J, Stabnikov V, Ivanov V (2012) Microbially induced calcium carbonate precipitation on surface or in the bulk of soil. *Geomicrobiol J* 29:544–549
- Guo W, Chu J, Yan SW (2009) Classification of geotubes and related analysis methods. In: Leung CF, Chu J, Shen RF (eds) *Ground improvement technologies and case histories*. Research Publishing, Singapore, pp 263–274
- He J (2012) Mitigation of liquefaction of sand using microbial methods. Ph.D. thesis, Nanyang Technological University, Singapore
- Lee EC (2009) Application of geotextile tubes as submerged dykes for long term shoreline management in Malaysia. In: Proceedings of 17th South East Asian geotechnical conference, Taipei, 10–13 May
- Okamura M, Ishihara M, Tamura K (2006) Degree of saturation and liquefaction resistances of sand improved with sand compaction pile. *J Geotech Geoenviron Eng ASCE* 132(2):258–264
- Saathoff F, Oumeraci H, Restall S (2007) Australian and German experiences on the use of geotextile containers. *Geotext Geomembr* 25(4–5):251–263
- Yan SW, Chu J (2010) Construction of an offshore dike using slurry filled geotextile mats. *Geotext Geomembr* 28:422–432
- Yan SW, Chu J, Fan QJ, Yan Y (2009) Construction of offshore breakwater on soft clay using prefabricated caissons. In: Proceeding of ICE geotechnical engineering, London, 2009, vol 162, GE1, pp 3–12
- Yegian MK, Eseller-Bayat E, Alshwabkeh A, Ali S (2007) Induced-partial saturation for liquefaction mitigation: experimental investigation. *J Geotech Geoenviron Eng ASCE* 133(4):372–380

Index

A

ABAQUS software, 312, 318
Abuel-Naga, H.M., 297, 298, 306, 307, 310
Aceh Earthquake, 34, 37
Aceh Province, 33
Active earth pressure
 coefficients, 248, 249
 postfailure stress system, 249
 statically admissible stress system, 248
Aftershocks, 48
Akai, N., 166, 167, 169
Akino, N., 157
AlaTau slope, 282, 283
Aldiamar, F., 33
Alluvial deposits, 282
Almaty
 alluvial soil, 281
 foundation pit wall, 292–294
 geological condition
 alluvial deposits, 282
 avalanches, 283
 clay soil, 282
 coarse crushed stones, 283
 exogenous processes, 282
 fluvioglacial deposits, 282
 geological profile, 282, 283
 proluvial deposits, 282
 slopes soil, 283
 laboratory test, soil
 petrographic analysis, 286
 shear deformation, 289
 static and dynamic load, 287, 289
 stress–strain conditions, 287
 landslide formation, 282
 shear test equipment, 284–286
 slope stability analysis, 290–291

 soil subsidence, 281
 tectonic breaches, 281
Anchor excavation, 272–273
Artidteang, S., 297
Asaoka, A., 105, 302, 303, 316
Asrurifak, M., 33
Avalanches, 61, 283

B

Balderhead Dam, 143–144
Baranov dynamometer, 284
Barradas, J., 253
Benioff Zone, 40
Bergado, D.T., 297, 310
Bioclogging approach, 380–381
Biogas. *See* Soil liquefaction and biogas
Biot, M.A., 150
Bishop, A.W., 217
Bjerrum, L., 80, 82
Breakwaters
 Kamaishi Harbor, 4–5
 Kamaishi Port Gate, 23–25
 Onagawa Bay, 5, 6

C

Cam-clay model, 181, 229, 238
Cauchy stress, 183
Centrifuge model test, 325–326, 330
Chai, J.C., 310, 317
Chen, F., 61
Chen, Z.P., 183, 216, 223, 227
Christian, J.T., 164, 166, 167, 169
Chu, J., 375–378, 380, 382
Clay soil, 282, 286, 289

- Clough, G., 150, 160–162, 362
 Collins, L.F., 244
 Colossal earthquakes, 47
 Consolidometer test program, 302–303,
 305–306
 Convention soil replacement method, 381
 Coppersmith, K.J., 40
 Creep-inclusive preconsolidation
 pressure, 82
- D**
- Damaged sea walls, Ofunato city, 27, 28
 Dasenbrock, D.D., 354
 Davis, E.H., 244
 Deep-mixing method (DMM)
 application, 345
 compensation cost, 348, 349, 351
 embankment and improvement ground, 346
 FEM, 345, 346
 robust probability, 347
 soil improvement cost, 348, 349
 Deformation analysis considering stress
 anisotropy and reorientation
 (DAC SAR), 178
 FEM program, 345
 finite volume method (FVM), 166
 Galerkin method, 165
 governing equations and boundary
 conditions, 164, 165
 hydraulic gradients, 166, 167
 orthogonal meshes, 166, 167
 spatial discretization formula, 166, 167
 total water head, 165, 166
 Deng, J.H., 61
 Detoumay, E., 244
 Dewatering process
 pore water pressure distribution, 327, 334
 strain distribution, 332
 Dike, 377, 378, 388
 Disaster mitigation technologies
 bioclogging approach, 380–381
 geosynthetic mats
 dike, 377, 378
 geotextile bags, 376, 377
 geotextile tubes, 376, 377
 quick setting materials, 381–383
 soil liquefaction and biogas
 categories, 378
 dynamic compaction, 380
 microorganisms, 379
 pore water pressure, 379, 380
 saturated and unsaturated sand, 379
- 3D linear finite element analysis, 271
 Donahue, M.J., 22
 Double suction method, 362
 Drescher, A., 244
 Drucker, D.C., 105
 Duncan, J.M., 138, 146
- E**
- Earthquake-induced landslide early warning
 system (ELEWS), 56
 Elastic viscoplastic (EVP) models
 creep settlement, 81
 geotechnical structure, 78
 Leneghans embankment, 80
 parameters, 80
 quasi-preconsolidation, 82
 soil model, 80
 Elasto-plastic constitutive model, 105–107
 original Cam clay mode, 229, 238
 S_e hardening model
 application, 218–220
 nonlinear contractancy description and
 subloading surface, 220–225
 soil-water retention characteristic curve,
 226–227
 yield function, 217–218
 stress-strain relationship (*See* Sekiguchi-
 Ohta's model)
- Embankments, soft clays
 axisymmetric unitcell analyses
 pwp response, 87–88
 settlement responses, 86–87
 creep-nonlinear analyses
 excess pwp response, 91–92
 geotextile strain, 92
 lateral displacement profiles, 90–91
 settlement profiles, 89–90
 EVP models (*see* Elastic viscoplastic
 (EVP) models)
 full embankment analysis
 permeability estimation, 88
 plane strain modeling, 88
 Leneghans embankment, 78–79
 MCC material parameters
 embankment fill, 83–84
 foundation clay, 3, 83
 geogrid reinforcement, 3, 84
 permeability, 84–86
 mechanical behavior and seepage, 77
 pore water pressure, 78
 prefabricated vertical drains, 78
 secondary compression, 77, 80–82

e Pinto, P.S.S., 253
 EVP models. *See* Elastic viscoplastic (EVP) models
 Exponential contractancy (EC) model, 220–223

F

Finite element method (FEM)
 deep-mixing method, 345, 346
 1-D FEM
 consolidation yield stress and vertical effective stress, 121
 groundwater compression, 116, 120
 groundwater pressure, 119–121
 mesh, 118, 119
 soil–water coupling analysis, 117
 2-D ground deformation
 countermeasures, 128, 129
 ground surface settlement, 126, 127
 lateral displacement, 126, 127
 soil parameters, 124, 125
 2011 Great East Japan Earthquake, 21, 22
 seawall, 21, 22
 soil-water coupled FEM analysis (*see* Soil-water coupled finite element method (FEM) analysis)
 Firmanti, A., 33
 Fluvioglacial deposits, 282
 Frankel, A., 40
 Fujiyama, T., 131, 163
 Full-scale field test embankment
 Taiyogaoka, Kanazawa in 1996, 100–104
 collapse, overhanging cliff, 103, 105
 cutters, 102
 embankment material, 100, 101
 experiment, 102, 103
 FEM simulation, 110–113
 field test, 96, 97
 material properties, 100, 102
 overhanging cliff, 102, 104
 soil bridge, 102, 104
 soil structure, 100, 101
 tensile test, 100, 102
 Yuhidera, Kanazawa in 1994
 collapse of embankment, 100, 101
 embankment, 96
 FEM simulation, 109–112
 field tests, 96, 97
 material properties, 96, 98
 Omma sand, 96, 98
 overhanging cliff, 96, 99
 uni-extension test, 96, 98

G

Galerkin method, 165
 Geosynthetic mats
 dike, 377, 378
 geotextile bags, 376, 377
 geotextile tubes, 376, 377
 Geosynthetics-reinforcement, soil structures
 complex dynamic interactions, 96
 dilatancy, compacted soil
 constitutive properties, 106–110
 elasto-plastic constitutive model, 105–107
 elasto-plastic constitutive models, 96
 full-scale field model tests (*see* Full-scale field test embankment)
 Gnanendran, C.T., 77, 81
 Grasp real 3D action of subsoils and pore water (GRASP3D), 150
 2011 Great East Japan Earthquake
 estimated slippage contours, 23, 24
 field survey, 26–28
 huge-scale event, 23
 moment of tsunami, 25
 safety and relief, 28–30
 tsunami hazard mitigation
 FEM analysis, 21, 22
 ground motion attacks structure, 20
 hazard maps, 20
 Kamaishi Port Gate breakwaters, 23–25
 proposed system, 22, 23
 seismic performance evaluation, 20–22
 tsunami inundation areas, 26
 Ground deformation
 2-D finite element method
 countermeasures, 128, 129
 ground surface settlement, 126, 127
 lateral displacement, 126, 127
 soil parameters, 124, 125
 ground settlement, 159
 Ground displacement, 123, 324, 330
 Ground upheaval phenomenon
 centrifuge model test, 325–326, 330
 consolidation time relation, 326
 data acquisition and mapping, 323–324
 distribution, Tokyo, 323
 ground displacement, 330, 331
 groundwater level, 326
 one dimensional consolidation theory, 328–330
 pore water pressure distribution, 327, 330
 strain distribution, 331, 332
 study activities, 322
 two dimensional FE analysis

- Ground upheaval phenomenon (*cont.*)
 analysis model and boundary condition,
 332, 333
 analysis schedule, 332, 334
 bending moment, tunnel, 332, 335
 parameters, 332, 333
 vertical distribution, pore pressure,
 332, 334
- Ground water, 324–326
 heavy deep well pumping (*see* Tokyo Bay,
 heavy deep well pumping)
 mini-greenhouse, 16
 room temperature control, 15
- Grundy, P., 36
- Gucheng Hydropower project, 68, 71
- Guo, W., 376
- Gutenberg-Richter (GR), 41
- Gutierrez, M., 191
- H**
- Hankour, R., 354
- Hansbo, S., 303, 310, 314
- Hashiguchi, K., 181–185, 191, 216, 223, 227
- Hata, S., 221
- Hendriyawan, B.B., 33
- Henkel, D.J., 354, 362
- Hilman, D., 33
- Hirata, M., 95
- Hird, C.C., 88, 91
- Hybrid-type penalty method (HPM)
 actual site, 175–178
 center of gravity, 173
 constant matrices, 173
 DACSAR (*see* Deformation analysis
 considering stress anisotropy and
 reorientation (DACSAR))
 hybrid residual equation, 172
 hybrid variation principle, 171–172
 hydraulic gradients, 167–169, 173
 Lagrange's undetermined multiplier,
 171–172
 one-dimensional consolidation, 170–171,
 174–175
 pore water pressure, 164
 spatial discretization formula, 174
 water head, 164
- I**
- Iai, S., 1
- Ichii, K., 19, 22
- Iizuka, A., 1, 95, 109, 117, 149, 215, 229,
 332, 353
- Imai, T., 157
- Indo-Australian plate, 47
- Indonesia Earthquake
 Aceh Province, 33
 buildings and facilities damages, Aceh
 Earthquake, 34, 37
 buildings failures and ground cracking,
 West Sumatera Earthquake, 34, 37
 catastrophic damage, 34
 earthquake engineering, 34
 estimated total losses, 34, 36
 great earthquakes, 34, 36
 ground cracking and landslide, Padang
 Earthquake, 34, 38
 Pacific Ring of Fire, 33, 34
 Seismic Hazard Map (*see* Seismic Hazard
 Map of Indonesia)
 tectonic plates, 33
 tectonic settings, 33, 35
- Indraratna, B., 85, 310, 317
- International Building Code, 38
- Ion-exchanged water (IEW), 359, 360
- Irsyam, M., 33
- Ishiguro, T., 131
- Ito, T., 321
- J**
- Japan Meteorological Agency (JMA), 4
- K**
- Kamaishi Harbor breakwater, 4–5
- Kamaishi Port Gate breakwaters, 23–25
- Kamihikawa Dam
 center-core rockfill dam, 134
 cross-section, 134
 earth pressure cells, 137
 elasto-plastic effective stress analysis, 133
 elasto-visco-plastic model, 134
 grain size correction, 135, 136
 mesh diagram, 134
 pore water pressure, 135, 136
 rock material, 135
 soil–water coupled effective stress
 analysis, 134
- Kanazawa, S.-i., 215
- Karim, M.R., 77, 80–83, 91
- Kato, S., 218
- Kawai, K., 215, 220
- Kennard, M.F., 138, 141
- Kertapati, E., 33
- Khomyakov, V.A., 281, 286
- Kikuchi, Y., 11
- Kjellmann, W., 297
- Kobayashi, A., 115

Kobayashi, I., 353
 Koizumi, A., 321
 Kusaka, T., 321
 Kutter, B.L., 81, 82
 Kuwano, J., 6, 181

L

Laboratory vane shear apparatus, 301
 Lai, Y.P., 297
 Landslide at Cikangkareng, 53, 55
 Large-scale consolidometer, 298–299
 Leneghans embankment, 78–79
 Liquefaction, 52, 55, 375. *See also* Soil
 liquefaction and biogas
 Lizuka, A., 163
 Longmenshan fault belt, 62–63
 Lo, S.R., 77, 78, 83, 85, 86
 Lukpanov, R.E., 281

M

Matsumoto, K., 115
 Maximum credible earthquake (MCE), 38
 Meilano, I., 33
 Mentawai Fault, 48
 Mercalli scale., 48
 Metastability, 237–238
 Microzonation maps, 41, 45
 Mikasa, M., 328, 335
 Mini-greenhouse, 15, 16
 Miura, K., 189, 192
 Modified Cam clay (MCC) model
 material parameters
 embankment fill, 83–84
 foundation clay, 3, 83
 geogrid reinforcement, 3, 84
 permeability, 84–86
 Mohamedelhassan, E., 310
 Mohr-Coulomb model, 83, 84
 Morioka, S., 3
 Muntohar, A.S., 47
 Murdoch, L.C., 138

N

Nadai, A.L., 200, 203, 212
 Nagae, T., 337
 Nakai, T.M., 7
 Nakayama, E., 353
 Natawidjaja, D., 38
 Natawijaya, D.H., 38
 Natural disasters, Indonesia

active volcanic mountain chain, 47
 colossal earthquakes, 47
 disaster management, 56
 ELEWS, 56
 geomorphologic features, 48
 Indo-Australian plate, 47
 landslides and high rainfalls, 48
 Padang Earthquake (*see* Padang
 Earthquake)
 recorded earthquake, 48, 49
 Situ Gintung dam (*see* Situ Gintung dam)
 weathered soils, 47
 West Java Earthquake (*see* West Java
 Earthquake)
 Next generation attenuations (NGA), 40, 41
 Nishida, H., 337
 Nishida, Y., 3
 Nishihara, A., 241
 Nobari, E.S., 146
 North Sumatra Province, 33

O

Ohkawa, H., 187, 194, 196
 Ohmori, K., 95
 Ohno, S., 183, 215–218, 221, 222, 227
 Ohta, H., 3, 15, 95, 96, 105, 107, 109, 112, 115,
 117, 131, 134, 149, 150, 155, 163,
 183, 199, 215, 221, 229, 241, 332,
 345, 353, 354
 Old Rossio railway station building
 corrosion protection tests
 grouts properties, 268
 internal and external protections, 267
 investigation test, 270–272
 steel tendon protection, 269, 272–273
 suitability test, 267
 visual inspections, 269–270
 Eurocodes 7 and 8, 255
 geological characteristics, 256
 geological profile, 255
 geotechnical characteristics, 256
 monitoring and environmental impacts
 horizontal displacements, inclinometer
 tube, 277
 logger, 278–279
 Portuguese Actions Code, 255
 principal facade, 274, 275
 reinforced concrete frames, 255
 retaining walls
 Bairro Alto, 263–264, 266–269
 experimental tests, 262–265
 numerical analyses, 258–261

Old Rossio railway station building (*cont.*)
 seismic analysis (*see* Seismic analysis)
 static conditions, 256–258
 SAP 90 code, 271
 tied back wall, 254
 underground gallery, 254
 Omma sand, 96, 98, 110
 One dimensional consolidation theory,
 328–330
 O'Rourke, T.D., 150, 160–162
 Osaka Bay clay
 anisotropic consolidation, 370
 constant volume undrained tests, 369
 effective stress paths, 371
 Ko-rebound and Ko-reloading, 370, 371
 properties, 369
 stress–strain relations, 371
 Osaka Prefecture, 21

P

Padang Earthquake, 34, 38
 aftershocks, 48
 debris and mud flows, 51, 52
 fault ruptures, 48, 50
 liquefaction and lateral spreading, 52, 53
 Mentawai Fault, 48
 Mercalli scale., 48
 Padang Pariaman village, 50, 52
 seismic intensity distribution, 48, 51
 shaking ground, 50
 Sumatera strike-slip fault, 48, 49
 Partial derivative equation (PDE), 207
 Passive earth pressure
 coefficient, 248
 Coulomb's earth pressure, 246
 limit equilibrium method, 246, 247
 slip line method, 247
 stress boundary block, 245
 velocity boundary block, 245
 Pipatpongsa, T., 199, 200, 210, 229
 Polarized principal axes (PPA), 200
 Pothiraksanon, C., 305
 Prefabricated vertical drains (PVDs)
 ABAQUS software, 312
 back-calculated compressibility
 parameters, 303–304, 310–312, 316
 consolidometer test program, 302–303,
 305–306
 2D drain analysis, 312
 heat source, 300–301
 heat transfer, 306–307
 laboratory vane shear apparatus, 301

large-scale consolidometer, 298–299
 physical properties and testing procedures,
 301–302
 PVDCON, 304
 smear zone effects, 313
 two-dimensional axisymmetric mesh,
 313, 314
 vacuum and thermal effects
 excess pore pressure, 309–310
 shear strength, 307–309
 water contents, 307
 vacuum generator, 299–300
 Probability of exceeding (PNCR), 261
 Proluvial deposits, 282
 Protective seawall embankment, Hiro, 7, 9
 Pubugou hydropower project, 68–70

Q

Quick dike construction method, 383

R

Rad, N.S., 362
 Reliability design. *See* Robust control approach
 Retaining walls
 Bairro Alto, 263–264, 266–269
 experimental tests, 262–265
 ground and earth-retaining diaphragm
 walls, 155–160
 numerical analyses, 258–261
 seismic analysis (*see* Seismic analysis)
 static conditions, 256–258
 Wenchuan Earthquake, 64, 65
 Reverse concreting excavation methods
 elasto-viscoplastic constitutive model, 150
 excavation process, 154
 excavation work, 152–153
 finite element mesh, 153–154
 finite element mesh and geometric
 boundary condition, 153–154
 geometric boundary condition, 153–154
 GRASP3D, 150
 ground-and earth-retaining diaphragm
 walls, 155–160
 ground conditions, 150–152
 groundwater measurement, 155
 load movement, 160, 161
 maximum ground surface settlements,
 160, 161
 Rice, J.R., 181
 Ridwan, M., 33
 Rikuzentakata City Office, 26–27, 31

- Robust control approach
 decision-making framework
 expected total cost, 343–344
 one state variable, 341–343
 relationship table, 344
 robust probability distribution, 343
 soil structure, 343
 deep-mixing method
 application, 345
 compensation cost, 348, 349
 embankment and improvement
 ground, 346
 FEM, 345, 346
 robust probability, 347
 soil improvement cost, 348, 349
 probability distribution gap, 339–340
 risk sensitivity, 340–341
 sensitivity analysis, 348–351
- Rockfill dams
 Balderhead Dam, 143–144
 core material, 138
 core zone, 140–141, 145–146
 current evaluation method, 132–133
 dam stability, 141–142
 earth pressure and pore water measurement
 data, 138
 field-compacted materials., 139
 minor effective stress contour, 140
 minor principal stress and pore water
 pressure, 139
 pore water pressure and flow rate, 139
 reservoir filling (*see* Kamihikawa Dam)
 soil and pore water pressure, 137
 stress–deformation behavior, 131, 132
- Roscoe, K.H., 237, 238
 Rudnicki, J.W., 181
- S**
- Safety factor (SF), 211–212
 Saito, T., 321
 Sand heap
 partial derivative equation, 207
 rectangular coordinate system, 204–205
 safety factor, 211–212
 self-similar solution, 208–211
 stress conditions
 angular coordination, 203–204
 direction of gravity, 202–203
 Mohr's circle, 201–202, 206
 octahedral stresses, 203
 stress orientations, 203
- Sandhu, R., 176–178
 Saowapakpiboon, J., 297, 305
 Sathialingam, N., 81, 82
- Sato, T., 337
 Savage, S.B., 210
 Seed, B., 138
 S_e hardening model
 application, 218–220
 nonlinear contractancy description and
 subloading surface
 exponential contractancy model,
 220–223
 stress–strain relationship, 224–225
 triaxial shear tests, 225–227
 yield function, 217–218
- Seismic activity areas. *See* Almaty
 Seismic analysis
 earthquake, 261
 Eurocode 8, 261
 horizontal seismic coefficient, 262
 local soil failure, 261
 overall soil stability, 261
 Portuguese territory, 259
 pseudostatic analysis, 261
 seismic source model, 40
- Seismic Code, 41
 Seismic Hazard Map of Indonesia
 Benioff Zone, 40
 fault characteristics, 38
 fault source model, 38
 Gutenberg–Richter (GR), 41
 International Building Code, 38
 MCE, 38
 microzonation maps, 41, 45
 PGA maps, 41–44
 Seismic Code, 41
 seismic hazard parameters, 38, 39
 seismic source model, 40
 SSZ and SFZ, 38
 subduction mechanism, 40
 two-dimensional (2-D) model, 38
 United States Geological Survey, 37
- Sekiguchi, H., 105, 112, 117, 134, 150, 155,
 183, 345
 Sekiguchi-Ohta's model, 322
 axisymmetric stress plane, 235
 deviatoric stress plane, 235
 K₀-consolidation, 232
 Koiter's associated flow rule, 233
 metastability, 237–238
 simulated stress path, 231–232
 yield surface of, 230–231
- Self-weight transmission. *See* Sand heap
 Semi-underground Reinforced earth walled
 AI-weather yard (SUREWAY),
 12, 13
- Shang, J.Q., 310
 Shear test equipment, 284–286

- Shibata, T., 221, 230, 333
- Shimamoto, S., 241
- Sieh, K., 38
- Situ Gintung dam
 - catchment area, 58, 59
 - conservation area, 58–59
 - disaster, 57–58
 - early warning system (EWS), 59
 - spatial planning law, 58
- Smart Triaxial* apparatus
 - control and measuring units, 358, 359
 - degasser, 359, 360
 - monitoring sensors, 358, 359
- Osaka Bay clay
 - anisotropic consolidation, 370
 - constant volume undrained tests, 369
 - effective stress paths, 371
 - Ko-rebound and Ko-reloading, 370, 371
 - properties, 369
 - stress–strain relations, 371
- pedestal displacement, 359
- pressure pump, 357, 358
- programmable logic controller, 358
- specifications, 355
- testing procedures
 - anisotropic consolidation, 364
 - back pressure set up process, 363
 - B-value measurement process, 363, 364
 - cell pressure, 361
 - compression and extension tests, 365, 366
 - double suction method, 362
 - flushing and saturation process, 362, 363
 - isotropic consolidation, 364, 365
 - Ko-consolidation process, 365, 366
 - pore water pressure measurement, 361
 - preliminary consolidation process, 361–362
 - random wave displacement control, 368
 - sawtooth wave displacement control, 368
 - sine wave displacement control, 367
 - specimen set up process, 360, 361
 - stress relaxation test, 366, 367
- test program, 355
- triaxial chamber, 356–357
- Soil liquefaction and biogas
 - categories, 378
 - dynamic compaction, 380
 - microorganisms, 379
 - pore water pressure, 379, 380
 - saturated and unsaturated sand, 379
- Soil-water coupled finite element method (FEM) analysis
- HPM
 - actual site, 175–178
 - center of gravity, 173
 - constant matrices, 173
 - DACSAR (*see* Deformation analysis considering stress anisotropy and reorientation (DACSAR))
 - hybrid residual equation, 172
 - hybrid variation principle, 171–172
 - hydraulic gradients, 167–169, 173
 - Lagrange’s undetermined multiplier, 171–172
 - one-dimensional consolidation, 170–171, 174–175
 - pore water pressure, 164
 - spatial discretization formula, 174
 - water head, 164
- reverse concreting excavation methods
 - elasto-viscoplastic constitutive model, 150
 - excavation process, 154
 - excavation work, 152–153
 - finite element mesh, 153–154
 - geometric boundary condition, 153–154
 - GRASP3D, 150
 - ground-and earth-retaining diaphragm walls, 155–160
 - ground conditions, 150–152
 - groundwater measurement, 155
 - load movement, 160, 161
 - maximum ground surface settlements, 160, 161
 - soil parameters, 155, 156
- Soil-water retention characteristic curve (WRC) model, 220
- Sokolovski, V.V., 241
- Sousa, A., 253
- Sowa, V.A., 354, 362
- Sreng, S., 321
- Stress relaxation test, 366, 367
- Sugano, T., 134
- Sugie, S., 149
- Suhardjono, 33
- Sumatera strike-slip fault, 48, 49
- Sumatran Fault Zone (SFZ), 38
- Sumatran Subduction Zone (SSZ), 38
- T**
- Tachibana, S., 181, 215
- Tai, J.J., 61
- Takada, N., 328
- Takeuchi, N., 164, 172, 178

- Takeyama, T., 163, 216, 229
- Talagabodas volcano, 56
- Tamura, T., 166, 167, 169
- Tanaka, H., 321
- Tatsuoka, F., 13, 157, 362
- Taya, M., 353
- Taylor, D.W., 84
- Tectonic breaches, 281
- Thermo-prefabricated vertical drains. *See*
Prefabricated vertical drains (PVDs)
- Three-dimensional soil–water coupled FEM
analysis. *See* Reverse concreting
excavation methods
- 2011 Tohoku-Pacific Ocean Earthquake
ground water in temperature, 14–17
inland highway, semi-underground
facilities, 10, 12–14
near-shore zones, Sanriku area, 3
seawall highway, residential functions,
8, 10, 11
tsunami disaster (*see* Tsunami disaster)
- Tokyo. *See* Ground upheaval phenomenon
- Tokyo Bay, heavy deep well pumping
Arakawa River, 116
DACSAR, 117
expanded poly-styrol (EPS), 117
field observations
 construction and planned ground
 monitoring, 121–123
 ground displacement, 123, 124
finite element method (*see* Finite element
method (FEM))
geohazard, 115
groundwater, 115–116, 118
pile deformation, 116
public aquarium, 116
reclamation record, 118
soil profile, 116–118
- Tokyo Sea Life Park, 116
- Tonouchi, K., 157
- Toyoura sand
 Cam-clay model, 181
 Cauchy stress, 183
 contract-dilate volume change, 192–195
 deviatoric-tangential stress rate, 184, 185
 elastic and inelastic stretching, 182
 elastic bulk and shear moduli, 183
 elastic response, 190–193
 elasto-plastic constitutive modeling, 182
 hypoeastic rate constitutive equation, 183
 noncoaxiality, 195–197
 p constant and b constant shear conditions,
 186–188
 plastic multiplier, 184
 plastic stretching, 184
 Poisson ratio, 183
 second-order tensor, 183
 stress ratio tensor, 183
 subloading surface, 183, 188–190
- Triaxial shear tests, 225–227
- Triaxial test equipment, 286
- Triyoso, W., 33
- Tsunami damage. *See* 2011 Great East Japan
Earthquake
- Tsunami disaster
 areas heavily protected by seawalls, 6, 9
 breakwaters, mouth of Onagawa Bay, 5, 6
 Japanese coastline, 6–7
 JMA, 4
 Kamaishi Harbor breakwater, 4–5
 modern design methodology, 4
 no protective seawall, 6, 8
 Onagawa harbor, 5, 7
 protective seawall embankment, Hiro, 7, 9
- Tsunami hazard mitigation
 2011 Great East Japan Earthquake
 FEM analysis, 21, 22
 ground motion attacks structure, 20
 hazard maps, 20
 Kamaishi Port Gate breakwaters, 23–25
 proposed system, 22, 23
 seismic performance evaluation, 20–22
- Tsutsumi, S., 181, 182, 184, 185, 191
- Two dimensional FE analysis
 analysis model and boundary condition,
 332, 333
 analysis schedule, 332, 334
 bending moment, tunnel, 332, 335
 parameters, 332, 333
 vertical distribution, pore pressure,
 332, 334
- U**
- Uchita, Y., 131
- ULEM. *See* Upper and lower equilibrium
methods (ULEM)
- United States Geological Survey, 37
- Unsaturated soils. *See* Elasto-plastic
constitutive model
- Upper and lower equilibrium methods (ULEM)
 active earth pressure (*see* Active earth
 pressure)
 equilibrium stress system, 244
 passive earth pressure (*see* Passive earth
 pressure)

- Upper and lower equilibrium methods (ULEM)
 (*cont.*)
 plastic limit theorems, perfect plasticity,
 242–243
 post-failure stress system, 244
 statically admissible stress system, 244, 245
 stress and velocity boundary block, 244, 245
 stress circles, 245, 246
- V**
 Vacuum consolidation method, 297
 Vacuum prefabricated vertical drains. *See*
 Prefabricated vertical drains (PVDs)
- W**
 Wangjiayan landslide, 66, 67
 Wardani, S.P.R., 47
 Water level rising process, 327
 Wayan Sengara, I., 33
 Wei, J.B., 61
 Wells, D.L., 40
 Wenchuan Earthquake
 Gucheng and Pubugou hydropower
 projects, 61
 intensity and geographical names, 61, 62
 Longmenshan fault belt, 62–63
 Longmenshan mountain area, 61
 protecting structures
 gravity-retaining walls, 64, 65
 protecting nets, 64, 65
 shotcrete, 64, 66
 retaining structures
 anchored concrete frames, 66
 cable bolts, 67–70, 72
 slide-resistant piles, 66–68
 Zipingpu reservoir, 61
- West Java Earthquake
 earthquake intensity distribution, 53
 joint, 55
 landslide at Cikangkareng, 53, 55
 landslide materials, 55
 liquefaction, 55
 mud flow, 56
 sand boiling, 55, 56
 seismotectonic map, 53
 Talagabodas volcano, 56
 Tasikmalaya District, 53
 2007 West Sumatera Earthquake, 34, 37
 Widiyantoro, S., 33
 Wilson, E.L., 176–178
- Y**
 Yamakami, T., 95
 Yanagisawa, E., 134
 Yan, S.W., 376, 377
 Yatomi, C., 181
 Yenkebayev, S.B., 281
 Yin, J.H., 80
 Yokota, Y., 95
- Z**
 Zhussupbekov, Z.A., 281
 Zipingpu dam site, 67, 69
 Zipingpu reservoir, 61